E. Edmund Kim
Vanessa Murad
Jin-Chul Paeng
Gi-Jeong Cheon
Editors

Atlas and Anatomy of PET/MRI, PET/CT and SPECT/CT

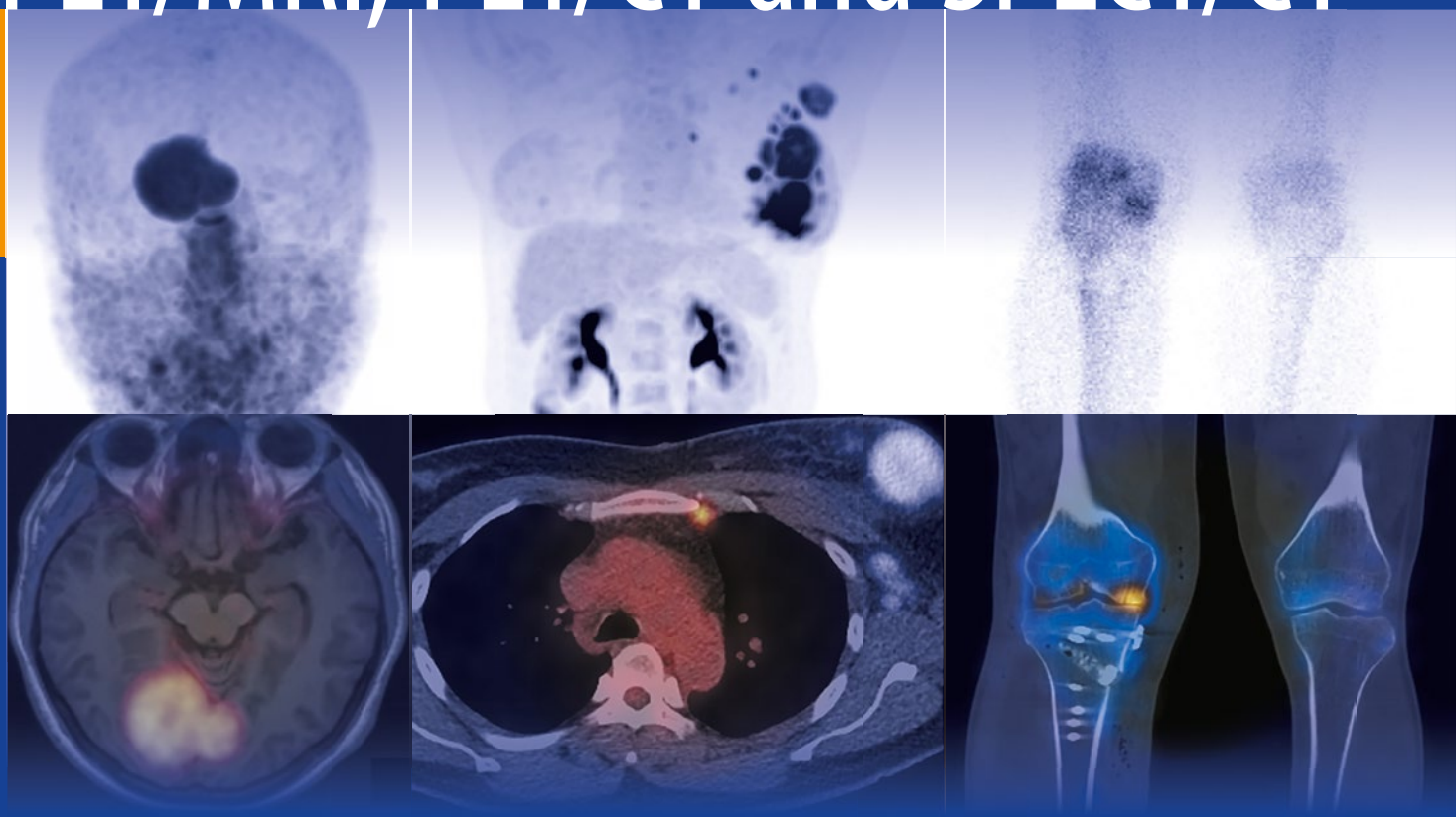

Second Edition

Springer

Atlas and Anatomy of PET/MRI, PET/CT and SPECT/CT

E. Edmund Kim • Vanessa Murad
Jin-Chul Paeng • Gi-Jeong Cheon
Editors

Atlas and Anatomy of PET/MRI, PET/CT and SPECT/CT

Second Edition

Springer

Editors
E. Edmund Kim
Department of Radiological Sciences
University of California, Irvine,
School of Medicine
Orange, CA, USA

Department of Nuclear Medicine and Department of Molecular Medicine
Graduate School of Convergence Science and Technology, Seoul National University College of Medicine
Seoul, Republic of Korea

Jin-Chul Paeng
Department of Nuclear Medicine
Seoul National University College of Medicine
Seoul, Republic of Korea

Vanessa Murad
Department of Nuclear Medicine
Seoul National University College of Medicine
Seoul, Republic of Korea

Department of Diagnostic Imaging
Fundacion Santa Fe de Bogotá University Hospital
Bogota, Colombia

Gi-Jeong Cheon
Department of Nuclear Medicine
Seoul National University College of Medicine
Seoul, Republic of Korea

ISBN 978-3-030-92348-8 ISBN 978-3-030-92349-5 (eBook)
https://doi.org/10.1007/978-3-030-92349-5

This Springer imprint is published by the registered company Springer Nature Switzerland AG
The registered company address is: Gewerbestrasse 11, 6330 Cham, Switzerland

Preface

Since we published the *Atlas and Anatomy of PET/MRI, PET/CT, and SPECT/CT* in 2016, we have been using more hybrid imaging with improved equipment and software in clinical practice. Technological advances allow us to have higher quality images, and with the increasing use of new radiopharmaceuticals, we can provide more accurate evaluation of physiological processes, diagnosis, and therapeutic evaluation.

Trainees in imaging specialties and non-imaging physicians need more knowledge of detailed imaging anatomy as well as imaging analysis with pattern recognition and differential diagnosis for better patient evaluation. They should also know the different studies available and their indications, to make a more frequent and appropriate use of them in their daily practice.

In this new edition, we have included many new cases of both frequent pathologies, with their typical and atypical presentations, and infrequent pathologies. In addition, there are examples of studies with common novel radiotracers and new techniques. Each case includes relevant clinical data as well as analytical imaging description and approach, and highlights of some pathologies to provide educational information. Additional and updated bibliographic references are also included.

Orange, CA, USA — E. Edmund Kim
Seoul, Republic of Korea — Vanessa Murad

Acknowledgements

We express our gratitude to our colleagues in the Department of Nuclear Medicine at Seoul National University as well as the University of Texas M. D. Anderson Cancer Center Hospitals.

We thank our families, who supported our work, and Mr. Lee Klein at Springer, who encouraged and helped with the creation of this book.

Contents

Contributors

Camilo Barragan, MD, MSc Joint Department of Medical Imaging, University Health Network, University of Toronto, Toronto, ON, Canada

Gi-Jeong Cheon, MD, PhD Department of Nuclear Medicine, Seoul National University College of Medicine, Seoul, Republic of Korea

Hyung-Jun Im, MD, PhD Departments of Applied Bioengineering, Molecular Medicine, and Biopharmaceutical Sciences, Graduate School of Convergence Science and Technology, Seoul National University, Seoul, Republic of Korea

E. Edmund Kim, MD, MS, FACR, FACNM Department of Radiological Sciences, University of California, Irvine, School of Medicine, Orange, CA, USA

Department of Nuclear Medicine and Department of Molecular Medicine, Graduate School of Convergence Science and Technology, Seoul National University College of Medicine, Seoul, Republic of Korea

Ji-Young Kim, MD, PhD Department of Nuclear Medicine, Bundang Seoul National University Hospital, Seoul Korea, Radiation Health Research Institute, Korea Hydro & Nuclear Power Co., Ltd., Seoul, Republic of Korea

Vanessa Murad, MD Department of Nuclear Medicine, Seoul National University College of Medicine, Seoul, Republic of Korea

Department of Diagnostic Imaging, Fundacion Santa Fe de Bogotá University Hospital, Bogota, Colombia

Jin-Chul Paeng, MD, PhD Department of Nuclear Medicine, Seoul National University College of Medicine, Seoul, Republic of Korea

Atlas and Anatomy of PET/MRI

Vanessa Murad, E. Edmund Kim, Jin-Chul Paeng, Hyung-Jun Im, and Gi-Jeong Cheon

Hybrid positron emission tomography/magnetic resonance image (PET/MRI) has undergone rapid evolution during the last years, moving from a predominantly research field to clinical practice. With the advances in faster silicon photomultiplier detectors, MRI-based attenuation correction, and image reconstruction, significant improvements in equipment and image quality have been achieved. Currently, there are fully integrated PET/MRI systems that allow simultaneous and more rapid acquisition, improving not only the technical quality but also the experience for patients who need a low radiation dose [1–3]. With this technology comes the possibility of performing multiparametric MRI studies, where detailed anatomical evaluation and functional evaluation are possible, not only considering the qualitative and quantitative data of PET but also integrating multiple parameters such as perfusion (contrast-enhanced sequences), cellularity (diffusion-weighted sequence), metabolites (spectroscopic analysis), and texture analysis. Additionally, recent developments are very promising in giving the possibility of incorporating advanced data and biomarkers to integrate with bioinformatics and allow a better understanding of the disease, as well as an efficient evaluation, prediction of response to treatment, and follow-up [4–7].

With the growing availability of PET/MRI, its main and differential applications have also been clarified. Nonspecific ^{18}F-fludeoxyglucose (FDG) PET/MRI continues to be the most widely used, and thus new radiotracers are expanding the field to be explored. Among the most frequent applications of ^{18}F-FDG PET/MRI, where its superiority over PET/CT has been demonstrated, are the evaluation of head and neck, colorectal, gynecological, bone and soft tissue tumors, as well as the evaluation and characterization of primary or secondary liver lesions [8–12]. It has also shown good results in non-tumor pathology such as epilepsy, inflammatory bowel disease, and cardiac sarcoidosis [4, 13].

The creation of new radiotracers that can be imaged both with PET/MRI and PET/CT, depending on the case and availability, has allowed great advances in the evaluation of other oncological and non-oncological pathologies. In the case of neuroendocrine tumors and prostate cancer, targeting somatostatin receptors with ^{68}Ga-DOTATOC, targeting PSMA with ^{68}Ga-PSMA-11 among others available tracers, and the inclusion of ^{177}Lu agents have revolutionized the diagnosis and treatment of these pathologies respectively [14, 15]. In the field of neuroimaging, the wide availability of radiotracers has made it possible to improve the evaluation of multiple targets different from glucose metabolism (FDG), such as DNA synthesis (^{18}F-fluorothymidine), protein synthesis (^{11}C-methionine, ^{18}F-fluoroethyl-L-tyrosine [FET], ^{18}F-fluoro-L-3,4-dihydroxyphenylalanine [DOPA]), and hypoxia (^{18}F-fluoromisonidazole) [16, 17]. In the field of degenerative diseases, where much remains to be explored and research is very promising, examples of emerging invaluable applications are amyloid PET and Tau PET for Alzheimer's disease, as well as ^{18}FP-CIT PET for Parkinson's disease [18, 19].

In this chapter, we present multiple demonstrative examples of the different uses of PET/MR, with the most relevant anatomical references for each case.

V. Murad (✉)
Department of Nuclear Medicine, Seoul National University College of Medicine, Seoul, Republic of Korea

Department of Diagnostic Imaging, Fundacion Santa Fe de Bogotá University Hospital, Bogota, Colombia

E. E. Kim
Department of Radiological Sciences, University of California, Irvine, School of Medicine, Orange, CA, USA

Department of Nuclear Medicine and Department of Molecular Medicine, Graduate School of Convergence Science and Technology, Seoul National University College of Medicine, Seoul, Republic of Korea

J.-C. Paeng · G.-J. Cheon
Department of Nuclear Medicine, Seoul National University College of Medicine, Seoul, Republic of Korea

H.-J. Im
Departments of Applied Bioengineering, Molecular Medicine, and Biopharmaceutical Sciences, Graduate School of Convergence Science and Technology, Seoul National University, Seoul, Republic of Korea

E. E. Kim et al. (eds.), *Atlas and Anatomy of PET/MRI, PET/CT and SPECT/CT*, https://doi.org/10.1007/978-3-030-92349-5_1

1 Head and Neck

1.1 Case 1

A 75-year-old male patient, with worsening dizziness and weakness in both legs. Brain malignancy was suspected on brain CT, so ^{18}F- FDG PET/MR was performed. Images revealed marked increased activity in a well-defined enhancing mass involving the corpus callosum, crossing the midline and with subependymal extension. Primary central nervous system (CNS) lymphoma was suspected, and stereotaxic biopsy confirmed a diffuse large B-cell lymphoma (Fig. 1) [20].

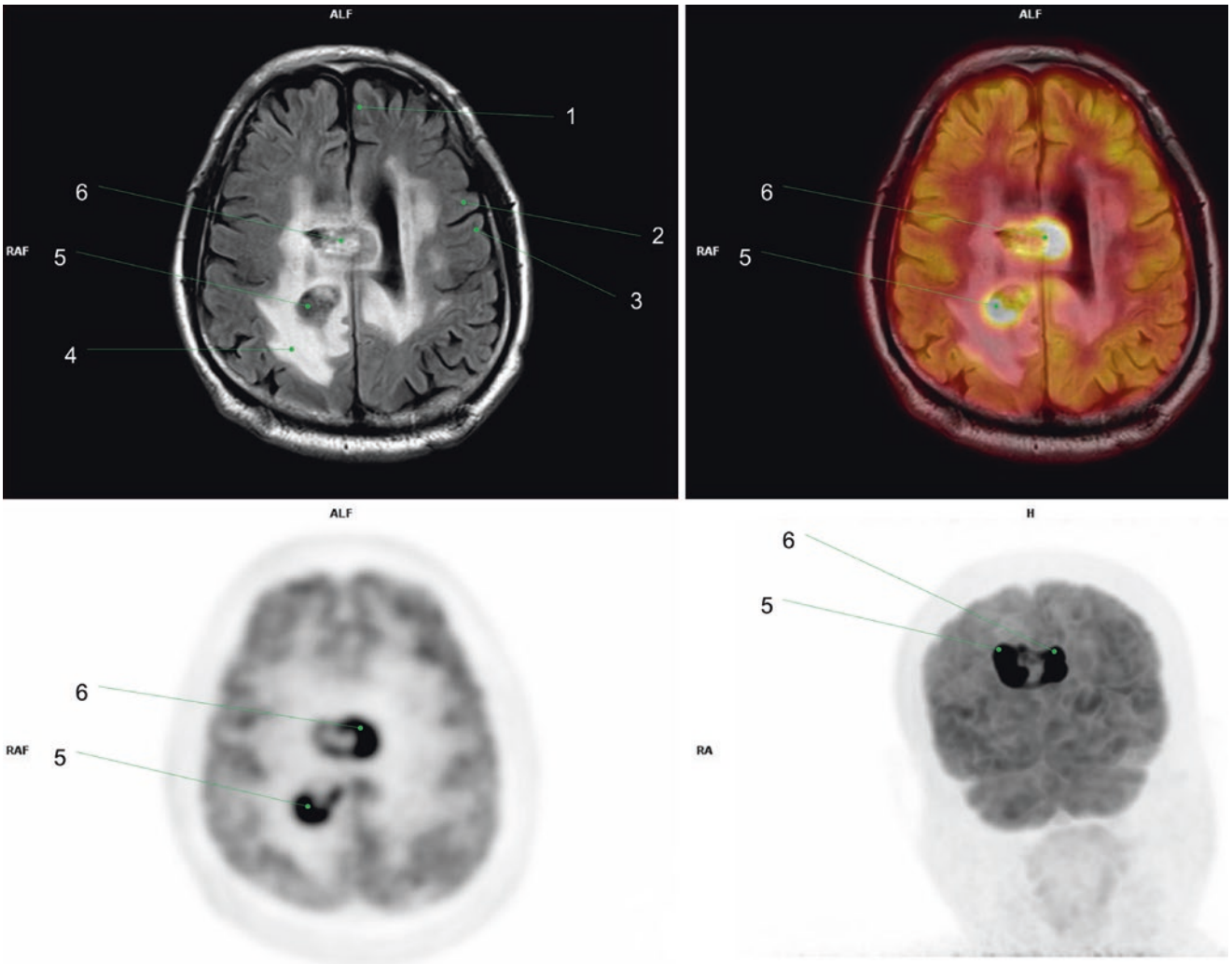

Fig. 1 1. Left superior frontal gyrus
2. Left precentral gyrus
3. Left postcentral gyrus
4. Peritumoral edema, right parietal lobe
5. Primary central nervous system lymphoma involving right parietal white matter
6. Primary central nervous system lymphoma involving corpus callosum

1.2 Case 2

A 72-year-old man with diagnosis of lymphoplasmacytic lymphoma (LPL)/Waldenström macroglobulinemia (WM) from marginal zone lymphoma, with central nervous system involvement. After surgery and chemotherapy, complete response was achieved, but the patient attended an early checkup with headache, so ^{18}F-FDG PET/MR was performed. Images showed focal increased activity in a lobulated mass at the periventricular white matter, adjacent to the posterior horn of the left lateral ventricle with perilesional edema, which showed predominantly low signal on T2WI and heterogeneous contrast enhancement, which are frequent findings of lymphoma involvement. With these findings, a relapse was confirmed, and treatment was initiated again (Fig. 2) [21].

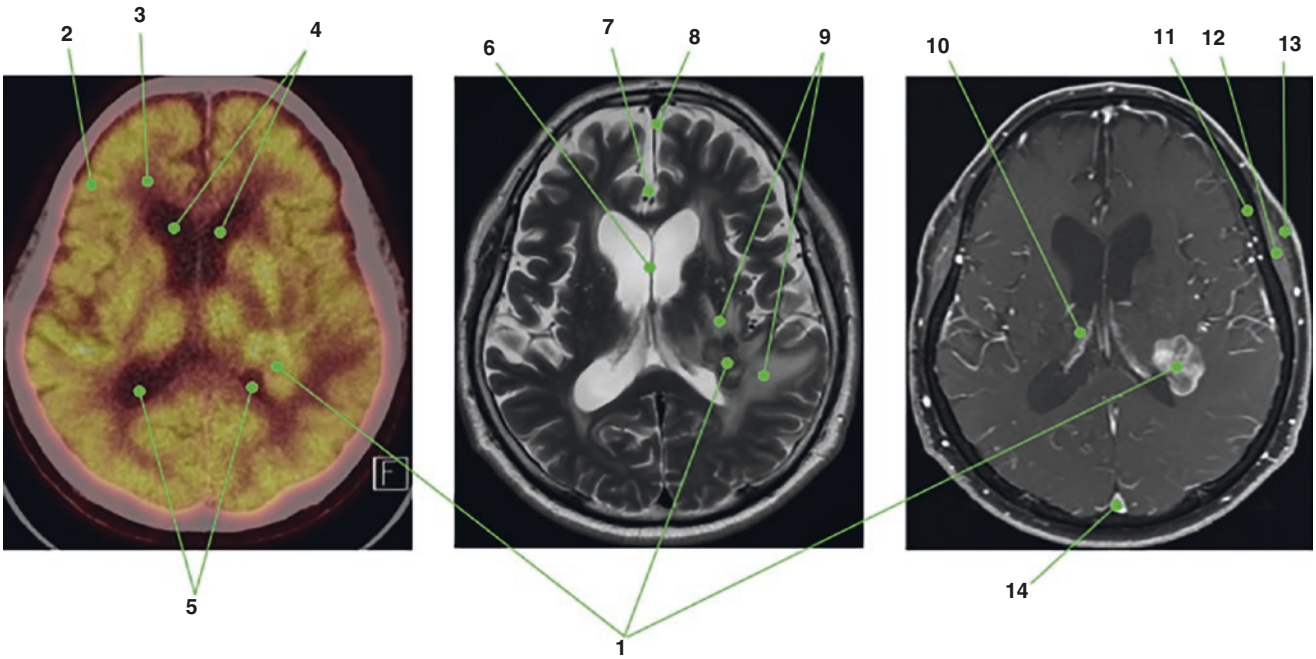

Fig. 2 1. Metabolically active lymphoma adjacent to the posterior horn of the left lateral ventricle
2. Normal FDG uptake in gray matter at the frontal cortex
3. Normal FDG uptake in the white matter at the frontal lobe
4. Anterior horns of the lateral ventricles
5. Posterior horns of the lateral ventricles
6. Septum pellucidum
7. Anterior cerebral arteries
8. Falx cerebri, frontal region
9. Perilesional edema
10. Choroid plexus at right lateral ventricle
11. Skull, left parietal area
12. Left temporal muscle
13. Scalp, left parietal area
14. Superior sagittal sinus

1.3 Case 3

A 5-year-old patient with gradual loss of vision in the right eye. Clinical examination and contrast-enhanced MRI were performed and confirmed the diagnosis of retinoblastoma. ^{18}F-FDG PET/MR was performed during initial workup and staging. Minimal uptake was found in the primary tumor and the presence of metabolically active metastases was ruled out (Fig. 3) [22].

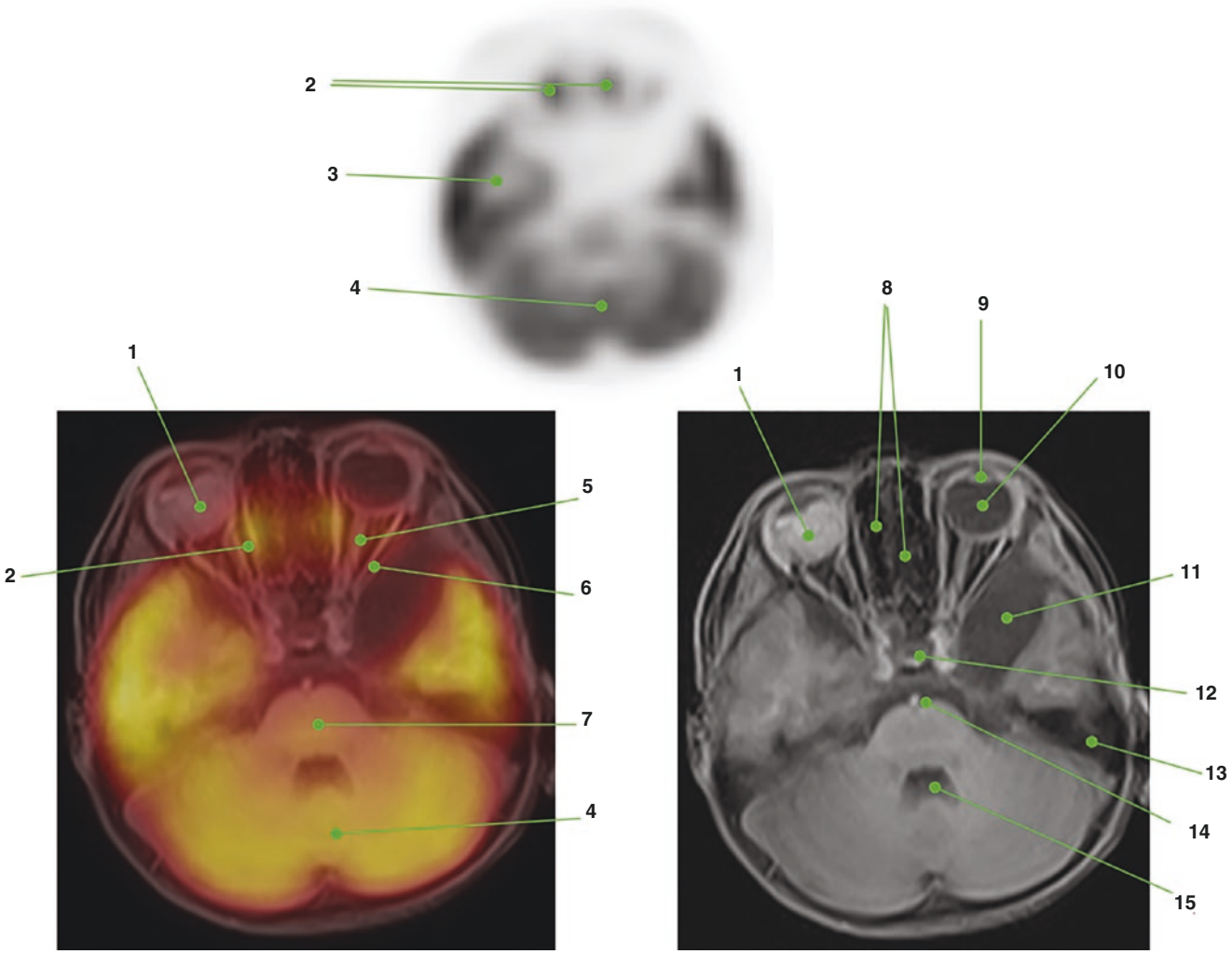

Fig. 3 1. Right eye retinoblastoma with minimal diffuse FDG uptake
2. Right medial rectus muscles
3. Right temporal lobe
4. Cerebellar vermis
5. Left optic nerve
6. Left lateral rectus muscle
7. Pons
8. Ethmoid air cells
9. Left eye, anterior chamber
10. Left eye, vitreous chamber
11. Left temporal arachnoid cyst
12. Pituitary gland
13. Left temporal bone
14. Basilar artery
15. Fourth ventricle

1.4 Case 4

A 49-year-old woman with a headache and decreased mobility of the right eye. ^{18}F-FDG PET/MR was performed, and images showed a metabolically active mass with heterogeneous enhancement in the olfactory recess involving the cribriform plate and ethmoid air cells. The lesion produced lateral displacement of the right medial rectus muscle, compression of the optic chiasm, and obstruction of the sphenoid sinuses. Subsequent biopsy confirmed the diagnosis of an olfactory neuroblastoma, also known as esthesioneuroblastoma (Fig. 4) [23].

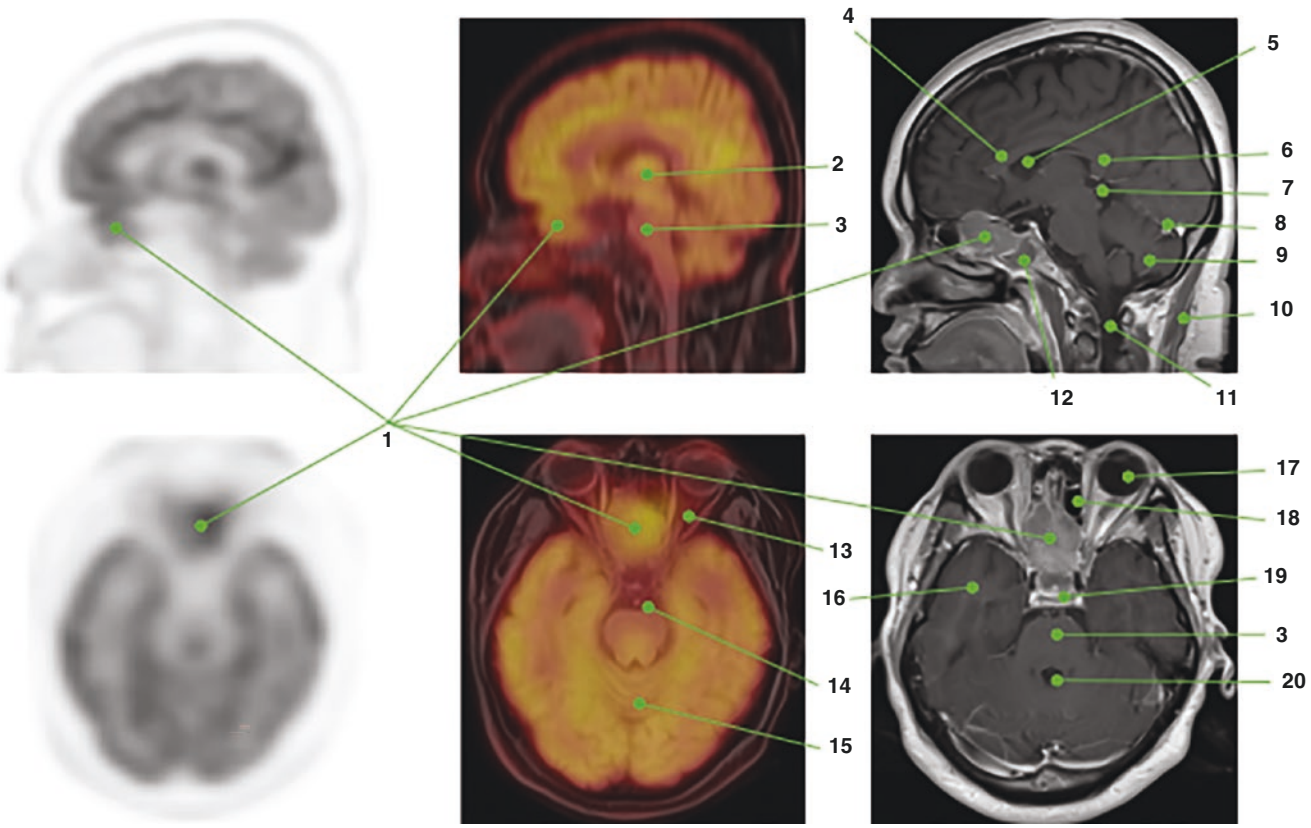

Fig. 4 1. Metabolically active tumor in the upper olfactory recess
2. Thalamus
3. Pons
4. Genu of corpus callosum
5. Lateral ventricle anterior horn
6. Splenium of corpus callosum
7. Pineal gland
8. Straight sinus
9. Cerebellum
10. Nuchal ligament
11. Spinal cord
12. Sphenoidal sinus with secretion due to obstruction
13. Left optic nerve
14. Basilar artery
15. Cerebellar vermis
16. Right temporal lobe
17. Left eye, vitreous chamber
18. Left ethmoid air cells
19. Optic chiasm
20. Fourth ventricle

1.5 Case 5

A 48-year-old male patient with progressive proptosis, impaired visual acuity, and headaches. ^{18}F-FDG PET/MR was performed, finding diffuse metabolically active infiltration of the soft tissues in both orbits and eyelids, with encasement and displacement of the optic nerves and muscles, without infiltration. Biopsy revealed the diagnosis of an extra nodal marginal zone B-cell lymphoma (EMZBC) (Fig. 5) [22].

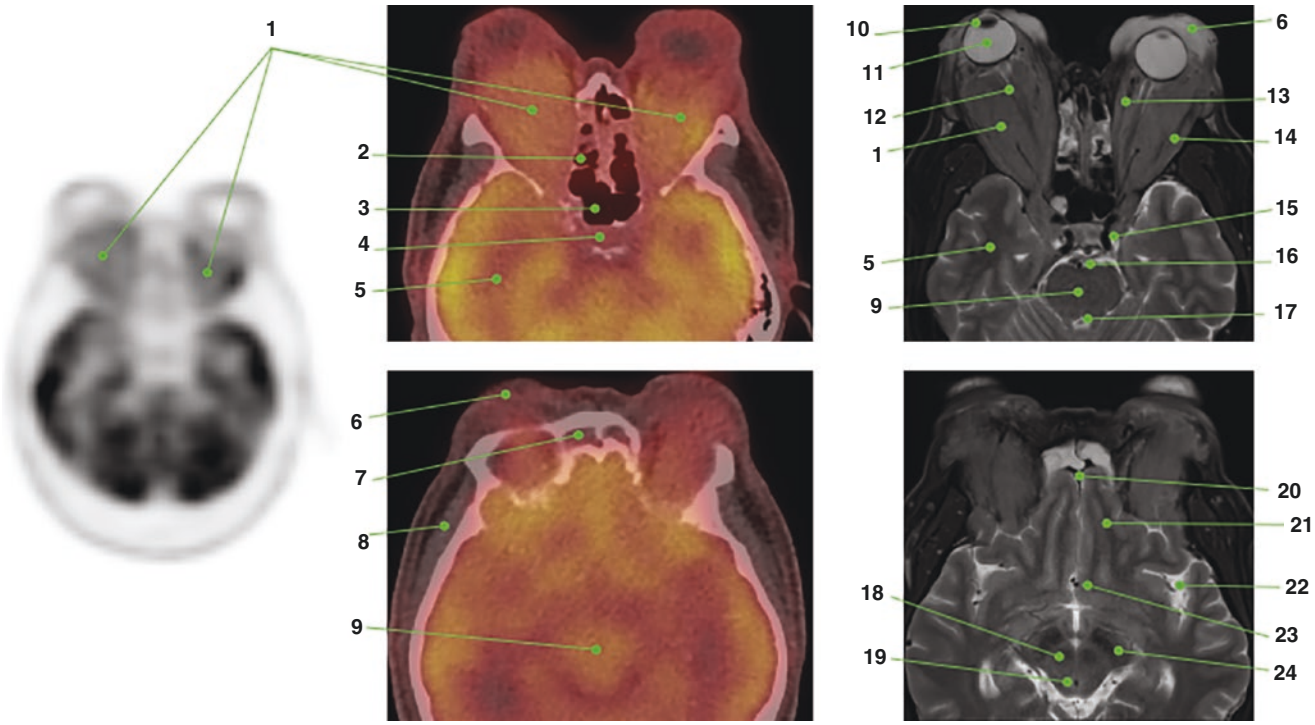

Fig. 5 1. Metabolically active bilateral orbital lymphoma infiltration
2. Right anterior ethmoid air cells
3. Right posterior ethmoid air cells
4. Sella turcica (pituitary gland)
5. Right temporal lobe
6. Right superior eyelid with lymphoma infiltration
7. Frontal sinuses
8. Right temporal muscle
9. Pons
10. Right eye lens
11. Right eye vitreous chamber
12. Right optic nerve
13. Left medial rectus muscle
14. Left lateral rectus muscle
15. Left internal carotid artery
16. Basilar artery
17. Fourth ventricle
18. Midbrain, red nucleus
19. Aqueduct of Sylvius
20. Crista galli
21. Left olfactory cortex
22. Left Sylvian fissure
23. Anterior cerebral arteries
24. Midbrain, sustancia nigra

1.6 Case 6

A 55-year-old male patient with sore throat and a soft tissue mass in the right nasopharyngeal wall on physical examination. Biopsy revealed nasopharyngeal squamous cell carcinoma, so ^{18}F-FDG PET/MR was performed for staging. Images showed increased metabolic activity in the right nasopharyngeal area at a soft tissue mass, consistent with the primary tumor. Hypermetabolic, enlarged, metastatic lymph node (LN) was also found in the right neck, level II (Figs. 6 and 7) [24].

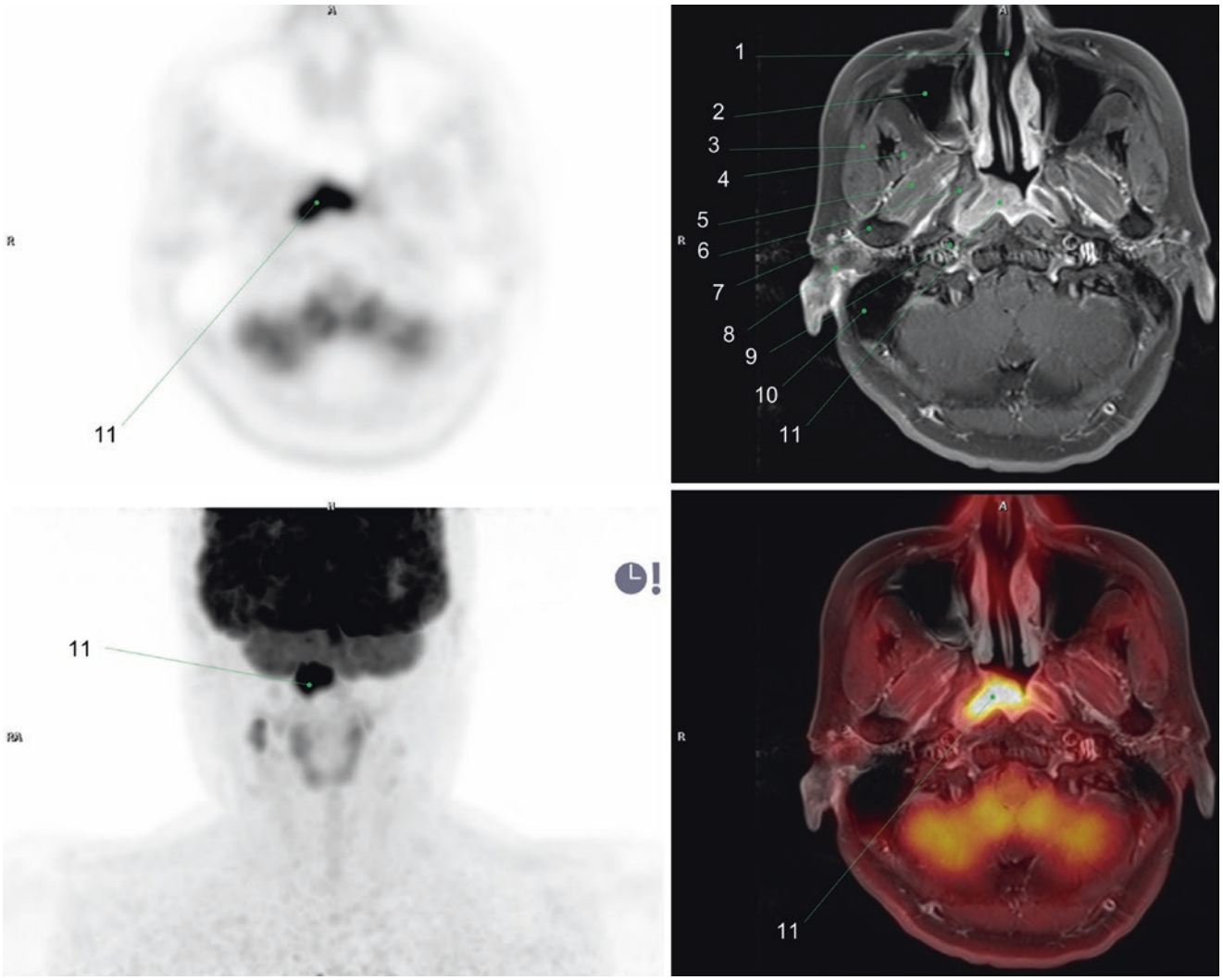

Fig. 6 1. Nasal septum
2. Right maxillary sinus
3. Right masseter muscle
4. Right temporalis muscle
5. Right lateral pterygoid muscle
6. Right medial pterygoid muscle
7. Right mandibular ramus
8. Right external auditory canal
9. Right internal carotid artery
10. Right mastoid air cells
11. Metabolically active tumor at the right fossa of Rosenmüller

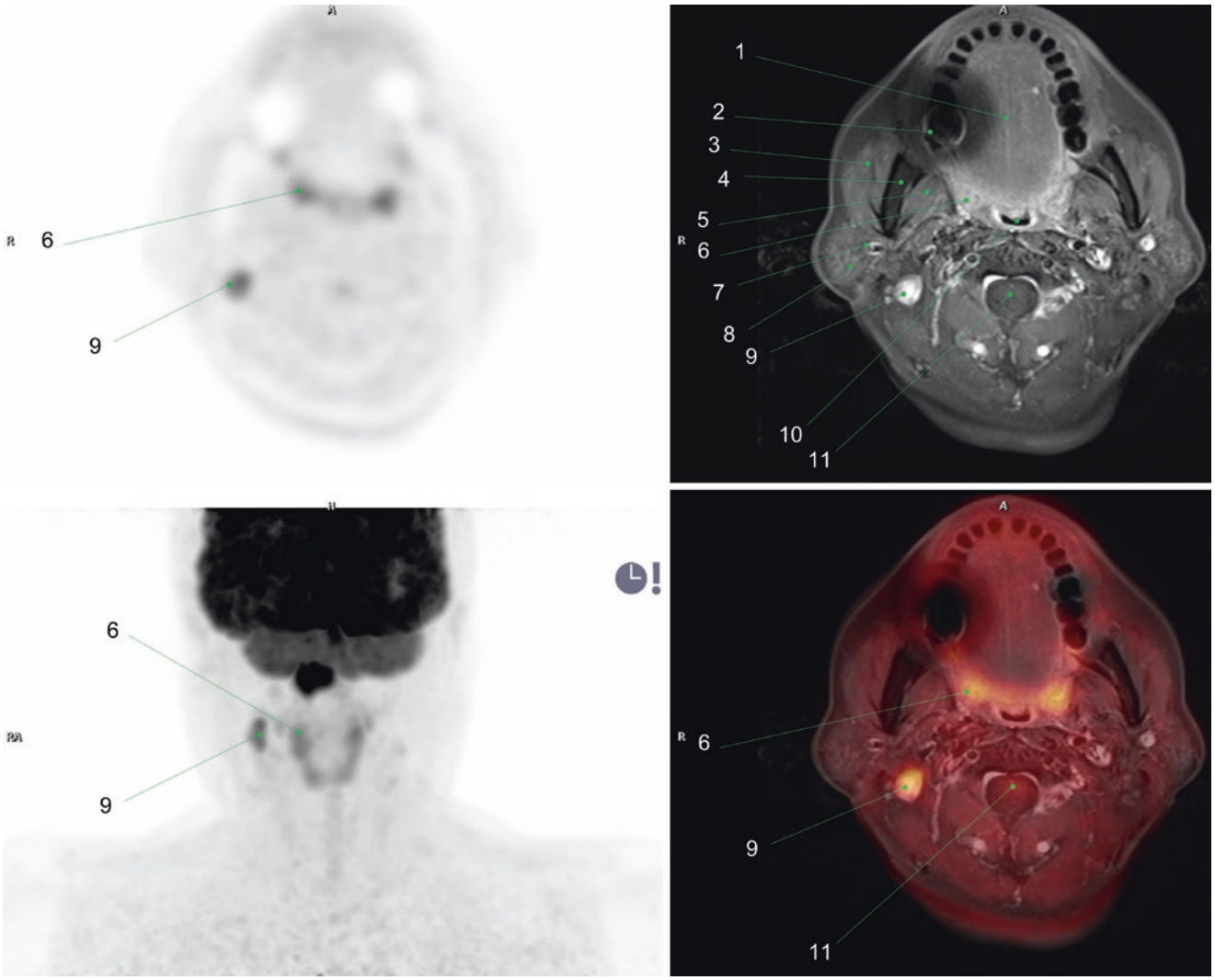

Fig. 7 1. Tongue
2. Right molar teeth with artifact due to dental implant
3. Right masseter muscle
4. Right mandibular ramus
5. Right medial pterygoid muscle
6. Right palatine tonsil
7. Right external maxillary vein
8. Right parotid gland
9. Metabolically active LN metastasis, right neck level II
10. Oropharynx
11. Spinal cord

1.7 Case 7

A 55-year-old female patient with a growing ulcerated mass in the right sublingual area. Biopsy was performed confirming an adenoid cystic carcinoma with cribriform pattern, so ^{18}F-FDG PET/MR was performed for staging. Images showed a focal hypermetabolic lesion in the right sublingual space, displacing the tongue's intrinsic muscles, without infiltrating them. Ipsilateral, level II, hypermetabolic lymph node metastasis was also found (Fig. 8) [10].

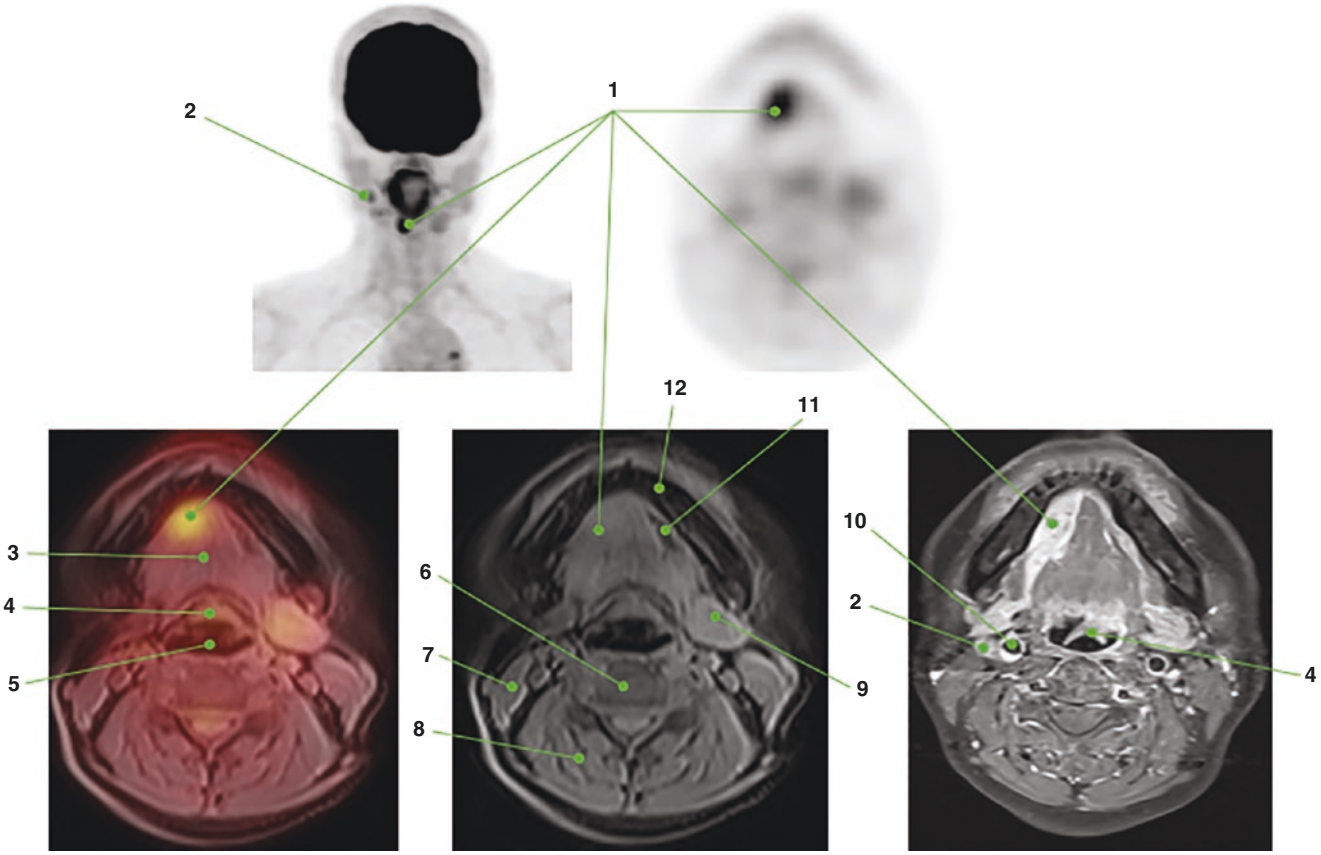

Fig. 8 1. Metabolically active tumor in the right sublingual space
2. Metastatic LN, right neck level II
3. Genioglossus muscle
4. Epiglottis
5. Larynx
6. Cervical vertebral body
7. Right sternocleidomastoid muscle
8. Posterior cervical muscles (inner to outer): semispinalis, splenius cervicis, and splenius capitis
9. Left submandibular gland
10. Right common carotid artery
11. Left sublingual space
12. Mandible, body

1.8 Case 8

A 55-year-old male patient with a history of persistent dysphagia and cough. Direct endoscopic examination was performed finding a laryngeal mass, consistent with an epiglottic squamous cell carcinoma. ^{18}F-FDG PET/MR was performed for staging, finding a prominent hypermetabolic mass in the superior aspect of the epiglottis, projecting towards the upper airway and decreasing its caliber. No hypermetabolic lymph nodes or distant metastases were observed (Fig. 9) [10].

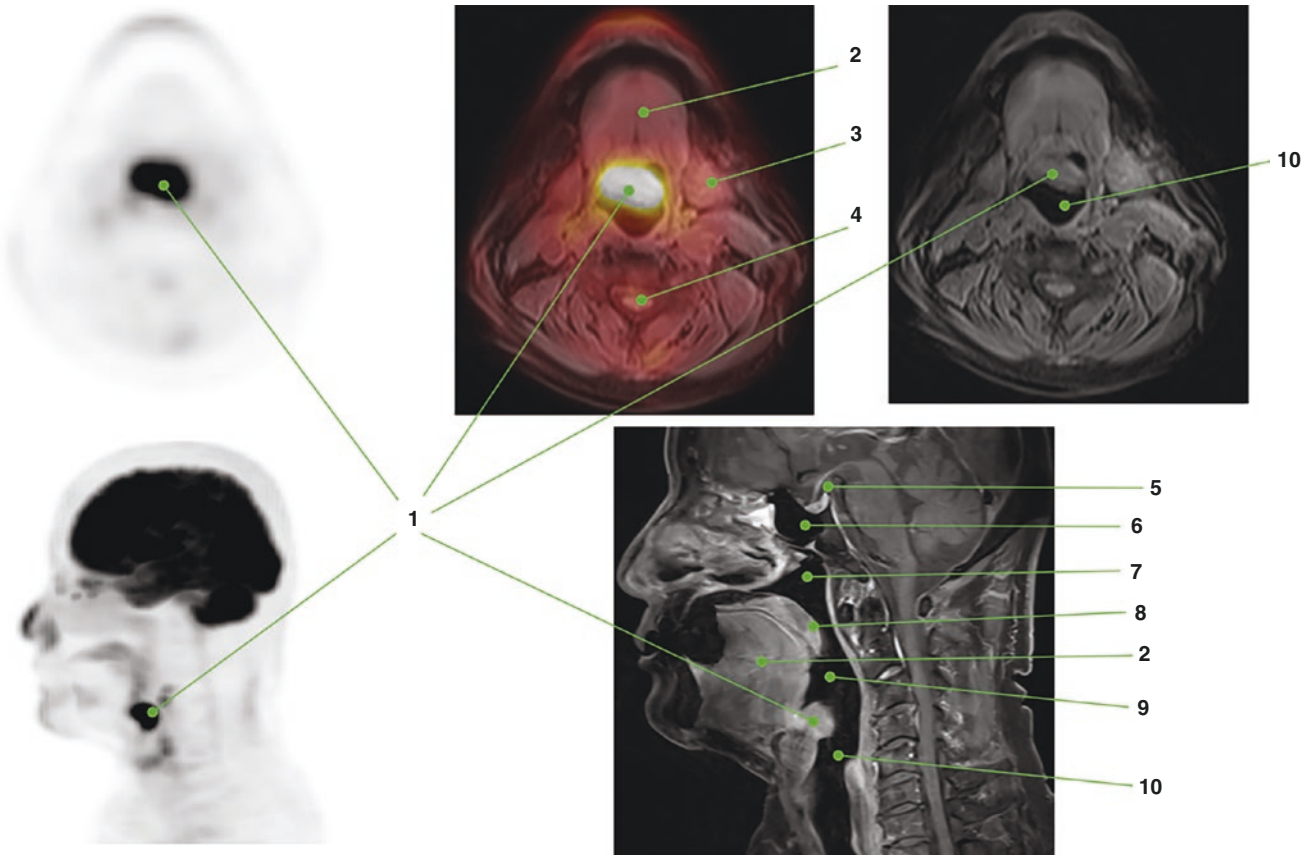

Fig. 9 1. Metabolically active epiglottic tumor
2. Intrinsic tongue muscles (genioglossus)
3. Left submandibular gland
4. Spinal cord
5. Pituitary gland and stalk
6. Sphenoid sinus
7. Nasopharynx
8. Uvula
9. Oropharynx
10. Larynx

1.9 Case 9

A 21-year-old man with a non-painful, progressively growing right parotid mass. Ultrasound-guided biopsy revealed a secretory carcinoma, so ^{18}F-FDG PET/MR was performed for staging. Images showed a hypermetabolic irregular mass involving both the superficial and deep lobes of the right parotid gland, without associated metastatic lymph nodes (Fig. 10) [25].

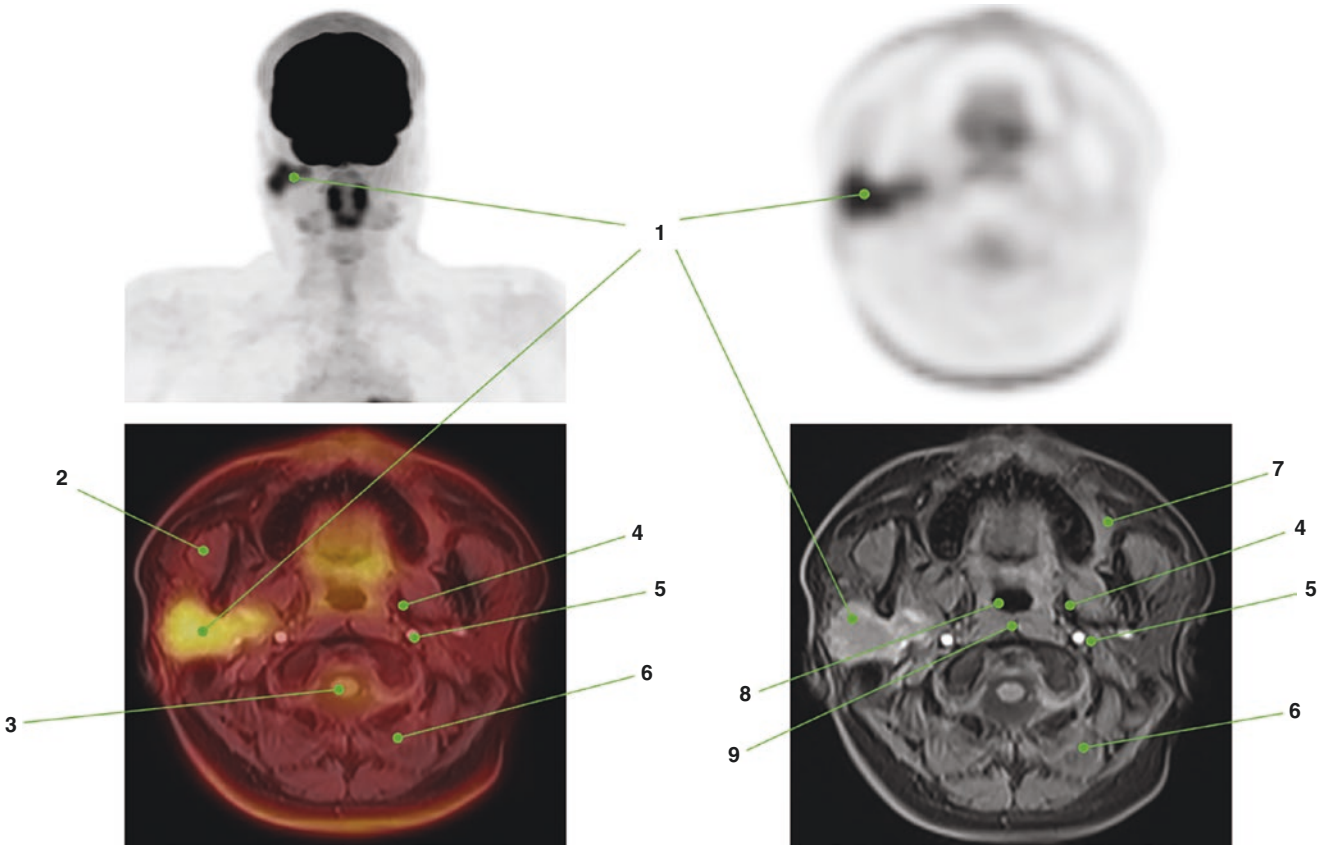

Fig. 10 1. Metabolically active right parotid tumor, involving both superficial and deep lobes
2. Right masticator space
3. Spinal cord
4. Left parapharyngeal space
5. Left carotid space
6. Left paraspinal space
7. Left buccal space
8. Oropharynx
9. Longus capitis muscles

1.10 Case 10

A 57-year-old man with a painful, rapidly growing left cervical mass. Ultrasound was performed finding an enlarged, necrotic lymph node, which biopsy revealed a metastatic carcinoma. ^{18}F-FDG PET/MR was performed suspecting primary head and neck malignancy, and images showed a hypermetabolic mass in the hypopharynx, predominantly left side, with multiple metastatic lymph nodes in the left neck. The diagnosis of primary squamous cell carcinoma in this location was confirmed (Fig. 11) [10].

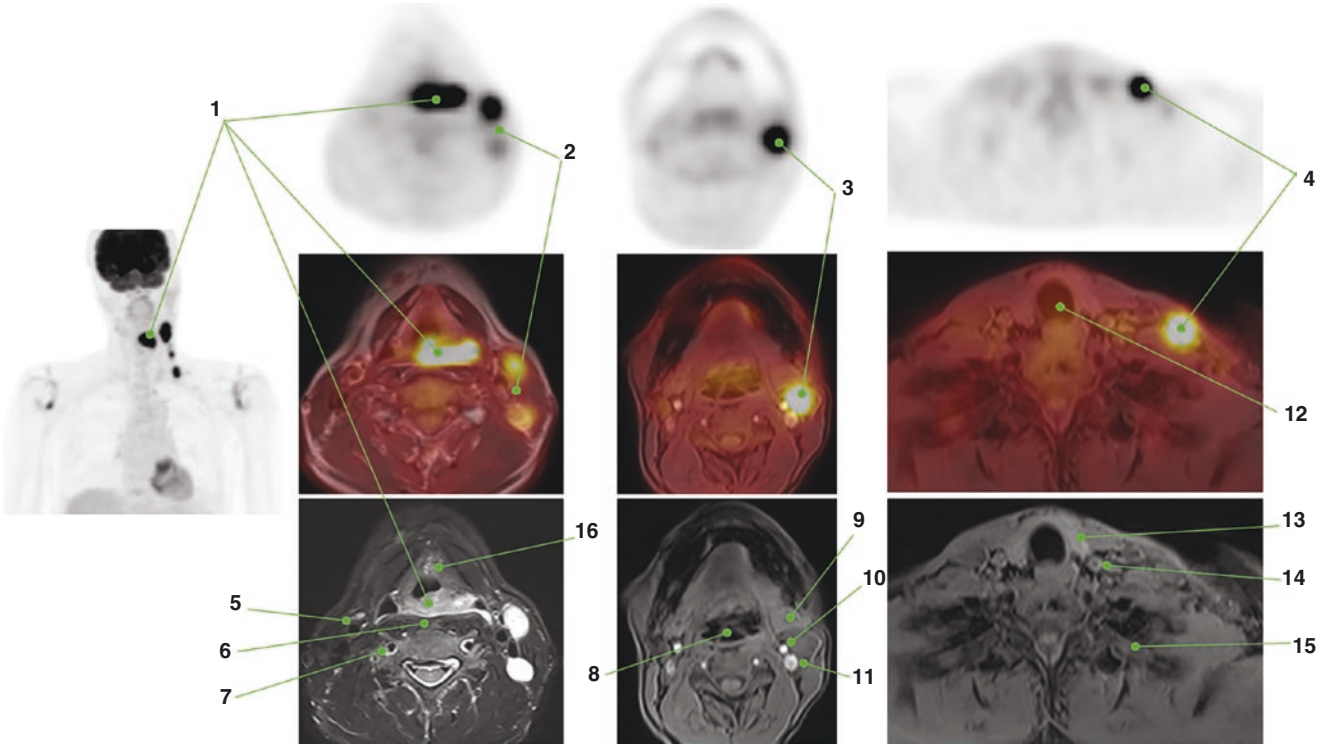

Fig. 11 1. Metabolically active hypopharyngeal tumor
2. Hypermetabolic metastatic neck lymph nodes: left, level III
3. Hypermetabolic metastatic neck lymph node: left, level II
4. Hypermetabolic metastatic neck lymph nodes: left, level IV
5. Right carotid artery
6. Retropharyngeal space
7. Right vertebral artery
8. Epiglottis
9. Left submandibular gland
10. Left carotid artery
11. Left jugular vein
12. Trachea
13. Left thyroid lobe
14. Left common carotid artery
15. Left second rib
16. Vocal cords

1.11 Case 11

A 22-year-old man with headache, occasional fever, and weakness in both arms. Laboratory tests did not show definite abnormalities, so ^{18}F-FDG PET/MR and MRI were performed to rule out unknown origin infection vs occult malignancy. Images showed diffusely increased activity along the spinal cord with corresponding ill-defined high signal intensity lesions in T2WI. With these findings and other neurological tests, the diagnosis of acute disseminated encephalomyelitis (ADEM) was confirmed (Fig. 12) [26].

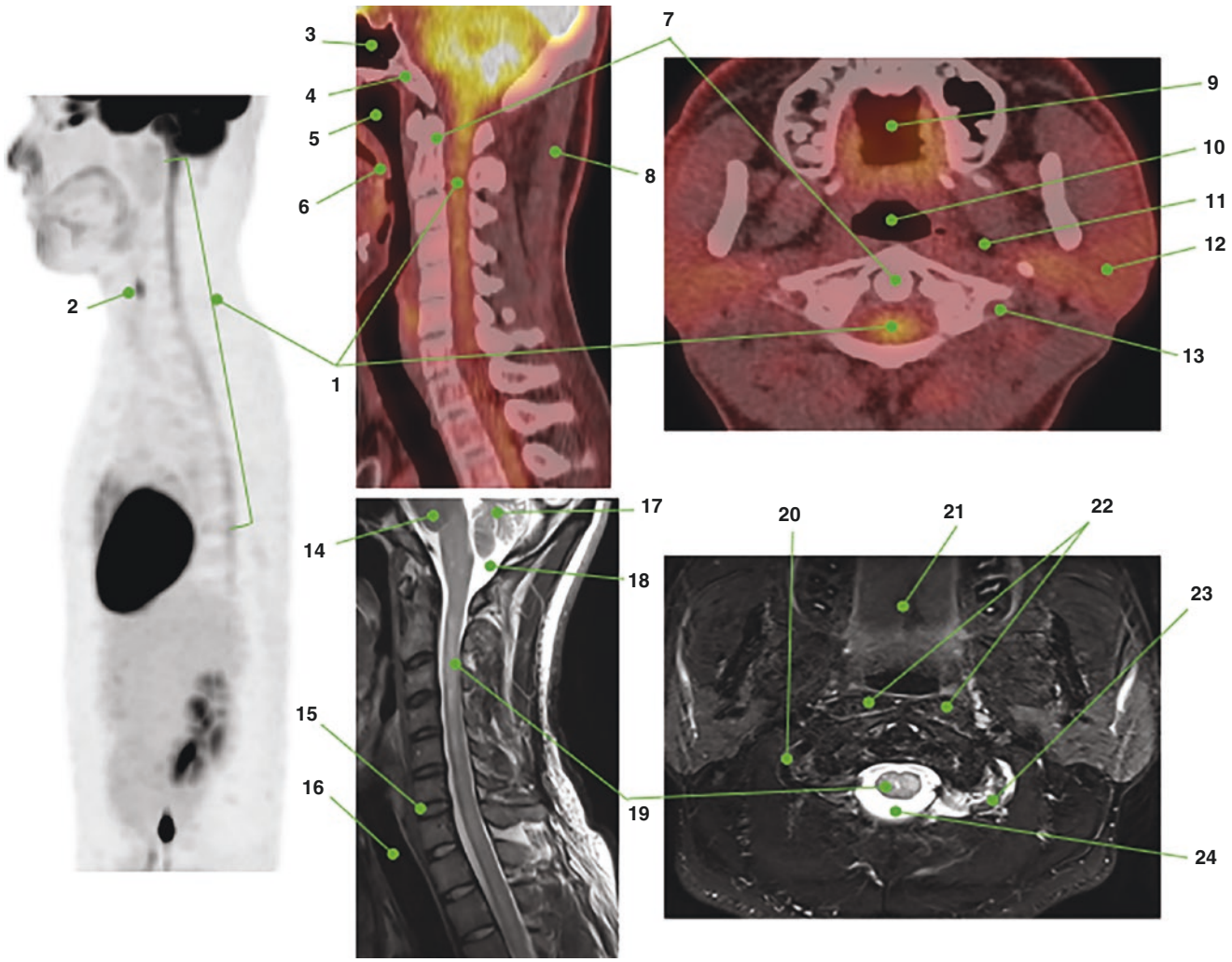

Fig. 12 1. Diffusely increased activity along the spinal cord
2. Focal increased activity at the vocal cords, physiologic
3. Sphenoid sinus
4. Clivus
5. Nasopharynx
6. Uvula
7. C2, odontoid process
8. Nuchal ligament
9. Oral cavity
10. Oropharynx
11. Left parapharyngeal space
12. Left parotid gland
13. Left vertebral foramen in C1
14. Brainstem
15. C6–C7 Intervertebral disc
16. Trachea
17. Cerebellum
18. Cisterna magna
19. Ill-defined high signal intensity lesions (T2WI)
20. Right vertebral artery
21. Hard palate
22. Longus capitis muscles
23. Left vertebral artery
24. Cerebrospinal fluid

1.12 Case 12

A 67-year-old male patient with a history of left maxillary sinus squamous cell carcinoma, treated 9 years ago with radiotherapy and surgery (resection with flap reconstruction). He attended his annual checkup completely asymptomatic and among other studies ^{18}F-FDG PET/MR was performed. Images showed focal increased activity in the lateral wall of the left nostril on the medial aspect of the surgical flap, which also presented heterogeneous contrast enhancement, which was not evident in the previous study. This finding was confirmed as a local recurrence (Fig. 13) [10].

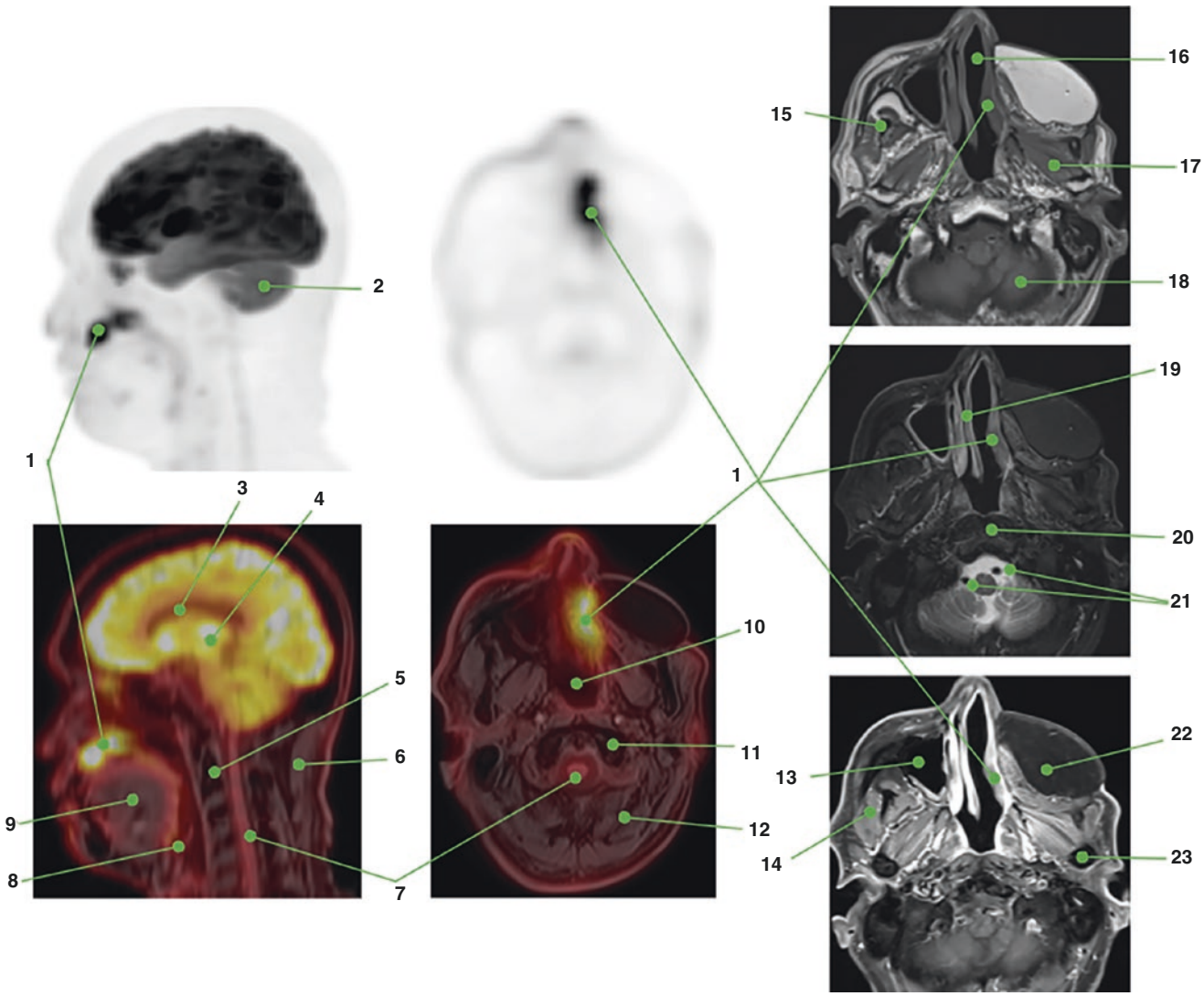

Fig. 13 1. Metabolically active recurred tumor in the surgical flap
2. Cerebellum
3. Lateral ventricles
4. Thalami
5. C2, odontoid process
6. Nuchal ligament
7. Medulla
8. Epiglottis
9. Tongue
10. Nasopharynx
11. Left occipital condyle
12. Left cervical paraspinal muscles (multifidus, longissimus capitis, splenius capitis)
13. Right maxillary sinus
14. Right masseter muscle
15. Right mandibular ramus
16. Left nostril
17. Left pterygoid muscles
18. Left cerebellar hemisphere
19. Nasal septum
20. Prevertebral muscles (longus capitis and rectus capitis muscles)
21. Proximal vertebral arteries
22. Surgical graft
23. Left mandibular condyle

2 Chest

2.1 Case 1

A 62-year-old male patient with a solitary pulmonary nodule and history of heavy smoking. ^{18}F-FDG PET/MR was performed during staging. Images showed moderately increased activity in a small solid nodule at the left lower lobe, which was later resected and confirmed as an adenocarcinoma. No metabolically active metastases were detected (Figs. 14, 15, 16, 17, 18, and 19) [27, 28].

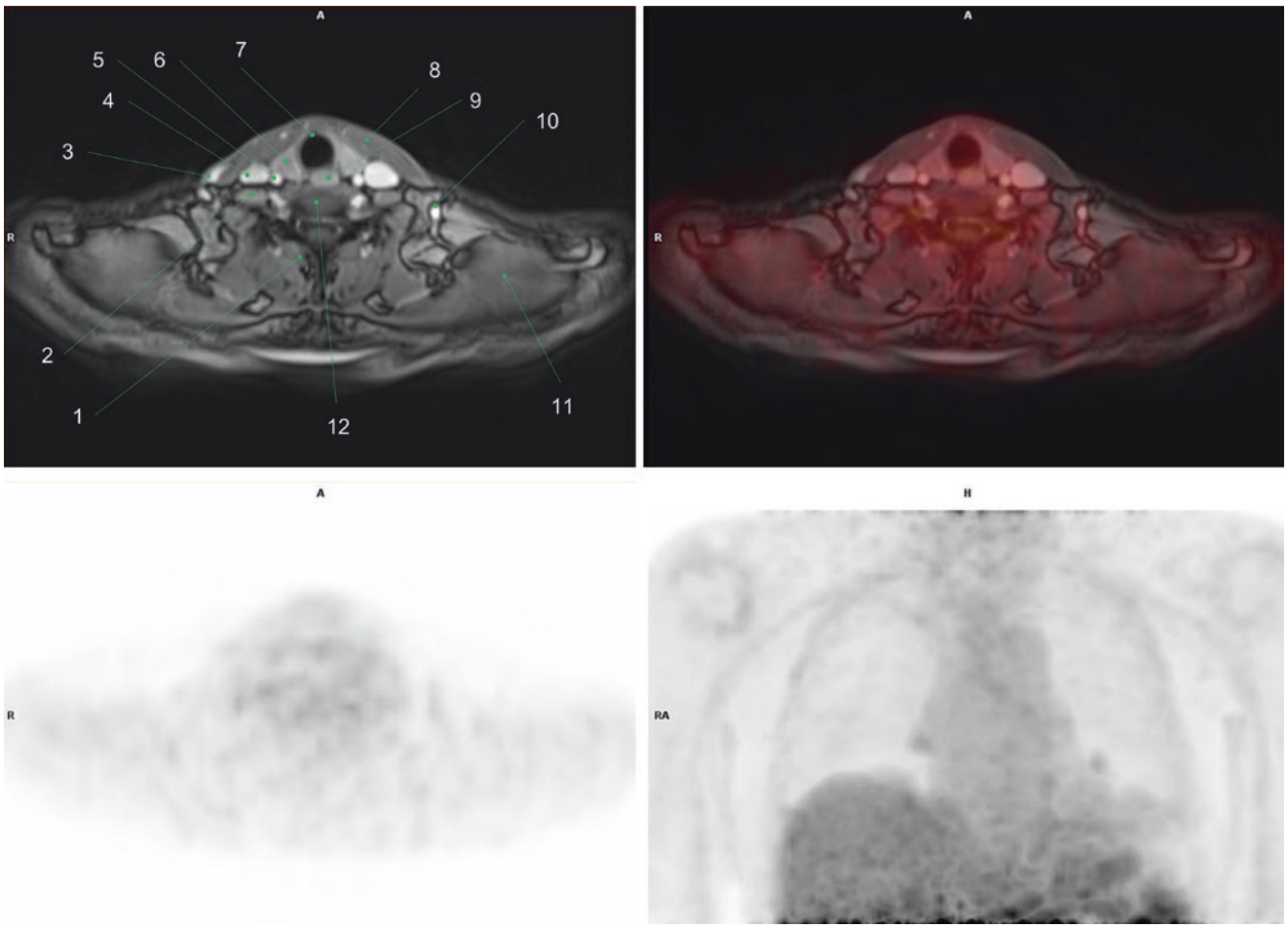

Fig. 14 1. Right erector spinae muscle
2. Right anterior scalene muscle
3. Right external jugular vein
4. Right internal jugular vein
5. Right common carotid artery
6. Thyroid gland, right lobe
7. Trachea
8. Left sternocleidomastoid muscle
9. Esophagus
10. Normal lymph node, left neck, level IV
11. Left trapezius muscle
12. Cervical vertebral body

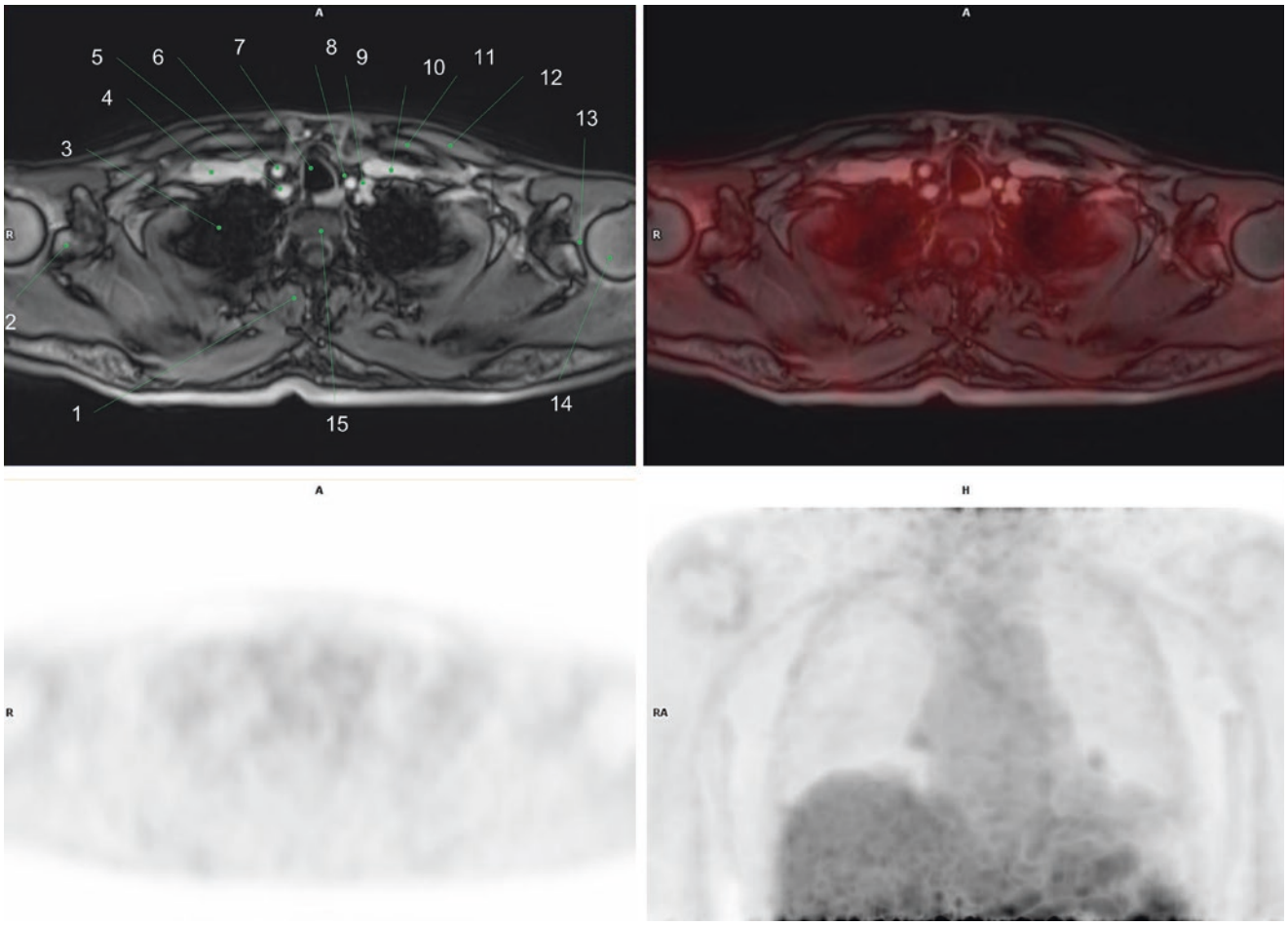

Fig. 15 1. Right erector spinae muscle
2. Right glenoid
3. Right lung apex, right upper lobe (RUL)
4. Right subclavian vein
5. Right subclavian artery
6. Right common carotid artery
7. Trachea
8. Left common carotid artery
9. Left subclavian artery
10. Left subclavian vein
11. Left pectoralis minor muscle
12. Left pectoralis major muscle
13. Left glenohumeral joint
14. Left humeral head
15. Thoracic vertebral body

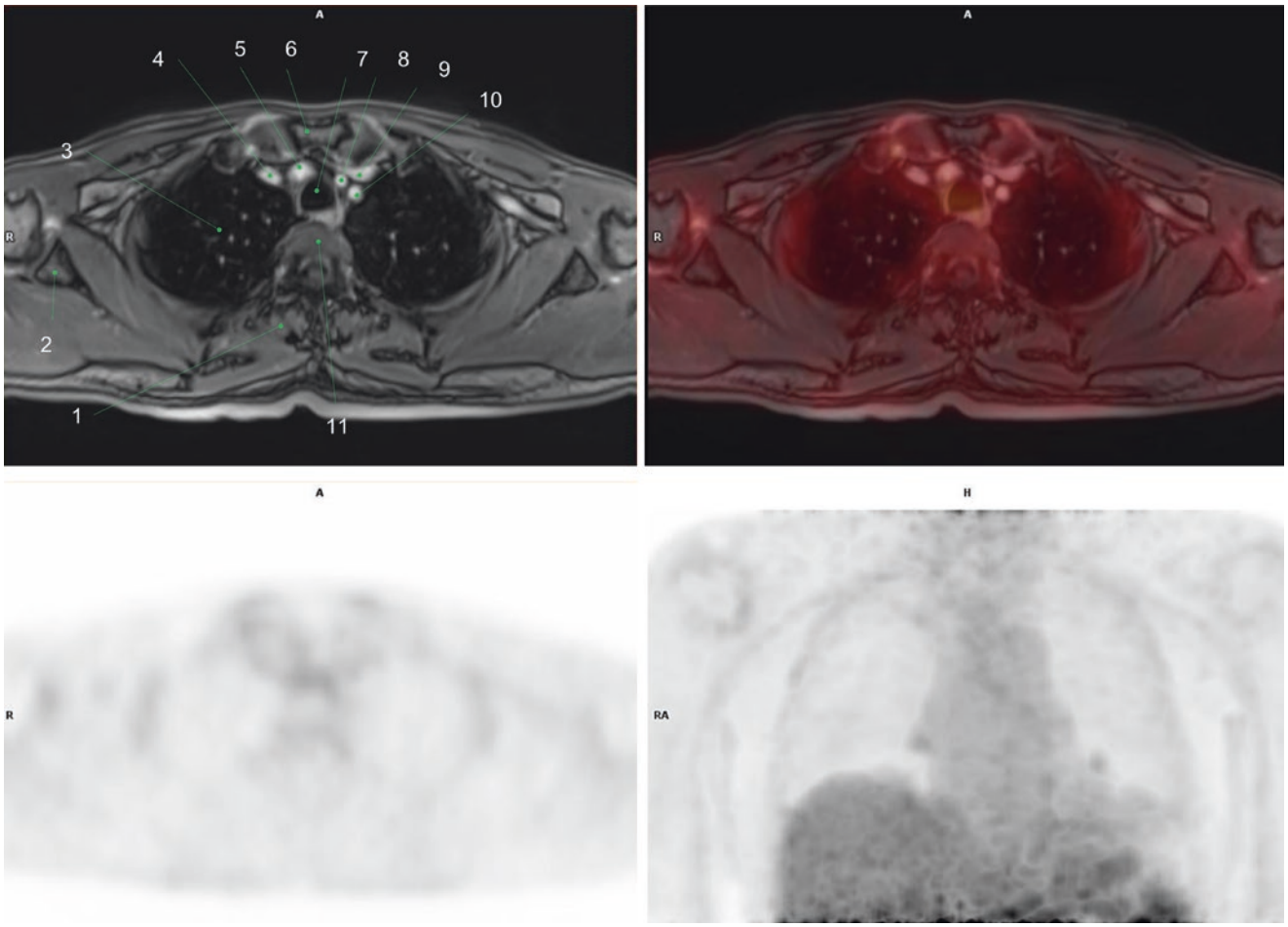

Fig. 16 1. Right erector spinae muscle
2. Right glenoid, scapula
3. Lung RUL
4. Right brachiocephalic vein
5. Right brachiocephalic artery
6. Sternal manubrium
7. Trachea
8. Left common carotid artery
9. Left brachiocephalic vein
10. Left subclavian artery
11. Thoracic vertebral body

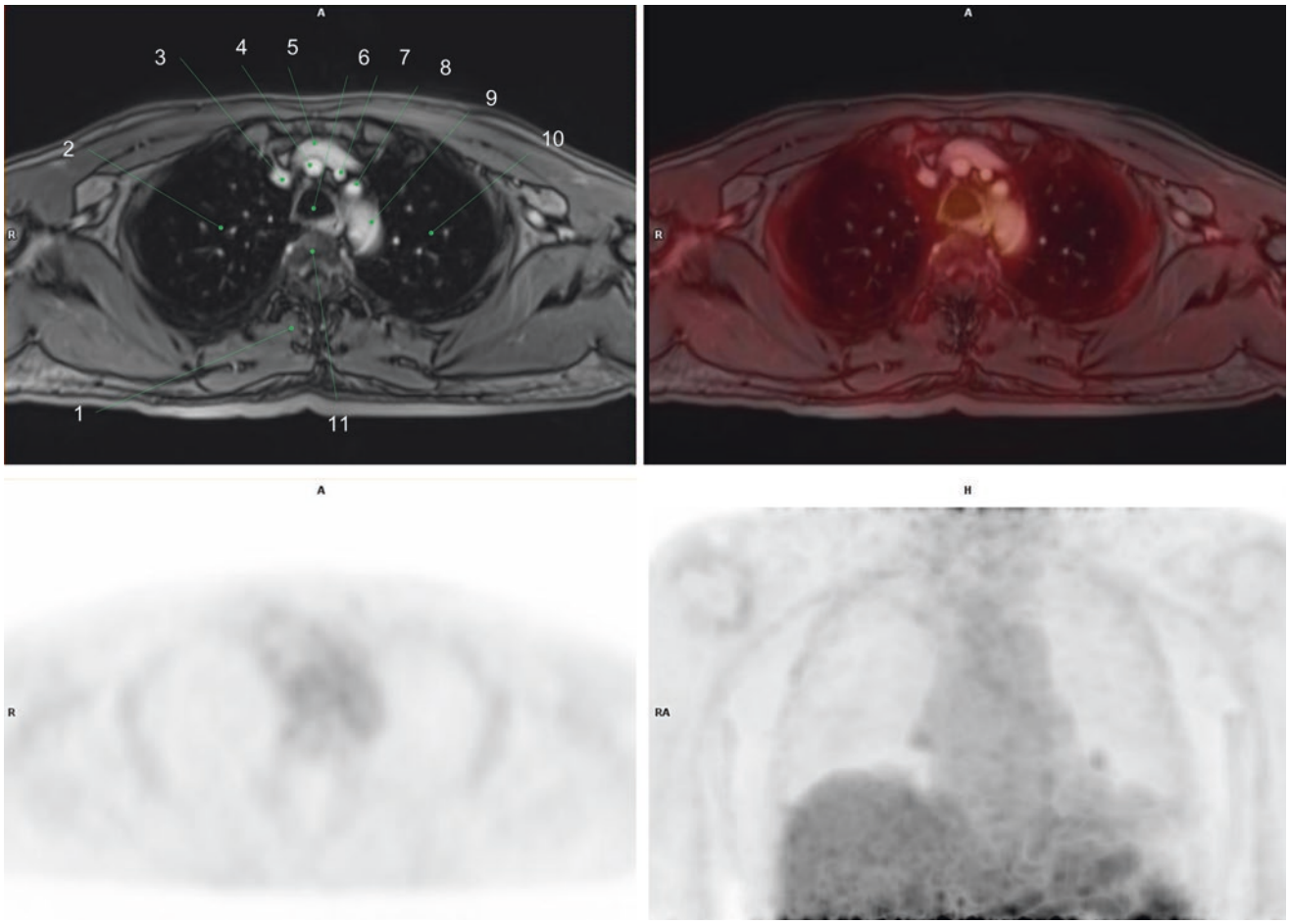

Fig. 17 1. Right erector spinae muscle
2. Lung RUL
3. Right brachiocephalic vein
4. Right brachiocephalic artery
5. Left brachiocephalic vein
6. Trachea
7. Left common carotid artery
8. Left subclavian artery
9. Aortic arch
10. Lung left upper lobe (LUL)
11. Thoracic vertebral body

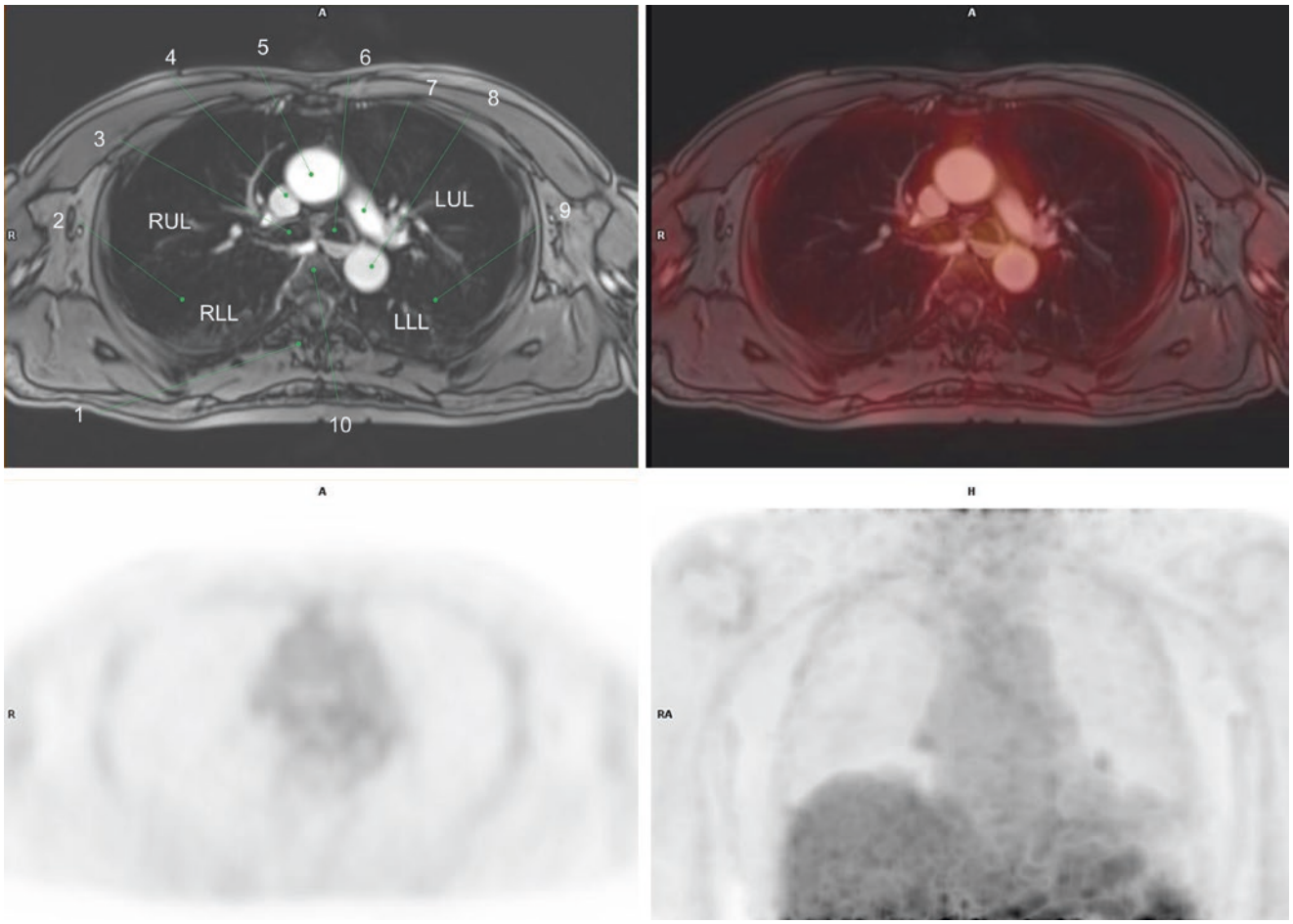

Fig. 18 1. Right erector spinae muscle
2. Right major fissure
3. Right main bronchus
4. Superior vena cava (SVC)
5. Ascending aorta
6. Left main bronchus
7. Left pulmonary artery
8. Descending aorta
9. Left lung fissure
10. Thoracic vertebral body

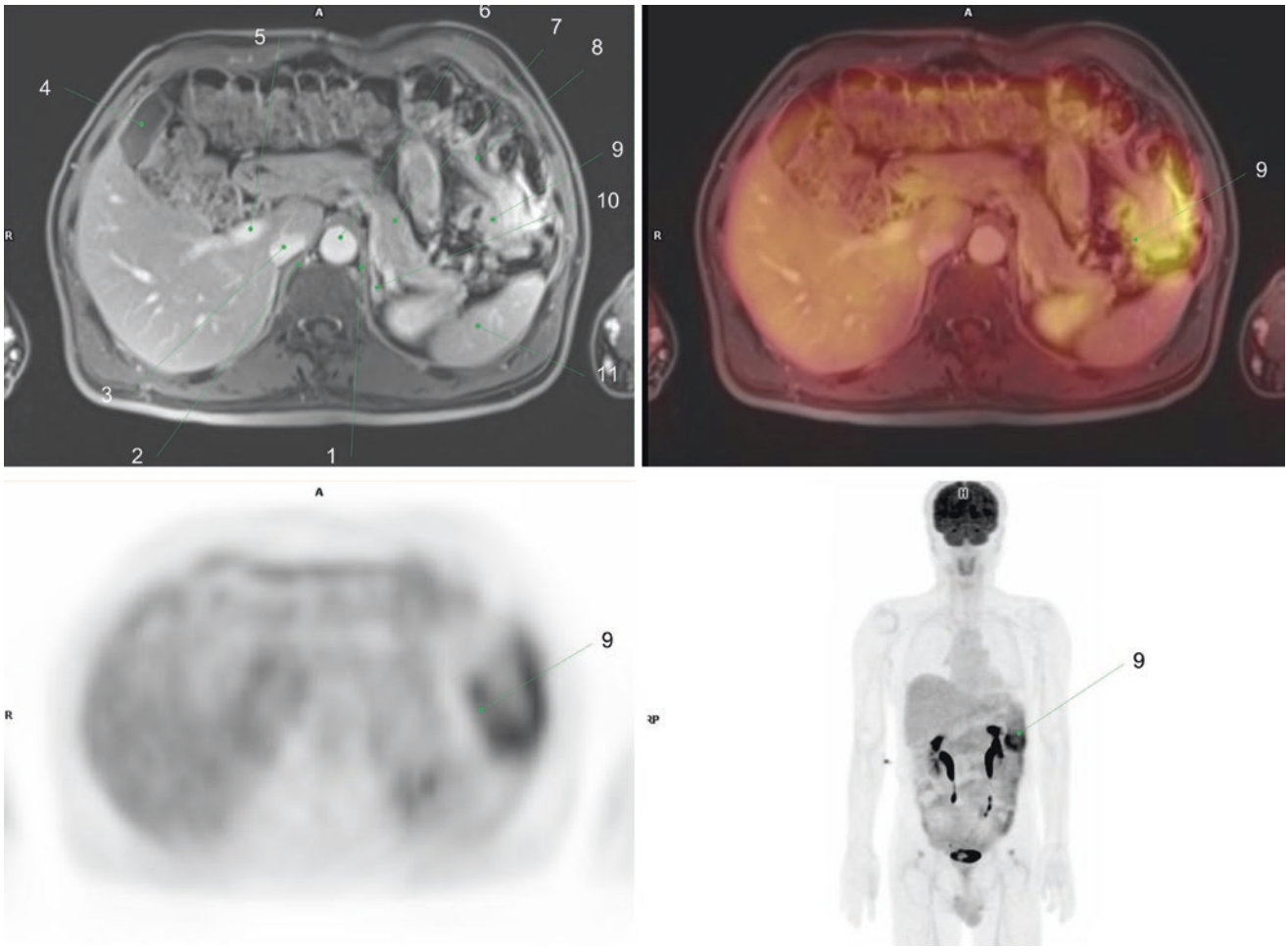

Fig. 19 1. Left diaphragmatic crura
2. Right diaphragmatic crura
3. Inferior vena cava
4. Gallbladder
5. Main portal vein
6. Abdominal aorta
7. Pancreas, body
8. Transverse colon
9. Descending colon
10. Left adrenal gland
11. Spleen

2.2 Case 2

Chest X-ray was performed on a 43-year-old woman due to a history of tuberculosis. A mediastinal mass was found, so evaluation with ^{18}F-FDG PET/MR was indicated. Images showed mild focal increased activity at an oval, well-defined mass in the anterior and superior mediastinum as the only finding. Posterior biopsy confirmed a low-grade thymoma, type A (Fig. 20) [29].

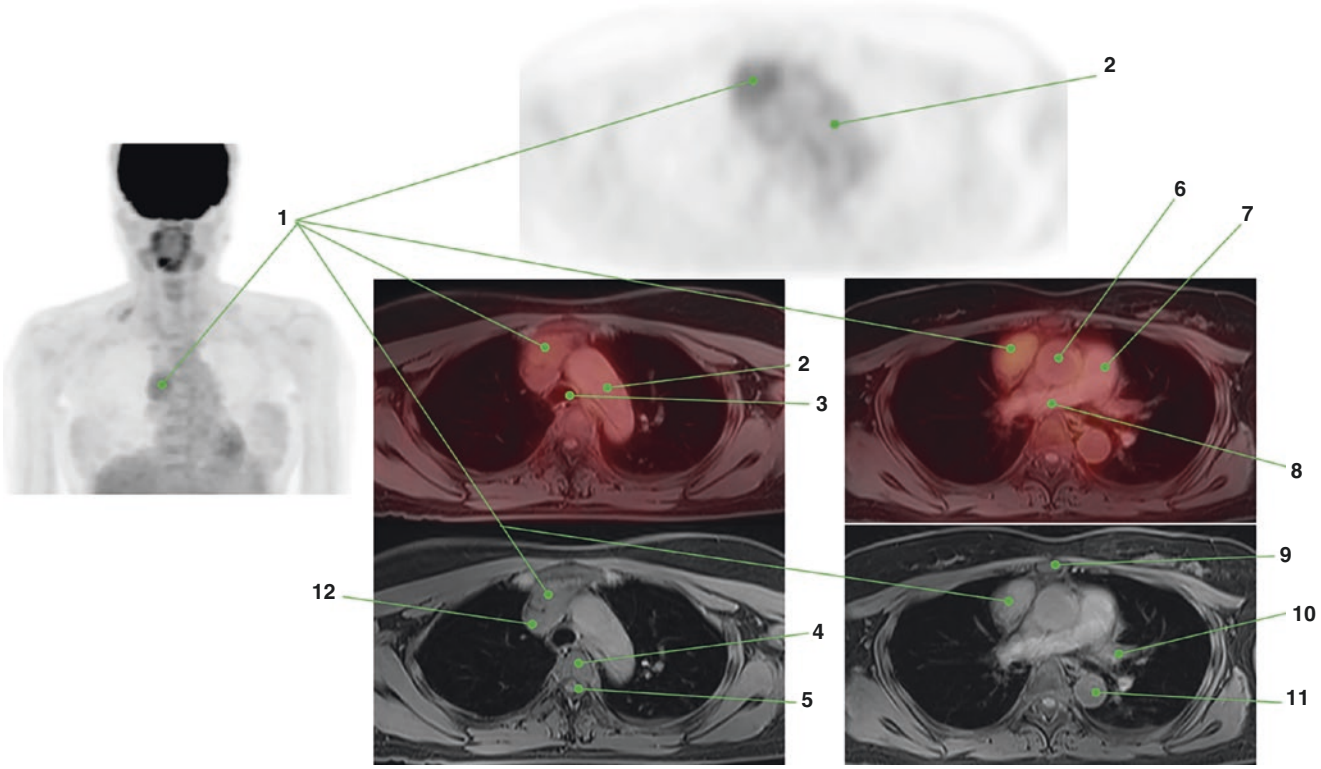

Fig. 20 1. Anterior mediastinal mass with mild, diffuse FDG uptake: low-grade thymoma
2. Aortic arch
3. Trachea
4. Thoracic vertebral body
5. Spinal cord
6. Ascending aorta
7. Main pulmonary artery
8. Right pulmonary artery
9. Sternum
10. Left pulmonary artery
11. Descending aorta
12. Superior vena cava

2.3 Case 3

A 39-year-old woman with family history of breast cancer (two sisters), who attended with a palpable mass in the right breast. Initial studies confirmed an invasive ductal carcinoma, so ^{18}F-FDG PET/MR was performed for staging. Images showed a metabolically active mass in the right breast with metastatic axillary lymph nodes in levels I and II. Intense FDG uptake was found in the left ventricular wall, probably related to poor fasting (Figs. 21 and 22).

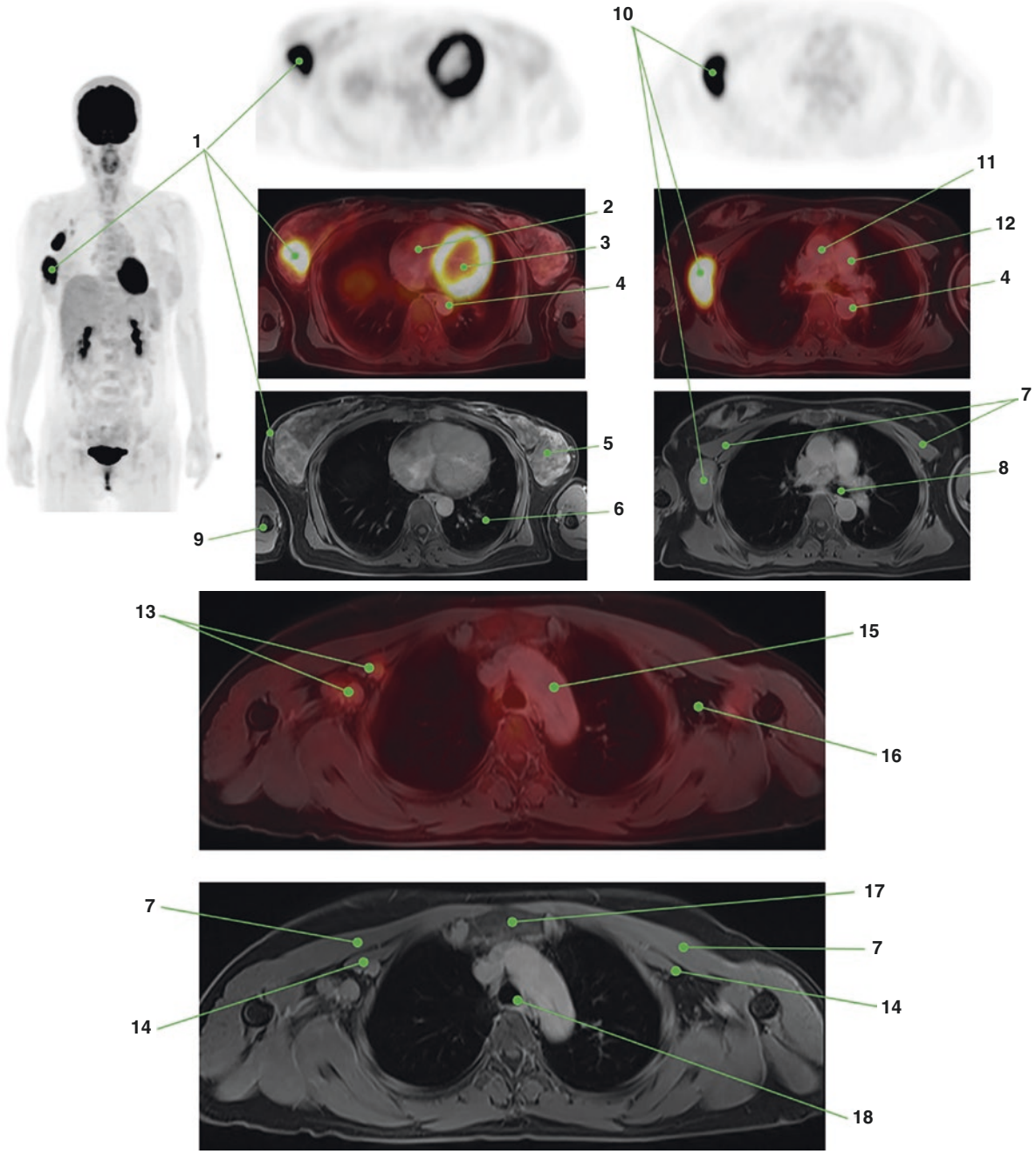

Figs. 21 and 22 1. Metabolically active tumor in the right breast
2. Right ventricle
3. Left ventricle (diffuse myocardial uptake)
4. Descending aorta
5. Left breast normal fibroglandular tissue
6. Lung, left lower lobe
7. Pectoralis major muscles
8. Left main bronchus
9. Right humeral shaft
10. Hypermetabolic LN metastasis, right axillary level I
11. Ascending aorta
12. Main pulmonary artery
13. Mild hypermetabolic LN metastasis, right axillary level II
14. Right pectoralis minor muscle
15. Aortic arch
16. Left axillary fossa
17. Sternum
18. Trachea

3 Abdomen and Pelvis

3.1 Case 1

A 60-year-old male patient with weight loss of 10 kg over 7 months. Endoscopy and biopsy confirmed the diagnosis of a gastric adenocarcinoma, so ^{18}F-FDG PET/MR was done for initial staging. Images showed a hypermetabolic lesion along the lesser curvature of the stomach, corresponding to the primary tumor. Another focal lesion with increased activity was found in the liver S5, which was confirmed as a liver metastasis [30]. As an incidental finding, a cystic lesion was observed in the left perineal soft tissues, which corresponded to a dermoid cyst (Figs. 23, 24, and 25).

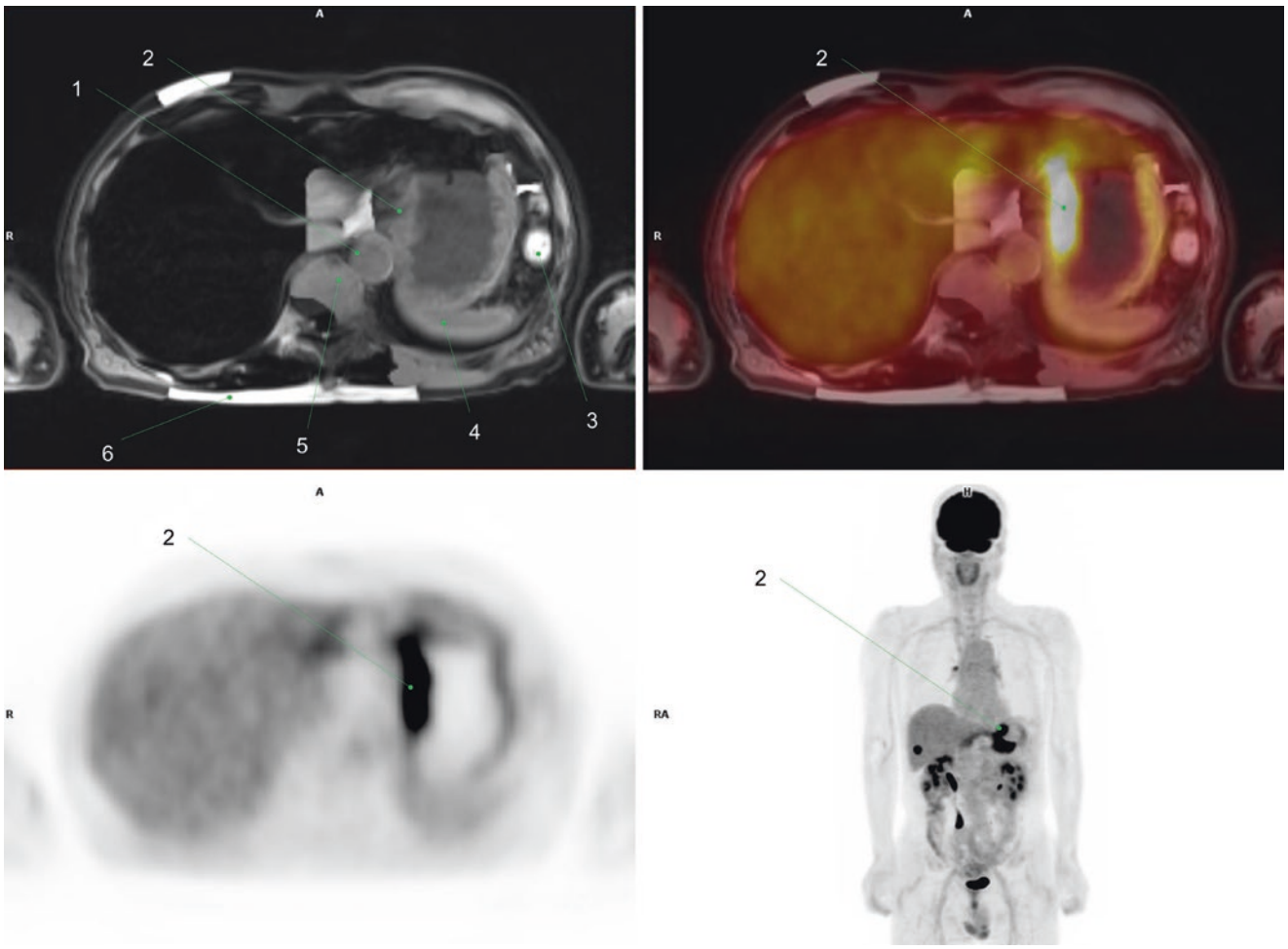

Fig. 23 1. Abdominal aorta
2. Metabolically active stomach cancer in lesser curvature
3. Splenic flexure of the colon
4. Spleen
5. Thoracic vertebral body
6. Magnetic resonance artifact

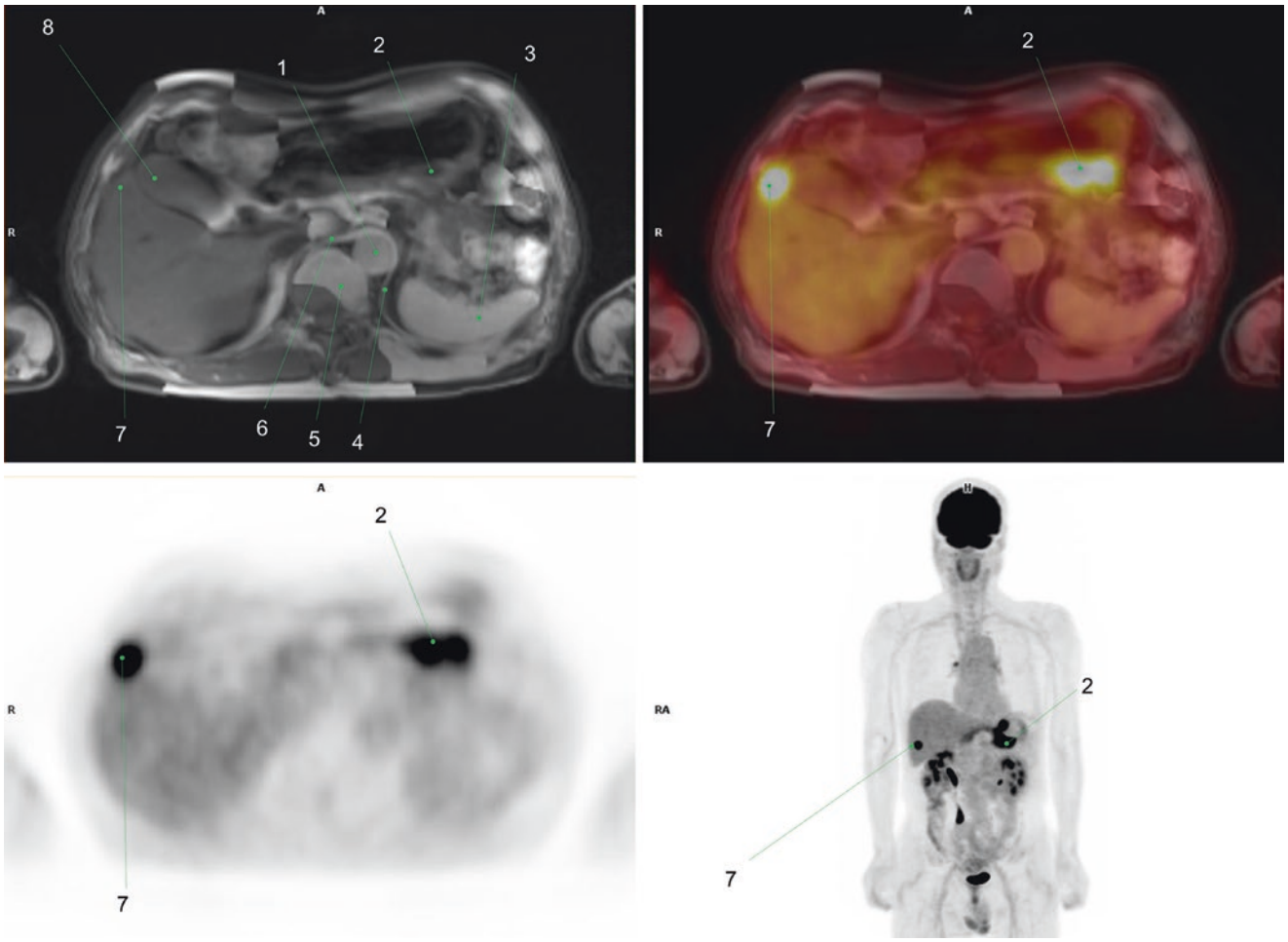

Fig. 24 1. Abdominal aorta
2. Metabolically active stomach cancer in lesser curvature
3. Spleen
4. Left diaphragmatic crura
5. Thoracic vertebral body
6. Right diaphragmatic crura
7. Metabolically active liver metastasis, S5
8. Gallbladder

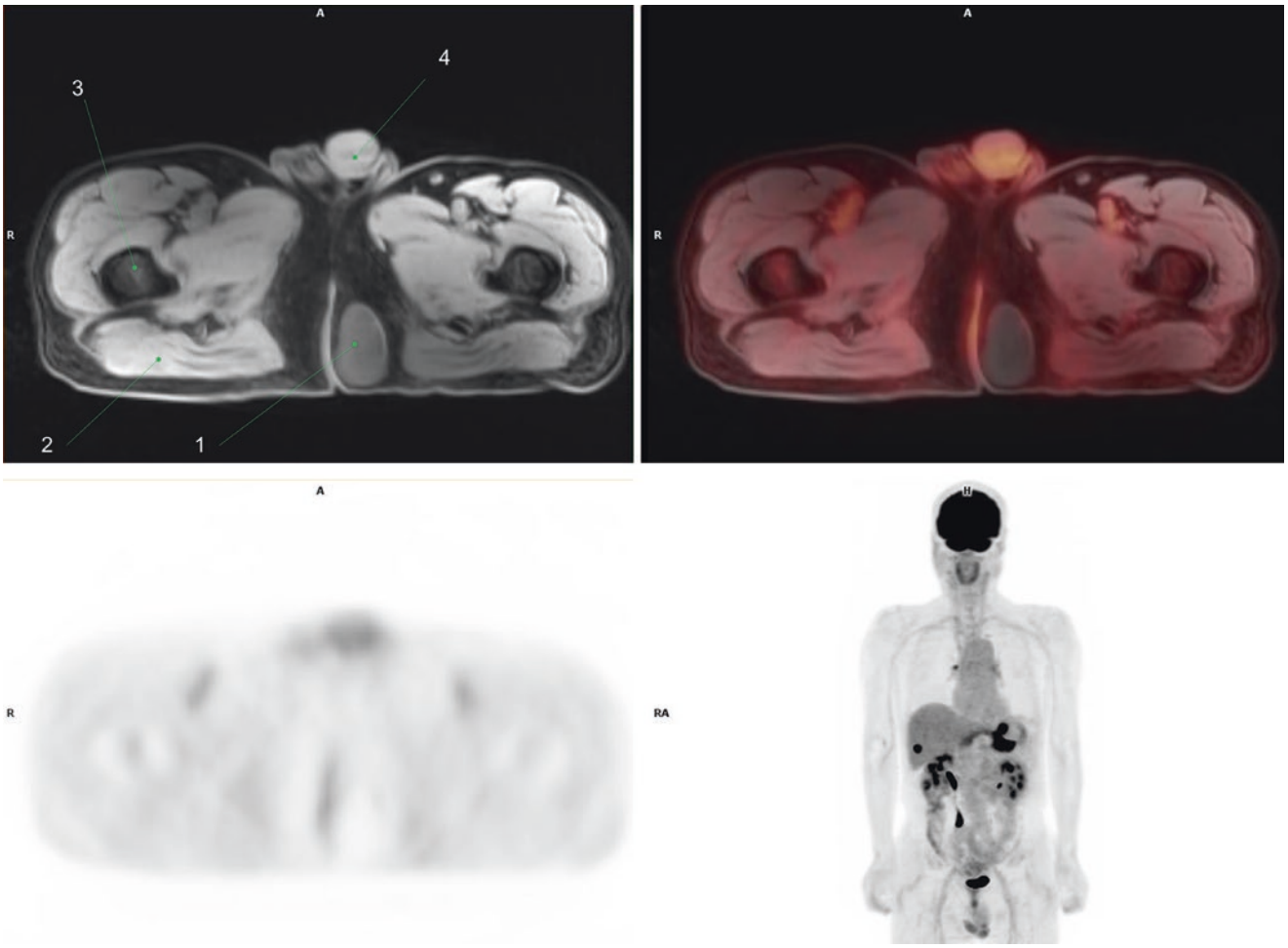

Fig. 25 1. Hypometabolic dermoid cyst in the left perineal area
2. Right gluteus maximus muscle
3. Right proximal femur
4. Penis

3.2 Case 2

A 69-year-old female patient with a history of right nephrectomy 10 years ago due to a renal liposarcoma, who presented with abdominal discomfort. Endoscopy was done and revealed a signet-ring cell gastric cancer, so ^{18}F-FDG PET/MR was done for initial staging. Focal increased activity was observed in the gastric antrum corresponding to the primary tumor, as well as in several enlarged lymph nodes (LNs) in the lesser curvature area, metastatic. Additionally, mild, diffuse, increased activity was found in fat-attenuating lesions at the retrocrural area and peritoneum, which were consistent with recurred liposarcoma (Figs. 26 and 27) [30, 31].

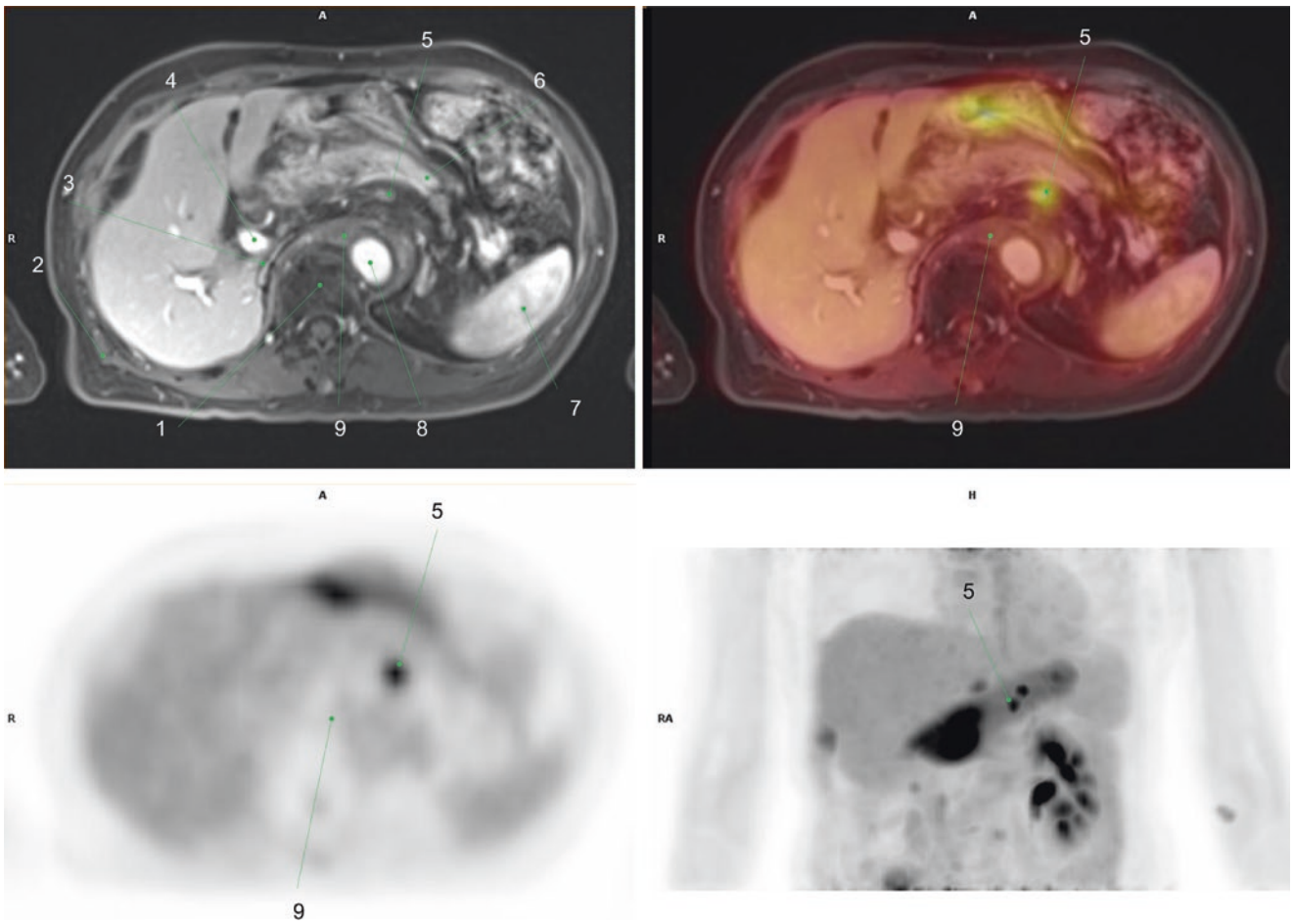

Fig. 26 1. Thoracic vertebral body
2. Right latissimus dorsi muscle
3. Collapsed inferior vena cava
4. Main portal vein
5. Hypermetabolic perigastric lymph node metastasis
6. Stomach, body
7. Spleen
8. Abdominal aorta
9. Mild, metabolically active recurred liposarcoma in retrocrural area

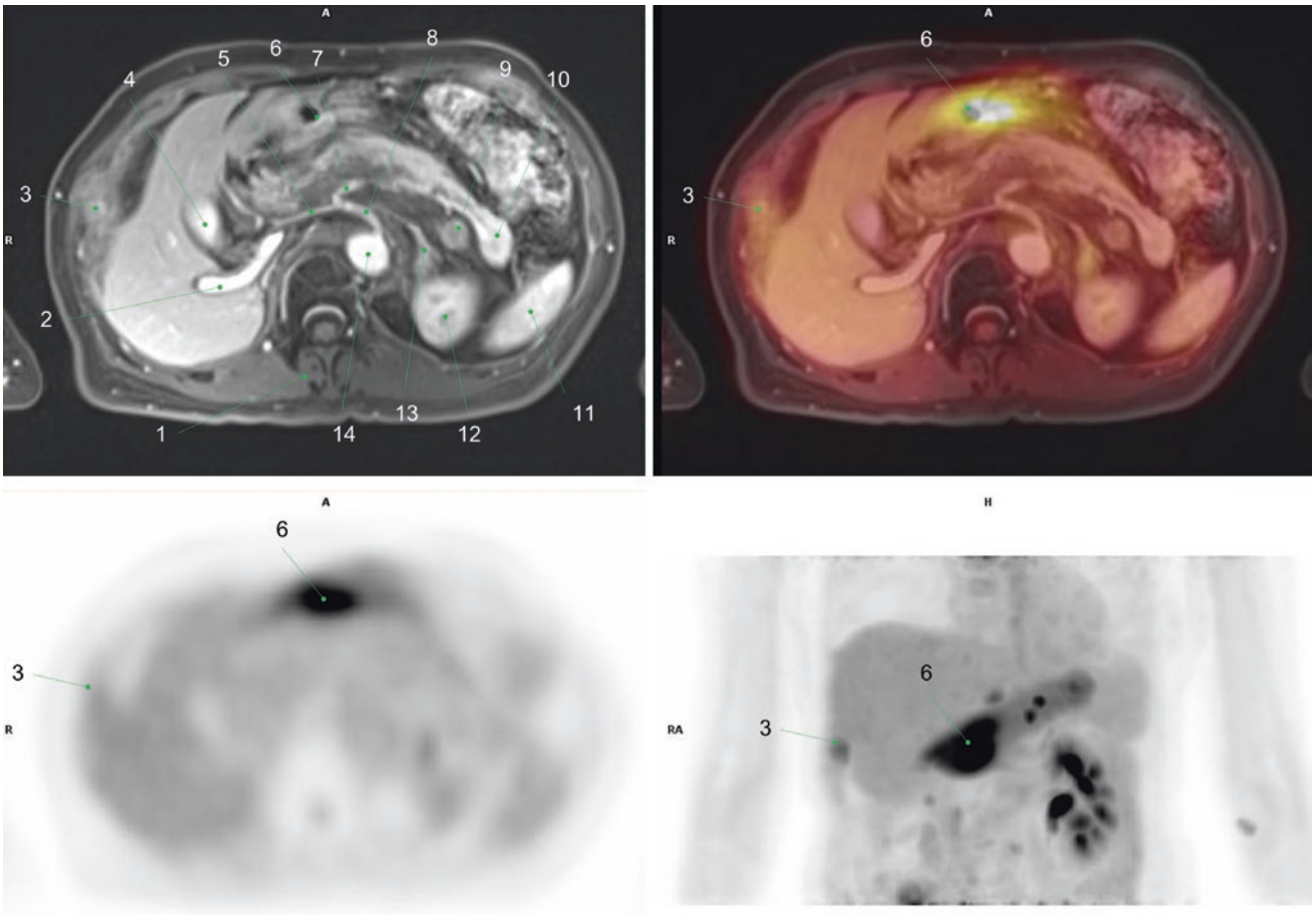

Fig. 27 1. Right paraspinal muscles
2. Right portal vein
3. Mild metabolically active peritoneal lesion, corresponding to recurred liposarcoma
4. Gallbladder
5. Common hepatic artery
6. Metabolically active stomach cancer, antrum
7. Splenic artery
8. Celiac trunk
9. Mild metabolically active peritoneal lesion, corresponding to recurred liposarcoma
10. Pancreatic tail
11. Spleen
12. Left kidney, inferior pole
13. Left adrenal gland
14. Abdominal aorta

3.3 Case 3

A 74-year-old male patient with persistent abdominal pain during the last 3 months. Ultrasound was performed finding a suspicious mass in the gallbladder, so he was referred for ^{18}F-FDG PET/MR evaluation. Images showed a marked hypermetabolic mass in the gallbladder fundus with intermediate, heterogeneous signal intensity in T2WI, consistent with a primary adenocarcinoma. Hypermetabolic liver invasion was excluded, as well as distant metastases (Fig. 28) [32].

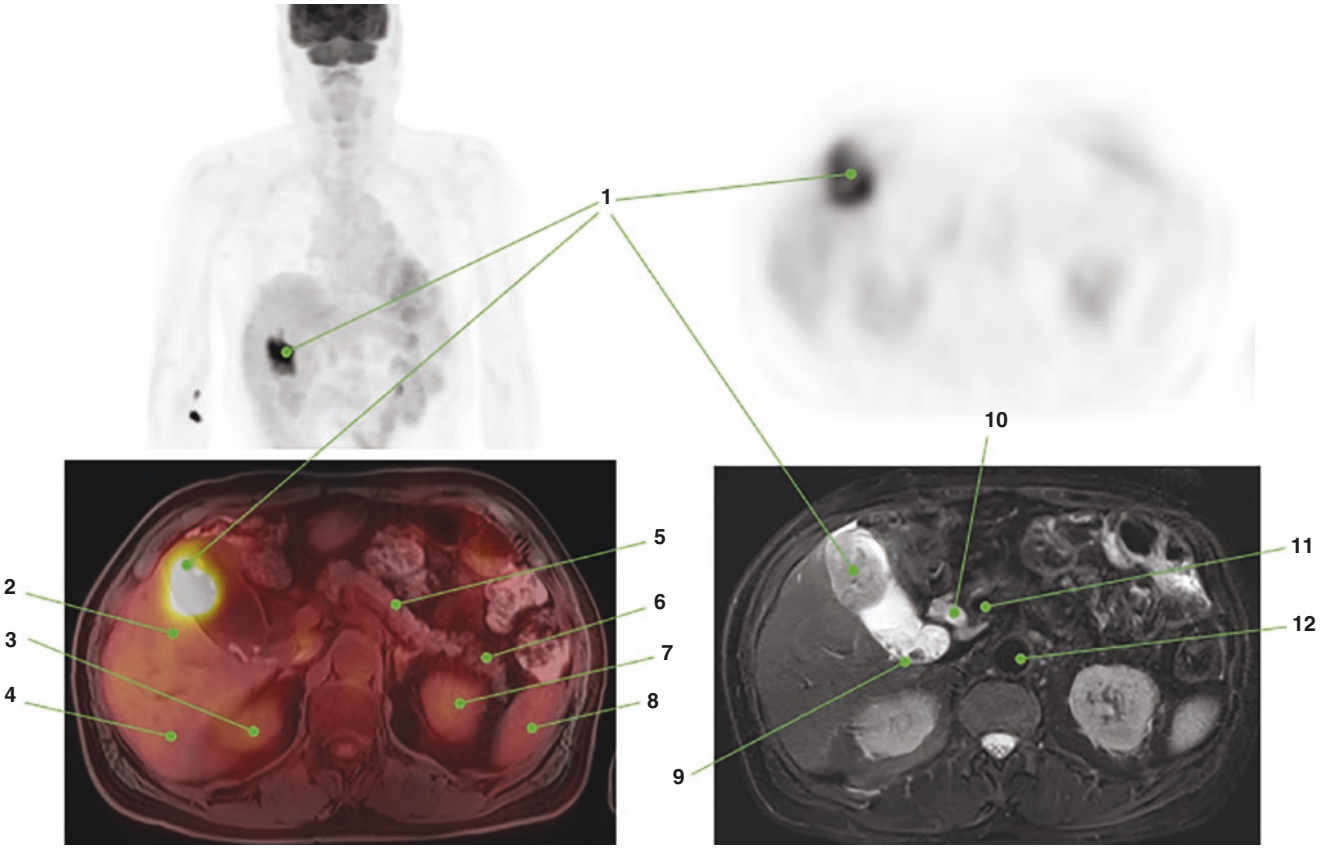

Fig. 28 1. Metabolically active gallbladder tumor
2. Liver segment 5
3. Right kidney, superior pole
4. Liver segment 6
5. Pancreatic body
6. Pancreatic tail
7. Left kidney, superior pole
8. Spleen, inferior pole
9. Gallbladder stones
10. Cystic duct
11. Portal vein
12. Abdominal aorta

3.4 Case 4

A 42-year-old patient, hepatitis B virus carrier, underwent abdominal ultrasonography for a routine health check. A liver mass was found, so ^{18}F-FDG PET/MR was indicated for further evaluation. Images showed moderate focal increased activity in the liver S7 at a lobulated mass with arterial enhancement and delayed washout, consistent with a hepatocarcinoma. The patient underwent right liver posterior sectionectomy and the final diagnosis was combined hepatocellular carcinoma (HCC) and cholangiocarcinoma (CCA), which explains the high FDG uptake of the lesion (Fig. 29) [33].

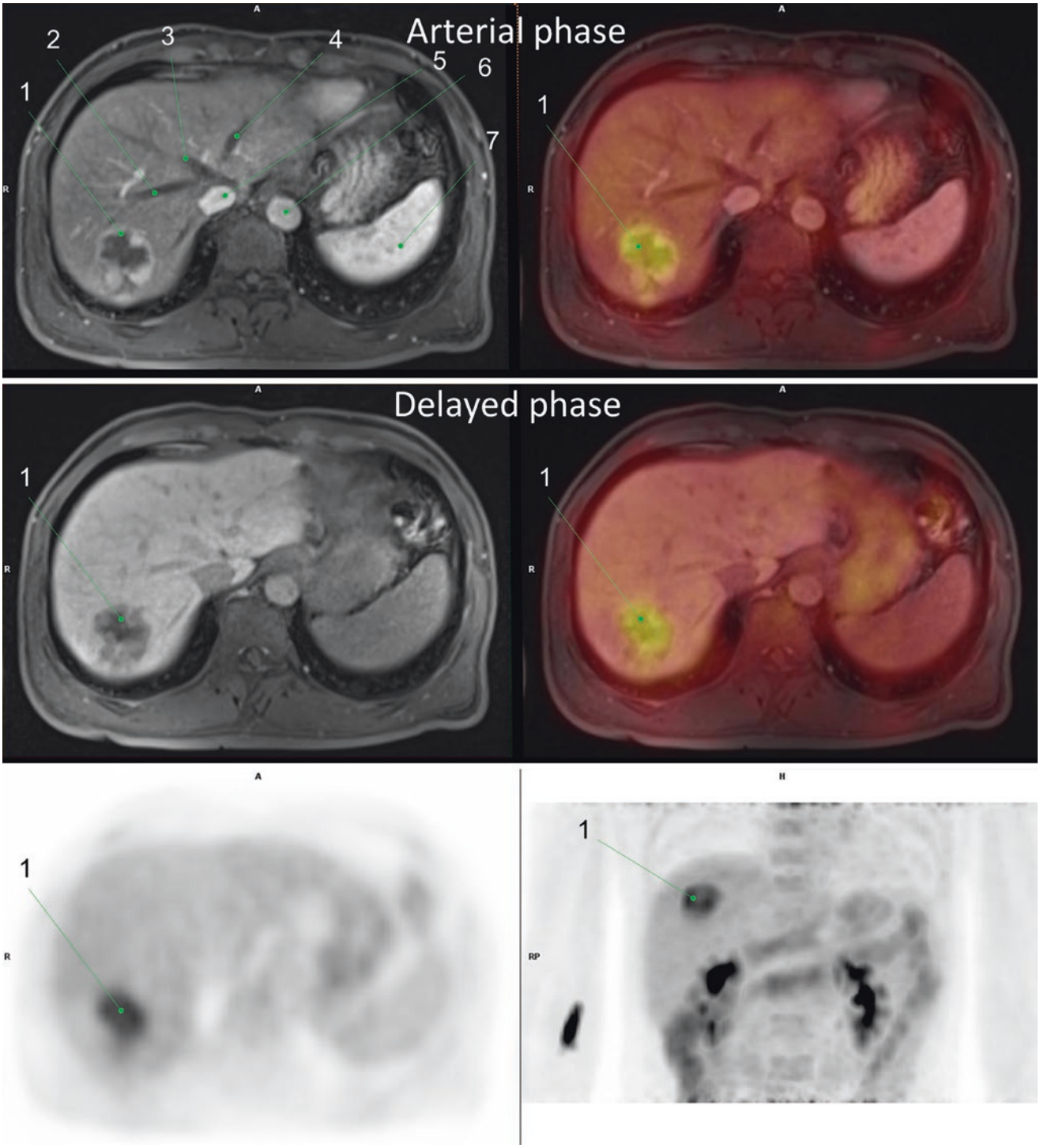

Fig. 29 1. Metabolically active liver tumor with heterogeneous arterial enhancement and delayed washout
2. Right hepatic vein
3. Middle hepatic vein
4. Left hepatic vein
5. Inferior vena cava
6. Abdominal aorta
7. Spleen

3.5 Case 5

A 58-year old patient with a history of a rare liver schwannoma, who presented with abdominal mass. ^{18}F-FDG PET/MR was done to search for malignant transformation. Images showed mild focal increased activity at the solid component of a complex irregular mass in the liver dome, which also showed heterogeneous signal intensity and delayed enhancement. Excisional biopsy was done, and a schwannoma with malignant transformation was confirmed (Figs. 30 and 31) [34].

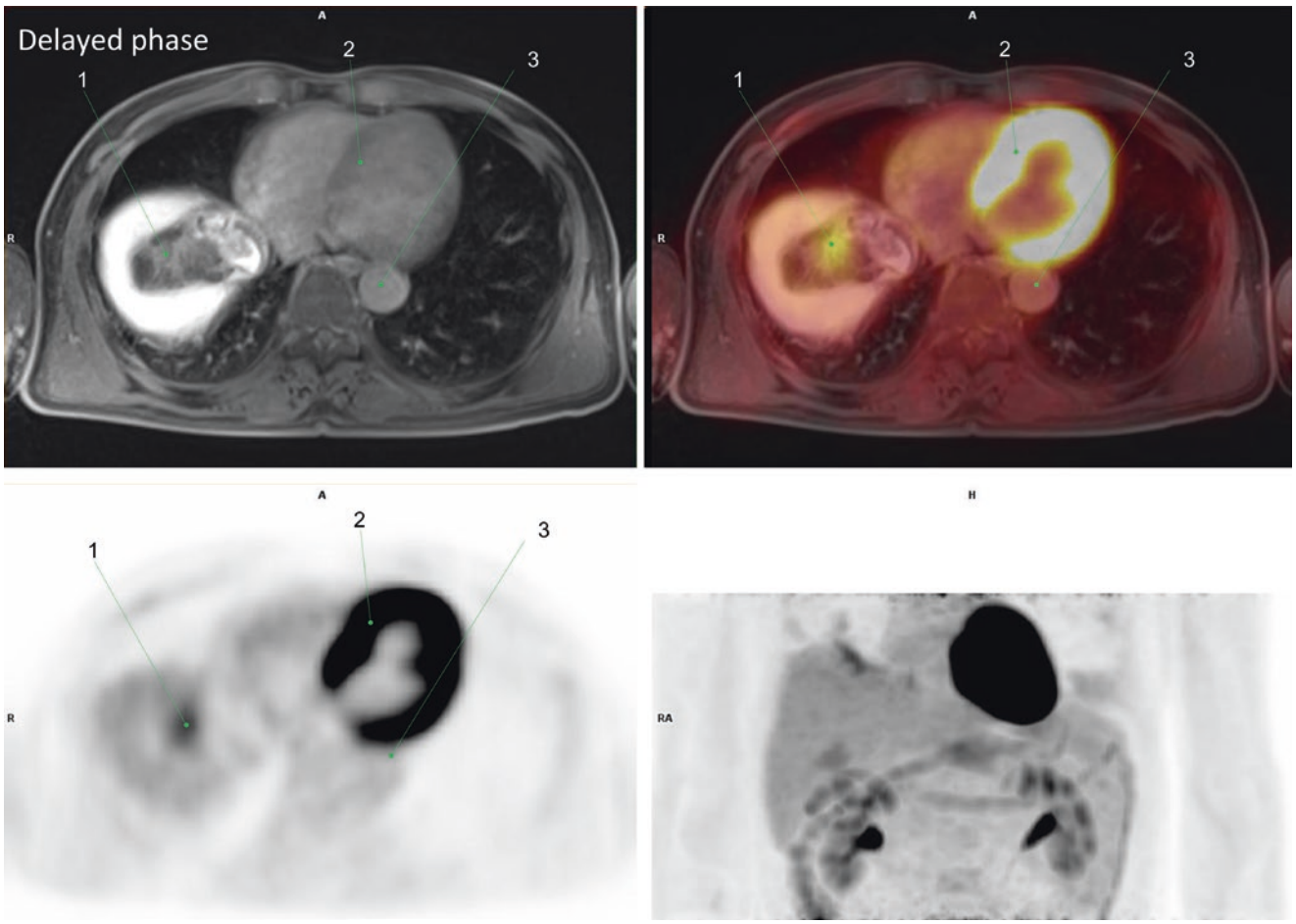

Fig. 30 1. Metabolically active liver schwannoma with delayed enhancement and central necrosis
2. Physiologic myocardial uptake, left ventricle
3. Descending aorta

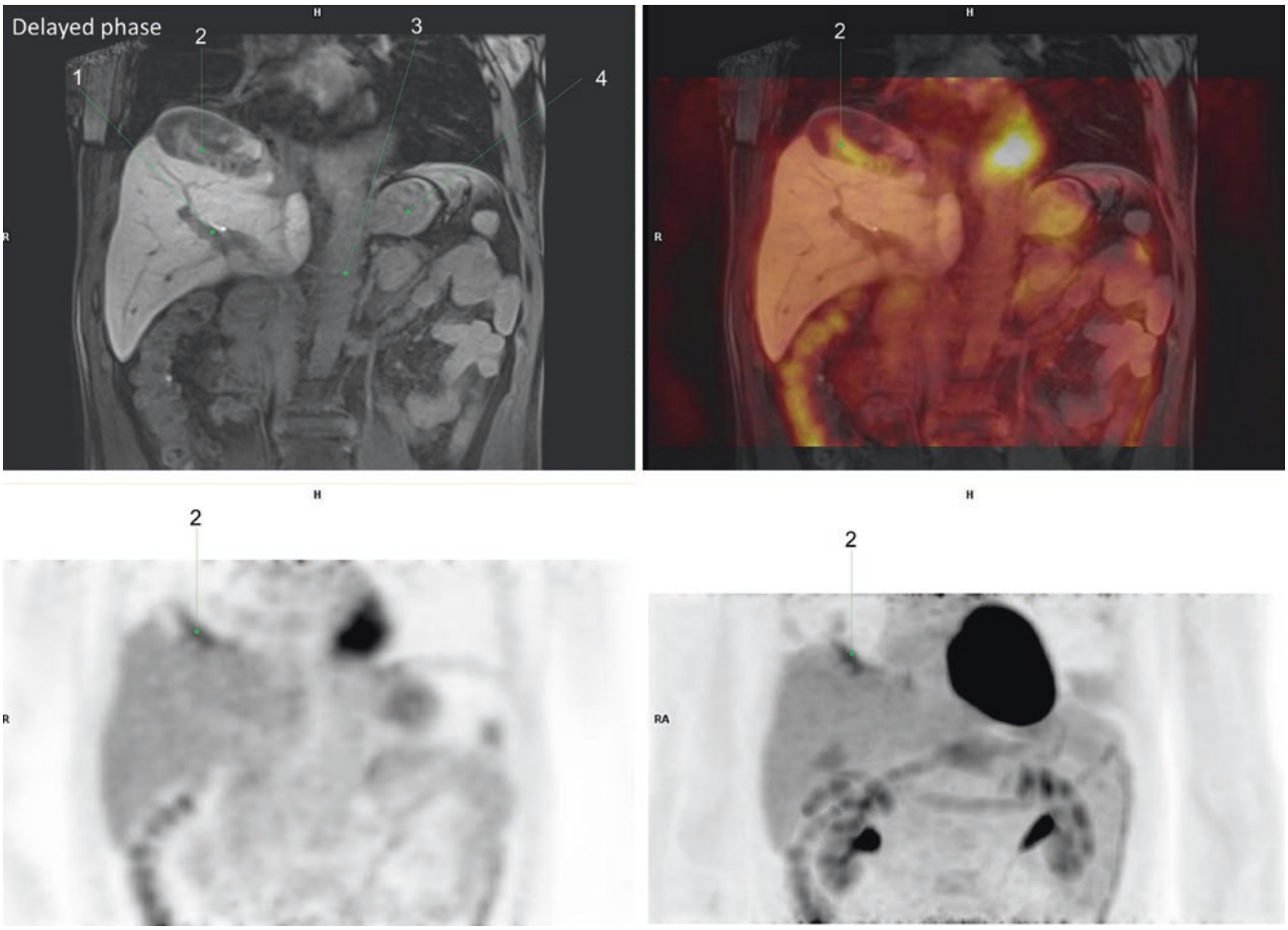

Fig. 31 1. Main portal vein
2. Metabolically active liver schwannoma with delayed enhancement and central necrosis
3. Abdominal aorta
4. Stomach

3.6 Case 6

A 72-year-old woman with recurrent abdominal pain, weight loss, and fever. Initial studies confirmed the diagnosis of a pancreatic tail adenocarcinoma and due to the suspicion of liver metastases, ^{18}F-FDG PET/MR was indicated. Images showed focal increased activity in a hypovascular pancreatic tail mass consistent with the primary tumor; due to the location of the lesion, no dilation of the main pancreatic duct was observed. Additionally, multiple focal hypermetabolic liver lesions were identified in the right hepatic lobe, corresponding to metastasis (Fig. 32) [32].

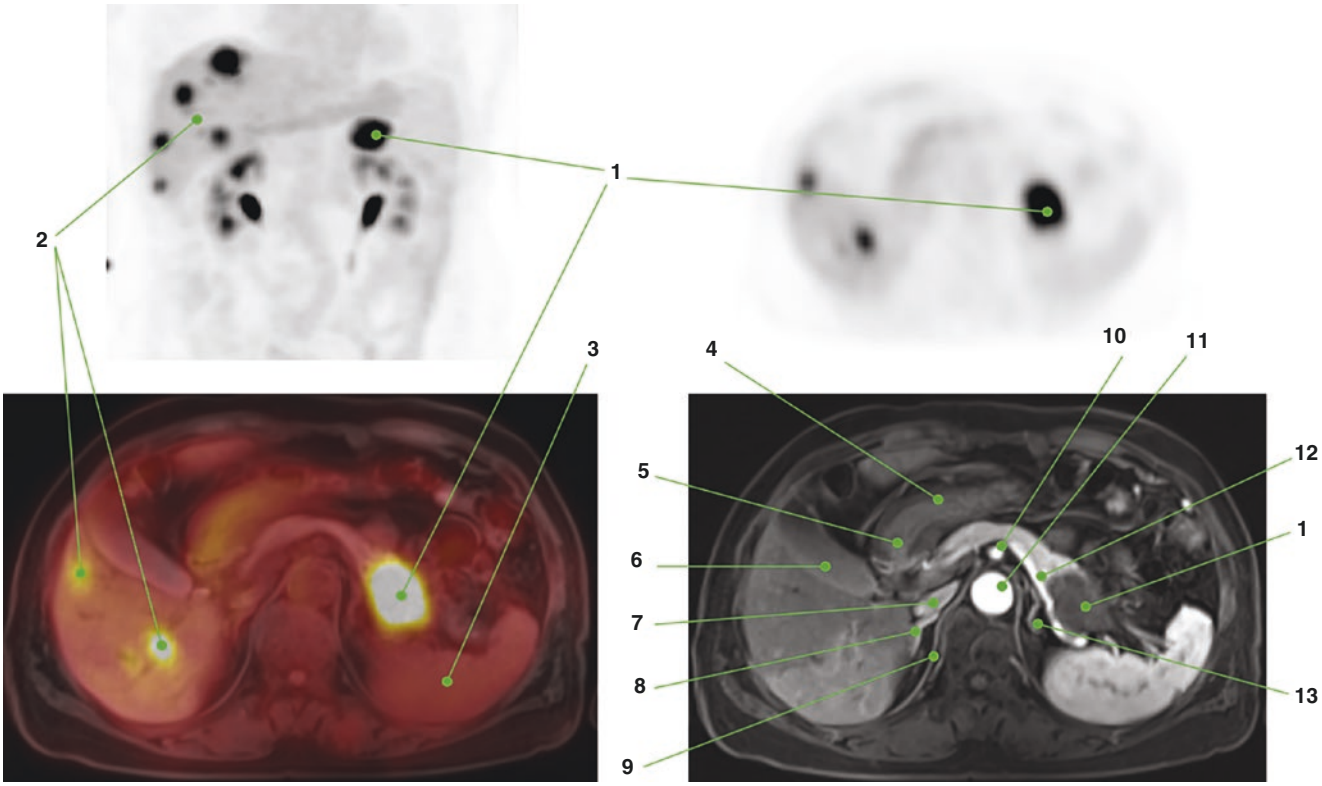

Fig. 32 1. Metabolically active pancreatic tail tumor
2. Multiple hypermetabolic liver metastasis in the right hepatic lobe
3. Spleen
4. Gastric antrum
5. Pylorus
6. Gallbladder
7. Inferior vena cava
8. Right adrenal gland
9. Right diaphragmatic crus
10. Superior mesenteric artery
11. Abdominal aorta
12. Splenic artery
13. Left adrenal gland

3.7 Case 7

A 69-year-old woman with persistent abdominal pain and distention. Abdominal ultrasound showed biliary dilatation and a suspicious pancreatic mass. ^{18}F-FDG PET/MR was done finding a hypermetabolic mass in the pancreatic head with dilatation of the main pancreatic duct and atrophy of the distal pancreatic parenchyma, typical findings of an adenocarcinoma at this location. No metabolically active metastases were detected (Fig. 33) [32].

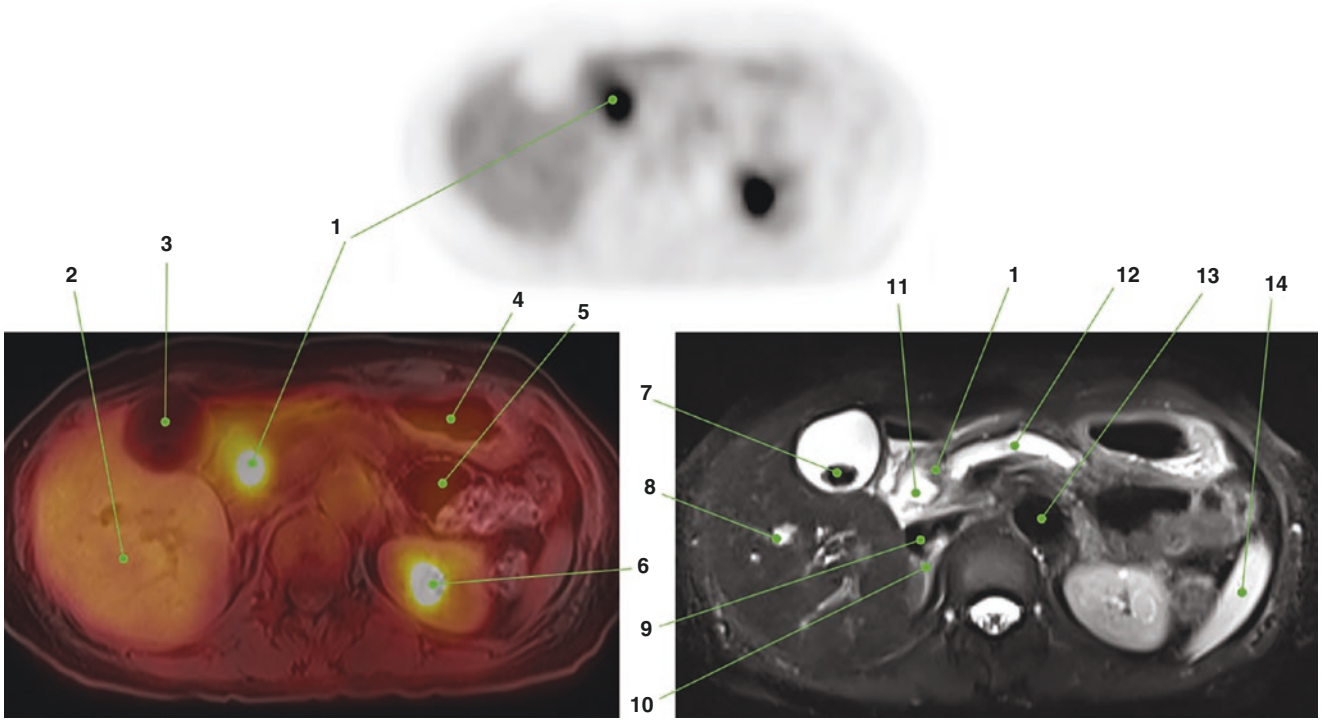

Fig. 33 1. Marked metabolically active pancreatic head adenocarcinoma
2. Right hepatic lobe
3. Gallbladder
4. Stomach
5. Transverse colon
6. Left kidney, upper pole
7. Gallbladder stone
8. Intrahepatic biliary duct dilation
9. Inferior vena cava
10. Right adrenal gland
11. Common bile duct, distal portion
12. Main pancreatic duct dilatation
13. Abdominal aorta
14. Spleen

3.8 Case 8

An 80-year-old woman with bloating, heaviness, and abdominal distention. Endoscopy was done finding a prominent mass in the stomach, so ^{18}F-FDG PET/MR was performed. Images showed slight and diffuse increased activity in a prominent rounded and very well-defined mass at the stomach, with heterogeneous contrast enhancement due to the presence of necrosis. Surgical resection of the lesion was done, and the final diagnosis was a low-grade gastrointestinal stromal tumor (GIST), as suspected (Fig. 34) [35].

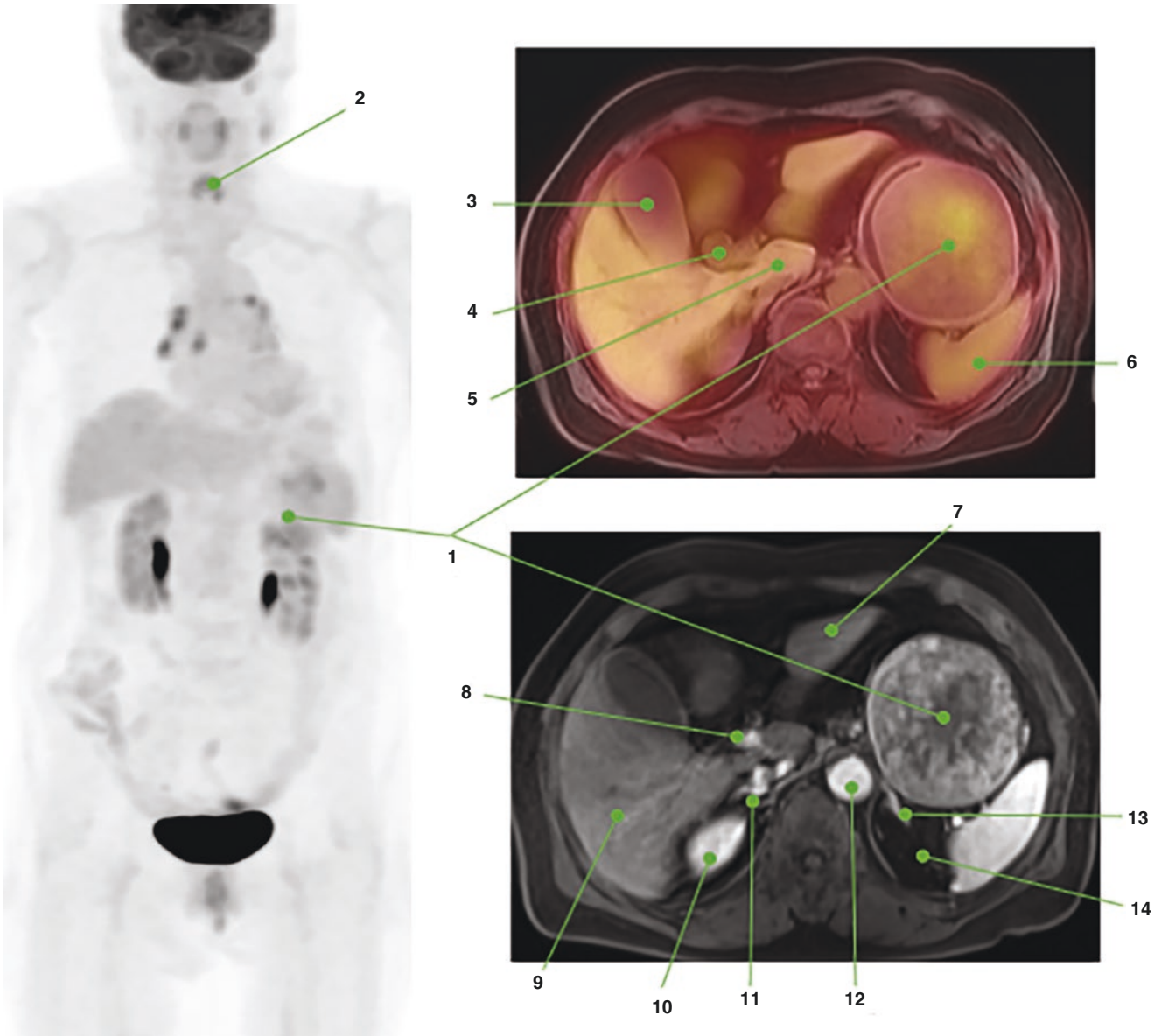

Fig. 34 1. Metabolically active gastric GIST
2. Physiologic activity in the vocal cords
3. Gallbladder
4. Common bile duct
5. Caudate lobe
6. Spleen
7. Left hepatic lobe, segment 3 (III)
8. Common hepatic artery
9. Right hepatic lobe, segment 6 (VI)
10. Right kidney, inferior pole
11. Right adrenal gland
12. Abdominal aorta
13. Left adrenal gland
14. Left perirenal space

3.9 Case 9

A 59-year-old man with a 3-month history of gradually increasing rectal bleeding. Colonoscopy was performed finding a circumferential mass in the sigmoid colon, consistent with an adenocarcinoma. During initial staging, liver metastases were suspected, so ^{18}F-FDG PET/MR was performed. Images show intense FDG uptake in the sigmoid colon at the primary tumor, without hypermetabolic pelvic or retroperitoneal lymph nodes. However, multiple metabolically active liver metastases were identified in both lobes (Fig. 35) [36].

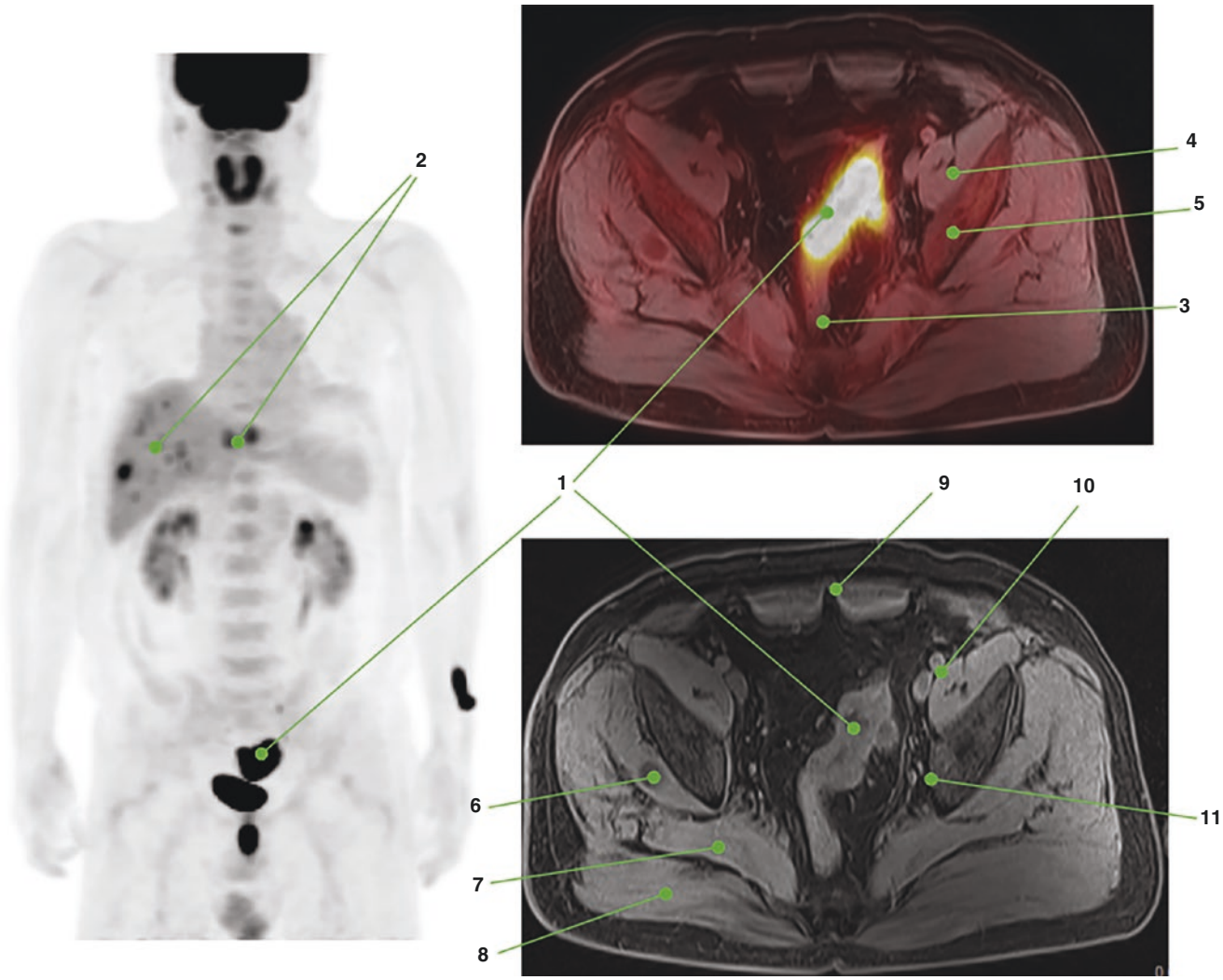

Fig. 35 1. Metabolically active sigmoid colon adenocarcinoma
2. Multiple hypermetabolic liver metastases in both lobes
3. Rectosigmoid junction
4. Left iliopsoas muscle
5. Left iliac bone
6. Right gluteus minimus muscle
7. Right gluteus medius muscle
8. Right gluteus maximus muscle
9. Rectus abdominis muscles
10. Left external iliac vessels
11. Left internal iliac vessels

3.10 Case 10

A 74-year-old man with prostate cancer, Gleason 8 (4 + 4), diagnosed with multiparametric MRI and transrectal biopsy. ^{18}F-Choline PET/CT was performed for staging and images showed focal increased activity in the primary tumor at the left peripheral zone of the prostate gland with exophytic extension to the recto-prostatic angle and probable involvement of the neurovascular bundle (see MRI correlation). Also, two different metastatic bone lesions were observed, one slightly hypermetabolic, ill-defined intramedullary lesion in the right ischial tuberosity, and other cortical sclerotic lesion in the left ischial tuberosity without FDG uptake (Fig. 36) [15].

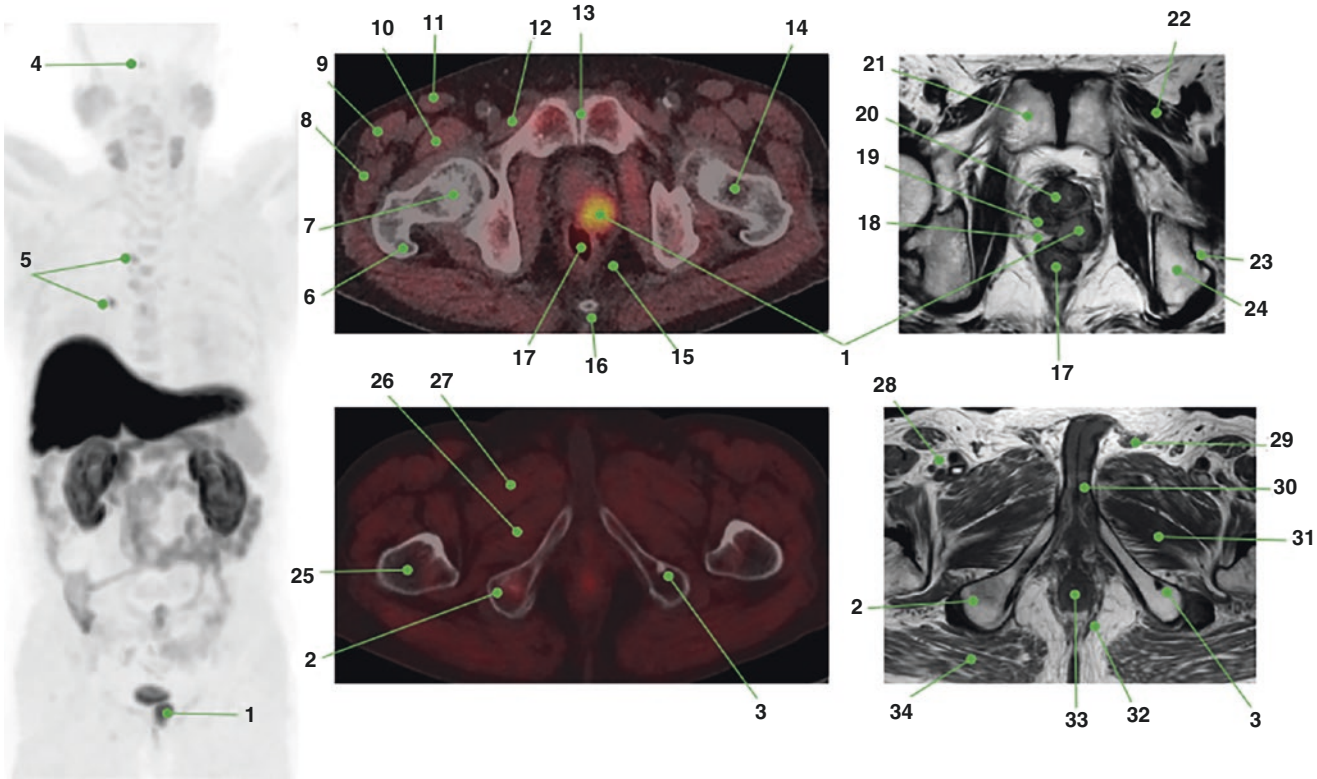

Fig. 36 1. Focal increased activity at primary prostate cancer in the left peripheral zone
2. Mild uptake in medullary bone metastasis
3. Sclerotic cortical bone metastasis without uptake
4. Pituitary gland
5. Mild metabolically active inflammatory lymph nodes
6. Right femur, greater trochanter
7. Right femoral head
8. Right vastus lateralis muscle
9. Right tensor fascia latae muscle
10. Right rectus femoris muscle
11. Right sartorius muscle
12. Right pectineus muscle
13. Pubic symphysis
14. Left femoral neck
15. Perirectal fat
16. Coccix
17. Rectum
18. Right recto-prostatic angle
19. Prostate gland, right peripheral zone
20. Prostate gland, transitional zone
21. Right pubic bone
22. Left pectineus muscle
23. Ischial tuberosity, cortical bone (T2WI hypointense)
24. Ischial tuberosity, medullary bone (T2WI hyperintense)
25. Right proximal femoral shaft
26. Right adductor magnus muscle
27. Right adductor brevis muscle
28. Right femoral vessels
29. Left spermatic cord
30. Base of penis
31. Left adductor magnus muscle
32. Left pubococcygeus muscle
33. Anal canal
34. Right gluteus maximus muscle

3.11 Case 11

A 41-year-old woman referred for ^{18}F-FDG PET/MR due to abnormal findings on her annual general checkup. At colonoscopy, a lobulated subepithelial mass was found on the anterior aspect of the rectum; there was no definite abnormal increased activity in the lesion, which was later confirmed as a leiomyoma. Also, a complex right adnexal cystic mass without abnormal increased FDG uptake was observed; the final diagnosis was a hemorrhagic cyst (Figs. 37 and 38) [36].

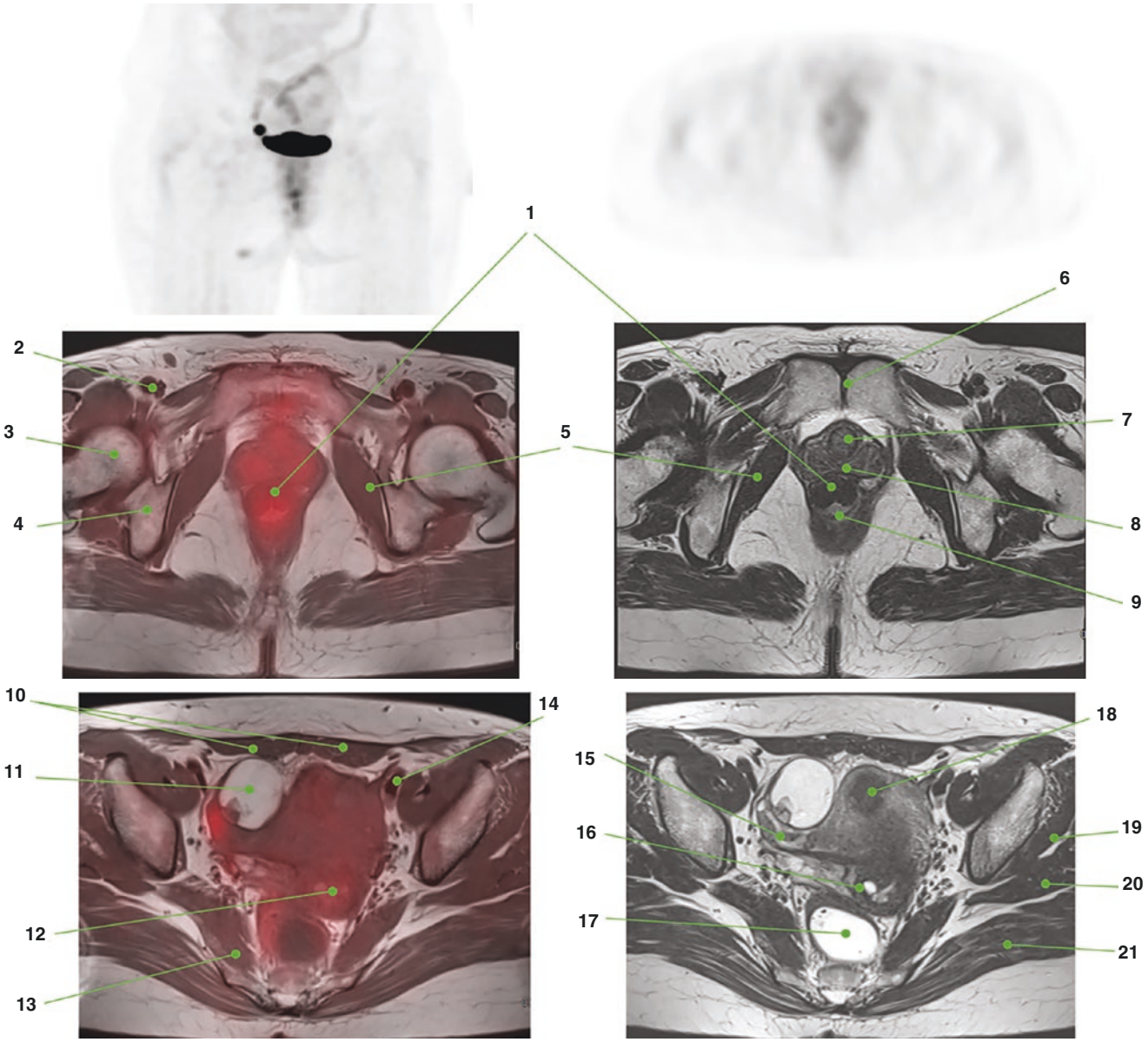

Figs. 37 and 38 1. Anterior rectal wall leiomyoma
2. Right femoral vessels
3. Right femoral head
4. Right acetabulum
5. Internal obturator muscles
6. Pubic symphysis
7. Urethra
8. Vagina
9. Rectal lumen
10. Rectus abdominis muscles
11. Complex right adnexal cyst with posterior papillary projection
12. Cervix
13. Right ischio-coccygeus muscle
14. Left external iliac vessels
15. Right fallopian tube
16. Nabothian cyst in the cervix
17. Proximal rectum
18. Uterine myoma
19. Gluteus minimus muscle
20. Gluteus medius muscle
21. Gluteus maximus muscle

3.12 Case 12

A 59-year-old female patient with an abnormal Pap smear test. Cervical punch biopsy revealed a squamous cell carcinoma, so ^{18}F-FDG PET/MR was done for initial staging. Images showed a hypermetabolic mass in the uterine cervix involving the posterior upper vaginal wall, but not the parametrium. No abnormal hypermetabolic lesions suggesting metastasis were found (Figs. 39 and 40) [37, 38].

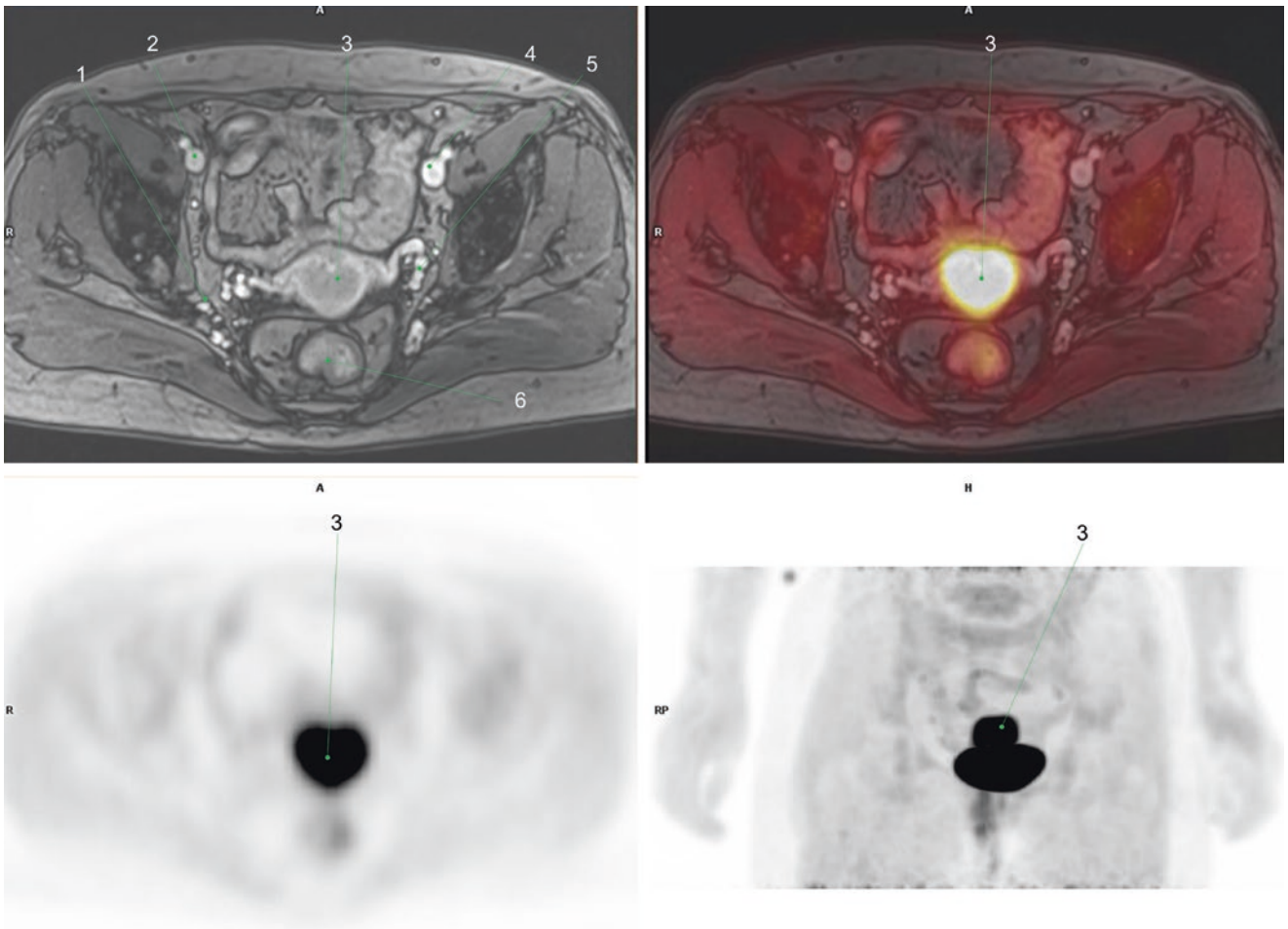

Fig. 39 1. Right internal iliac vessels
2. Right external iliac vessels
3. Metabolically active cervical cancer
4. Left external iliac vessels
5. Left internal iliac vessels
6. Rectum

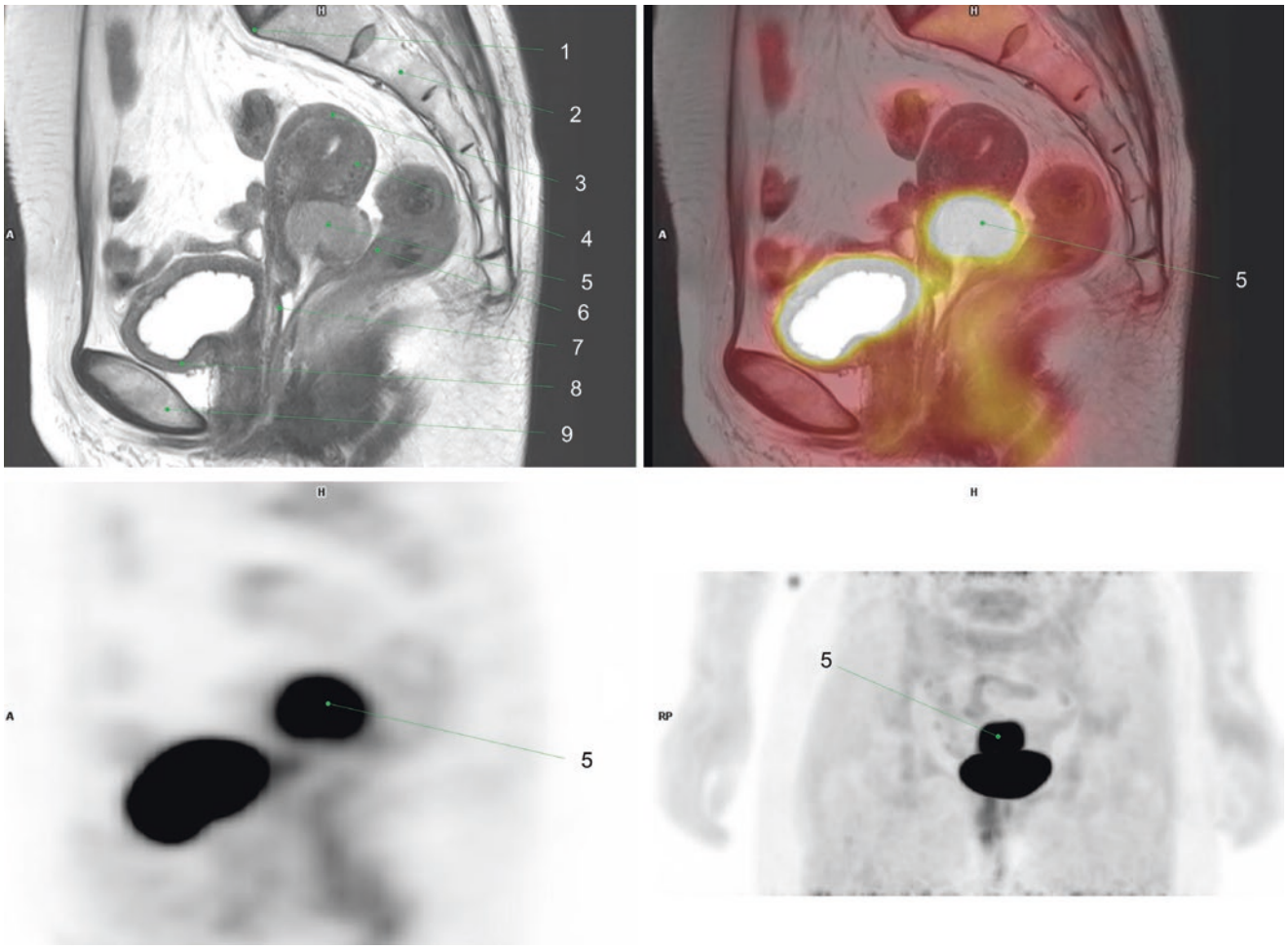

Fig. 40 1. Sacral promontory
2. Sacrum, S2
3. Uterine fundus
4. Uterine body (myometrium)
5. Metabolically active cervical cancer involving posterior vaginal fornix
6. Rectum
7. Vagina
8. Urinary bladder
9. Pubic bone

3.13 Case 13

A 41-year-old female patient with vaginal bleeding. Cervical biopsy revealed a squamous cell carcinoma, so ^{18}F-FDG PET/MR was done for staging. Images showed a hypermetabolic uterine cervical mass involving the parametrium and the lower third of the vagina. Hypermetabolic and enlarged metastatic LNs were also found in both the external iliac and left internal and perirectal areas (Figs. 41, 42, 43, and 44) [37, 38].

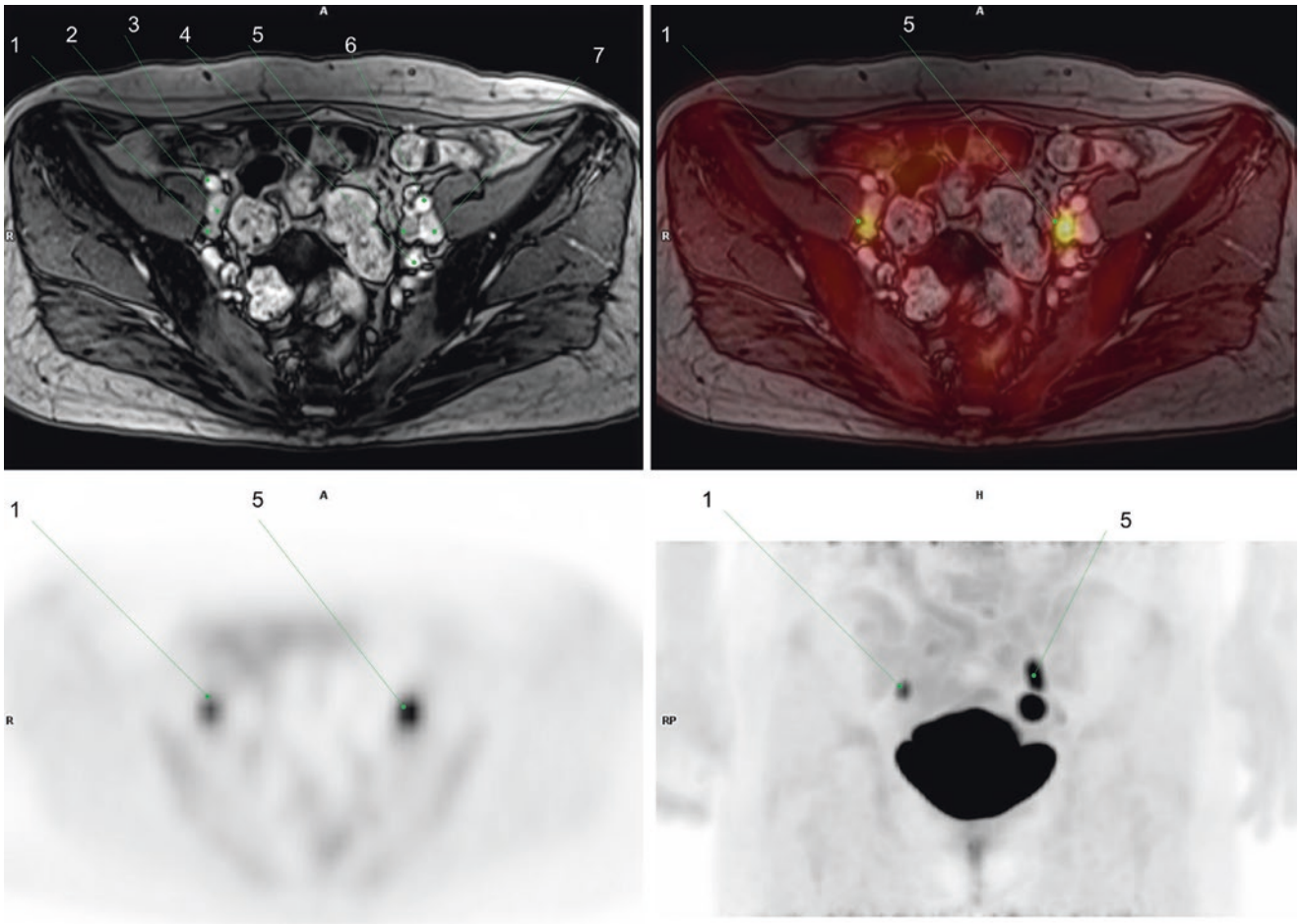

Fig. 41 1. Right external iliac LN metastasis
2. Right external iliac vein
3. Right external iliac artery
4. Left internal iliac artery
5. Left external iliac LN metastasis
6. Left external iliac artery
7. Left external iliac vein

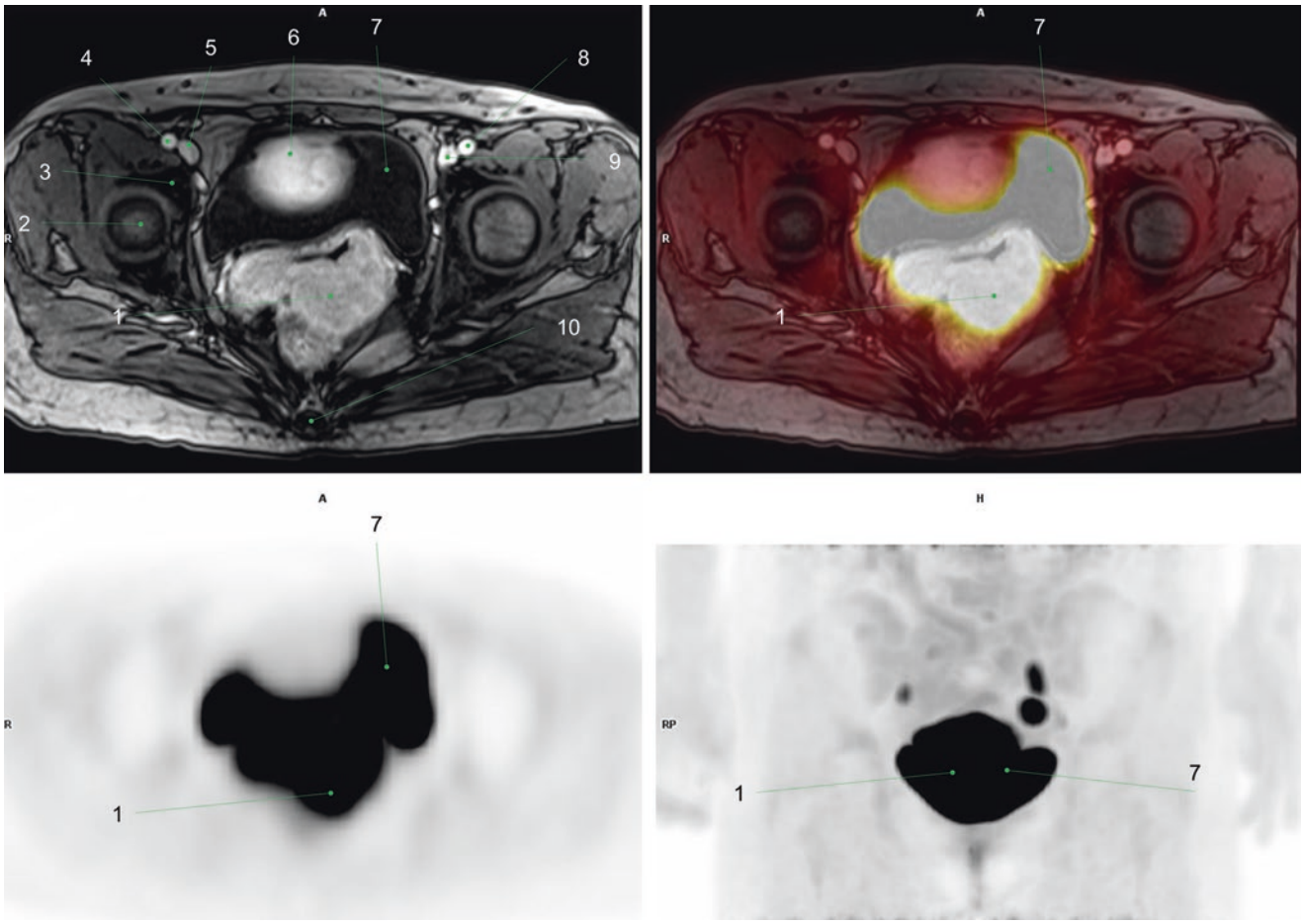

Fig. 42 1. Metabolically active cervical cancer
2. Right femoral head
3. Right acetabulum
4. Right femoral artery
5. Right femoral vein
6. Uterus, fundus
7. Urinary bladder
8. Left femoral artery
9. Left femoral vein
10. Coccyx

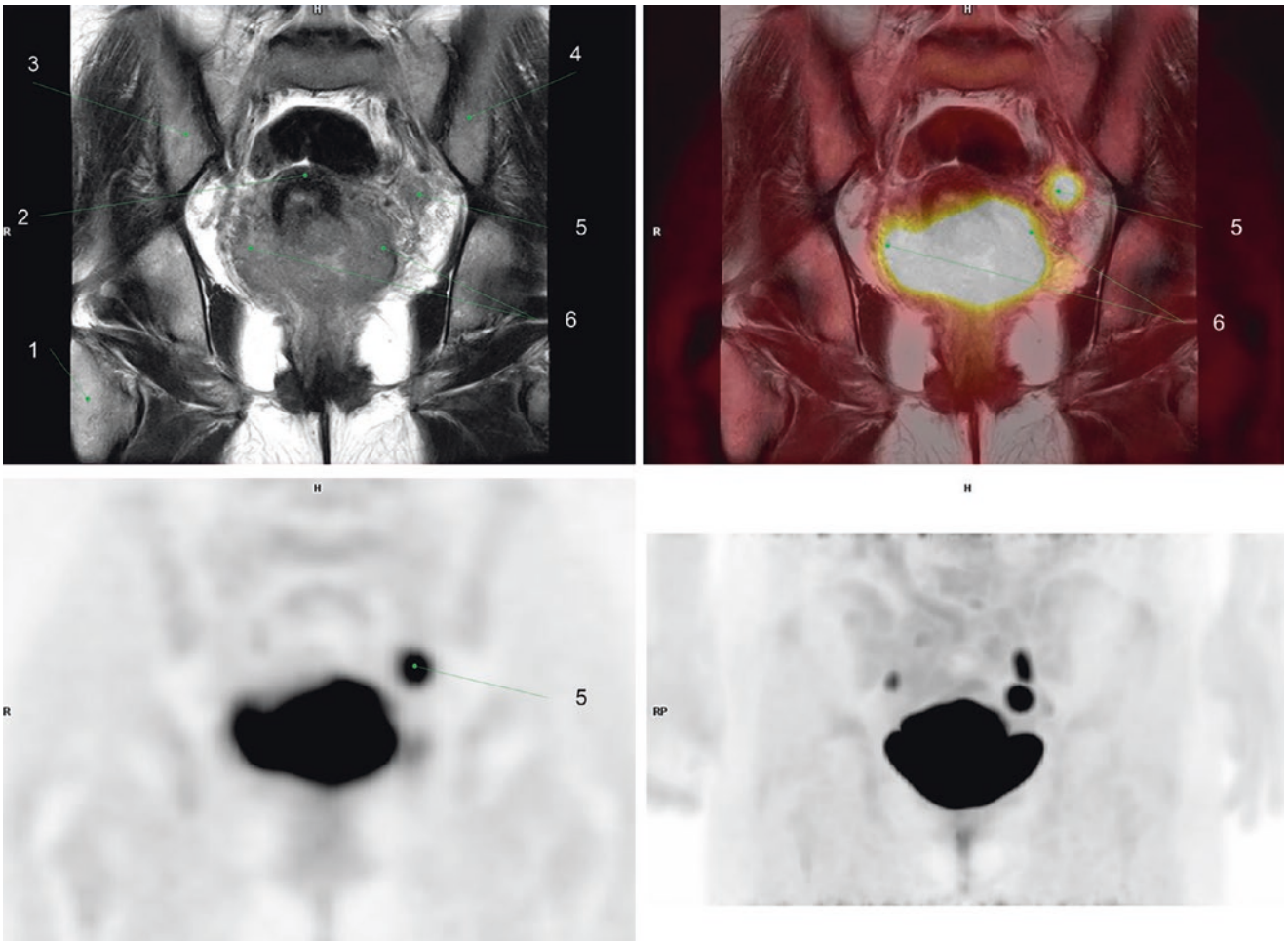

Fig. 43 1. Right proximal femur
2. Uterus
3. Right Ilium
4. Left ilium
5. Left pelvic LN metastasis
6. Bilateral parametrial invasion of cervical cancer

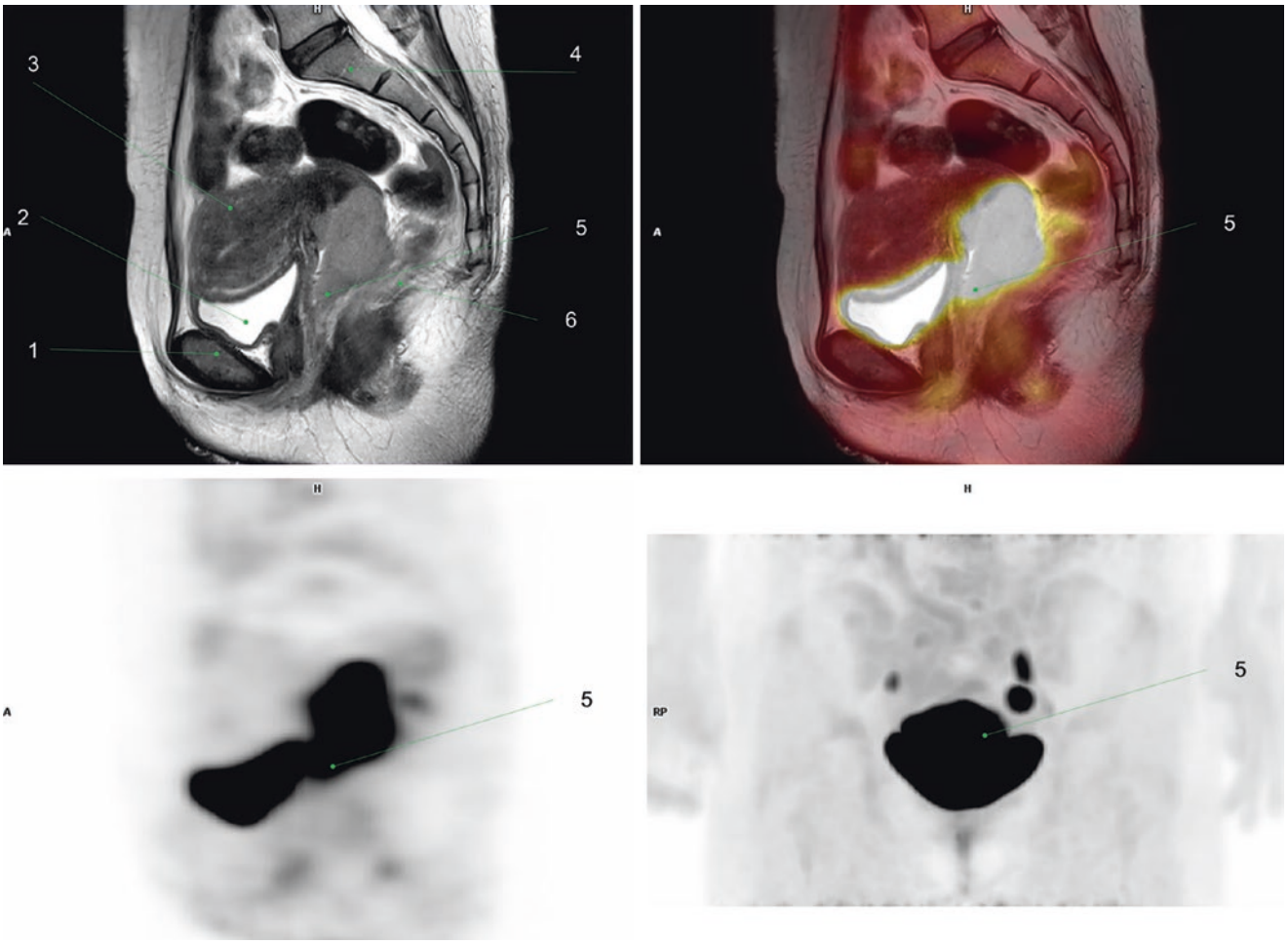

Fig. 44 1. Pubic bone
2. Urinary bladder
3. Uterus fundus
4. Sacrum S1
5. Metabolically active cervical cancer, lower vaginal extension
6. Rectum

4 Musculoskeletal System

4.1 Case 1

A 42-year-old female patient with a palpable mass in the right lower leg. ^{18}F-FDG PET/MR was performed for further evaluation, finding a multilobulated soft tissue mass with moderately increased activity at the posterior compartment of the right lower leg. Enlarged LNs with mildly increased metabolism were also observed in the right external iliac, inguinal, and popliteal regions. Posterior biopsy confirmed synovial sarcoma in the primary mass, and reactive inflammatory LNs in other locations, which is an expected finding since sarcomas very rarely metastasize to LNs (Figs. 45, 46, 47, 48, and 49) [39, 40].

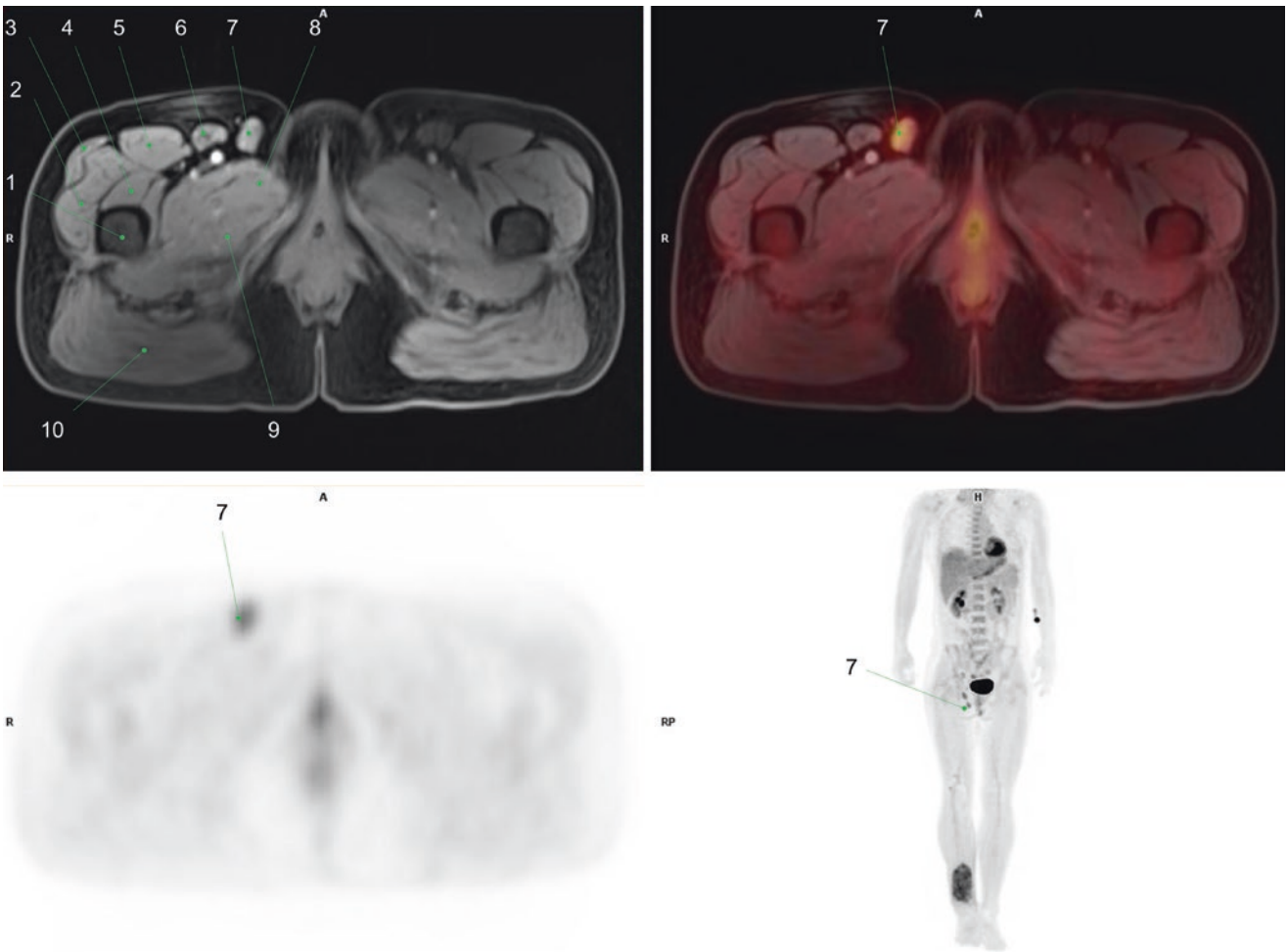

Fig. 45 1. Right femoral shaft
2. Right vastus lateralis muscle
3. Right tensor fasciae latae muscle
4. Right vastus intermedius muscle
5. Right rectus femoris muscle
6. Right sartorius muscle
7. Right inguinal LN with mild increased activity, reactive
8. Right adductor brevis muscle
9. Right adductor magnus muscle
10. Right gluteus maximus muscle

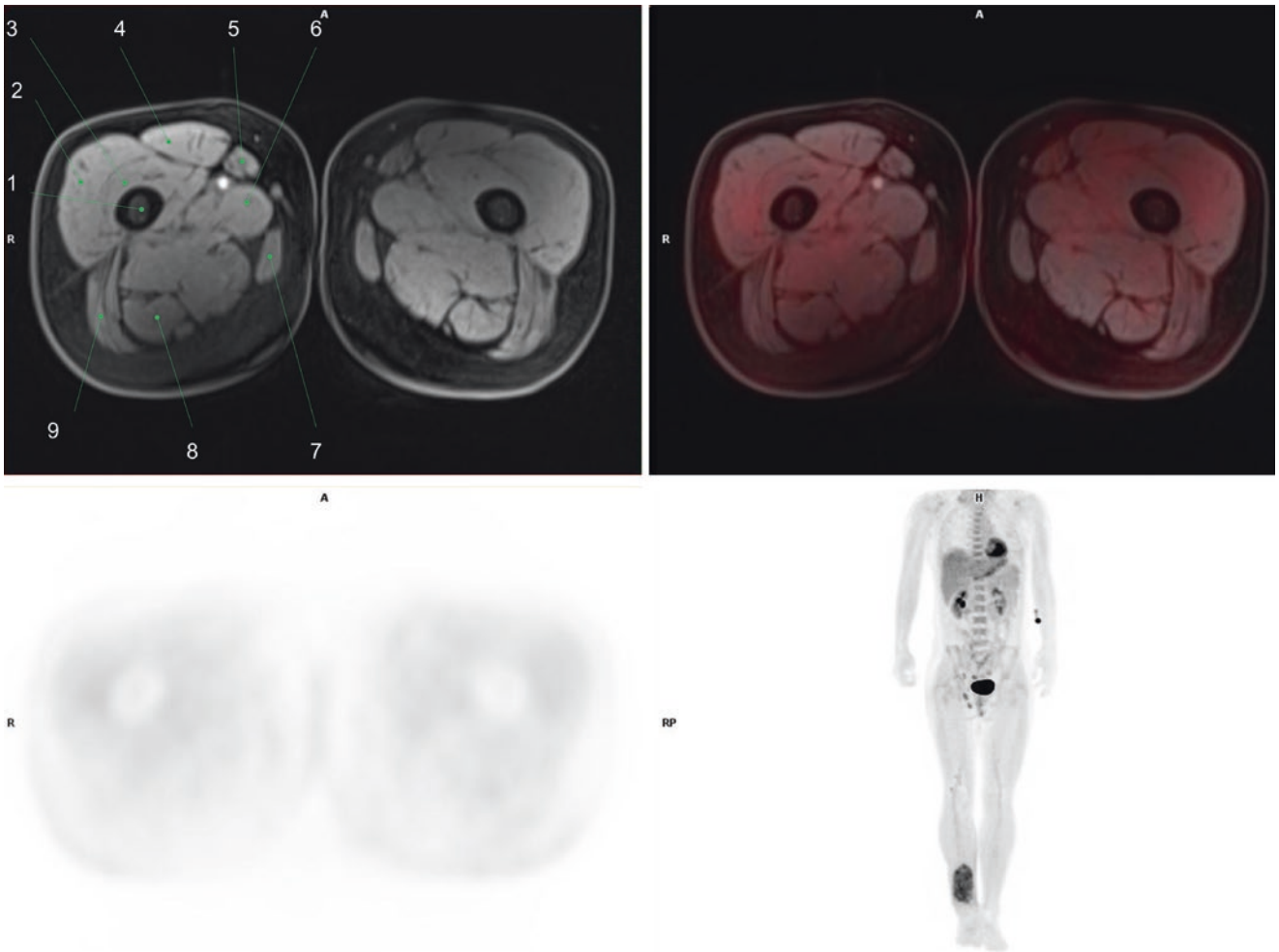

Fig. 46 1. Right femur
2. Right vastus lateralis muscle
3. Right vastus medialis and intermedius muscle
4. Right rectus femoris muscle
5. Right sartorius muscle
6. Right adductor longus muscle
7. Right gracilis muscle
8. Right semitendinosus muscle
9. Right gluteus maximus muscle

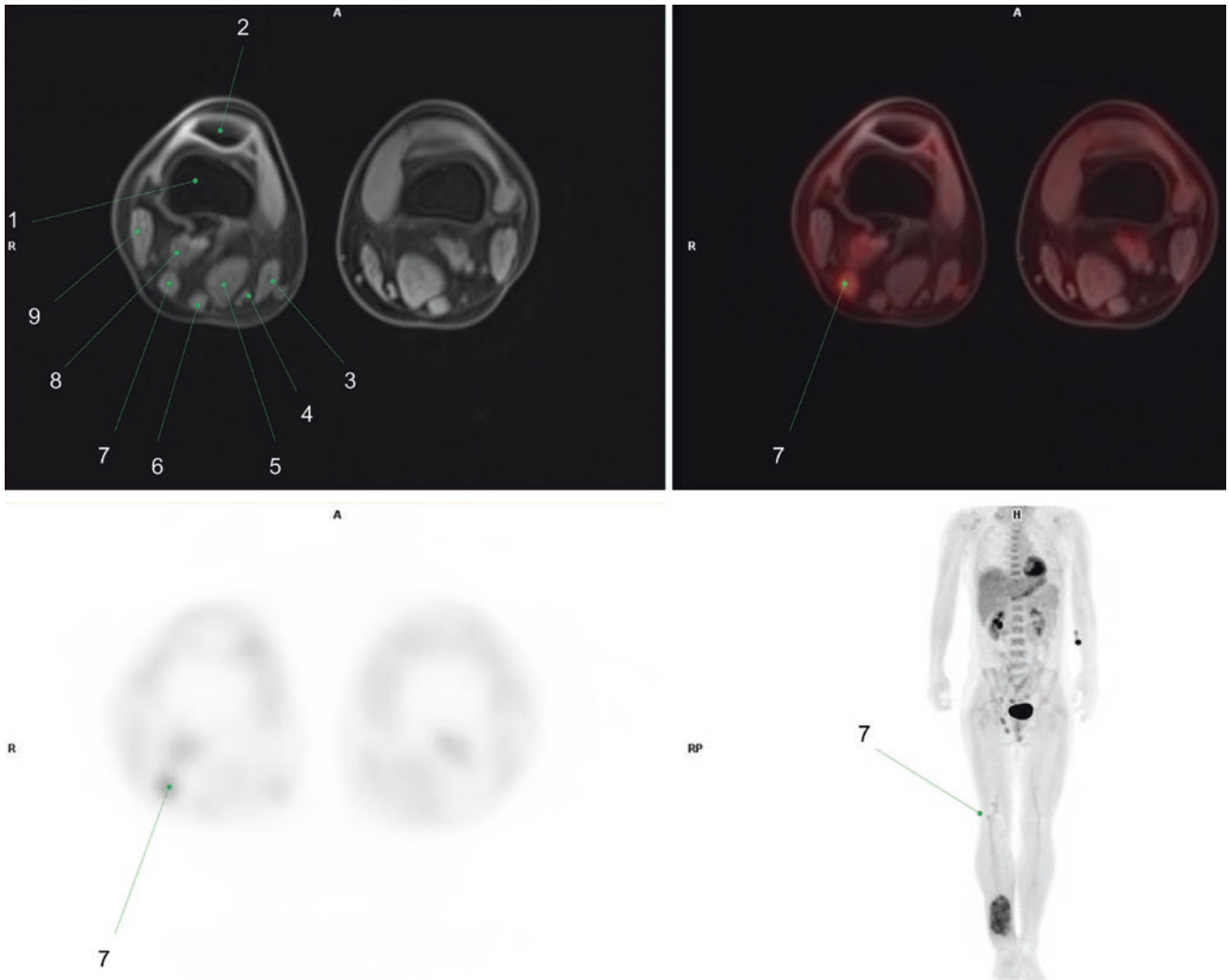

Fig. 47 1. Right femur
2. Right patella
3. Right sartorius muscle
4. Right gracilis muscle
5. Right semimembranosus
6. Right semitendinosus muscle
7. Right popliteal LN with mild increased activity, reactive
8. Right gastrocnemius muscle
9. Right biceps femoris muscle

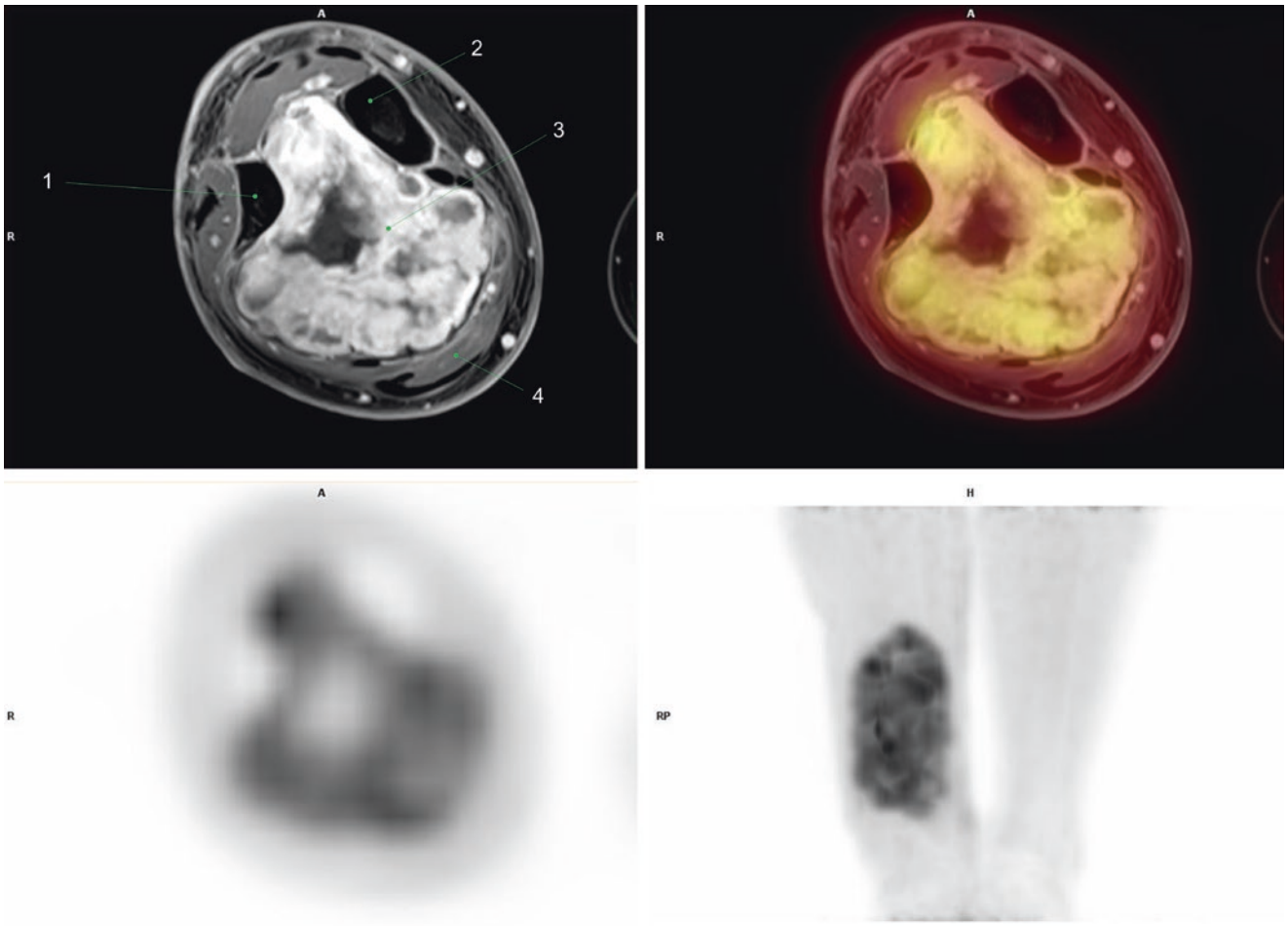

Fig. 48 1. Fibula shaft
2. Tibial shaft
3. Metabolically active synovial sarcoma
4. Gastrocnemius muscle

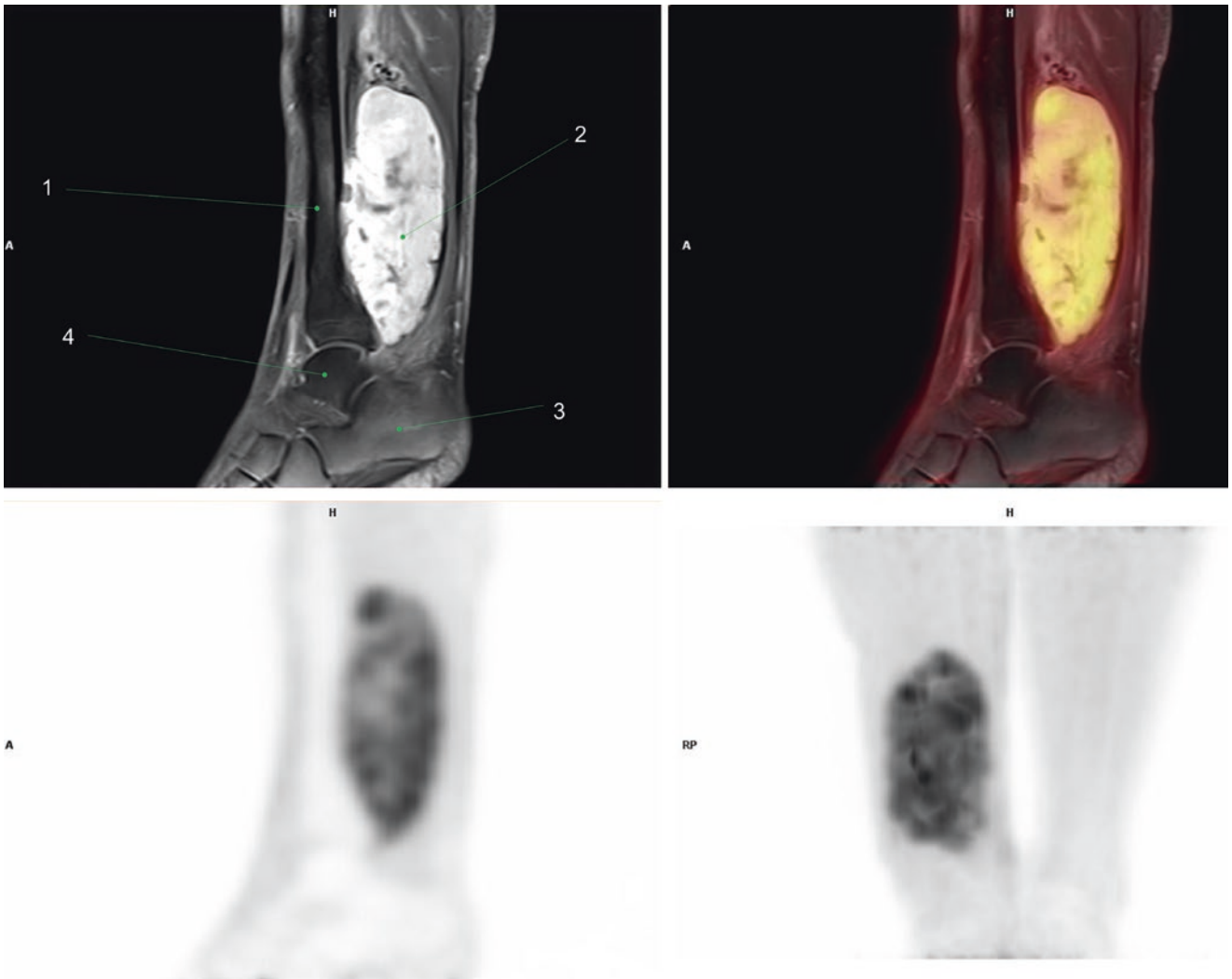

Fig. 49 1. Tibial shaft
2. Metabolically active synovial sarcoma
3. Calcaneus
4. Talus

4.2 Case 2

A 39-year-old male patient with a palpable mass in the right thigh. ^{18}F-FDG PET/MR was done for initial evaluation and staging. Images showed mild increased activity at a well-marginated enhancing mass in the right inner thigh. Myxoid liposarcoma was revealed by needle biopsy (Fig. 50) [39].

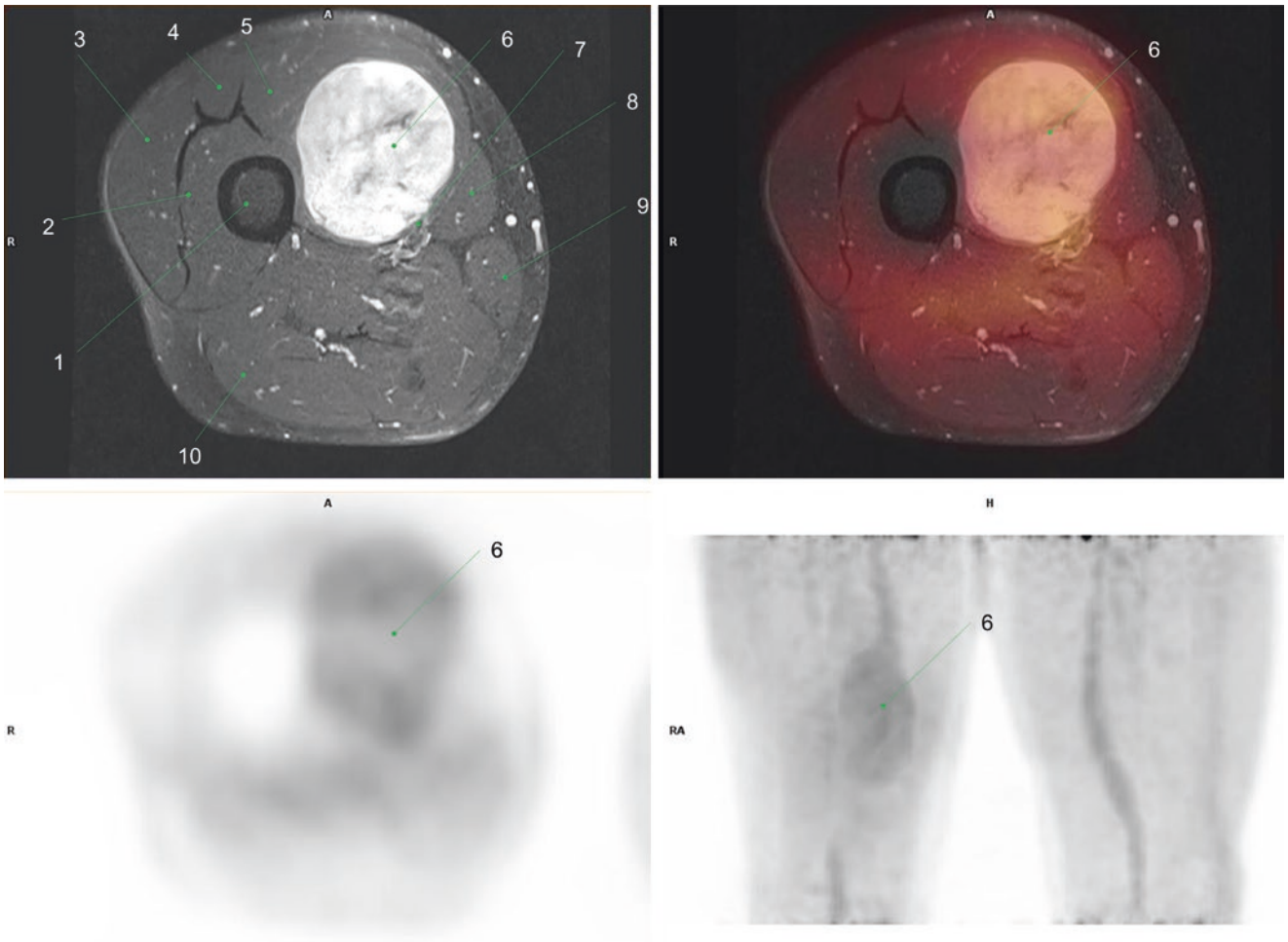

Fig. 50 1. Femoral shaft
2. Vastus intermedius muscle
3. Vastus lateralis muscle
4. Rectus femoris muscle
5. Vastus medialis muscle
6. Mild hypermetabolic liposarcoma
7. Femoral vessel
8. Sartorius muscle
9. Gracilis muscle
10. Biceps femoris muscle

4.3 Case 3

A 16-year-old female patient with chronic pelvic pain. X-ray and CT scan revealed an aggressive bone lesion in the left pelvic bone, and needle biopsy confirmed the diagnosis of osteosarcoma, so ^{18}F-FDG PET/MR was performed for staging. Images showed increased activity at a destructive bony lesion in the left pelvic bone involving the ilium, sacrum, and acetabulum, and encasing the left internal iliac vessels and sacral plexus. Inside the mass, an area with signal void on T2WI and marked contrast enhancement was identified, suggestive of intratumoral aneurysm. Multiple mild hypermetabolic metastatic lung nodules were also found (Figs. 51 and 52) [41, 42].

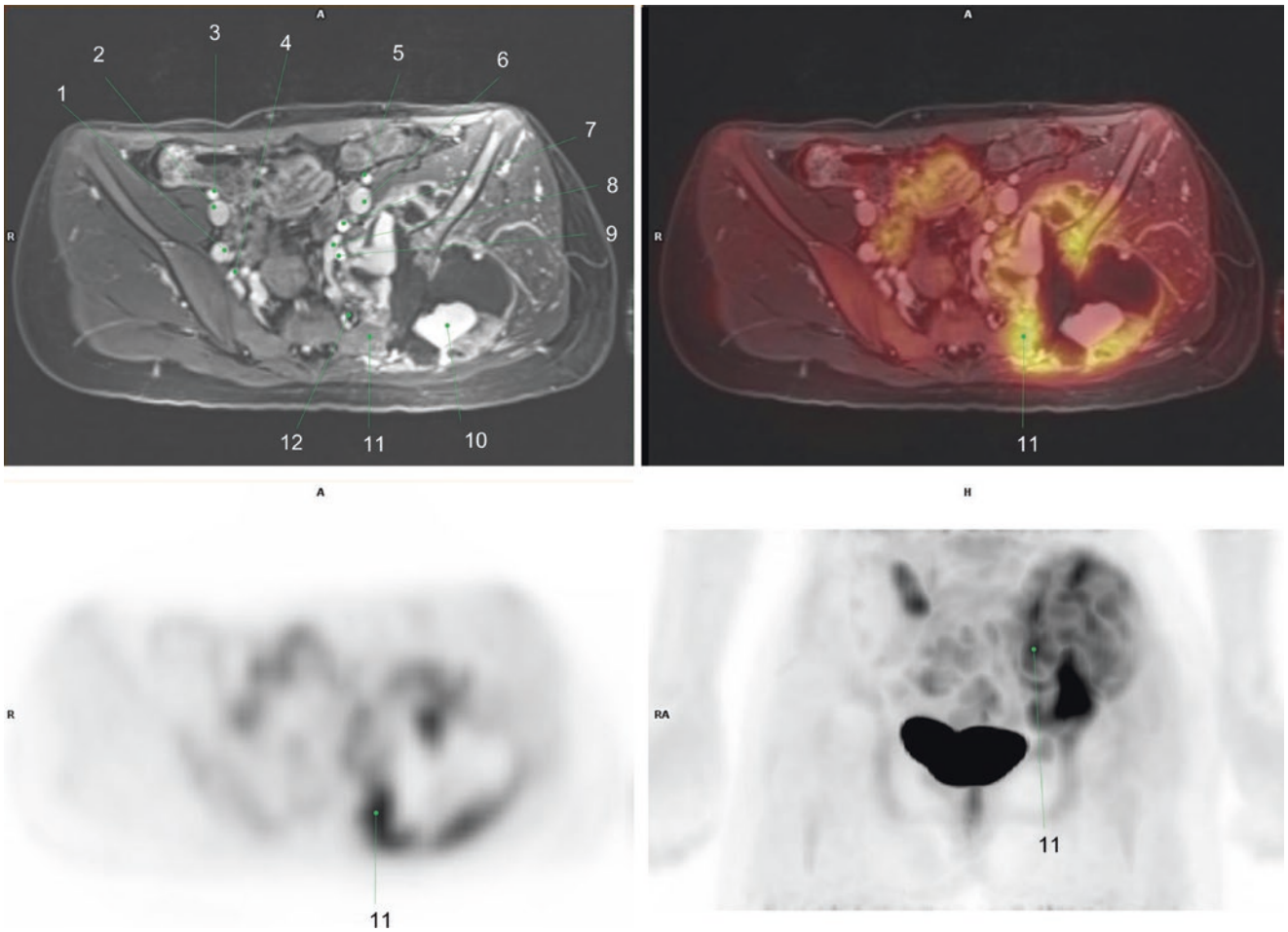

Fig. 51 1. Right internal iliac vein
2. Right external iliac vein
3. Right external iliac artery
4. Right internal iliac artery
5. Left external iliac artery
6. Left external iliac vein
7. Left internal iliac artery
8. Left internal iliac vein
9. Obturator artery
10. Intratumoral aneurysmal change of tumor vessel
11. Metabolically active osteosarcoma involving the left sacral ala
12. Sacral plexus

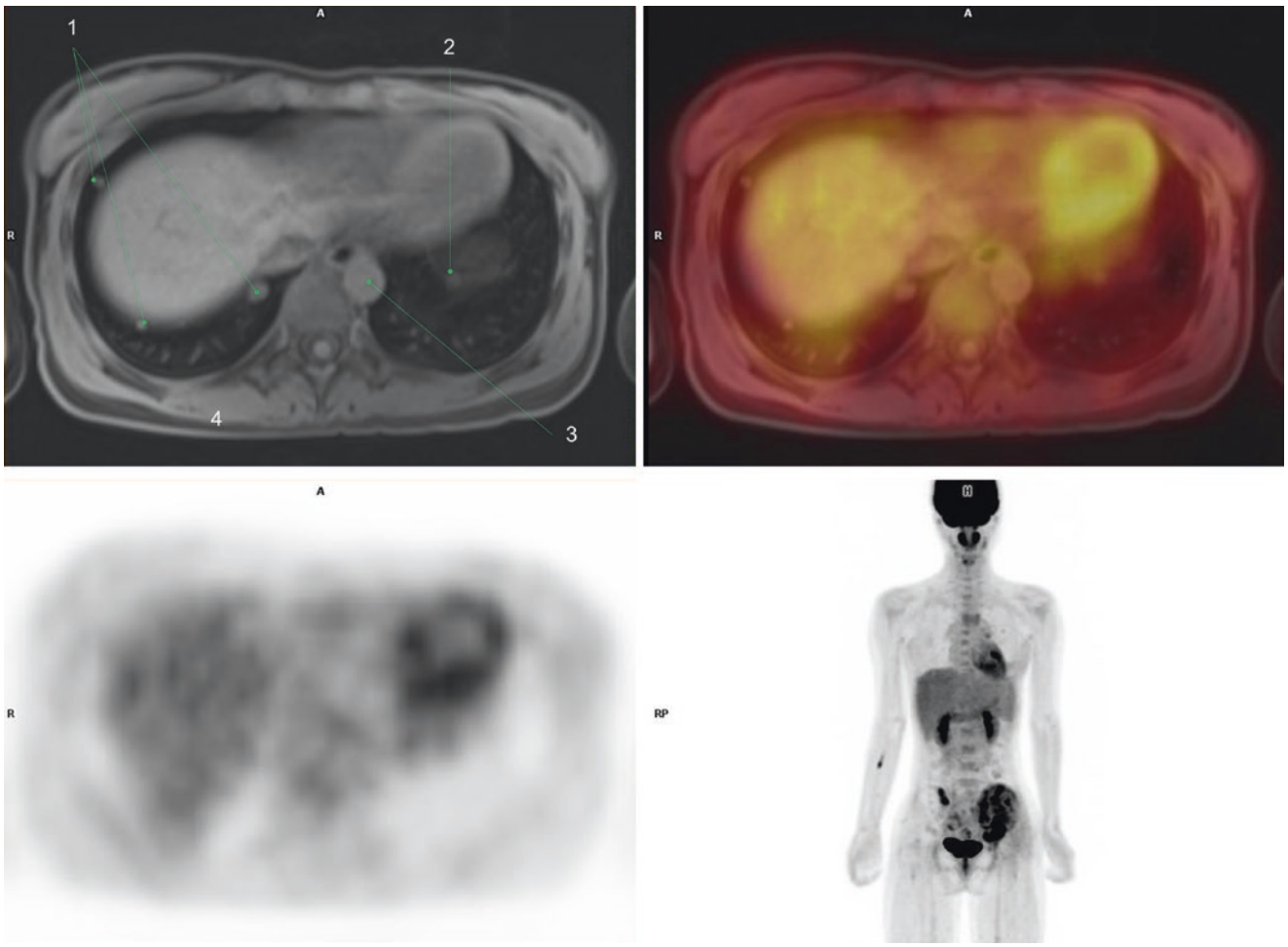

Fig. 52 1. Mild metabolically active lung metastases, right left lobe (RLL)
2. Mild metabolically active lung metastasis, Left lower lobe (LLL)
3. Descending aorta

Acknowledgments *The authors gratefully acknowledge Dr. Dong Soo Lee and Dr. Keon Wook Kang for their contributions to this chapter as it appeared in the previous edition.*

References

1. Levin CS, Maramraju SH, Khalighi MM, Deller TW, Delso G, Jansen F. Design features and mutual compatibility studies of the time-of-flight PET capable GE SIGNA PET/MR system. IEEE Trans Med Imaging. 2016;35:1907–14.
2. Chen Y, An H. Attenuation correction of PET/MR imaging. Magn Reson Imaging Clin N Am. 2017;25:245–55.
3. Fayad H, Lamare F, Merlin T, Visvikis D. Motion correction using anatomical information in PET/CT and PET/MR hybrid imaging. Q J Nucl Med Mol Imaging. 2016;60:12–24.
4. Bronski SM, Goenka AH, Kemp BJ, Johnson GB. clinical PET/MRI: 2018 update. AJR. 2018;211:295–313.
5. Kaufmann S, Kruck S, Gatidis S, et al. Simultaneous whole-body PET/MRI with integrated multiparametric MRI for primary staging of high-risk prostate cancer. World J Urol. 2020;38:2513–21.
6. Leithner D, Horvat JV, Bernard-Davila B, et al. A multiparametric [^{18}F]FDG PET/MRI diagnostic model including imaging biomarkers of the tumor and contralateral healthy breast tissue aids breast cancer diagnosis. Eur J Nucl Med Mol Imaging. 2019;46:1878–88.
7. Öztürk H. PET/MRI: the future of cancer restaging. Cancer Treatment Res Commun. 2020;25:100250.
8. Kirchner J, Sawicki LM, Deuschl C, et al. ^{18}F-FDG PET/MR imaging in patients with suspected liver lesions: value of liver-specific contrast agent gadobenate dimeglumine. PLoS One. 2017;12:e0180349.
9. Rutegård MK, Båtsman M, Axelsson J, et al. PET/MRI and PET/CT hybrid imaging of rectal cancer - description and initial observations from the RECTOPET (REctal Cancer trial on PET/MRI/CT) study. Cancer Imaging. 2019;19(1):52.
10. Huellner MW. PET/MR in head and neck cancer - an update. Semin Nucl Med. 2021;51(1):26–38.
11. Virarkar M, Devine C, Bassett R Jr, Javadi S, De Castro FS, Bhosale P. Update on diagnostic performance of PET/MRI in gynecological malignancies: a systematic review and meta-analysis. J Belgian Soc Radiol. 2020;104(1):4.
12. Cassarino G, Evangelista L, Giraudo C. et al. ^{18}F-FDG PET/MRI in adult sarcomas. Clin Transl Imaging. 2020;8:405–12.
13. Sgard B, Brillet PY, Bouvry D, Djelbani S, Nunes H, Meune C, Valeyre D, Soussan M. Evaluation of FDG PET combined with cardiac MRI for the diagnosis and therapeutic monitoring of cardiac sarcoidosis. Clin Radiol. 2019;74(1):81.

14. Nguyen NC, Moon C-H, Muthukrishnan A, Furlan A. 68Ga-DOTATATE PET/MRI for neuroendocrine tumors. Clin Nucl Med. 2020;45(9):e406–10.
15. Evangelista L, Zattoni F, Cassarino G, et al. PET/MRI in prostate cancer: a systematic review and meta-analysis. Eur J Nucl Med Mol Imaging. 2021;48:859–73.
16. Overcast WB, Davis KM, Ho CY, et al. Advanced imaging techniques for neuro-oncologic tumor diagnosis, with an emphasis on PET-MRI imaging of malignant brain tumors. Curr Oncol Rep. 2021;23:34.
17. Laudicella R, Iagaru A, Minutoli F, et al. PET/MR in neuro-oncology: is it ready for prime-time? Clin Transl Imaging. 2020;8:233–5.
18. Ortner M, Drost R, Heddderich D, et al. Amyloid PET, FDG-PET or MRI? - the power of different imaging biomarkers to detect progression of early Alzheimer's disease. BMC Neurol. 2019;19:264.
19. Kerstens VS, Varrone A. Dopamine transporter imaging in neurodegenerative movement disorders: PET vs. SPECT Clin Transl Imaging. 2020;8:349–56.
20. Mohile NA, Deangelis LM, Abrey LE. The utility of body FDG PET in staging primary central nervous system lymphoma. Neuro Oncol. 2008;10:223–8.
21. Thomas R, Braschi-Amirfarzan M, Laferriere SL, Jagannathan JP. Imaging of Waldenström Macroglobulinemia: a comprehensive review for the radiologist in the era of personalized medicine. AJR. 2019;213:248–56.
22. Natarajan A, Chandra P, Purandare N, Agrawal A, Shah S, Puranik A, et al. Role of fluorodeoxyglucose positron emission tomography/computed tomography in various orbital malignancies. IJNM. 2018;33(2):118–24.
23. Dadgar H, Norouzbeigi N, Ahmadzadehfar H, Assadi M. 68Ga-DOTATATE and 18F-FDG PET/CT for the management of esthesioneuroblastoma of the sphenoclival region. Clin Nucl Med. 2020;45(8):e363–4.
24. Platzek I, Beuthien-Baumann B, Schneider M, Gudziol V, Langner J, Schramm G, et al. PET/MRI in head and neck cancer: initial experience. Eur J Nucl Med Mol Imaging. 2013;40:6–11.
25. Larson CR, Wiggins RH. FDG-PET imaging of salivary gland tumors. Seminars in Ultrasound, CT and MRI. 2018;40(5):391–9.
26. Higashiyama A, Komori T, Inada Y, Nishizawa M, Nakajima H, Narumi Y. Diffuse ^{18}F-FDG uptake throughout the spinal cord in the acute phase of Neuromyelitis Optica Spectrum disorder. Eur J Nucl Med Mol Imaging. 2017;44(9):1609–10.
27. Heusch P, Buchbender C, Kohler J, Nensa F, Gauler T, Gomez B, et al. Thoracic staging in lung cancer: prospective comparison of 18F-FDG PET/MR imaging and 18F-FDG PET/CT. J Nucl Med. 2014;55:373–8.
28. Kohan AA, Kolthammer JA, Vercher-Conejero JL, Rubbert C, Partovi S, Jones R, et al. N staging of lung cancer patients with PET/MRI using a three-segment model attenuation correction algorithm: initial experience. Eur Radiol. 2013;23:3161–9.
29. Lee J, Cho YS, Kim J, Shim YM, Lee K-H, Choi JY. Prognostic significance of metabolic parameters by 18F-FDG PET/CT in thymic epithelial tumors. Cancer. 2021;13:712.
30. Wu CX, Zhu ZH. Diagnosis and evaluation of gastric cancer by positron emission tomography. World J Gastroenterol. 2014;20:4574–85.
31. Francis IR, Cohan RH, Varma DGK, Sondak VK. Retroperitoneal sarcomas. Cancer Imaging. 2005;5:89–94.
32. Moradi F, Ladaru A. The role of positron emission tomography in pancreatic cancer and gallbladder cancer. Semin Nucl Med. 2020;50(5):434–46.
33. Lu RC, She B, Gao WT, Ji YH, Xu DD, Wang QS, et al. Positron-emission tomography for hepatocellular carcinoma: current status and future prospects. World J Gastroenterol. 2019;25(32):4682–95.
34. Ota Y, Aso K, Watanabe K, Einama T, Imai K, Karasaki H, et al. Hepatic schwannoma: imaging findings on CT, MRI and contrast-enhanced ultrasonography. World J Gastroenterol. 2012;18:4967–72.
35. Wei K, Pan B, Yang H, Lu C, Ge L, Cao N. F-18 FDG PET, CT, and MRI for detecting the malignant potential in patients with gastrointestinal stromal tumors. Medicine. 2018;97(16):e0389.
36. Lee DH, Lee JM. Whole-body PET/MRI for colorectal cancer staging: is it the way forward? J Magn Reson Imaging. 2017;45(1):21–35.
37. Sala E, Wakely S, Senior E, Lomas D. MRI of malignant neoplasms of the uterine corpus and cervix. AJR Am J Roentgenol. 2007;188:1577–87.
38. Son H, Kositwattanarerk A, Hayes MP, Chuang L, Rahaman J, Heiba S, et al. PET/CT evaluation of cervical cancer: spectrum of disease. Radiographics. 2010;30:1251–68.
39. Schuler MK, Richter S, Beuthien-Baumann B, Platzek I, Kotzerke J, van den Hoff J, et al. PET/MRI imaging in high-risk sarcoma: first findings and solving clinical problems. Case Rep Oncol Med. 2013;2013:793927.
40. Partovi S, Kohan AA, Zipp L, Faulhaber P, Kosmas C, Ros PR, et al. Hybrid PET/MR imaging in two sarcoma patients — clinical benefits and implications for future trials. Int J Clin Exp Med. 2014;7:640–8.
41. Brenner W, Bohuslavizki KH, Eary JF. PET imaging of osteosarcoma. J Nucl Med. 2003;44:930–42.
42. Im HJ, Kim TS, Park SY, Min HS, Kim JH, Kang HG, et al. Prediction of tumour necrosis fractions using metabolic and volumetric 18F-FDG PET/CT indices, after one course and at the completion of neoadjuvant chemotherapy, in children and young adults with osteosarcoma. Eur J Nucl Med Mol Imaging. 2012;39:39–49.

Atlas and Anatomy of PET/CT

Vanessa Murad, E. Edmund Kim, Jin-Chul Paeng,
Camilo Barragan, and Gi-Jeong Cheon

PET/CT is a combined system of positron emission tomography (PET) and computed tomography (CT) scanners. PET can detect abnormal metabolic activity in organs or lesions even before they show morphological changes and CT enables precise localization, so co-registration of functional and anatomic information is achieved in the same study, obtained on the same scanner [1]. This technology, available now for at least 10 years, has allowed great advances especially in the field of oncology, and every day it opens more fields to explore in this and other multiple pathologies [2]. Nowadays there is also the possibility of carrying out total body PET studies, which encompasses the entire body within the field of view of the scanner, allowing imaging of all the tissues and organs simultaneously. The increase in geometric coverage of total body PET and multiple adjusted parameters make the whole-body image a very sensitive study with major implications for medical imaging.

PET/CT is currently widely available in the world and many guidelines already recommend it as part of the diagnosis, staging, follow-up, or re-evaluation of various pathologies. As for PET/MR, nonspecific ^{18}F-FDG is the most widely used an available radiotracer for PET/CT studies, and thus many other new tracers are available or under investigation, to offer better possibilities to patients and not only in the field of oncology [2, 3]. Indications for FDG PET/CT are continuously evolving according to the advances that current research allows; however, in oncology it can be useful in various stages of the disease depending on the pathology: initial diagnosis, staging, therapeutic approach, evaluation of response to treatment and recurrence. A great example, and perhaps one of the most frequently used with multiple indications is lymphoma [3, 4]. Other frequent scenarios in which it has a diagnostic utility are the evaluation of a solitary pulmonary nodule, multiple myeloma, and search for a primary tumor of unknown origin [5–7]. Its usefulness in staging due to the ability to evaluate the whole body, detect lymph node or distant metastasis, and offer some prognostic information can be extended to almost all cancer pathology, but it has been evaluated with better results in melanoma, head and neck, lung, colorectal, gynecological and esophageal cancers among others, as well as in bone and soft tissue sarcomas [3, 8–11]. Likewise, in some cases such as lung, esophageal, and colorectal cancers, it has shown great utility in radiotherapy planning with excellent results [12, 13]. Response assessment utility depends on the characteristics of the primary tumor and stage, but in lung, esophageal, and colorectal cancers, the results have been promising [10, 13, 14]. Finally, in the evaluation of recurrence, its diagnostic accuracy may also be subject to the characteristics of the primary tumor, but since a large part of the metastases are more aggressive and metabolically active, it represents a good tool for almost all tumors, especially for head and neck, lung, gynecological, and bone and soft tissue tumors. It is important to bear in mind that although it is not indicated for the diagnosis or staging of a series of non-FDG avid tumors (stomach, pancreas, hepatoma, genitourinary tract, ovary, among others), when there is a suspicion of relapse it may play an important role [3, 15, 16].

As in PET/MRI, the availability of multiple novel radiotracers has allowed great advances, especially in neuroendocrine tumors, prostate cancer, and neuro-oncology and degenerative diseases, having the same tracers previously described available for PET/CT studies [17].

V. Murad (✉)
Department of Nuclear Medicine, Seoul National University College of Medicine, Seoul, Republic of Korea

Department of Diagnostic Imaging, Fundacion Santa Fe de Bogotá University Hospital, Bogota, Colombia

E. E. Kim
Department of Radiological Sciences, University of California, Irvine, School of Medicine, Orange, CA, USA

Department of Nuclear Medicine and Department of Molecular Medicine, Graduate School of Convergence Science and Technology, Seoul National University College of Medicine, Seoul, Republic of Korea

J.-C. Paeng · G.-J. Cheon
Department of Nuclear Medicine, Seoul National University College of Medicine, Seoul, Republic of Korea

C. Barragan
Joint Department of Medical Imaging, University Health Network, University of Toronto, Toronto, ON, Canada

E. E. Kim et al. (eds.), *Atlas and Anatomy of PET/MRI, PET/CT and SPECT/CT*, https://doi.org/10.1007/978-3-030-92349-5_2

In this chapter, we present multiple demonstrative examples of the different uses of FDG and non-FDG PET/CT, with the most relevant anatomical references for each case.

1 ^{18}F-FDG PET/CT

1.1 Head and Neck

1.1.1 Case 1

A 56-year-old female patient with frontal headaches during the last 3 months. Brain ^{18}F-FDG PET/CT was performed for malignancy work-up. Images showed mild and irregular increased activity in the cingulate cortex and corpus callosum, at a lobulated and calcified extra axial mass, and later proved to be a meningioma (WHO grade I). The increased activity in this case may represent an artifact due to the dense and irregular calcification, rather than a definite uptake by the mass (Figs. 1 and 2).

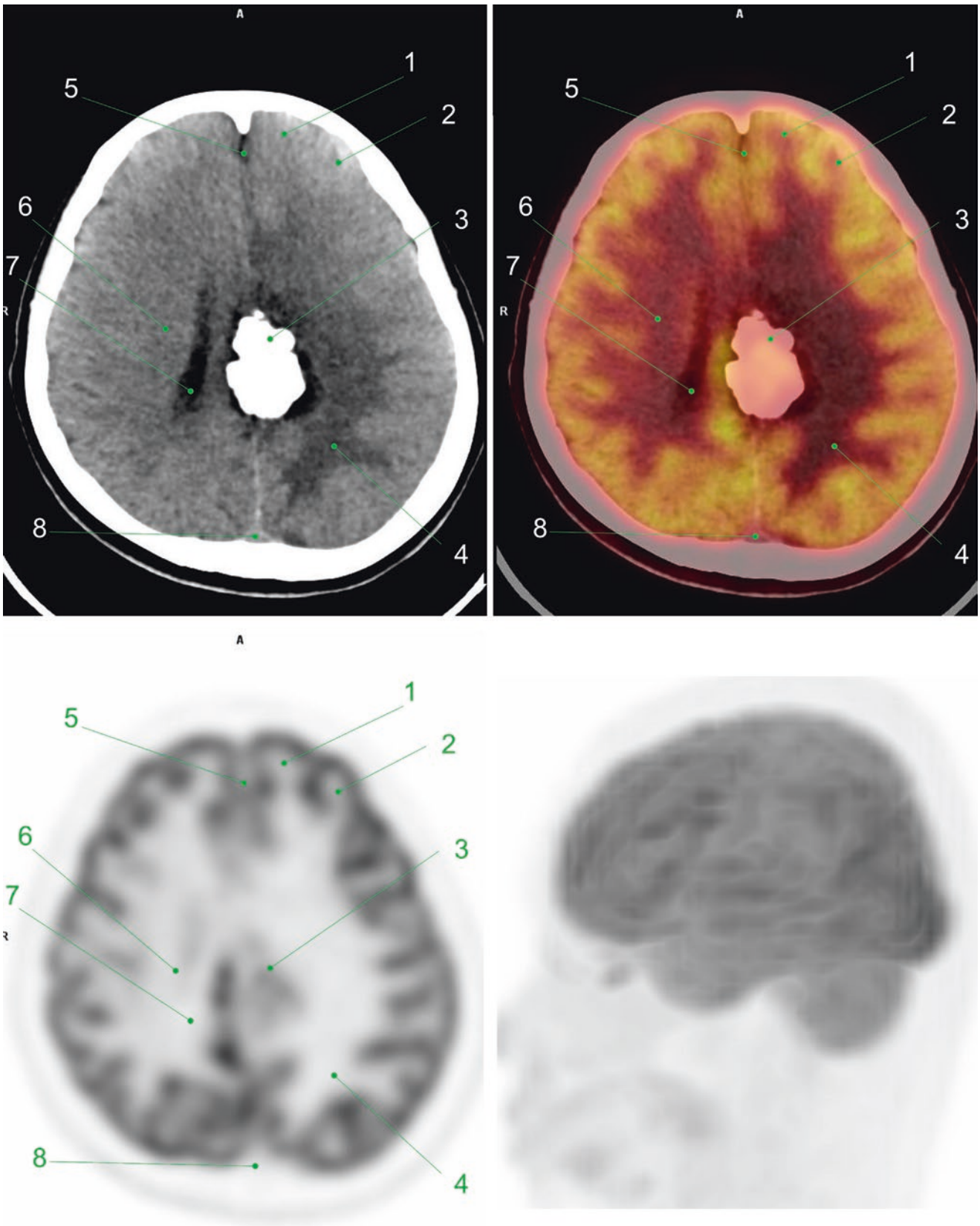

Fig. 1 1. Left superior frontal gyrus
2. Left middle frontal gyrus
3. Calcified meningioma in the corpus callosum
4. Perilesional edema in the posterior left periventricular area
5. Falx cerebri
6. Right corona radiata
7. Right lateral ventricle
8. Superior sagittal sinus

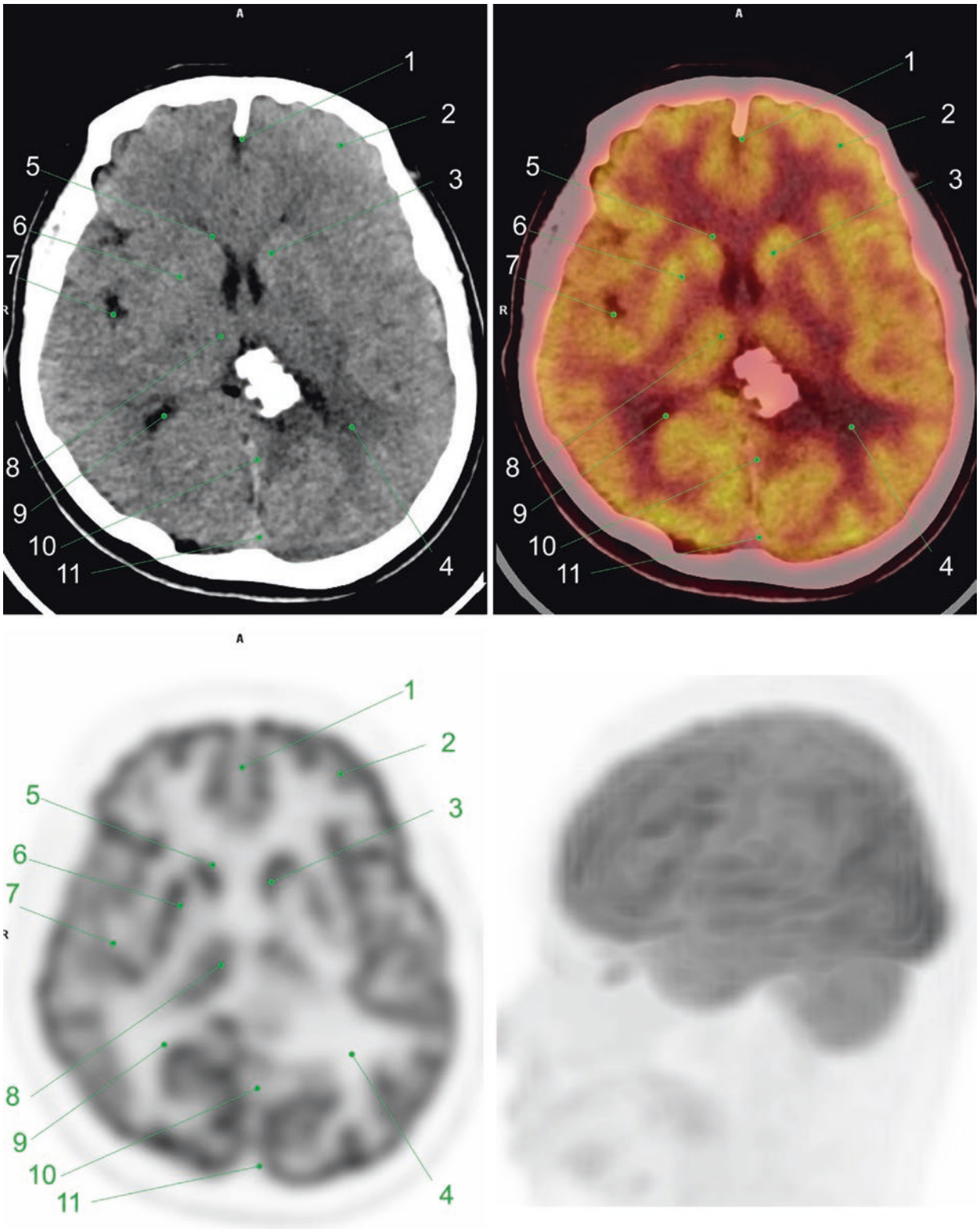

Fig. 2 1. Falx cerebri
2. Left medial frontal gyrus
3. Left caudate nucleus head
4. Perilesional edema in the posterior left periventricular area
5. Right lateral ventricle, anterior horn
6. Right putamen
7. Right cistern of lateral cerebral fossa (insular cistern)
8. Right thalamus
9. Right lateral ventricle, posterior horn
10. Straight sinus
11. Superior sagittal sinus

1.1.2 Case 2

A 65-year-old woman with a history of lung squamous cell carcinoma undergoing chemotherapy, who attended her routine follow-up completely asymptomatic. ^{18}F-FDG PET/CT was performed finding a newly developed focal hypometabolic lesion in the left parietal cortex with peripheral mild, diffuse hypometabolism, which was confirmed to be a metastatic lesion with surrounding edema on contrast MRI (Figs. 3 and 4) [18].

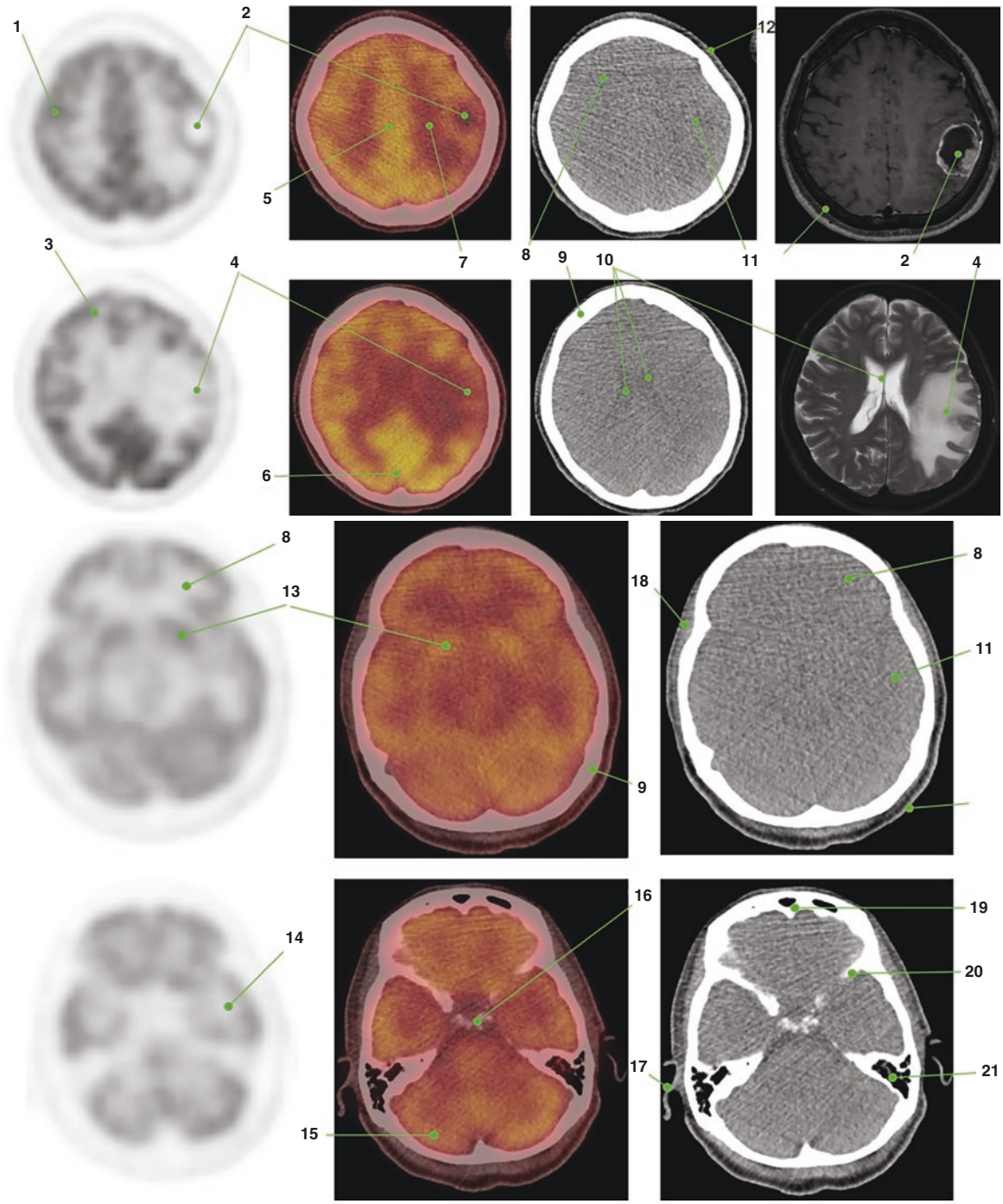

Figs. 3 and 4 1. Right parietalcortex, precentral gyrus
2. Hypometabolic metastasis in left parietal cortex
3. Right frontal cortex, superior frontal gyrus
4. Diffuse hypometabolism in the left parietal cortex and white matter representing perilesional edema
5. Right cingulate gyrus
6. Occipital cortex
7. Left centrum semiovale
8. Right frontal lobe
9. Right frontal skull
10. Lateral ventricles
11. Left parietal lobe
12. Left frontal scalp
13. Head of caudate nucleus
14. Left temporal lobe
15. Right occipital lobe
16. Sella turcica
17. Right auricle
18. Right temporal muscle
19. Frontal sinuses
20. Left sphenoid bone
21. Left mastoid air cells

1.1.3 Case 3

A 17-year-old male patient with persistent headache and obstructive hydrocephalus on brain CT. ^{18}F-FDG PET/CT was performed finding two lesions, one located in the suprasellar region and the other in the pineal region. Both lesions showed very low FDG uptake and heterogeneous density with cystic components and calcifications. Biopsy revealed the diagnosis of bifocal germinoma, which can be found in 2–18% of cases. It remains unclear if this represents synchronous tumors or metastatic disease, but it is known that these patients have a worse prognosis (Fig. 5) [19].

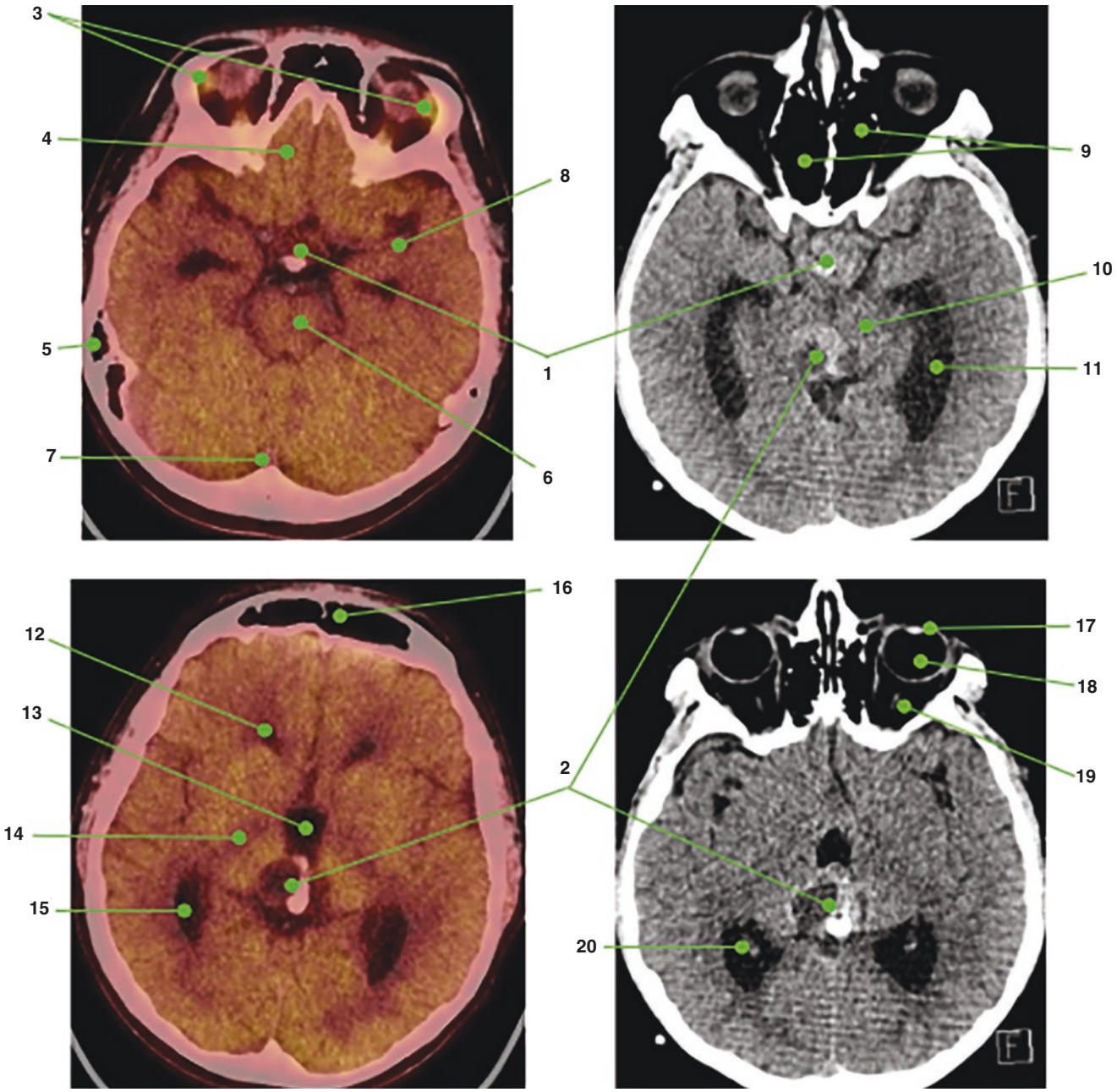

Fig. 5 1. Suprasellar germinoma
2. Pineal germinoma
3. Lacrimal glands with mild increased activity
4. Olfactory cortex
5. Right mastoid air cells
6. Midbrain
7. Torcula Herophili (confluence of the sinuses)
8. Left middle cerebral artery
9. Ethmoid air cells
10. Left thalamus
11. Body of the left lateral ventricle
12. Anterior horn of the right lateral ventricle
13. Third ventricle
14. Posterior limb of the right internal capsule
15. Posterior horn of the right lateral ventricle
16. Frontal sinuses
17. Left eye lens
18. Left eye vitreous chamber
19. Left optic nerve
20. Choroid plexus at the right lateral ventricle

1.1.4 Case 4

A 64-year-old man with occasional headache. Initial brain CT revealed an expansive heterogeneous lesion in the clivus, so ^{18}F-FDG PET/CT was performed to determine its nature. Images showed minimal diffusely increased activity in an expansive, well-defined, lytic lesion in the superior and central aspect of the clivus. These findings favored the diagnosis of a chordoma, which differs from chondrosarcoma because the latter generally presents greater FDG uptake and a chondroid matrix with typical calcifications in rings and arcs (Fig. 6) [20].

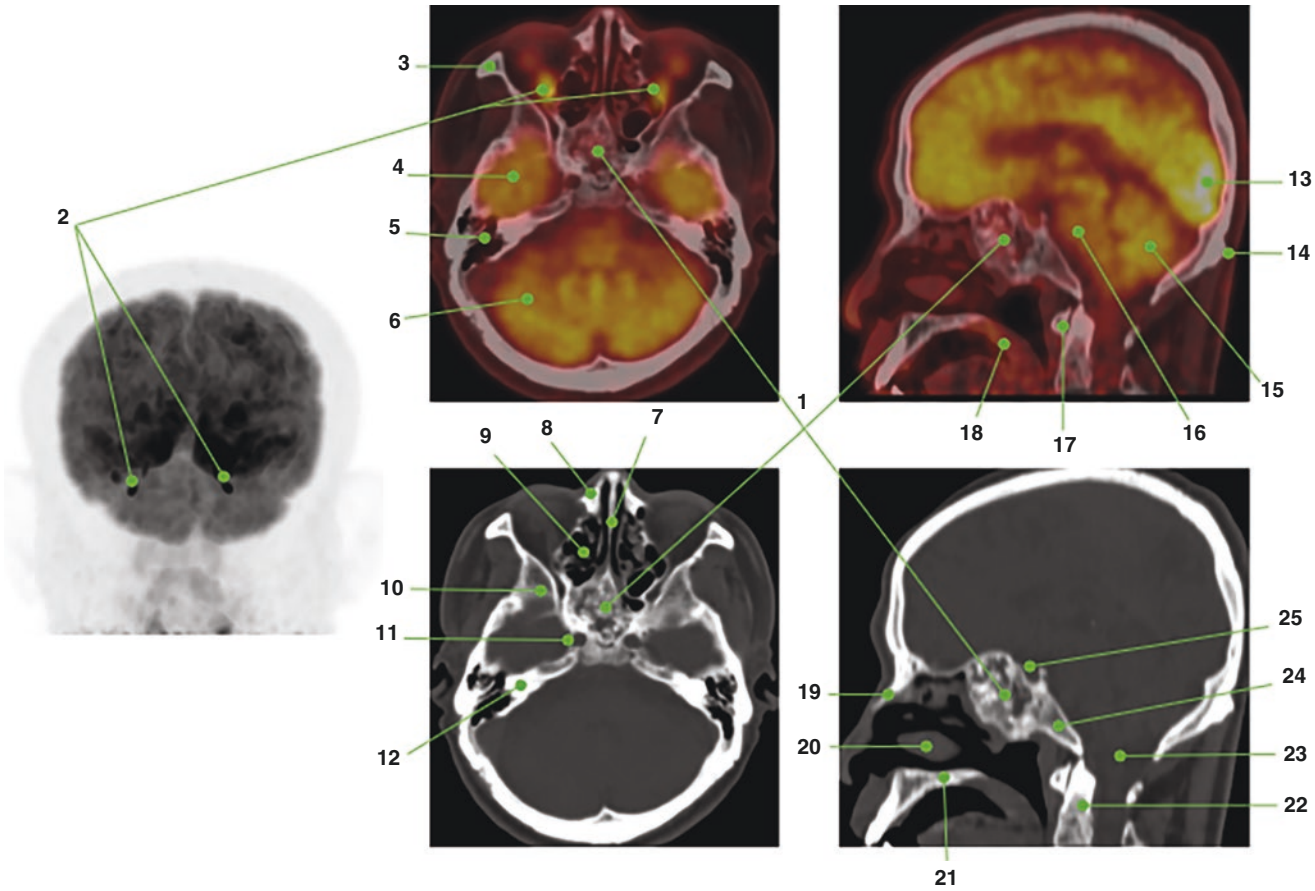

Fig. 6 1. Clival chordomas
2. Optic nerves
3. Right zygomatic bone
4. Right temporal lobe
5. Right mastoid air cells
6. Right cerebellum
7. Nasal septum
8. Right nasal bone
9. Right ethmoid sinus
10. Right sphenoid bone
11. Right internal carotid artery
12. Right petrous pyramid
13. Physiologic increased uptake at the visual cortex
14. External occipital protuberance
15. Cerebellum
16. Brainstem
17. Atlantoaxial joint
18. Soft palate
19. Nasal bones
20. Middle nasal concha
21. Hard palate
22. C2, odontoid process (dens)
23. Foramen magnum
24. Clivus
25. Sella turcica/pituitary gland

1.1.5 Case 5

A 65-year-old man with progressive hoarseness. In otolaryngology consultation, physical examination and laryngoscopy revealed a tiny lesion in the right side of the glottis. Biopsy confirmed a squamous cell carcinoma, so ^{18}F-FDG PET/CT scan was requested for staging. Images showed focal increased uptake in the right side of the glottis, at the site of the primary tumor, which represents a metabolic change without an evident anatomical abnormality. No hypermetabolic lymph nodes or distant metastases were found [9] (Figs. 7 and 8).

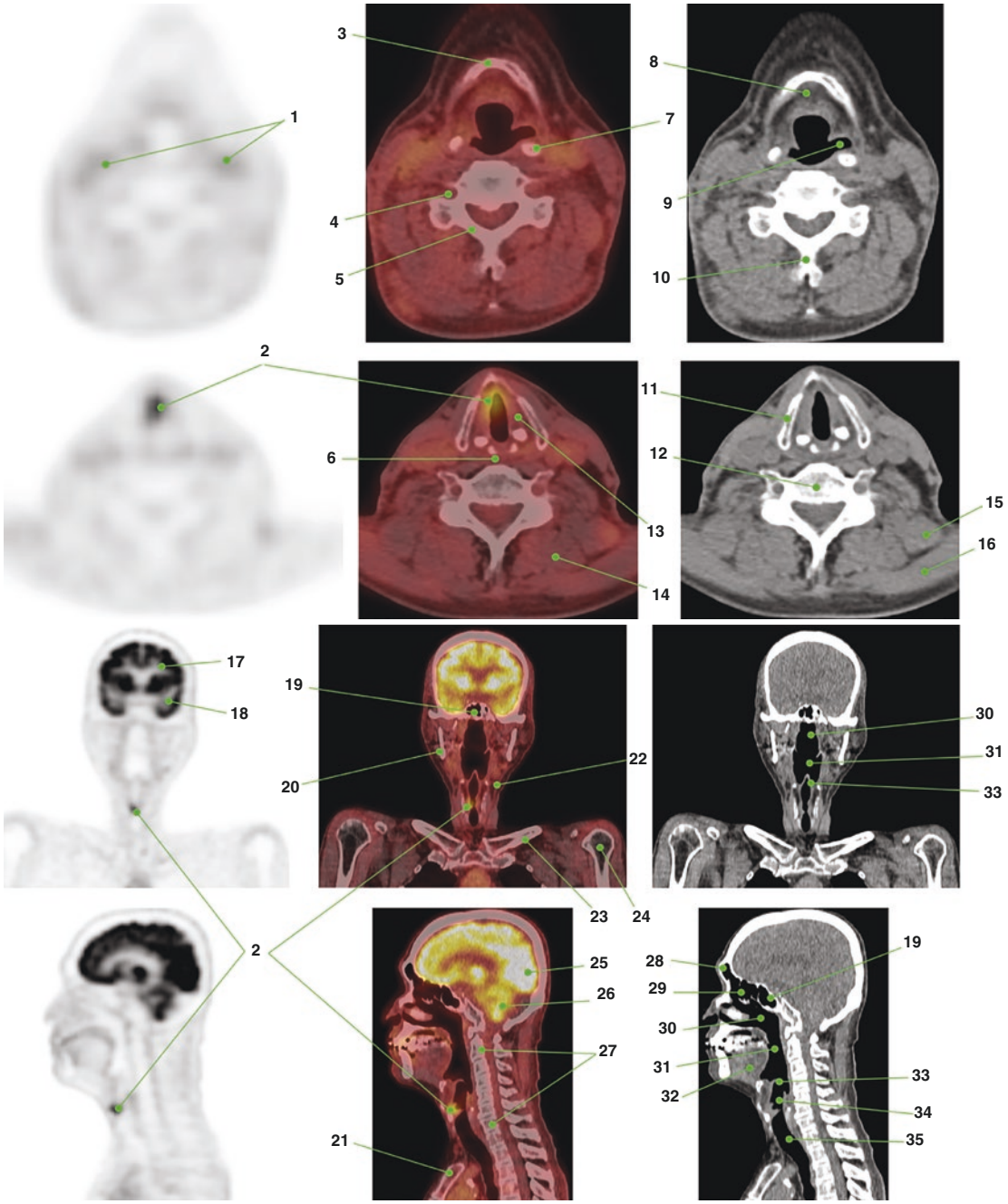

Figs. 7 and 8 1. Submandibular glands
2. Metabolically active glottis squamous cell carcinoma
3. Hyoid bone
4. Cervical transverse foramen, vertebral artery
5. Cervical vertebral body posterior arch
6. Arytenoid cartilages
7. Cricoid cartilage
8. Pre-epiglottic fat
9. Left pyriform sinus
10. Cervical vertebrae, spinous process
11. Thyroid cartilage
12. Cervical vertebral body
13. Left vocal cord
14. Left splenius capitis muscle
15. Left levator scapula muscle
16. Left trapezius muscle
17. Left parietal lobe
18. Left temporal lobe
19. Sphenoid sinus
20. Right mandible ramus
21. Sternum
22. Left parapharyngeal space
23. Left clavicle
24. Left humerus
25. Occipital lobe
26. Cerebellum
27. Cervical spine
28. Frontal sinus
29. Ethmoid cells
30. Nasopharynx
31. Oropharynx
32. Tongue
33. Epiglottis
34. Glottis
35. Trachea

1.1.6 Case 6

A 45-year-old woman with progressive enlargement of the thyroid gland and occasional pain. Ultrasound and ultrasound-guided biopsy confirmed the diagnosis of diffuse, large B-cell lymphoma, so ^{18}F-FDG PET/CT was performed for staging. Images showed marked increased activity in the diffusely enlarged thyroid gland. No hypermetabolic lymph nodes or distant metastasis were noted (Fig. 9) [21].

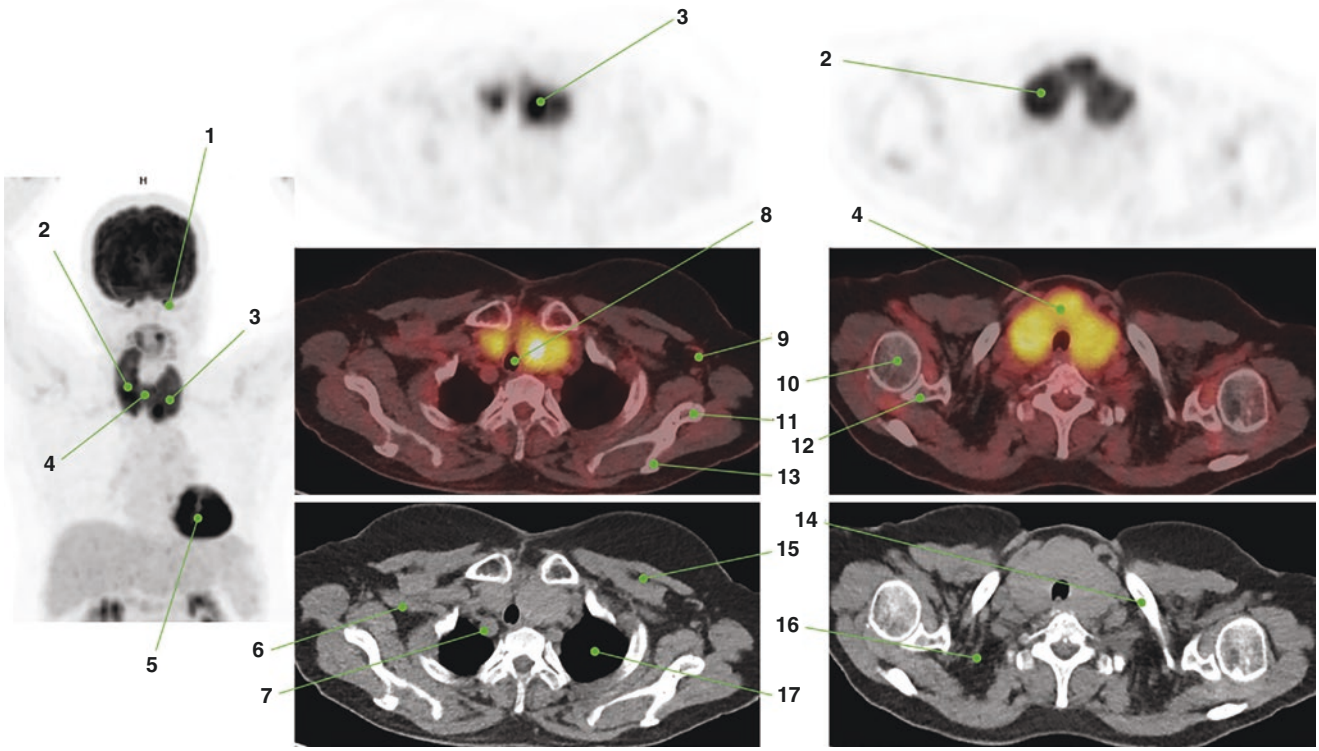

Fig. 9 1. Left optic nerve
2. Right thyroid lobe, lymphoma involvement
3. Left thyroid lobe, lymphoma involvement
4. Thyroid isthmus
5. Heart, left ventricular wall uptake
6. Right subclavian vein
7. Right brachiocephalic vein
8. Trachea
9. Normal left axillary lymph nodes
10. Right humeral head
11. Left acromion
12. Right glenoid
13. Left scapular spine
14. Left clavicle
15. Left interpectoral area
16. Posterior cervical fat
17. Left pulmonary apex

1.1.7 Case 7

An 85-year-old man with odynophagia. Physical examination revealed enlargement and ulceration of the right palatine tonsil and biopsy confirmed the diagnosis of a squamous cell carcinoma, so FDG was performed for staging. Images showed focal increased activity in the right palatine tonsil at the primary tumor, as well as two hypermetabolic metastatic lymph nodes in the right upper neck, level II. Note the obliteration of the right parapharyngeal space, which is one of the indirect signs of lesions at this location (Fig. 10) [9].

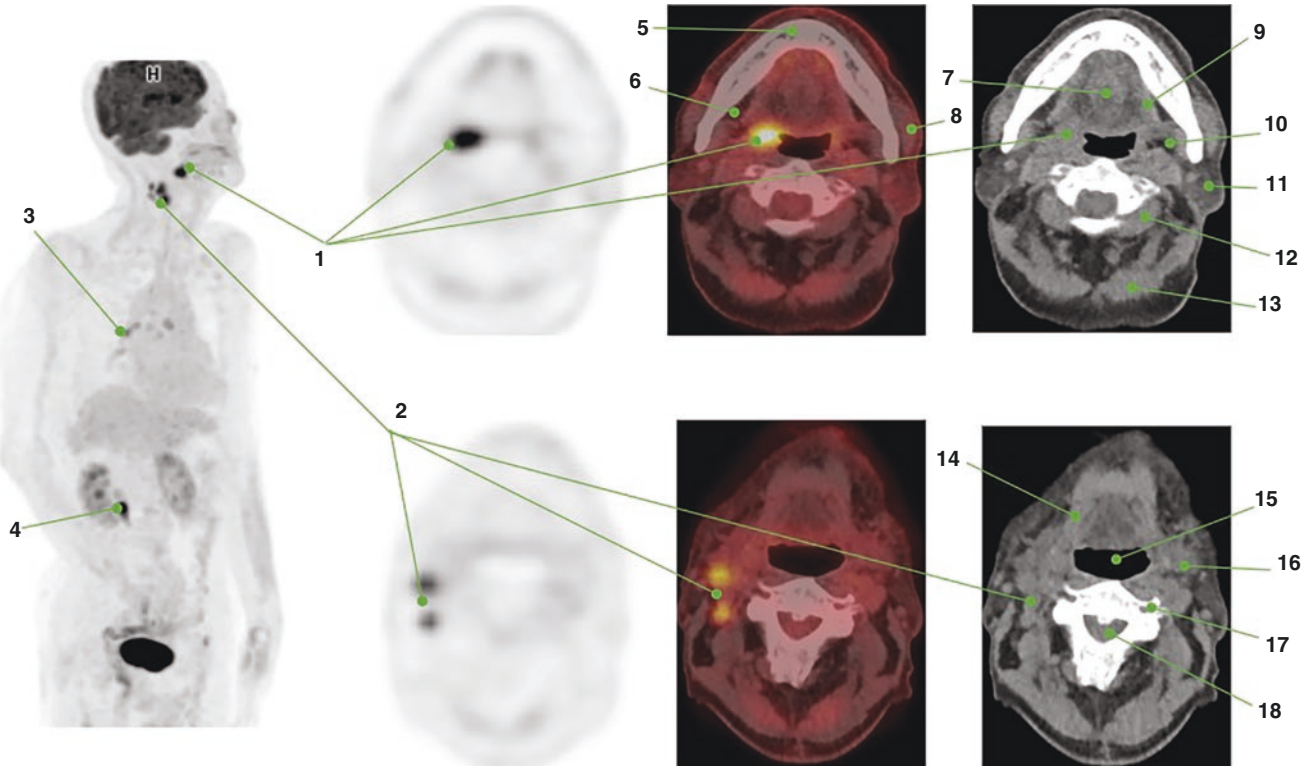

Fig. 10 1. Metabolically active primary tumor in the right tonsil
2. Metabolically active metastatic lymph nodes in the right neck, level II
3. Mild hypermetabolic lymph nodes in the right lung hilum, inflammatory
4. Right renal pelvis
5. Mandible
6. Right sublingual space
7. Genioglossus muscle
8. Left masseter muscle
9. Left mylohyoid muscle
10. Left parapharyngeal space
11. Left parotid gland
12. Left oblique capitis muscle
13. Left splenius capitis muscle
14. Right mylohyoid muscle
15. Oropharynx
16. Left submandibular gland
17. Left vertebral foramen
18. Spinal canal

1.2 Chest

1.2.1 Case 1

A 25-year-old man with rapid weight loss. Initial studies showed high alpha-fetoprotein (AFP) and a mediastinal mass in the chest X-ray, so ^{18}F-FDG PET/CT was performed on suspicion of a germ cell tumor. Images showed a well-defined, cystic-necrotic anterior mediastinal mass, with a peripheral hypermetabolic solid component, which suggested a more aggressive behavior favoring a non-seminomatous tumor. Posterior biopsy confirmed the diagnosis of a yolk sac tumor (Fig. 11).

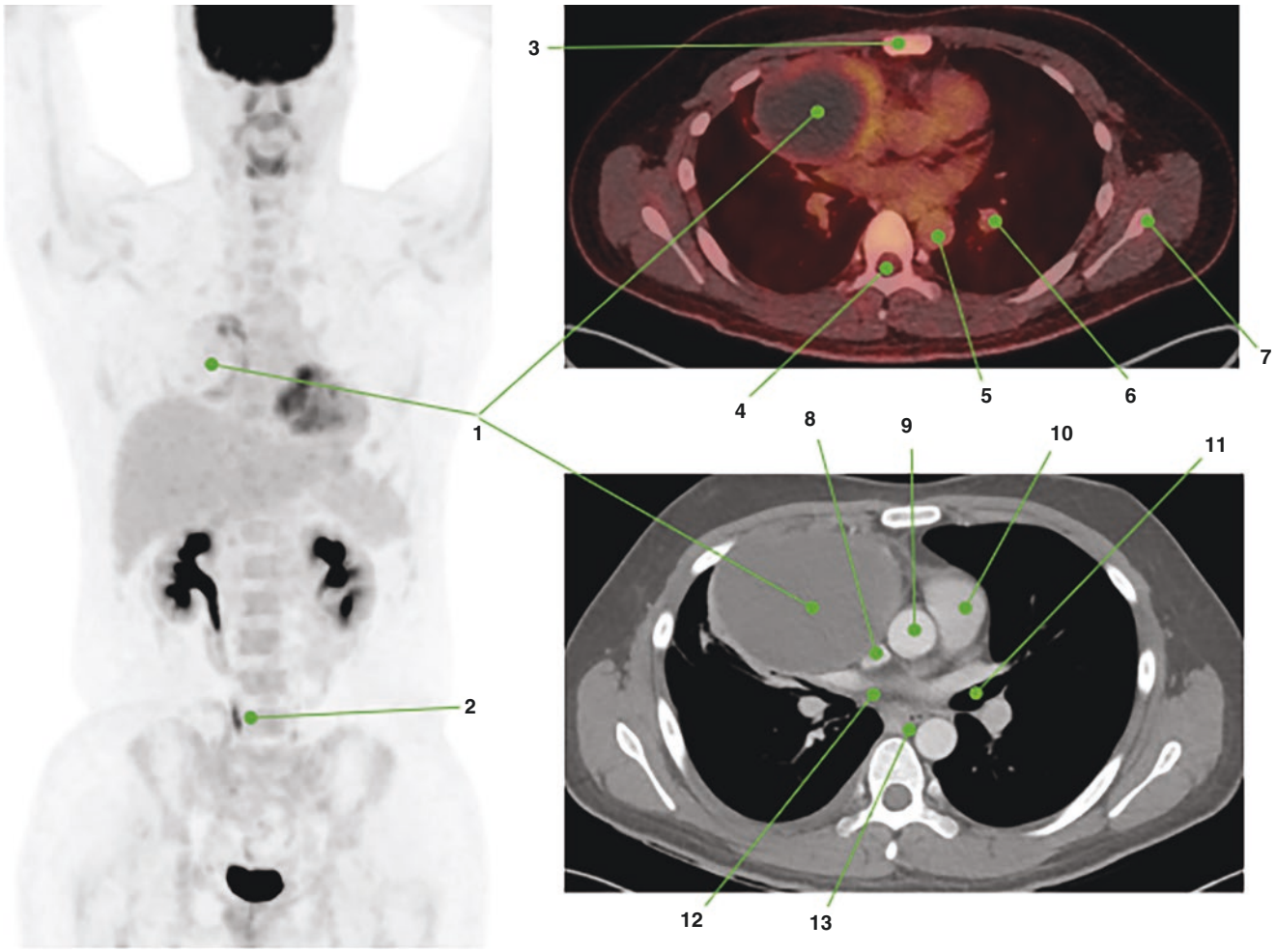

Fig. 11 1. Primary tumor with large cystic-necrotic component and hypermetabolic solid peripheral component
2. Right ureter
3. Sternum
4. Spinal canal
5. Descending aorta
6. Left pulmonary artery, upper lobe branch
7. Left scapula
8. Superior vena cava
9. Ascending aorta
10. Main pulmonary artery
11. Left main bronchus
12. Right atrium, superior aspect
13. Esophagus

1.2.2 Case 2

A 43-year-old woman with occasional dyspnea and chest tightness. Chest X-ray and CT were performed, finding a mediastinal mass and considering lymphoma or thymoma as differential diagnoses, so ^{18}F-FDG PET/CT was performed. Images showed an irregular, well-defined anterior mediastinal mass, with an adequate cleavage plane with the vascular structures, with mild homogeneous FDG uptake. With these findings, the diagnosis of low-grade thymoma was suggested and biopsy confirmed a type AB thymoma (Fig. 12) [22].

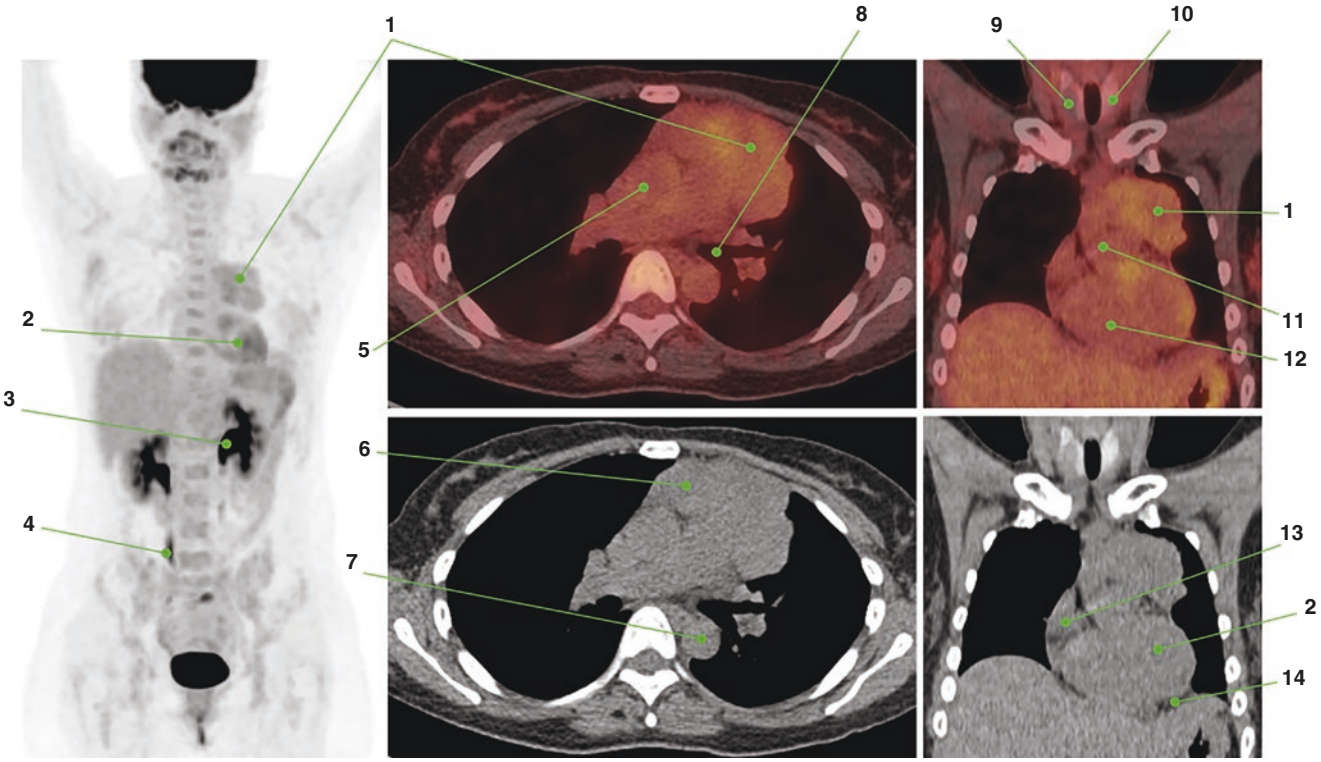

Fig. 12 1. Anterior mediastinal mass with mild homogeneous FDG uptake, consistent with thymoma type AB
2. Left ventricle
3. Left renal pelvis
4. Right middle ureter
5. Cavo-atrial junction
6. Ascending aorta
7. Descending aorta
8. Left main bronchus
9. Homogeneous cystic lesion in the right thyroid lobe
10. Left thyroid lobe
11. Aortic root
12. Right ventricle
13. Right atrium
14. Left pericardial recess

1.2.3 Case 3

A 50-year-old man with progressive dyspnea and chest pain. Chest X-ray and CT showed an anterior mediastinal mass, so ^{18}F-FDG PET/CT was performed. Images showed a large, irregular, but not infiltrative, mild, metabolically active anterior mediastinal mass with dystrophic calcifications. Extensive pleural invasion with the same mild, diffuse uptake as the primary tumor was observed. The findings suggested a low-grade thymoma and later biopsy confirmed a thymoma type B1 (Fig. 13) [22].

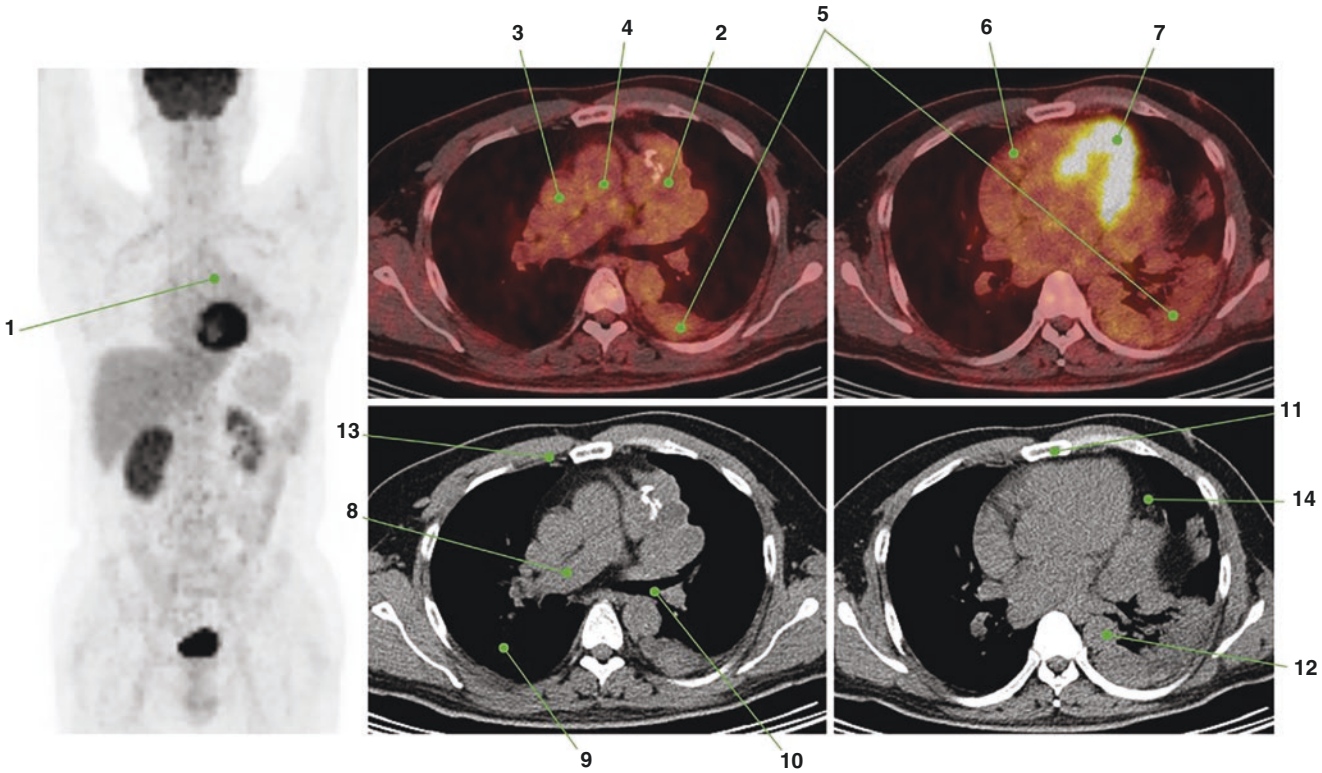

Fig. 13 1. Slight hypermetabolic anterior mediastinal mass corresponding to thymoma type B1
2. Thymoma type B1, left superior aspect with dystrophic calcifications
3. Superior vena cava
4. Common pulmonary artery
5. Extensive left pleural invasion
6. Thymoma type B1, right inferior aspect
7. Left ventricular wall
8. Right main pulmonary artery
9. Right lung lower lobe
10. Left main bronchus
11. Sternum
12. Descending aorta
13. Right internal mammary vessels
14. Pericardial fat

1.2.4 Case 4

A 58-year-old patient with atypical and occasional chest pain who underwent an echocardiogram, finding a poorly defined mediastinal lesion. Contrast CT and ^{18}F-FDG PET/CT revealed a poorly defined infiltrative mediastinal lesion with high and homogeneous FDG uptake, as well as a right inferior pleural seeding. The findings were suspicious of a high-grade thymoma, and postsurgical pathology of the pleural lesion confirmed the diagnosis of a thymoma type B3 (Fig. 14) [22].

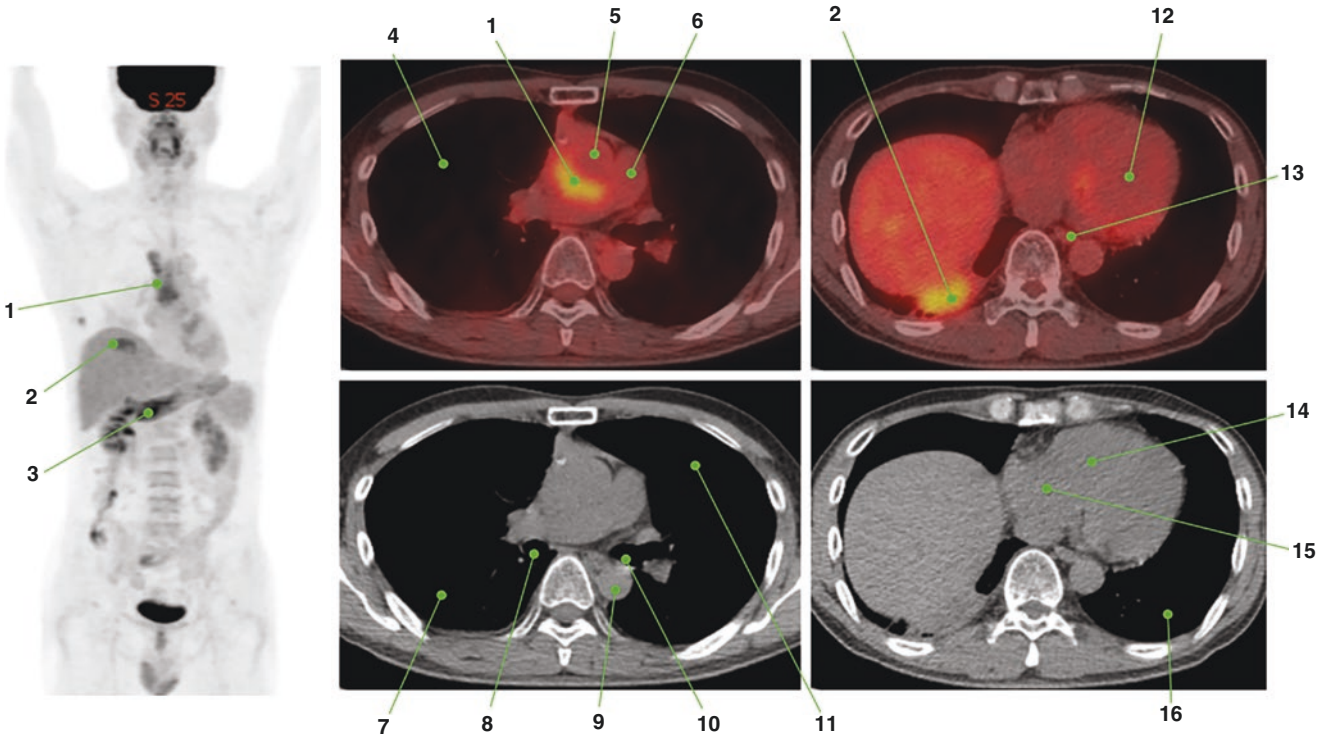

Fig. 14 1. Increased activity in the infiltrating mass, consistent with thymoma type B3
2. Metabolically active right lower lobe pleural seeding
3. Gastric antrum physiologic FDG uptake
4. Right upper lobe
5. Ascending aorta
6. Common pulmonary artery
7. Right lower lobe
8. Right main bronchus
9. Descending aorta
10. Left main bronchus
11. Left upper lobe
12. Left ventricle
13. Lower esophagus
14. Right ventricle
15. Right atrium
16. Left lower lobe

1.2.5 Case 5

A 58-year-old female patient with a history of diffuse, large B-cell lymphoma with lymph node involvement, treated with chemotherapy achieving complete metabolic response. In the last ^{18}F-FDG PET/CT checkup, multiple new hypermetabolic mediastinal lymph nodes were noted, with a distribution in bilateral hilar, subcarinal, and right paratracheal areas (lambda sign). Also, diffusely increased activity was detected in the soft tissues of the lower lumbar region and left gluteal region. Given the suspicion of lymphoma recurrence, biopsy of both the lymph nodes and the soft tissue lesions was performed, where chronic granulomatous changes consistent with sarcoidosis were reported (Fig. 15).

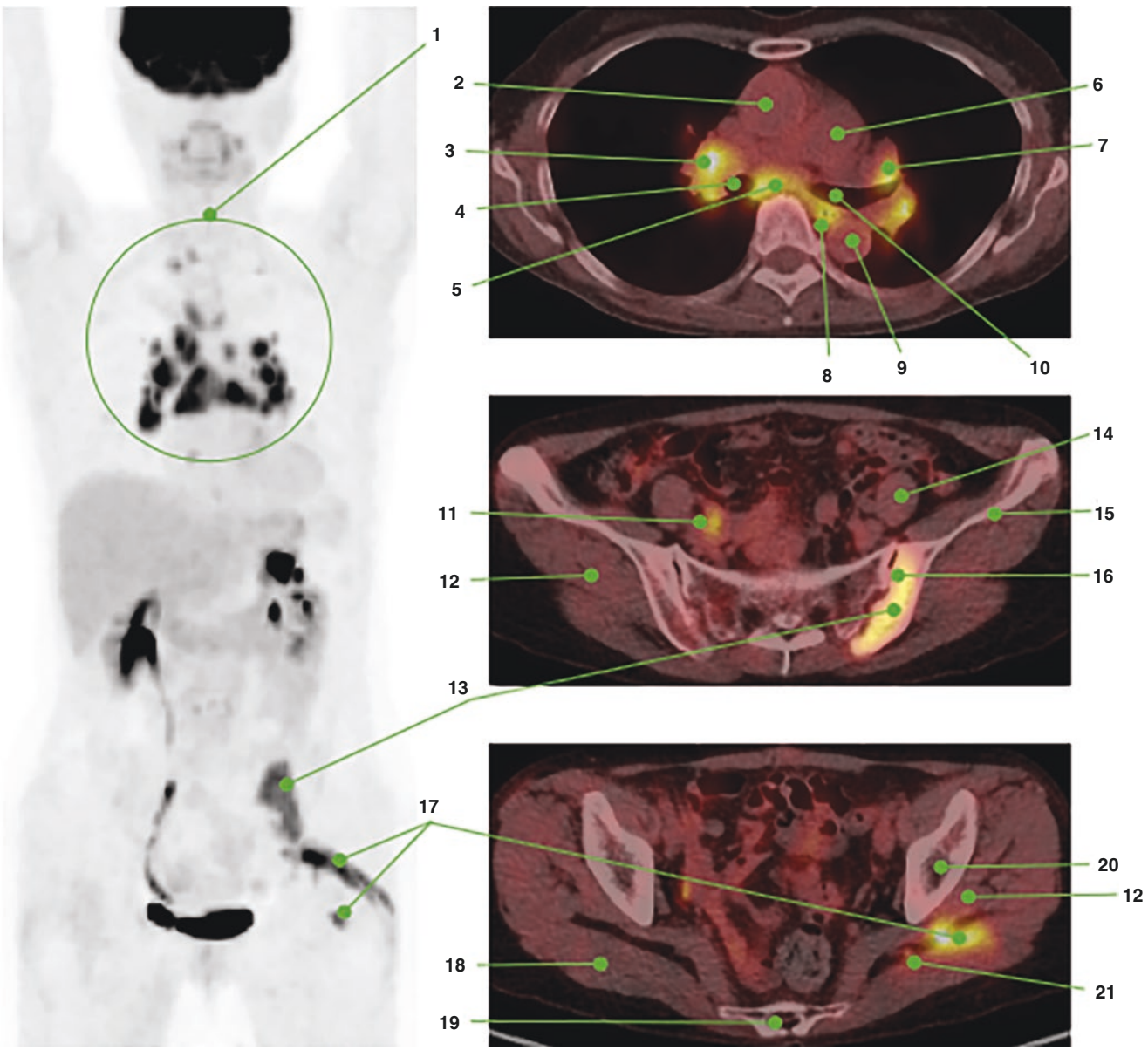

Fig. 15 1. Metabolically active mediastinal lymph nodes, lambda sign
2. Ascending aorta
3. Right hilar lymph nodes, level 10R
4. Right main bronchus
5. Subcarinal lymph nodes, level 7
6. Main pulmonary artery
7. Left hilar lymph nodes, 10L
8. Esophagus
9. Descending aorta
10. Left main bronchus
11. Right ureter, distal third
12. Gluteus medius muscles
13. Increased activity at left iliac bone involvement
14. Left iliopsoas muscle
15. Left iliac wing
16. Left sacroiliac joint
17. Increased activity at left gluteal soft tissue involvement
18. Right gluteus maximus muscle
19. Sacrum
20. Left acetabular roof
21. Metabolically active intergluteal lymph node

1.2.6 Case 6

A 51-year-old man with dyspnea and chest pain, with normal chest X-ray. Suspecting pulmonary embolism (PE), chest CT angiography was requested, finding an extensive filling defect in the pulmonary trunk, the entire right pulmonary artery and the branch for the superior lobe, as well as in the proximal left pulmonary artery. However, the filling defect was irregular and showed enhancement, indicating that it was more likely a soft tissue lesion or a tumor thrombus, so ^{18}F-FDG PET/CT was performed. Images showed marked increased activity in the irregular intravascular lesion without other findings. A primary angiosarcoma of the pulmonary artery was suggested as the diagnosis, which was later confirmed with biopsy (Fig. 16) [23].

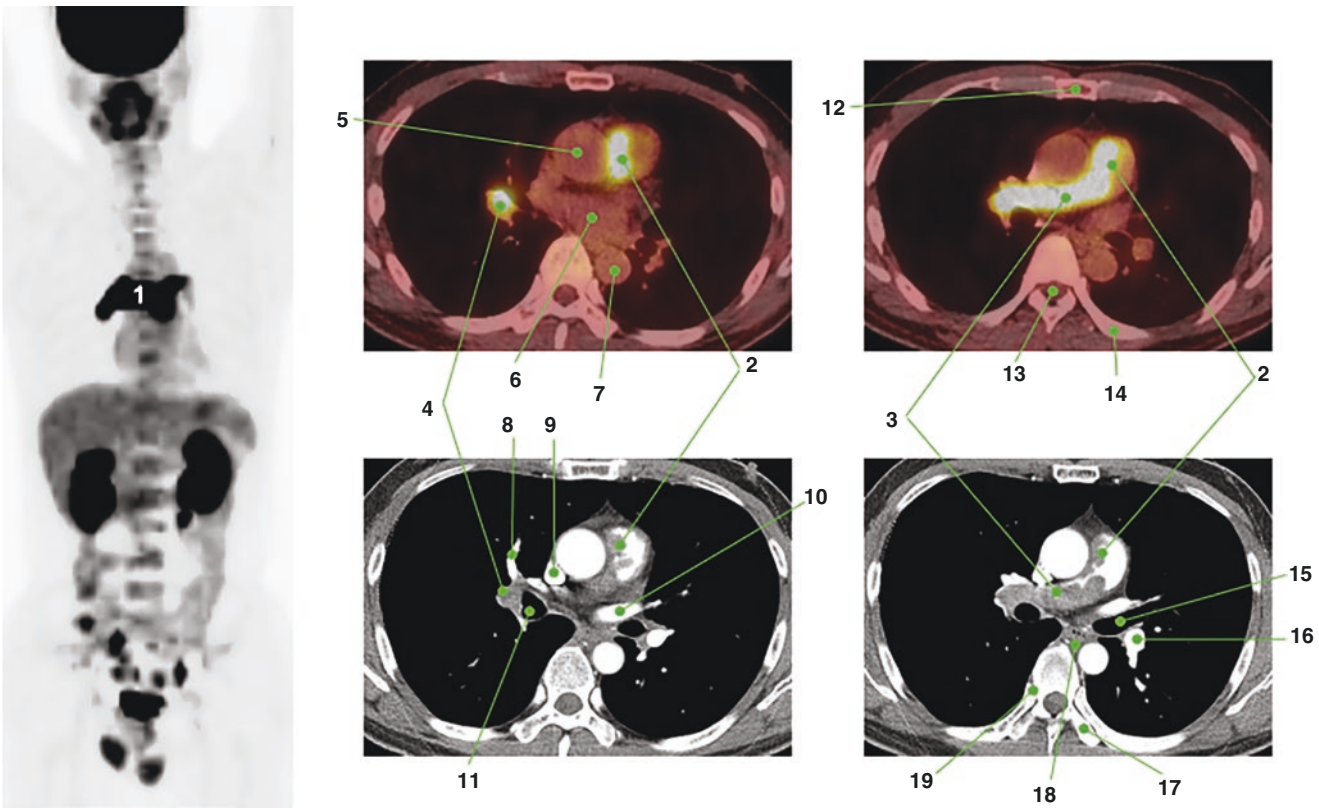

Fig. 16 1. Metabolically active tumor in the pulmonary artery
2. Angiosarcoma involvement at the main pulmonary artery
3. Angiosarcoma involvement at the right pulmonary artery
4. Angiosarcoma involvement at the right upper lobe artery
5. Ascending aorta
6. Left atrium superior aspect
7. Descending aorta
8. Right interlobar artery
9. Superior vena cava
10. Left pulmonary artery
11. Right main bronchus
12. Sternum
13. Spinal canal
14. Left rib posterior arc
15. Left main bronchus
16. Left upper lobe pulmonary artery
17. Thoracic vertebra left transverse process
18. Esophagus
19. Right costovertebral joint

1.2.7 Case 7

A 28-year-old woman with occasional chest pain. Chest X-ray was performed finding a mediastinal mass, so ^{18}F-FDG PET/CT was ordered for further evaluation. Initial images (superior) showed intense FDG uptake in a bulky anterior mediastinal mass, as well as metabolically active enlarged lymph nodes at the lower neck and right cardiophrenic and left retroperitoneal areas. The diagnosis of primary mediastinal B-cell lymphoma was confirmed and first-line chemotherapy was started. Two cycles later, in the follow-up ^{18}F-FDG PET/CT, complete metabolic resolution of the previously visualized lesions was observed. This unique and rare subtype of non-Hodgkin lymphoma occurs in only 2–3% of cases (Fig. 17) [24].

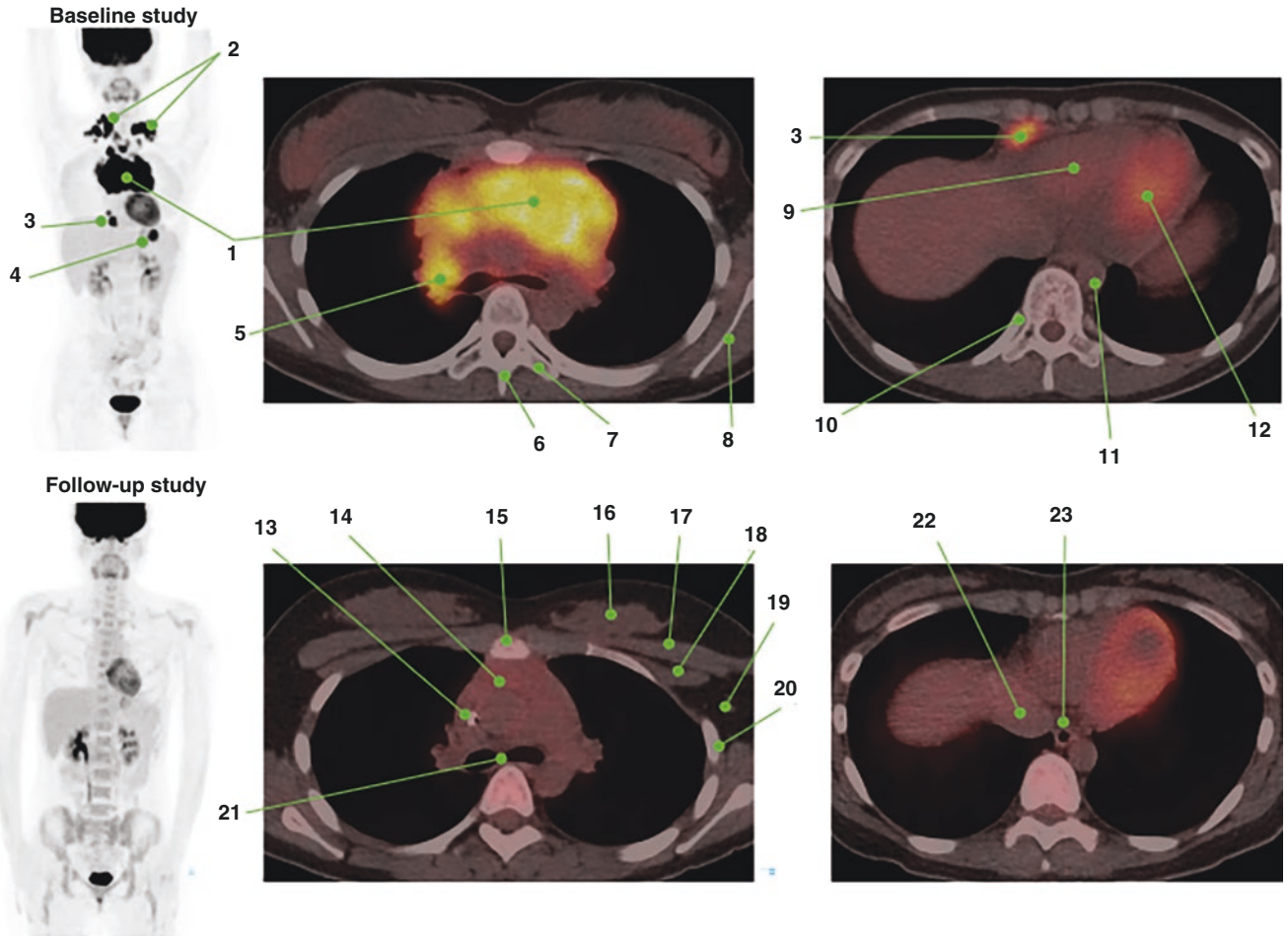

Fig. 17 1. Metabolically active bulky anterior mediastinal mass
2. Hypermetabolic enlarged lymph nodes in the bilateral lower neck
3. Focal increased activity in right cardiophrenic lymph node
4. Focal increased activity in left retroperitoneal lymph node
5. Focal increased activity in right hilar lymph node
6. Thoracic vertebral body spinous process
7. Thoracic vertebral body left transverse process
8. Left scapula
9. Right ventricle
10. Right costovertebral junction
11. Descending aorta
12. Left ventricle
13. Posttreatment residual calcification
14. Residual soft tissue lesion in the anterior mediastinum with no definite FDG uptake (Deauville 1)
15. Sternum
16. Left breast tissue
17. Left major pectoralis muscle
18. Left minor pectoralis muscle
19. Left axillary fossa
20. Left rib, lateral arc
21. Carina
22. Superior vena cava
23. Esophagus

1.2.8 Case 8

A 54-year-old woman with diagnosis of infiltrating ductal carcinoma of the left breast and suspected axillary lymph node metastases. As part of staging, ^{18}F-FDG PET/CT was performed. Images showed diffuse, increased activity in the left breast, predominantly toward the lower outer quadrant, where the primary lesion was confirmed. Furthermore, multiple metabolically active lymph node metastases were observed at all left axillary levels, supraclavicular region, and mediastinum. In the normal right breast parenchyma, diffuse FDG uptake is perceived, which represents normal physiologic activity frequently seen in premenopausal women (Figs. 18 and 19) [25].

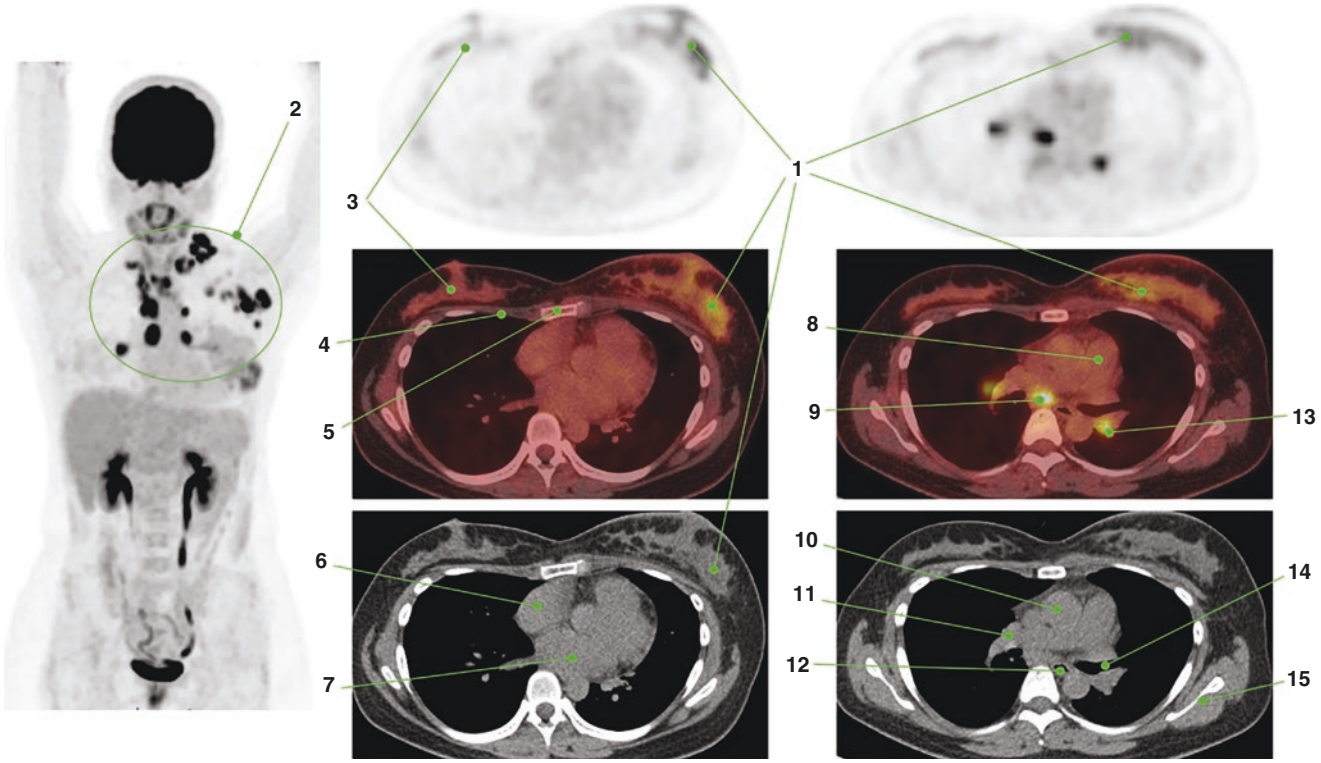

Fig. 18 1. Hypermetabolic diffuse infiltrative left breast cancer
2. Multiple hypermetabolic lymph node metastasis
3. Normal right breast tissue with mild, diffuse FDG uptake
4. Right internal mammary chain, normal
5. Sternum
6. Right atrium
7. Left atrium
8. Common pulmonary artery
9. Hypermetabolic infracarinal lymph node (level 7)
10. Ascending aorta
11. Right hilum (11R metastasis)
12. Lower esophagus
13. Left hypermetabolic lymph node (level L11)
14. Left main bronchus
15. Left scapula

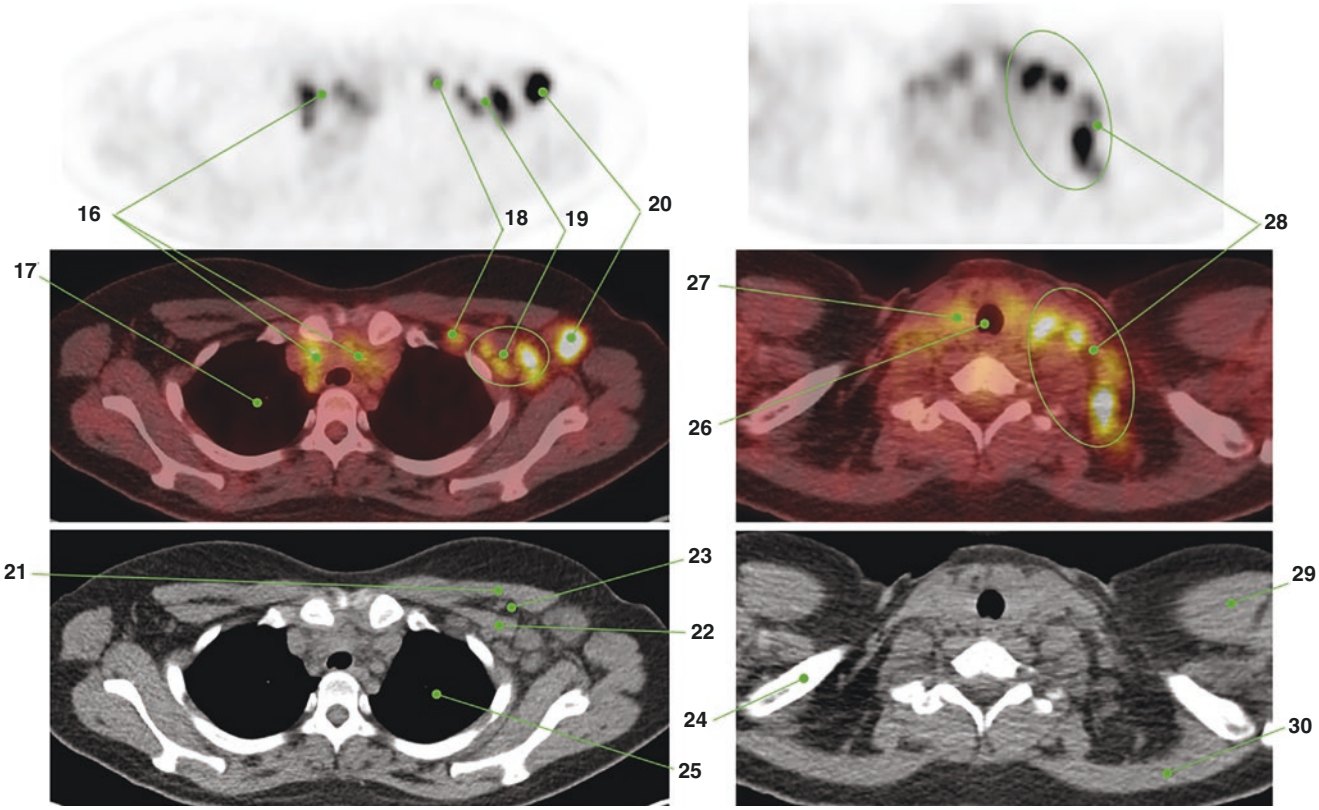

Fig. 19 1. Bilateral superior mediastinal lymph nodes (level 1–2)
2. Right lung, upper lobe
3. Level III hypermetabolic lymph node
4. Level II hypermetabolic lymph nodes
5. Level I hypermetabolic lymph node
6. Left major pectoralis muscle
7. Left minor pectoralis muscle
8. Interpectoral lymph node (Rotter lymph node)
9. Right clavicle
10. Left lung, upper lobe
11. Trachea
12. Right thyroid lobe with mild, diffuse uptake
13. Hypermetabolic left supraclavicular lymph nodes
14. Left deltoid muscle
15. Left trapezius muscle

1.2.9 Case 9

A 48-year-old woman with progressive pain, redness, and hardening of the left breast, associated with bloody nipple discharge. Ultrasound and biopsy were performed confirming the diagnosis of an inflammatory carcinoma and ^{18}F-FDG PET/CT was requested for staging. Images showed a metabolically active multifocal left breast cancer with increased activity at marked skin thickening. Multiple hypermetabolic metastatic lymph nodes were also observed, predominantly in the axillary level I, as well as same-side interpectoral area and internal mammary chain (Fig. 20) [25].

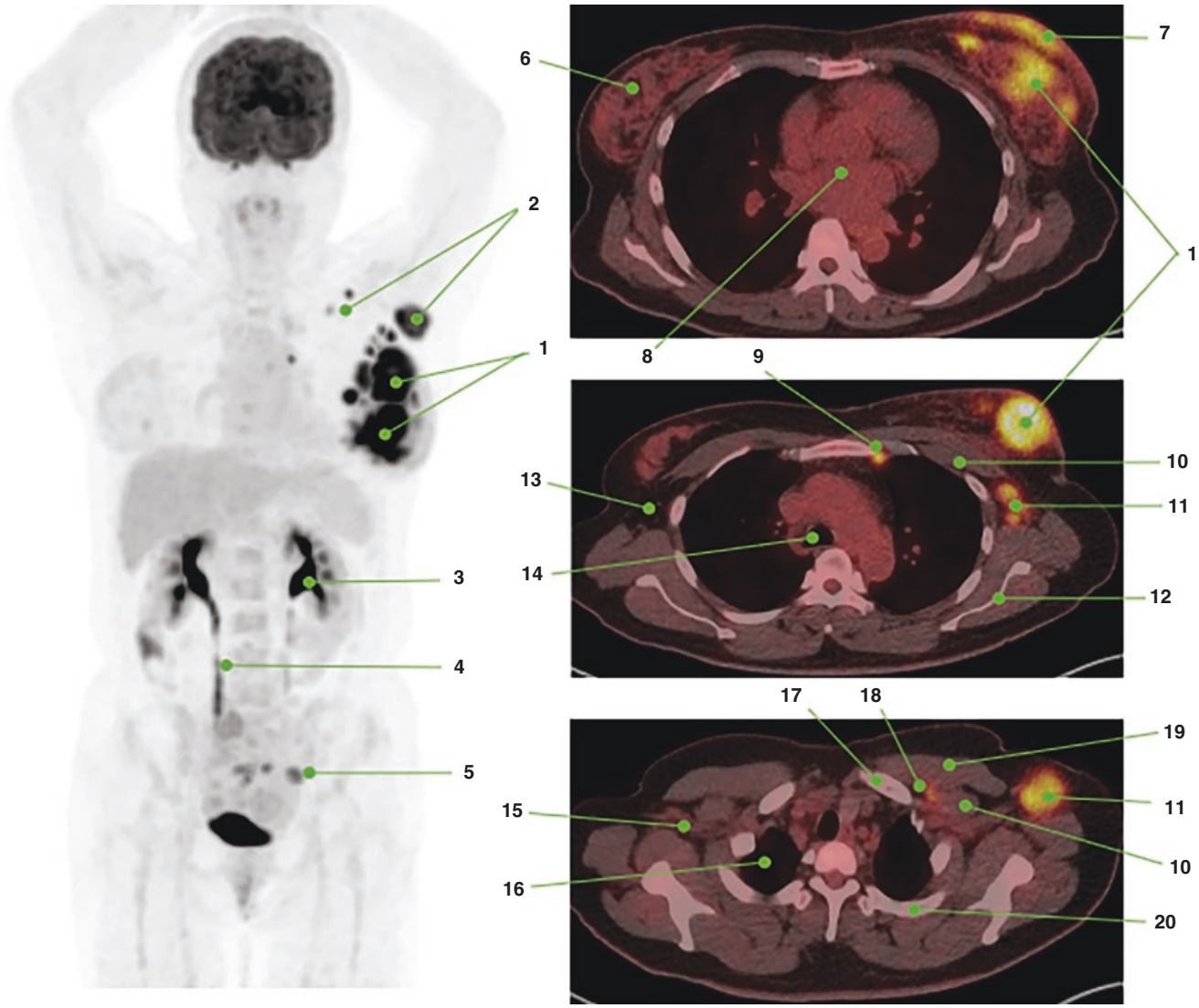

Fig. 20 1. Metabolically active multifocal left breast cancer
2. Multiple hypermetabolic metastatic lymph nodes
3. Left renal pelvis
4. Right ureter
5. Left adnexal physiologic activity
6. Normal right breast tissue
7. Increased activity at skin thickening in the left breast
8. Mediastinal vessels
9. Left internal mammary lymph node metastasis
10. Minor pectoralis muscle
11. Metastatic left axillary lymph nodes, level I
12. Left scapula
13. Right axillary fossa
14. Trachea
15. Right subclavian vessels
16. Right lung apex
17. Left first rib, anterior arc
18. Interpectoral lymph node (Rotter) metastasis
19. Left major pectoralis muscle
20. Left second rib, posterior arc

1.2.10 Case 10

An 80-year-old male patient with history of scalp angiosarcoma, treated with surgery and chemotherapy. Follow-up ^{18}F-FDG PET/CT was performed 8 months after surgery and showed multiple new lesions, including a small left upper lobe pneumothorax chamber, increased activity at a right middle lobe ground glass opacity, and multiple randomly distributed, thin-walled cystic lesions, some with peripheral FDG uptake. Hypermetabolic lymph nodes were also noted in the subcarinal and bilateral hilar areas. Ultrasound-guided endobronchial biopsy revealed the suspected diagnosis: angiosarcoma metastasis (Fig. 21) [26].

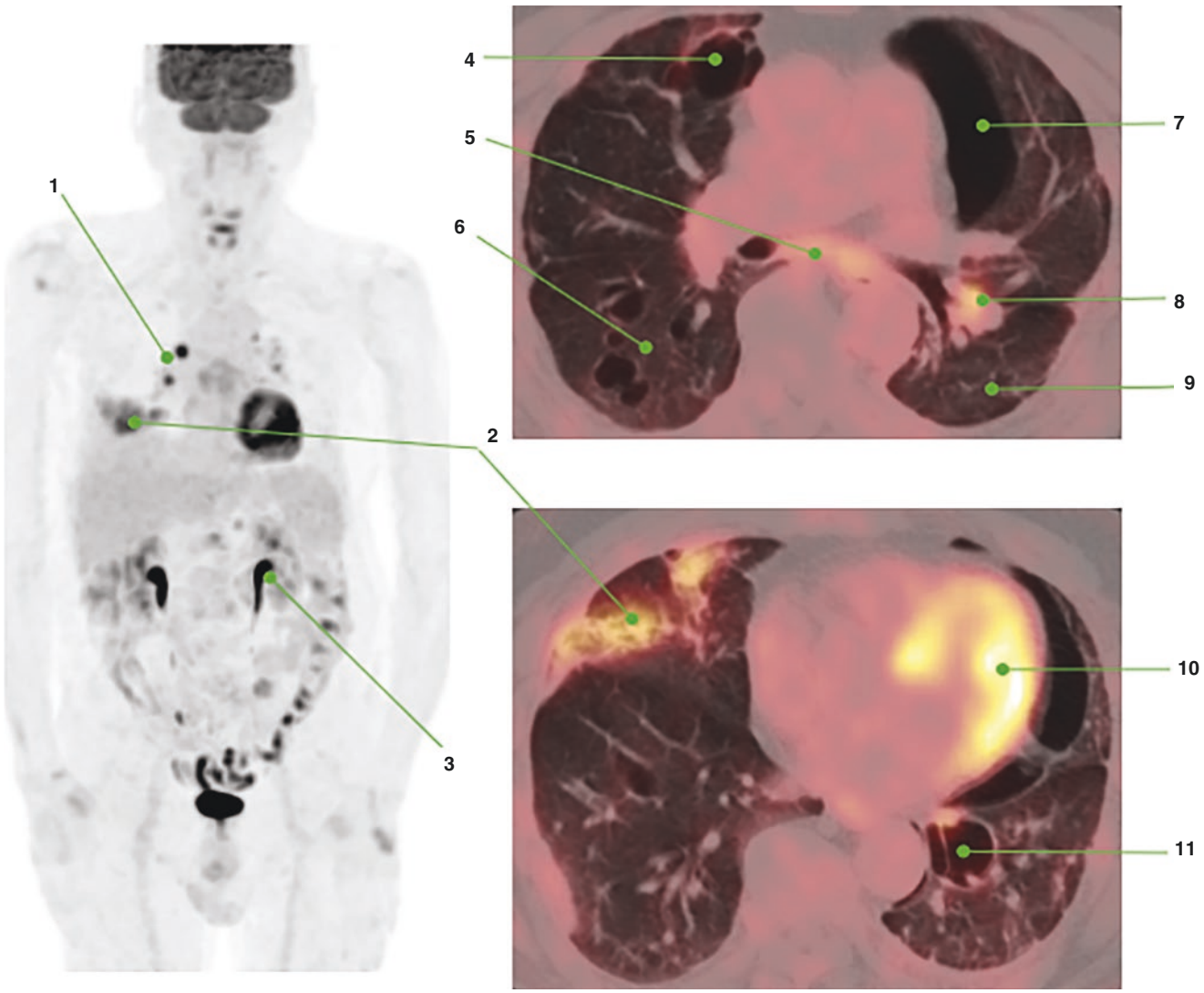

Fig. 21 1. Metabolically active right hilar lymph nodes
2. Diffusely increased activity in ground-glass opacities at the right middle lobe
3. Left renal pelvis
4. Thin-walled cystic metastasis with peripheral uptake at the right upper lobe
5. Hypermetabolic subcarinal lymph nodes
6. Right lower lobe with multiple thin-walled cystic metastasis
7. Small left upper lobe pneumothorax chamber
8. Hypermetabolic left hilar lymph node
9. Left lower lobe
10. Diffusely increased uptake in the left ventricular wall
11. Thin-walled cystic metastasis with peripheral uptake at the left lower lobe

1.2.11 Case 11

A 43-year-old male patient, currently smoker, who presented with persistent productive cough with occasional drops of blood. ^{18}F-FDG PET/CT was performed, finding multiple metabolically active solid nodules with random distribution in both lungs, with two dominant lesions at the right lung, one of them with central cavitation. Ultrasound-guided endobronchial biopsy confirmed the diagnosis of primary pulmonary melanoma at the right upper lobe, with multiple bilateral metastases. Additionally, a metastatic mediastinal lymph node conglomerate with necrotic components was found involving levels 7, 10R, and 11R, as well as a right neck level II metabolically active lymph node (Figs. 22 and 23) [27].

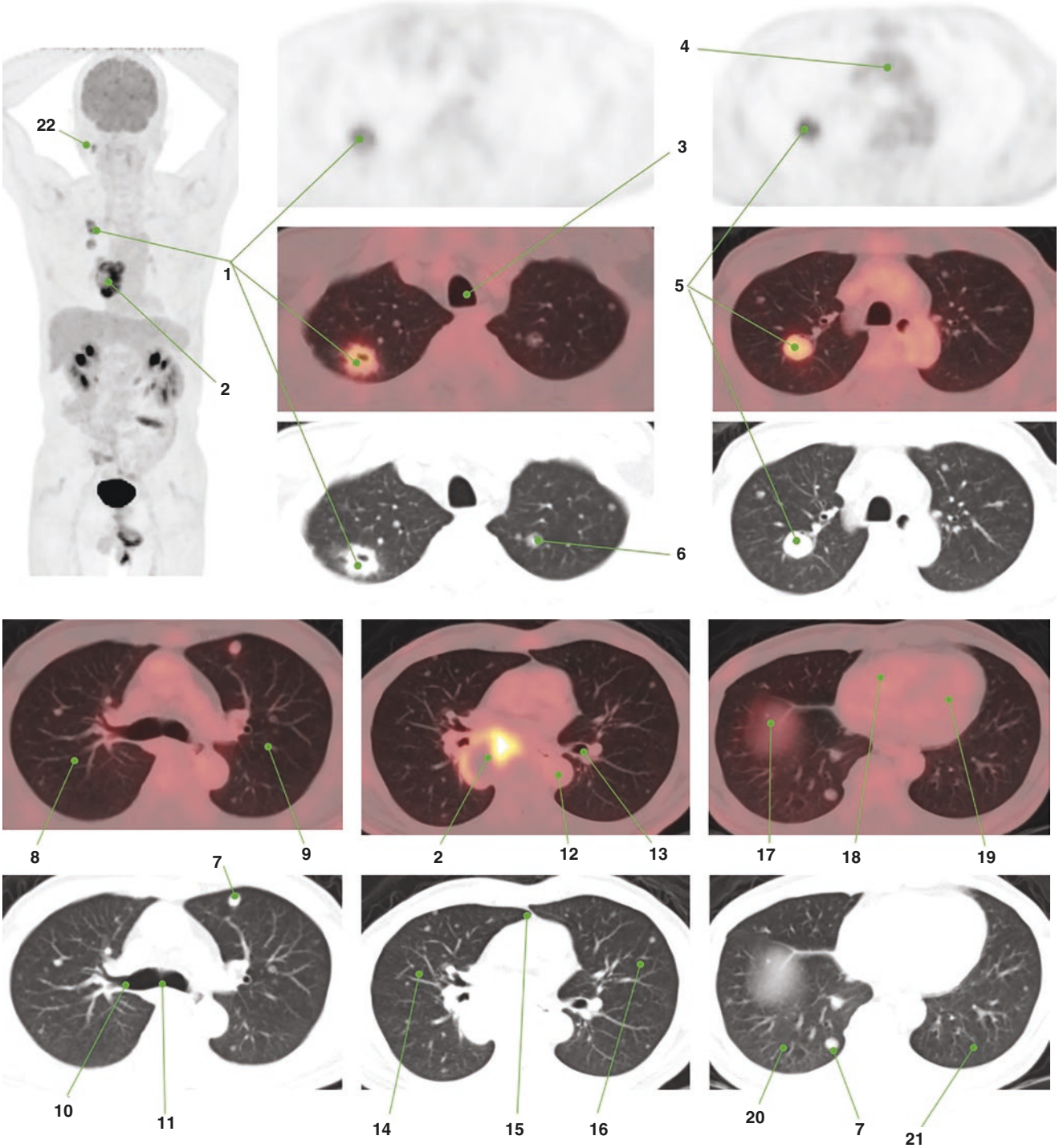

Figs. 22 and 23 1. Right upper lobe hypermetabolic cavitated nodule
2. Mediastinal lymph node conglomerate with uneven uptake due to necrosis
3. Trachea
4. Aortic arch
5. Right upper lobe hypermetabolic solid nodule
6. Left upper lobe metastatic ground glass nodule
7. Solid metastases
8. Right upper lobe
9. Left upper lobe
10. Right main bronchus
11. Carina
12. Descending aorta
13. Left bronchus
14. Right middle lobe
15. Anterior junction line of the pleura
16. Left lower lobe, lingula
17. Diaphragm, liver dome
18. Right ventricle
19. Left ventricle
20. Right lower lobe
21. Left lower lobe
22. Right neck level II lymph node metastasis

1.2.12 Case 12

A 74-year-old woman with significant weight loss. Chest X-ray showed a mediastinal mass, so ^{18}F-FDG PET/CT was performed. Images revealed a high metabolically active left hilar mass with multiple mediastinal and lower neck metastatic lymph nodes, as well as a retroperitoneal lymph node. The diagnosis of a primary lung cancer was suggested, but transbronchial biopsy confirmed a diffuse, large B-cell lymphoma. Findings that favor the diagnosis of lymphoma include the presence of a bulky mass with bulky lymph nodes, which surrounds or encases the bronchial and vascular structures, without compressing or invading them. Also, the presence of lymph nodes in other locations can give a clue, although there is no definitive finding to differentiate them from metastasis of a primary lung tumor (Fig. 24) [28].

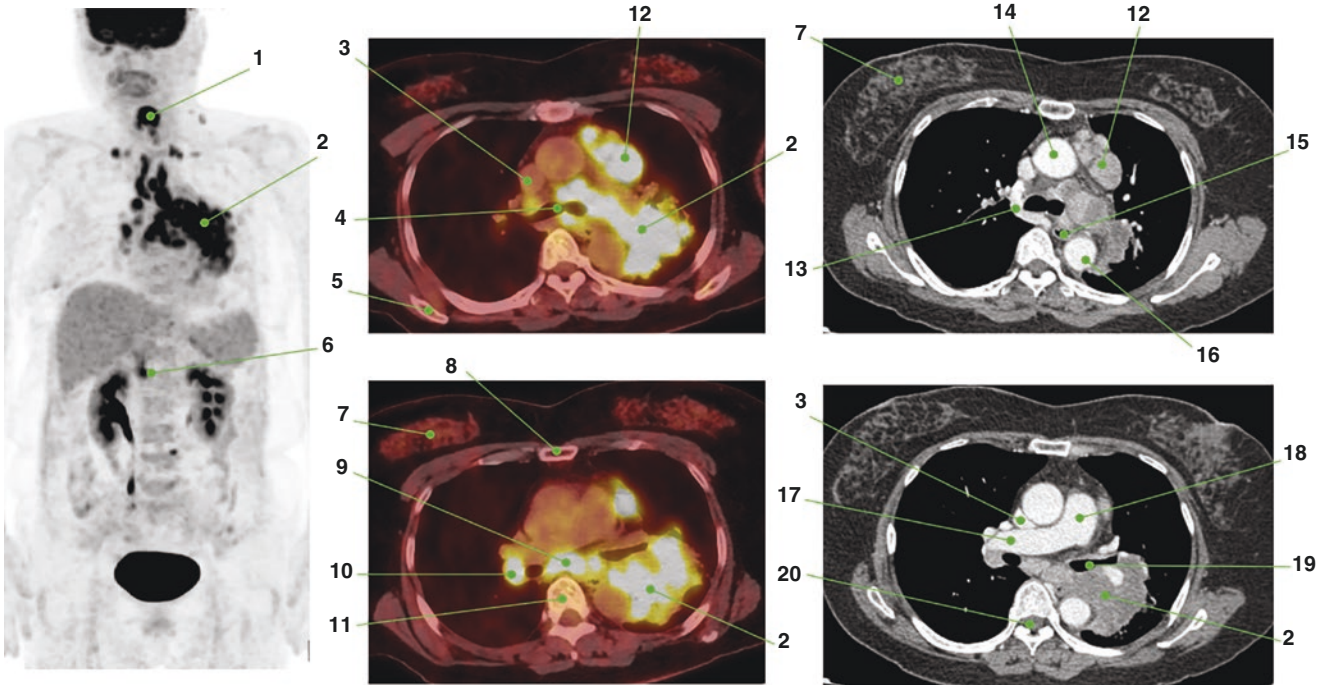

Fig. 24 1. Lymphoma involvement at lower cervical lymph nodes
2. Metabolically active left hilar mass, consistent with diffuse large B-cell lymphoma
3. Superior vena cava
4. Carina
5. Tip of the right scapula
6. Lymphoma involvement at upper aortocaval lymph node
7. Right breast fibroglandular tissue
8. Sternum
9. Lymphoma involvement at subcarinal lymph nodes
10. Lymphoma involvement at right hilar lymph nodes
11. Thoracic vertebral body
12. Lymphoma involvement at prevascular lymph nodes
13. Azygos vein
14. Ascending aorta
15. Esophagus
16. Descending aorta
17. Right main pulmonary artery
18. Common pulmonary artery
19. Left main bronchus
20. Spinal cord

1.2.13 Case 13

A 75-year-old female patient with history of breast cancer and recent diagnosis of small cell lung cancer, in treatment with immunotherapy (atezolizumab). Follow-up ^{18}F-FDG PET/CT showed increased size of metabolically active primary tumor in the left upper lobe, with a peripheral area of necrosis, as well as increased activity in two lesions that were previously not so evident, one in the left diaphragmatic crus and other in the right perirenal area. At this time, the possibility of a pseudo-progression due to the ongoing treatment was considered, which was confirmed with the following follow-up, where metabolic response of all the described lesions was observed (Fig. 25) [29].

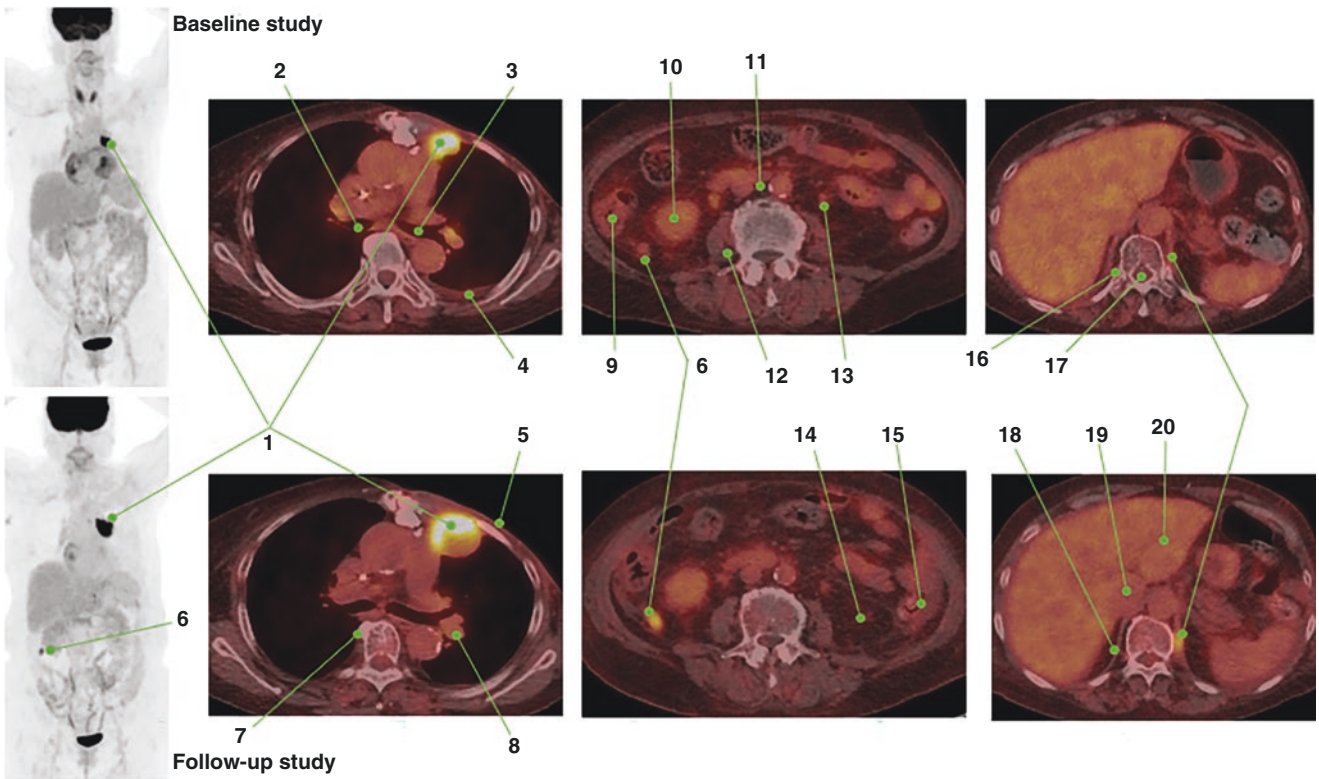

Fig. 25 1. Metabolically active primary tumor in the left upper lobe. Note the posterior necrotic component of the mass in the follow-up study
2. Right main bronchus
3. Left main bronchus
4. Small amount of left pleural effusion
5. Left mastectomy post-op changes
6. Increased activity at nodular lesion in the right perirenal space
7. Thoracic vertebral body osteophyte
8. Left pulmonary hilum
9. Ascending colon
10. Right kidney, inferior pole
11. Aortocaval space
12. Right psoas muscle
13. Left ureter
14. Left perirenal fat
15. Descending colon
16. T11 right costovertebral junction
17. Spinal canal
18. Right diaphragmatic crus
19. Caudate lobe
20. Left hepatic lobe
21. Increased activity at nodular lesion in the left diaphragmatic crus

1.2.14 Case 14

A 59-year-old woman with a history of breast cancer 25 years ago. She attended due to progressive dyspnea and chest radiograph showed diffuse opacity of the left lung, so ^{18}F-FDG PET/CT was performed. Images showed marked increased activity in diffuse nodular pleural thickening of the left lung, with involvement of the major fissure; there was no significant pleural effusion or mediastinal lymph nodes. Pleural mesothelioma was initially suspected, but biopsy confirmed the diagnosis of pleural metastases from breast carcinoma. Although it is not the most frequent site of metastasis, the pleura can be the only manifestation of recurrent disease in up to 40% of cases (Fig. 26) [30].

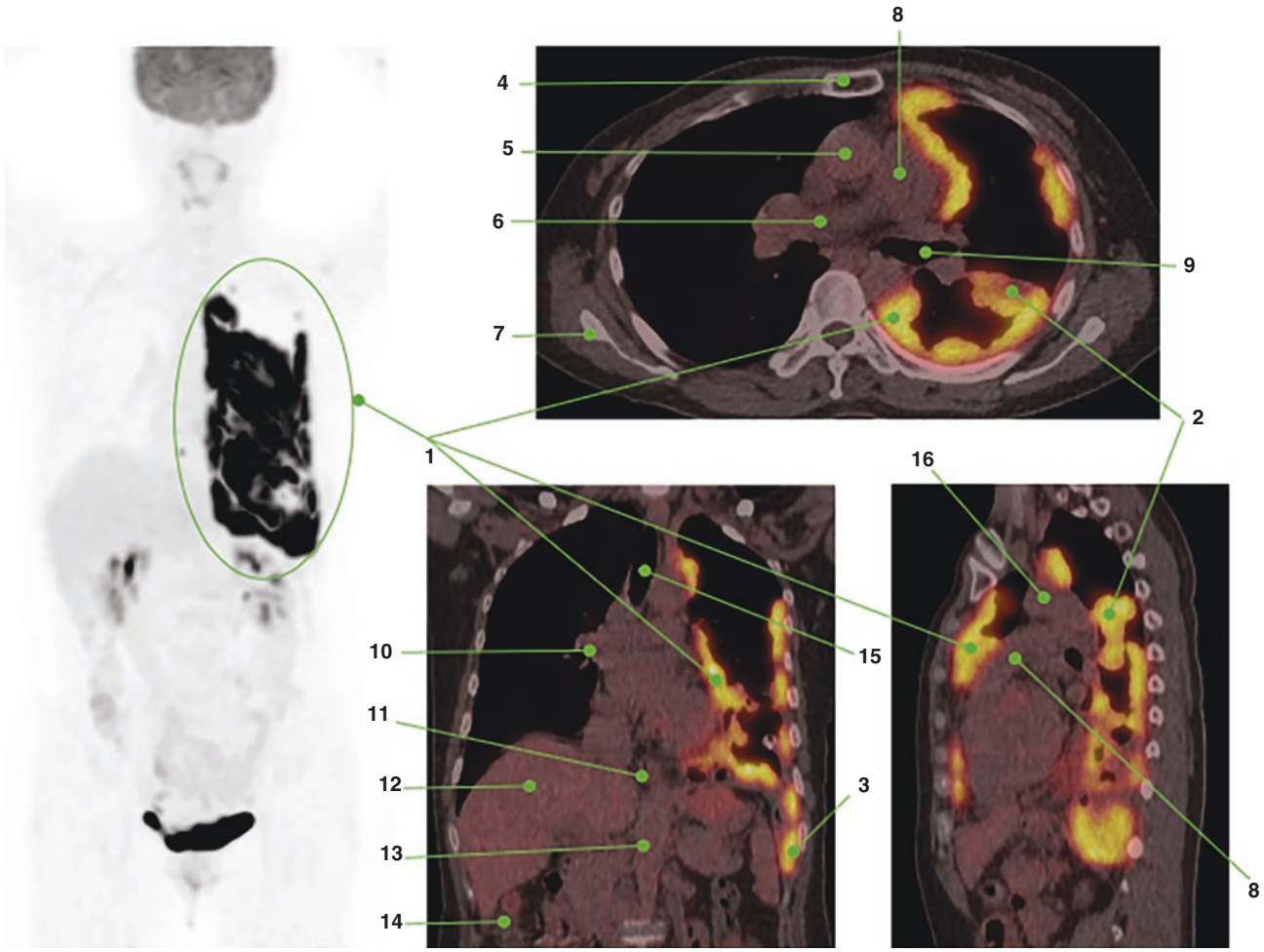

Fig. 26 1. Marked increased activity at diffuse left pleural nodular thickening
2. Increased activity at left major fissure involvement
3. Increased activity at the deep left costophrenic angle involvement
4. Sternum
5. Ascending aorta
6. Right main pulmonary artery
7. Right scapula
8. Pulmonary trunk
9. Left main bronchus
10. Right pulmonary hilum
11. Gastroesophageal junction
12. Right hepatic lobe
13. Abdominal aorta
14. Ascending colon
15. Trachea
16. Aortic arch

1.2.15 Case 15

A 54-year-old woman with dyspnea and fatigue for several months. Chest X-ray was performed, finding bilateral pleural effusion and cardiomegaly. Given the suspicion of pulmonary embolism, contrast-enhanced CT was performed, finding a soft tissue mass involving the right ventricle, superior vena cava, and innominate veins, as well as mild pericardial effusion. ^{18}F-FDG PET/CT was performed for whole body evaluation, observing moderate, diffuse, increased activity in the soft tissue lesion described in tomography. Final diagnosis was consistent with a superior vena cava angiosarcoma (Fig. 27) [23].

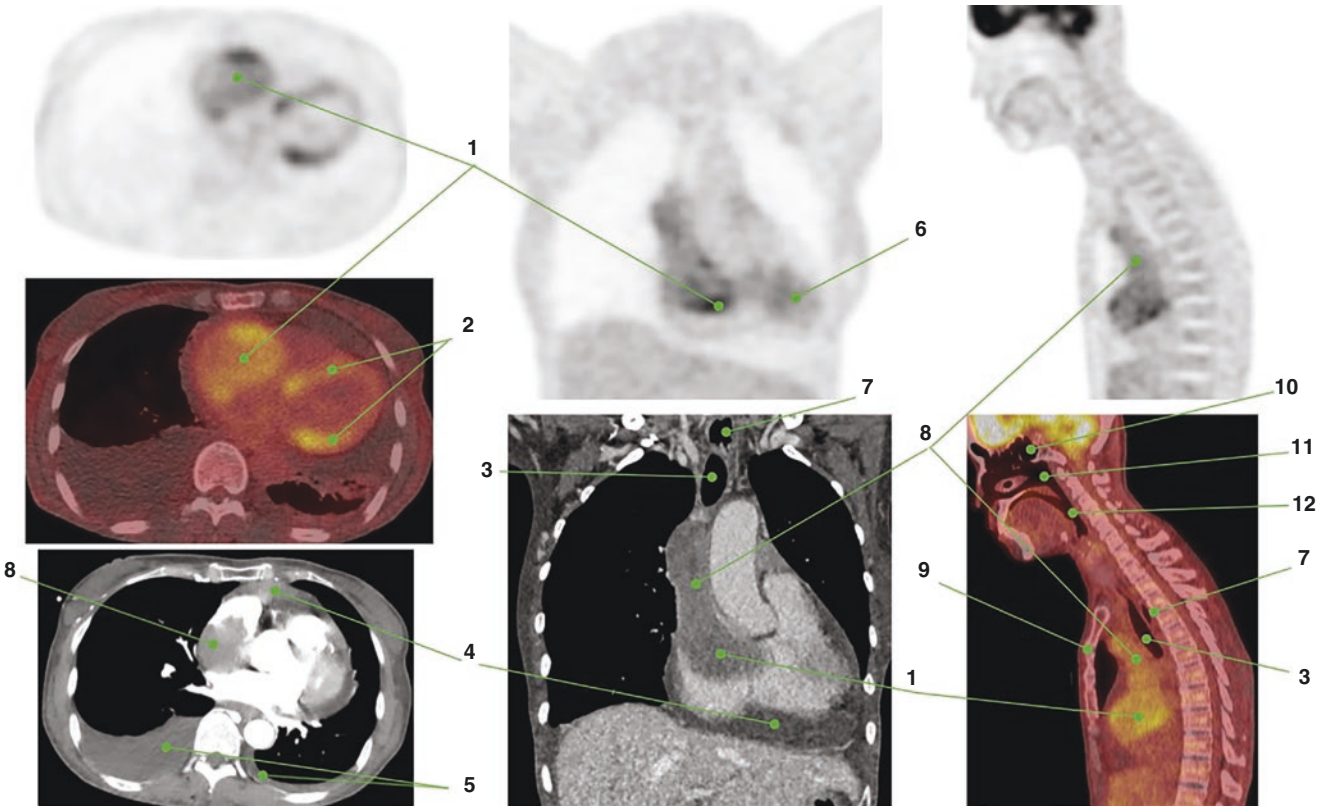

Fig. 27 1. Hypermetabolic angiosarcoma, right ventricle component
2. Physiologic uptake in the left ventricle wall
3. Trachea
4. Pericardial effusion
5. Bilateral pleural effusion
6. Left ventricle
7. Esophagus
8. Hypermetabolic angiosarcoma, superior vena cava component
9. Sternum
10. Sphenoid sinus
11. Nasopharynx
12. Oropharynx

1.2.16 Case 16

A 34-year-old male patient with progressive odynophagia and night sweats. ^{18}F-FDG PET/CT was performed finding a metabolically active mass in the oropharynx, consistent with biopsy-confirmed diffuse, large B-cell lymphoma; no other hypermetabolic lesion suggestive of lymphoma involvement was found. However, two incidental cardiac findings were found: (1) diffuse increase in FDG uptake at the right ventricular wall, secondary to pulmonary hypertension and (2) focal FDG uptake at the upper portion of the interventricular septum, protruding into the left ventricle. The last finding corresponds to an asymmetric or isolated septal hypertrophy, also known as interventricular septal bulge (Fig. 28) [31].

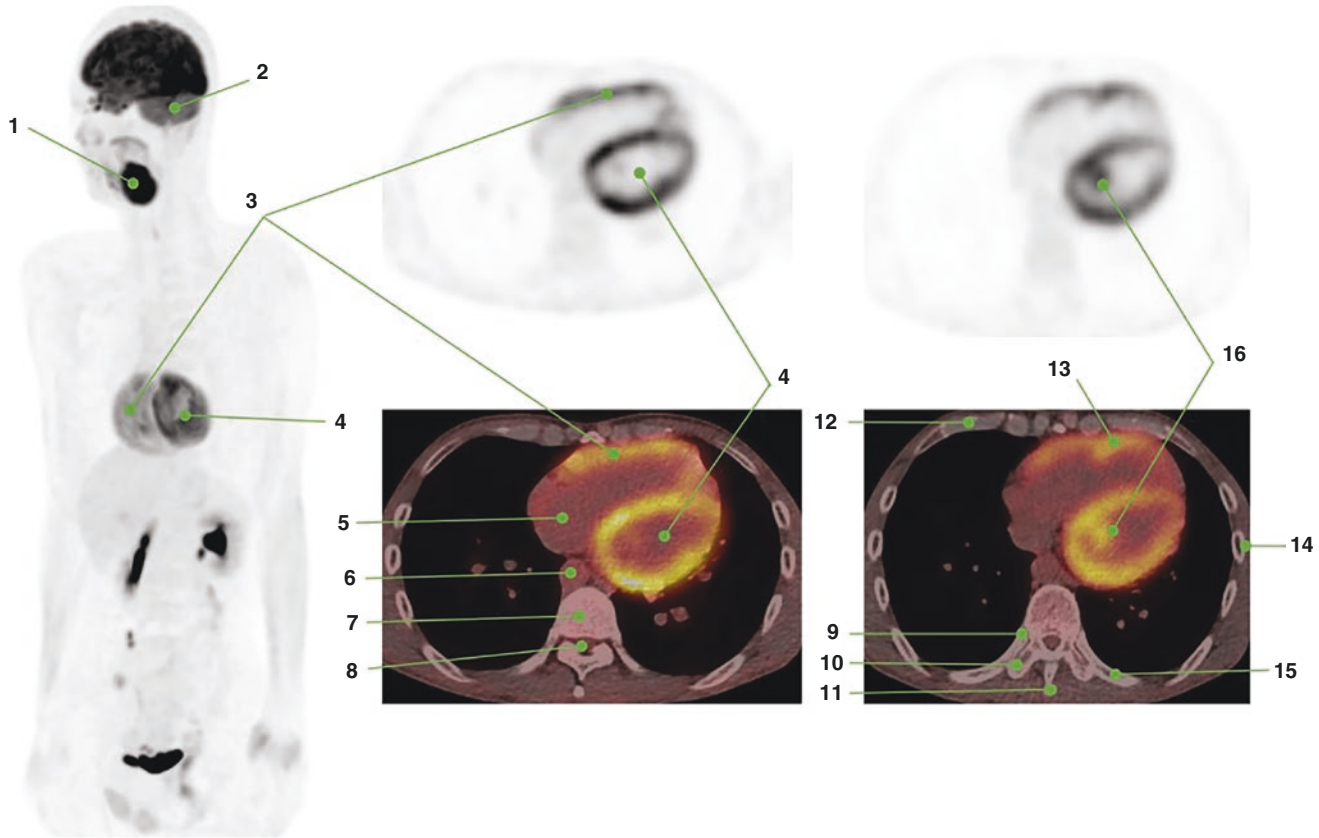

Fig. 28 1. Metabolically active oropharyngeal lymphoma
2. Cerebellum
3. Diffuse FDG uptake in the right ventricular wall
4. Diffuse FDG uptake in the left ventricular wall
5. Right atrium
6. Descending aorta
7. Thoracic vertebral body
8. Spinal cord
9. Right costovertebral junction
10. Vertebral right transverse process
11. Vertebral spinous process
12. Right costal cartilage
13. Right ventricle papillary muscle
14. Left rib, lateral arc
15. Left rib, posterior arc
16. Asymmetric or isolated septal hypertrophy, also known as interventricular septal bulge

1.2.17 Case 17

An 18-year-old man with diagnosis of Hodgkin lymphoma with inguinal lymph nodes involvement, undergoing treatment with first-line chemotherapy. After the second cycle, follow-up ^{18}F-FDG PET/CT was performed, where complete resolution of the previously visualized lymph nodes was observed. However, as a new finding, increased activity was found at the aortic root, consistent with inflammatory changes (aortitis), more likely related to the established treatment (Fig. 29) [32].

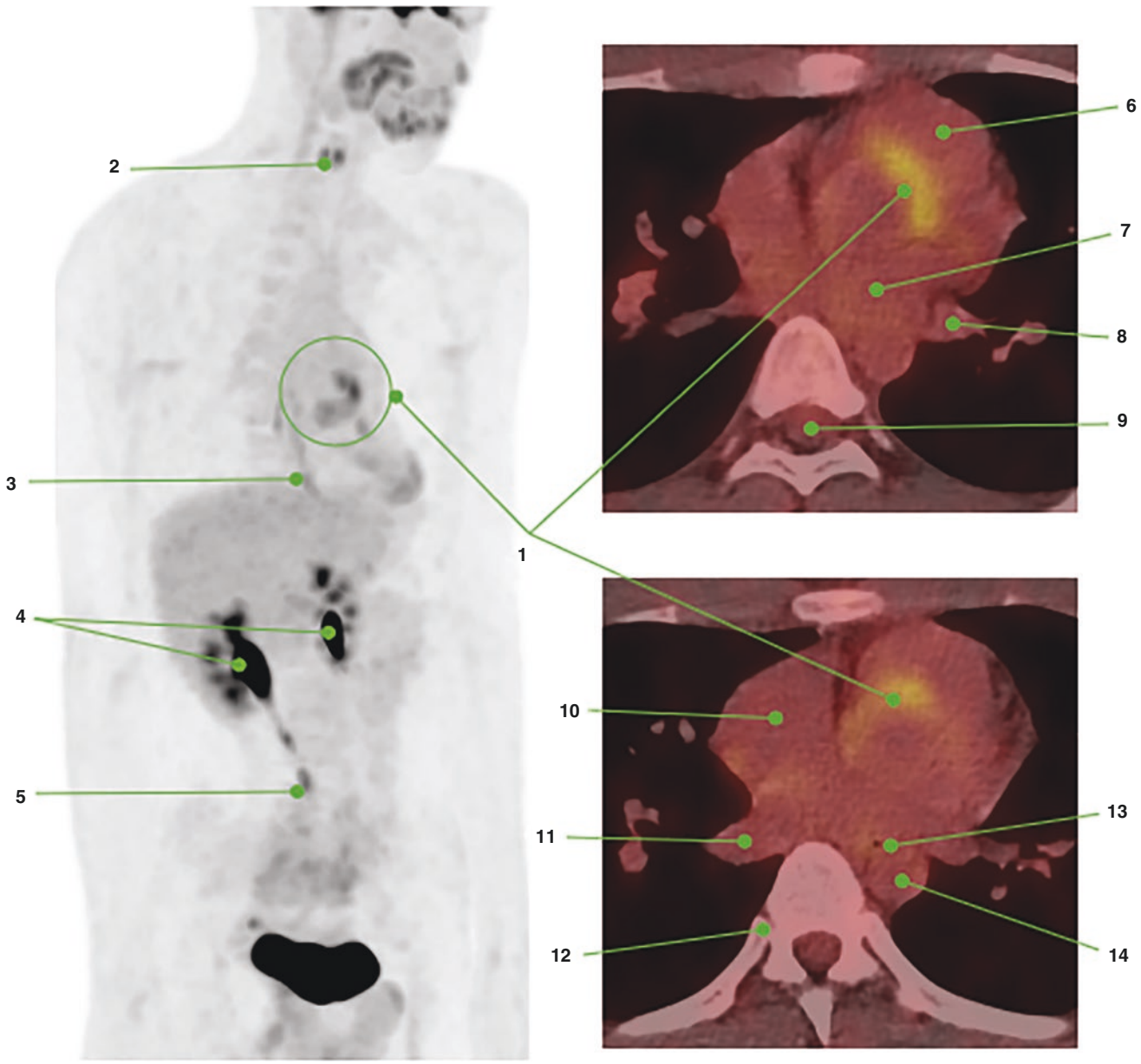

Fig. 29 1. Diffusely increased activity at the aortic root
2. Increased activity at the vocal cords
3. Increased activity at the distal esophagus, probable esophagitis
4. Renal pelvis
5. Right middle ureter
6. Right ventricle
7. Left atrium
8. Left pulmonary vein
9. Spinal canal
10. Right atrium
11. Right pulmonary vein
12. Right costovertebral junction
13. Esophagus
14. Descending aorta

1.2.18 Case 18

A 32-year-old man diagnosed with Hodgkin lymphoma with nodal involvement. ^{18}F-FDG PET/CT was performed for end-of-therapy follow-up, where complete resolution of previously identified lymph nodes was found, consistent with metabolic complete response. However, increased activity was found in the bilateral neck, supraclavicular fossae, and thoracic paravertebral areas, corresponding in the CT to fat with no underlying lesion. This finding represents metabolically active adipose tissue or brown fat and is a common finding specially related to cold temperatures (Fig. 30) [33].

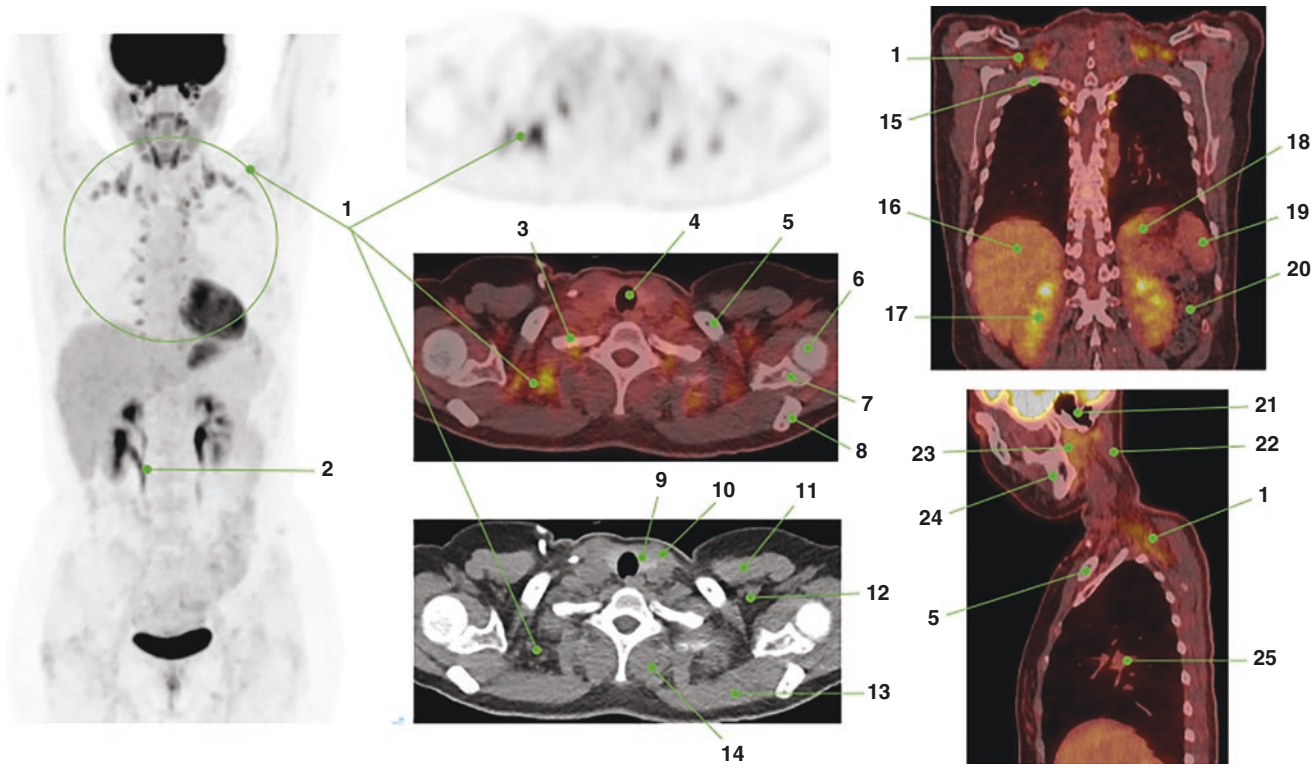

Fig. 30 1. Brown adipose tissue in typical locations: neck, supraclavicular fossa and paravertebral space
2. Right double collecting system
3. Right first rib
4. Trachea
5. Left clavicle
6. Left humeral head
7. Left glenoid
8. Left scapula
9. Thyroid gland, left lobe
10. Left sternohyoid muscle
11. Left pectoralis major muscle
12. Left subclavian vessels
13. Left trapezius muscle
14. Left paraspinal muscles
15. Right third rib posterior arc
16. Liver
17. Right kidney
18. Stomach
19. Spleen
20. Descending colon
21. Mastoid air cells
22. Nuchal ligament
23. Parotid gland
24. Mandible ramus
25. Pulmonary hilum

1.2.19 Case 19

A 71-year-old man with progressive fatigue, weight loss, and dyspnea, as well as fever in the last 3 weeks. Chest X-ray and CT did not show any remarkable findings, so ^{18}F-FDG PET/CT was performed to rule out occult malignancy. Images showed multiple hypermetabolic mediastinal lymph nodes in paratracheal and bilateral hilar areas, as well as markedly increased activity in the enlarged spleen. Widespread FDG uptake was noted in both lungs without any CT abnormality. Transbronchial lymph node biopsy confirmed the diagnosis of diffuse, large B-cell lymphoma. Although the initial bronchoalveolar lavage only showed increased alveolar macrophages, without evidence of abnormal lymphocytes, in the follow-up study all pulmonary findings disappeared as did the lymph nodes and splenomegaly. There are some cases with similar lung findings reported in the literature, where the histopathologic diagnosis of intravascular large B-cell lymphoma has been confirmed with the presence of large atypical lymphocytes in the lumina of the capillary vessels, so in this case, these findings and their evolution most likely represent lymphoma involvement (Fig. 31) [34].

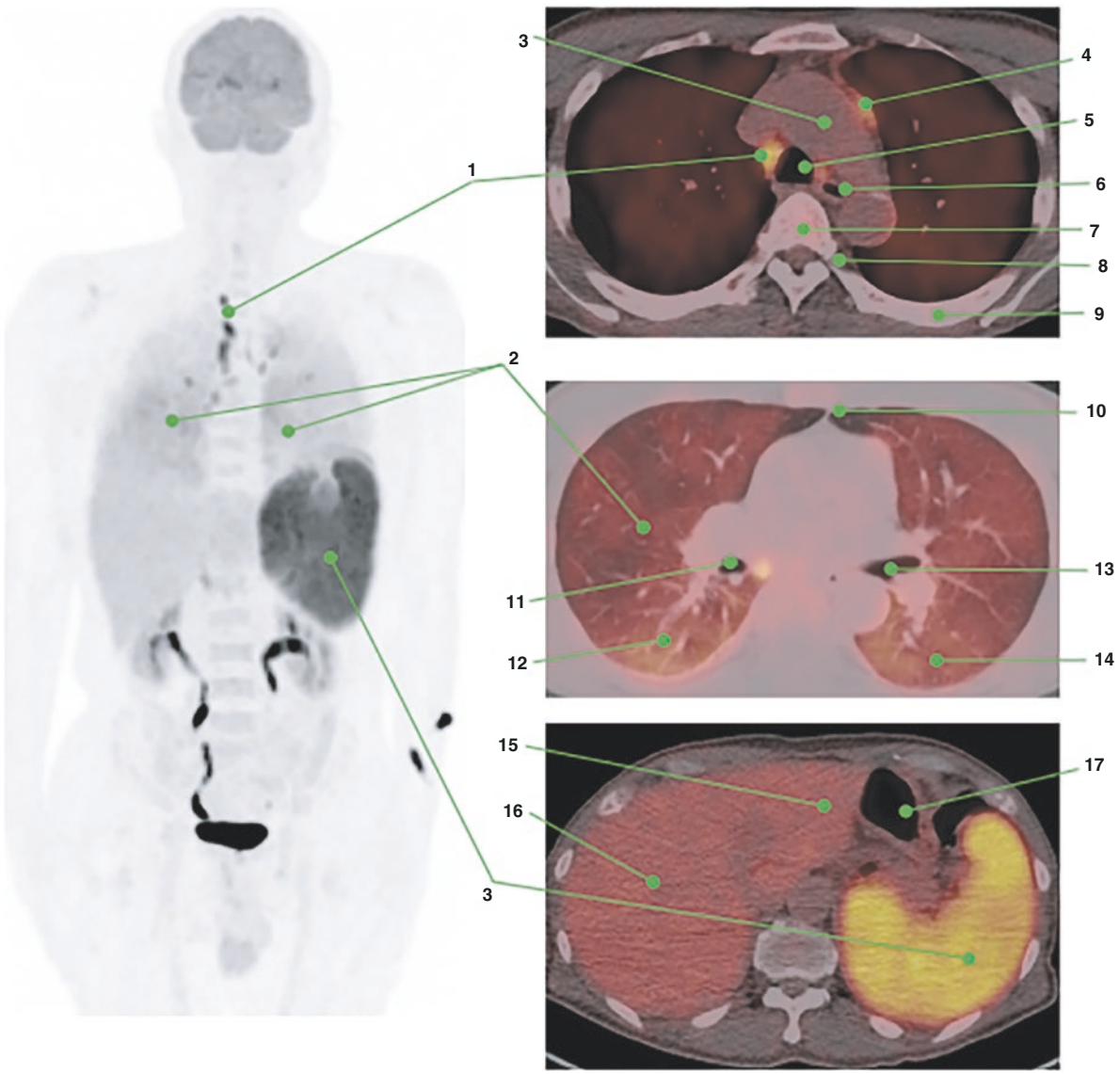

Fig. 31 1. Hypermetabolic right paratracheal lymph nodes
2. Diffusely increased activity at bilateral lungs without discernible CT abnormality
3. Metabolically active splenomegaly
4. Hypermetabolic lymph nodes in prevascular area
5. Trachea
6. Esophagus
7. Thoracic vertebral body
8. Left costovertebral junction
9. Left rib posterior arc
10. Anterior junction line
11. Right main bronchus
12. Right lower lobe
13. Left main bronchus
14. Left lower lobe
15. Left hepatic lobe
16. Right hepatic lobe
17. Stomach

1.2.20 Case 20

A 62-year-old woman with a history of Takayasu arteritis, who consulted for acute thoracoabdominal pain. Other possible causes of pain were ruled out, and ^{18}F-FDG PET/CT was performed to assess disease activity and thus define treatment. Images showed generalized increased activity in the walls of the thoracoabdominal aorta, with involvement of the main cervical trunks, the iliac bifurcation, and the proximal iliac arteries. These findings indicate an active acute phase of the disease. No areas of stenosis or aneurysmal dilatation were observed (Fig. 32) [35].

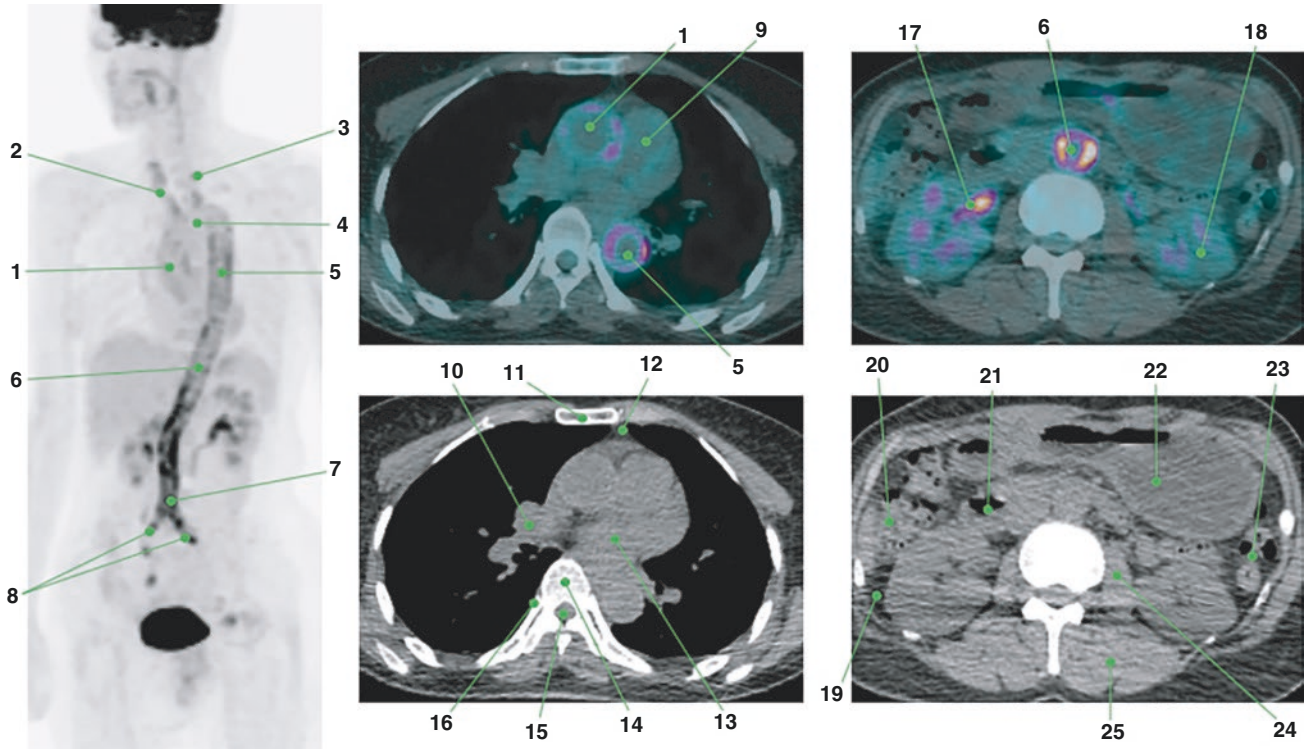

Fig. 32 1. Ascending aorta
2. Brachiocephalic trunk
3. Left common carotid artery
4. Aortic arch
5. Descending aorta
6. Abdominal aorta
7. Iliac bifurcation
8. Common iliac arteries
9. Main pulmonary artery
10. Right pulmonary hilum
11. Sternum
12. Anterior junction line
13. Left atrium
14. Thoracic vertebral body
15. Spinal canal
16. Right costovertebral joint
17. Right renal pelvis
18. Left kidney
19. Right perirenal space
20. Ascending colon
21. Proximal duodenum
22. Stomach
23. Descending colon
24. Left psoas muscle
25. Left paraspinal muscles (multifidus and erector spinae)

1.2.21 Case 21

A 52-year-old male patient with a known diagnosis of Langerhans cell histiocytosis (LCH). After almost 2 years asymptomatic, he presented with lower back pain, so imaging studies including ^{18}F-FDG PET/CT were performed. Images showed diffusely increased activity in a permetative and aggressive lytic lesion involving the left iliac bone and sacral ala, as well as a smaller lesion with same characteristics in the right iliac bone; both lesions corresponded to LCH involvement. Additionally, minimal diffuse increased uptake was observed in both lungs, with multiple small irregular cystic lesions and septal thickening, with findings also corresponding to LCH involvement (Fig. 33).

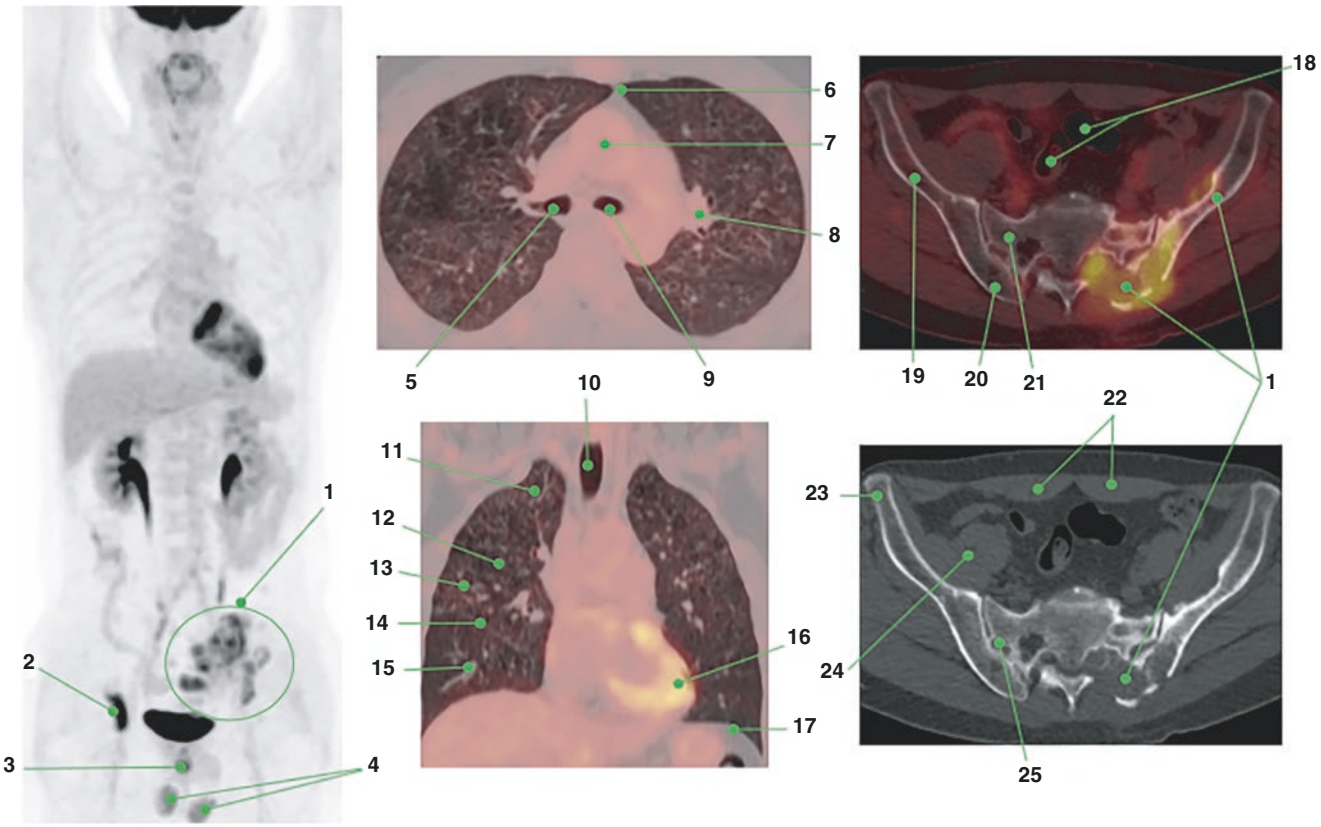

Fig. 33 1. LCH involvement at the left iliac bone and sacral ala
2. LCH involvement at the right iliac bone
3. Prostatic urethra
4. Testes
5. Right main bronchus
6. Anterior junction line
7. Ascending aorta
8. Left pulmonary hilum
9. Left main bronchus
10. Trachea
11. Right lung apex
12. Horizontal lung fissure
13. Right middle lobe
14. Oblique lung fissure
15. Right lower lobe
16. Left ventricle
17. Left diaphragmatic cupola
18. Sigmoid colon
19. Right iliac wing
20. Right iliac tuberosity
21. Sacral ala
22. Abdominis rectus muscles
23. Right anterior superior iliac spine
24. Right iliopsoas complex
25. Right sacroiliac joint

1.3 Abdomen and Pelvis

1.3.1 Case 1

A 73-year-old man with a history of occasional dysphagia and weight loss. Upper digestive tract endoscopy showed suspicious findings of malignancy, so ^{18}F-FDG PET/CT was performed. Images showed focal increased activity at the distal third of the esophagus in a concentric solid mass, which was later confirmed to correspond to a squamous cell carcinoma. No abnormal lymph nodes or distant metastasis were noted (Fig. 34) [14, 36].

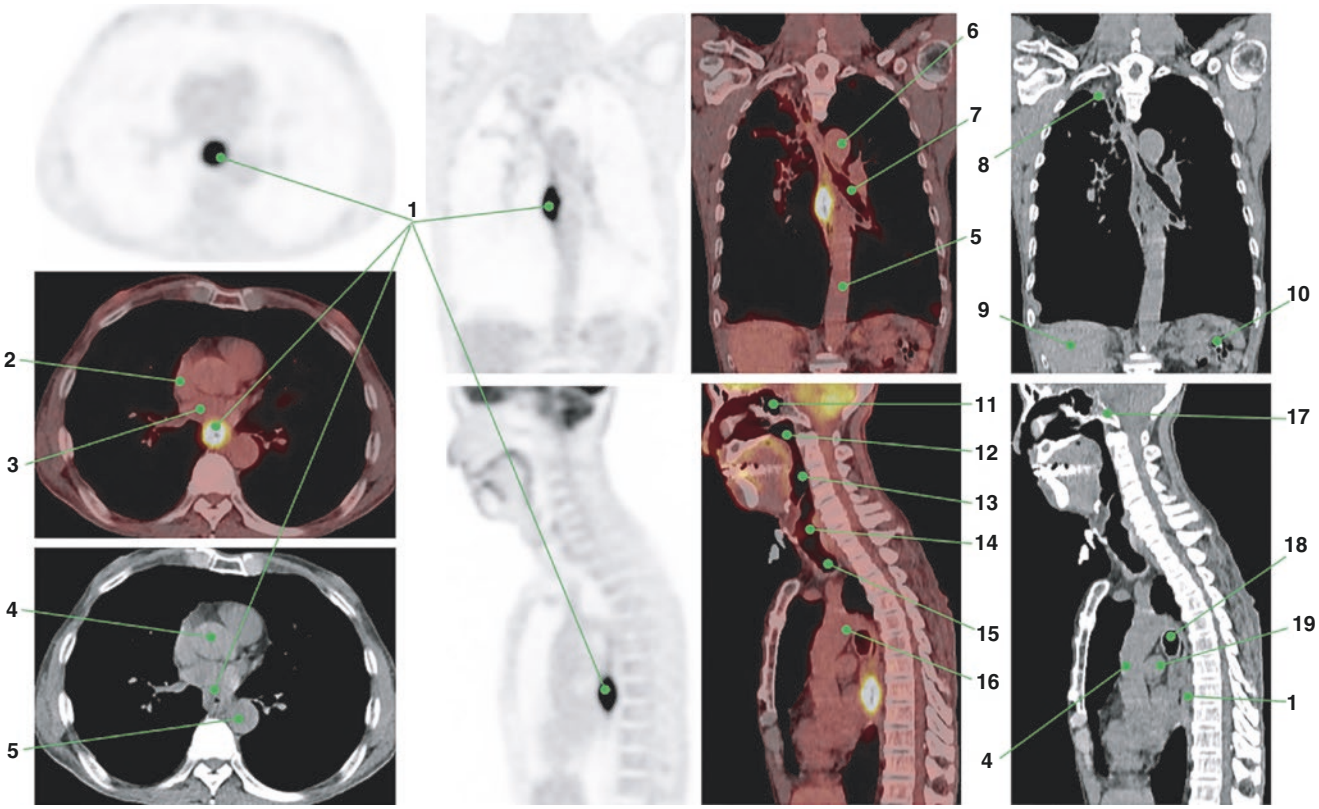

Fig. 34 1. Metabolically active esophageal squamous cell carcinoma
2. Right atrium
3. Left atrium
4. Ascending aorta
5. Descending aorta
6. Aortic knob
7. Left main bronchus
8. Fibrotic changes at the right lung apex
9. Liver dome
10. Gastric fundus
11. Sphenoid sinus
12. Nasopharynx
13. Oropharynx
14. Pharynx
15. Trachea
16. Aortic arch
17. Clivus
18. Right main bronchus
19. Pulmonary artery

1.3.2 Case 2

A 26-year-old female patient with occasional chest pain and reflux. Chest X-ray showed a mediastinal mass, so ^{18}F-FDG PET/CT was performed, finding markedly increased activity in a prominent wall-based mass at the distal esophagus, with exophytic growth and no lumen obstruction or mucosal involvement. The diagnosis of a gastrointestinal stromal tumor (GIST) was considered as the first possibility, which was later confirmed with biopsy (Fig. 35) [36].

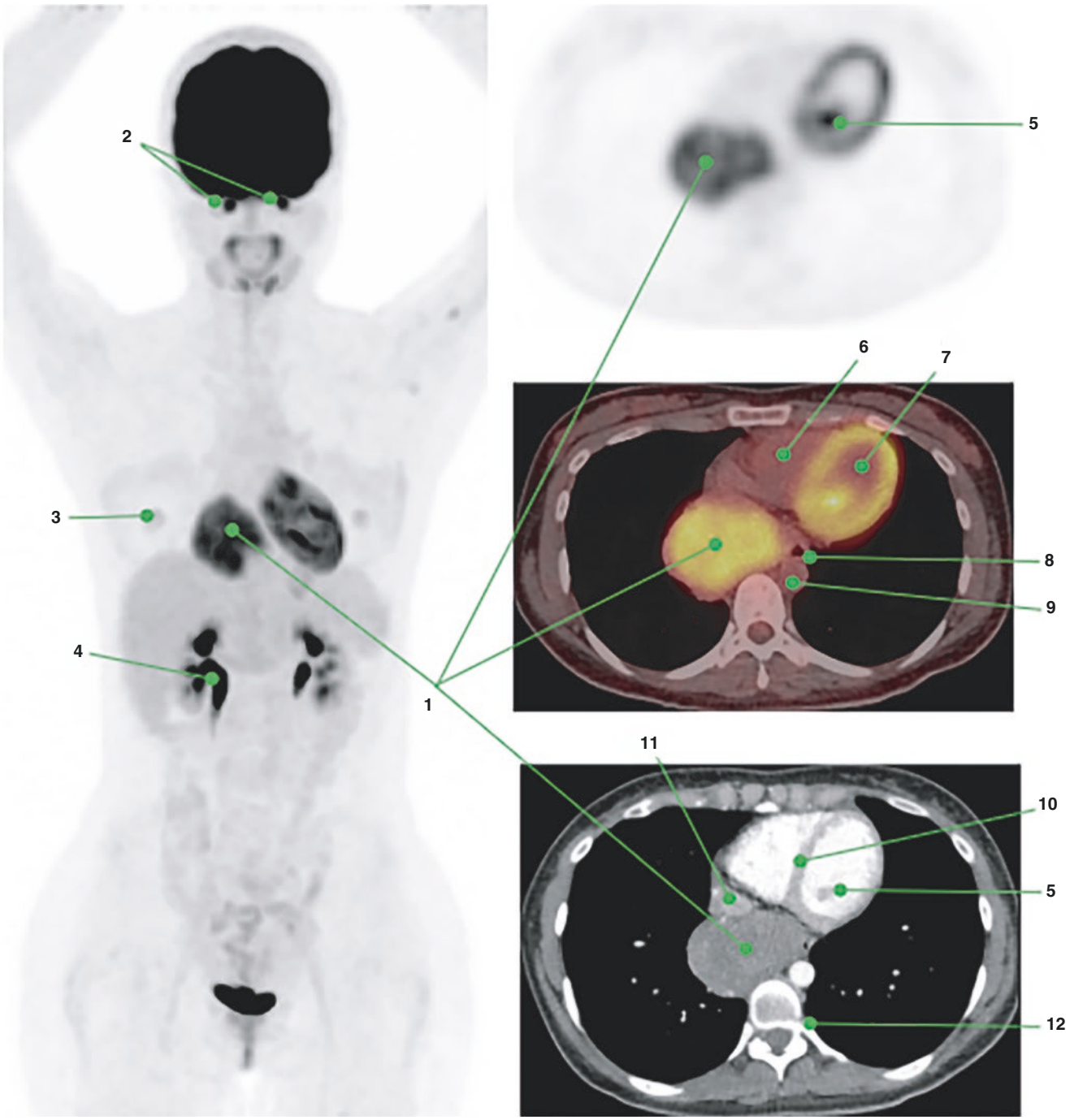

Fig. 35 1. Large metabolically active mass in the wall of the distal esophagus
2. Optic nerves
3. Right nipple
4. Right renal pelvis
5. Left ventricle papillary muscle
6. Right ventricle
7. Left ventricle
8. Esophageal lumen
9. Descending aorta
10. Interventricular septum
11. Superior vena cava
12. Left T9 costovertebral junction

1.3.3 Case 3

A 49-year-old man with chronic upper abdominal pain and weight loss. Endoscopic evaluation and biopsy were performed, finding an advanced gastric adenocarcinoma, so ^{18}F-FDG PET/CT was performed for staging. Images showed increased metabolic activity in the gastric fundus and body at irregular wall thickening, consistent with the primary tumor. Metabolically active enlarged lymph nodes at the gastrohepatic and right retrocrural areas were also noted (Figs. 36 and 37) [16].

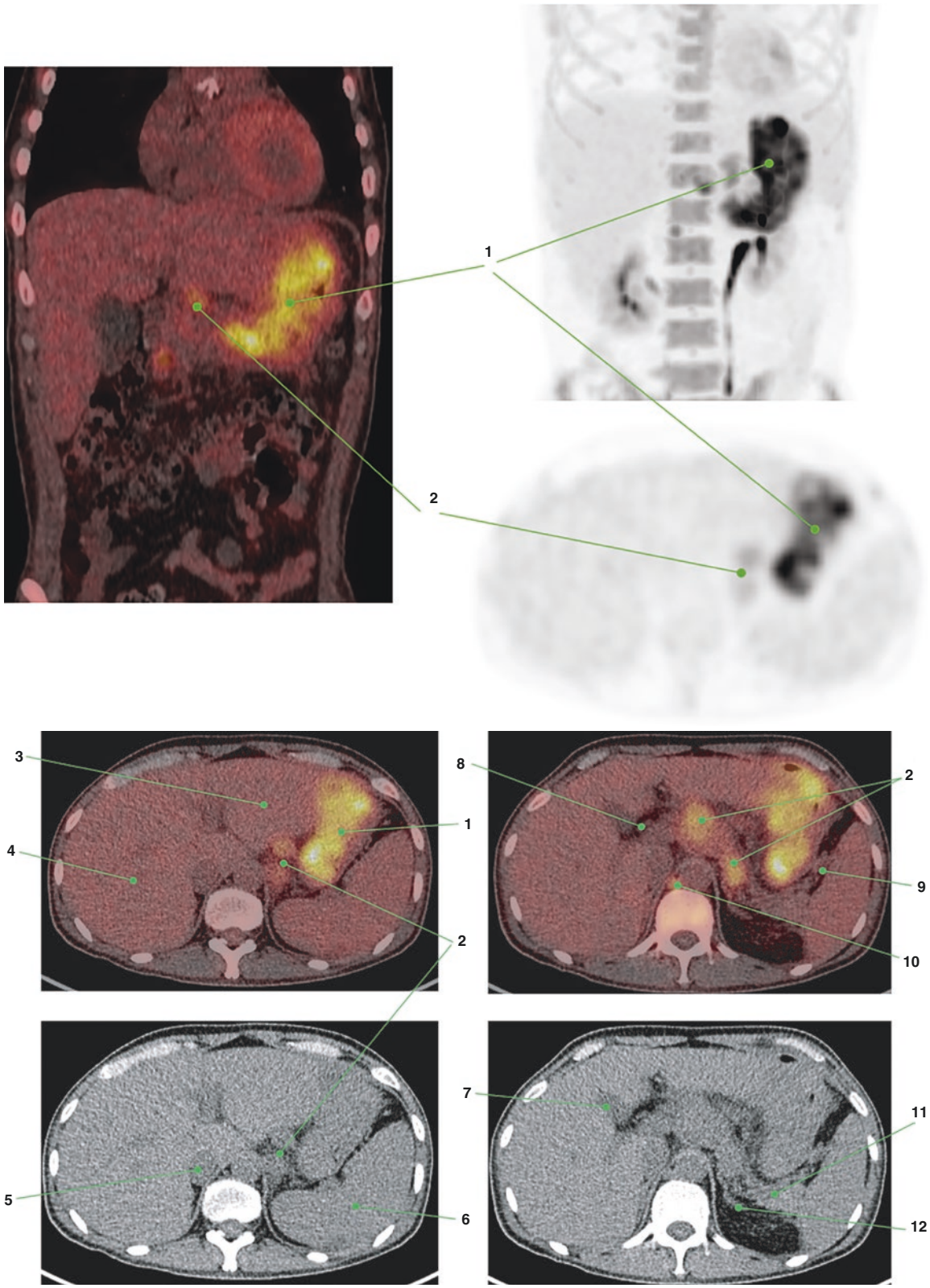

Figs. 36 and 37 1. Metabolically active gastric wall thickening: primary gastric adenocarcinoma
2. Hypermetabolic lymph node metastasis at the gastro-hepatic ligament
3. Left hepatic lobe
4. Right hepatic lobe
5. Inferior vena cava
6. Spleen
7. Gallbladder
8. Hepato-duodenal ligament
9. Gastro-splenic ligament
10. Right retrocrural lymph node metastasis
11. Pancreatic tail
12. Left adrenal gland

1.3.4 Case 4

A 54-year-old male patient with weight loss and night sweats during the last 2 months. ^{18}F-FDG PET/CT was performed on suspicion of malignancy, where a bulky metabolically active mass was found in the stomach, as well as multiple prominent hypermetabolic retroperitoneal lymph nodes. With these findings, a lymphoma was suggested, and the subsequent biopsy confirmed the diagnosis: diffuse, large B-cell lymphoma (Fig. 38) [37].

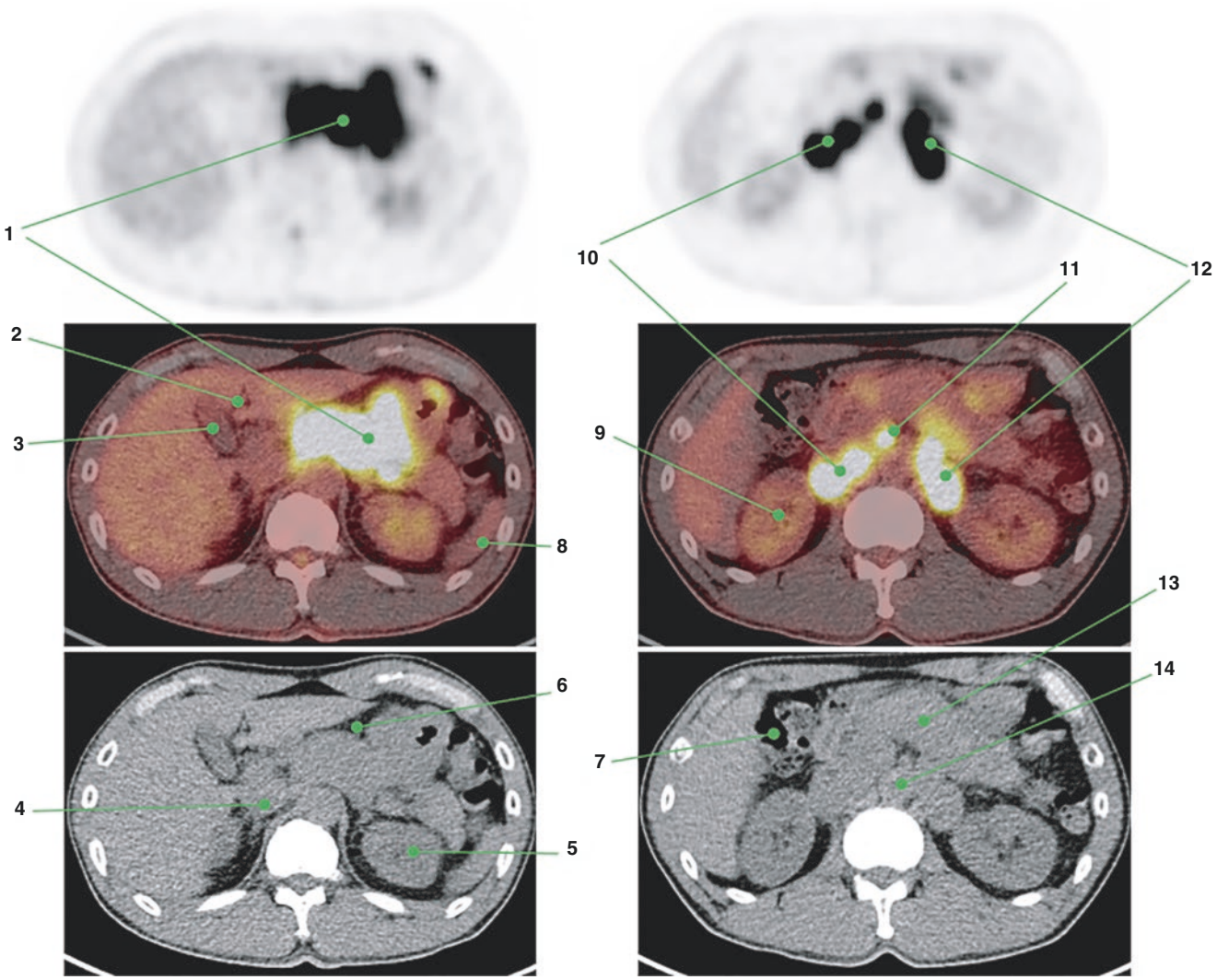

Fig. 38 1. Metabolically active bulky stomach mass
2. Falciform ligament
3. Gallbladder
4. Inferior vena cava
5. Left kidney
6. Gastro-hepatic ligament
7. Hepatic flexure of the colon
8. Spleen
9. Right kidney
10. Hypermetabolic aortocaval lymph nodes
11. Hypermetabolic preaortic lymph nodes
12. Hypermetabolic left paraaortic lymph nodes
13. Pancreatic body
14. Abdominal aorta

1.3.5 Case 5

A 79-year-old woman with acute abdominal pain and vomiting. Contrast-enhanced CT was performed, finding a partial low-grade bowel obstruction with transition zone at the distal ileum. After managing the acute condition, ^{18}F-FDG PET/CT was performed, finding a metabolically active concentric mass at the distal ileum with lumen reduction, without adjacent mesenteric fat stranding or other findings. Surgical resection was performed, confirming a primary large B-cell lymphoma (Fig. 39) [37].

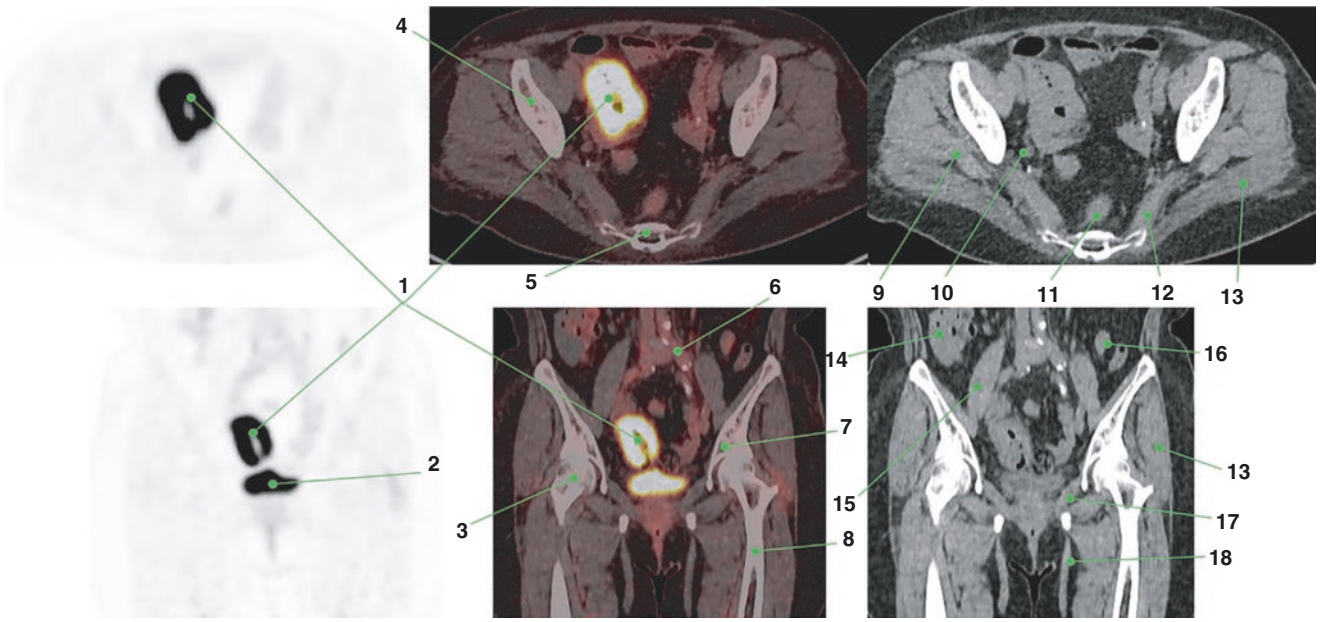

Fig. 39 1. Hypermetabolic concentric mass in the distal ileum
2. Urinary bladder
3. Right femoral head
4. Right iliac wing
5. Sacrum
6. Iliac bifurcation
7. Left acetabulum
8. Left femoral shaft
9. Right gluteus medius muscle
10. Right external iliac vessels
11. Rectum
12. Left piriformis muscle
13. Left gluteus Maximus muscle
14. Ascending colon
15. Right psoas muscle
16. Small bowel loops
17. Left levator ani muscle
18. Left femoral artery

1.3.6 Case 6

A 38-year-old man who attended an annual checkup completely asymptomatic. Colonoscopy and biopsy revealed a colon adenocarcinoma. ^{18}F-FDG PET/CT was performed for staging, finding a focal increased activity in the distal transverse colon corresponding to the primary tumor, as well as a metabolically active mesenteric lymph node metastasis. No distant metastases were noted (Fig. 40) [13].

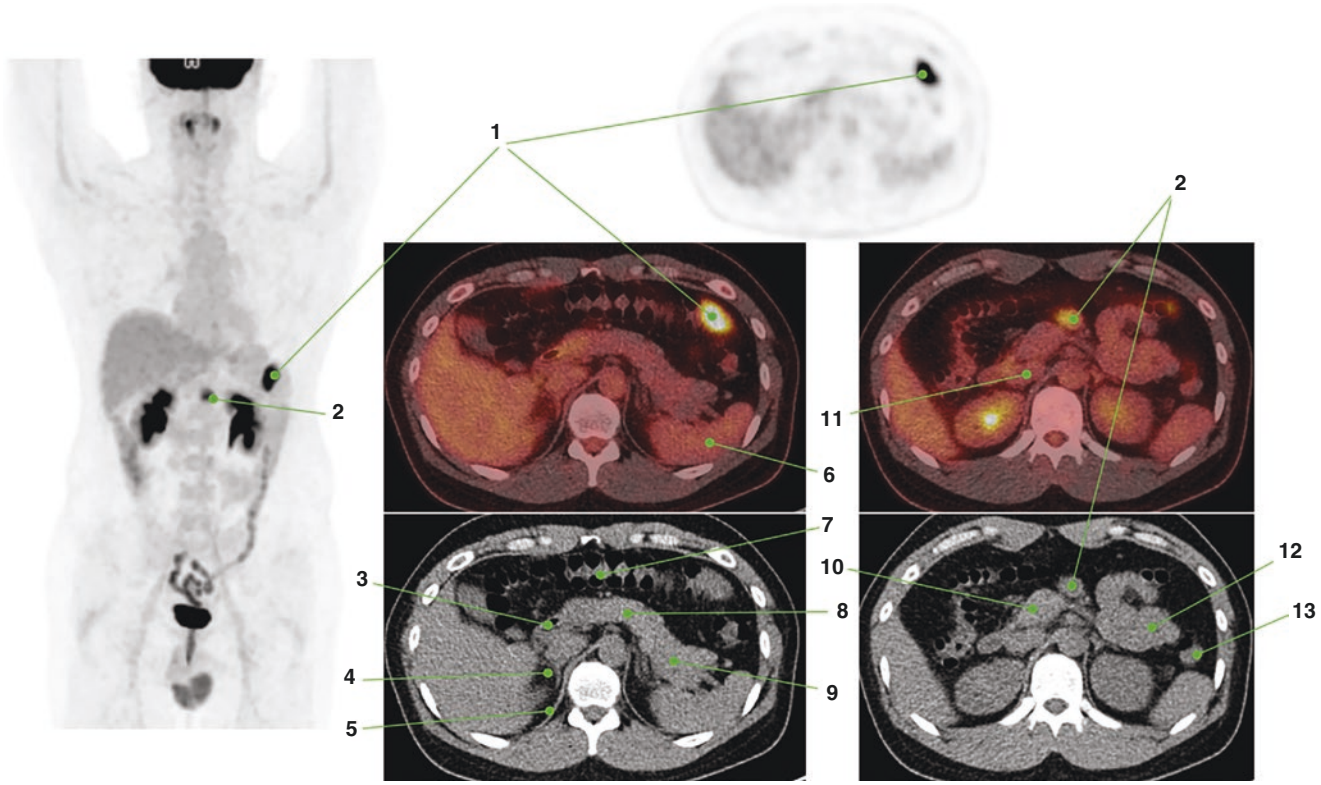

Fig. 40 1. Metabolically active distal transverse colon adenocarcinoma
2. Metastatic mesenteric lymph node
3. Second portion of duodenum
4. Right adrenal gland
5. Right diaphragmatic crus
6. Spleen
7. Transverse colon
8. Pancreatic body
9. Pancreatic tail
10. Pancreatic head, uncinate process
11. Inferior vena cava
12. Proximal small bowel loops
13. Accessory spleen

1.3.7 Case 7

A 52-year-old woman with a history of constipation and occasional rectal bleeding. ^{18}F-FDG PET/CT was performed to rule out malignancy. Images showed focal increased activity at the sigmoid colon suggesting a polypoid lesion. Colonoscopy and biopsy were performed confirming the diagnosis of sigmoid colon adenocarcinoma. No abnormal hypermetabolic lymph nodes or metastasis were detected (Fig. 41) [13].

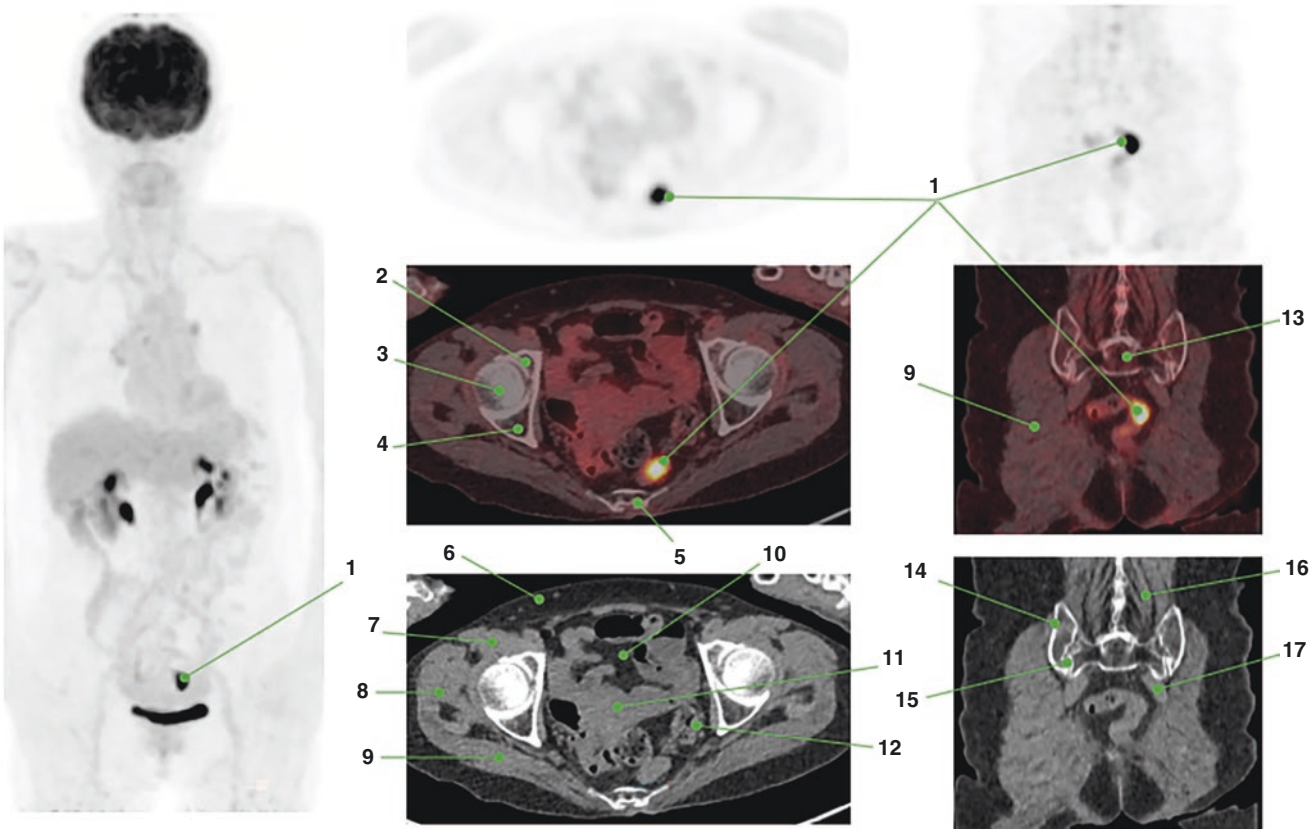

Fig. 41 1. Metabolically active sigmoid colon adenocarcinoma
2. Right acetabulum anterior wall
3. Right femoral head
4. Right acetabulum posterior wall
5. Coccygeal vertebral body
6. Subcutaneous fat, anterior abdominopelvic wall
7. Right iliacus muscle
8. Right gluteus medius muscle
9. Right gluteus maximus muscle
10. Mesenteric fat, normal appearance
11. Small bowel loops
12. Descending colon loops
13. Sacrum
14. Right sacral ala
15. Right sacroiliac joint
16. Left paraspinal muscles
17. Left piriformis muscle

1.3.8 Case 8

A 60-year-old man with a history of occasional rectal bleeding worsened in the last 2 weeks. Clinical examination and rectoscopy were performed and confirmed the presence of a mass, so ^{18}F-FDG PET/CT was performed. Images showed a focal increased activity in the lower rectum at the primary tumor site, with no other hypermetabolic lesions suggesting metastasis. Final biopsy confirmed an adenocarcinoma (Fig. 42) [13].

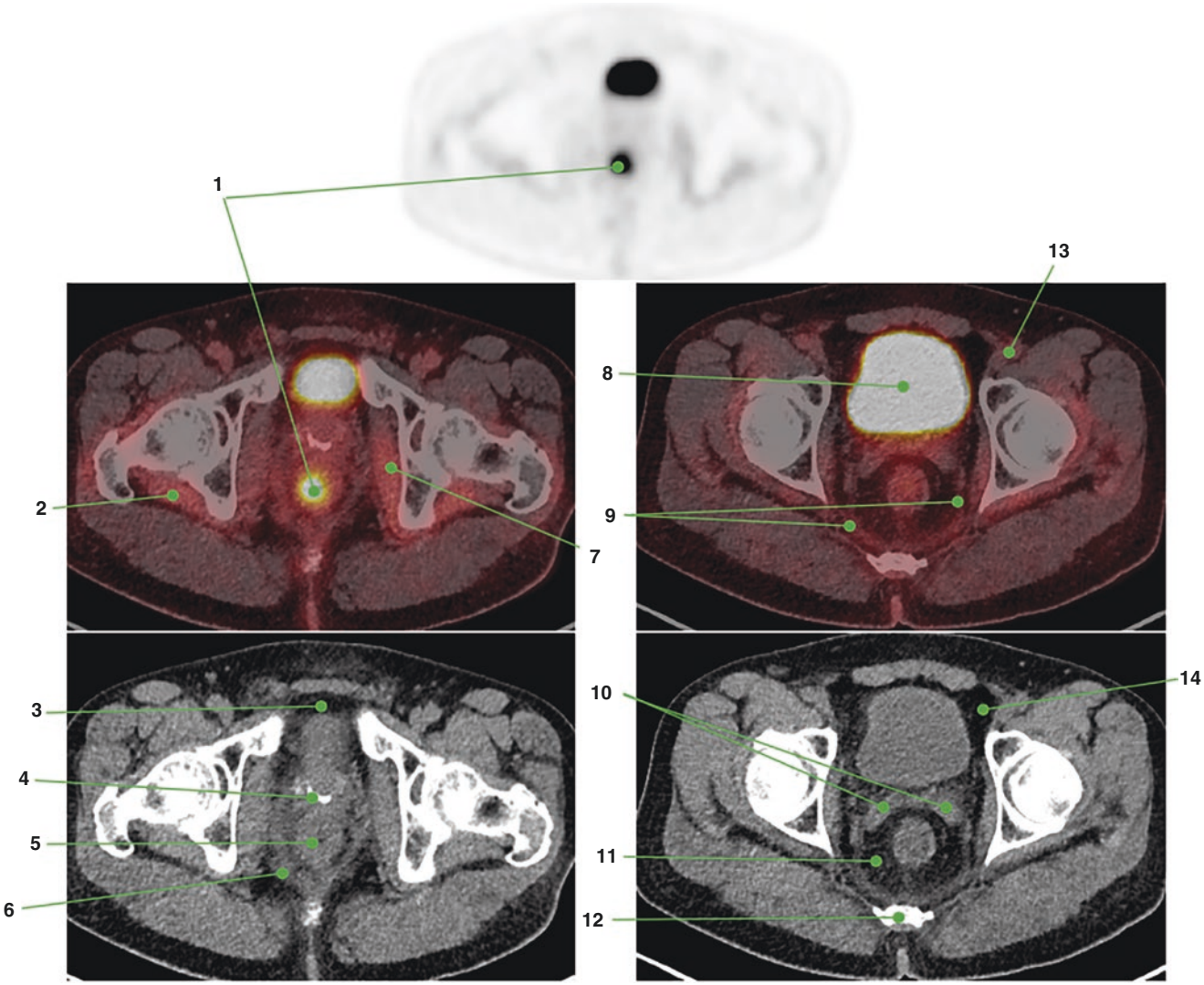

Fig. 42 1. Metabolically active rectal adenocarcinoma
2. Right obturator internus muscle, posterior aspect
3. Prevesical space
4. Prostate gland with dystrophic calcifications
5. Rectum, thickened
6. Right levator ani muscle, puborectalis
7. Left obturator internus muscle, medial aspect
8. Urinary bladder
9. Levator ani muscles, pubococcygeus
10. Seminal vesicles
11. Perirectal fat
12. Coccyx
13. External iliac vessels
14. Perivesical fat

1.3.9 Case 9

A 71-year-old man with a history of ascending colon adenocarcinoma 2 years ago, treated with laparoscopic right hemicolectomy and chemotherapy. He attended due to nodular feeling at the umbilical port scar where ultrasound showed a suspicious mass, so ^{18}F-FDG PET/CT was performed. Images showed a metabolically active spiculated lesion involving the subcutaneous tissue and both rectus abdominis muscles. Biopsy confirmed the presence of metastatic adenocarcinoma, probably secondary to a seeding during prior surgery (Fig. 43) [38].

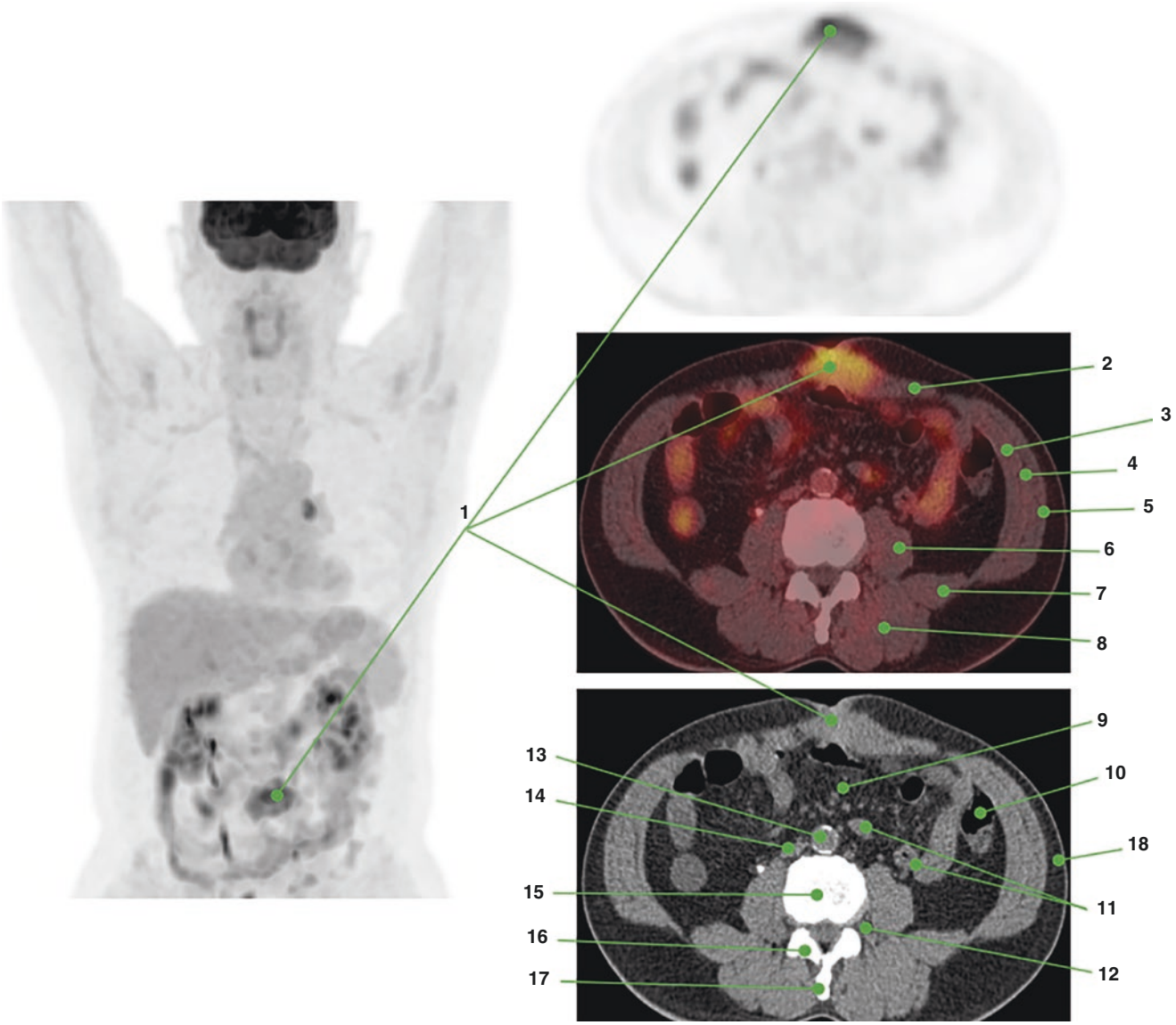

Fig. 43 1. Hypermetabolic recurred colon cancer in the umbilical port scar
2. Left rectus abdominis muscle
3. Left transversus abdominis muscle
4. Left internal oblique muscle
5. Left external oblique muscle
6. Left psoas muscle
7. Left quadratus lumborum muscle
8. Left erector spinatus muscle
9. Small bowel mesentery
10. Descending colon
11. Small bowel loops
12. Left lumbar neural foramen
13. Abdominal aorta
14. Inferior vena cava
15. Lumbar vertebral body
16. Right vertebral lamina
17. Spinous process
18. Subcutaneous fat, left abdominal wall

1.3.10 Case 10

A 52-year-old male patient with persistent abdominal discomfort and occasional fever. Initial work-up showed high Ca19-9 (2540 units/ml), so contrast-enhanced CT and ^{18}F-FDG PET/CT were performed. Images showed focal increased activity in the pancreatic body, at a well-defined hypovascular mass on CT, with distal pancreatic duct dilatation and parenchymal atrophy, which are typical findings of adenocarcinoma. Vascular involvement, lymph nodes, and distant metastases were excluded. Endoscopic ultrasound-guided biopsy confirmed the diagnosis of adenocarcinoma (Fig. 44) [15].

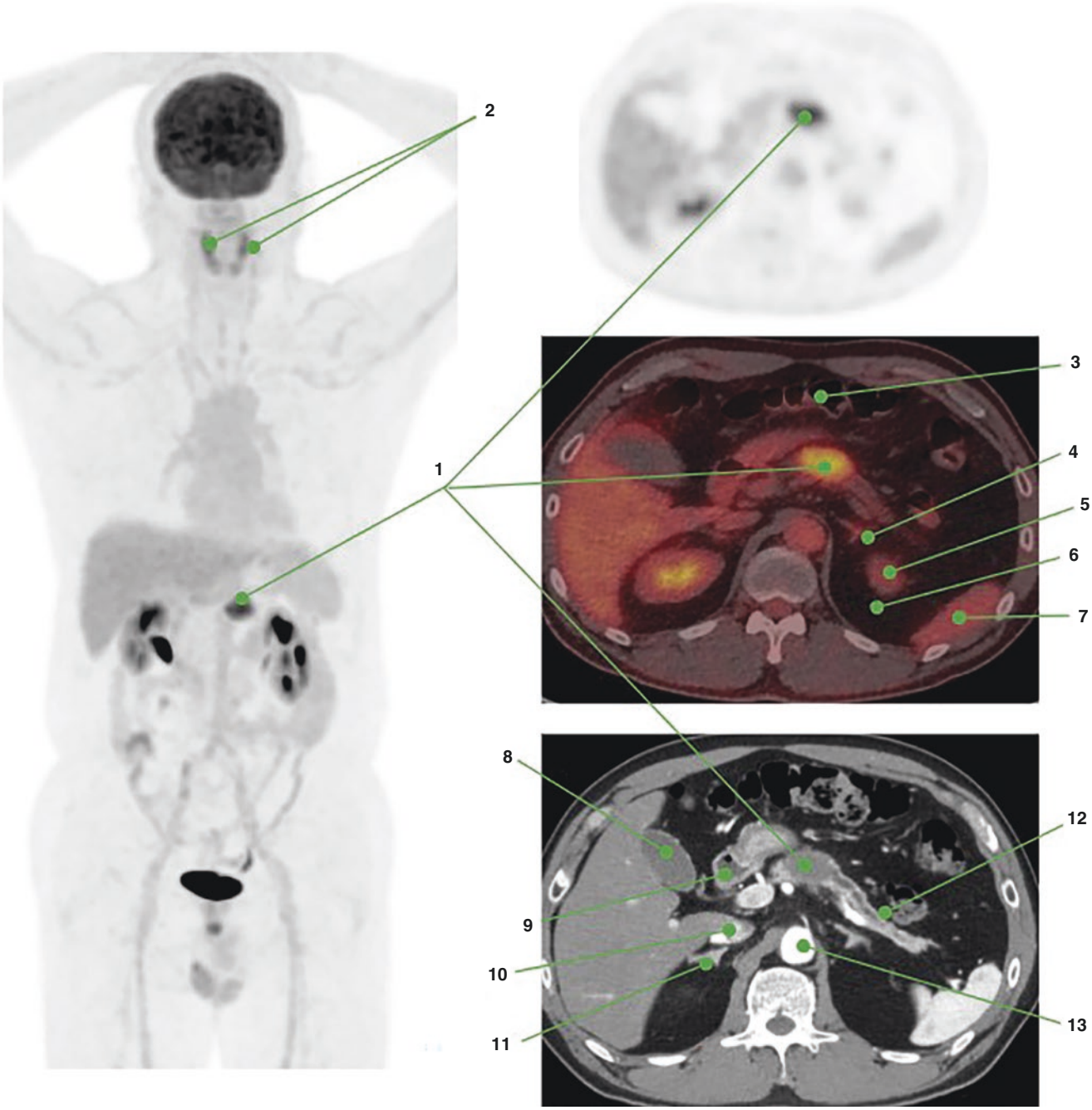

Fig. 44 1. Metabolically active pancreatic body tumor
2. Palatine tonsils symmetric uptake, physiologic
3. Transverse colon
4. Left adrenal gland
5. Left kidney inferior pole
6. Left perirenal space
7. Spleen
8. Gallbladder
9. Duodenum, second portion
10. Inferior vena cava
11. Right adrenal gland
12. Pancreatic duct dilatation and parenchymal atrophy distal to the tumor
13. Abdominal aorta

1.3.11 Case 11

A 67-year-old man with abdominal pain who attended the emergency department. Abdominal ultrasound was performed finding slight dilation of the biliary tree and multiple focal liver lesions, suspicious of metastasis; the gallbladder was filled with sludge. Given the suspicion of a liver or pancreatic neoplasm, ^{18}F-FDG PET/CT was indicated. Images showed a hypermetabolic mass in the gallbladder fundus with adjacent hepatic parenchyma involvement and multiple liver and lymph node metastases. The diagnosis of primary gallbladder carcinoma was later confirmed (Fig. 45) [15].

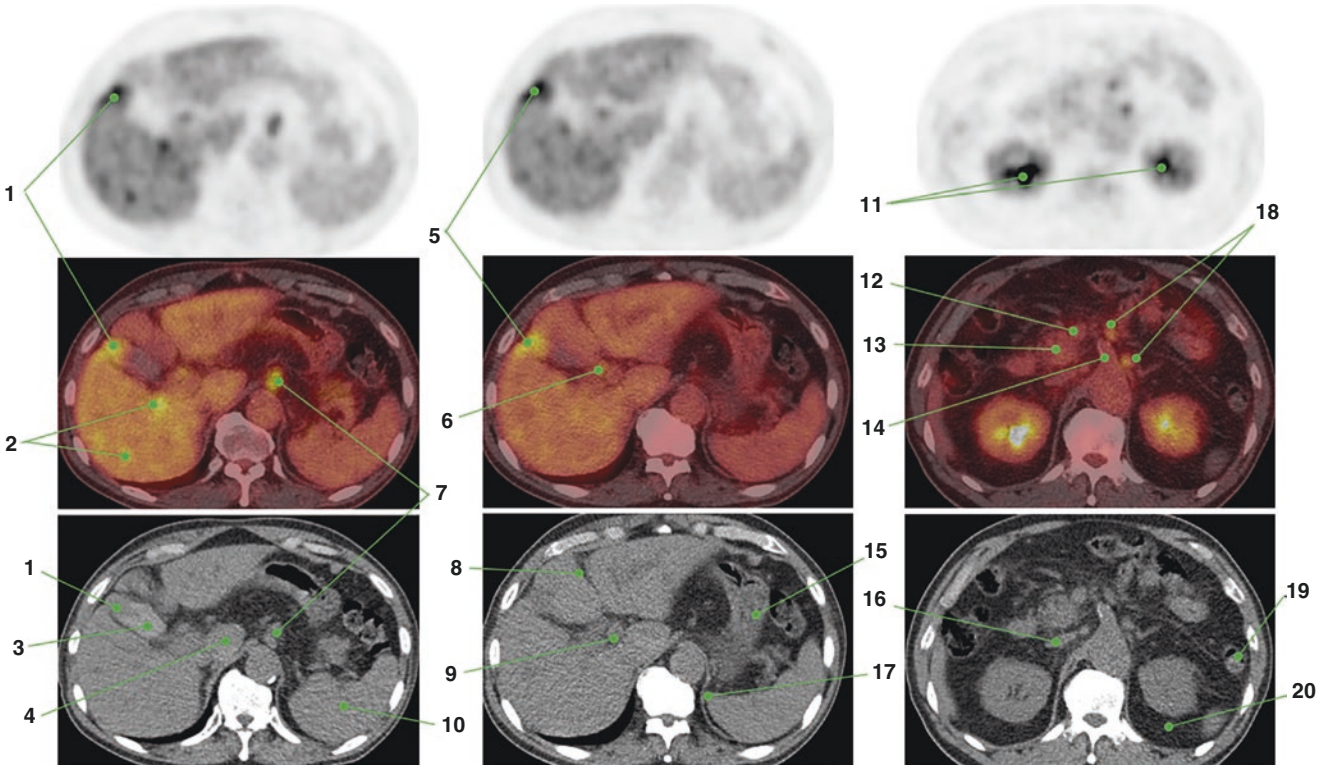

Fig. 45 1. Metabolically active tumor in the gallbladder fundus
2. Hypermetabolic liver metastases
3. Gallbladder sludge
4. Caudate lobe
5. Hypermetabolic contiguous involvement of the liver, segment 5
6. Mild hypermetabolic porta hepatis lymph node
7. Hypermetabolic preaortic lymph node
8. Falciform ligament
9. Portal vein
10. Spleen
11. Renal pelvis
12. Superior mesenteric vein
13. Pancreas uncinate process
14. Superior mesenteric artery
15. Gastric body
16. Inferior vena cava
17. Left diaphragmatic crus
18. Hypermetabolic superior mesenteric lymph nodes
19. Descending colon
20. Left perirenal fat

1.3.12 Case 12

An 82-year-old man with known diagnosis of hepatocellular carcinoma treated with transarterial radioembolization. During follow-up, alpha-fetoprotein (AFP) was rising, so ^{18}F-FDG PET/CT was performed in order to evaluate the amount of remaining viable tumor. Images showed a prominent mass in the right hepatic lobe without significant FDG uptake, isometabolic to the liver parenchyma, with heterogeneous enhancement due to central areas of necrosis and posterior dystrophic calcifications related to treatment. FDG uptake in this type of tumors is highly variable and is determined by low expression of GLUT1 transporters, high activity of FDG-6-phosphatase and high expression of P-glycoprotein mainly, which also depend on tumor grade (Fig. 46) [39].

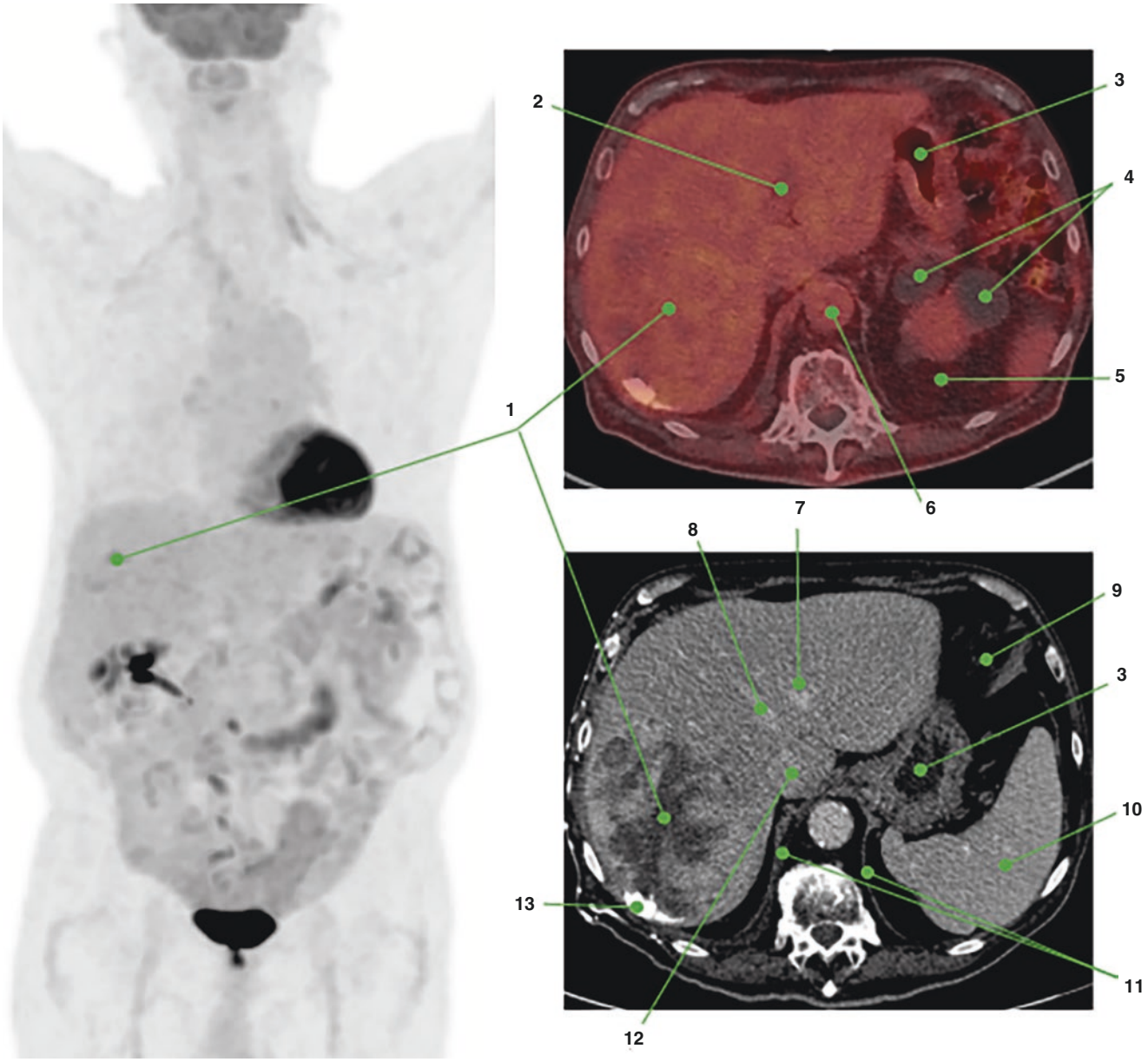

Fig. 46 1. Isometabolic hepatocellular carcinoma
2. Falciform ligament
3. Stomach
4. Left renal cysts
5. Left perirenal space
6. Abdominal aorta
7. Left hepatic vein
8. Middle hepatic vein
9. Splenic flexure of the colon
10. Spleen
11. Diaphragmatic crura
12. Inferior vena cava
13. Posttreatment calcifications

1.3.13 Case 13

A 91-year-old female patient who attended the emergency department for abdominal pain. Abdominal ultrasound was performed, finding a heterogeneous mass in the left hepatic lobe, so ^{18}F-FDG PET/CT was performed. Images showed a mild metabolically active tumor in the left hepatic lobe, corresponding to the primary tumor, as well as multiple metastatic lymph nodes and peritoneal involvement with ascites and diffuse hypermetabolism in peritoneal fat stranding with nodularity. Biopsy confirmed the diagnosis of cholangiocarcinoma (Fig. 47) [15].

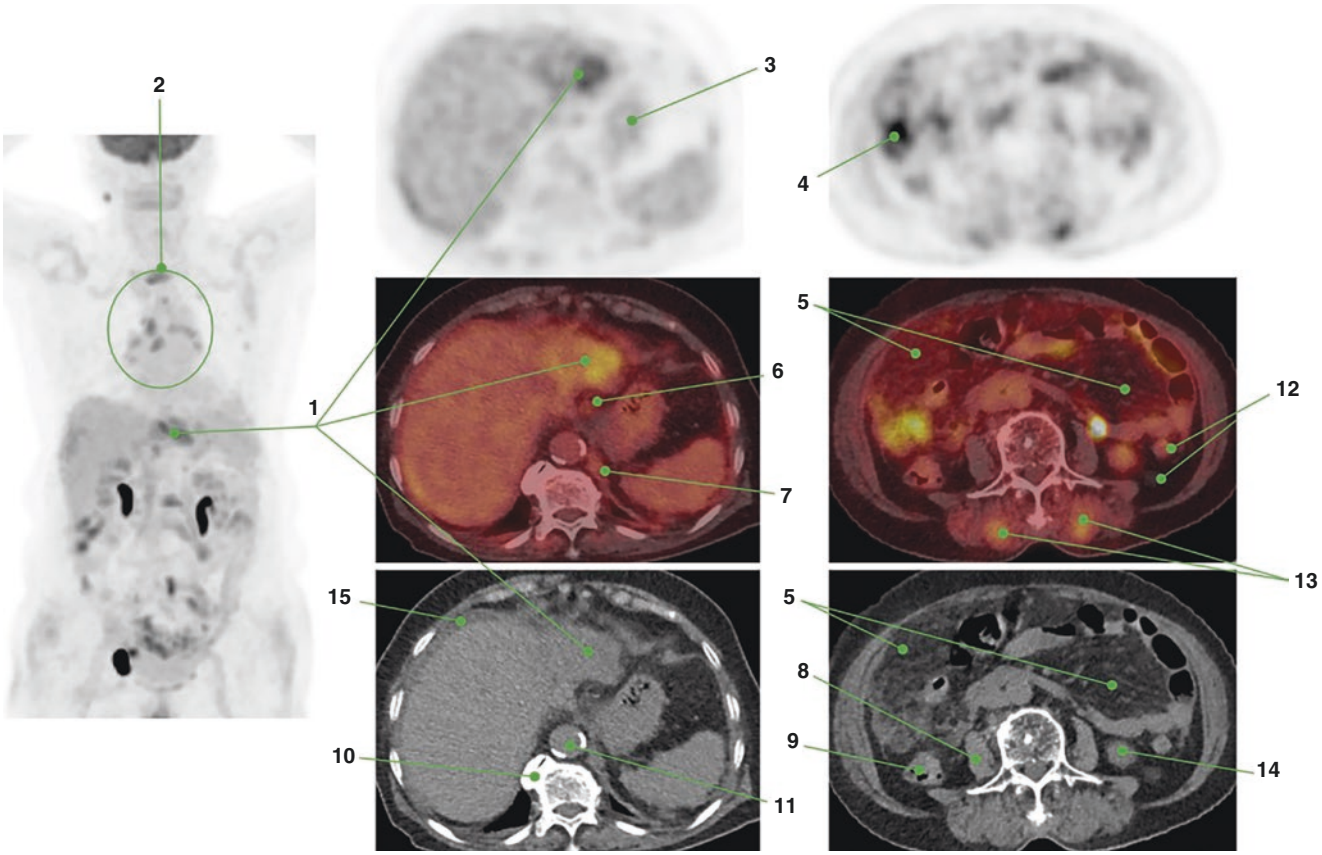

Fig. 47 1. Mild hypermetabolic mass in the left hepatic lobe: cholangiocarcinoma
2. Multiple hypermetabolic mediastinal inflammatory lymph nodes
3. Physiologic activity at the gastric fundus
4. Physiologic activity in small bowel loops
5. Peritoneal fat stranding with diffuse hypermetabolism
6. Mild hypermetabolic celiac lymph node metastasis
7. Mild hypermetabolic diaphragmatic crus metastasis
8. Right psoas muscle
9. Ascending colon
10. Thoracic vertebral body prominent osteophyte
11. Abdominal aorta
12. Hypermetabolic peritoneal nodules
13. Increased uptake at stressed paraspinal muscles
14. Left kidney inferior pole
15. Perihepatic ascites

1.3.14 Case 14

A 48-year-old patient with abdominal pain and elevated Ca19-9. Abdominal ultrasound showed slight dilatation of the common bile duct and posterior endoscopic ultrasound-guided fine needle aspiration (FNA) biopsy confirmed the diagnosis of a small, distal, common bile duct adenocarcinoma; ^{18}F-FDG PET/CT was performed for staging. Images showed moderate diffuse increased activity surrounding the biliary drain, without any discernible macroscopic lesion. This increased uptake is due to attenuation correction artifacts with high-density material, and it is important to recognize it to avoid false-positive results (Fig. 48) [40].

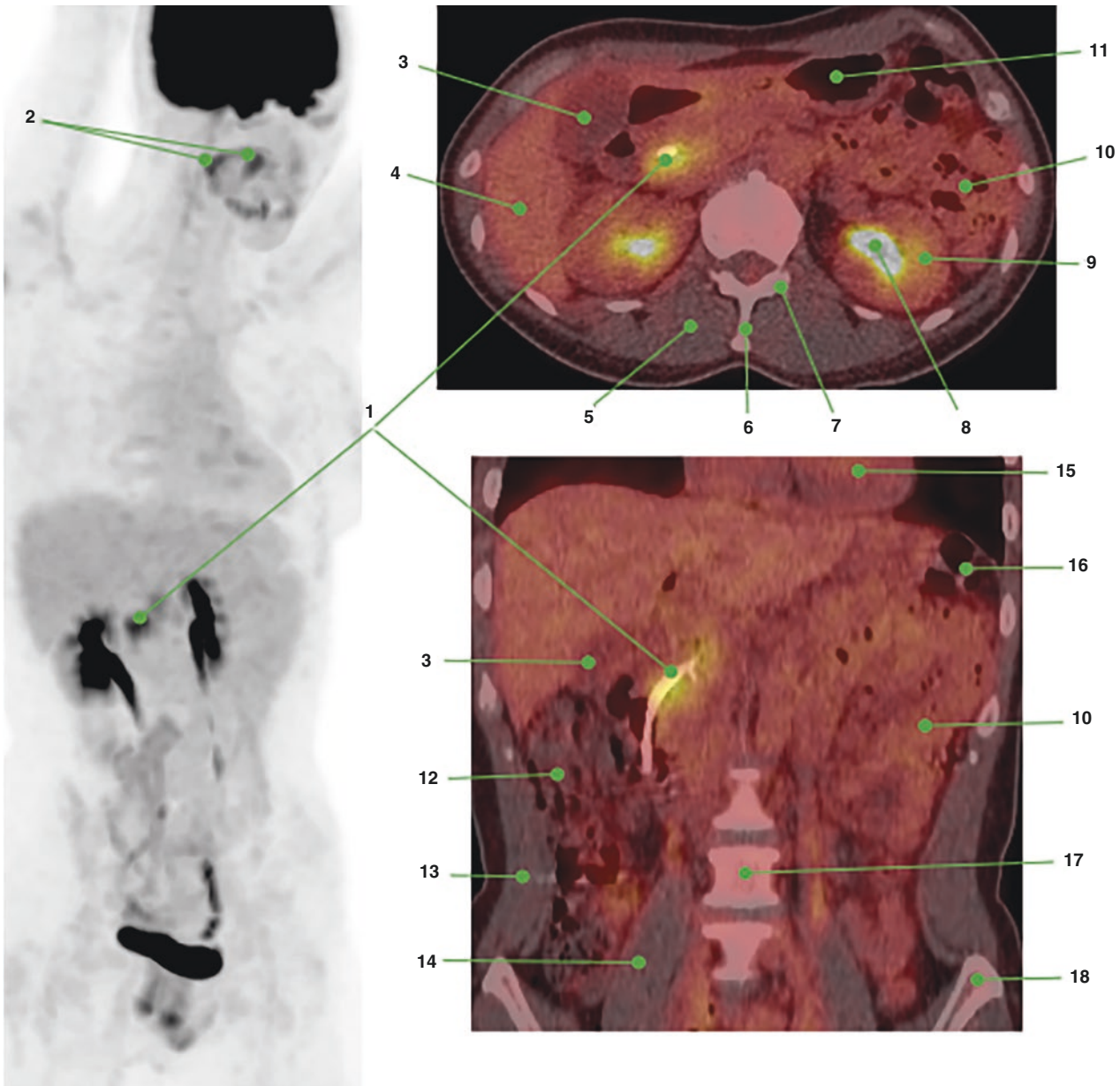

Fig. 48 1. Attenuation correction artifact related to biliary drainage
2. Physiologic symmetric activity in the tonsils
3. Gallbladder
4. Liver, segment 6(VI)
5. Right erector spinae muscle
6. Lumbar spinous process
7. Lumbar vertebral lamina
8. Left renal pelvis
9. Left renal parenchyma
10. Descending colon
11. Gastric chamber
12. Ascending colon
13. Right abdominal wall muscles: external oblique, internal oblique and transversus abdominis
14. Right psoas muscle
15. Left ventricle
16. Splenic flexure of the colon
17. Lumbar vertebral body (L4)
18. Left iliac crest

1.3.15 Case 15

A 38-year-old man with a known diagnosis of IgG4-related disease. He attends his routine control, asymptomatic, finding serum IgG4 levels slightly elevated so ^{18}F-FDG PET/CT was performed to monitor the underlying disease. Images showed diffuse FDG uptake in the pancreas, without peripancreatic fat stranding or fluid collections, consistent with chronic autoimmune pancreatitis. Additionally, both submandibular glands showed increased uptake compared with the parotid glands, suggestive of chronic inflammation related to IgG4 deposits (Fig. 49) [41].

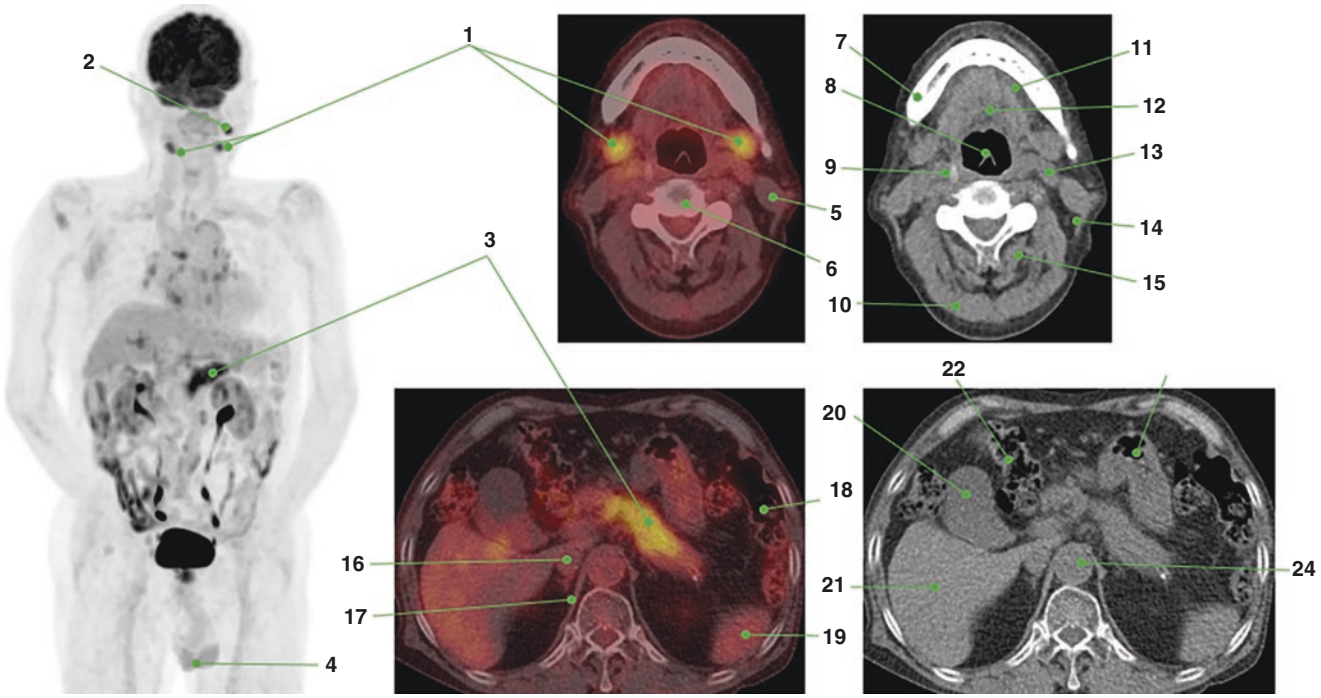

Fig. 49 1. Increased activity in bilateral submandibular glands
2. Metabolically active, left, level II lymph node
3. Diffuse FDG uptake in the pancreas consistent with IgG4-related pancreatitis
4. Scrotum, normal mild uptake
5. Sternocleidomastoid muscle
6. Cervical vertebral body
7. Right mandible
8. Epiglottis
9. Right styloid process
10. Right posterior neck muscles (semispinalis capitis, splenius capitis, and cervicis)
11. Left sublingual space
12. Genioglossus muscles
13. Left internal jugular vein
14. Normal lymph node, left neck, level V
15. Left deep posterior neck muscles (rotator, multifidus, and semispinalis cervicis)
16. Inferior vena cava
17. Right diaphragmatic crus
18. Descending colon
19. Spleen
20. Gallbladder
21. Right hepatic lobe
22. Transverse colon
23. Stomach
24. Abdominal aorta

1.3.16 Case 16

A 71-year-old male patient with history of inoperable pancreatic cancer under treatment with systemic chemotherapy. He attended an early checkup with abdominal pain, so ^{18}F-FDG PET/CT was performed. Images showed interval metabolic response of the primary tumor with no definite uptake; however, new diffusely increased activity was noted in diffuse peritoneal fat stranding with nodularity and ascites, representing peritoneal spread of the tumor (Fig. 50) [42].

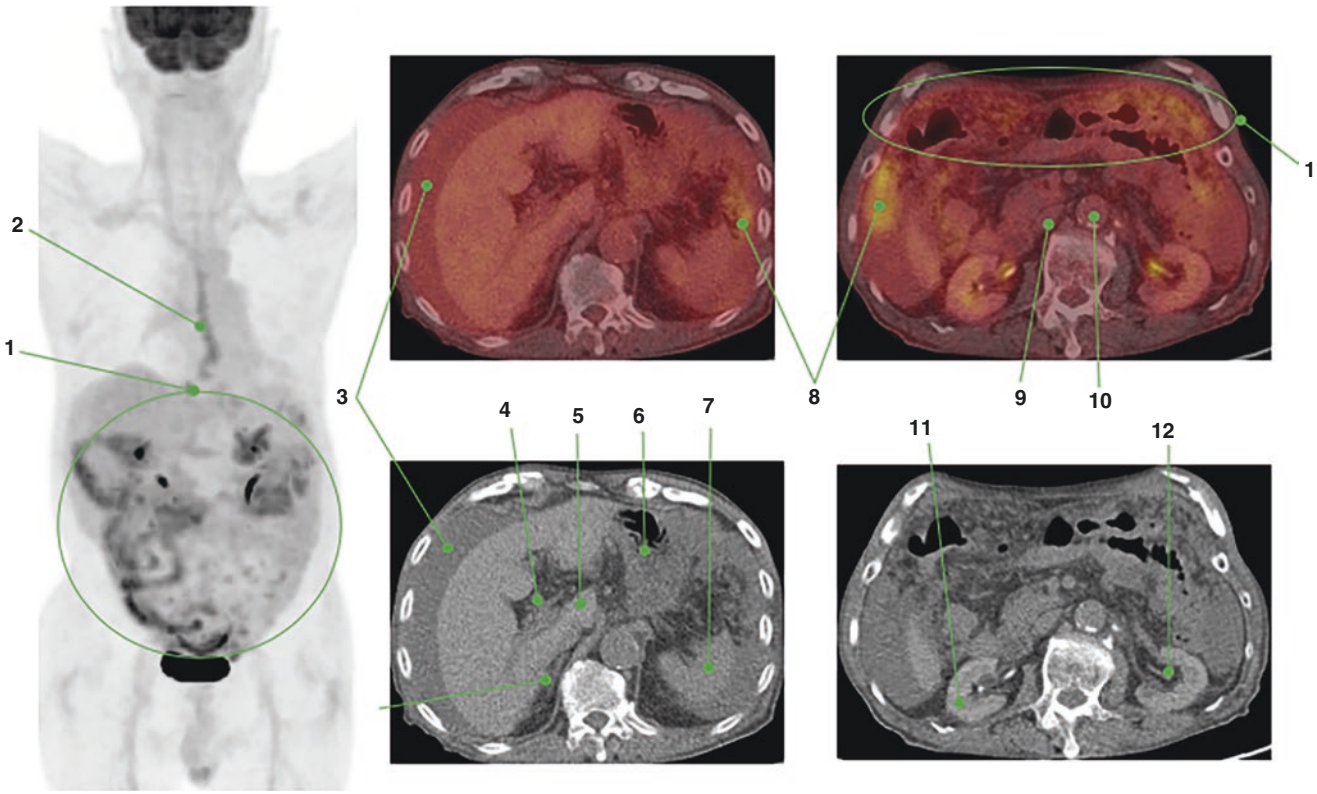

Fig. 50 1. Diffusely increased activity in peritoneal fat stranding with nodularity
2. Linear increased activity at the esophagus, probably related to inflammatory changes
3. Perihepatic ascites
4. Hepatic hilum, porta hepatis
5. Caudate lobe
6. Stomach
7. Spleen, inferior pole
8. Hypermetabolic nodular peritoneal seeding
9. Inferior vena cava
10. Abdominal aorta
11. Right renal cortex
12. Left renal sinus

1.3.17 Case 17

A 28-year-old man with a history of diffuse, large B-cell lymphoma, with complete metabolic response 1 year earlier. He attended an early checkup due to a growing abdominal mass and night sweating. ^{18}F-FDG PET/CT was initially performed due to suspected lymphoma recurrence, finding splenomegaly with mild, diffuse, increased activity, as well as a focal hypermetabolic lesion. Small hypermetabolic retroperitoneal lymph nodes were also noted, so lymphoma recurrence was confirmed (Fig. 51).

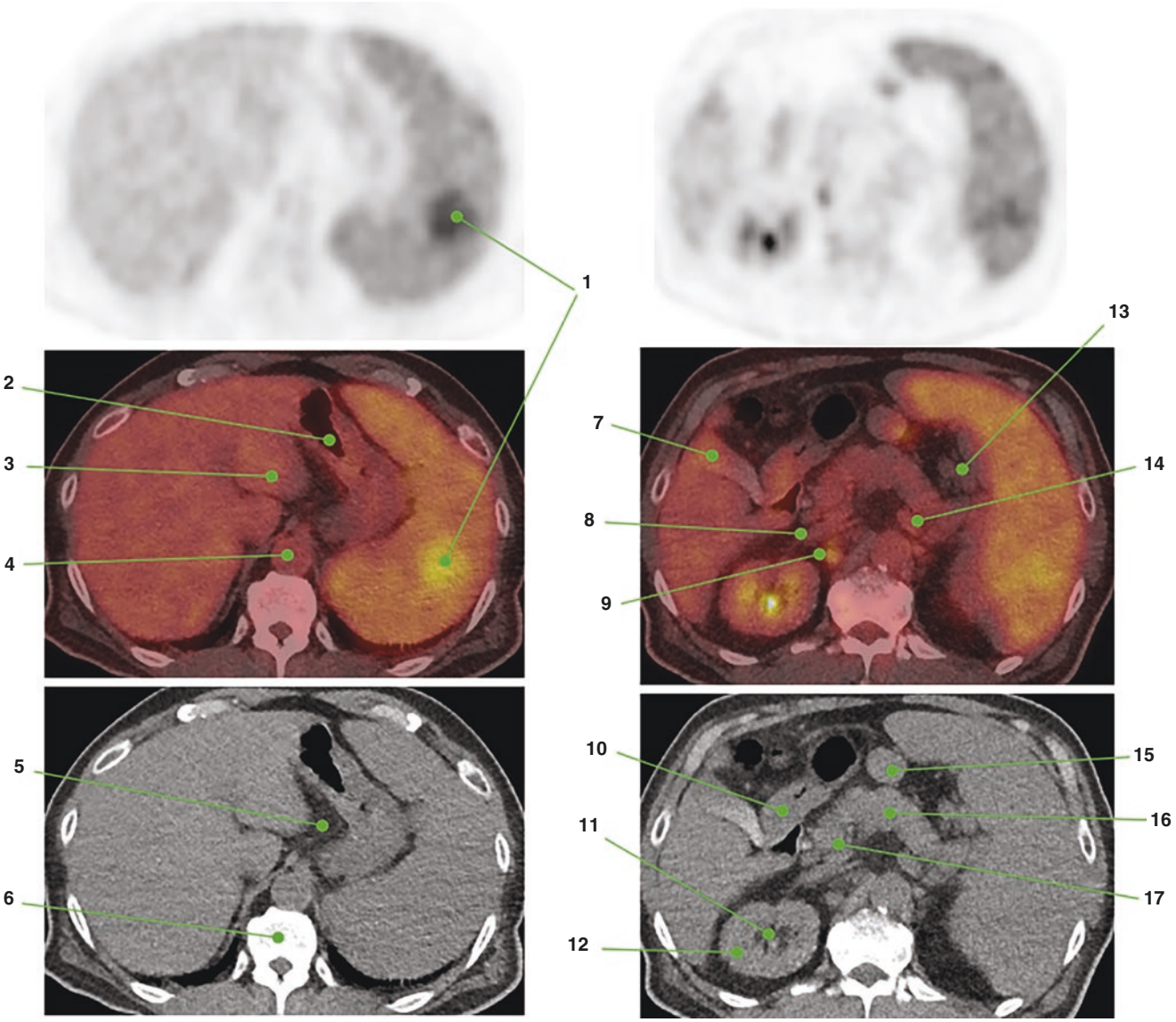

Fig. 51 1. Splenomegaly with diffuse hypermetabolism as well as a focal hypermetabolic lesion
2. Stomach
3. Caudate lobe
4. Abdominal aorta
5. Gastrohepatic ligament
6. Thoracic vertebral body
7. Gallbladder
8. Right renal vein
9. Hypermetabolic retrocaval lymph node
10. Pylorus
11. Right renal sinus
12. Right renal parenchyma
13. Splenic hilum lymph nodes
14. Mildly hypermetabolic periaortic lymph node
15. Accessory spleen
16. Pancreatic body
17. Portal vein

1.3.18 Case 18

A 20-year-old man with fever, fatigue, and gingival bleeding. Laboratory tests revealed low levels of white blood cells, red blood cells, and platelets, so a lymphoproliferative disease was suspected. Contrast-enhanced CT and ^{18}F-FDG PET/CT were performed and images showed hepatosplenomegaly and two small, hypometabolic, hypodense, poorly defined splenic lesions with increased FDG uptake. No other findings, especially lymphadenopathy, were identified. Subsequently, a bone marrow biopsy was performed, reaching the final diagnosis of hemophagocytic lymphohistiocytosis. Treatment with dexamethasone was carried out, and 2 weeks later, follow-up studies were completely normal (Fig. 52) [43].

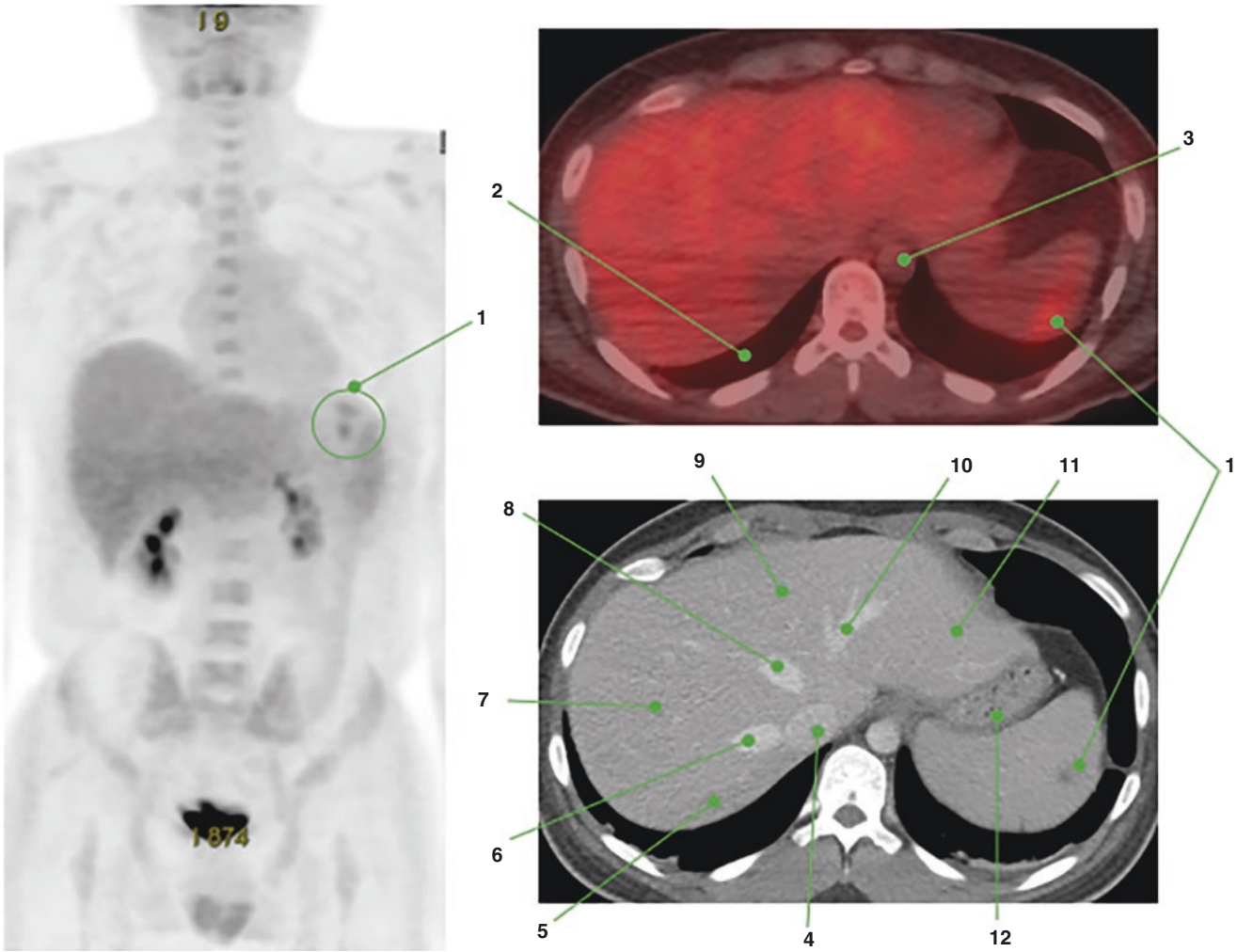

Fig. 52 1. Metabolically active hypodense splenic lesions
2. Right lung, lower lobe
3. Descending aorta
4. Inferior vena cava
5. Liver segment VII (7)
6. Right hepatic vein
7. Liver segment VIII (8)
8. Middle hepatic vein
9. Liver segment IV (4)
10. Left hepatic vein
11. Liver segment II (2)
12. Stomach

1.3.19 Case 19

A 5-year-old girl with pain and palpable mass in the left hemiabdomen. Abdominal ultrasound showed a left renal mass, so contrast-enhanced CT and ^{18}F-FDG PET/CT were performed. Images showed uneven increased activity in a prominent, well-defined mass at the lower pole of the left kidney, with heterogeneous contrast enhancement due to the presence of necrosis. The lesion showed the "claw sign", representing how the normal parenchyma wraps the mass forming sharp angles with it, which confirms its renal origin and the diagnosis of Wilms tumor over neuroblastoma, which is one of the most frequent tumors at this age. Other features favoring the diagnosis in this case are the well-defined margins, displacement of adjacent organs and structures without invasion, and the absence of retroperitoneal lymphadenopathies. Neuroblastoma is usually larger, crosses the midline, and is less defined, encasing vascular structures and sometimes invading the spinal canal; it is also associated with lymph nodes and metastases with greater frequency (Fig. 53) [44].

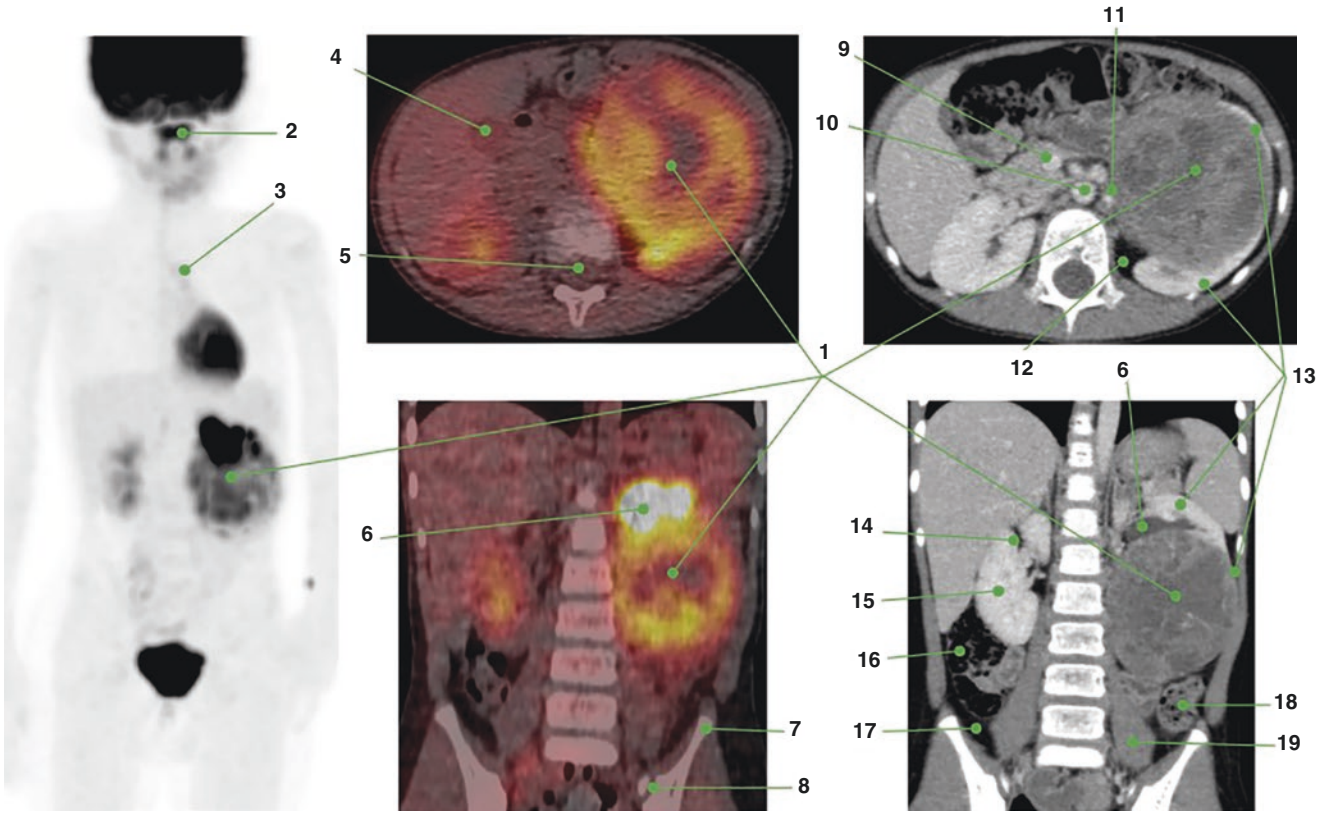

Fig. 53 1. Metabolically active left renal mass with necrosis: Wilms tumor
2. Prominent, hypermetabolic adenoid tissue; normal finding in children
3. Mild physiologic uptake in the thymus
4. Gallbladder
5. Spinal canal
6. Left renal pelvis, displaced by the mass
7. Left iliac bone
8. Left sacroiliac joint
9. Inferior mesenteric vein
10. Abdominal aorta
11. Left renal artery
12. Left perirenal fat
13. Normal left renal parenchyma, "claw sign"
14. Junctional parenchymal defect at the superior pole of the right kidney
15. Right kidney
16. Ascending colon
17. Right paracolic gutter
18. Descending colon
19. Left psoas muscle

1.3.20 Case 20

A 73-year-old man with a 3-month history of hematuria. Renal ultrasound was performed, finding a suspicious mass in the left kidney, so contrast-enhanced CT and ^{18}F-FDG PET/CT were performed. Images showed mild, diffuse, increased activity at the left kidney primary tumor, corresponding to a renal cell carcinoma, as well as hypermetabolism in the lumen of the enlarged left renal vein, consistent with a tumor thrombus. No distant metastases were observed (Fig. 54) [45].

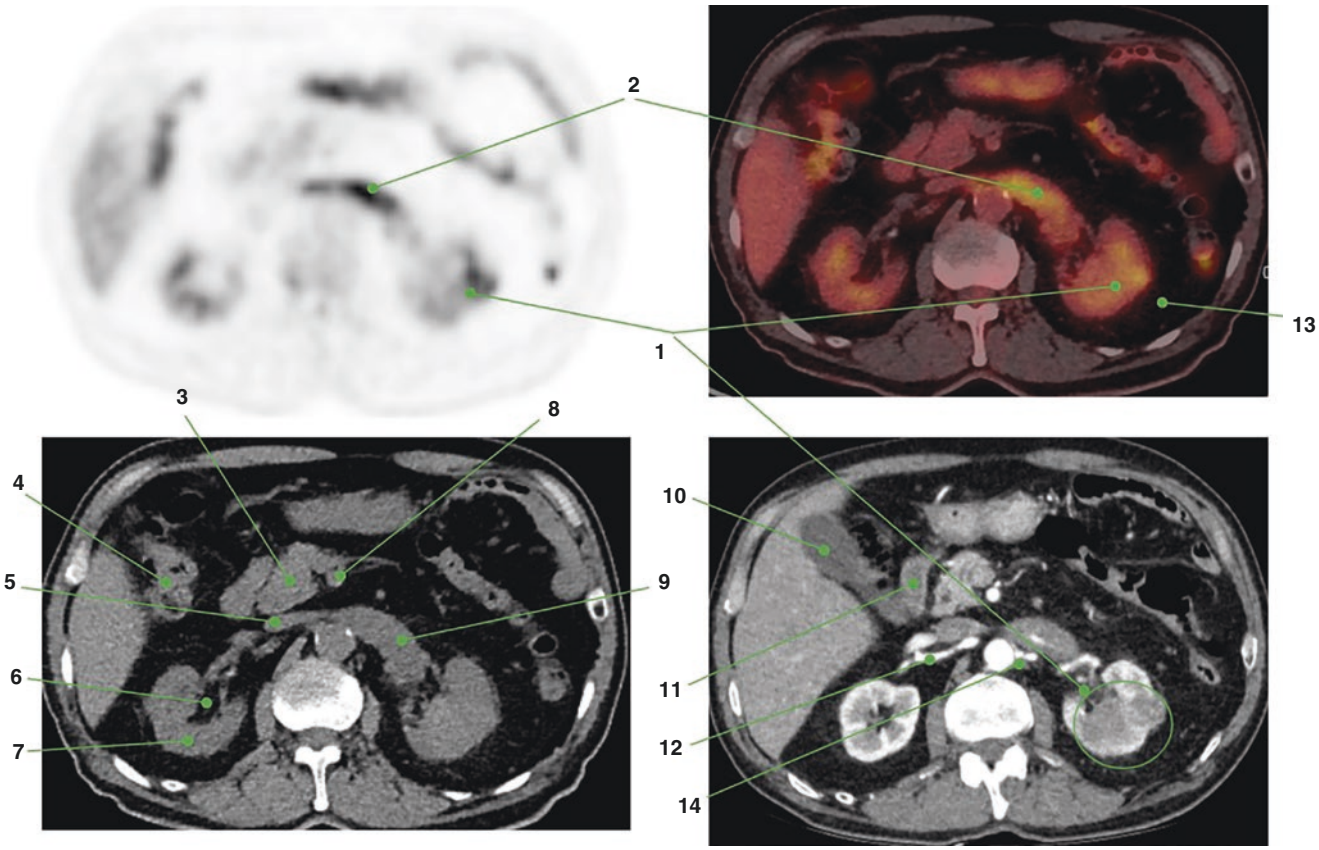

Fig. 54 1. Mild hypermetabolic left renal cell carcinoma
2. Metabolically active tumor thrombus in the left renal vein
3. Pancreatic head
4. Hepatic flexure of the colon
5. Right renal vein
6. Renal sinus fat
7. Renal parenchyma
8. Superior mesenteric artery
9. Dilated left renal vein
10. Gallbladder
11. Duodenum, second portion
12. Right renal artery
13. Left perirenal fat
14. Left renal artery

1.3.21 Case 21

A 77-year-old female patient scheduled for retinal surgery. In the pre-surgical studies, blood count showed as an incidental finding, elevated leukocyte count with atypical cells. Bone marrow biopsy confirmed the diagnosis of diffuse, large B-cell lymphoma. ^{18}F-FDG PET/CT was performed for staging, finding diffusely increased activity in a soft-tissue infiltration of the right perirenal space, without a definite mass. The right kidney morphology and parenchyma were completely preserved. Also, metabolically active retroperitoneal lymph nodes were observed (Fig. 55) [46].

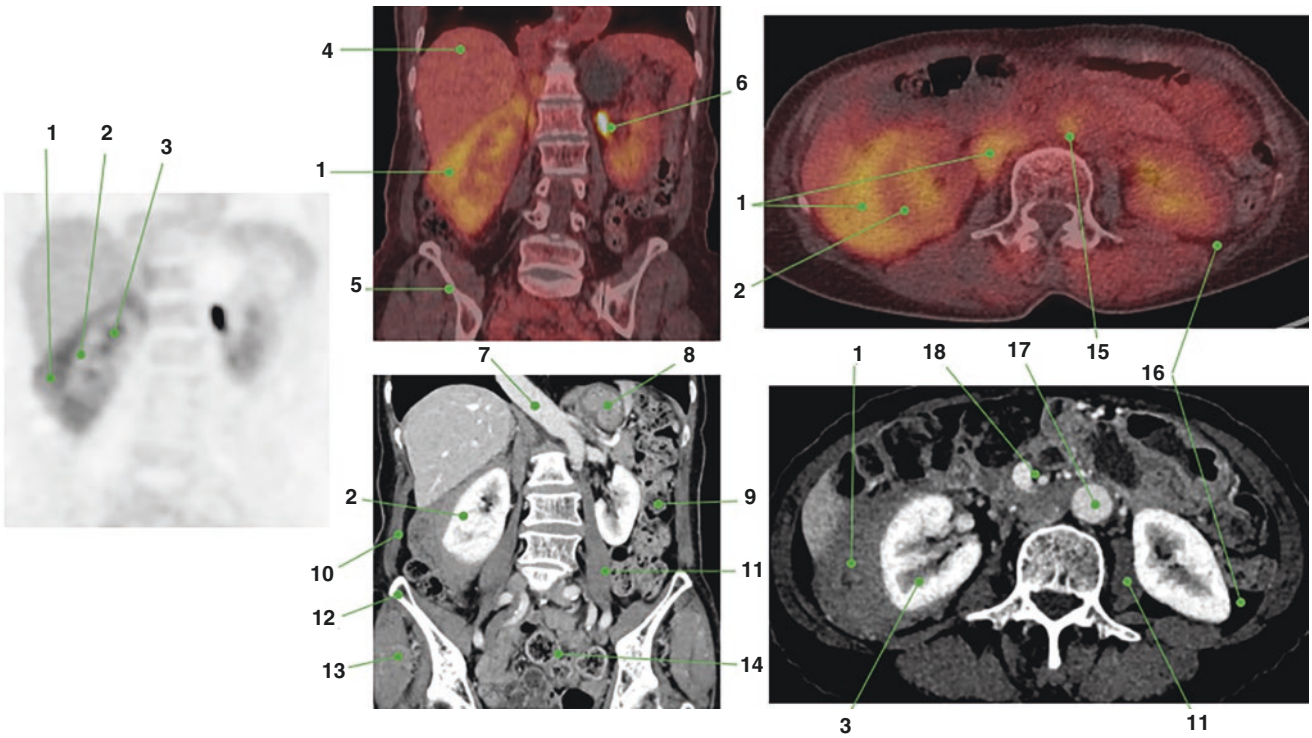

Fig. 55 1. Diffusely increased activity at soft-tissue infiltration of the right perirenal space, corresponding to lymphoma involvement
2. Right renal cortex
3. Right renal superior calyces
4. Liver dome
5. Right iliac bone
6. Left renal pelvis
7. Tortuous thoracoabdominal aorta
8. Gastric fundus
9. Descending colon
10. Right lateral abdominal wall muscles
11. Left psoas muscle
12. Right anterior superior iliac crest
13. Right gluteus muscles
14. Sigmoid colon
15. Hypermetabolic retroperitoneal paraaortic lymph node
16. Left perirenal fat, normal appearance
17. Abdominal aorta
18. Mesenteric vessels

1.3.22 Case 22

A 71-year-old male patient with persistent hematuria and ultrasound documented left hydronephrosis. Ureteroscopy was performed, finding a solid mass in the middle portion of the left ureter, so ^{18}F-FDG PET/CT was performed. Images showed markedly increased activity at the middle third of the left ureter, in a soft tissue mass, corresponding to biopsy-confirmed urothelial carcinoma, obstructing and leading to proximal dilatation and renal parenchymal atrophy. Periureteral fat stranding and small metabolically active lymph nodes around the mass were also noted (Fig. 56) [47].

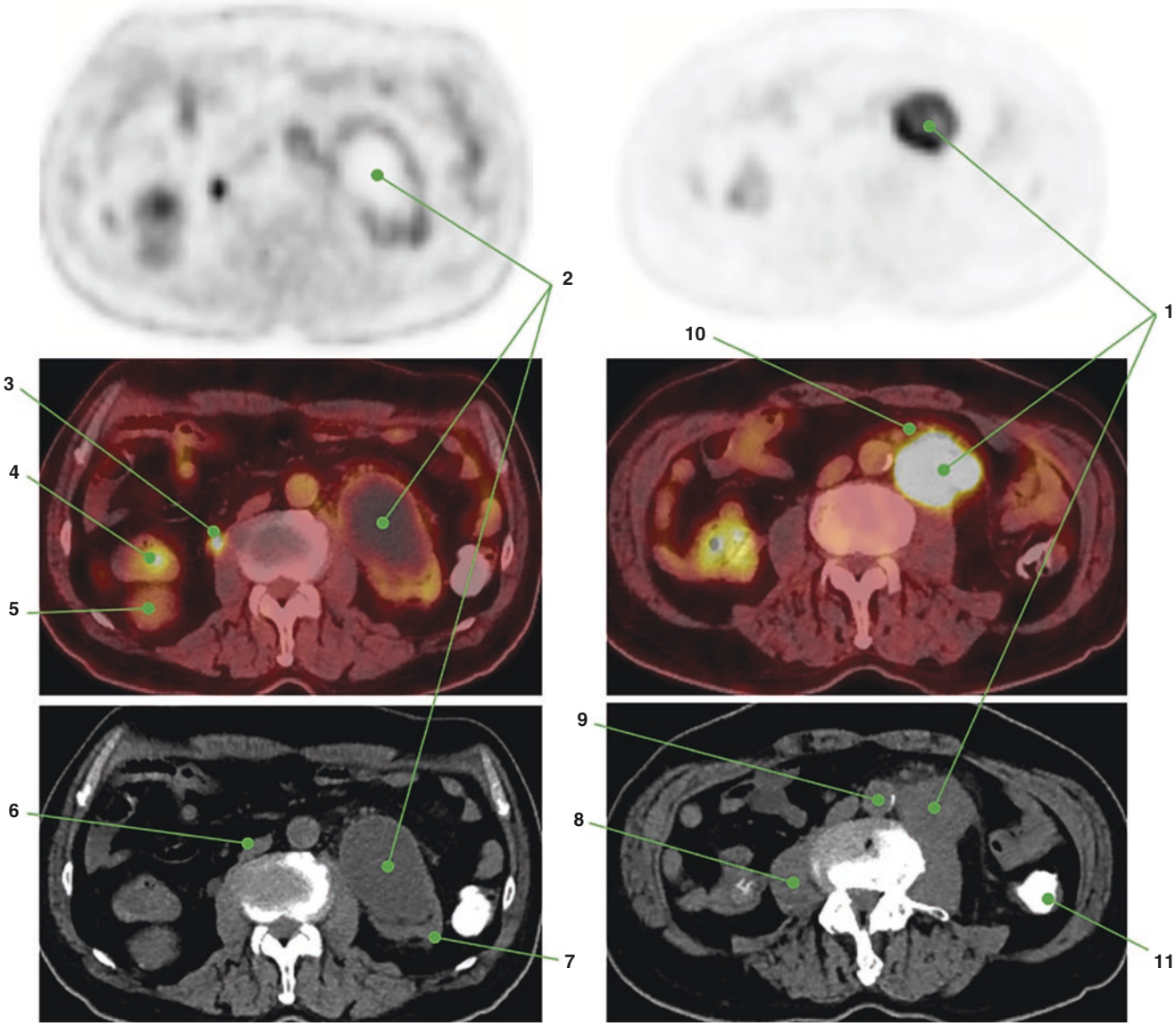

Fig. 56 1. Marked metabolically active left ureter urothelial carcinoma
2. Dilated left renal pelvis: hydronephrosis
3. Right ureter
4. Ascending colon
5. Right kidney, inferior pole
6. Inferior vena cava
7. Left atrophic renal parenchyma
8. Right psoas muscle
9. Abdominal aorta
10. Periureteral fat stranding and small metabolically active lymph nodes
11. Hyperdense oral contrast in the descending colon

1.3.23 Case 23

A 64-year-old female patient with history of right renal cell carcinoma, treated with partial nephrectomy and chemotherapy 2 years ago. She attended a routine checkup, where abdominal CT reported postoperative changes with a small residual collection in the right pararenal space. When performing the complementary ^{18}F-FDG PET/CT, focal nodular increased activity was noted at the postsurgical changes, later confirmed as tumor recurrence. No other hypermetabolic metastases were found (Fig. 57) [45].

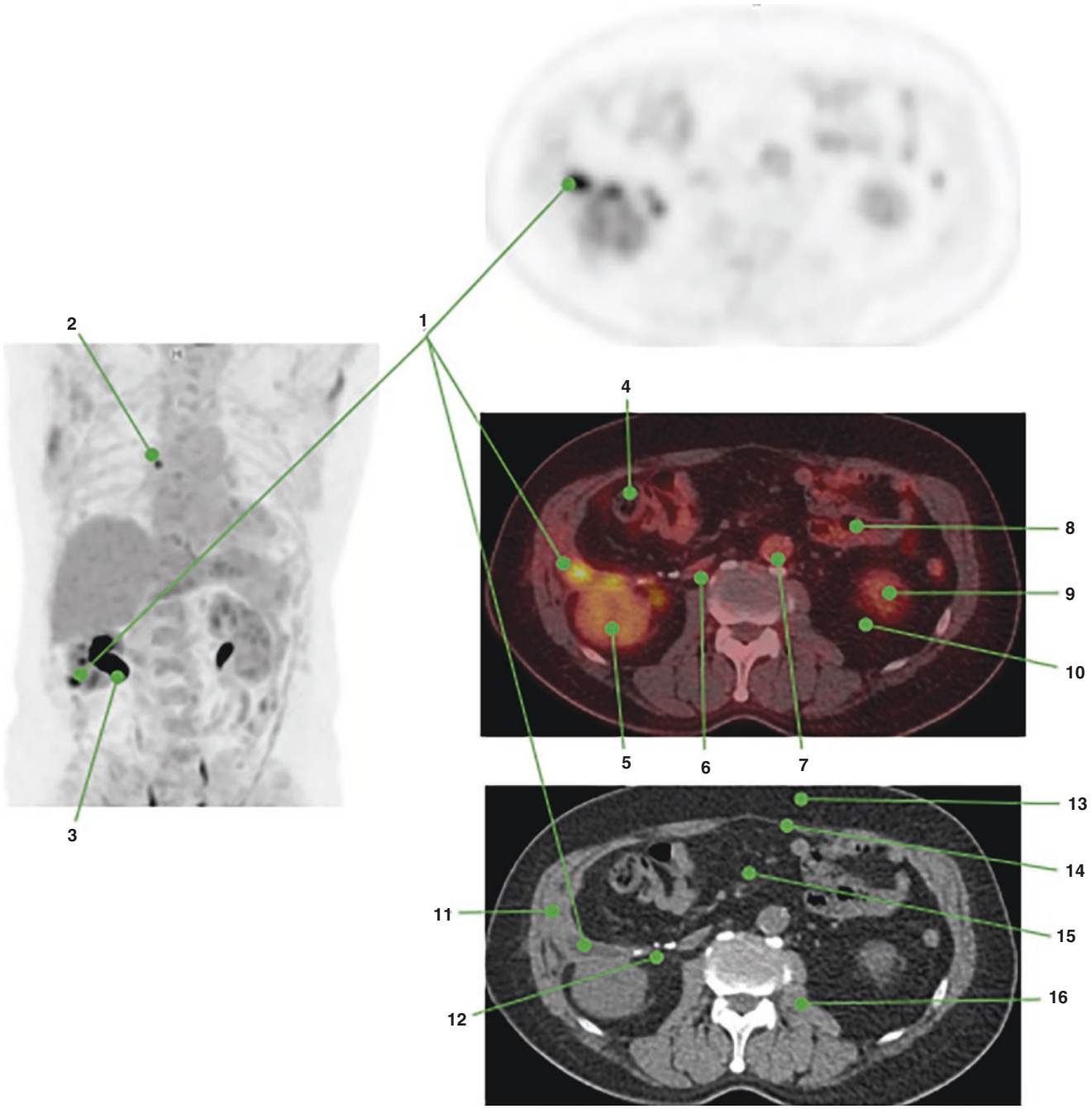

Fig. 57 1. Focal increased activity at postsurgical changes in the right perirenal space and lateroconal fascia
2. Hypermetabolic right hilar lymph node, reactive more likely
3. Right renal pelvis
4. Ascending colon
5. Right kidney inferior pole
6. Inferior vena cava
7. Abdominal aorta
8. Small bowel loops
9. Left kidney, inferior pole
10. Left perirenal space, normal fat appearance
11. Right lateral abdominal wall muscles (inner to outer: transverse, internal oblique, external oblique)
12. Surgical clips
13. Anterior abdominal wall subcutaneous fat
14. Rectus sheath
15. Small bowel mesentery
16. Left psoas muscle

1.3.24 Case 24

A 54-year-old male patient with history of stage III lung adenocarcinoma, treated with external radiation therapy and posterior surgery. A routine chest CT reported partial visualization of a left adrenal lesion, so ^{18}F-FDG PET/CT was performed. Images showed increased metabolic activity in the diffusely enlarged left adrenal gland, corresponding to a newly developed infrequent-shaped metastasis. No other hypermetabolic lesions were observed (Fig. 58).

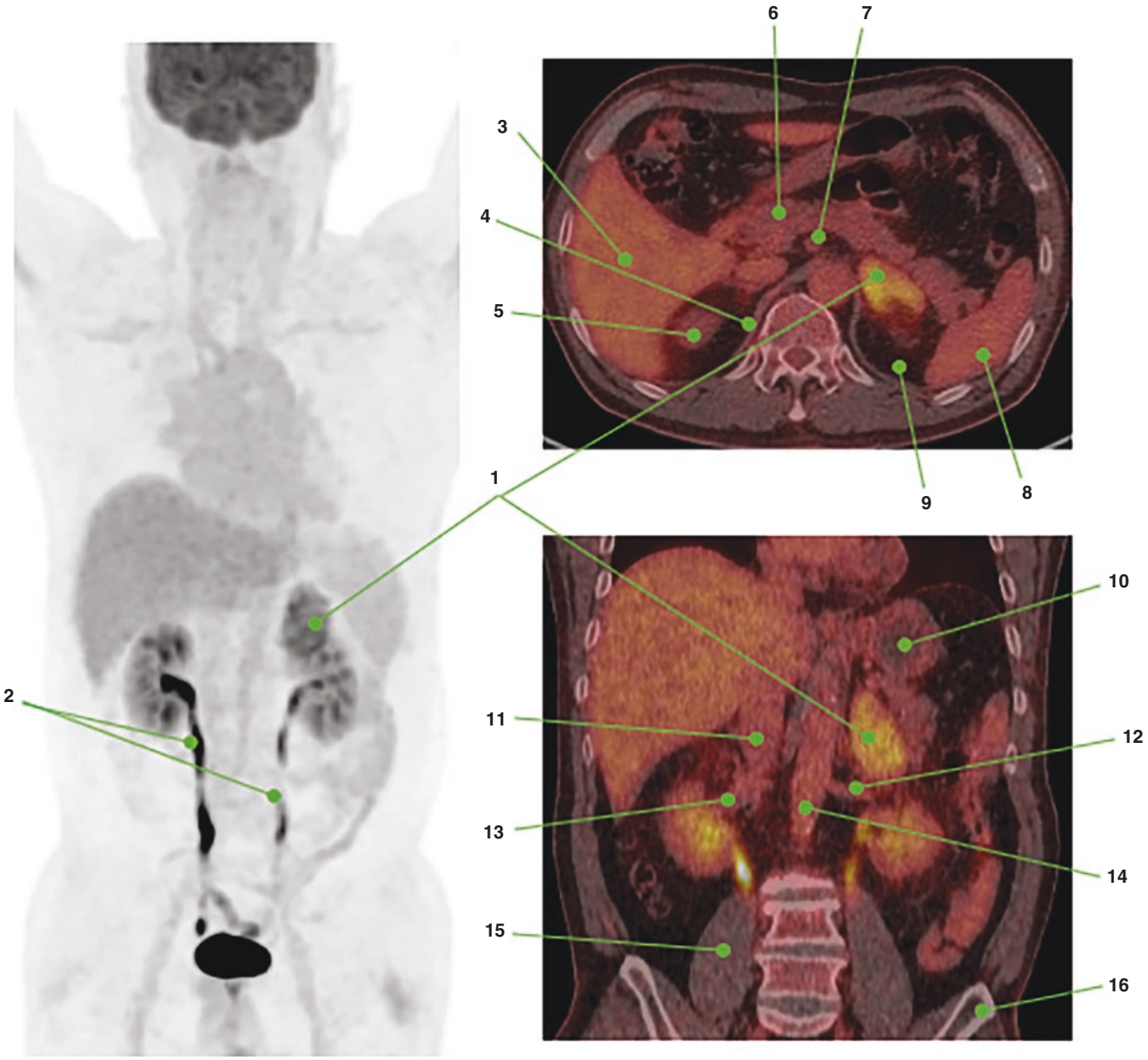

Fig. 58 1. Metabolically active left adrenal metastasis
2. Ureters
3. Liver, segment 6
4. Right diaphragmatic crus
5. Right kidney, inferior pole
6. Pancreatic head
7. Superior mesenteric artery
8. Spleen
9. Left perirenal fat
10. Stomach
11. Inferior vena cava
12. Left renal artery
13. Right renal vein
14. Abdominal aorta
15. Right psoas muscle
16. Left anterior superior iliac spine

1.3.25 Case 25

A 64-year-old man with a history of diffuse, large B-cell lymphoma, treated 2 years ago with complete metabolic response, and a history of prostate cancer treated with surgery and radiotherapy 1 year ago. He attended hemato-oncology checkup with a follow-up ^{18}F-FDG PET/CT, where multiple slightly hypermetabolic lymph nodes were found in the right internal and external iliac chains, as well as multiple moderately hypermetabolic bone lesions in thoracic and lumbar vertebral bodies, in both pelvic bones and the right femur. Subsequently, a PSA of 40 ng/ml was found and metastatic disease from an aggressive prostate cancer was confirmed with biopsy (Fig. 59) [48].

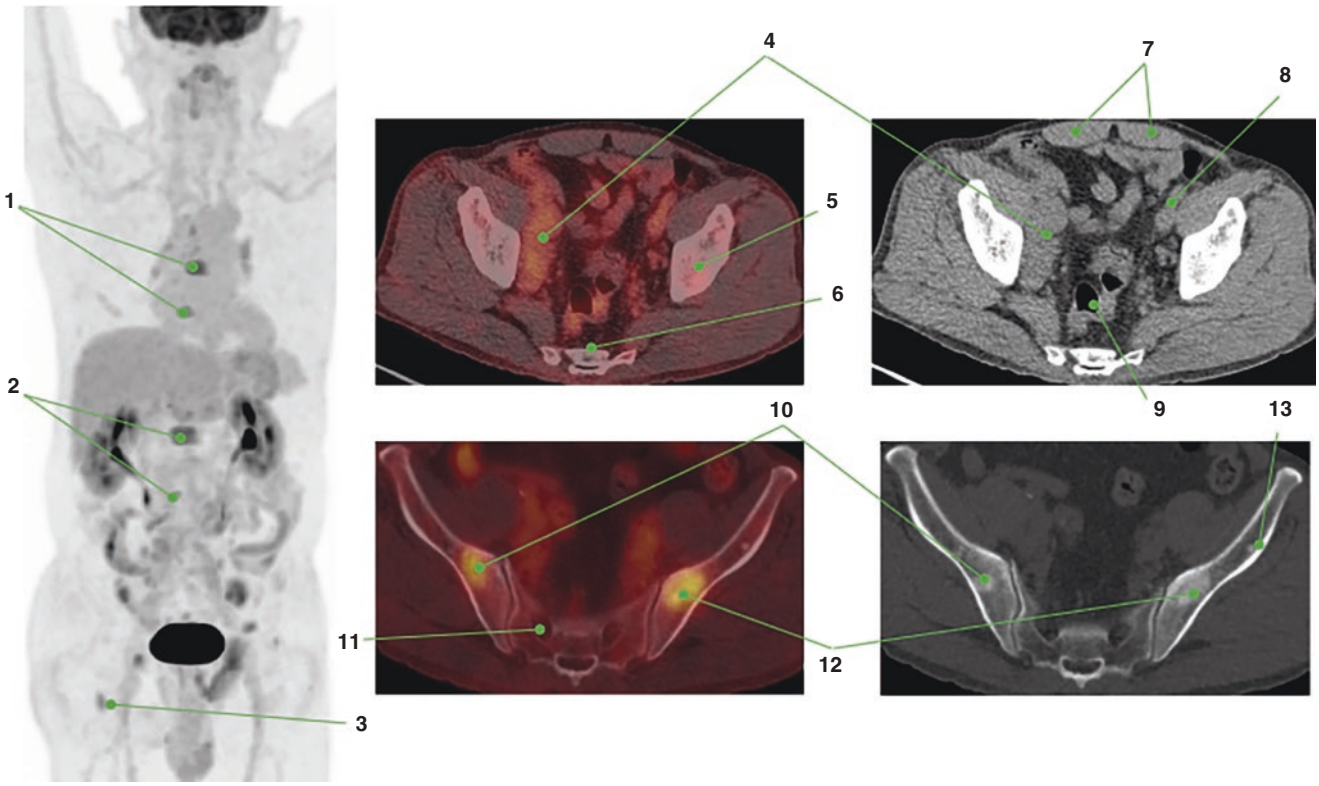

Fig. 59 1. Thoracic vertebral bodies metastases
2. Lumbar vertebral bodies metastases
3. Right proximal femur metastasis
4. Right iliac chains metastatic lymph nodes
5. Left acetabular roof
6. Sacrum
7. Abdominis rectus muscles
8. Left external iliac vessels
9. Sigmoid colon
10. Right iliac bone sclerotic metastasis
11. Right sacral foramen
12. Left iliac bone sclerotic metastasis
13. Left iliac wing sclerotic metastasis without FDG uptake

1.3.26 Case 26

A 46-year-old woman with occasional abdominal pain and suspected lymphoma due to a retroperitoneal lesion described in abdominal ultrasound. Contrast-enhanced CT and ^{18}F-FDG PET/CT were performed to confirm the diagnosis and stage the disease. Images showed focal increased activity at an irregular thickening of the soft tissues surrounding the abdominal aorta just below the renal hilum, encasing it without compression. Subsequent biopsy confirmed an initial stage of retroperitoneal fibrosis and when carrying out extension studies, IgG4-related disease was confirmed as its etiology (Fig. 60) [49].

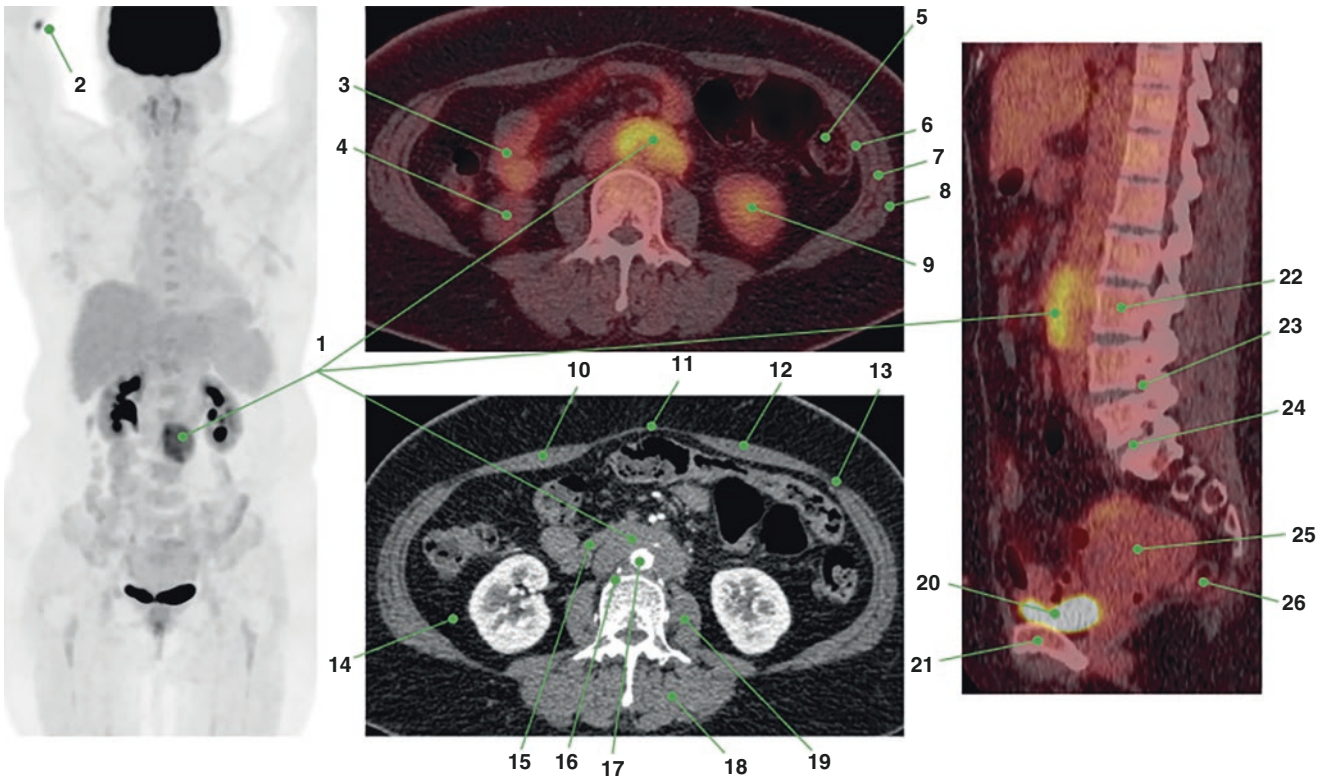

Fig. 60 1. Increased activity at periaortic thickened soft tissues
2. Right arm injection site
3. Small bowel loops
4. Right kidney inferior pole
5. Descending colon
6. Left transversus abdominis muscle
7. Left internal oblique muscle
8. Left external oblique muscle
9. Left kidney
10. Right rectus abdominis muscle
11. Rectus sheath
12. Left rectus abdominis muscle
13. Left lateral fascia
14. Right perirenal space
15. Inferior vena cava
16. Right lumbar artery
17. Abdominal aorta
18. Left erector spinae muscle
19. Left psoas muscle
20. Bladder
21. Pubis
22. L3 vertebral body
23. L4-L5 spinal foramen
24. L5-S1 intervertebral space
25. Retroverse uterus
26. Rectum

1.3.27 Case 27

A 79-year-old man with persistent fever and night sweats. Initial studies showed low white blood cell count and elevation of serum lactate dehydrogenase (LDH), so ^{18}F-FDG PET/CT was performed to confirm and stage the diagnosis of lymphoma. Images showed multiple hypermetabolic mediastinal lymph nodes and a bulky retroperitoneal aortocaval lymph node conglomerate at the level of the renal hilum, as well as markedly increased activity in a right perirenal mass involving the perirenal fascia. Subsequent biopsy of the right perirenal mass confirmed the diagnosis of diffuse, large B-cell lymphoma (Fig. 61).

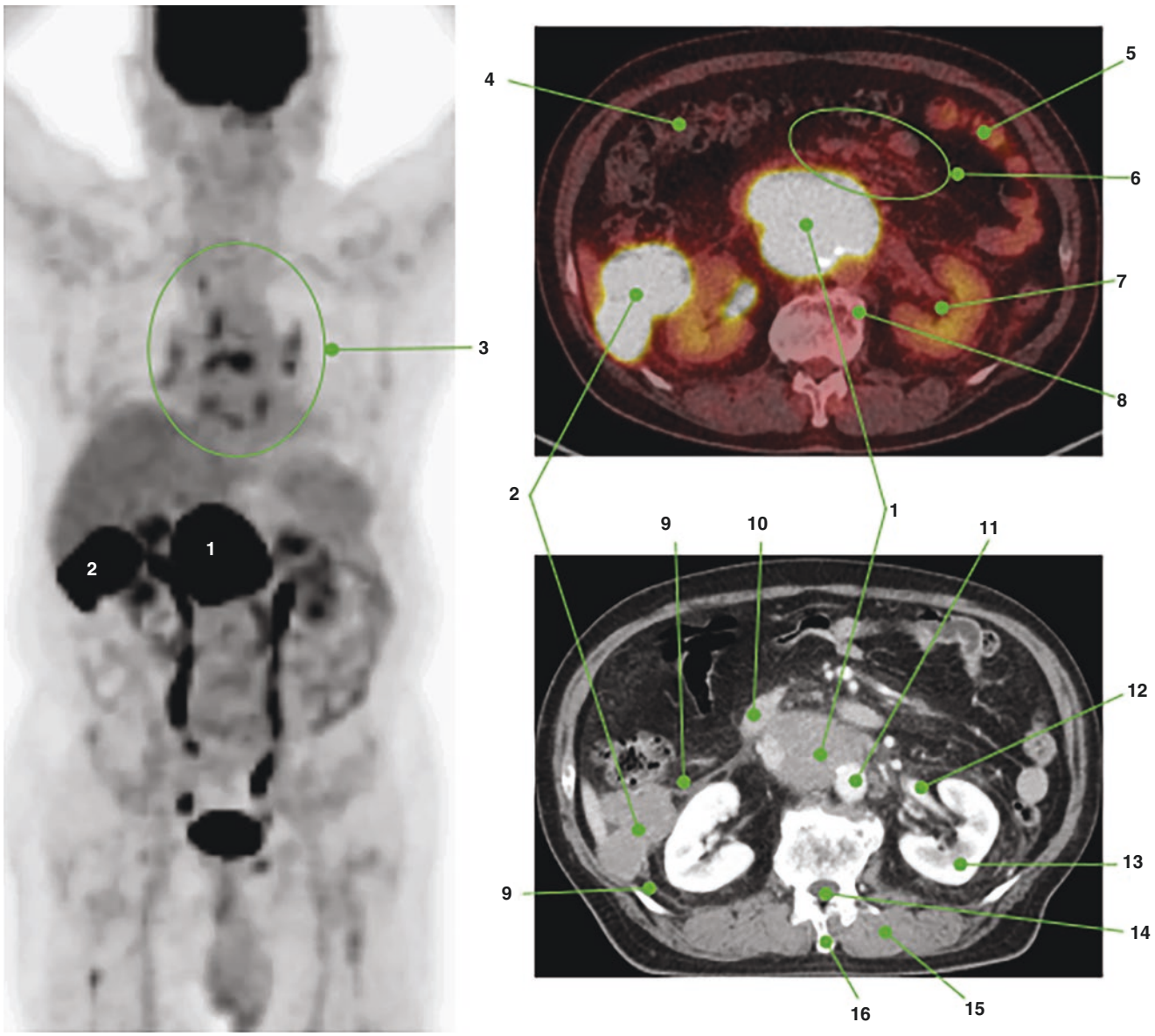

Fig. 61 1. Metabolically active retroperitoneal lymph node conglomerate
2. Metabolically active right perirenal mass
3. Hypermetabolic mediastinal lymph nodes
4. Proximal transverse colon
5. Small bowel loops
6. Probably reactive lymph nodes in the small bowel mesentery
7. Left renal sinus
8. Lumbar vertebral body osteophyte
9. Right perirenal fascia
10. Inferior vena cava
11. Abdominal aorta
12. Left renal vein
13. Left renal parenchyma
14. Spinal canal
15. Left erector spinae muscle
16. Lumbar spinous process

1.3.28 Case 28

A 70-year-old woman with a growing abdominal mass and fever. Ultrasound-guided biopsy of the mass confirmed the diagnosis of germinal center B-cell (GCB) diffuse large B-cell lymphoma (DLBCL), so ^{18}F-FDG PET/CT was performed for staging. Images showed a bulky hypermetabolic mass with a central area of necrosis, surrounding the abdominal aorta below the renal hilum, as well as two small metabolically active lymph nodes in the right pelvis and minimal, diffuse, increased uptake in the spleen (greater than that of the liver). DLBCL is the most common type of non-Hodgkin lymphoma and there are two main biological subtypes to consider, GCB, like in this patient, and activated B-cell (ABC) subtypes, the latter with a more aggressive behavior and worse prognosis. Other less frequent subtypes include double-hit and double-expressor lymphomas (Fig. 62) [50].

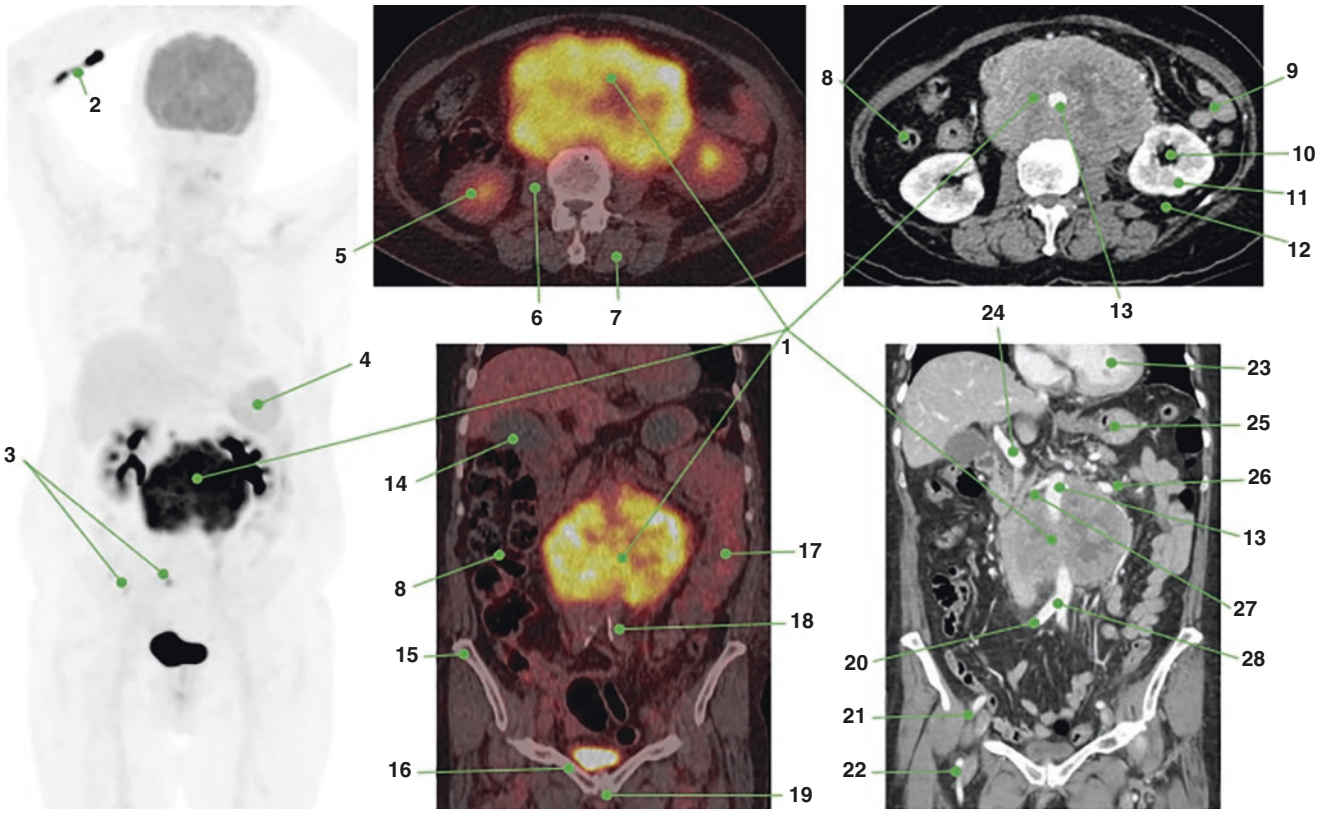

Fig. 62 1. Metabolically active retroperitoneal lymphoma
2. Injection site at the right proximal forearm
3. Mild hypermetabolic pelvic lymph nodes
4. Spleen, minimal, diffuse, increased uptake
5. Right kidney
6. Right psoas muscle
7. Left erector spinae muscle (includes longissimus and iliocostalis muscles)
8. Ascending colon
9. Small bowel loops
10. Left renal sinus
11. Left renal parenchyma
12. Left perirenal space
13. Abdominal aorta
14. Gallbladder
15. Right iliac crest
16. Right pubic bone, superior ramus
17. Descending colon
18. Left common iliac artery with atherosclerotic calcifications
19. Pubic symphysis
20. Right common iliac artery
21. Right external iliac artery
22. Right femoral artery
23. Left ventricle
24. Portal vein
25. Stomach
26. Superior mesenteric artery
27. Right renal artery
28. Iliac bifurcation

1.3.29 Case 29

A 44-year-old man with a history of acute myeloid leukemia (AML), treated 1 year ago. He attended an early checkup with a left cervical mass, so ^{18}F-FDG PET/CT was performed. Images showed multiple metabolically active lesions including a prominent left submandibular mass, multiple left neck, mediastinal and retroperitoneal lymph nodes, nodular lesions at the right lung, stomach, pancreas and left kidney, as well as diffuse infiltration of the abdominal aorta wall. Biopsy of the cervical mass was performed and the diagnosis of myeloid sarcoma (MS), as an AML relapse, was confirmed (Fig. 63) [51].

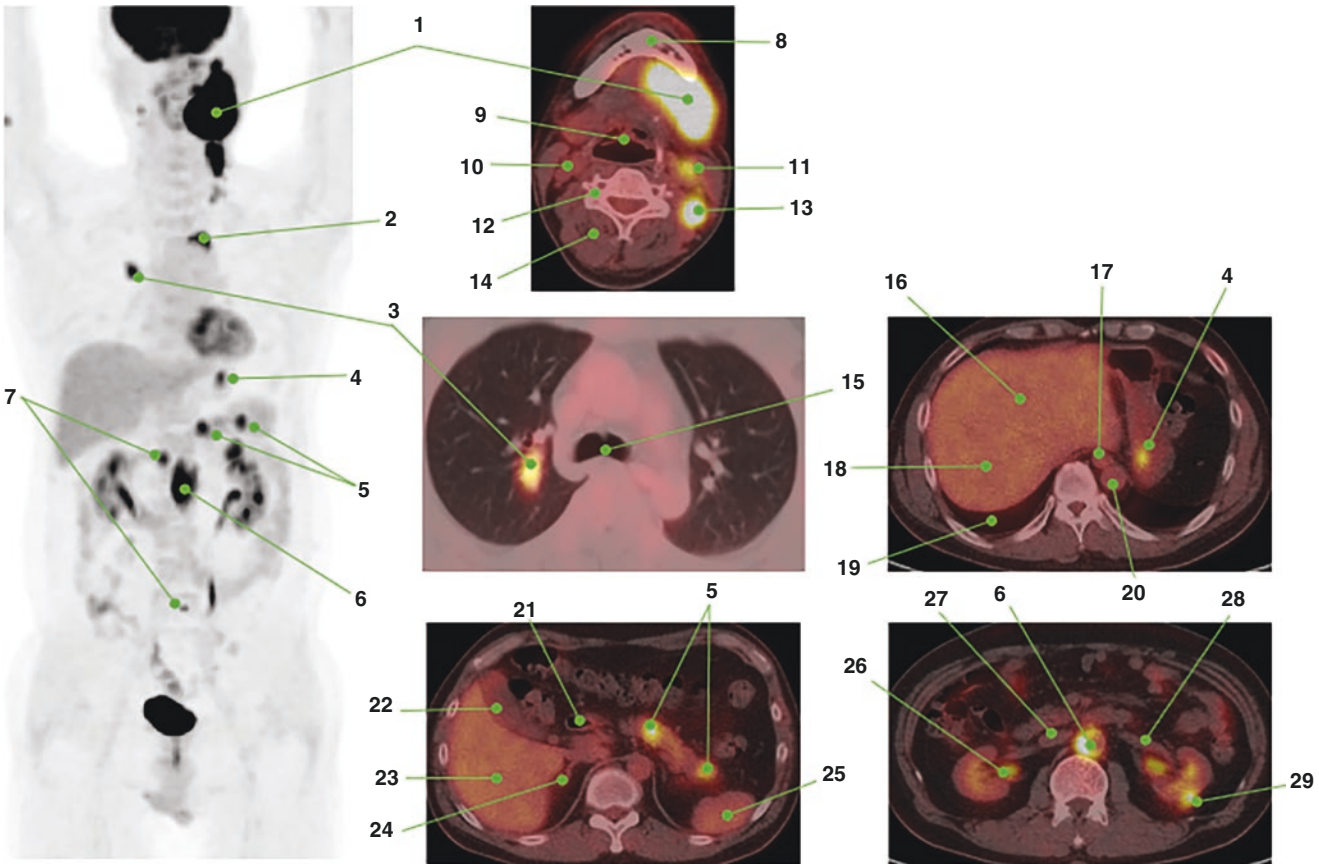

Fig. 63 1. Metabolically active left submandibular mass
2. Metabolically active mediastinal lymph node
3. Metabolically active right lung nodule
4. Metabolically active nodule at the gastric cardia
5. Metabolically active nodules at the pancreatic body and tail
6. Metabolically active involvement of the abdominal aorta wall
7. Metabolically active retroperitoneal lymph nodes
8. Mandible
9. Epiglottis
10. Right carotid space (common carotid artery and internal jugular vein)
11. Metabolically active left neck lymph node, level III
12. Right vertebral foramen
13. Metabolically active left neck lymph node, level V
14. Right posterior cervical muscles
15. Carina
16. Liver, segment 4(IV)
17. Gastroesophageal junction
18. Liver, segment 7(VII)
19. Right lung base
20. Distal thoracic aorta
21. Duodenum, second portion
22. Gallbladder
23. Liver, segment 6(VI)
24. Right adrenal gland
25. Spleen, inferior pole
26. Right renal pelvis
27. Inferior vena cava
28. Left renal vein
29. Metabolically active nodule in the Lt kidney

1.3.30 Case 30

A 5-year-old girl who attended the emergency room for pelvic pain. They performed abdominal ultrasound identifying a complex pelvic mass, so contrast-enhanced CT and ^{18}F-FDG PET/CT were performed. Images showed diffusely increased activity in a prominent pelvic mass with heterogeneous enhancement, displacing the bladder and invading the uterus and adnexa. The lesion was removed and the diagnosis of rhabdomyosarcoma was confirmed. Pelvic location is rare and almost exclusive in the pediatric population; in girls, the vagina is the most frequently involved organ (Fig. 64).

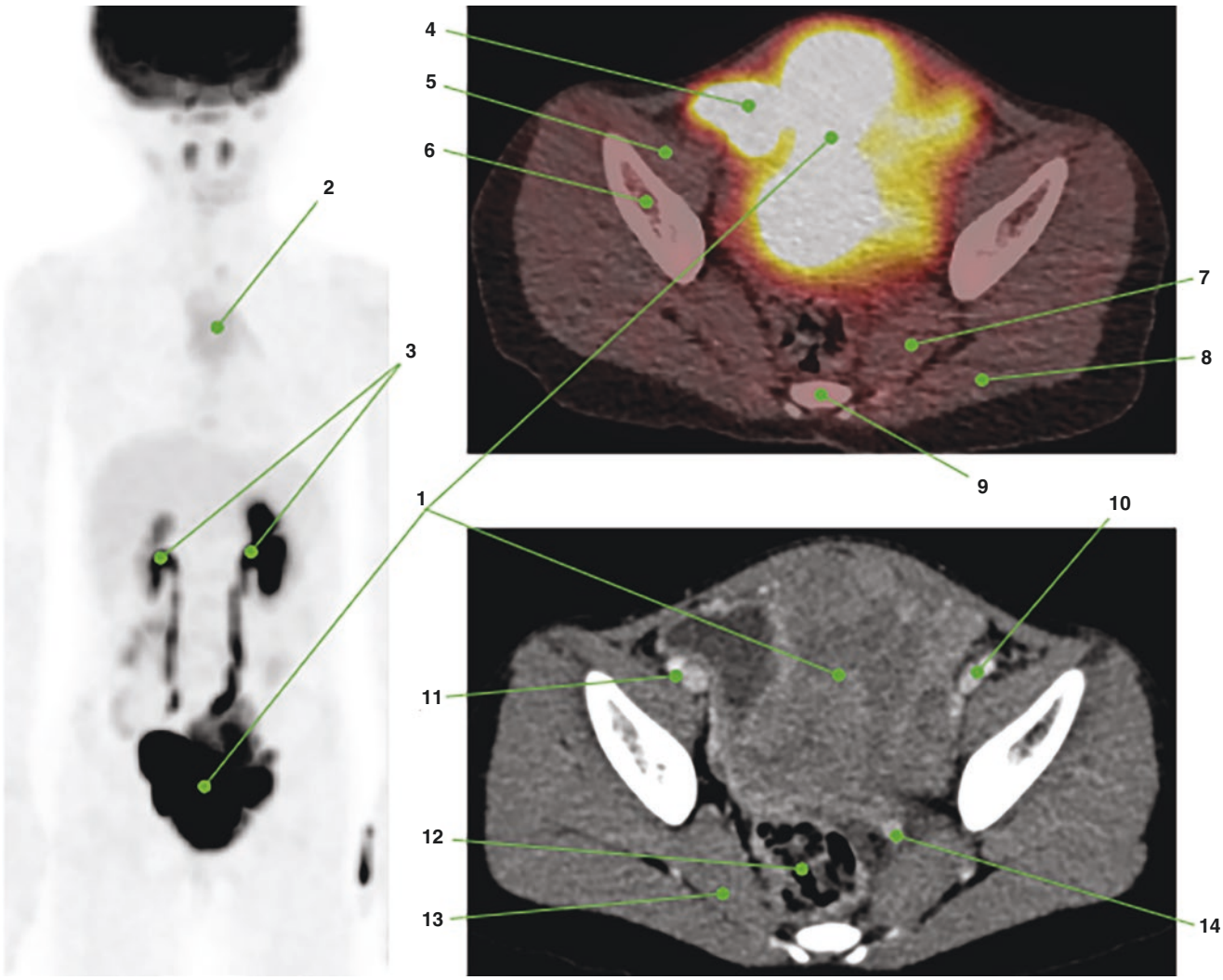

Fig. 64 1. Metabolically active irregular pelvic mass with heterogeneous contrast enhancement
2. Mild physiologic uptake in the thymus
3. Renal pelvis
4. Displaced urinary bladder
5. Right iliacus muscle
6. Right iliac bone
7. Left piriformis muscle
8. Left gluteus maximus muscle
9. Coccyx
10. Left external iliac vessels
11. Right external iliac vessels
12. Rectum
13. Right piriformis muscle
14. Left internal iliac vessels

1.3.31 Case 31

A 67-year-old female patient with abnormal uterine bleeding. Gynecological ultrasound reported a heterogeneous uterine mass and to rule out malignancy vs fibroma with degenerative changes, so ^{18}F-FDG PET/CT was performed. Images showed a prominent uterine mass with markedly increased activity and central necrosis, involving the perituterine soft tissues, which was later confirmed to correspond to endometrial stromal sarcoma. Multiple hypermetabolic pelvic and retroperitoneal lymph nodes were also noted (Figs. 65 and 66) [52].

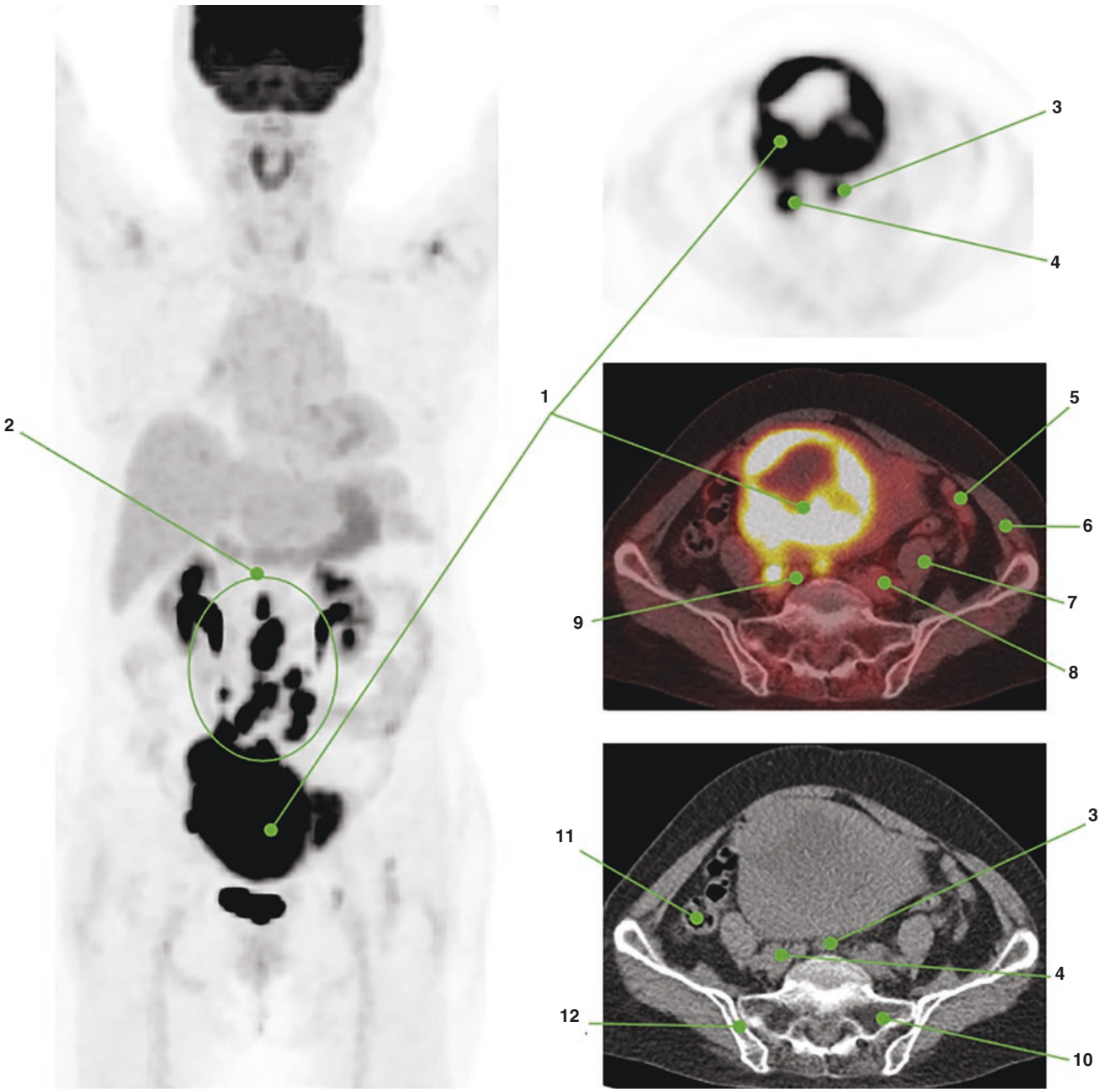

Fig. 65 1. Metabolically active uterine tumor with central necrosis
2. Multiple hypermetabolic retroperitoneal lymph nodes
3. Hypermetabolic pelvic lymph node: iliac bifurcation
4. Hypermetabolic pelvic lymph node: right common iliac chain
5. Small bowel loops at left lower quadrant
6. Left internal oblique muscle
7. Left psoas muscle
8. Left common iliac vessels
9. Right common iliac vein
10. Left sacral ala
11. Ascending colon
12. Right sacroiliac joint

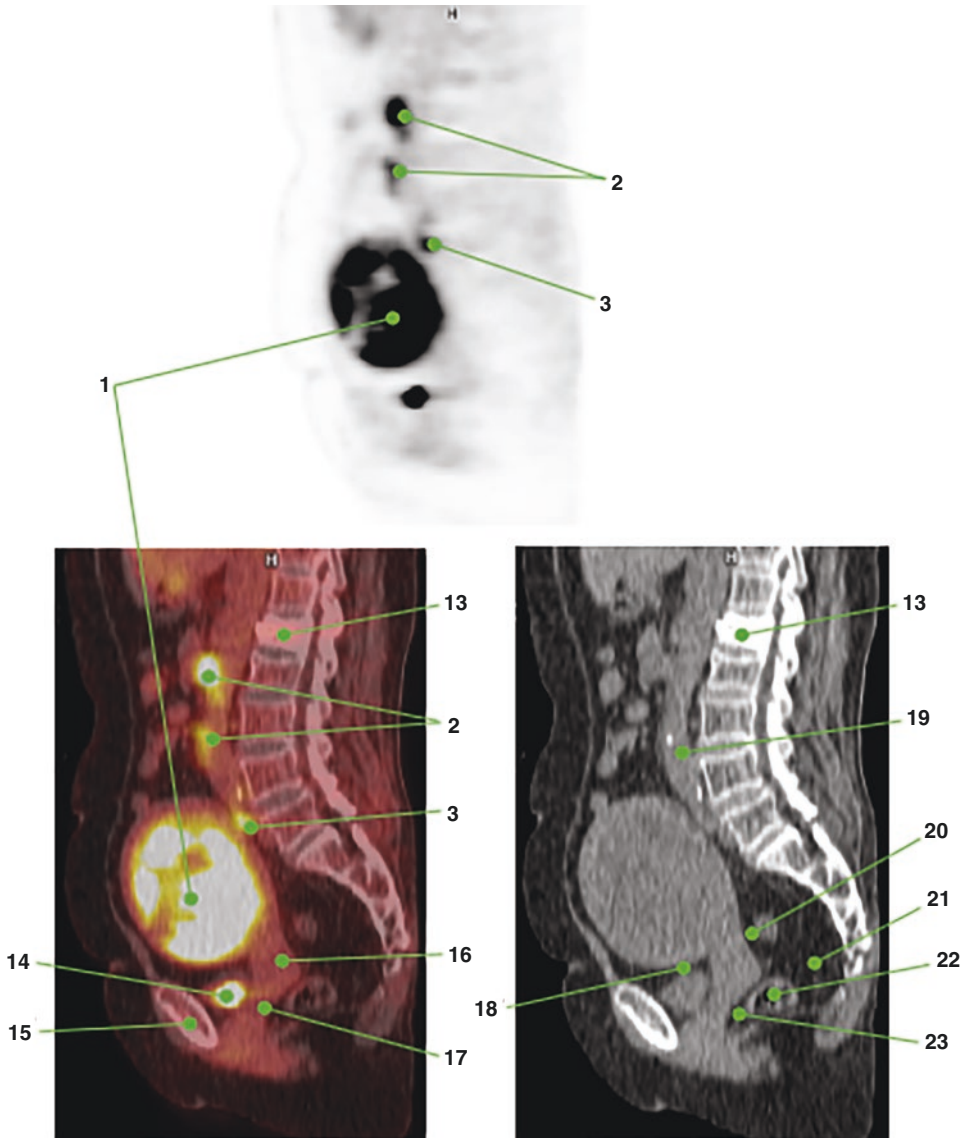

Fig. 66 13. L1 compression fracture with treatment changes
14. Bladder
15. Pubic bone
16. Cervix
17. Vagina
18. Vesicouterine pouch
19. Abdominal aorta
20. Recto-uterine pouch (pouch of Douglas)
21. Perirectal fat
22. Rectum
23. Recto-vaginal septum

1.3.32 Case 32

A 62-year-old woman with abnormal vaginal bleeding and perineal pain. On physical examination, an ulcerated vulvar mass was found and excisional biopsy confirmed the diagnosis of carcinoma. They requested ^{18}F-FDG PET/CT for whole body evaluation. Images showed markedly focal increased activity at the uterine cavity in posteriorly confirmed primary endometrial carcinoma, as well as two focal hypermetabolic lesions in the vaginal wall, corresponding to infrequent carcinoma metastases, just as the previously removed vulvar lesion (Fig. 67).

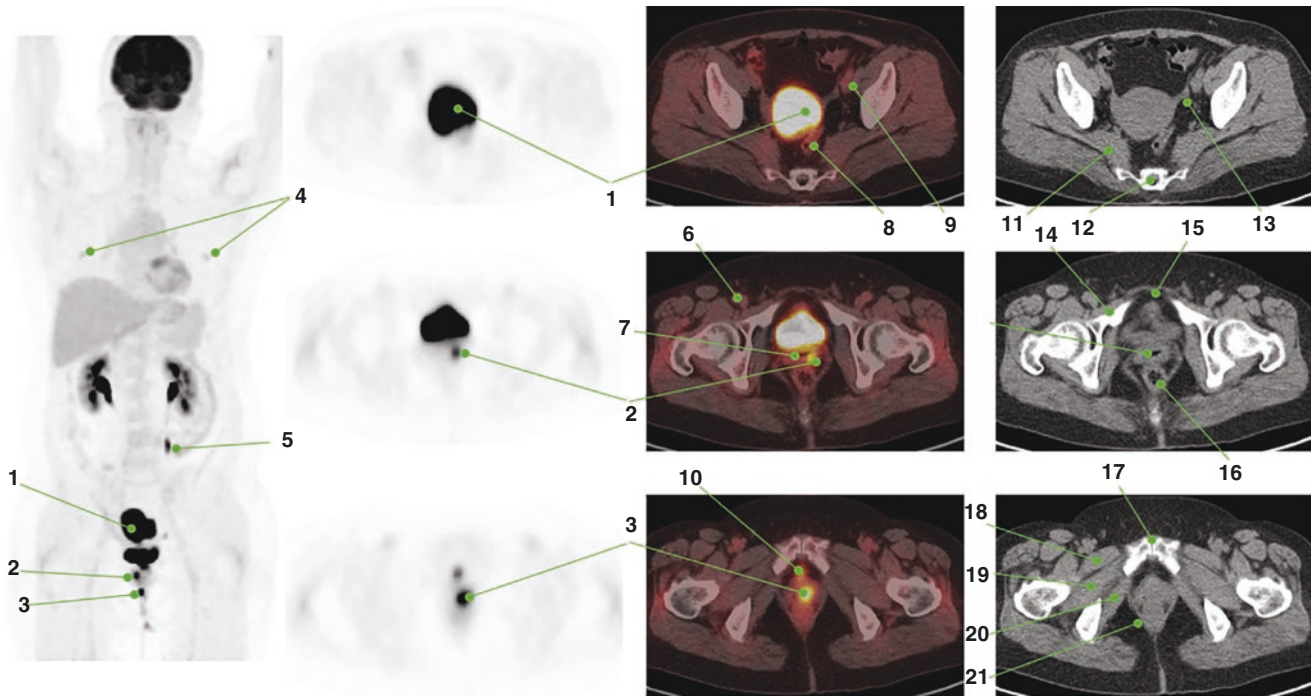

Fig. 67 1. Metabolically active uterine primary tumor
2. Superior vaginal wall hypermetabolic metastasis
3. Inferior vaginal wall hypermetabolic metastasis
4. Nipples
5. Left ureter, middle third
6. Right femoral vessels
7. Vaginal canal
8. Distal sigmoid colon
9. Left external iliac vessels
10. Uretra
11. Right piriformis muscle
12. Inferior sacrum
13. Left round ligament
14. Right pubic ramus
15. Prevesical space
16. Rectum
17. Pubic symphysis
18. Right pectineus muscle
19. Right external obturator muscle
20. Right internal obturator muscle
21. Right levator ani muscle

1.3.33 Case 33

A 57-year-old female patient with occasional abdominal pain, who attended a general checkup, with elevated CA 125. Gynecological ultrasound revealed a mixed solid and cystic mass, so contrast-enhanced CT and ^{18}F-FDG PET/CT were performed. Images showed a large complex pelvic mass originated in the right ovary, with increased activity in the peripheral solid enhancing component, highly suspicious of malignancy. No other hypermetabolic lesions were detected. Later biopsy confirmed the diagnosis of a clear cell carcinoma (Fig. 68) [53].

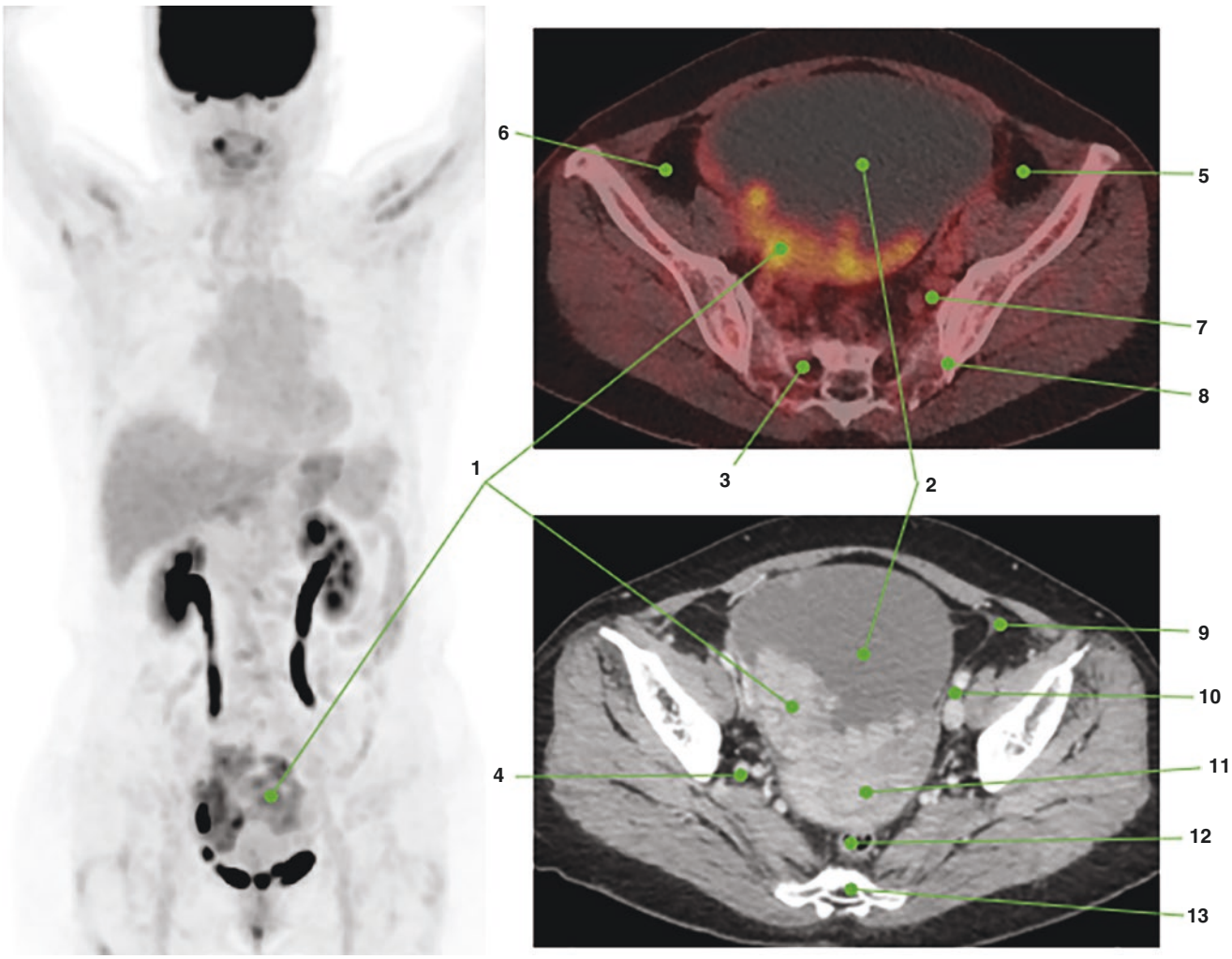

Fig. 68 1. Metabolically active solid component of complex pelvic mass
2. Cystic component of pelvic mass
3. Right sacral foramen
4. Right internal iliac vessels
5. Left paracolic gutter
6. Right paracolic gutter
7. Left internal iliac vessels
8. Left sacroiliac joint
9. Left round ligament
10. Left external iliac vessels
11. Uterus
12. Rectum
13. Sacrum

1.3.34 Case 34

A 51-year-old woman with a history of gastric cancer treated with total gastrectomy and chemotherapy. She attended an early checkup due to abdominal pain and distension, so contrast-enhanced CT and ^{18}F-FDG PET/CT were performed. Images showed diffusely increased activity at a prominent pelvic mass with solid and cystic components, with thick enhancing septa, dependent on the left ovary. There was also increased activity at the enlarged and heterogeneous right ovary, as well as diffuse FDG uptake in pelvic ascites. Given the suspicion of metastasis, the lesions were surgically resected and the presence of signet ring cells, consistent with a Krukenberg tumor, confirmed the diagnosis (Fig. 69).

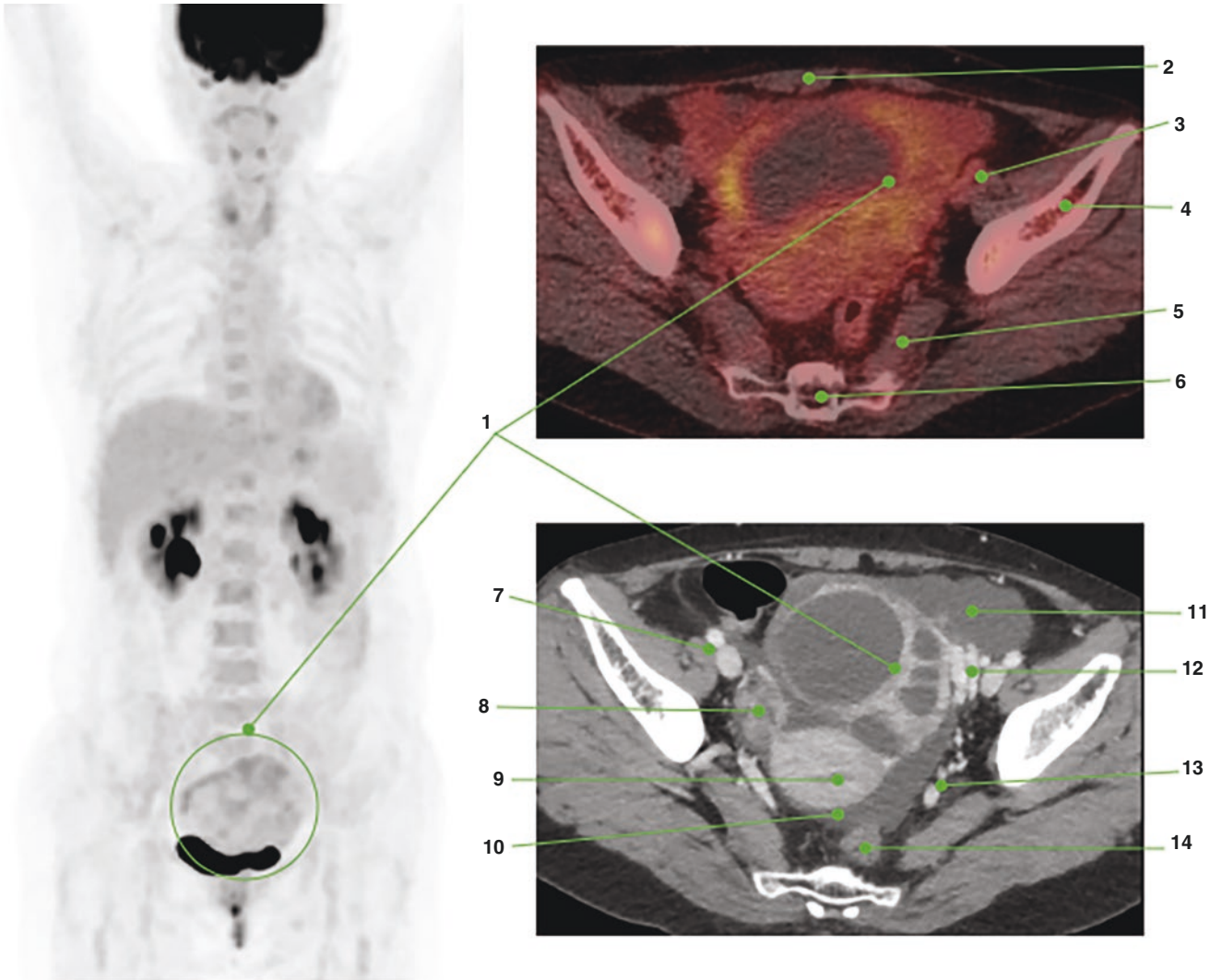

Fig. 69 1. Metabolically active left ovarian complex mass
2. Right abdominal rectus muscle
3. Left external iliac vessels
4. Left iliac wing
5. Left piriformis muscle
6. Sacrum
7. Right external iliac vessels
8. Right ovary with mild heterogeneous uptake and enhancement
9. Uterus
10. Ascites at Douglas cul-de-sac
11. Ascites at left paracolic gutter
12. Tortuous and dilated periuterine veins
13. Left internal iliac vessels
14. Rectum

1.3.35 Case 35

A 57-year-old woman with abdominal distention and elevated tumor markers (CA125: 5138 and HE4: 212). Abdominal ultrasound revealed a complex pelvic mass and ascites, so an ovarian cancer was suspected and ^{18}F-FDG PET/CT was suggested. Images showed diffuse increased activity at the irregular pelvic mass with heterogeneous enhancement involving both adnexal regions, as well as in ascites and sub-hepatic peritoneal seeding. The final diagnosis was bilateral ovarian cancer, high-grade serous carcinoma. Additionally, hypermetabolic mediastinal and left internal mammary lymph nodes were found, corresponding to uncommon metastases (Fig. 70) [53].

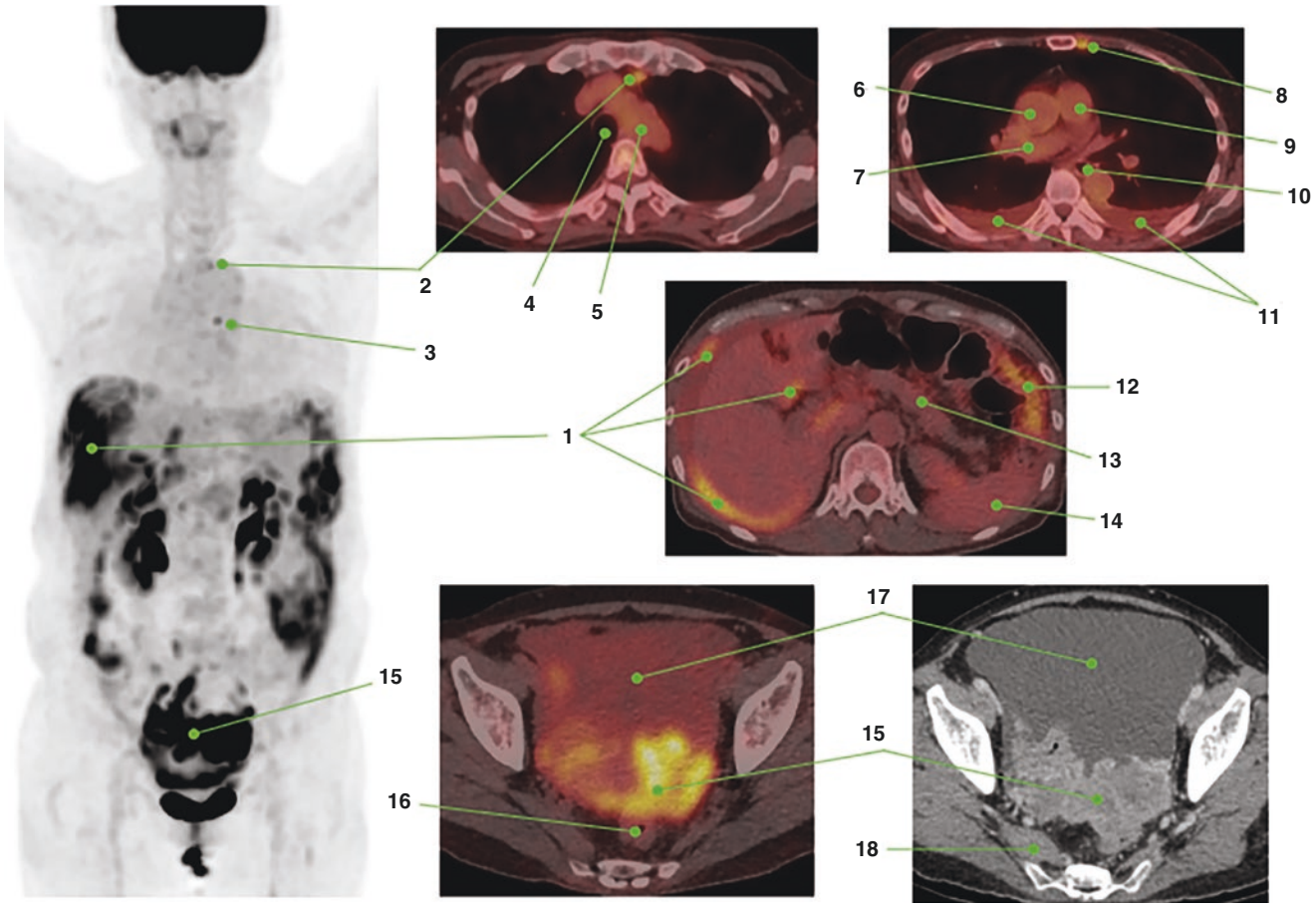

Fig. 70 1. Perihepatic peritoneal seeding
2. Prevascular lymph node metastasis
3. Lower pretracheal lymph node metastasis
4. Trachea
5. Aortic arch
6. Ascending aorta
7. Right pulmonary artery
8. Left internal mammary lymph node metastasis
9. Main pulmonary artery
10. Esophagus
11. Bilateral pleural effusion
12. Physiologic activity at the proximal descending colon
13. Pancreas
14. Spleen
15. Metabolically active irregular pelvic mass with heterogeneous enhancement
16. Rectum
17. Ascites
18. Right piriformis muscle

1.3.36 Case 36

A 51-year-old woman with pelvic pain and vaginal discharge. Gynecological ultrasound showed an elongated complex solid-cystic lesion in the left adnexal region, suspicious of hydrosalpinx. However, tumor markers were elevated (CA125: 2130 and HE4: 162), so ^{18}F-FDG PET/CT and contrast-enhanced CT were performed. Images showed marked increased activity in the left adnexal region at an irregular elongated lesion with heterogeneous enhancement, as well as small amounts of fluid within the endometrial cavity and the cul-de-sac. With these findings, malignancy was suspected, so the lesion was resected, and the pathology revealed a primary salpingeal carcinoma with ovarian involvement. These are extremely infrequent tumors originated in the fallopian tubes which account for less than 1.1% of gynecologic tumors (Fig. 71) [54].

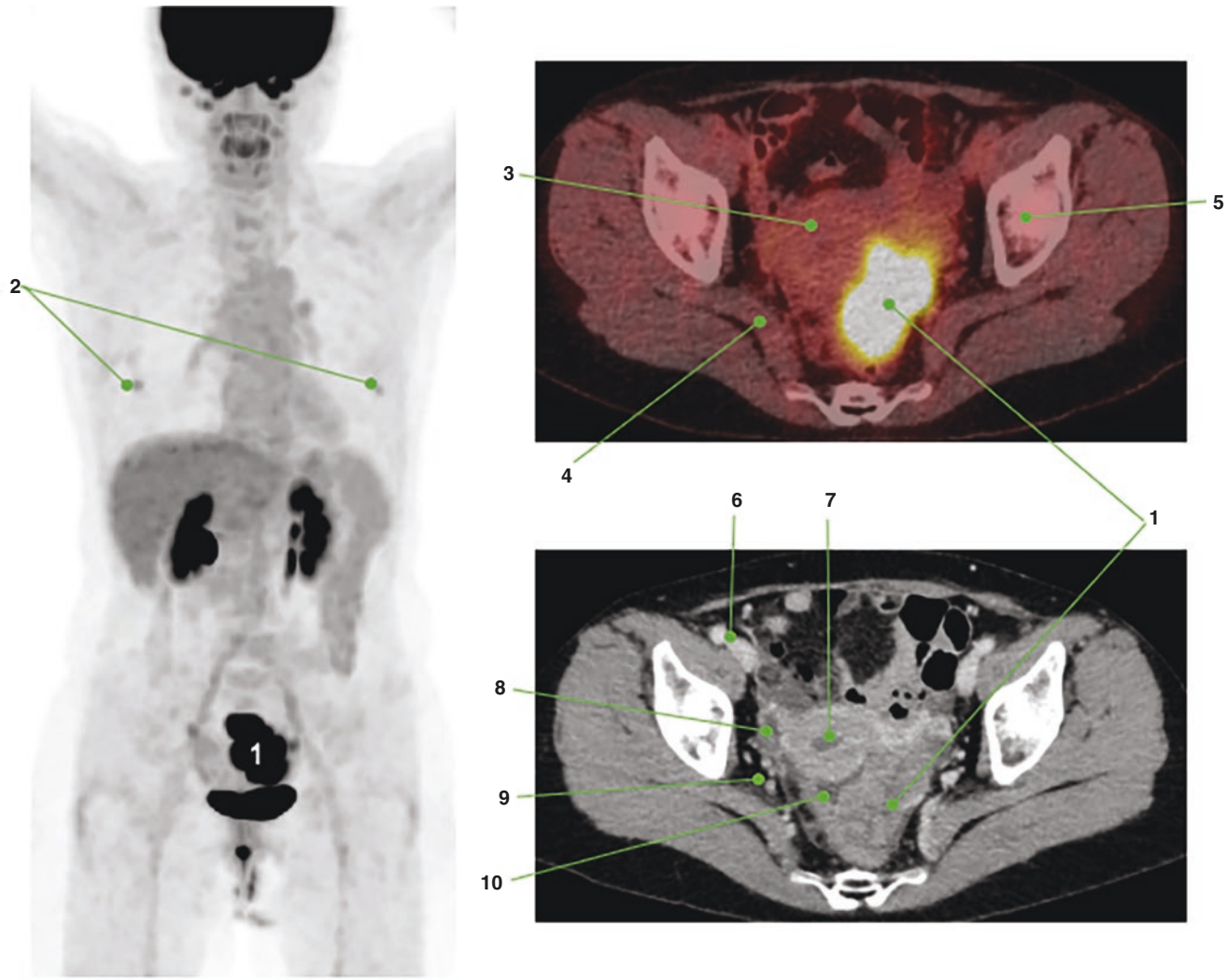

Fig. 71 1. Markedly increased activity in complex left adnexal mass; salpingeal carcinoma
2. Nipples
3. Uterus
4. Right piriformis muscle
5. Left acetabular roof
6. Right external iliac vessels
7. Small amount of fluid within the endometrial cavity
8. Right ovary
9. Right internal iliac vessels
10. Small amount of fluid at the cul-de–sac

1.3.37 Case 37

A 69-year-old man with progressive testicular pain and swelling. Ultrasound demonstrated bilateral diffuse enlargement of the testes with ill-defined hypoechoic signal, so lymphoma was suspected. ^{18}F-FDG PET/CT was performed for staging, finding focal increased activity in both testes and in multiple mediastinal and retroperitoneal enlarged lymph nodes, as well as in diffuse peritoneal involvement. Subsequent biopsy confirmed the diagnosis of diffuse, large B-cell lymphoma (Fig. 72) [4].

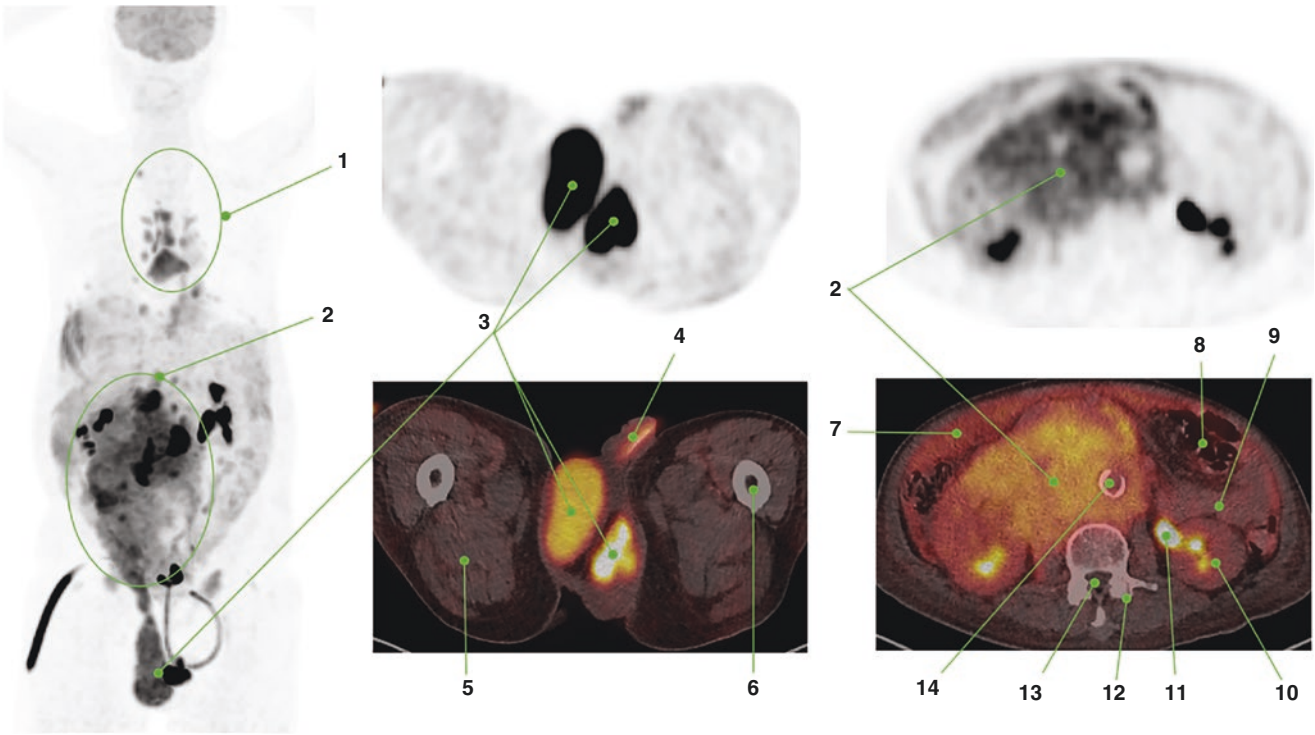

Fig. 72 1. Metabolically active mediastinal lymph nodes; lymphoma involvement
2. Metabolically active retroperitoneal lymph nodes; lymphoma involvement
3. Metabolically active testicular lymphoma involvement
4. Urinary catheter
5. Right hamstring muscles (biceps femoris, semimembranosus, semitendinosus)
6. Left femoral shaft
7. Metabolically active peritoneal thickening; lymphoma involvement
8. Transverse colon
9. Small bowel loops
10. Left kidney
11. Left renal pelvis
12. Left facet joint
13. Spinal canal
14. Abdominal aorta with atherosclerosis

1.4 Musculoskeletal System

1.4.1 Case 1

A 71-year-old male patient, ex-smoker, with diagnosis of a right solitary pulmonary nodule. ^{18}F-FDG PET/CT was performed, finding focal increased activity in the nodule (later confirmed adenocarcinoma) and a single metastatic mediastinal lymph node. As an incidental finding, diffuse, increased uptake was observed in a fusiform soft tissue structure at the left scapular region, which represents physiological uptake in the Teres minor muscle, associated with probable muscle stress due to FDG injection (Fig. 73) [55].

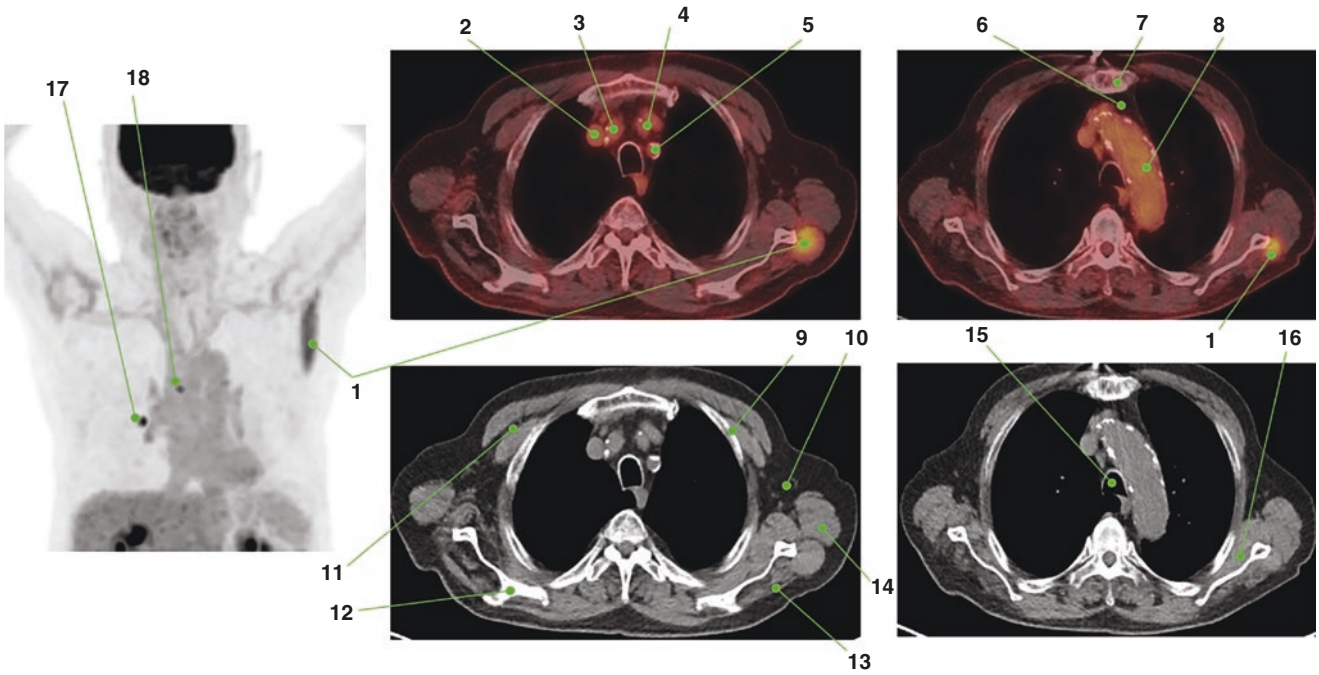

Fig. 73 1. Increased activity at the left Teres minor muscle: physiologic uptake related to IV FDG injection
2. Right brachiocephalic vein
3. Right brachiocephalic artery
4. Left common carotid artery
5. Left subclavian artery
6. Prevascular fat
7. Sternum
8. Aortic arch
9. Left rib anterior arch
10. Left axillary fossa
11. Right pectoralis muscles
12. Right scapula
13. Left infraspinatus muscle
14. Left latissimus dorsi muscle
15. Trachea
16. Left subscapularis muscle
17. Metabolically active primary lung adenocarcinoma
18. Hypermetabolic metastatic mediastinal lymph node

1.4.2 Case 2

A 54-year-old man with small erythematous nodular lesion on the right anterior chest wall. Biopsy was performed and the final diagnosis was a non-upper aerodigestive tract (NUAT) extranodal natural killer T-cell lymphoma (NTCL), so ^{18}F-FDG PET/CT was performed for staging. Images showed focal increased activity at nodular lesions in the right anterior chest wall, the left elbow, and the right vastus medialis muscle. No other cutaneous lesions or enlarged lymph nodes and splenic or bone marrow involvement were identified. This type of lymphoma is frequent in Asia and with its counterpart – UAT (upper aerodigestive tract) lymphoma which can be nasal or extranasal – it represents 10.5% of all non-Hodgkin lymphomas (Fig. 74) [56].

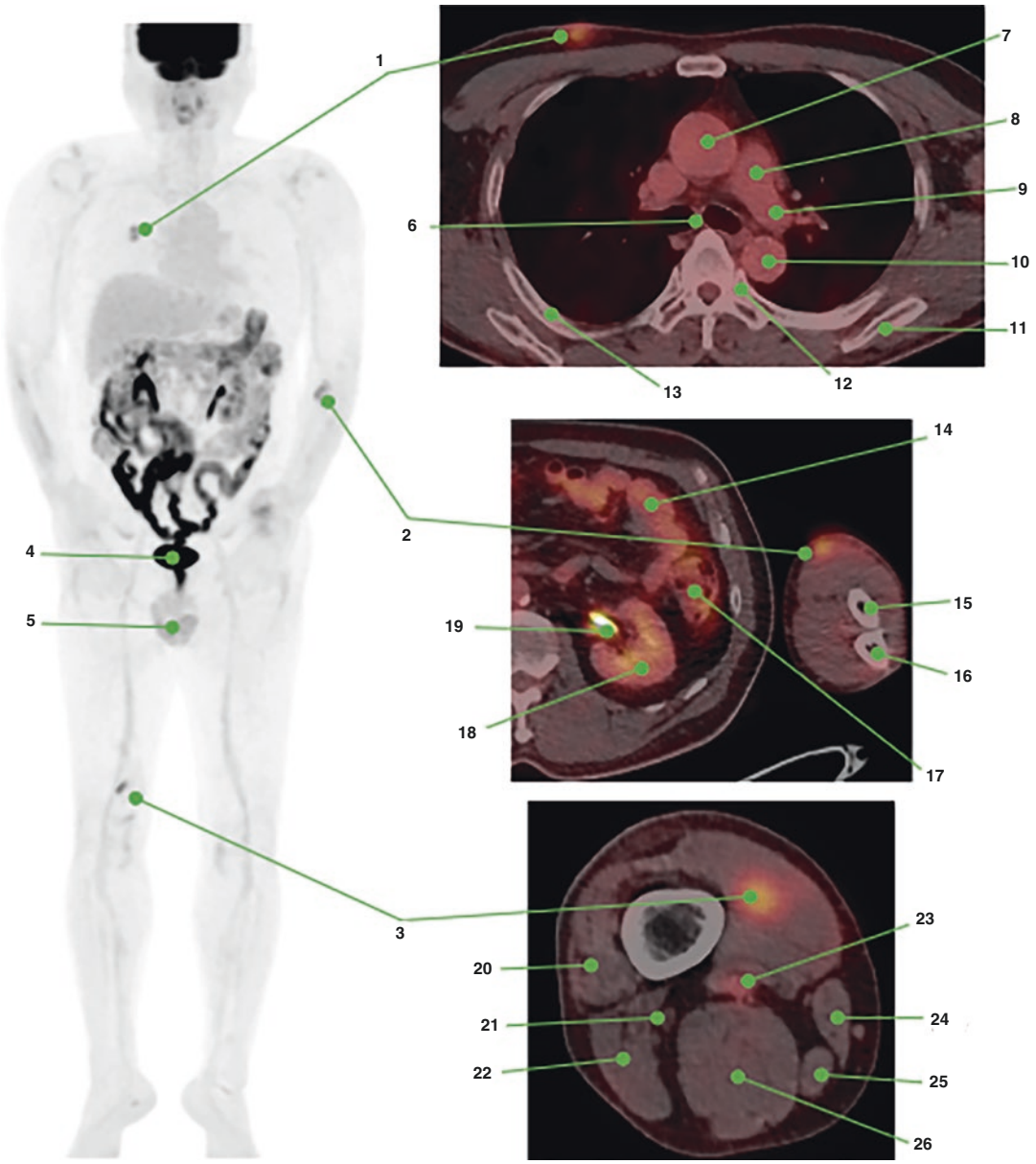

Fig. 74 1. NUAT-NTCL involvement at the right anterior chest wall
2. NUAT-NTCL involvement at the left elbow
3. NUAT-NTCL involvement at the right vastus medialis muscle
4. Bladder
5. Testes
6. Carina
7. Ascending aorta
8. Main pulmonary artery
9. Left pulmonary artery
10. Descending aorta
11. Left scapula
12. Left costovertebral junction
13. Right rib posterior arc
14. Small bowel loops
15. Proximal radial shaft
16. Proximal ulnar shaft
17. Descending colon
18. Left kidney
19. Left renal pelvis
20. Right vastus lateralis muscle
21. Normal popliteal lymph node
22. Right biceps femoris, short head
23. Right semimembranosus muscle
24. Right gracilis muscle
25. Right sartorius muscle
26. Femoral artery

1.4.3 Case 3

A 59-year-old man with a right mid-back painful and growing mass. X-ray was performed finding a right rib expansive sclerotic lesion, so ^{18}F-FDG PET/CT was performed suspecting malignancy. Images showed a metabolically active expansive lesion at the right fifth rib posterior arc, with wide transition zone, chondroid matrix, and soft tissue involvement. Posterior biopsy confirmed a primary chondrosarcoma (Fig. 75).

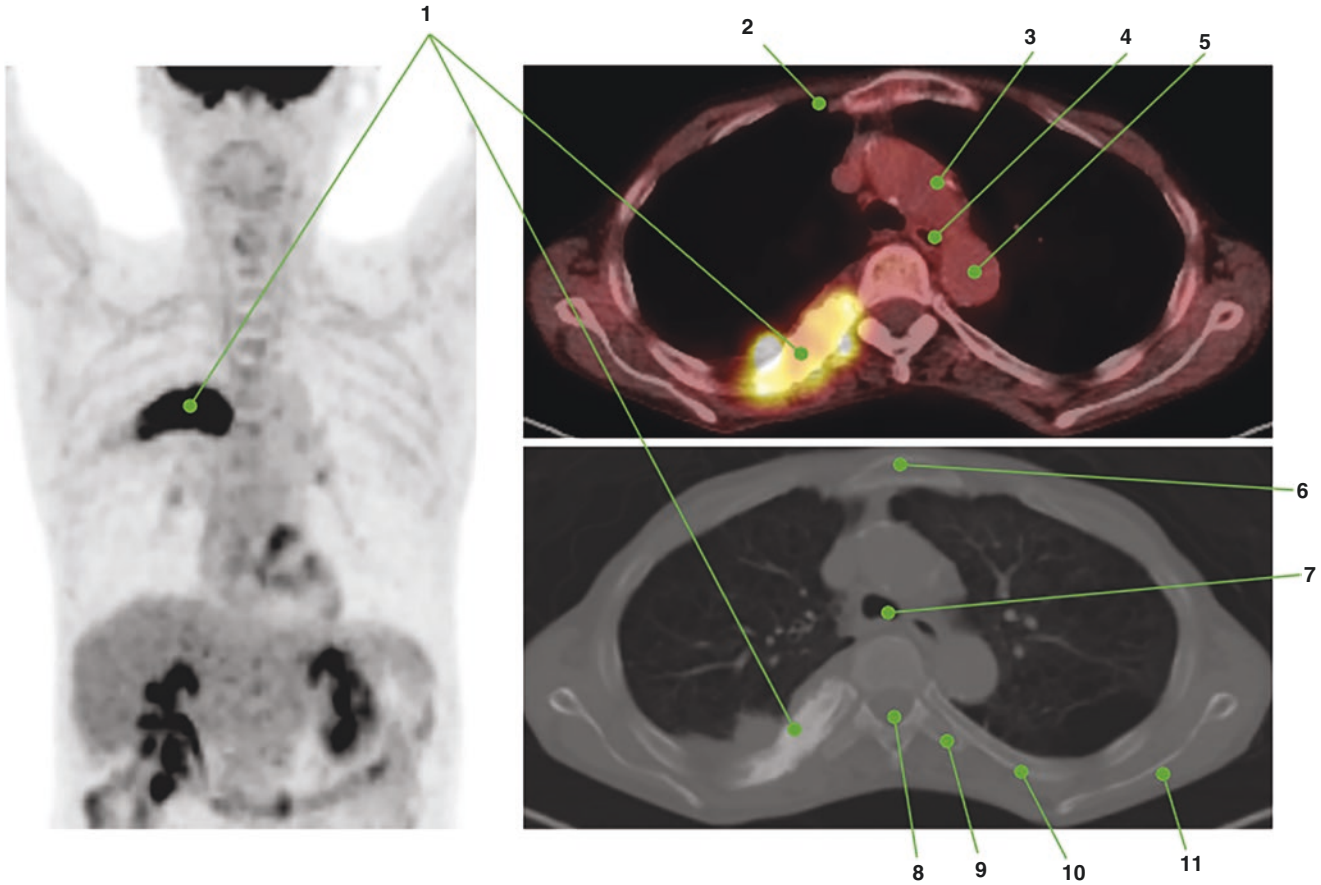

Fig. 75 1. Metabolically active chondrosarcoma at the right fifth rib posterior arc
2. Right internal mammary vessels
3. Aortic arch
4. Esophagus
5. Descending aorta
6. Sternum manubrium
7. Trachea
8. Spinal canal
9. Left transverse process of T5
10. Normal left fifth rib, posterior arc
11. Left scapula

1.4.4 Case 4

A 24-year-old female patient with diagnosis of non-Hodgkin lymphoma with cervical nodal involvement, undergoing end-of-therapy control. She reported mild back pain as the only symptom. ^{18}F-FDG PET/CT was performed, finding complete resolution of previously identified hypermetabolic lymph nodes. However, as a new finding, symmetric FDG uptake was observed in the thoracic and lumbar spinal roots, as well as accumulation of the tracer in the thecal sac. The findings corresponded to neurolymphomatosis, a rare manifestation of non-Hodgkin lymphoma due to nerve infiltration by neurotrophic neoplastic cells (Fig. 76) [57].

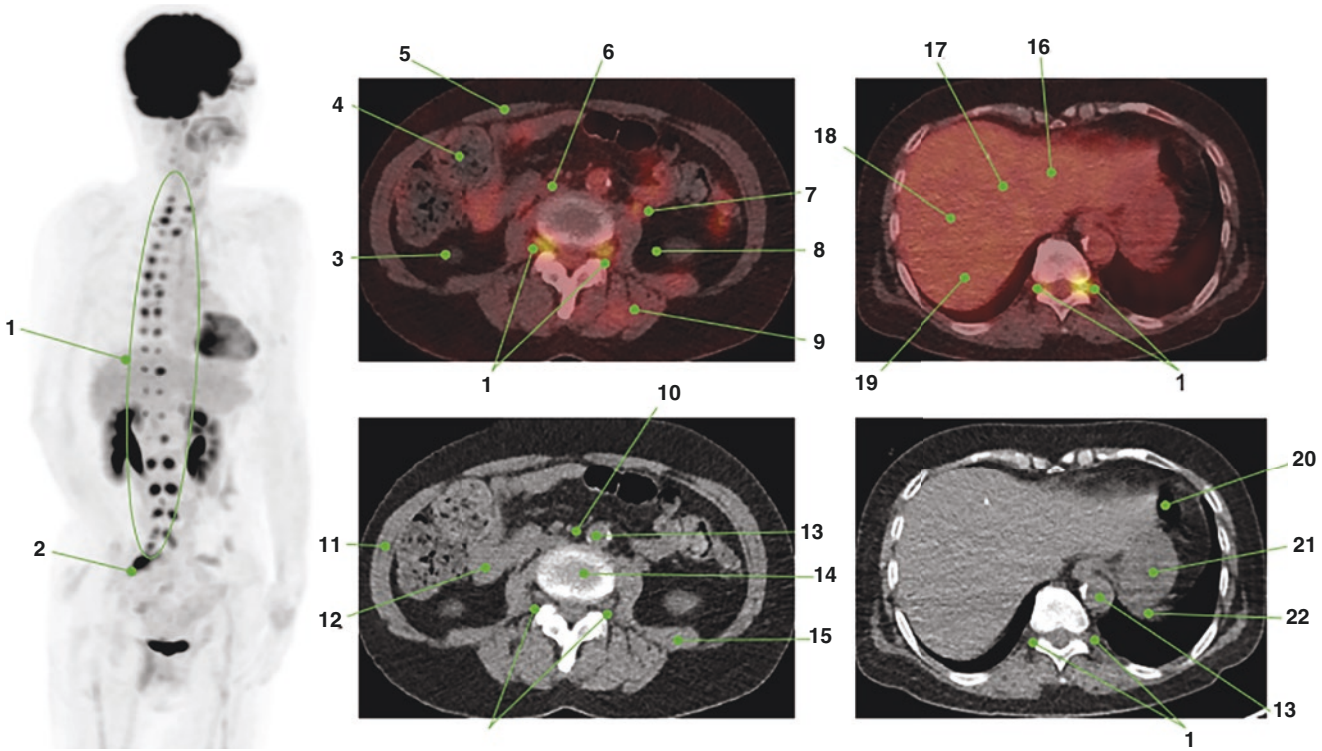

Fig. 76 1. Focal FDG uptake in the bilateral thoracic and lumbar spinal roots
2. FDG uptake in the thecal sac dependent portion
3. Right kidney, inferior pole
4. Ascending colon
5. Right abdominal rectus muscle
6. Inferior vena cava
7. Left ureter
8. Left perirenal fat
9. Left erector spinae muscles
10. Aortocaval space
11. Right lateral abdominal wall muscles (inner to outer: transverse, internal oblique, external oblique)
12. Small bowel loops
13. Abdominal aorta
14. Lumbar intervertebral disc
15. Left quadratus lumborum muscle
16. Liver segment 2
17. Liver segment 4
18. Liver segment 7
19. Liver segment 8
20. Gastric body
21. Gastric fundus
22. Diaphragm

1.4.5 Case 5

A 17-year-old man with acute right shoulder pain after trauma lifting weights in the gym. X-ray and MRI were performed, finding a pathological fracture of the right clavicle, so ^{18}F-FDG PET/CT was done. Images showed increased activity at the middle third of the right clavicle in the site of the fracture, with a subjacent osteolytic lesion; no other hypermetabolic lesions were noted. Posterior biopsy confirmed the diagnosis of a primary osteosarcoma (Fig. 77) [58].

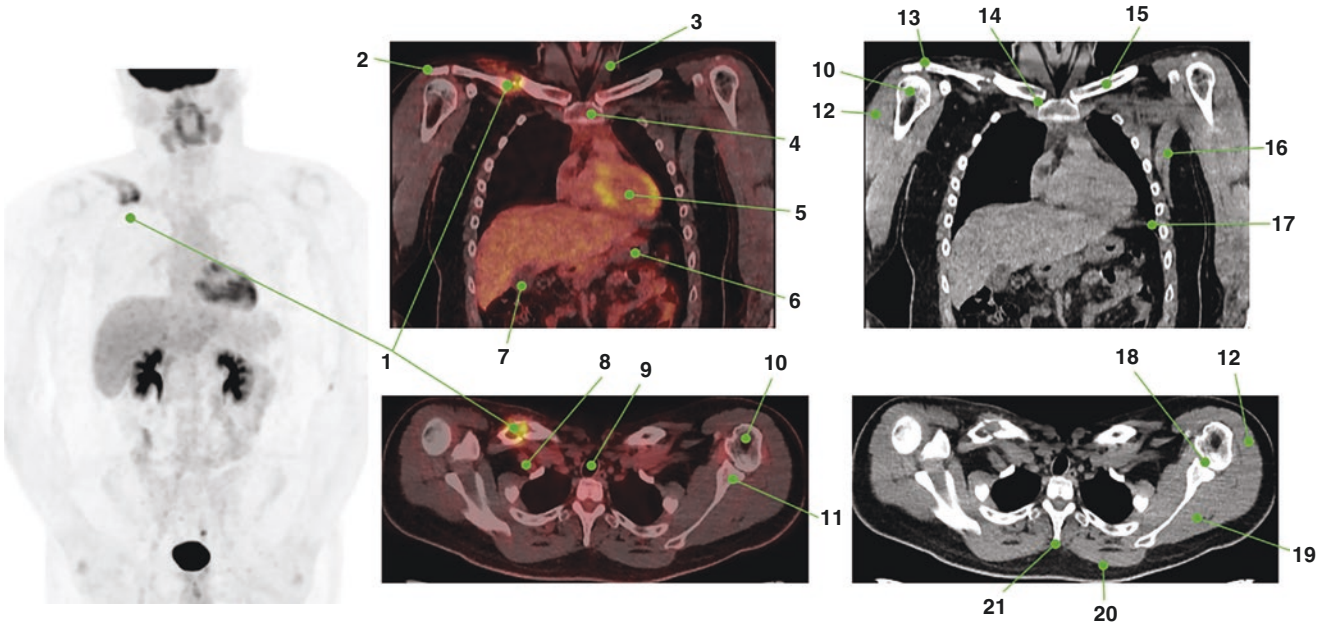

Fig. 77 1. Metabolically active osteolytic lesion with pathologic fracture at the right clavicle
2. Acromion
3. Left sternocleidomastoid muscle
4. Sternum manubrium
5. Left ventricle
6. Stomach
7. Gallbladder
8. Right subclavian vein
9. Trachea
10. Left humeral head
11. Left glenoid
12. Right deltoid muscles
13. Right acromioclavicular joint
14. Right sternoclavicular joint
15. Left clavicle
16. Left serratus muscle
17. Diaphragm
18. Left glenohumeral joint
19. Left supraspinatus muscle
20. Left trapezius muscle
21. Thoracic vertebra spinous process

1.4.6 Case 6

A 37-year-old woman with a history of right breast cancer, treated with neoadjuvant chemotherapy and subsequent surgery. She attended an early checkup due to back pain, and an initial bone scan suggested new vertebral metastases. ^{18}F-FDG PET/CT was performed finding, in addition to vertebral metastases, other small hypermetabolic lesions in both pelvic bones and the right proximal femur, which were not evident in bone scan (Fig. 78).

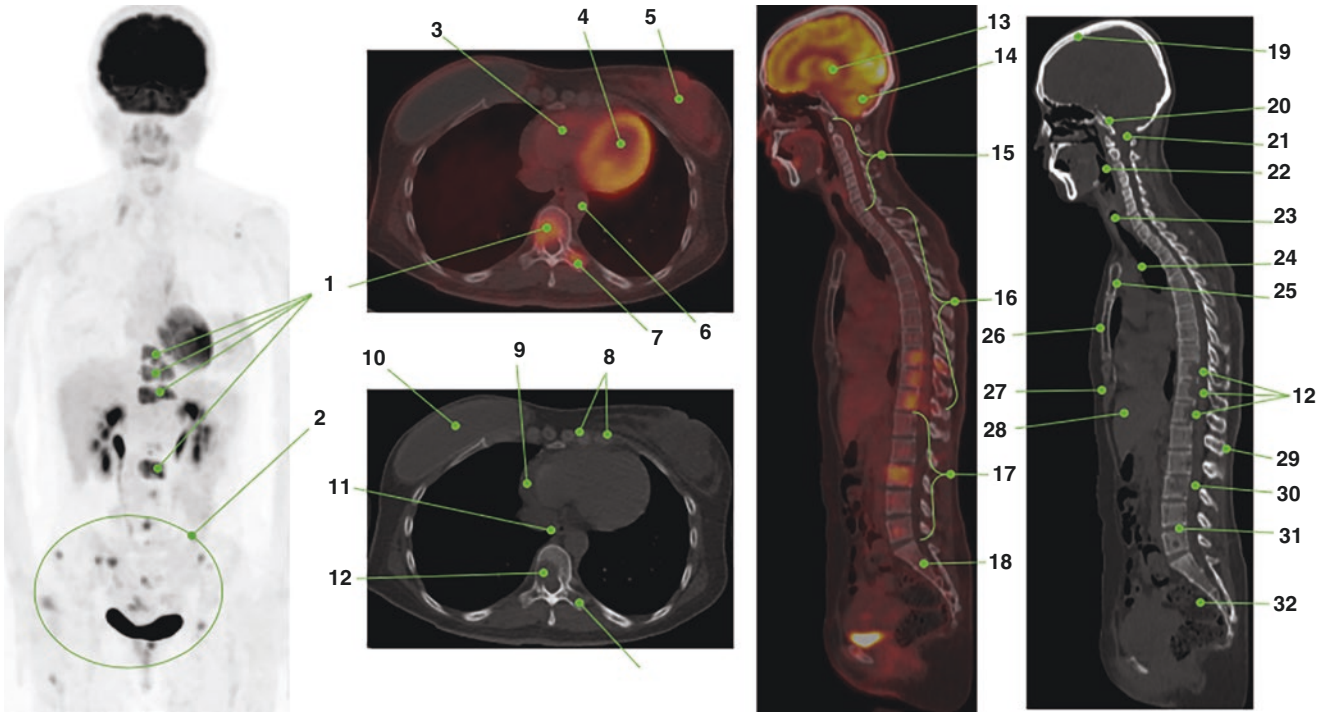

Fig. 78 1. Metabolically active thoracic and lumbar vertebral bodies metastases
2. Multiple hypermetabolic metastases in both pelvic bones and right femur
3. Right ventricle
4. Left ventricle with myocardial homogeneous FDG uptake
5. Left breast tissue, normal appearance
6. Descending aorta
7. Hypermetabolic metastasis, left thoracic vertebral pedicle
8. Costochondral junctions
9. Small amount of pericardial effusion
10. Right breast implant
11. Esophagus
12. Lytic vertebral body metastasis
13. Thalamus
14. Cerebellum
15. Cervical vertebral bodies
16. Thoracic vertebral bodies
17. Lumbar vertebral bodies
18. Sacrum
19. Skull
20. Clivus
21. Foramen magnum
22. Oropharynx
23. Pharynx
24. Trachea
25. Sternum manubrium
26. Sternum body
27. Xiphoid process
28. Liver
29. Lumbar vertebra spinous process
30. Thecal sac
31. Lumbar intervertebral space
32. Rectum

1.4.7 Case 7

A 61-year-old man with a history of meningeal hemangiopericytoma resection 6 years ago. He attended an early checkup due to lower back and hip pain, so ^{18}F-FDG PET/CT was performed. Images showed multiple metabolically active lytic bone lesions with soft tissue mass component at the skull base, ribs, thoracic and lumbar vertebral bodies, and both pelvic bones, as well as mediastinal and retroperitoneal lymph nodes. Focal lesions in the liver, the soft tissues of the right scapular region, and the right gluteal region were also noted. Biopsy, performed at the left iliac bone lesion, confirmed the diagnosis of metastatic anaplastic hemangiopericytoma. This is a rare mesenchymal tumor that can affect bone structures and soft tissues anywhere in the body. Currently, it is known to share genetic and histological characteristics with solitary fibrous tumors, so this aggressive and disseminated behavior is expected (Fig. 79) [59].

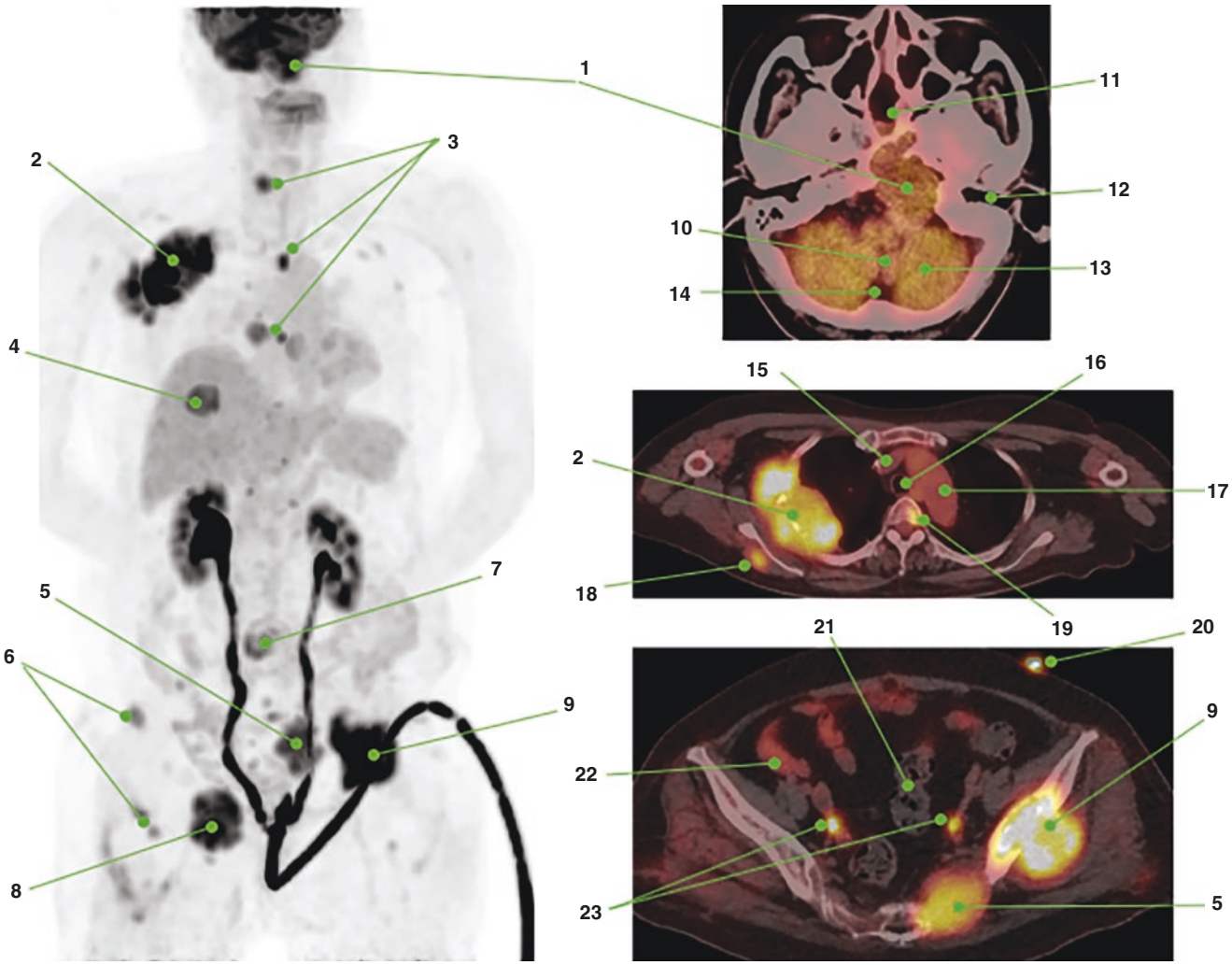

Fig. 79 1. Skull base metastasis involving the left clivus
2. Right rib metastasis
3. Metastatic lower neck and mediastinal lymph nodes
4. Right hepatic lobe metastasis
5. Left sacroiliac metastasis
6. Soft tissue metastasis in the right gluteal region
7. Retroperitoneal lymph node metastasis
8. Right ischium metastasis
9. Left iliac bone metastasis
10. Cerebellar vermis
11. Right sphenoid sinus with secretions
12. Left external auditory canal
13. Left cerebellar hemisphere
14. Cisterna magna
15. Brachiocephalic vein
16. Trachea
17. Aortic arch
18. Soft tissue metastasis at right scapular area
19. Thoracic vertebral body metastasis
20. Activity at the urinary catheter
21. Sigmoid colon
22. Small bowel loops
23. Normal activity at both ureters

1.4.8 Case 8

A 64-year-old woman with a recent diagnosis of multiple myeloma, with few lytic lesions evident in conventional radiology studies but marked generalized bone pain. ^{18}F-FDG PET/CT was performed to assess the distribution and activity of the disease. Images showed innumerable hypermetabolic lesions involving the whole axial and proximal appendicular skeleton, most of them lytic, but others expansive with soft tissue components in the ribs and vertebral bodies. With these findings, it was possible to determine that it was an active and disseminated form of myeloma, and treatment was started (Fig. 80) [6, 60].

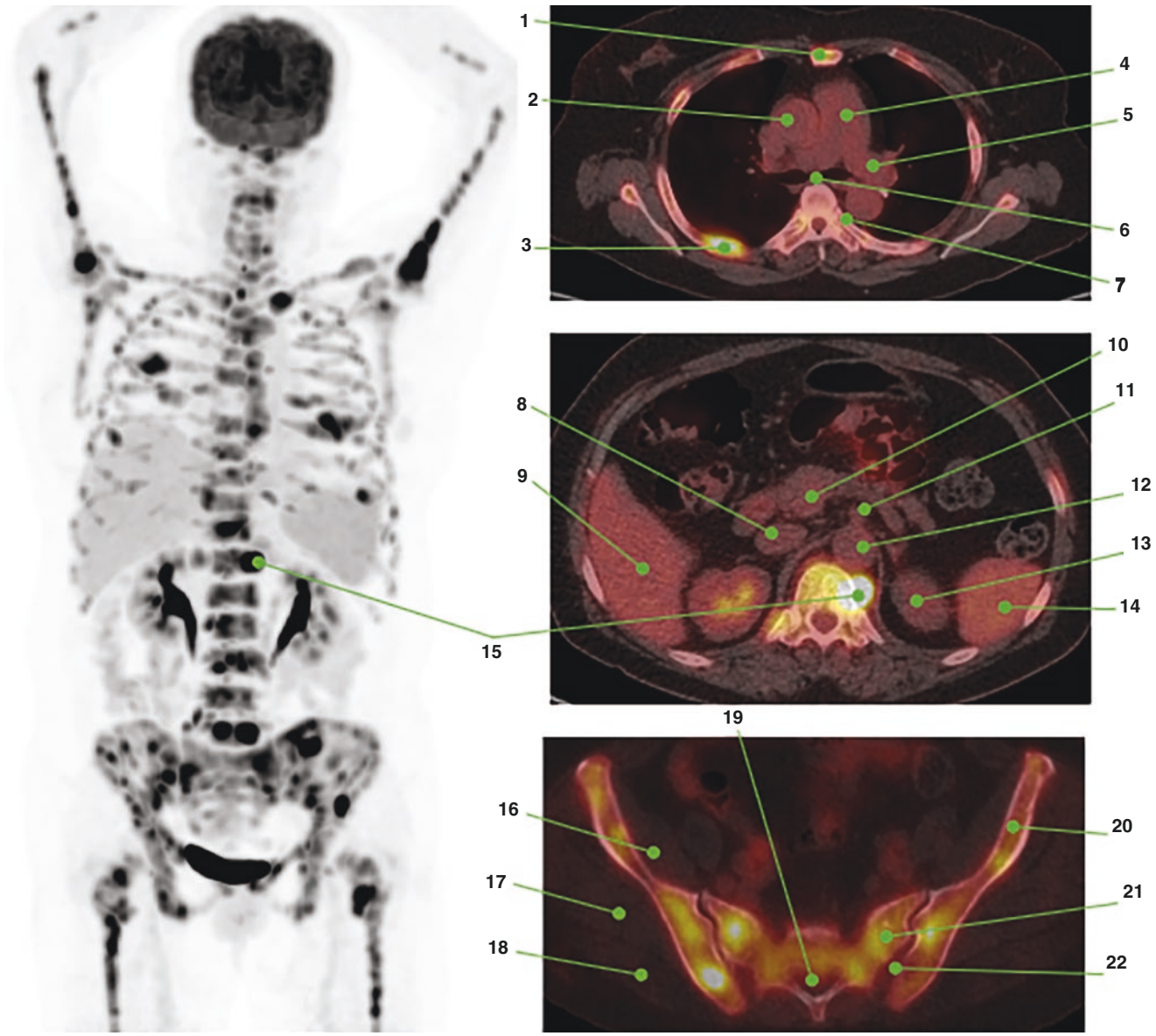

Fig. 80 1. Sternum
2. Ascending aorta
3. Metabolically active expansive lesion in right rib
4. Main pulmonary artery
5. Left pulmonary artery
6. Carina
7. Left costovertebral junction
8. Inferior vena cava
9. Liver, segment 6 (VI)
10. Inferior mesenteric vein
11. Inferior mesenteric artery
12. Abdominal aorta
13. Left kidney inferior pole
14. Spleen
15. Metabolically active expansile lesion with soft tissue mass component at T12
16. Right iliacus muscle
17. Right gluteus medius muscle
18. Right gluteus maximus muscle
19. Sacral canal
20. Left iliac bone
21. Left ala of sacrum
22. Left sacroiliac joint

1.4.9 Case 9

A 42-year-old man with lower back pain and a lytic lesion on conventional radiography. ^{18}F-FDG PET/CT was performed for evaluation and images showed a prominent mass in the right hemiabdomen with a hypermetabolic peripheral solid component and central necrosis. The mass was clearly arising from the neural foramen and had a small component in the medullary canal, displacing the spinal cord ("dumbbell sign"). With these findings, a peripheral nerve sheath tumor was suspected and considering its large size, the associated bone destruction, and the necrotic component, malignancy was suggested. Subsequent biopsy of the lesion confirmed the diagnosis of a malignant peripheral nerve sheath tumor (Fig. 81) [61].

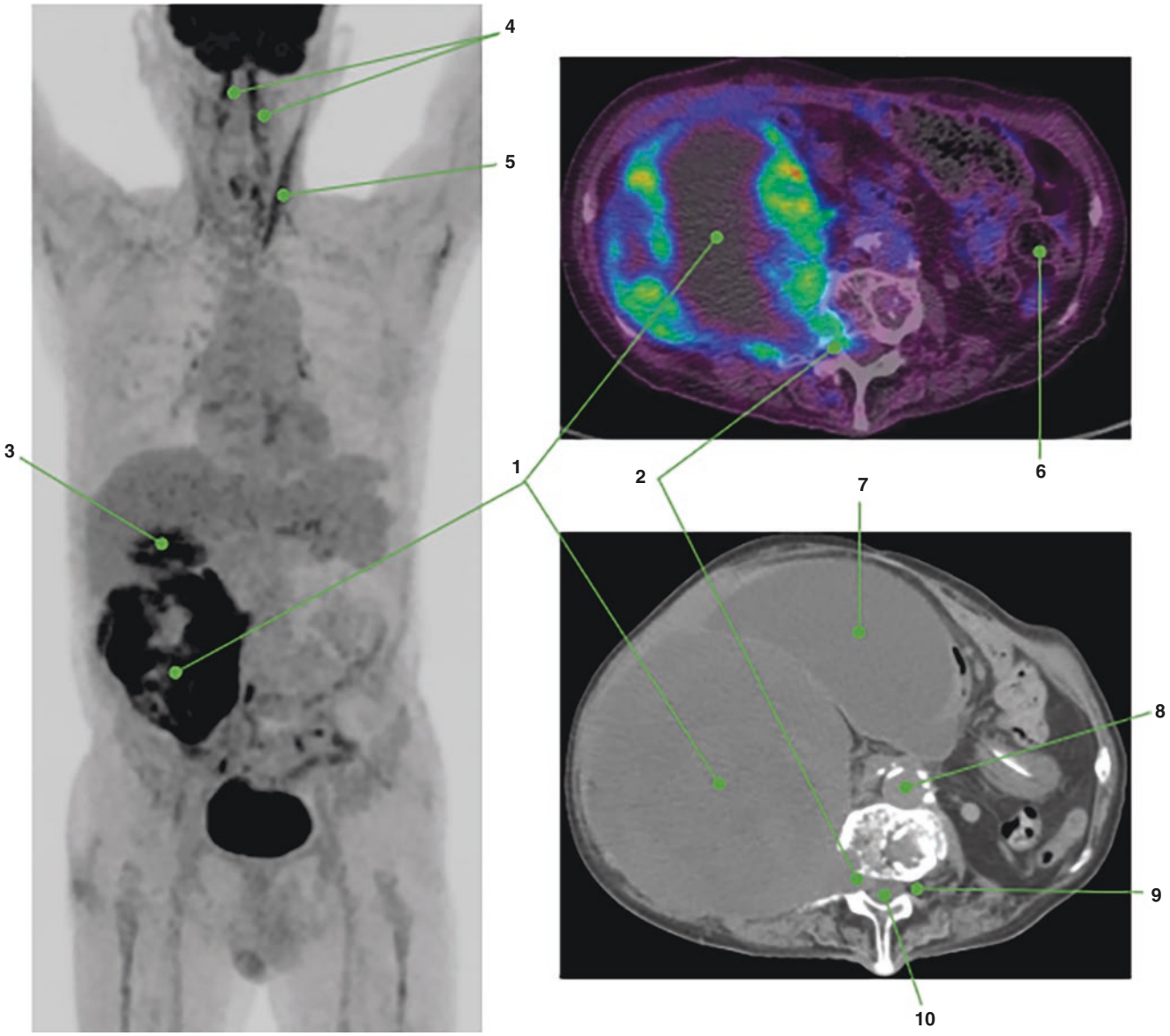

Fig. 81 1. Malignant peripheral nerve sheath tumor, heterogeneous retroperitoneal mass component
2. Malignant peripheral nerve sheath tumor, medullary component with enlarged neural foramen ("dumbbell sign")
3. Right kidney superiorly displaced
4. Diffuse uptake in longus colli muscles
5. Diffuse uptake in the left sternocleidomastoid muscle
6. Descending colon
7. Distended stomach
8. Abdominal aorta with atherosclerotic calcifications
9. Left neural foramen
10. Spinal cord

1.4.10 Case 10

A 25-year-old man with a history of brachial plexus peripheral nerve sheath tumor, treated with wide excision and nerve graft 2 years ago. He attended an early checkup because of left hip pain, and X-ray showed a pathological fracture of the iliac bone, so ^{18}F-FDG PET/CT was performed. Images showed intense increased activity at a soft tissue mass surrounding the left iliac wing with a pathological fracture. Another smaller lesion but with the same characteristics was found in the soft tissues of the left ninth intercostal space. Posterior biopsies confirmed the diagnosis of malignant peripheral nerve sheath tumor in both locations (Figs. 82 and 83).

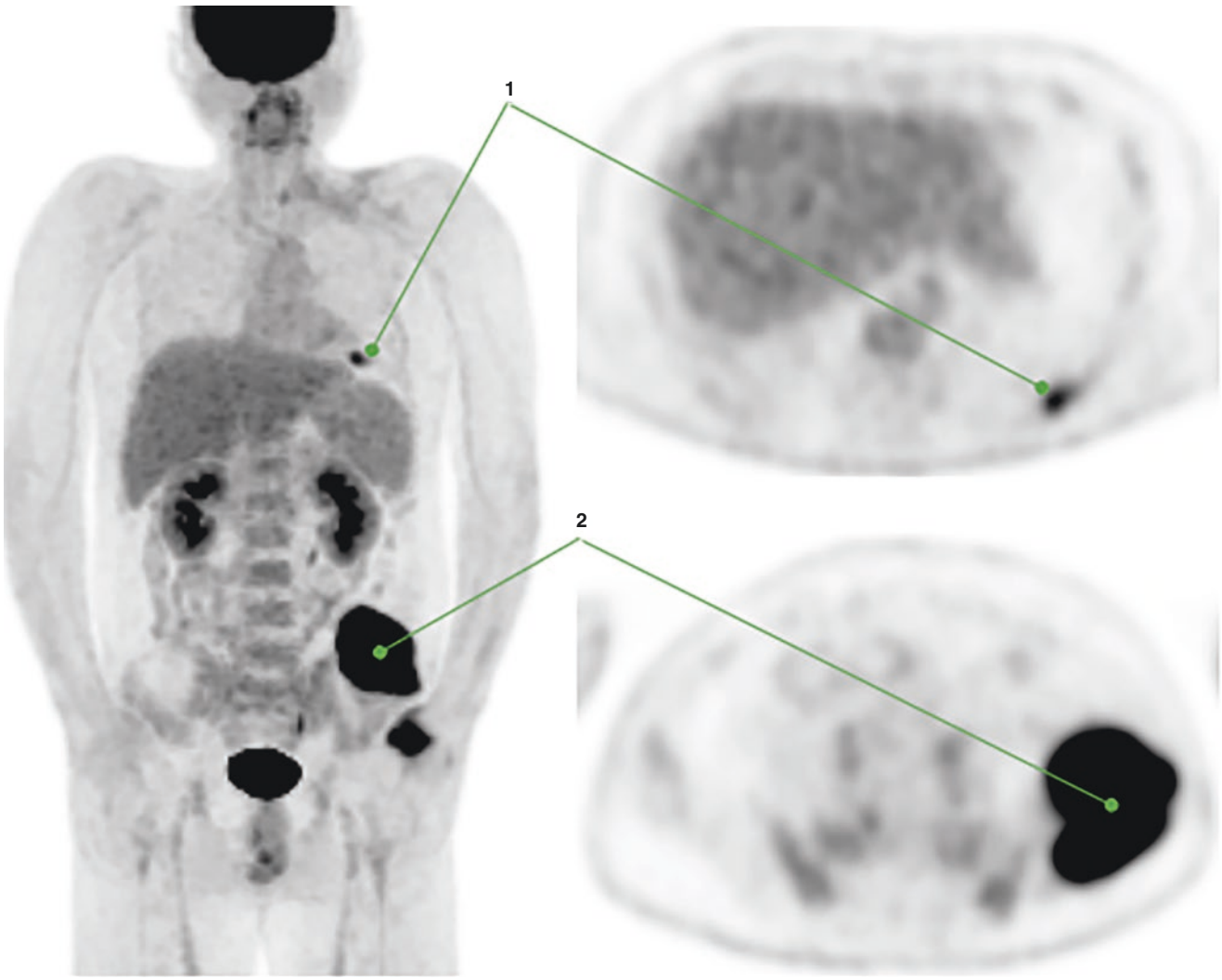

Figs. 82 and 83 1. Metabolically active tumor at the left ninth intercostal space
2. Metabolically active tumor at the left iliac wing with pathologic fracture
3. Sternum
4. Azygos vein
5. Distal esophagus
6. Right inferior rib, posterior arch
7. Descending aorta
8. Right common iliac vessels
9. Right psoas muscle
10. Right sacro-iliac joint
11. Root of the mesentery
12. Left iliac wing pathological fracture
13. Left paraspinal muscles

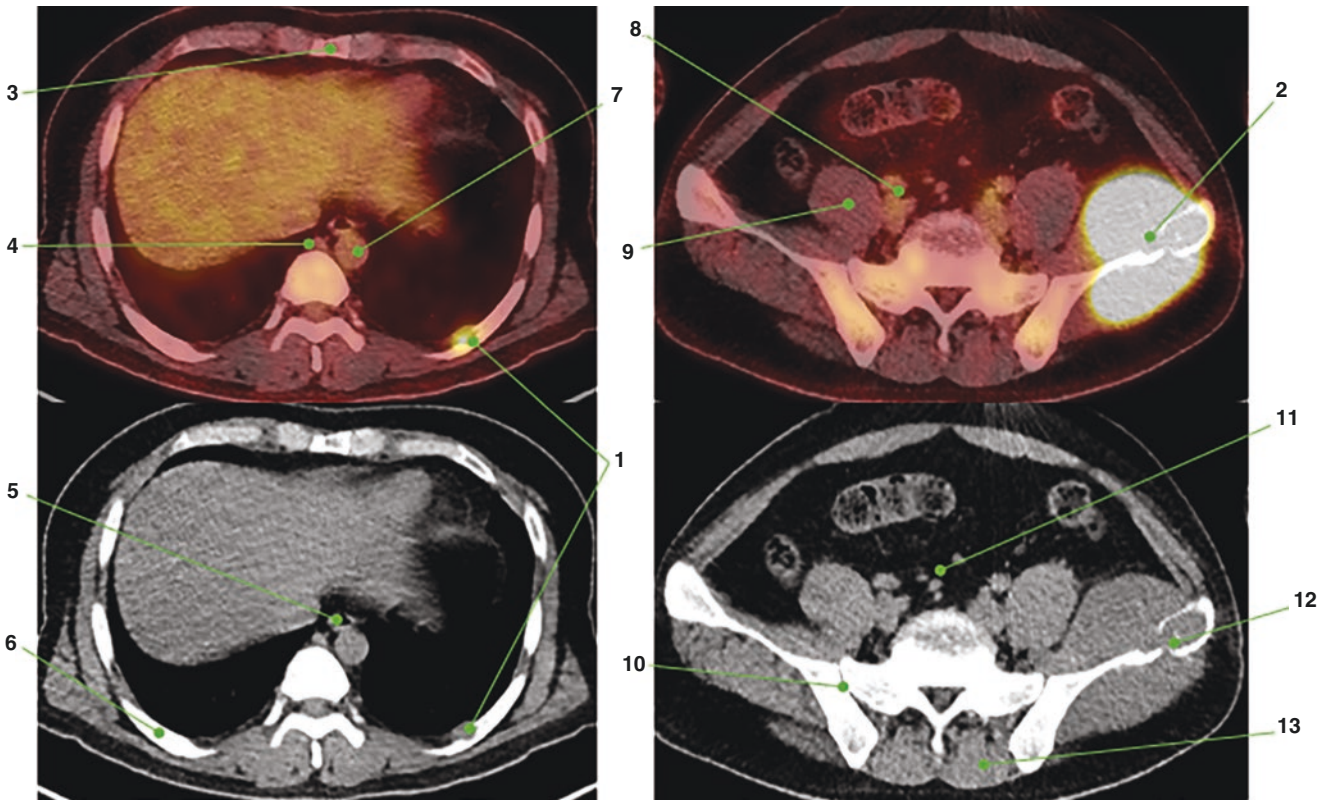

Figs. 82 and 83 (continued)

1.4.11 Case 11

A 43-year-old man complaining of left hip pain with decreased range of motion. Hip X-ray showed slightly diffuse disturbance of the trabecular pattern in the left iliac bone, so ^{18}F-FDG PET/CT was performed to rule out malignancy. Images showed minimal, diffuse, increased activity in the left iliac bone, where on CT, small osteolytic lucent areas were observed with some coarsened trabeculae. The findings correspond to early-phase changes of Paget's disease (Fig. 84).

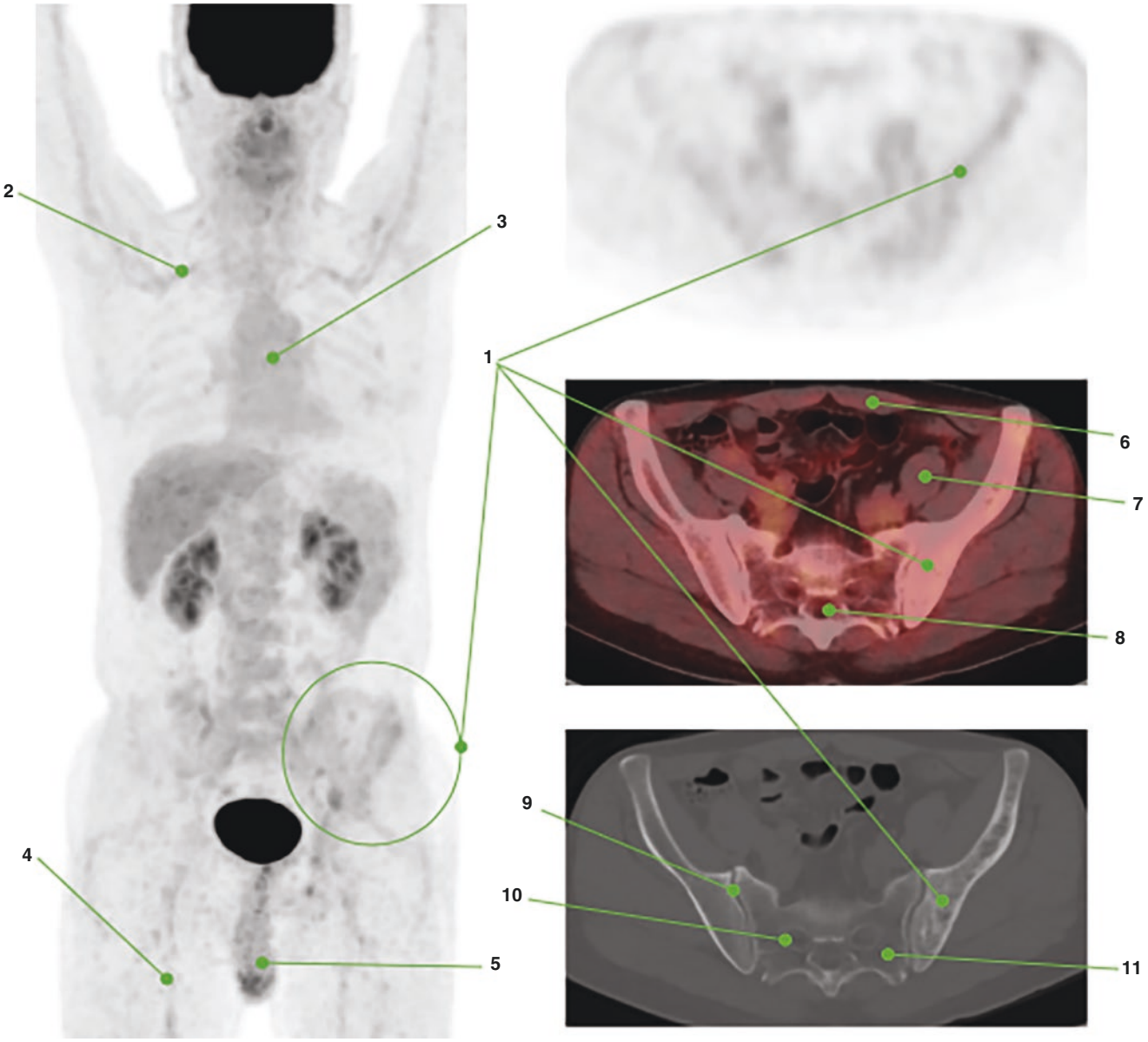

Fig. 84 1. Mild, diffuse, increased activity at the left iliac bone Paget's disease
2. Right subclavian vessels
3. Normal mediastinal diffuse uptake
4. Right femoral vessels
5. Scrotum
6. Left abdominal rectus
7. Left ilio-psoas muscle
8. Sacral canal
9. Right sacroiliac joint
10. Right sacral foramen
11. Sacrum

1.4.12 Case 12

A 75-year-old man with a rapidly growing painful mass in the right leg. ^{18}F-FDG PET/CT was performed, finding markedly increased activity at a rounded, well-defined soft tissue mass in the right thigh, involving the external obturator and adductor longus muscles. Biopsy confirmed the suspected diagnosis of an undifferentiated pleomorphic sarcoma (UPS) (Fig. 85) [62].

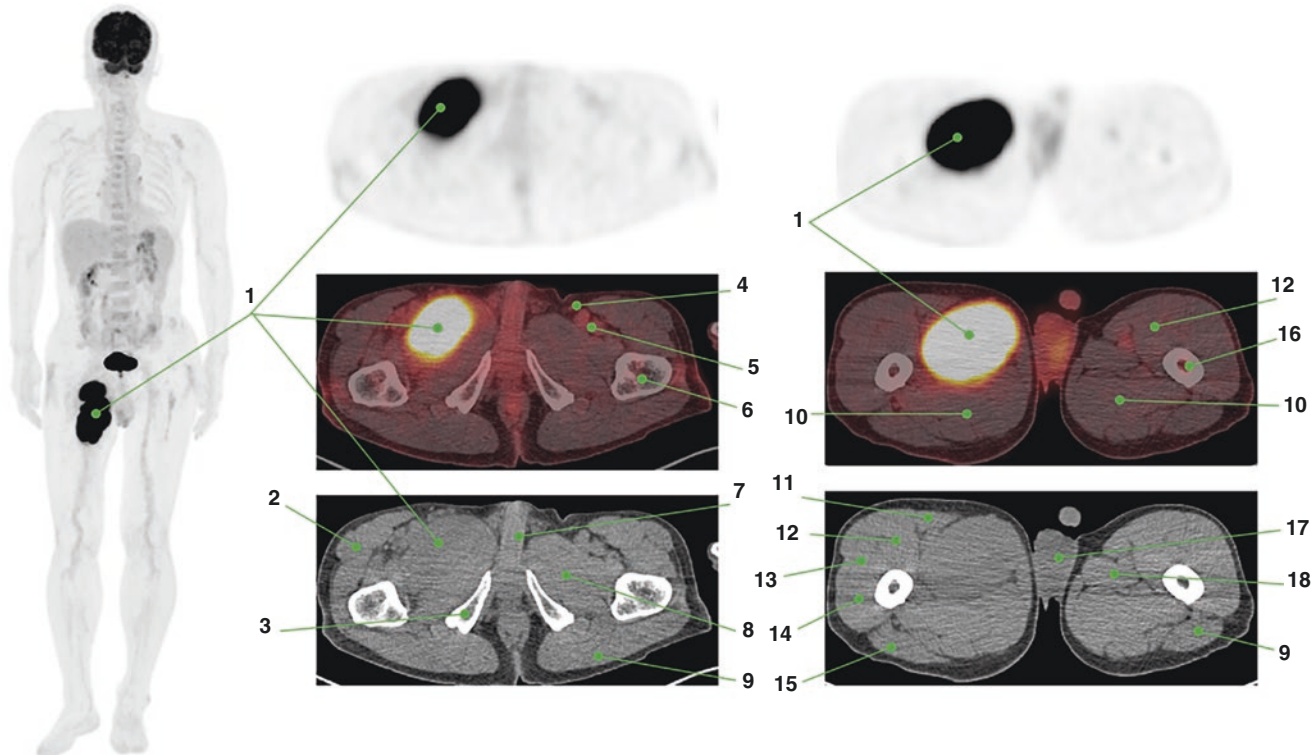

Fig. 85 1. Metabolically active tumor involving right external obturator and adductor longus muscles
2. Right tensor fascia latae muscle
3. Right ischial tuberosity
4. Normal left inguinal lymph node
5. Left common femoral vessels
6. Left femoral neck
7. Base of penis
8. Left external obturator muscle
9. Left gluteus maximus muscle
10. Adductor magnus muscles
11. Right Sartorius muscle
12. Vastus medialis muscles
13. Right vastus intermedius muscle
14. Right vastus lateralis muscle
15. Right gluteus maximus muscle
16. Left proximal femoral shaft
17. Scrotum
18. Right pectineus muscle

1.4.13 Case 13

A 27-year-old man with a non-painful growing mass in the left thigh. Ultrasound showed a solid soft tissue mass, so ^{18}F-FDG PET/CT was performed. Images showed diffuse and homogeneously increased activity at a well-defined, hypodense oval mass in the posterior aspect of the left thigh, with displacement of the adjacent muscles without infiltration. With these characteristics, the diagnosis of a myxoid liposarcoma was suspected, which is the second most frequent subtype of liposarcoma, and at this age, the extremities are the most frequent location. The diagnosis was confirmed later with biopsy (Fig. 86) [62].

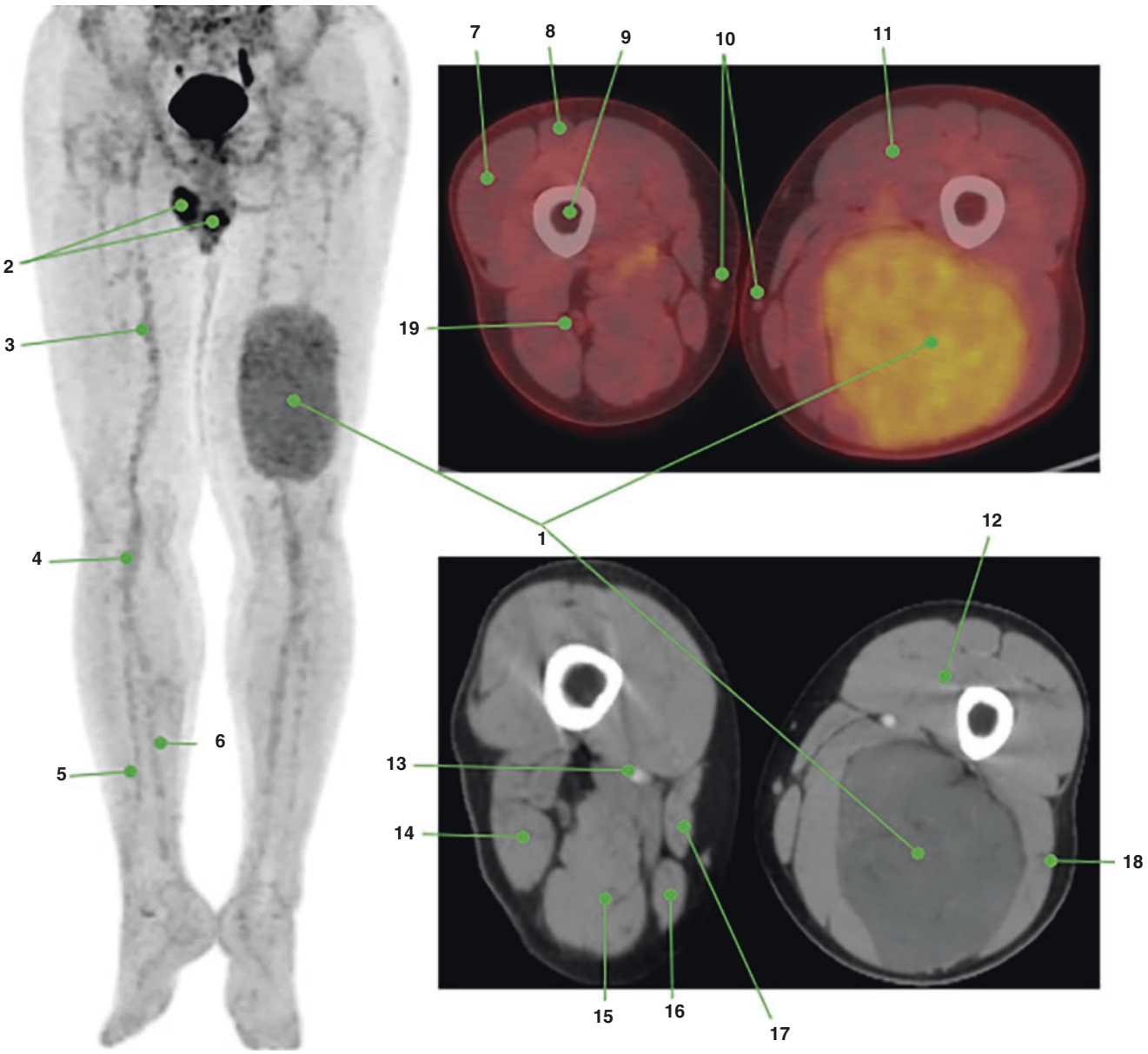

Fig. 86 1. Left posterior myxoid liposarcoma
2. Testes
3. Right femoral artery
4. Right popliteal artery
5. Right anterior tibial artery
6. Right posterior tibial artery
7. Right vastus lateralis muscle
8. Right rectus femoris muscle
9. Right femoral shaft
10. Greater saphenous vein
11. Left vastus medialis muscle
12. Left vastus intermedius muscle
13. Right femoral artery
14. Right biceps muscle, long head
15. Right semitendinosus muscle
16. Right semimembranosus muscle
17. Right gracilis muscle
18. Left biceps muscle, long head
19. Normal right popliteal Lymph node

1.4.14 Case 14

A 36-year-old man with a growing mass in the right gluteal region. Hip X-ray did not show any bone abnormality, but US revealed a heterogeneous and infiltrating mass, so ^{18}F-FDG PET/CT and MRI were performed. Images showed mild, diffuse, increased activity in an oval, well-defined mass at the right gluteal region, involving the gluteus maximus and medius muscles at their insertion, with heterogeneous signal intensity on T2WI, mainly hyperintense. Subsequent biopsy confirmed the diagnosis of low-grade synovial sarcoma, which explains the mild FDG uptake (Fig. 87) [62].

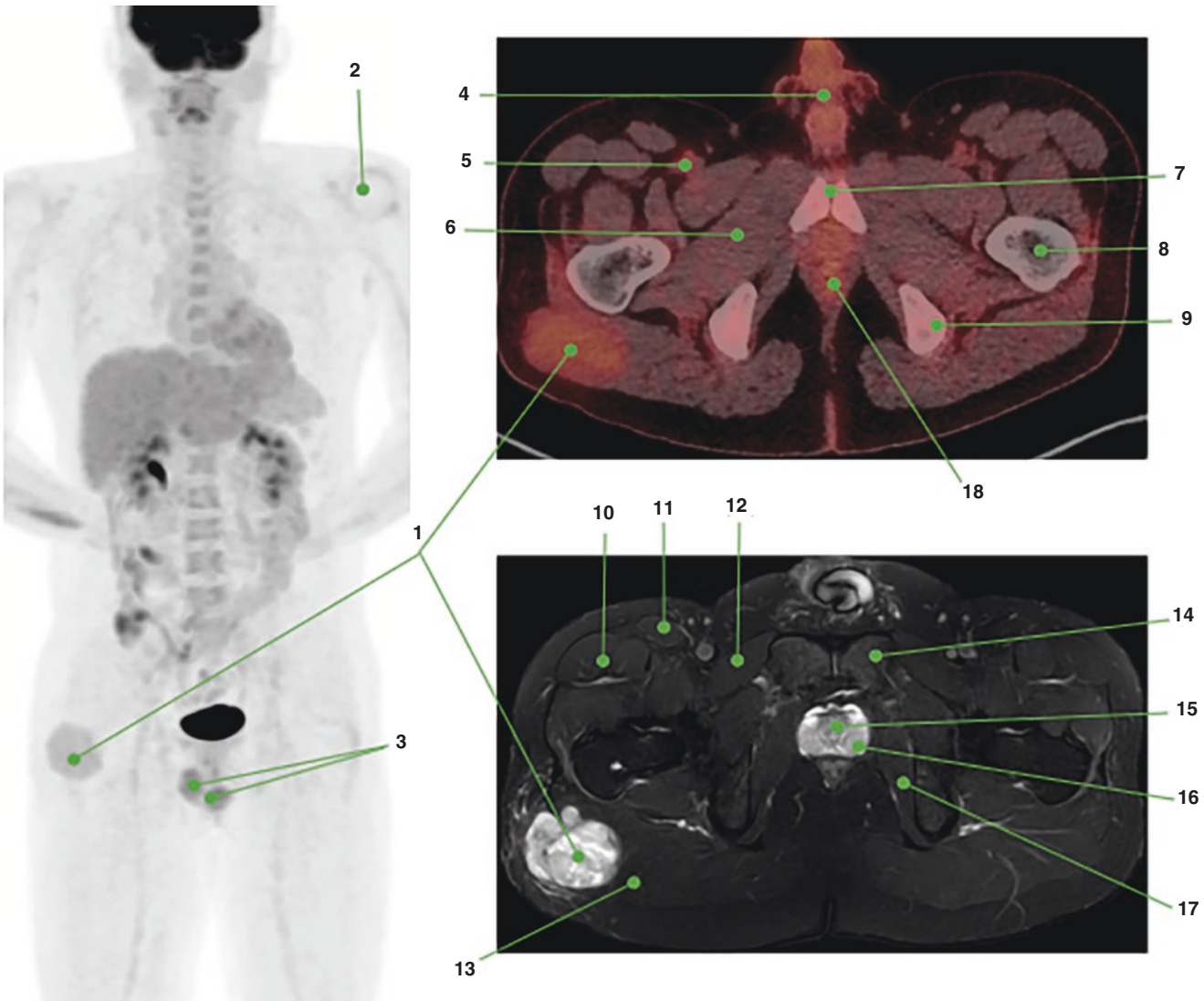

Fig. 87 1. Mild hypermetabolic mass in the right gluteus muscles
2. Diffuse increased activity around the left shoulder joints, probably related to capsulitis
3. Testes
4. Base of the penis
5. Right external iliac vessels
6. Right external obturator muscle
7. Pubic symphysis
8. Left femoral neck
9. Left ischial tuberosity
10. Right rectus femoris muscle
11. Right sartorius muscle
12. Right pectineus muscle
13. Right gluteus maximus muscle
14. Left pubic bone
15. Prostate gland, transitional zone
16. Prostate gland, peripheral zone
17. Left internal obturator muscle
18. Rectum

1.4.15 Case 15

A 28-year-old woman with a history of Ewing's sarcoma in the left iliac bone, treated with hemipelvectomy and radiotherapy. Twelve years later, she attended an early checkup for pelvic pain, so ^{18}F-FDG PET/CT was performed. Images showed a poorly defined and infiltrating lytic lesion at the sacrum and the right iliac bone, with increased peripheral multifocal activity. Biopsy of the lesion confirmed the diagnosis of radiation-induced osteosarcoma (Fig. 88) [63].

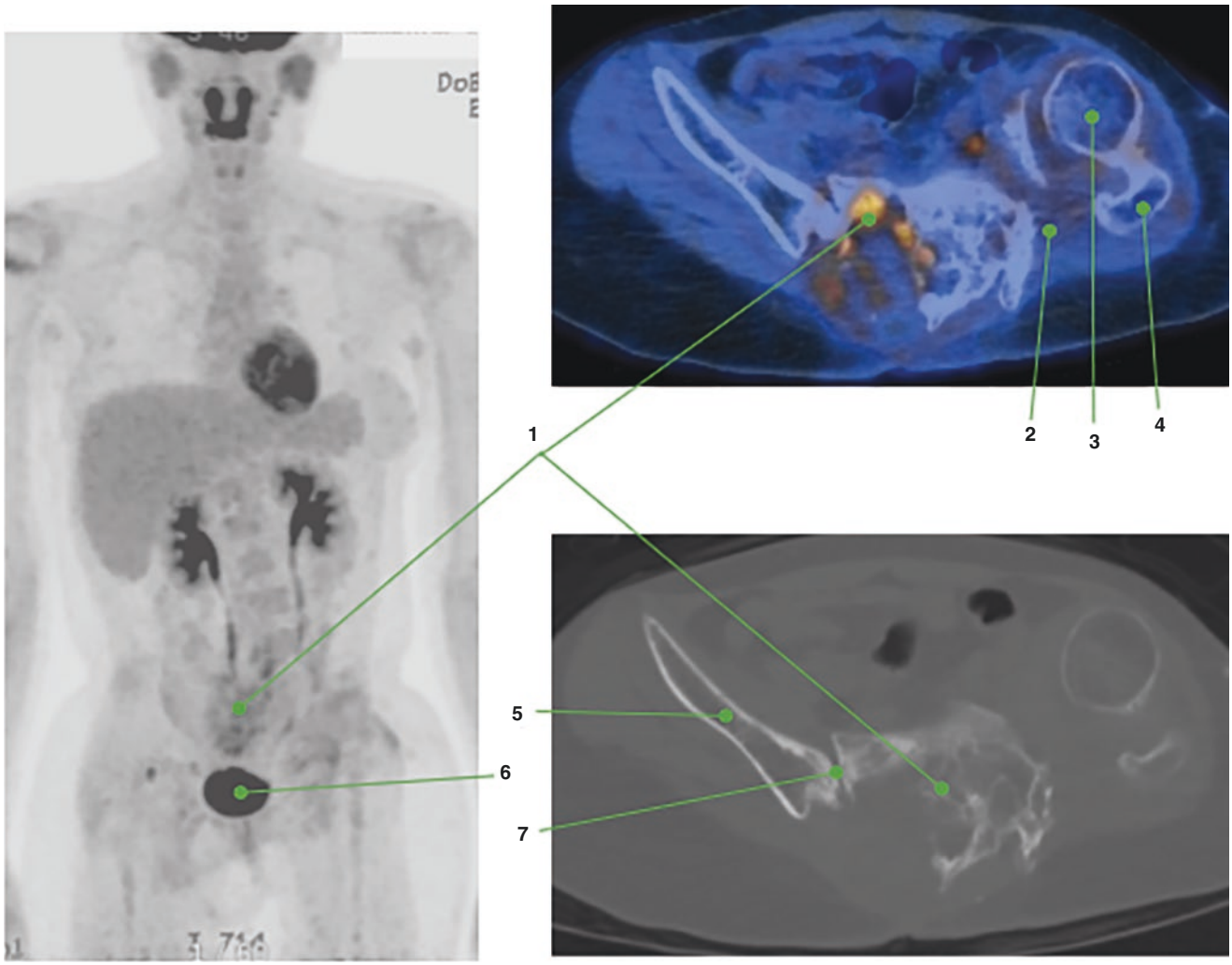

Fig. 88 1. Extensive lytic lesion with peripheral hypermetabolic component involving the sacrum and right iliac bone
2. Left hemipelvectomy postoperative changes
3. Left femoral head
4. Left femur greater trochanter
5. Right iliac wing
6. Bladder
7. Right sacroiliac joint

1.4.16 Case 16

A 66-year-old man with a history of rectal adenocarcinoma treated with surgery and adjuvant chemotherapy. Follow-up chest CT showed multiple new lymphadenopathies, so ^{18}F-FDG PET/CT was performed to rule out disease progression. Images showed increased activity in multiple mediastinal lymph nodes at peritracheal, prevascular, and hilar areas, as well as in few retroperitoneal lymph nodes. Additionally, multiple linear foci of increased FDG uptake were found in the muscles of both upper limbs, lumbar region, gluteal regions, and thighs. Subsequent biopsy of one of the muscle lesions confirmed the diagnosis of sarcoidosis. Muscular involvement in sarcoidosis can be detected in random biopsy in up to 80% of cases; however, it is usually underdiagnosed because symptoms only present in less than 3% of patients (Fig. 89) [64].

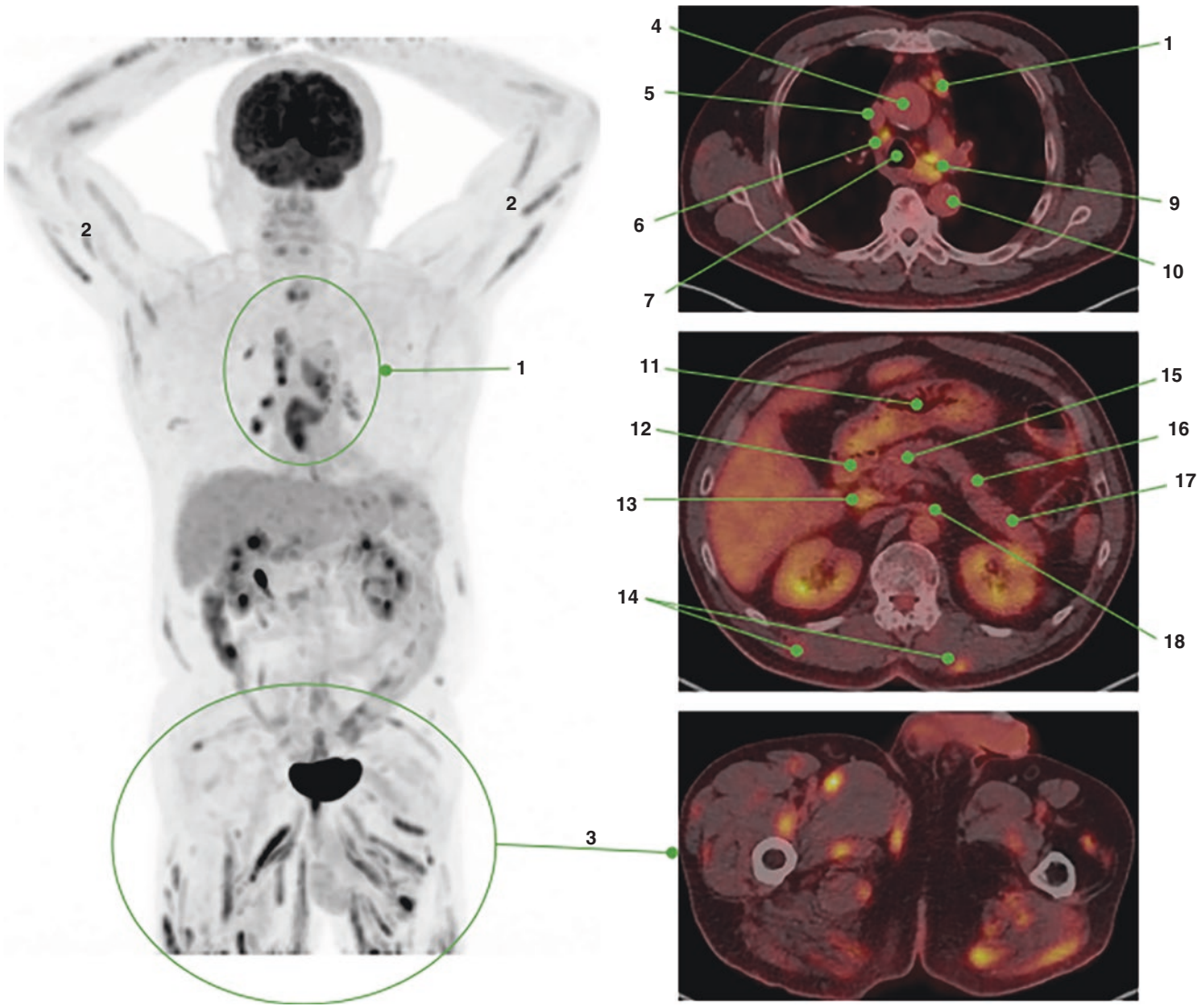

Fig. 89 1. Multiple metabolically active mediastinal lymph nodes
2. Multifocal linear increased activity at both arm muscles
3. Multifocal linear increased activity at both gluteal regions and proximal thighs
4. Ascending aorta
5. Superior vena cava
6. Hypermetabolic right paratracheal lymph node
7. Trachea
8. Hypermetabolic prevascular lymph nodes
9. Hypermetabolic left paratracheal lymph nodes
10. Descending aorta
11. Gastric antrum
12. Duodenum, second portion
13. Hypermetabolic portocaval lymph node
14. Linear increased activity at both paraspinal muscles
15. Pancreatic head
16. Pancreatic body
17. Pancreatic tail
18. Left renal vein

1.4.17 Case 17

An 80-year-old woman with chronic pain in the left knee, without a history of trauma. X-ray showed an aggressive sclerotic lesion in the distal femur, so ^{18}F-FDG PET/CT was performed. Images showed marked increased activity in an extensive intramedullary bone lesion at the distal femur, compromising the diaphysis, metaphysis, and epiphysis, with a dense bone matrix, a narrow transition zone and without significant periosteal reaction or soft tissue involvement. No skip lesions or distant metastases were found. Subsequent biopsy confirmed the diagnosis of osteosarcoma. Joint effusion with diffuse FDG uptake was also found in the suprapatellar bursa (Fig. 90).

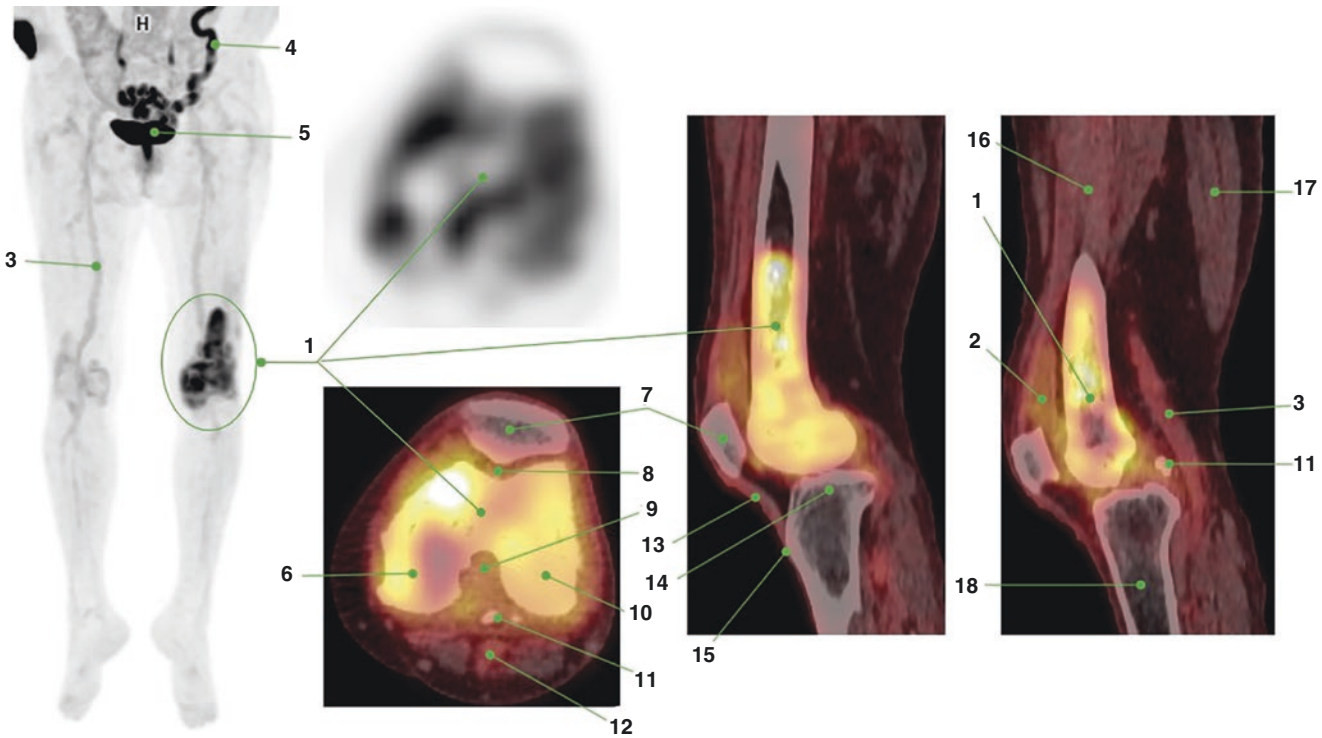

Fig. 90 1. Metabolically active osteosarcoma in the distal femur
2. Metabolically active joint effusion in the suprapatellar bursa
3. Femoral artery
4. Descending colon
5. Bladder
6. Medial femoral condyle
7. Patella
8. Patellofemoral space
9. Intercondylar notch
10. Lateral femoral condyle
11. Fabella
12. Femoral vessels
13. Patellar ligament
14. Tibial plateau
15. Anterior tibial tuberosity
16. Quadriceps muscle
17. Hamstring muscles (biceps femoris, semitendinosus, and semimembranosus)
18. Proximal tibia shaft

2 Non-FDG PET/CT

2.1 ^{18}F-Fluciclovine PET/CT

2.1.1 Case 1

A 68-year-old man with a history of prostate cancer treated with radical prostatectomy and radiotherapy. He attended routine control with a biochemical relapse, so ^{18}F-fluciclovine PET/CT was performed, finding focal increased activity in the surgical bed behind the bladder, consistent with recurrent tumor. This new radiotracer, a synthetic analog of the amino acid L-leucine, has the main advantage that the activity in the excreted urine is minimal or null, which allows the detection of lesions in the surgical bed with high precision, as in this case. Additionally, it has been shown that it allows the detection of small lesions with high diagnostic accuracy (Fig. 91) [65, 66].

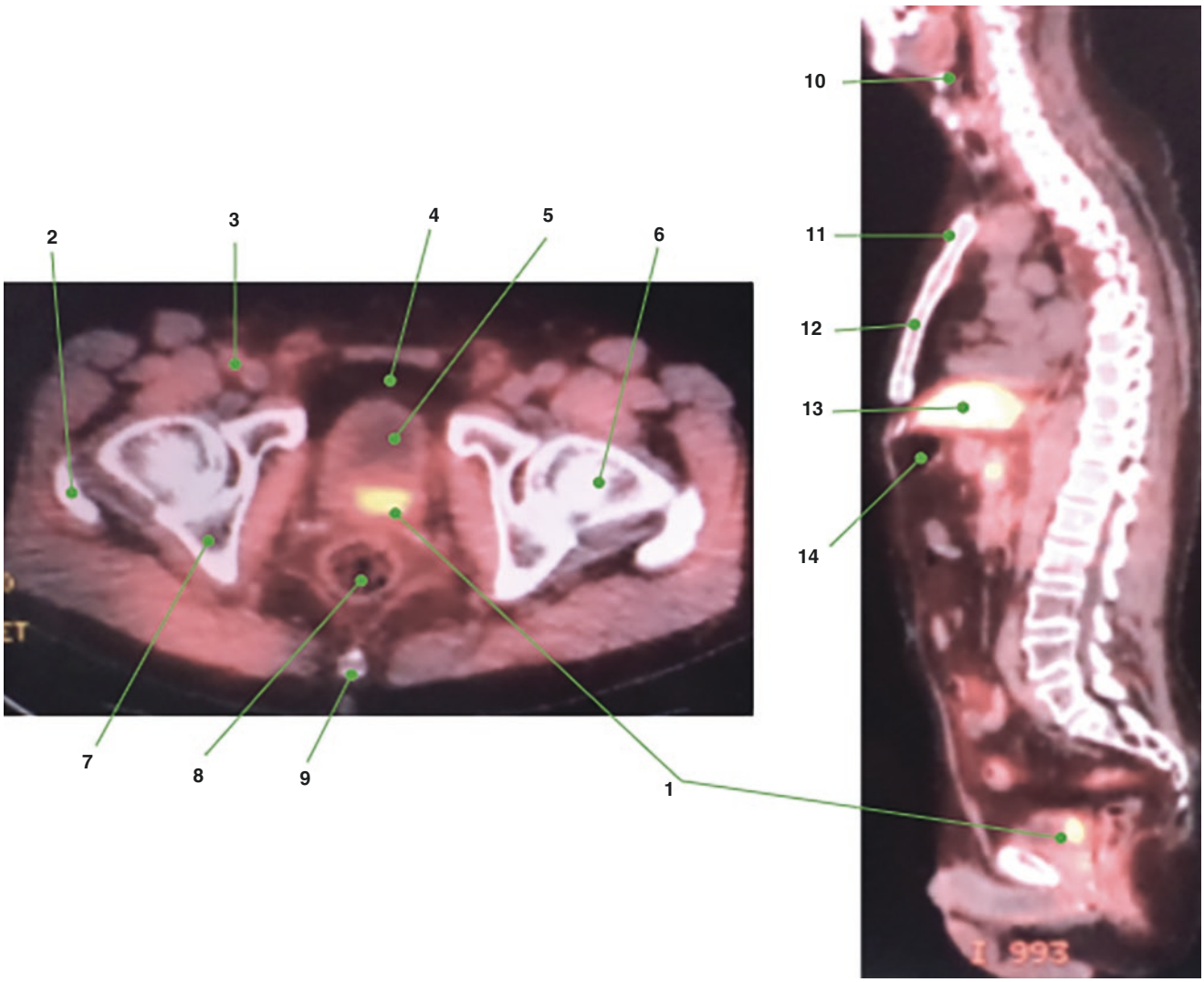

Fig. 91 1. Metabolically active recurrent tumor in the prostatic surgical bed
2. Right femur, greater trochanter
3. Right femoral vessels
4. Prevesical space
5. Bladder
6. Left femoral head
7. Right acetabulum, posterior column
8. Rectum
9. Coccix
10. Larynx
11. Sternal manubrium
12. Sternal body
13. Left hepatic lobe
14. Stomach

2.1.2 Case 2

A 55-year-old man with a history of prostate cancer treated with radical prostatectomy and radiotherapy. He presented biochemical relapse and conventional images did not show any suspicious lesions of local recurrence or metastasis, so ^{18}F-fluciclovine PET/CT was performed. Images showed focal increased uptake in small metastatic lymph nodes at both iliac chains, which, due to their size, had been considered reactive in conventional images. As previously mentioned, one of the advantages of this new radiotracer is the detection of small lesions with high sensitivity and specificity (Fig. 92) [65, 66].

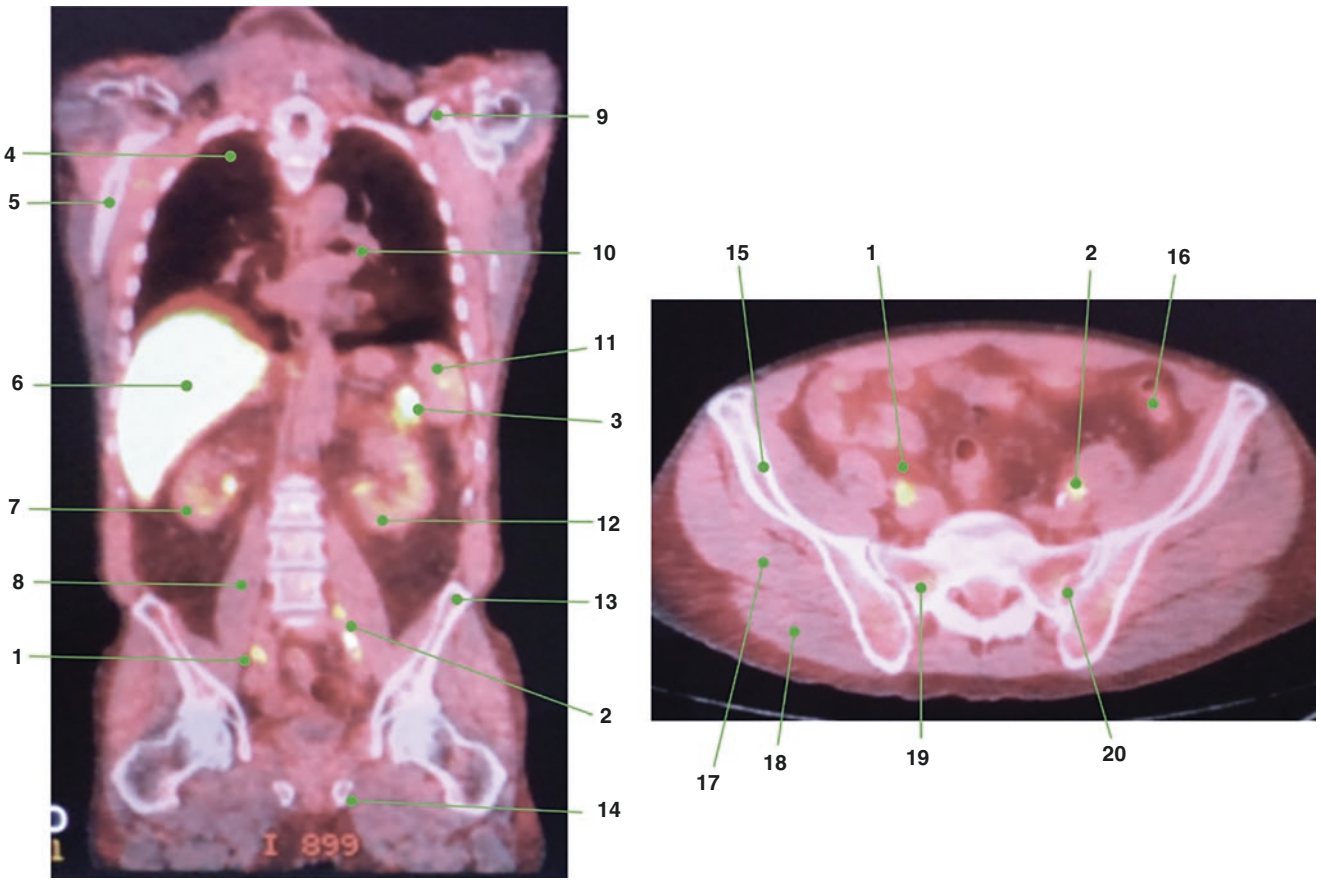

Fig. 92 1. Small metabolically active right common iliac lymph node metastasis
2. Small metabolically active left common iliac lymph node metastasis
3. Tip of the left hepatic lobe
4. Right lung apex
5. Right scapula
6. Liver
7. Right kidney
8. Right psoas muscle
9. Left acromioclavicular joint
10. Left lung hilum
11. Spleen
12. Left kidney
13. Left iliac bone
14. Left pubic bone
15. Right iliac wing
16. Descending colon
17. Right gluteus medius muscle
18. Right gluteus maximus muscle
19. Right sacral ala
20. Left sacroiliac joint

2.2 ^{68}Ga-DOTA TOC PET/CT

2.2.1 Case 1

A 38-year-old patient with a history of secondary hyperparathyroidism due to a parathyroid adenoma, 1 year earlier. On routine follow-up, fasting hypoglycemia and elevated chromogranin A were found, so ^{68}Ga-DOTA-TOC PET/CT was performed suspecting a pancreatic neuroendocrine tumor. Images showed multifocal increased activity in the body and tail of the pancreas, as well as two focal hypermetabolic liver lesions and increased size of both adrenal glands with diffuse uptake. The diagnosis of a grade 2 pancreatic neuroendocrine tumor was later confirmed, and the other lesions were consistent with liver metastasis, right adrenocortical hyperplasia, and left adrenal adenoma. With these findings and the previous diagnosis of parathyroid adenoma, additional studies were carried out confirming the diagnosis of multiple endocrine neoplasia type 1 (MEN1) (Fig. 93) [67].

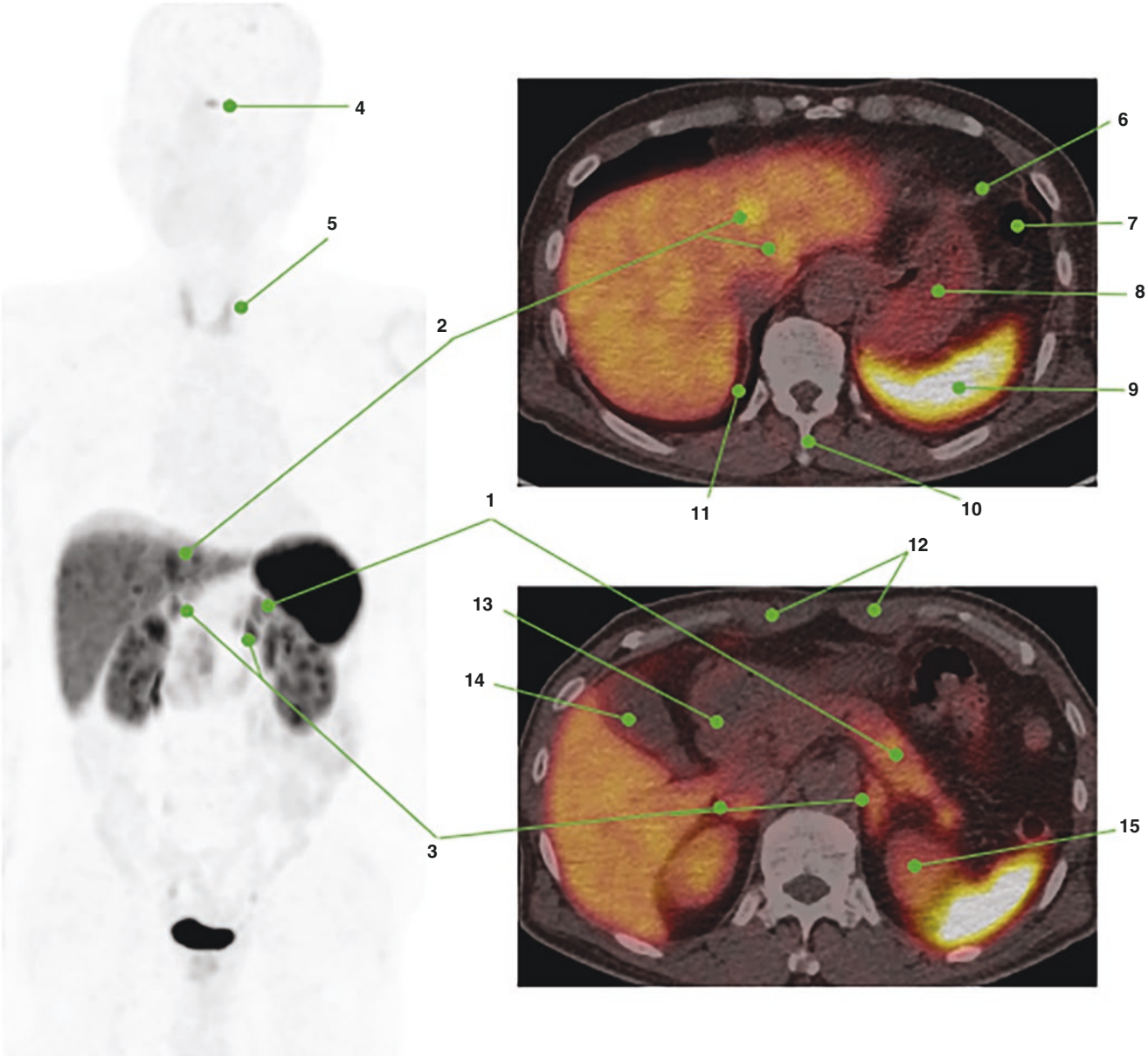

Fig. 93 1. Multifocal increased activity at the pancreatic body and tail; insulinoma
2. Focal hypermetabolic liver lesions; neuroendocrine tumor metastasis
3. Diffusely increased uptake in bilateral enlarged adrenal glands
4. Pituitary gland
5. Diffuse physiologic uptake in thyroid gland
6. Diaphragmatic cupula
7. Splenic flexure of the colon
8. Stomach
9. Spleen, physiologic activity
10. Thoracic vertebra spinous process
11. Right diaphragmatic crus
12. Rectus abdominis muscles
13. Duodenum, second portion
14. Gallbladder
15. Left kidney inferior pole

2.2.2 Case 2

A 65-year-old woman with a history of occasional headaches. Outside CT reported a left temporal mass and she was referred for evaluation with the suspected diagnosis of a meningioma. ^{68}Ga-DOTA-TOC PET/MR was performed, finding a metabolically active left temporal extra-axial well-defined mass, with broad dural base, consistent with a typical meningioma. Contrast-enhanced MRI showed marked and homogeneous enhancement (Fig. 94) [68].

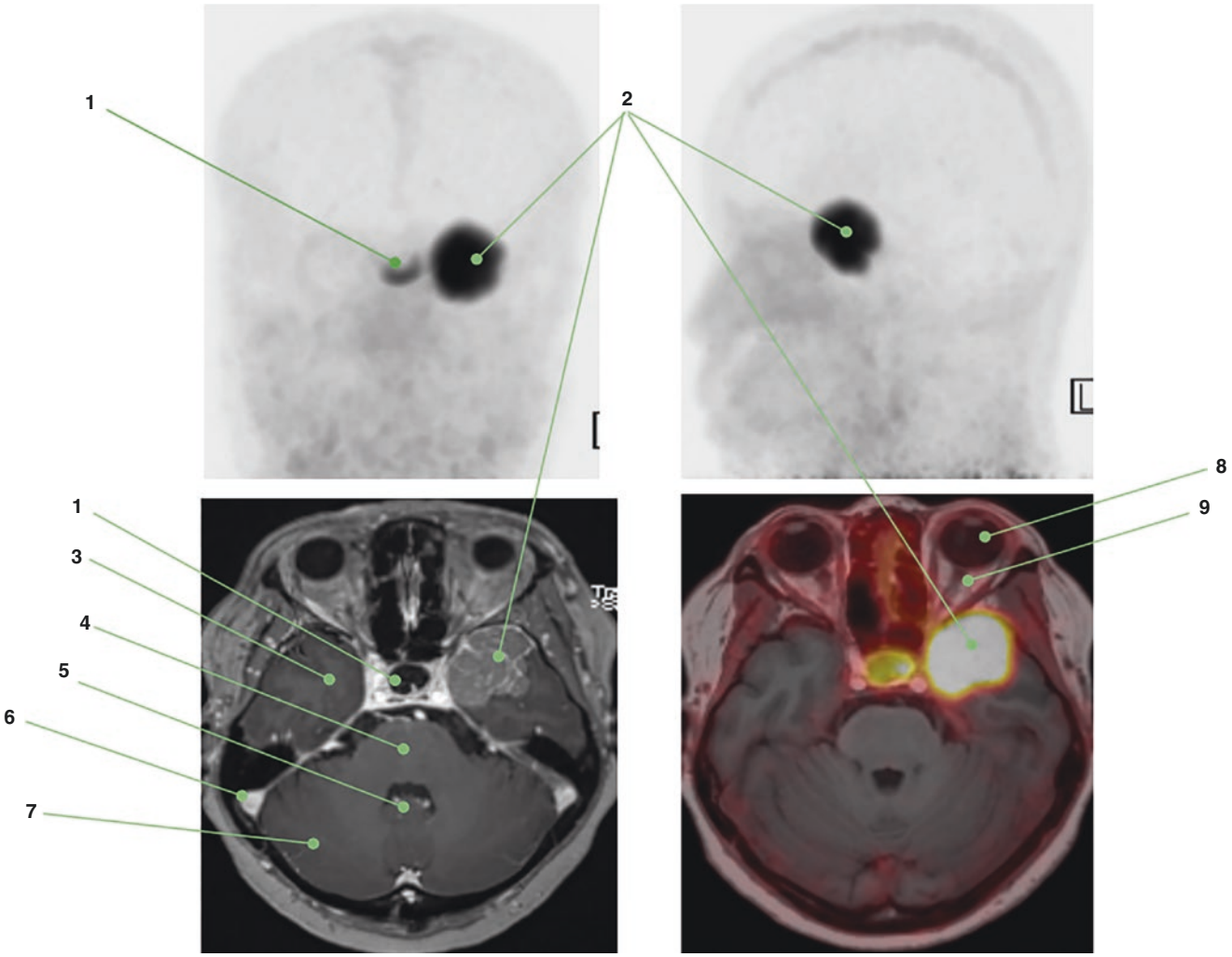

Fig. 94 1. Pituitary gland
2. Metabolically active left temporal meningioma
3. Right temporal lobe
4. Pons
5. Fourth ventricle
6. Right sigmoid sinus
7. Cerebellum, right
8. Left eyeball
9. Left optic nerve

2.2.3 Case 3

A 51-year-old female patient with progressive behavior and personality changes. Contrast-enhanced brain MRI was performed, finding a prominent enhancing extra-axial, dural-based, well-defined mass involving both frontal lobes. A ^{68}Ga-DOTA-TOC PET/MR was performed, confirming a metabolically active meningioma. Additionally, the presence of small hypermetabolic spinal and right parietal leptomeningeal seeding was found, which is characteristic of atypical meningioma, with more aggressive behavior (Figs. 95 and 96) [68].

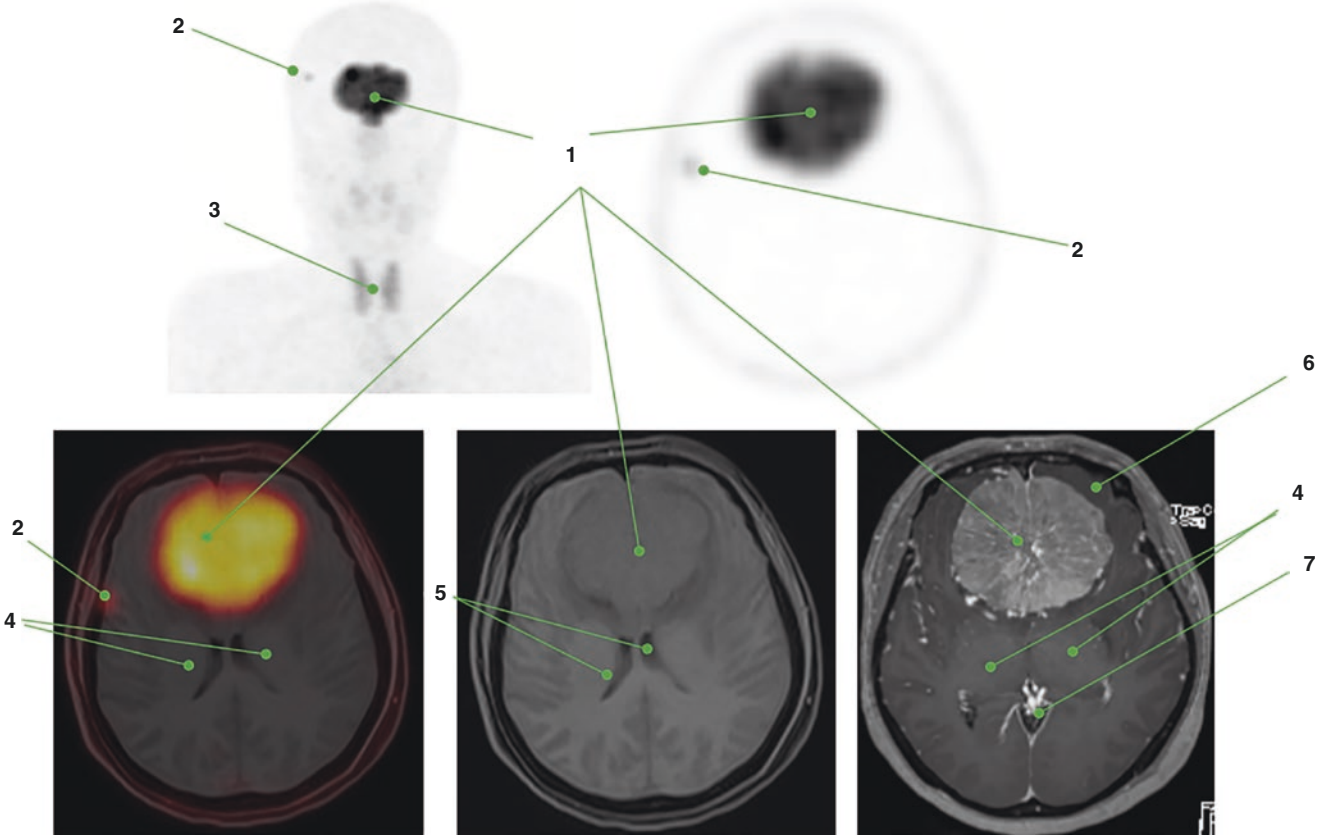

Fig. 95 1. Metabolically active meningioma involving bilateral frontal lobes
2. Hypermetabolic right parietal meningeal seeding
3. Thyroid gland with diffuse uptake
4. Thalami
5. Lateral ventricles
6. Left frontal lobe
7. Fourth ventricle

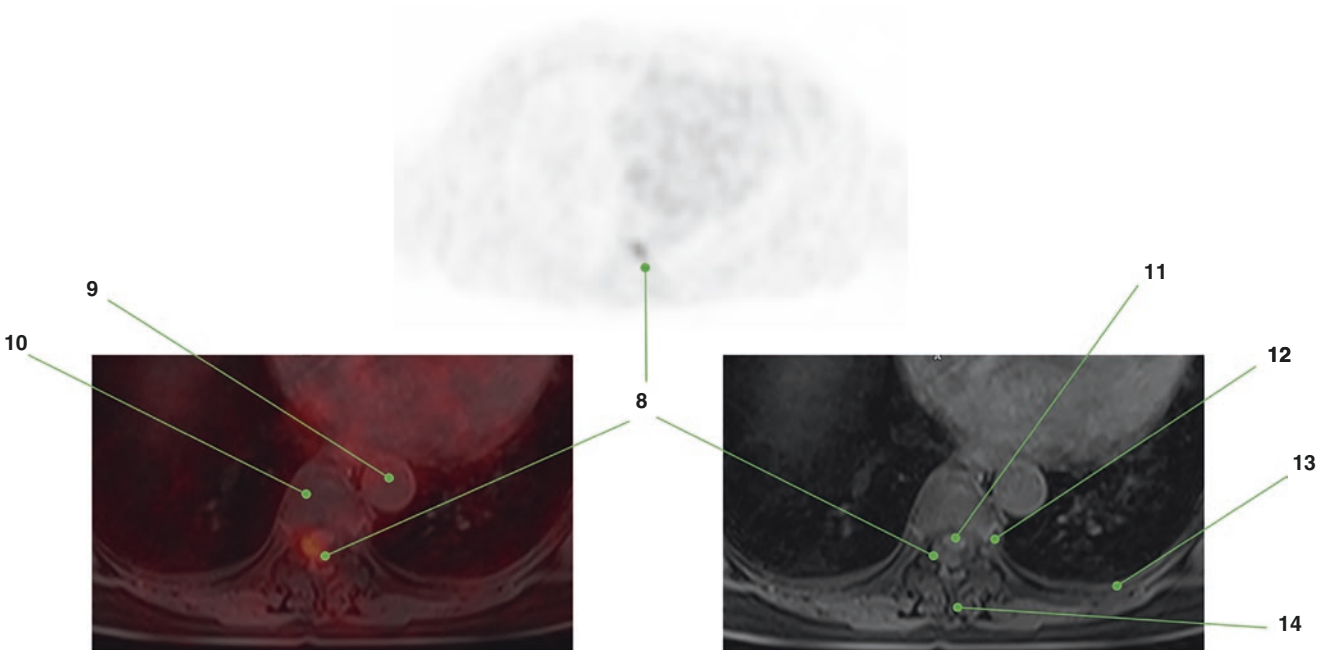

Fig. 96 8. Hypermetabolic spinal seeding at the level of thoracic spine
9. Descending aorta
10. Thoracic vertebral body
11. Spinal cord
12. Left costovertebral joint
13. Left rib, posterior arc
14. Spinous process

2.2.4 Case 4

A 52-year-old woman with a history of breast cancer. During initial staging, contrast-enhanced brain MRI was performed finding a well-defined, bilobulated, dural-based mass involving both occipital lobes. In order to differentiate between a meningioma and metastasis, ^{68}Ga-DOTA-TOC PET/MR was performed, as this is one of its indications. The avid uptake of the mass confirmed the diagnosis of meningioma and the patient did not require any additional management (Fig. 97).

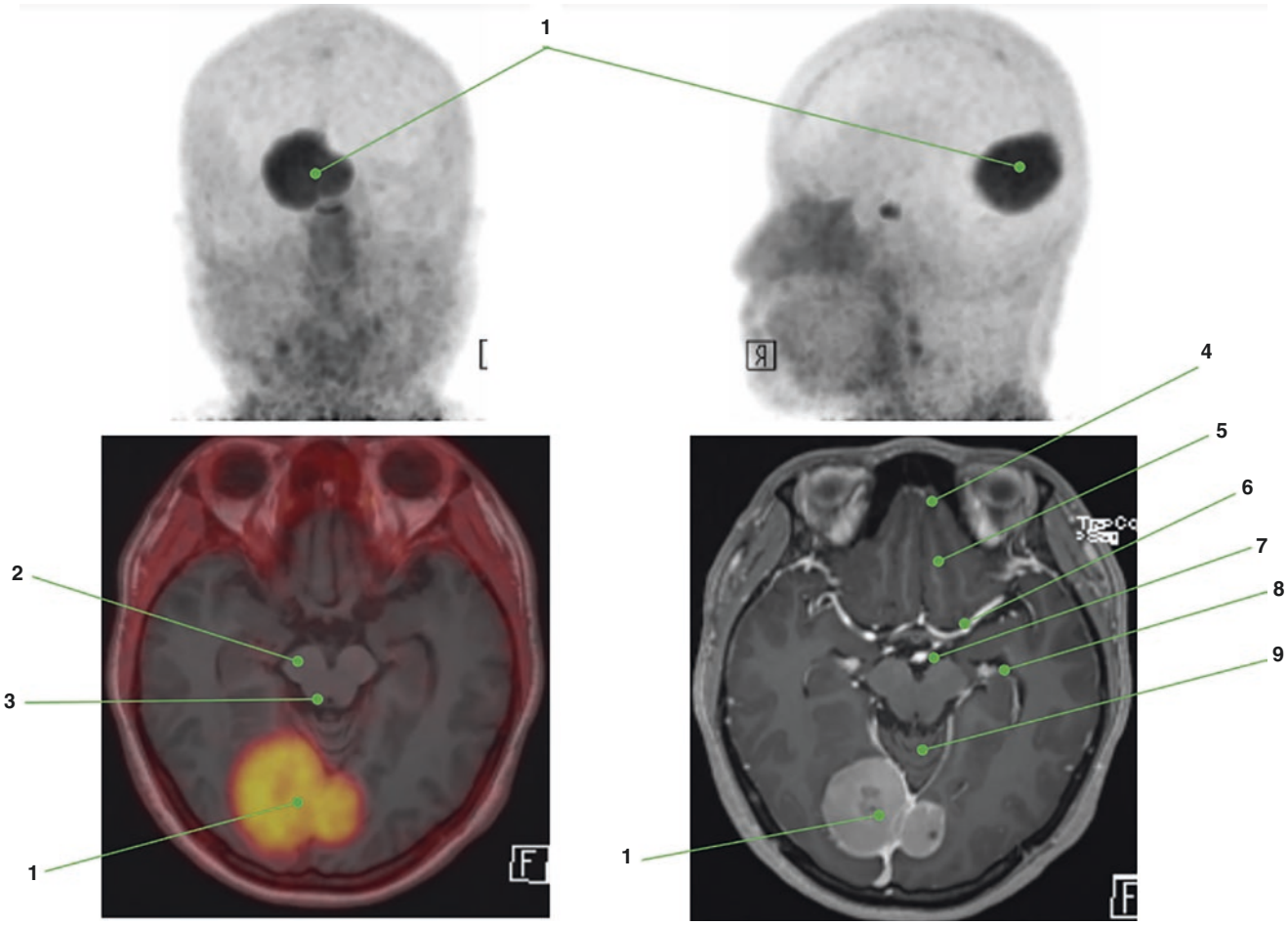

Fig. 97 1. Metabolically active falx meningioma involving both occipital lobes
2. Right cerebral peduncle
3. Cerebral aqueduct
4. Left olfactory sulcus
5. Left straight gyrus
6. Left middle cerebral artery
7. Basilar artery
8. Left lateral ventricle, temporal horn
9. Cerebellum

2.2.5 Case 5

A 71-year-old man who attended an annual routine checkup. Esophagogastroduodenoscopy was performed identifying a small nodular lesion in the proximal duodenum and biopsy confirmed the diagnosis of a grade 1 neuroendocrine tumor, so ^{68}Ga-DOTA-TOC PET/CT was performed. Images showed focal increased activity in the duodenal bulb, where a small nodular lesion with marked enhancement in the arterial phase was identified on CT, corresponding to the primary tumor; no hypermetabolic liver lesions were identified. As an additional finding, there was focal increased FDG uptake in a small right thyroid nodule, corresponding to a known adenomatous nodule. Note normal tracer uptake in the liver, spleen, kidneys, pituitary, adrenal glands, salivary glands, bowel, and prostate gland (Fig. 98) [67].

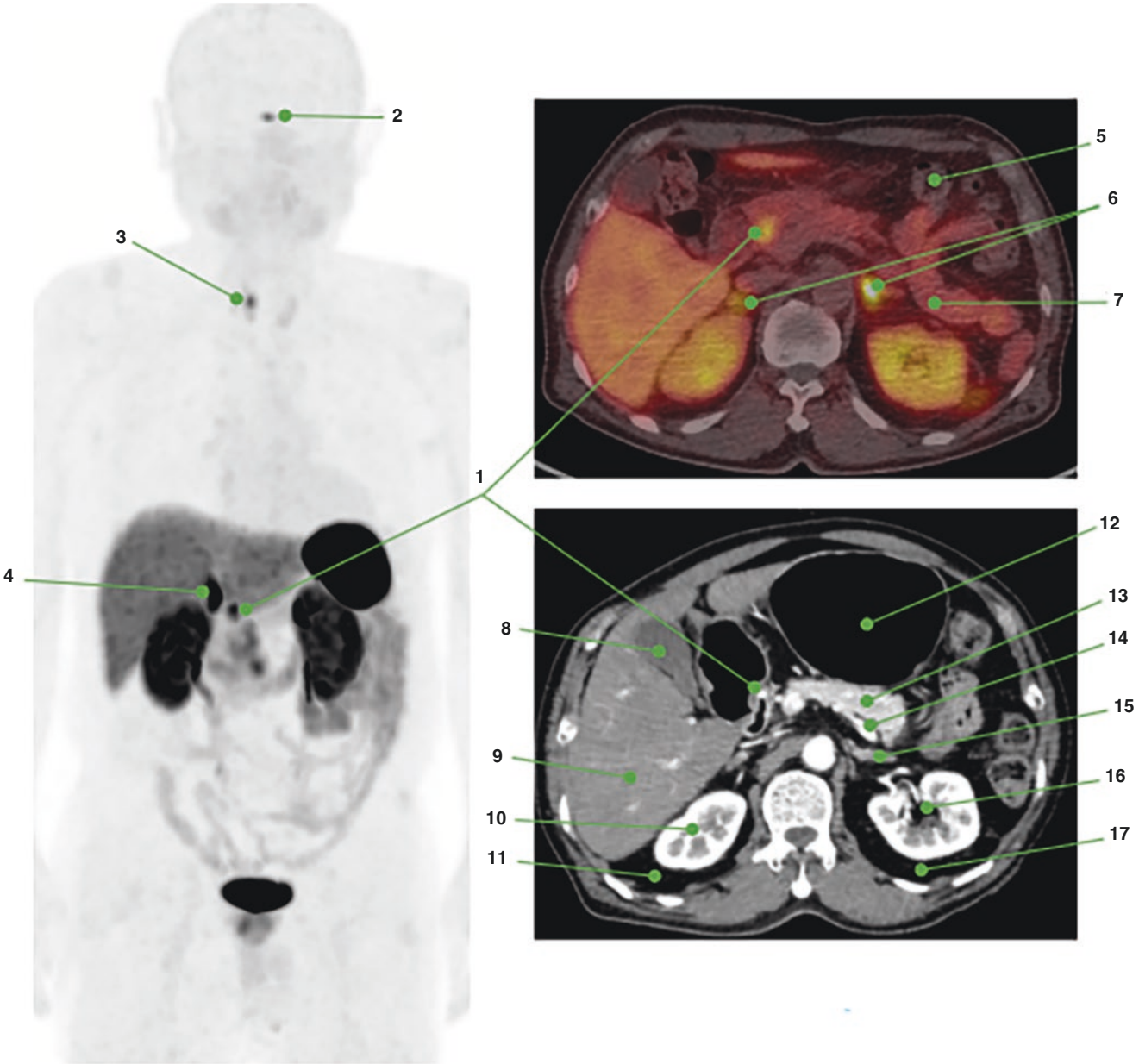

Fig. 98 1. Metabolically active neuroendocrine tumor in the duodenal bulb
2. Physiologic uptake in pituitary gland
3. Increased activity at right thyroid nodule
4. Physiologic uptake in right adrenal gland
5. Transverse colon
6. Physiologic uptake in both adrenal glands
7. Small bowel loops
8. Gallbladder
9. Liver, segment VI(6)
10. Right kidney
11. Right perirenal fat
12. Distended stomach
13. Pancreatic body
14. Splenic artery
15. Left adrenal gland
16. Left renal sinus
17. Left perirenal space

2.3 ^{68}Ga-NOTA Glu-Urea-Lys (NGUL) PET/CT

2.3.1 Case 1

^{68}Ga-NOTA Glu-urea-lys (NGUL) study in a 60-year-old male patient diagnosed with prostate cancer and treated with radical prostatectomy and chemotherapy. The follow-up study with this novel prostate-specific membrane antigen (PSMA) targeting tracer shows normal distribution at lacrimal glands, parotid and submandibular glands, mediastinal blood pool, liver, spleen, and urinary system. Studies have shown that compared with ^{68}Ga-PSMA-11, the most widely used tracer, ^{68}Ga-NGUL shows lower uptake in normal organs and a trend of relatively low tumor-to-background ratio (Fig. 99) [69].

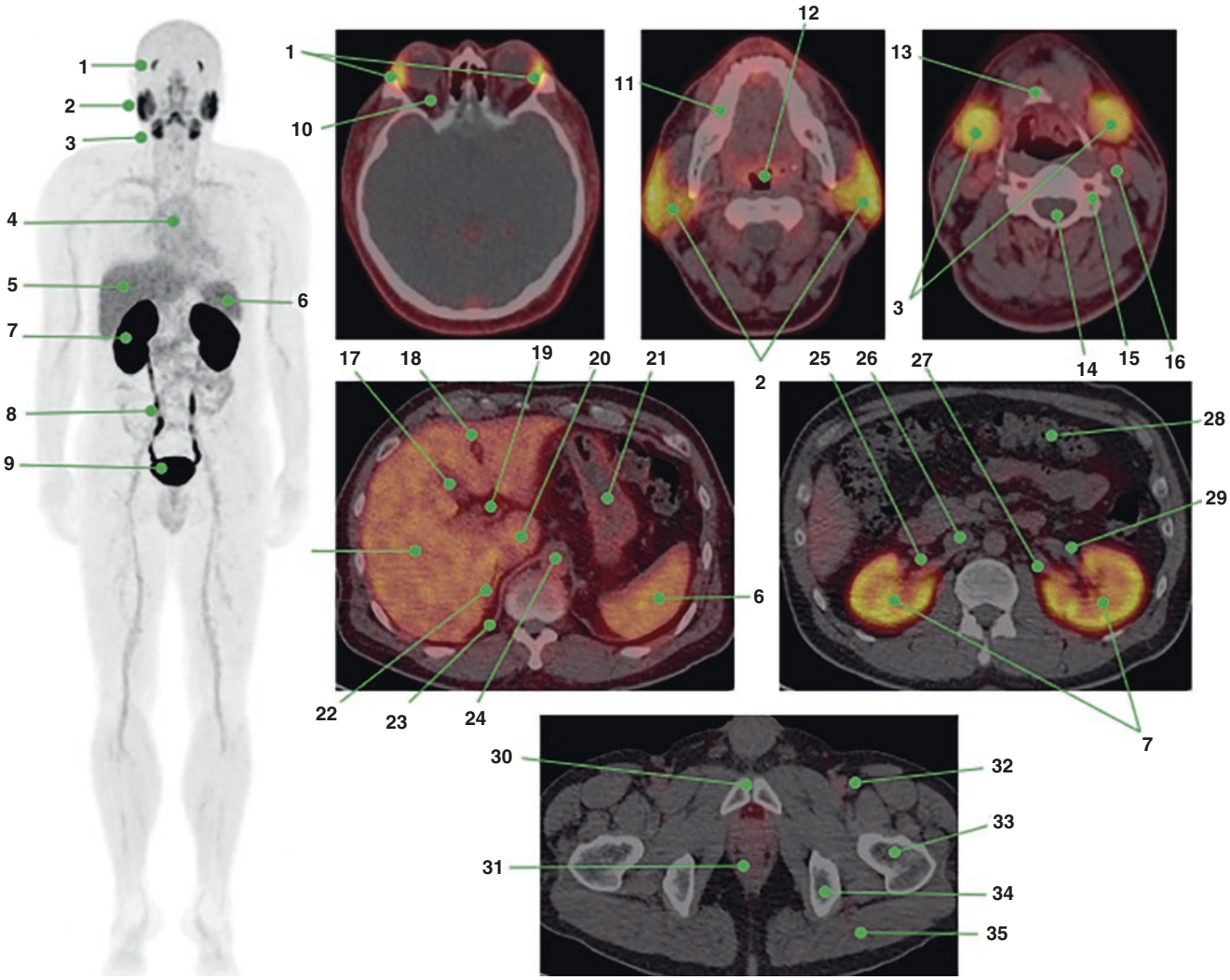

Fig. 99 1. Physiologic uptake in lacrimal glands
2. Physiologic uptake in parotid glands
3. Physiologic uptake in submandibular glands
4. Physiologic uptake in mediastinal blood pool
5. Physiologic uptake in the liver
6. Physiologic uptake in the spleen
7. Physiologic uptake in the kidneys
8. Physiologic uptake in ureters
9. Physiologic uptake in the bladder
10. Right optic nerve
11. Right side of the mandible
12. Oropharynx
13. Hyoid bone
14. Spinal canal
15. Vertebral foramen
16. Left carotid space (common carotid artery and jugular vein)
17. Gallbladder fossa
18. Falciform ligament
19. Hepatic hilum, porta hepatis
20. Caudate lobe of the liver
21. Stomach
22. Right adrenal gland
23. Right diaphragmatic crus
24. Abdominal aorta
25. Right renal vein
26. Inferior vena cava
27. Left renal artery
28. Transverse colon
29. Left renal vein
30. Pubic symphysis
31. Prostatic surgical bed
32. Left external iliac vessels
33. Left femoral neck
34. Left ischial tuberosity
35. Left gluteus maximus muscle

2.4 ^{11}C-Acetate PET/CT

2.4.1 Case 1

A 56-year-old male patient with left flank pain. A left renal mass was found on CT and biopsy revealed a renal cell carcinoma. ^{11}C-acetate PET/CT was performed for initial staging. Images demonstrated moderate increased activity at the primary tumor in the left kidney, as well as in a right adrenal gland metastasis and multiple LNs metastases in both retrocrural areas and retroperitoneum, metastatic (Figs. 100 and 101) [70].

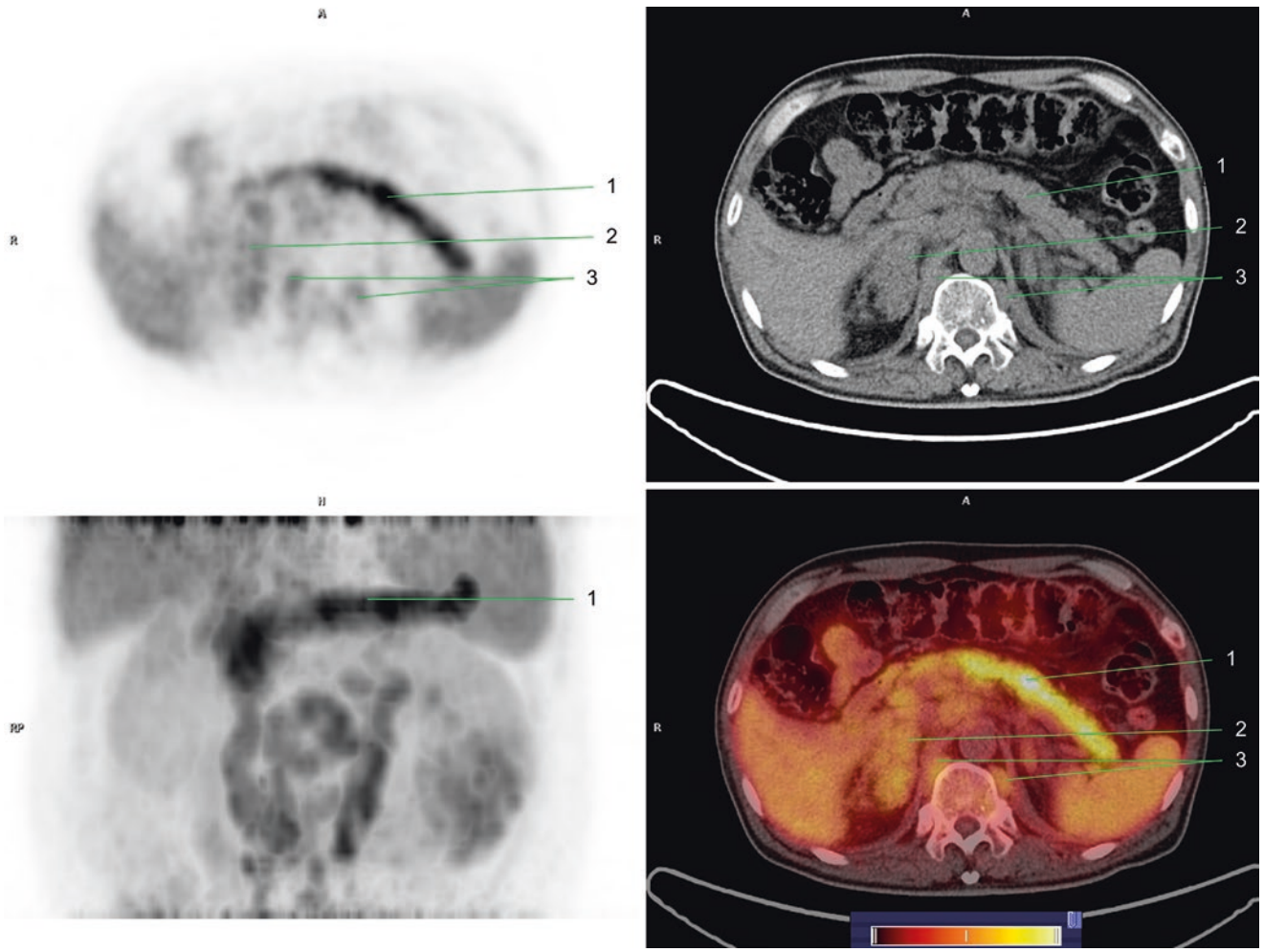

Fig. 100 1. Pancreas
2. Metabolically active metastasis in the right adrenal gland
3. Hypermetabolic retrocrural lymph node metastases

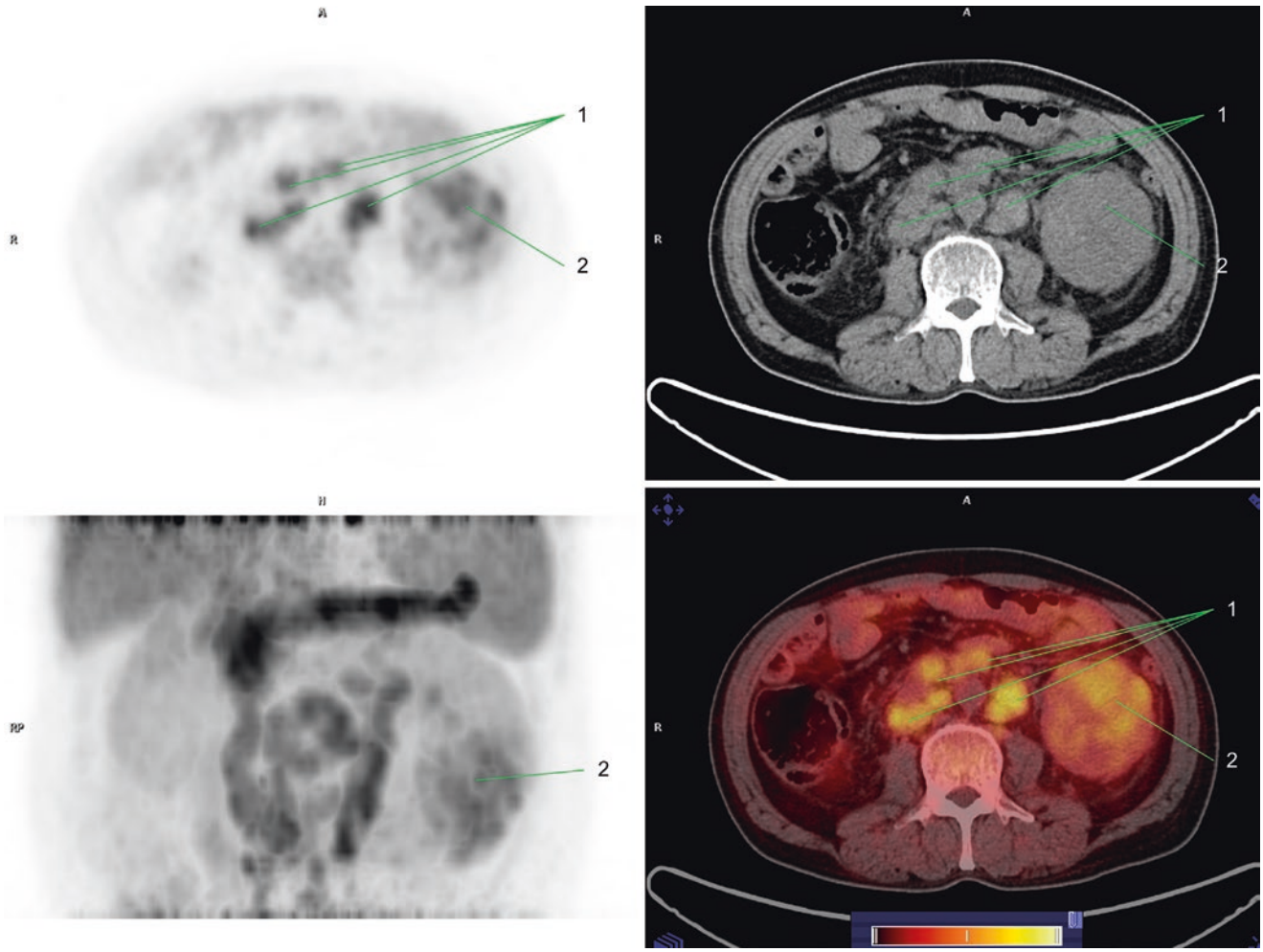

Fig. 101 1. Hypermetabolic retroperitoneal lymph nodes metastases
2. Metabolically active left renal cell carcinoma

2.4.2 Case 2

A 69-year-old woman attended her routine health checkup, where a lung nodule was found on a chest X-ray. ^{11}C-acetate PET/CT was done for differential diagnosis, and images showed increased activity in the partly solid lung nodule at the right lower lobe, which was proved to be an adenocarcinoma after surgery (Figs. 102 and 103) [70].

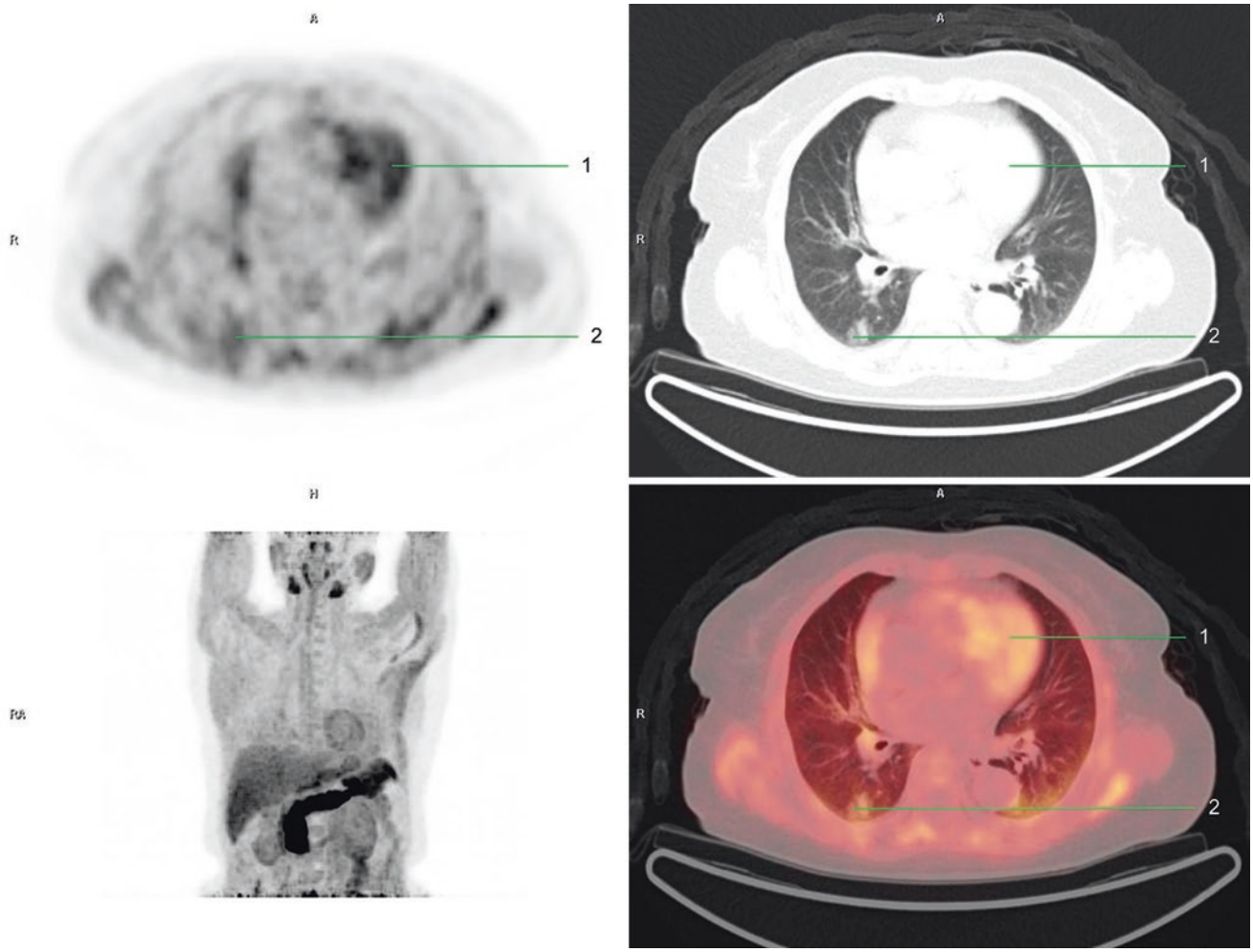

Fig. 102 1. Left ventricle
2. Mild metabolically active, right, lower lobe adenocarcinoma

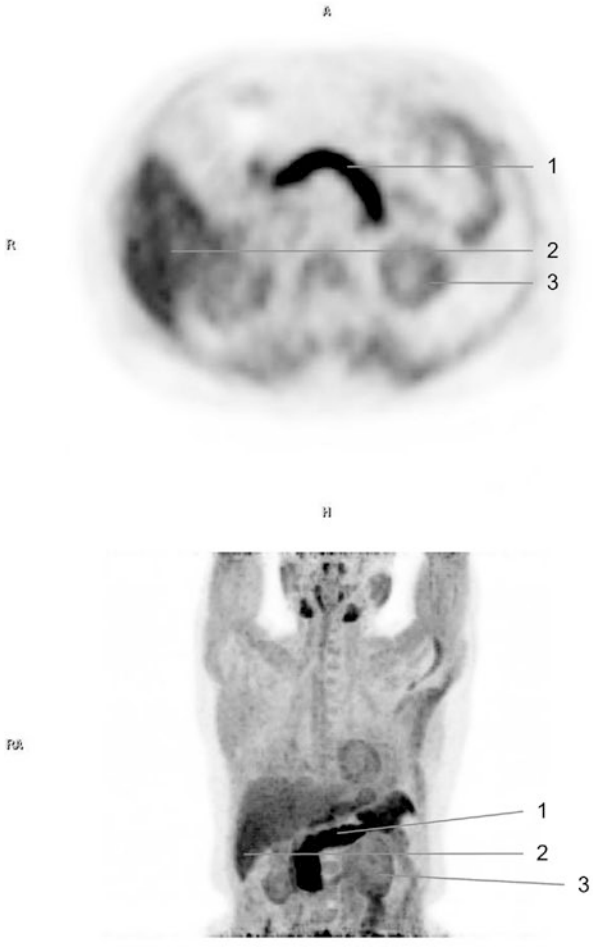

Fig. 103 1. Pancreas, physiologic activity
2. Liver, physiologic activity
3. Left kidney, physiologic activity

2.5 ^{11}C-Methionine PET/CT

2.5.1 Case 1

A 5-year-old boy with dizziness and vomiting. A brain tumor was suspected on CT and MRI, so ^{11}C-methionine PET/CT was performed for differential diagnosis. Images demonstrated focal increased activity in a right cerebellar mass, which was later proved to be a pilocytic astrocytoma (WHO grade I) (Figs. 104 and 105) [70].

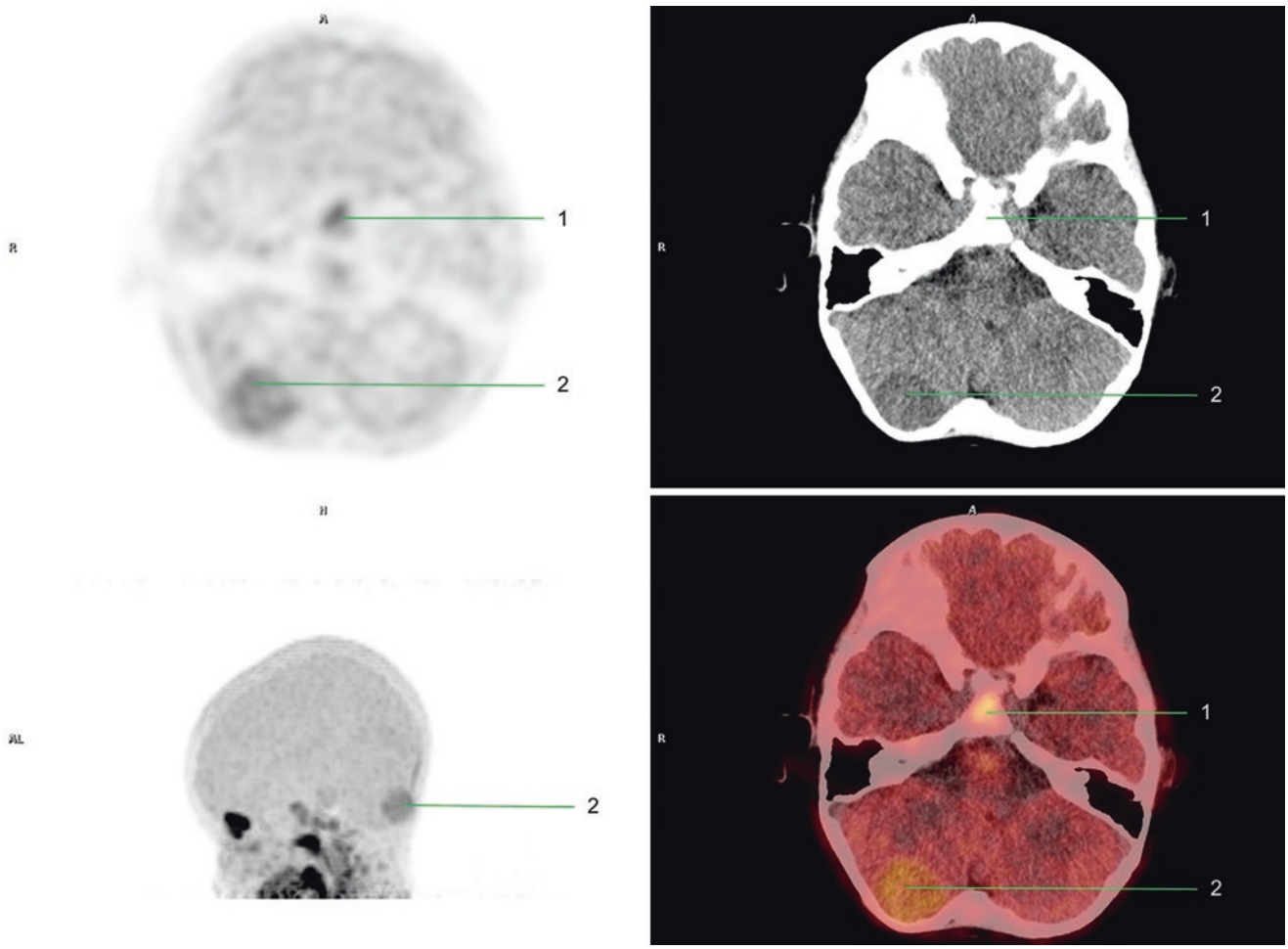

Fig. 104 1. Mild uptake in pituitary gland (physiologic uptake)
2. Brain tumor in right cerebellum (pathology: pilocytic astrocytoma)

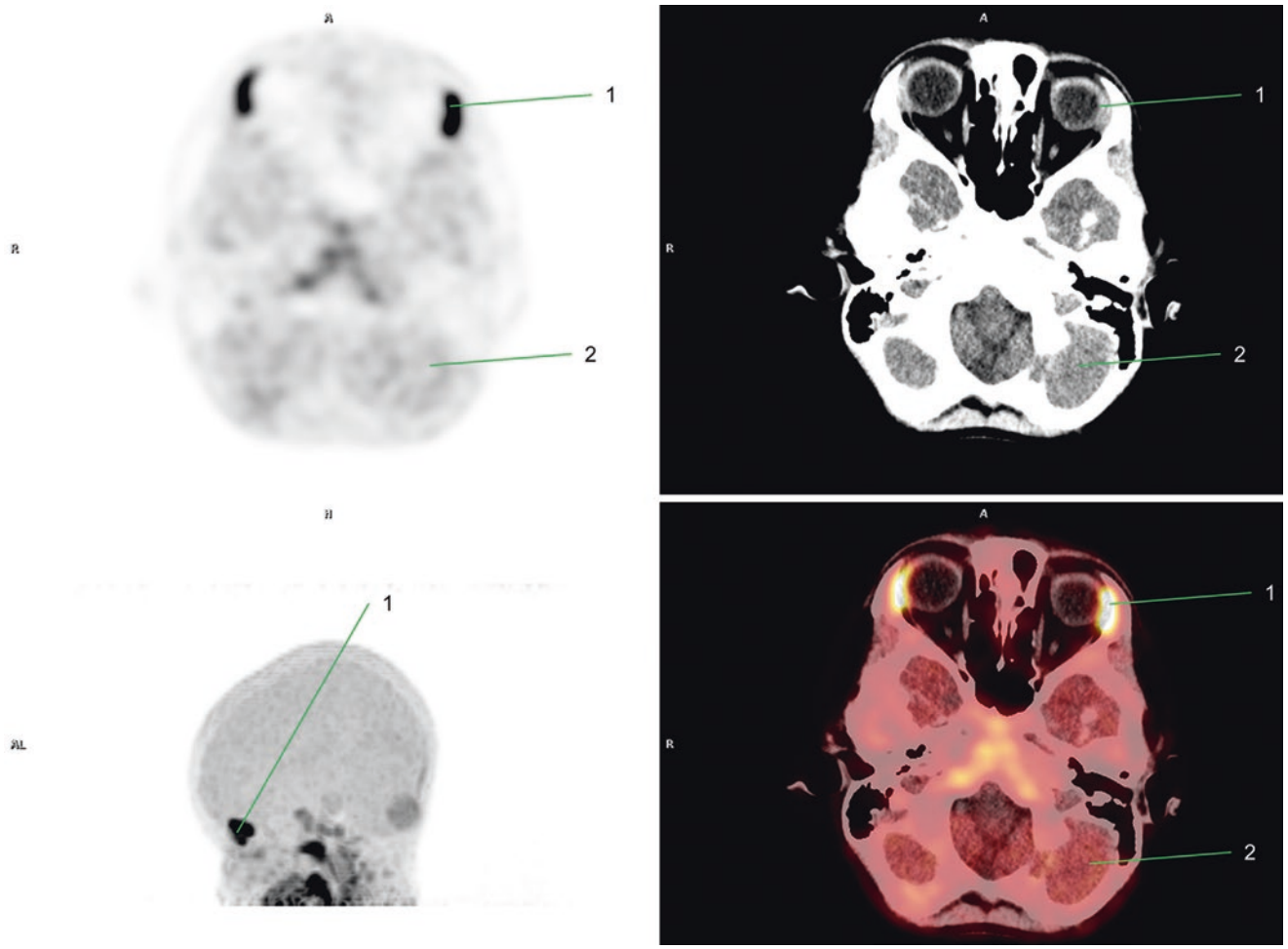

Fig. 105 1. Intense uptake in lacrimal gland (physiologic uptake)
2. Cerebellum

2.5.2 Case 2

A 14-year-old male patient with frequent vomiting, tremor, and recent memory loss. Brain MRI showed multiple masses, so ^{11}C-methionine PET/CT was performed for characterization. Images showed focal increased uptake in a suprasellar irregular mass with peripheral calcifications, which was confirmed to be a germ cell tumor, as suspected (Figs. 106 and 107).

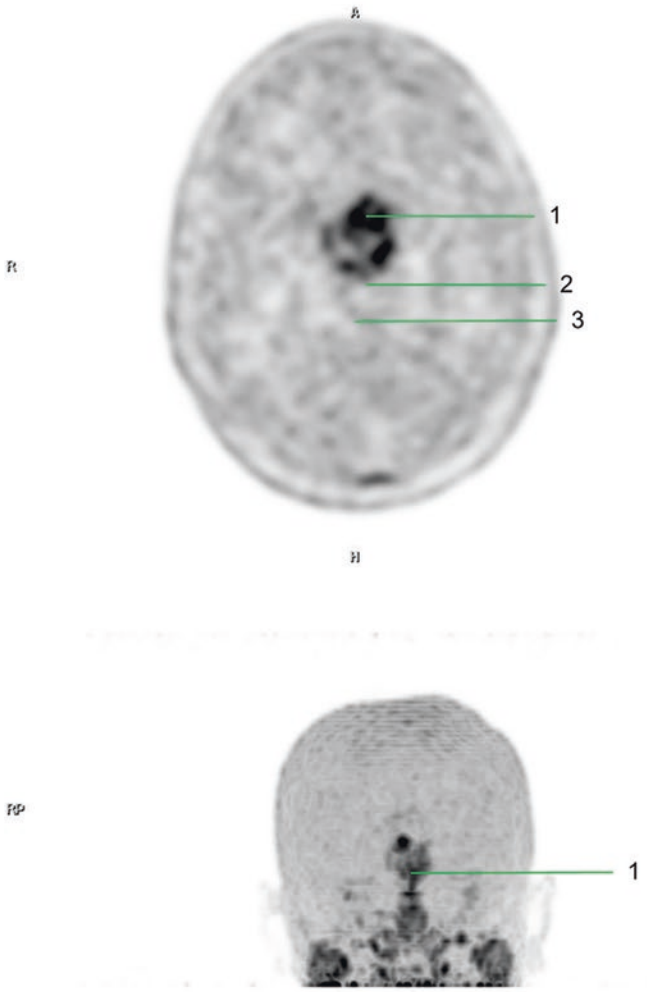

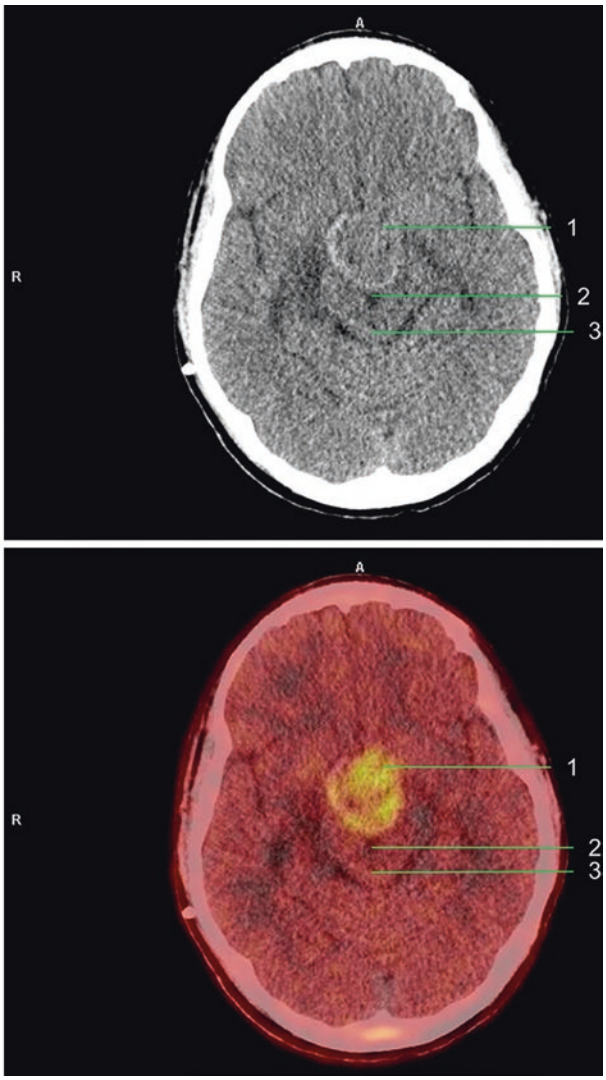

Fig. 106 1. Metabolically active suprasellar germ cell tumor 2. Interpeduncular fossa 3. Midbrain

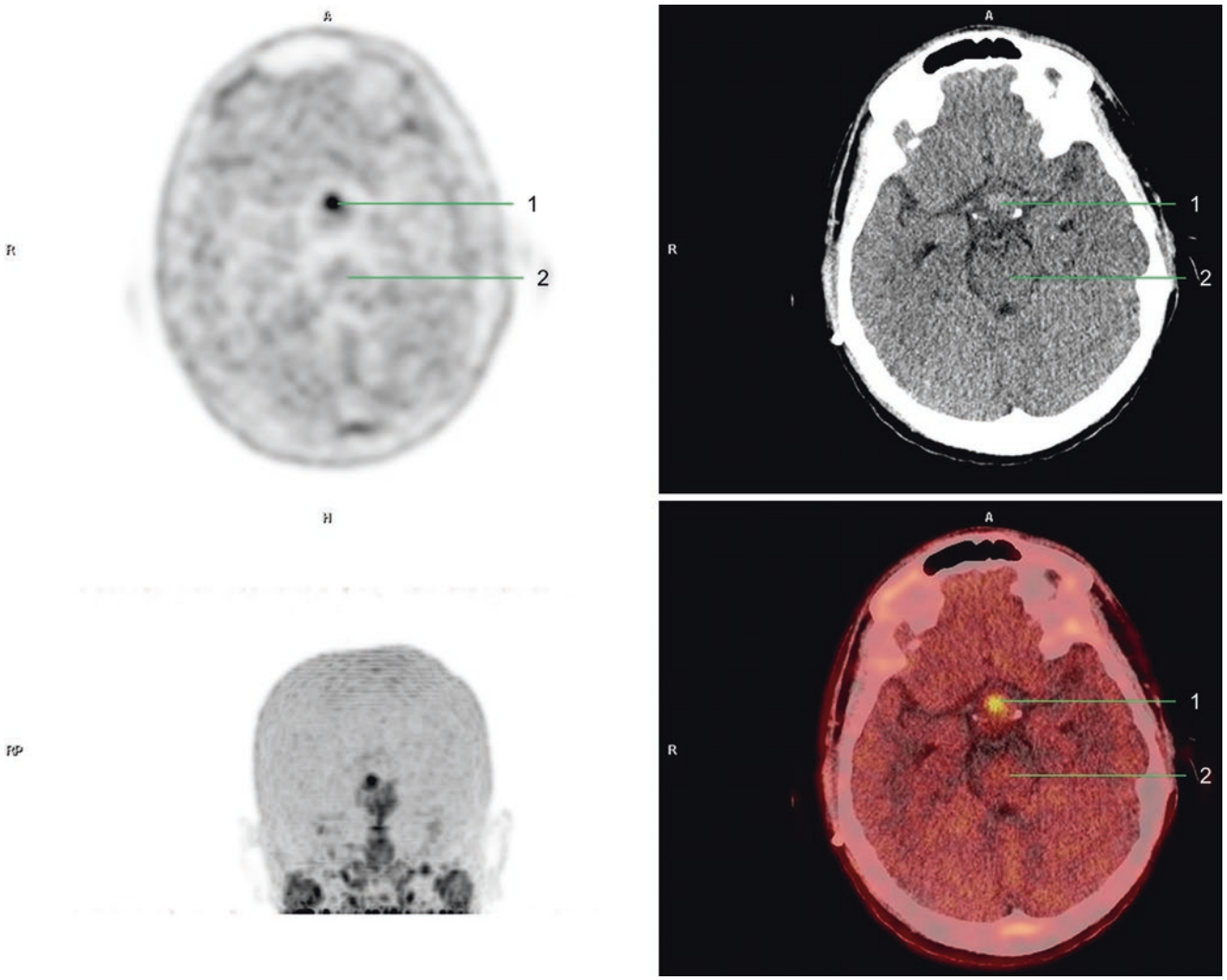

Fig. 107 1. Metabolically active suprasellar germ cell tumor
2. Midbrain

2.6 ^{11}C-PIB PET/CT

2.6.1 Case 1

A 66-year-old woman attended for dementia work-up. ^{11}C-PIB PET/CT was done demonstrating normal findings which include diffusely increased uptake in the white matter and no definite uptake in the gray matter (Figs. 108 and 109) [71].

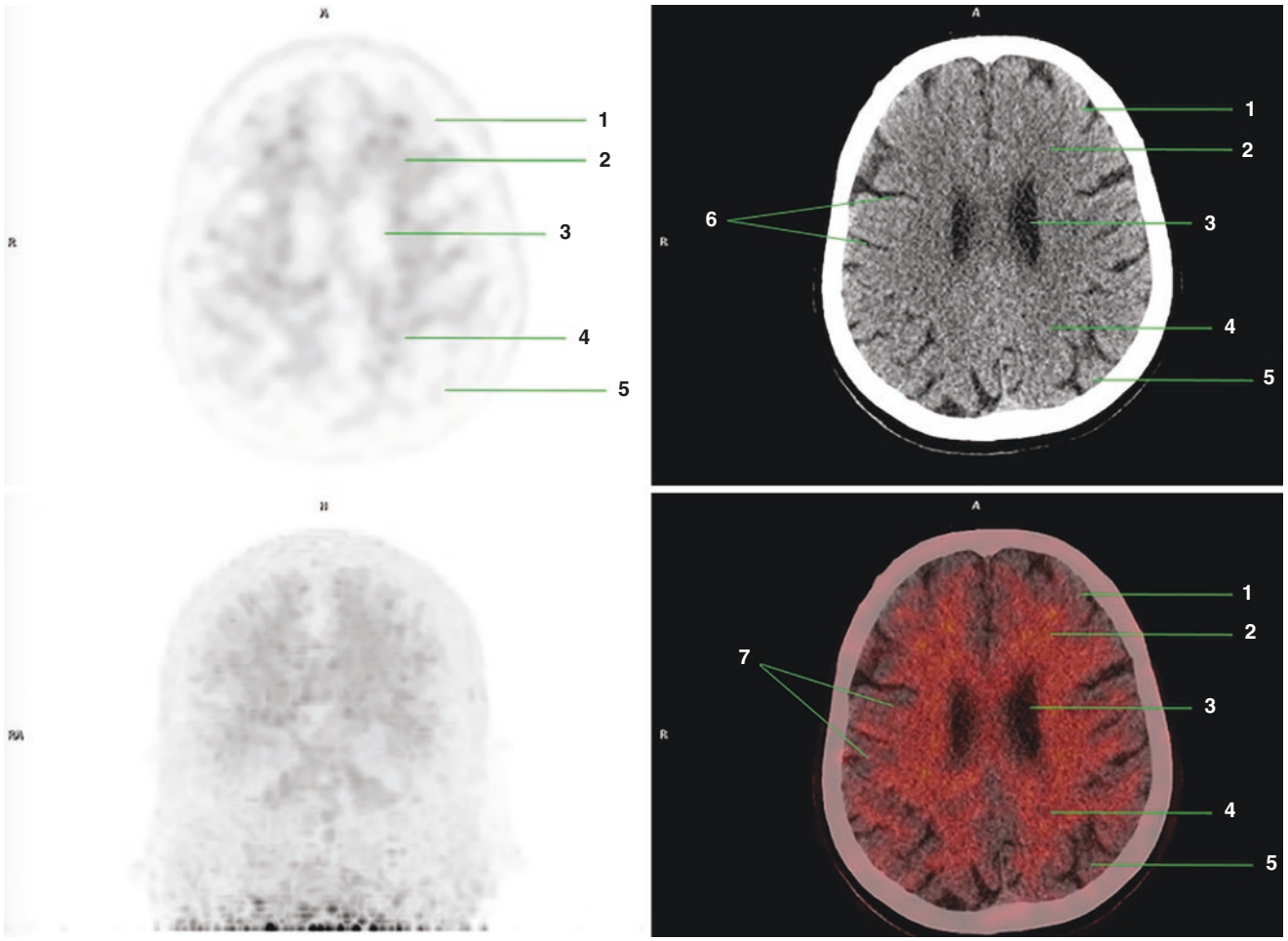

Fig. 108 1. Frontal lobe, gray matter
2. Frontal lobe, white matter
3. Lateral ventricle
4. Parietal lobe, white matter
5. Parietal lobe, gray matter
6. Brain sulci
7. Brain gyri

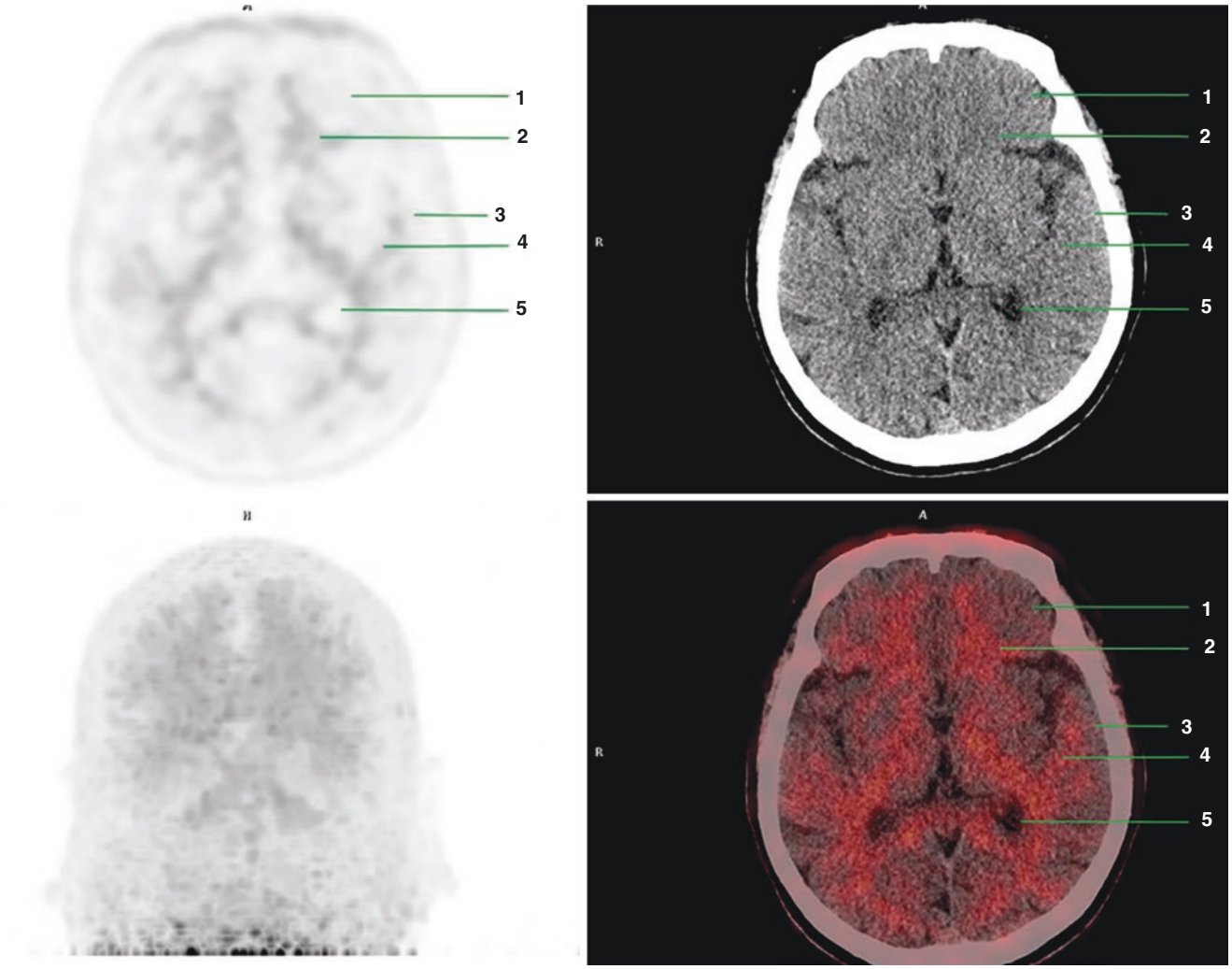

Fig. 109 1. Frontal lobe, gray matter
2. Frontal lobe, white matter
3. Temporal lobe, gray matter
4. Temporal lobe, white matter
5. Lateral ventricle

2.6.2 Case 2

A 71-year-old female showed memory loss symptoms. ^{11}C-PIB PET/CT was performed on a suspicion of dementia and images showed diffusely increased uptake in the gray matter and basal ganglia, which are consistent with the diagnosis of Alzheimer's disease (Figs. 110 and 111) [71].

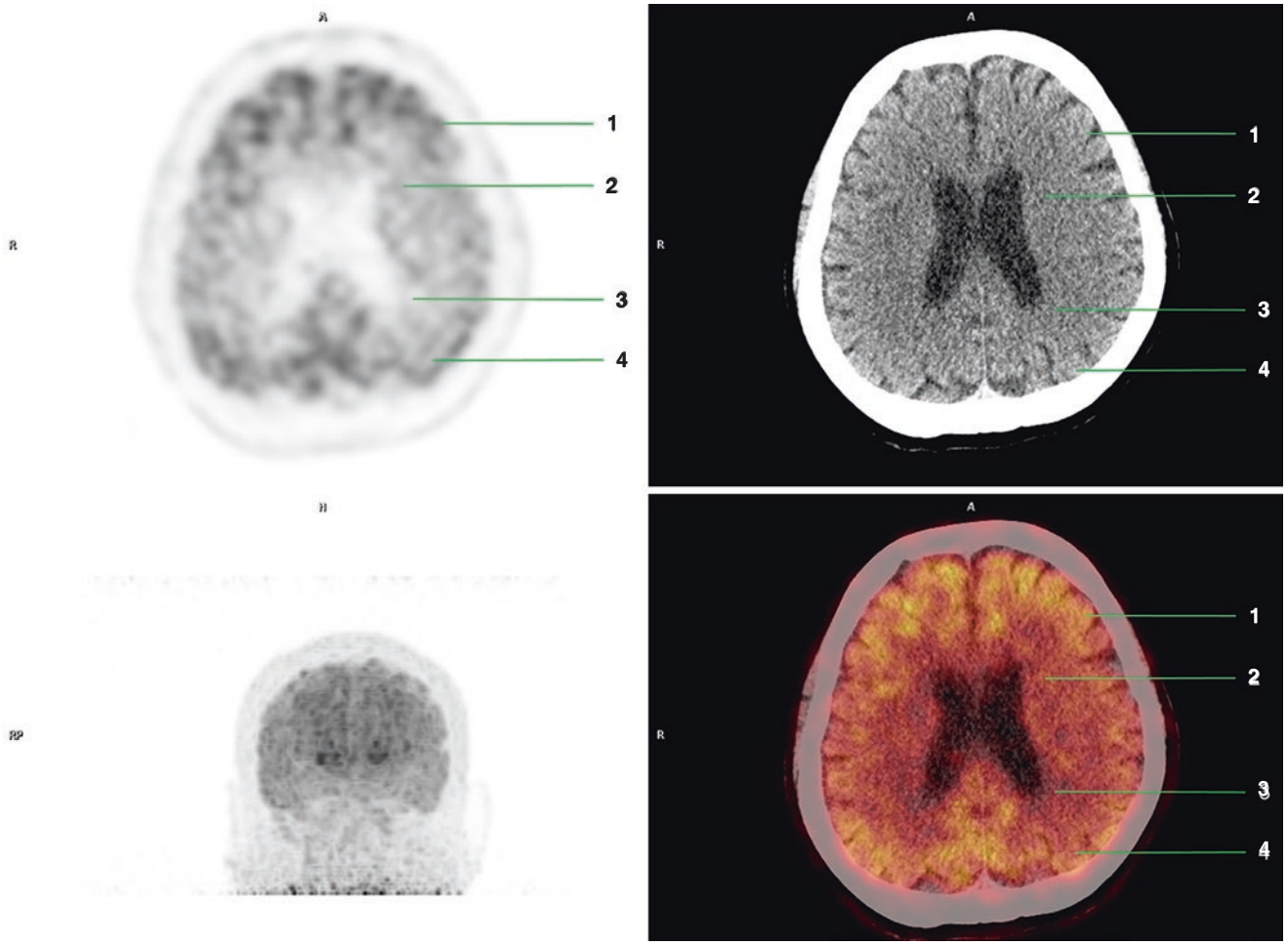

Fig. 110 1. Frontal lobe, gray matter
2. Frontal lobe, white matter
3. Parietal lobe, white matter
4. Parietal lobe, gray matter

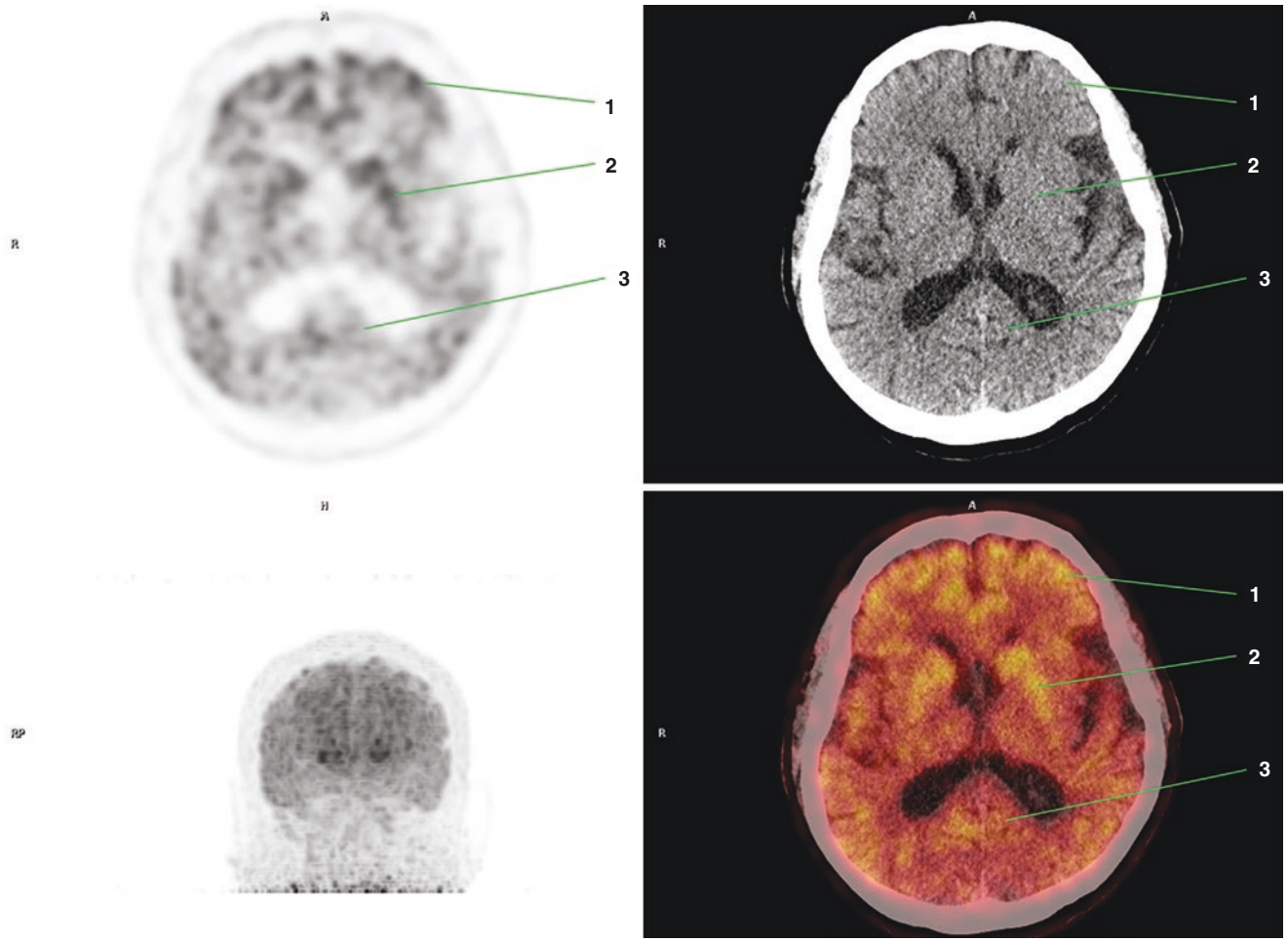

Fig. 111 1. Frontal cortex
2. Caudate putamen
3. Posterior cingulate

2.7 ^{18}F-FP-CIT PET/CT

2.7.1 Case 1

A 66-year-old male patient suffering from tremor for 2 months. ^{18}F-FP-CIT PET/CT was performed, finding marked increased uptake in the caudate nucleus, putamen, and midbrain. The patient was diagnosed with essential tremor (Figs. 112 and 113) [72].

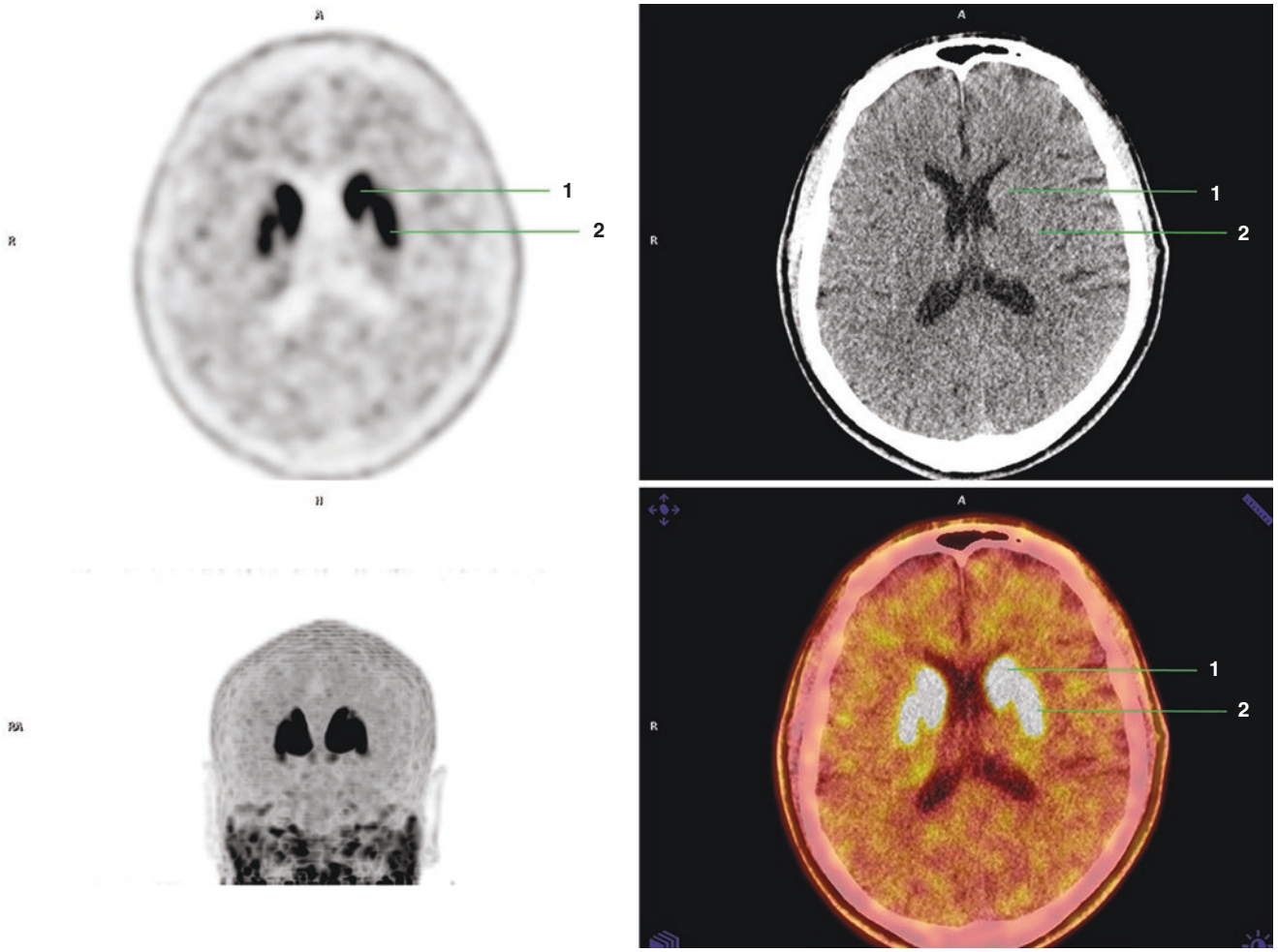

Fig. 112 1. Head of caudate nucleus
2. Putamen + globus pallidus

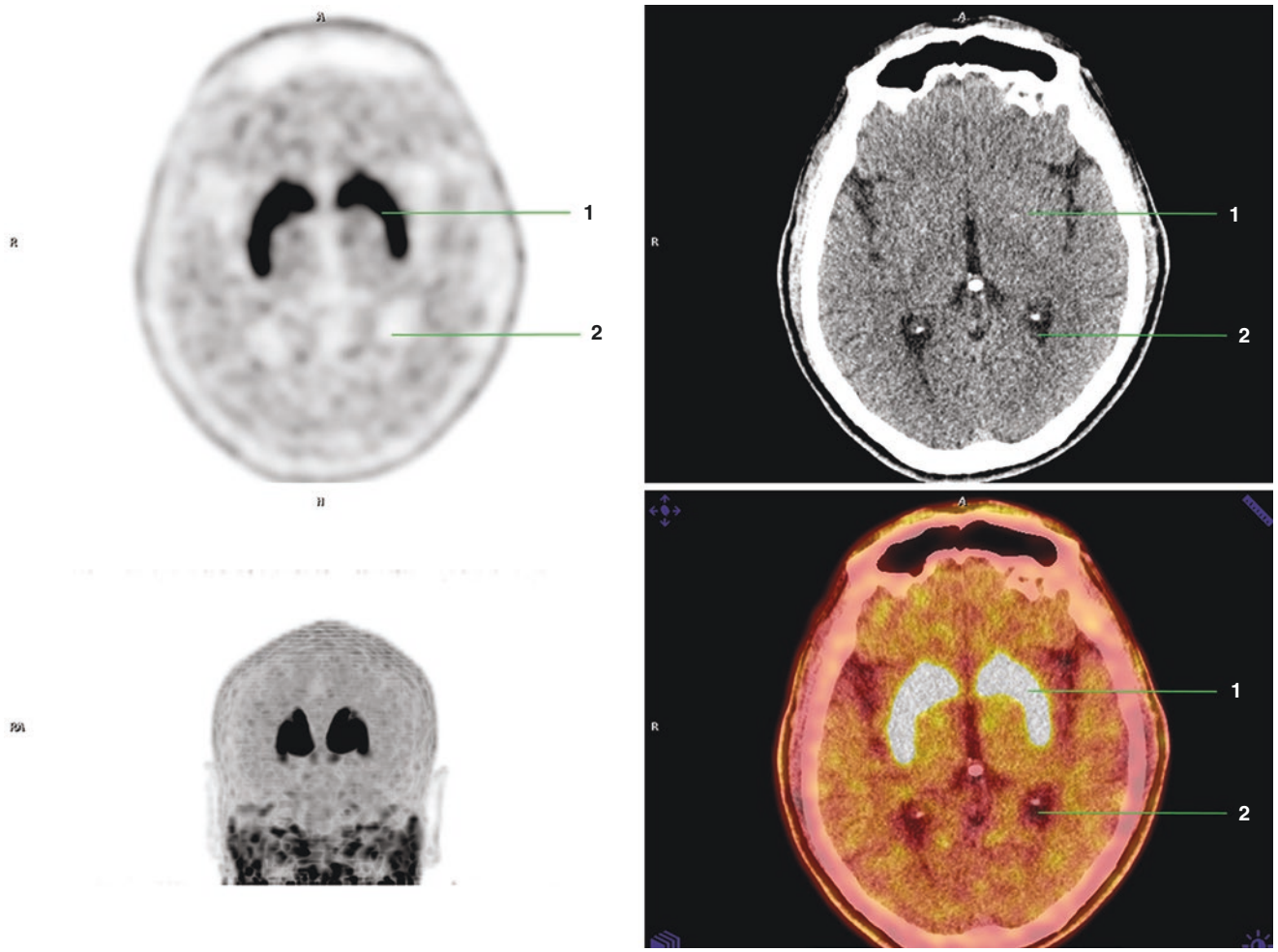

Fig. 113 1. Putamen + globus pallidus
2. Lateral ventricle

2.7.2 Case 2

A 54-year-old male patient with a known diagnosis of Parkinson's disease, who underwent ^{18}F-FP-CIT PET/CT in routine checkup. Images showed decreased activity in the bilateral putamina, mainly in the dorsal portion, which are the characteristic findings of Parkinson's disease (Figs. 114 and 115) [72].

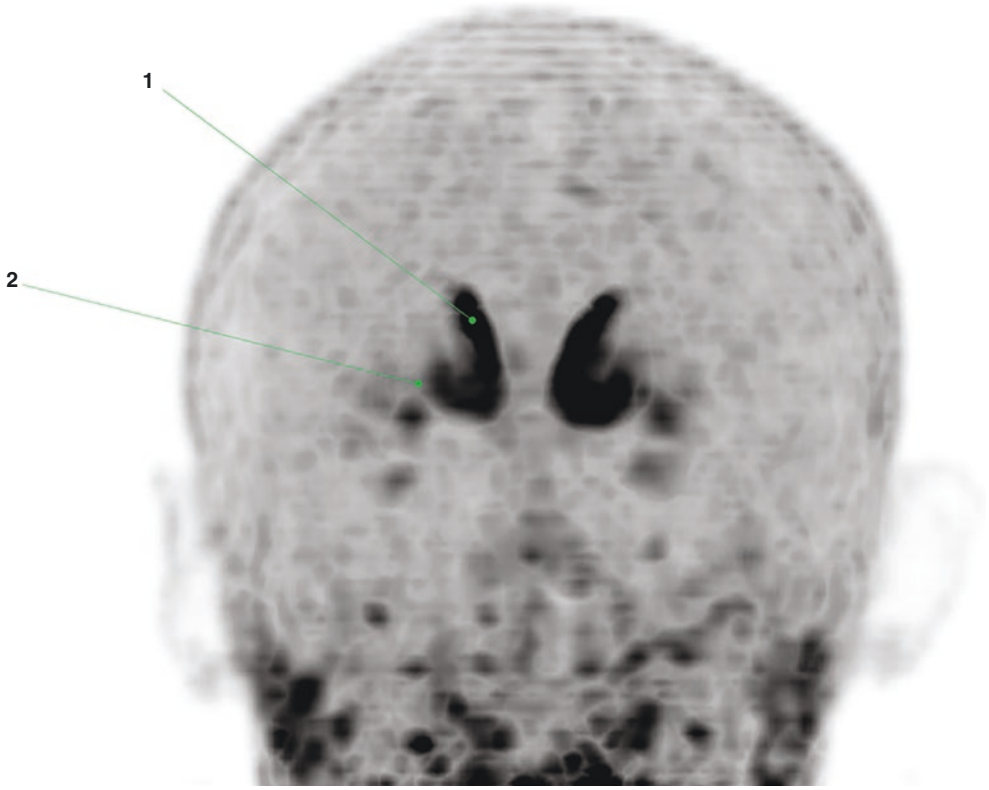

Fig. 114 1. Caudate nucleus
2. Putamen (decreased uptake)

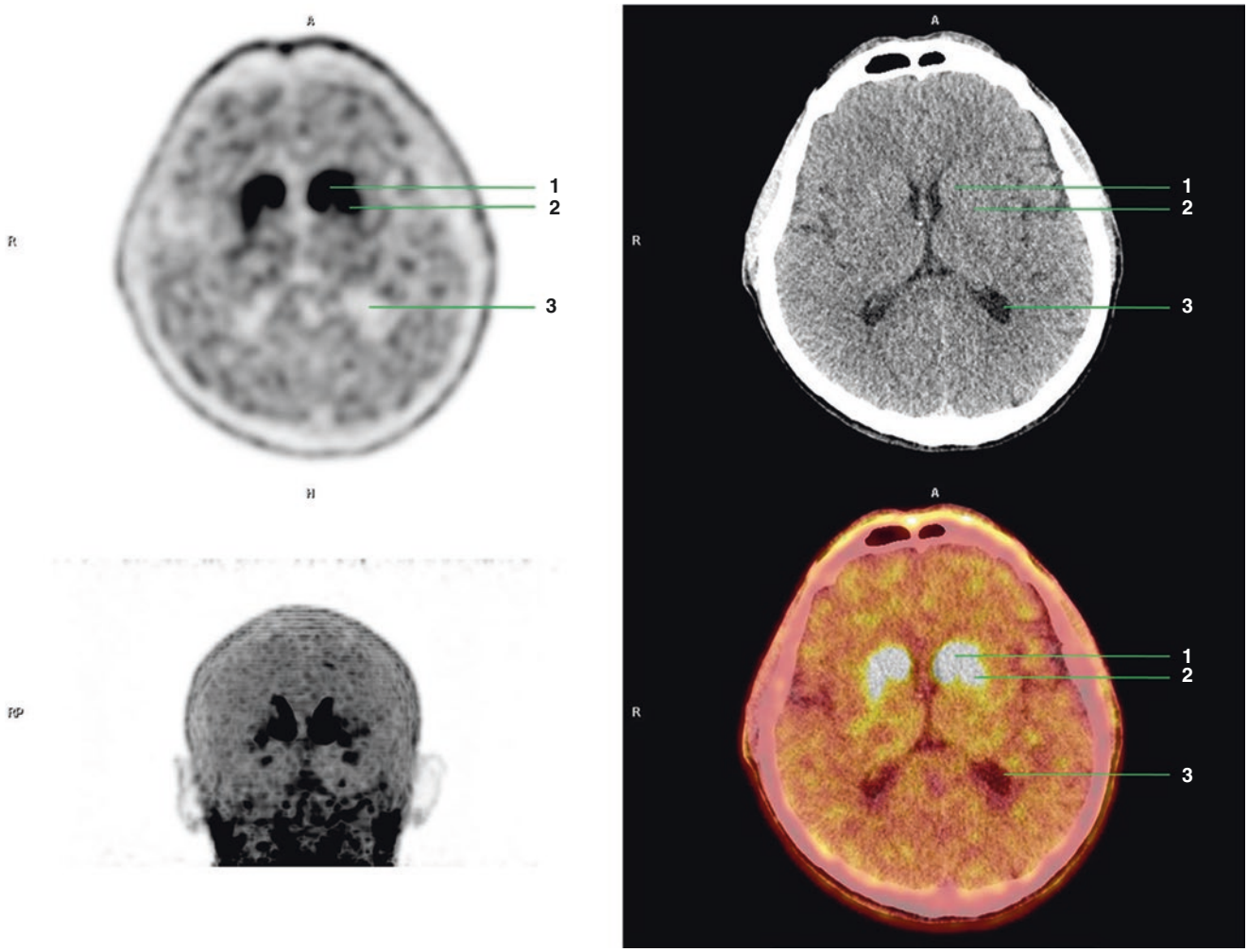

Fig. 115 1. Head of caudate nucleus
2. Putamen (decreased uptake in dorsal portion)
3. Lateral ventricle, posterior horn

2.8 ^{18}F-Flumazenil PET/CT

2.8.1 Case 1

A 39-year-old man with a history of epilepsy diagnosed during childhood, who underwent a ^{18}F-flumazenil PET/CT for follow-up. Images showed normal findings which consist of diffusely increased uptake in the cerebral cortex and relatively mildly increased uptake in the basal ganglia (Figs. 116 and 117) [70].

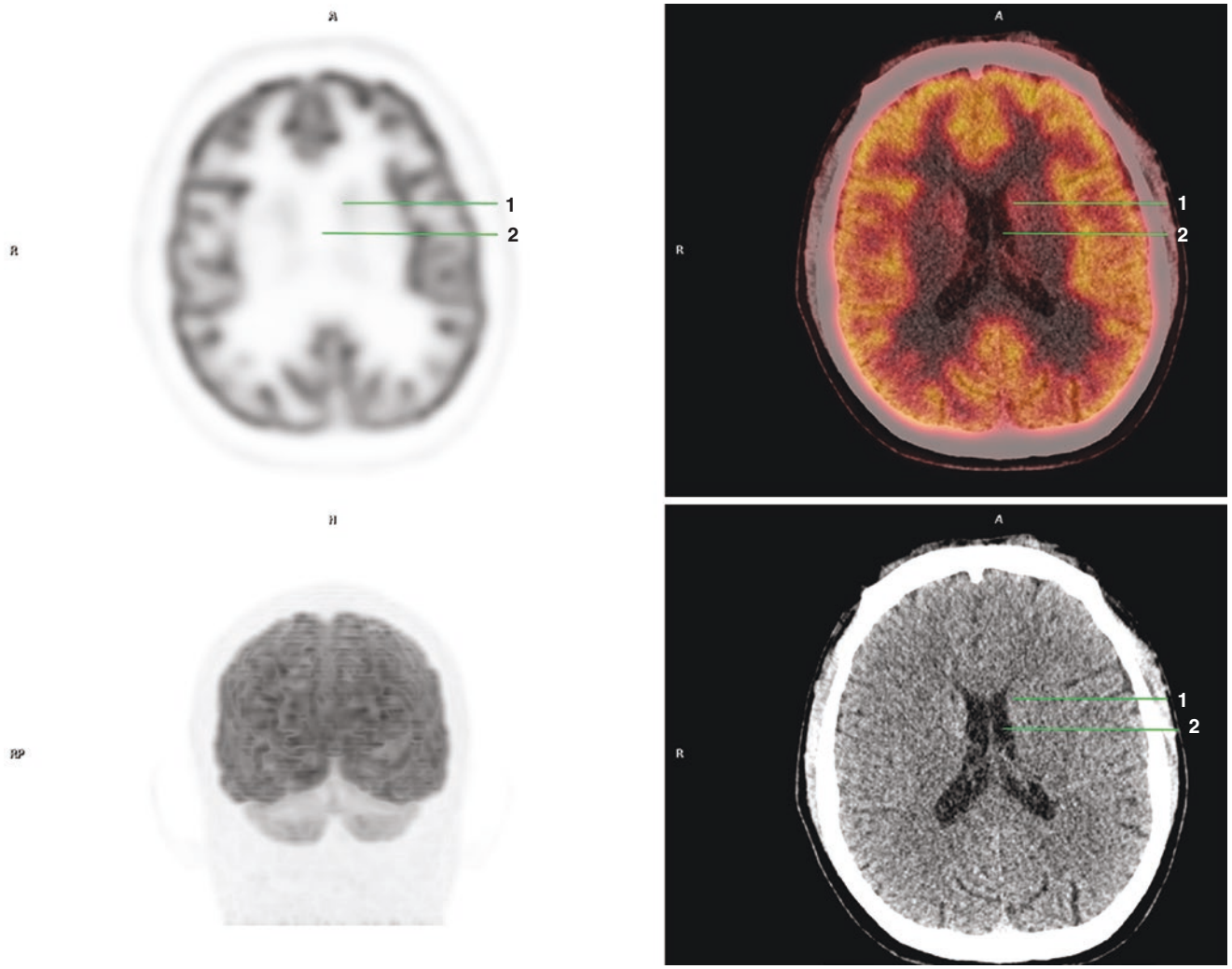

Fig. 116 1. Caudate nucleus
2. Lateral ventricle

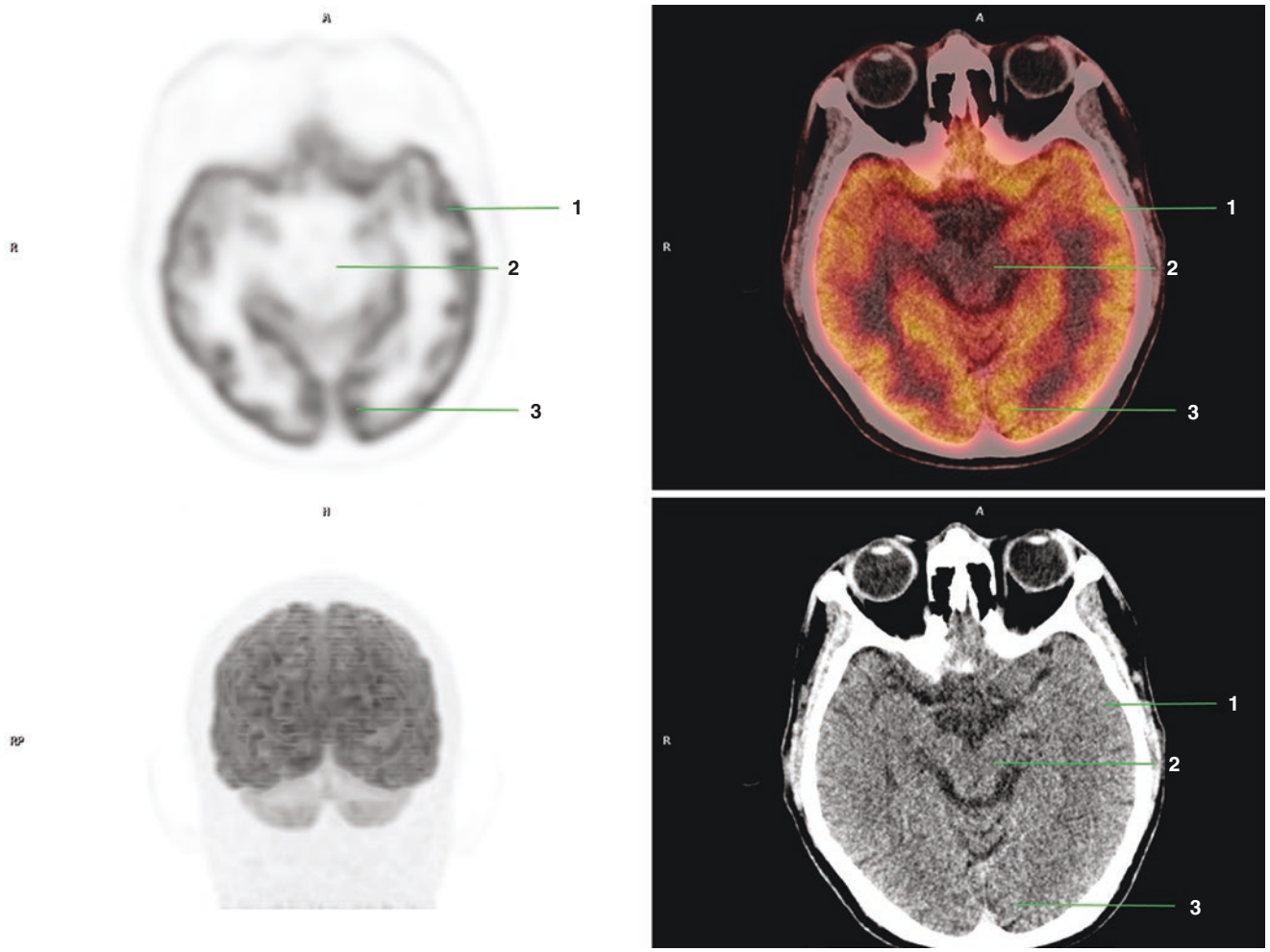

Fig. 117 1. Temporal cortex
2. Midbrain
3. Occipital cortex

2.9 ^{68}Ga-Arginine-Glycine-Aspartic Acid (RGD) PET/CT

2.9.1 Case 1

A 50-year-old female patient with biopsy proven breast cancer. ^{68}Ga-arginine-glycine-aspartic acid (RGD) PET/CT was done for staging. Images showed focal increased activity in the left breast at the primary tumor, as well as in an enlarged LN at the left axillary level I. These lesions were confirmed as infiltrating ductal carcinoma and metastatic LN. Mild uptake was found in the right thyroid gland, which was proved to be a benign nodule (Figs. 118 and 119) [73].

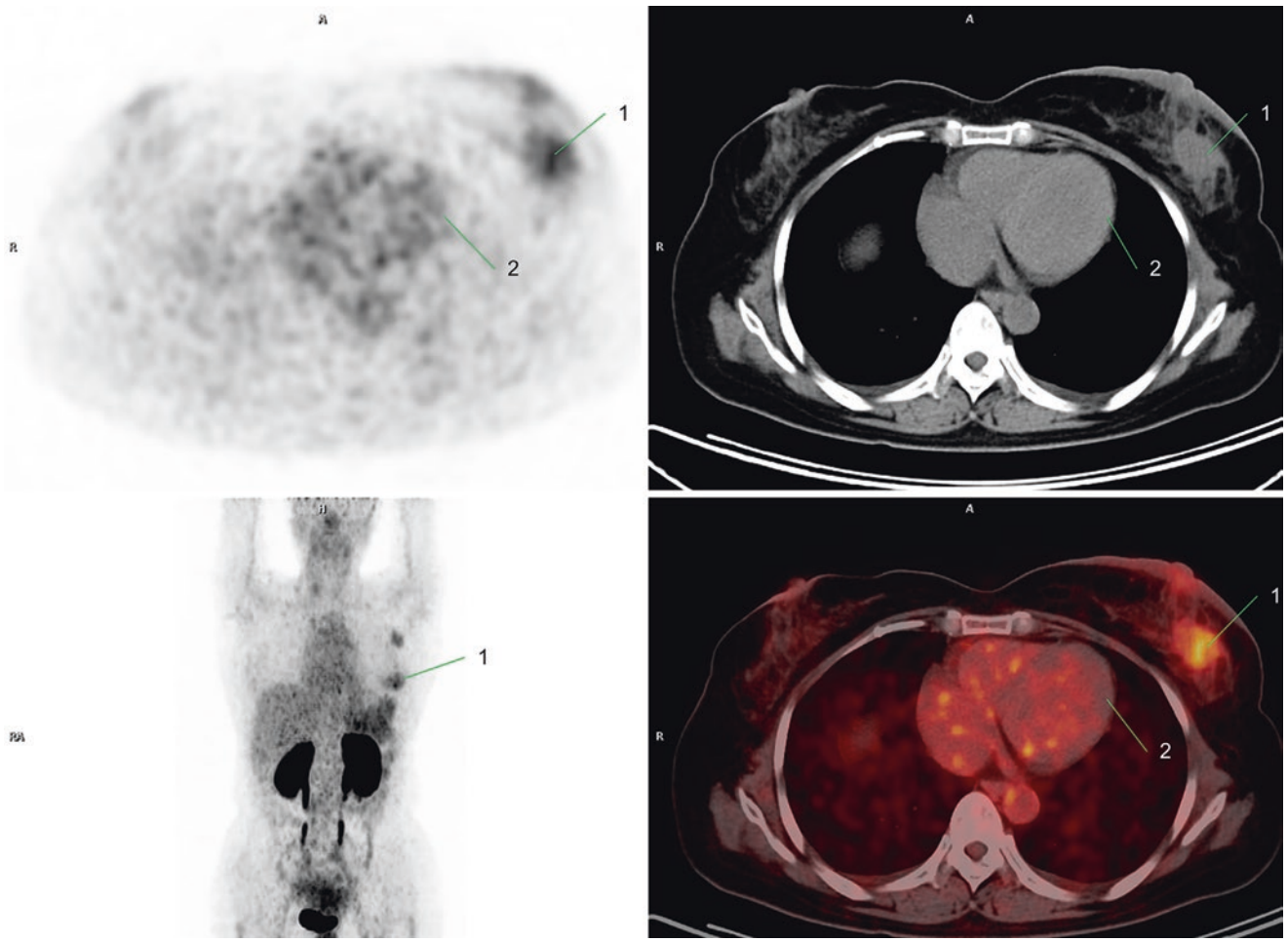

Fig. 118 1. Metabolically active left breast cancer
2. Myocardium, left ventricle

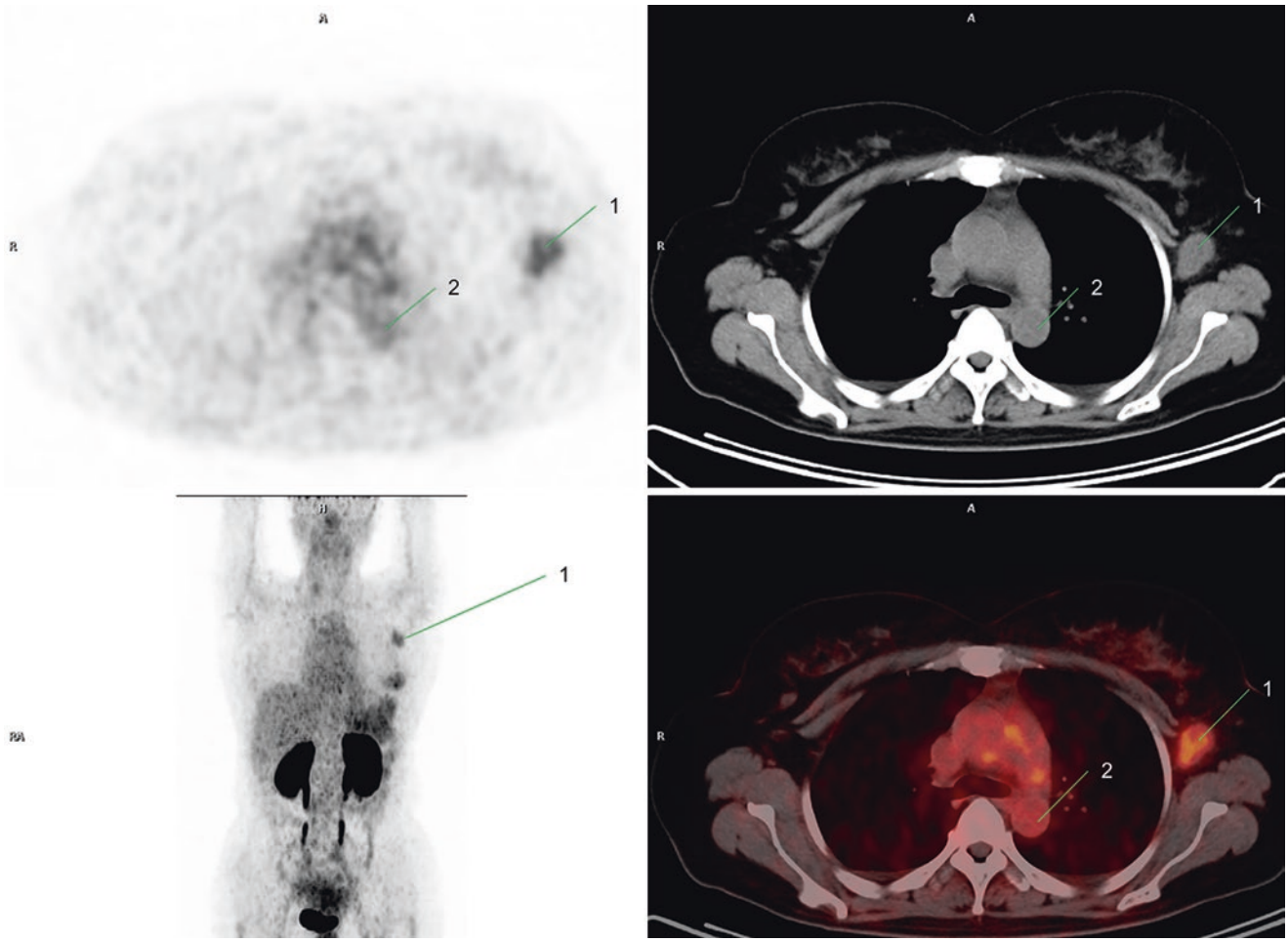

Fig. 119 1. Hypermetabolic LN metastasis in the left axillary level I
2. Descending aorta

2.10 ^{18}F-Florbetaben PET/CT

2.10.1 Case 1

^{18}F-florbetaben-PET/CT represents a very important diagnostic tool for the diagnosis and follow-up of patients with Alzheimer's disease, which is used to estimate β-amyloid plaque deposits. Visual assessment, which has a high sensitivity and specificity, is made according to the differential uptake between gray matter and white matter. When the differentiation is preserved, as in the figure on the left, a normal study is considered. However, when the differentiation is not clear and there is diffuse uptake in the gray matter, as the figure in the right, the presence of β-amyloid deposits is confirmed (Fig. 120) [70].

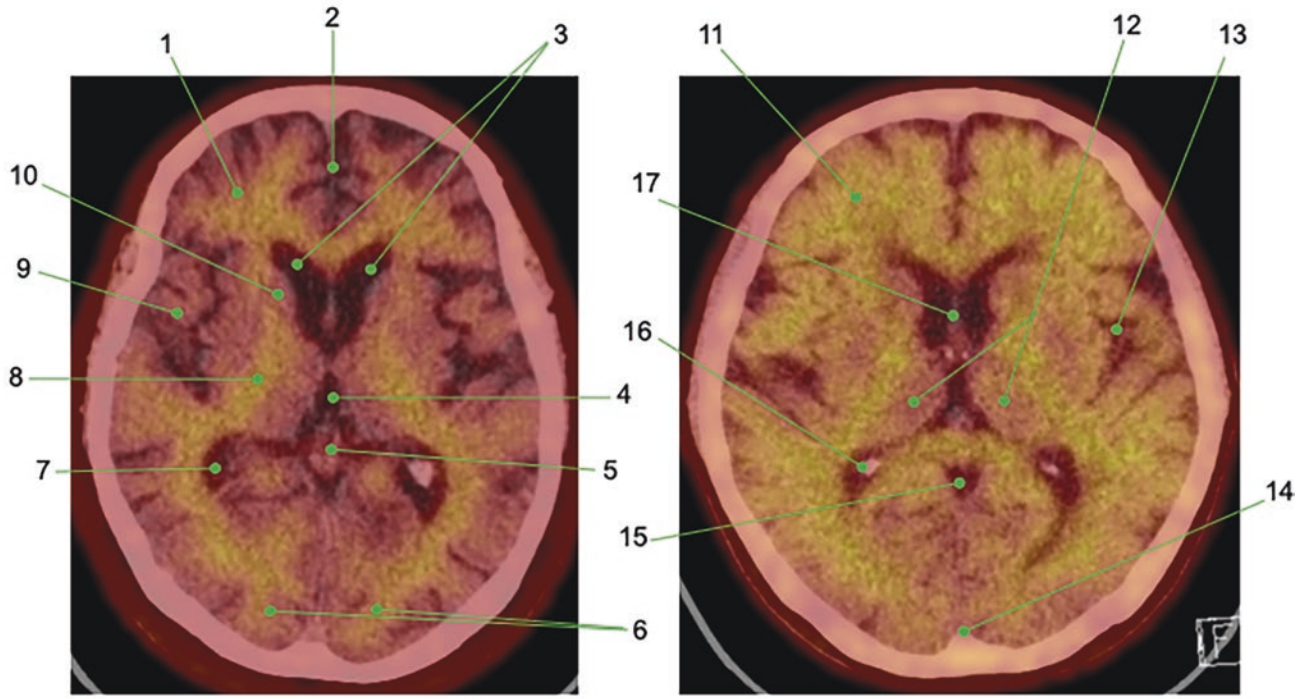

Fig. 120 1. Right frontal lobe: preserved gray matter–white matter differentiation, normal study
2. Falx cerebri, median interhemispheric fissure
3. Frontal horns of lateral ventricles
4. Third ventricle
5. Pineal gland
6. Visual cortex
7. Right occipital horn of lateral ventricle
8. Posterior limb of the right internal capsule
9. Right insular cortex
10. Head of the right caudate nucleus
11. Right frontal lobe: loss of gray matter - white matter differentiation, abnormal study
12. Talami
13. Left Sylvian fissure
14. Torcula Herophili (confluence of the sinuses)
15. Fourth ventricle
16. Choroid plexus calcification at the right lateral ventricle
17. Septum pellucidum

2.11 ^{18}F-Florastamin PET/CT

2.11.1 Case 1

A 64-year-old man with a history of prostate cancer, currently in biochemical relapse. ^{18}F-florastamin PET/CT was performed for further evaluation, finding multiple prostate-specific membrane antigen (PSMA) avid metastatic lymph nodes in the neck, mediastinum, retroperitoneum and iliac chains, as well as bilateral lung and liver metastasis. Prostate-specific membrane antigen (PSMA) is a transmembrane glycoprotein overexpressed in prostate cancer cells. Multiple radiolabeled molecules that bind to it, such as ^{18}F-florastamin, have emerged and currently represent the diagnostic standard for prostate cancer diagnosis (Fig. 121) [74].

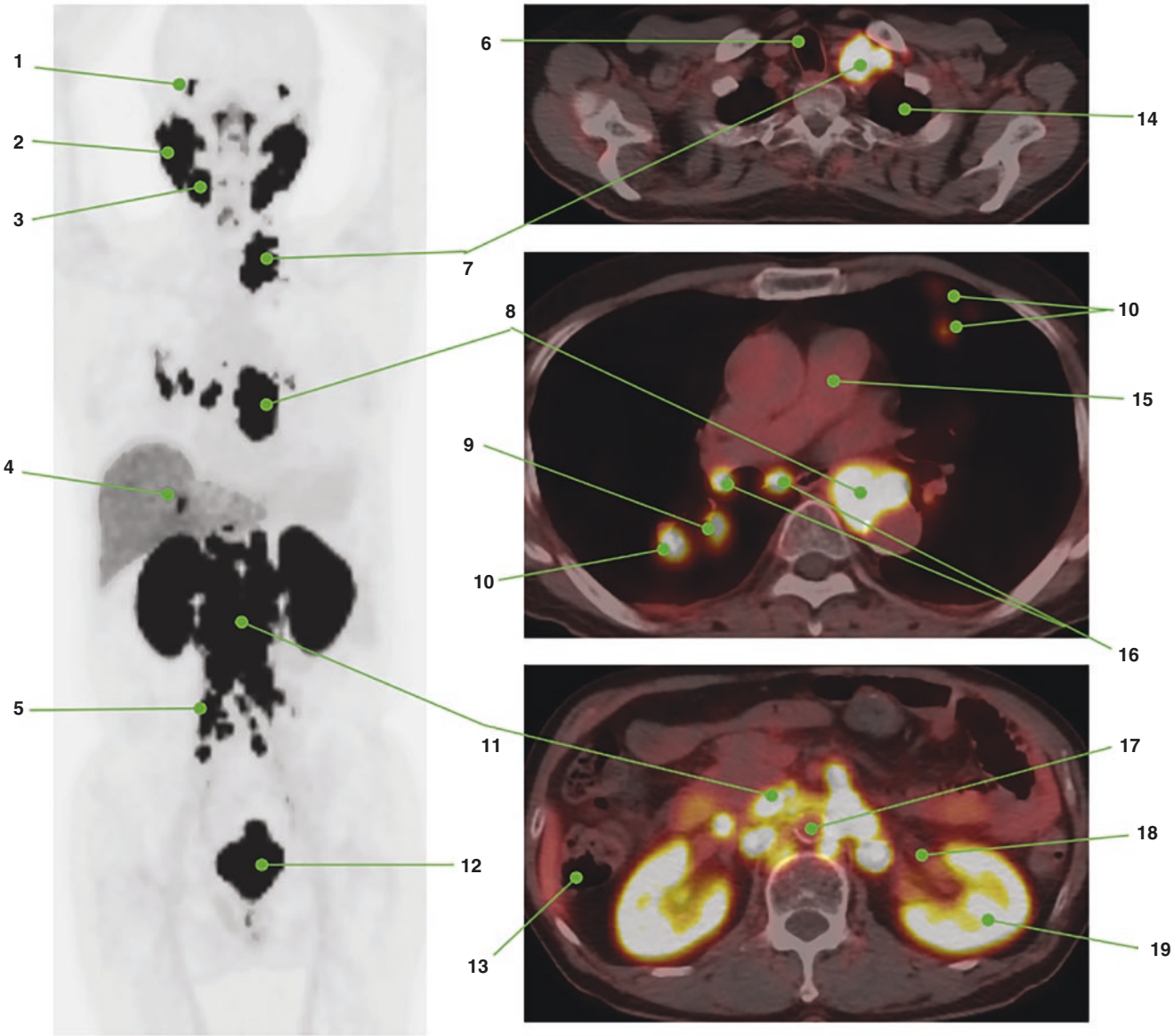

Fig. 121 1. Physiologic uptake in lacrimal glands
2. Physiologic uptake in parotid glands
3. Physiologic uptake in submandibular glands
4. PSMA avid liver metastasis
5. Metastatic lymph nodes in right iliac chain
6. Trachea
7. Metastatic lymph nodes, left supraclavicular notch
8. Metastatic mediastinal lymph nodes, 10L
9. Metastatic mediastinal lymph nodes, 11R
10. PSMA avid lung metastases
11. Metastatic retroperitoneal lymph nodes
12. Bladder
13. Ascending colon
14. Left lung apex
15. Main pulmonary artery
16. Metastatic mediastinal lymph nodes, 10R
17. Abdominal aorta
18. Left renal vein
19. Left kidney

2.12 ^{18}F-FDOPA PET/CT

2.12.1 Case 1

A 47-year-old woman with diagnosis of multiple endocrine neoplasia type 2 (MEN2) who underwent an ^{18}F-FDOPA PET/CT during follow-up. Images showed focal increased activity in both thyroid lobes, where suspicious heterogeneous nodules were identified on CT and US. Total thyroidectomy and lymph node dissection were performed, with a final diagnosis of bilateral medullary thyroid carcinoma (Fig. 122).

2.12.2 Case 2

A 31-year-old woman who consulted for abnormal sweating, dizziness, and occasional palpitations. At physical examination she was hypertensive, so the diagnosis of pheochromocytoma was suspected and ^{18}F-FDOPA PET/CT was performed for evaluation. Images showed marked increased activity in a left adrenal mass with heterogeneous enhancement in contrast images due to the presence of necrosis, with typical findings of a pheochromocytoma (Fig. 123).

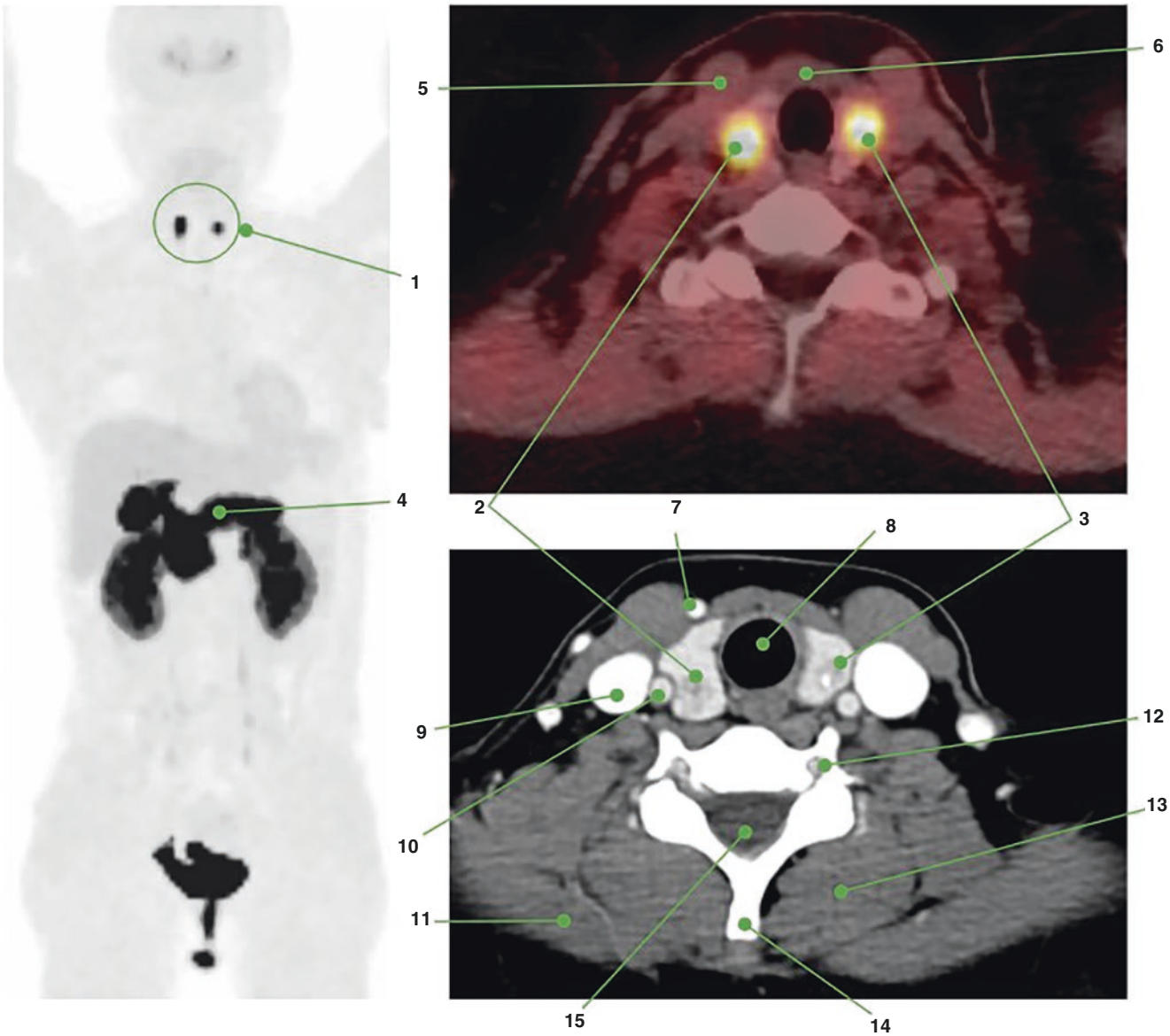

Fig. 122 1. Focal increased uptake in bilateral thyroid lobes
2. Metabolically active heterogeneous nodule in the right thyroid lobe
3. Metabolically active heterogeneous nodule with calcifications in the left thyroid lobe
4. Pancreas, physiologic activity
5. Right sternocleidomastoid muscle
6. Strap muscles
7. Right external jugular vein
8. Trachea
9. Right internal jugular vein
10. Right common carotid artery
11. Right trapezius muscle
12. Left vertebral artery
13. Left paravertebral space, paravertebral muscles
14. Cervical spinous process
15. Spinal canal

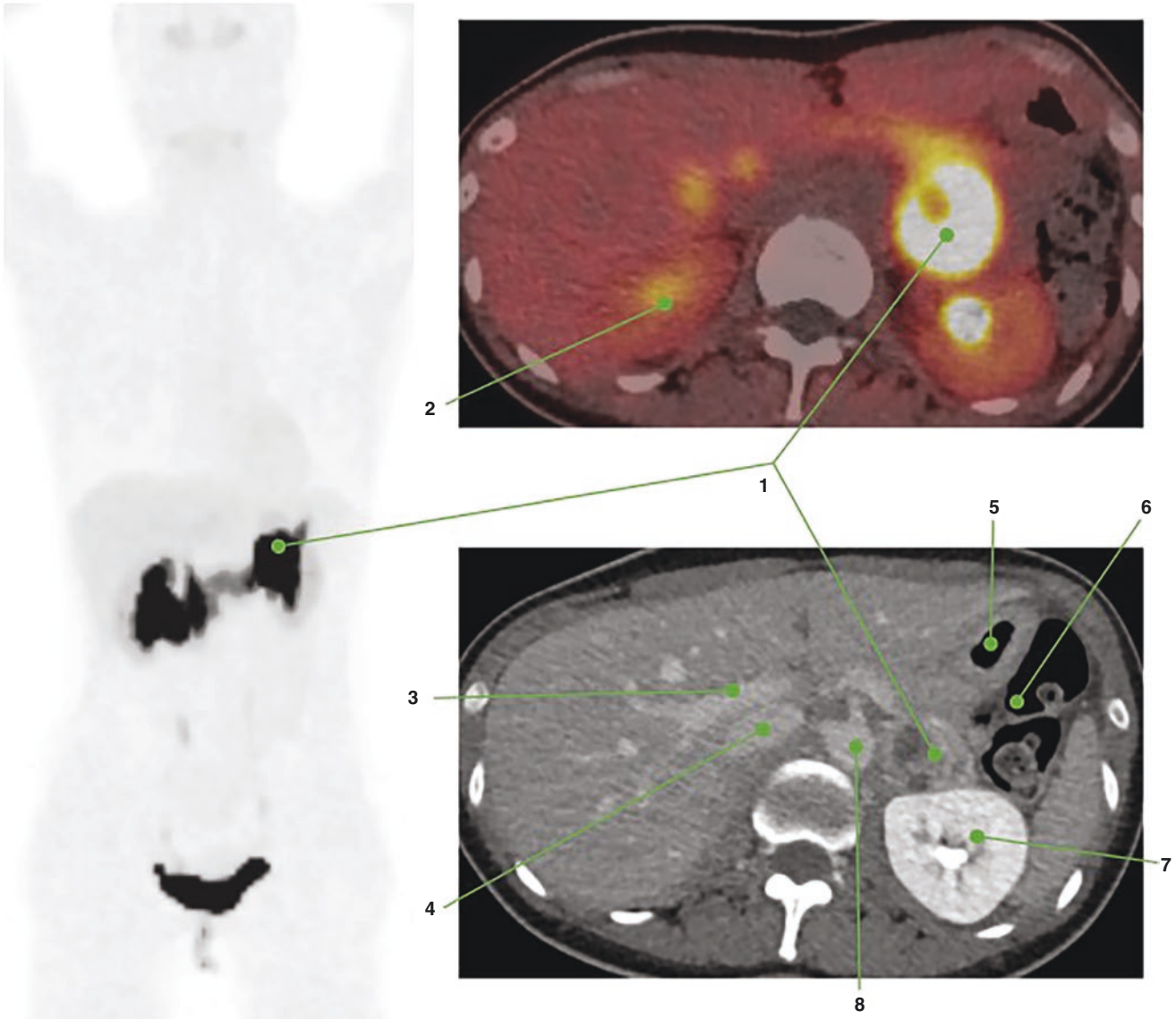

Fig. 123 1. Marked metabolically active left adrenal necrotic mass
2. Right kidney
3. Main portal vein
4. Inferior vena cava
5. Stomach
6. Proximal descending colon
7. Left kidney
8. Abdominal aorta

2.13 ^{18}F-Choline PET/CT

2.13.1 Case 1

A 44-year-old man who attended an annual checkup finding elevated PSA (9.53 ng/ml). Digital rectal examination was normal, as well as prostate volume (36 cc). However, multiparametric MRI showed a 2 cm PI RADS 5 lesion on the right side of the peripheral zone. Posterior biopsy confirmed the diagnosis of adenocarcinoma and an ^{18}F-choline PET/CT scan was performed for staging. Images showed focal increased activity in the right peripheral zone at the primary tumor location. No metabolically active metastases were noted (Fig. 124) [70, 66].

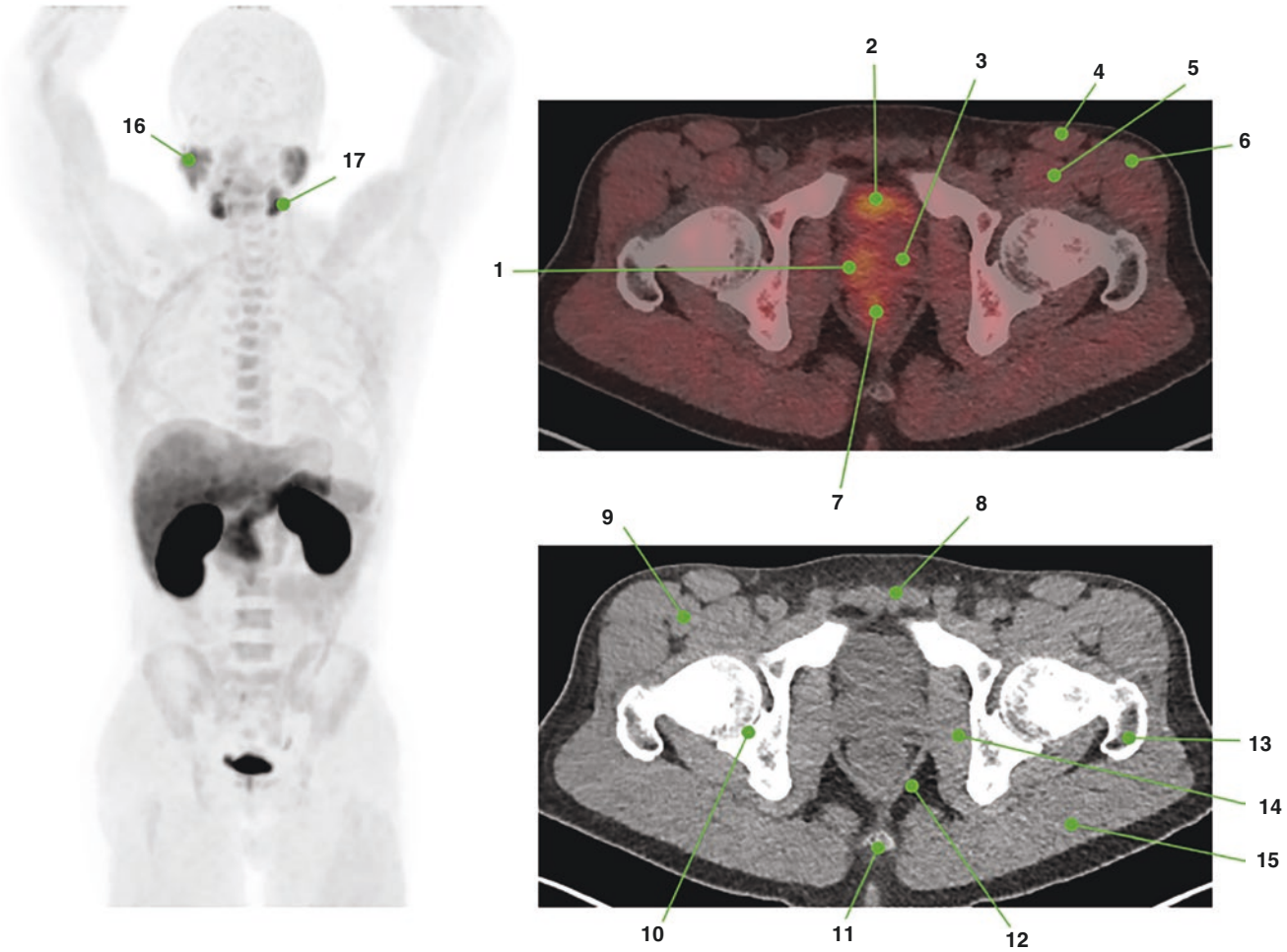

Fig. 124 1. Focal increased activity in the right peripheral zone at primary tumor
2. Bladder
3. Left prostate lobe
4. Left sartorius muscle
5. Left iliopsoas muscle
6. Left tensor fascia lata muscle
7. Rectum
8. Rectus abdominis muscles
9. Right rectus femoris muscle
10. Right coxofemoral joint
11. Coccix
12. Left levator ani muscle
13. Left femur, greater trochanter
14. Left internal obturator muscle
15. Left gluteus maximus muscle
16. Right parotid gland
17. Left submandibular gland

References

1. Kapoor V, McCook BM, Torok F. An introduction to PET-CT imaging. RadioGraphics. 2004;24:523–43.
2. Walrand S, Hesse M, Jamar F. Update on novel trends in PET/CT technology and its clinical applications. Br J Radiol. 2016;89:20160534.
3. Salaun PY, Abgral R, Mallard O, Querellou-Lefranc S, Quere G, Wartski M, et al. Good clinical practice recommendations for the use of PET/CT in oncology. Eur J Nucl Med Mol Imaging. 2020;47:28–50.
4. Voltin CA, Mettler J, Grosse J, Dietlein M, Baues C, Schmitz C, et al. FDG-PET imaging for Hodgkin and diffuse large B-cell lymphoma-an updated overview. Cancers. 2020;12(3):601.
5. Hadique S, Jain P, Hadi Y, et al. Utility of FDG PET / CT for assessment of lung nodules identified during low dose computed tomography screening. BMC Med Imaging. 2020;20:69.
6. Matteucci F, Paganelli G, Martinelli G, Cerchione C. PET/CT in multiple myeloma: beyond FDG. Front Oncol. 2021;25(10):622501.
7. Nikolova PN, Hadzhiyska VH, Mladenov KB, Ilcheva MG, Veneva S, Grudeva VV, et al. The impact of 18F-FDG PET/CT in the clinical management of patients with lymph node metastasis of unknown primary origin. Neoplasma. 2021;68(1):180–9.
8. El-Shourbagy KH, Mashaly EM, Khodair SA, et al. PET / CT in restaging, prognosis, and recurrence in patients with malignant melanoma. Egypt J Radiol Nucl Med. 2020;51:167.
9. Grosse J, Hellwig D. PET / CT und PET / MRT bei Tumoren des Kopf-Hals-Bereichs [PET / CT and PET / MRI in head and neck cancer]. Laryngorhinootologie. 2020;99(1):12–21.
10. Kaseda K. Recent and current advances in FDG-PET imaging within the field of clinical oncology in NSCLC: a review of the literature. Diagnostics. 2020;10(8):561.
11. Adam JA, Loft A, Chargari C, et al. EANM / SNMMI practice guideline for [18F] FDG PET / CT external beam radiotherapy treatment planning in uterine cervical cancer v1.0. Eur J Nucl Med Mol Imaging. 2021;48:1188–99.
12. Jelercic S, Rajer M. The role of PET-CT in radiotherapy planning of solid tumors. Radiol Oncol. 2015;49(1):1–9.
13. Maffione AM, Rubello D, Caroli P, Colletti P, Matteucci F. Is it time to introduce PET / CT in colon cancer guidelines? Clin Nucl Med. 2020;45(7):525–30.
14. Bruzzi JF, Munden RF, Truong MT, Marom EM, Sabloff BS, Gladish GW, et al. PET / CT of esophageal cancer: its role in clinical management. RadioGraphics. 2007;27(6):1635–52.
15. Lan BY, Kwee SA, Wong LL. Positron emission tomography in hepatobiliary and pancreatic malignancies: a review. Am J Surg. 2012;204(2):232–41.
16. Dascălu RI, Nicolae P, Bolocan A, Ion D, Andronic O. The role of PET-CT in gastric cancer - a narrative review. Sudan J Med Sci (SJMS). 2020;15(3):332–44.
17. Giammarile F, Castellucci P, Dierckx R, et al. Non-FDG PET / CT in diagnostic oncology: a pictorial review. Eur J Hybrid Imaging. 2019;3:20.
18. Hasan O, Nguyen M, Son H, Puri S. Role of FDG PET/CT in detecting unsuspected brain metastases during routine staging work up in oncology practice and its impact on patient management. J Nucl Med. 2014;55(supplement 1):1303.
19. Ghosh PS, Tekautz T, Mitra S. Pearls & Oy-sters: bifocal germinoma of the brain. Neurology. 2012;78(2):e8–10.
20. Fernandez-Miranda JC, Gardner PA, Snyderman CH, Devaney KO, Mendenhall WM, Suárez C, et al. Clival chordomas: a pathological, surgical, and radiotherapeutic review. Head Neck. 2014;36(6):892–906.
21. Nakadate M, Yoshida K, Ishii A, Koizumi M, Tochigi N, Suzuki Y, et al. Is 18F-FDG PET/CT useful for distinguishing between primary thyroid lymphoma and chronic thyroiditis? Clin Nucl Med. 2013;38(9):709–14.
22. Murad V, Kim EE. 18F-FDG PET/CT evaluation of thymomas: a pictorial review. Nucl Med Mol Imaging. 2021; https://doi.org/10.1007/s13139-021-00705-7.
23. Chong S, Kim TS, Kim B-T, Cho EY, Kim J. Pulmonary artery sarcoma mimicking pulmonary thromboembolism: integrated FDG PET/CT. AJR. 2007;188:1691–3.
24. Pfau D, Smith DA, Beck R, Gilani KA, Gupta A, Caimi P, et al. Primary mediastinal large B-cell lymphoma: a review for radiologists. AJR. 2019;213(5):194–210.
25. Rosen EL, Eubank WB, Mankoff DA. FDG PET, PET/CT, and breast cancer imaging 1. RadioGraphics. 2007;27:S215–9.
26. Tateishi U, Hasegawa T, Kusumoto M, Yamazaki N, Linuma G, Muramatsu Y, et al. Metastatic angiosarcoma of the lung: spectrum of CT findings. AJR. 2003;180:1671–4.
27. Deng S, Sun X, Zhu Z, et al. Primary malignant melanoma of the lung: a case report and literature review. BMC Pulm Med. 2020;20:94.
28. Angirish B, Sanghavi P, Jankharia B. Pulmonary manifestations of lymphoma: a pictorial essay. Lung India. 2020;37(3):263–7.
29. Costa L, Queiroz M, Barbosa F, Nunes RF, Zaniboni EC, Mazo M, et al. Reassessing patterns of response to immunotherapy with PET: from morphology to metabolism. RadioGraphics. 2020;41(1):120–43.
30. Schwarz C, Lübbert H, Rahn W, Schönfeld N, Serke M, Loddenkemper R. Medical thoracoscopy: hormone receptor content in pleural metastases due to breast cancer. Eur Respir J. 2004;24:728–30.
31. Ko SM, Kim TH, Chun EJ, Kim JY, Hwang SH. Assessment of left ventricular myocardial diseases with cardiac computed tomography. Korean J Radiol. 2019;20(3):333–51.
32. Ulaner G, Lyall A. Identifying and distinguishing treatment effects and complications from malignancy at FDG PET/CT. RadioGraphics. 2013;33(6):1817–34.
33. Gaspar RC, Pauli JR, Shulman GI, Muñoz VR. An update on brown adipose tissue biology: a discussion of recent findings. Am J Physiol Endocrinol Metab. 2021;320(3):488–95.
34. Wagner T, Brechemier D, Duget E, Le Guellec SL, Julian A, Hitzel A, Beyne O. Diffuse pulmonary uptake on FDG-PET with normal CT diagnosed as intravascular large B-cell lymphoma: a case report and a discussion of the causes of diffuse FDG uptake in the lungs. Cancer Imaging. 2012;12(1):7–12.
35. Parihar A, Kumar R, Singh H, Mittal B. 18F-FDG PET/CT in Takayasu arteritis – active or inactive? J Nucl Med. 2020;61(supplement 1):643.
36. Lewis RB, Mehrotra AK, Rodriguez P, Levine MS. From the radiologic pathology archives: esophageal neoplasms: radiologic-pathologic correlation. RadioGraphics. 2013;33(4):1083–108.
37. Phongkitkarun S, Varavithya V, Kazama T, Faria SC, Mar MV, Podoloff DA, et al Lymphomatous involvement of gastrointestinal tract: evaluation by positron emission tomography with (18)F-fluorodeoxyglucose. World J Gastroenterol 2005;11(46):7284–7289.
38. Bărbulescu M, Alecu L, Boeţi P, Popescu I. Port-site metastasis after laparoscopic surgery for colorectal cancer--still a real concern? Case report and review of the literature. Chirurgia (Bucur). 2012;107(1):103–7. PMID: 22480124.
39. Lu RC, She B, Gao WT, Ji YH, Xu DD, Wang QS, et al. Positron-emission tomography for hepatocellular carcinoma: current status and future prospects. World J Gastroenterol. 2019;25(32):4682–95.
40. Sureshbabu W, Mawlawi O. PET/CT imaging artifacts. J Nucl Med Technol. 2005;33(3):156–61.
41. Martínez-de-Alegría A, Baleato-González S, García-Figueiras R, Bermúdez-Naveira A, Abdulkader-Nallib I, Díaz-Peromingo

JA. IgG4-related disease from head to toe. RadioGraphics. 2015;35(7):2007–25.
42. Chang MC, Chen JH, Liang JA, Huang WS, Cheng KY, Kao CH. PET or PET/CT for detection of peritoneal carcinomatosis: a meta-analysis. Clin Nucl Med. 2013;38(8):623–9.
43. Recht H, Solnes L, Merrill S, Siegelman S. 18-FDG PET/CT findings in hemophagocytic lymphohistiocytosis: a pictorial review. J Nucl Med. 2020;61(supplement 1):1140.
44. Dickson PV, Sims TL, Streck CJ, et al. Avoiding misdiagnosing neuroblastoma as Wilms tumor. J Pediatr Surg. 2008;43(6):1159–63.
45. Wang HY, Ding HJ, Chen JH, et al. Meta-analysis of the diagnostic performance of [18F]FDG-PET and PET/CT in renal cell carcinoma. Cancer Imaging. 2012;12:464–74.
46. Almodovar S, Israel D, Sakellis C. PET/CT findings of renal lymphoma. J Nuc Med. 2008;49(supplement 1):175.
47. Zattoni F, Incerti E, Dal Moro F, Moschini M, Castellucci P, Panareo S. 18F-FDG PET/CT and urothelial carcinoma: impact on management and prognosis-a multicenter retrospective study. Cancers. 2019;11(5):700.
48. Shen G, Liu J, Hao Z, Huang R, Kuang A. Is 18F-FDG PET/CT a useful tool in prostate cancer? J Nucl Med. 2017;58(supplement 1):1077.
49. Lian L, Wang C, Tian JL. IgG4-related retroperitoneal fibrosis: a newly characterized disease. Int J Rheum Dis. 2016;19(11):1049–55.
50. Nowakowski GS, Czuczman MS. ABC, GCB, and double-hit diffuse large B-cell lymphoma: does subtype make a difference in therapy selection? Am Soc Clin Oncol Educ Book. 2015:e449–57. https://doi.org/10.14694/EdBook_AM.2015.35.e449.
51. Phin EY, Anthony M-P, Yu-Hung A, Loong F, Khong P-L. Utility of FDG PET/CT in the assessment of myeloid sarcoma. AJR. 2012;198:1175–9.
52. Murad V, Kim EE. Uterine endometrial stromal sarcoma on MRI and 18F-FDG PET/CT: a case report with literature review. J Med Imaging Case Rep. 2021;5(1):3–5.
53. Narayanan P, Sahdev A. The role of 18F-FDG PET CT in common gynaecological malignancies. Br J Radiol. 2017;90:1079.
54. Pectasides D, Pectasides E, Economopoulos T. Fallopian tube carcinoma: a review. Oncologist. 2006;11(8):902–12.
55. Nakatani K, Nakamoto Y, Togashi K. Unilateral physiological FDG uptake in teres minor muscle seems well associated with IV tracer injection procedures. Clin Nucl Med. 2015;40(1):62–4.
56. Lin N, Song Y, Zheng W, Tu M, Xie Y, Wang X, et al. Non-upper aerodigestive tract NK/T- cell lymphoma: an analysis of clinical features and survival from a single center in China. Zhonghua Xue Ye Xue Za Zhi. 2015;36(1):29–33.
57. Lin M, Kilanowska J, Taper J, Chu J. Neurolymphomatosis—diagnosis and assessment of treatment response by FDG PET-CT. Hematol Oncol. 2008;26:43–5.
58. Liu F, Zhang Q, Zhou D, Dong J. Effectiveness of 18F-FDG PET/CT in the diagnosis and staging of osteosarcoma: a meta-analysis of 26 studies. BMC Cancer. 2019;19(1):323.
59. Gengler C, Guillou L. Solitary fibrous tumor and hemangiopericytoma: evolution of a concept. Histopathology. 2006;48(1):63–74.
60. Lee K, Kim KW, Ko Y, Park HY, Chae EJ, Lee JH, et al. Comprehensive updates in the role of imaging for multiple myeloma management based on recent international guidelines. Korean J Radiol. 2021;22:80.
61. Kivrak AS, Koc O, Emlik D, Kiresi D. Differential diagnosis of dumbbell lesions associated with spinal neural foraminal widening: imaging features. Eur J Radiol. 2008;71(1):29–41.
62. Sambri A, Bianchi G, Longhi A, Righi A, Donati DM, Nanni C, et al. The role of 18F-FDG PET/CT in soft tissue sarcoma. Nucl Med Commun. 2019;40(6):626–31.
63. O'Regan K, Hall M, Jagannathan J, Giardino A, Kelly P, Butrynski J, et al. Imaging of radiation- associated sarcoma. AJR. 2011;197:30–6.
64. Han EJ, Jang YS, Lee IS, Lee JM, Kang S, Kim HS. Muscular sarcoidosis detected by F-18 FDG PET/CT in a hypercalcemic patient. J Korean Med Sci. 2013;28(9):1399–402.
65. Rais-Bahrami S, Efstathiou JA, Turnbull CM, et al. ^{18}F-Fluciclovine PET/CT performance in biochemical recurrence of prostate cancer: a systematic review. Prostate Cancer Prostatic Dis. 2021; https://doi.org/10.1038/s41391-021-00382-9.
66. Junaid M, Sun M, Skafida M, Obaid M, Ivanidze J, Osborne J, et al. Review of commonly used prostate specific PET tracers used in prostate cancer imaging in current clinical practice. Clin Imaging. 2021;79:278–88.
67. Tirosh A, Kebebew E. The utility of 68Ga-DOTATATE positron-emission tomography/computed tomography in the diagnosis, management, follow-up and prognosis of neuroendocrine tumors. Future Oncol. 2018;14(2):111–22.
68. Unterrainer M, Ruf V, Ilhan H, Vettermann FJ, Cyran CC, Niyazi M, et al. 68Ga-DOTATOC PET/CT differentiates meningioma from dural metastases. Clin Nucl Med. 2019;44(5):412–3.
69. Suh M, Im HJ, Ryoo HG, Kang KW, Jeong JM, Prakash S, Ballal SS, Yadav MP, Bal C, Jeong CW, Kwak C, Cheon GJ. Head to head comparison of 68Ga-NGUL and 68Ga-PSMA-11 in patients with metastatic prostate cancer: a prospective study. J Nucl Med. 2021; https://doi.org/10.2967/jnumed.120.258434.
70. Giammarile F, Castellucci P, Dierckx R, et al. Non-FDG PET/CT in diagnostic oncology: a pictorial review. Eur J Hybrid Imaging. 2019;3(20):3–20.
71. Cohen AD, Klunk WE. Early detection of Alzheimer's disease using PiB and FDG PET. Neurobiol Dis. 2014;72, Part A(0):117–22.
72. Oh M, Lee N, Kim C, et al. Diagnostic accuracy of dual-phase 18F-FP-CIT PET imaging for detection and differential diagnosis of Parkinsonism. Sci Rep. 2021;11:14992.
73. Beer AJ, Haubner R, Sarbia M, Goebel M, Luderschmidt S, Grosu AL, et al. Positron emission tomography using [18F]Galacto-RGD identifies the level of integrin αvβ3 expression in man. Clin Cancer Res. 2006;12:3942–9.
74. Farolfi A, Calderoni L, Mattana F, Mei R, Telo S, Fanti S, et al. Current and emerging clinical applications of PSMA PET diagnostic imaging for prostate cancer. J Nucl Med. 2021;62(5):596–604.

Atlas and Anatomy of SPECT/CT

E. Edmund Kim, Vanessa Murad, Jin-Chul Paeng,
Hyung-Jun Im, Ji-Young Kim, and Gi-Jeong Cheon

Single-photon emission computed tomography (SPECT) imaging has evolved rapidly during the past decades since the introduction of the Anger camera in 1970, the posterior rotating gantry and dual detectors with better reconstruction processes, and quantitative data analysis. In the late 1990s, hybrid SPECT/CT imaging appeared to improve diagnostic accuracy with precise anatomical location and image quality with attenuation correction. In the last 10 years, the improvements in this equipment and the evolution in radiopharmaceuticals have allowed us to improve in the evaluation of physiological processes and in the characterization of pathologies based on morphological patterns [1]. Conventional analog technologies have advanced to multidetector devices with direct conversion digital detectors that improve efficiency, resolution and image quality, resulting in faster studies with lower doses and even the ability to image multiple radionuclides simultaneously. This includes the last generation cadmium-zinc-telluride (CZT) scanners, which bring more possibilities in research and clinical practice, especially in nuclear cardiology [2–4]. There is no denying that SPECT is still the go-to choice for most cardiologists.

There are multiple SPECT/CT applications, and in this chapter, we introduce most of them with demonstrative examples. In tumor pathology, its best-known applications are the evaluation of bone tumors, especially osteoblastic metastases, neuroendocrine tumors, and parathyroid adenomas [5, 6]. However, there are other multiple uses such as the evaluation of hepatocellular carcinoma, liver metastasis, neuroblastoma, paraganglioma, and thyroid cancer. In non-tumor bone pathology, it is indicated in trauma, degenerative disease, and infection, for example – also in the evaluation of benign thyroid pathology, gastrointestinal bleeding, lymphatic system pathology, and pulmonary physiology, among others [5, 7–9]. SPECT systems as well as radiopharmaceuticals are more available and probably cost-effective than PET, so they remain and will remain at the forefront.

E. E. Kim
Department of Radiological Sciences, University of California, Irvine, School of Medicine, Orange, CA, USA

Department of Nuclear Medicine and Department of Molecular Medicine, Graduate School of Convergence Science and Technology, Seoul National University College of Medicine, Seoul, Republic of Korea

V. Murad (✉)
Department of Nuclear Medicine, Seoul National University College of Medicine, Seoul, Republic of Korea

Department of Diagnostic Imaging, Fundacion Santa Fe de Bogotá University Hospital, Bogota, Colombia

J.-C. Paeng · G.-J. Cheon
Department of Nuclear Medicine, Seoul National University College of Medicine, Seoul, Republic of Korea

H.-J. Im
Departments of Applied Bioengineering, Molecular Medicine, and Biopharmaceutical Sciences, Graduate School of Convergence Science and Technology, Seoul National University, Seoul, Republic of Korea

J.-Y. Kim
Department of Nuclear Medicine, Bundang Seoul National University Hospital, Seoul Korea, Radiation Health Research Institute, Korea Hydro & Nuclear Power Co., Ltd., Seoul, Republic of Korea

E. E. Kim et al. (eds.), *Atlas and Anatomy of PET/MRI, PET/CT and SPECT/CT*, https://doi.org/10.1007/978-3-030-92349-5_3

1 Tumors

1.1 Hepatocellular Carcinoma

1.1.1 Case 1

A 51-year-old man with a diagnosis of hepatocellular carcinoma. Selected SPECT (*top*) and SPECT/CT (*bottom*) of the liver with ^{99m}Tc-MAA particles injected into a hepatic arterial catheter showed several focal areas of slightly to moderately increased activity in the right and left hepatic lobes corresponding to multicentric hepatoma. Only 50% of hepatomas can be imaged with FDG-PET, mainly because of the high levels of phosphatase that dephosphorylate FDG and allow it to diffuse out of cells (Fig. 1) [10].

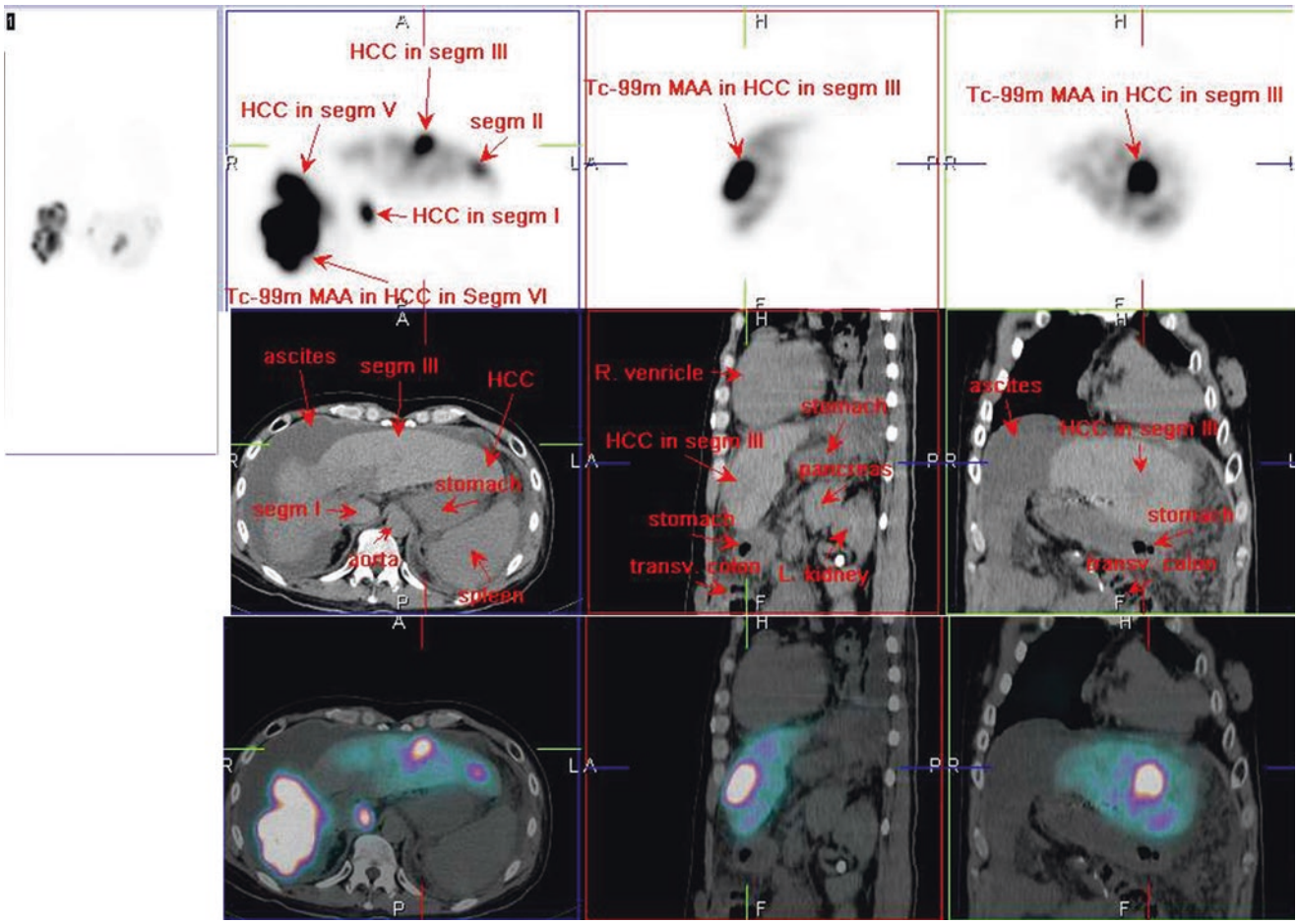

Fig. 1 ^{99m}Tc-MAA SPECT/CT

1.2 Liver Metastases

1.2.1 Case 1

A 68-year-old female patient with liver metastasis from breast cancer. Selected SPECT (*top*) and SPECT/CT (*bottom*) of the liver with ^{99m}Tc-MAA into the hepatic arterial catheter showed markedly heterogeneous activity in the liver caused by known metastases. There was no extra hepatic activity (Fig. 2) [11].

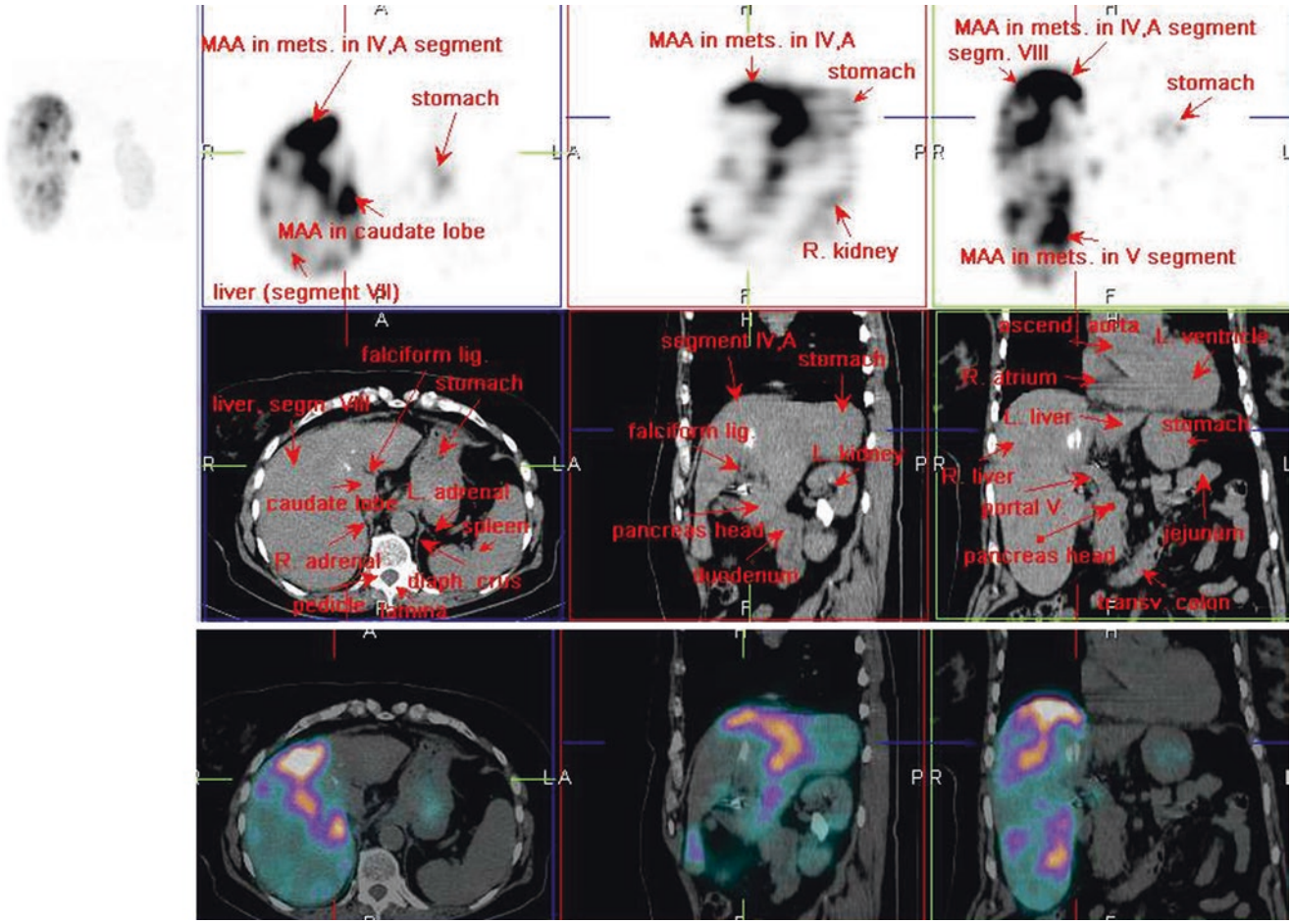

Fig. 2 ^{99m}Tc-MAA SPECT/CT

1.2.2 Case 2

Selected SPECT (*top*) and SPECT/CT (*bottom*) of the upper abdomen with ^{99m}Tc-MAA particles into a hepatic arterial catheter showed curvilinear activity along the gastric wall, indicating the suboptimal position of the hepatic arterial catheter (Fig. 3) [12].

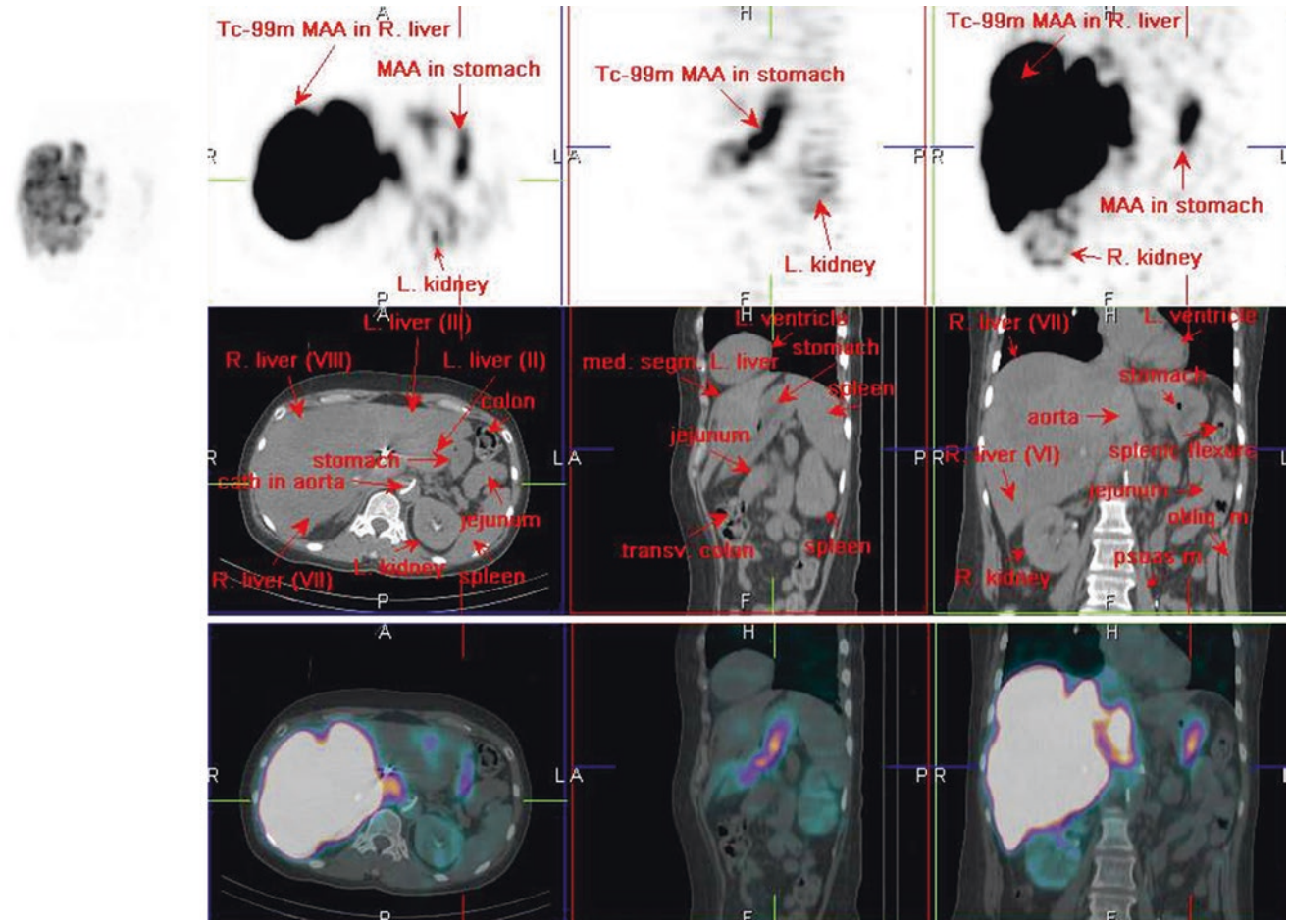

Fig. 3 ^{99m}Tc-MAA SPECT/CT

1.2.3 Case 3

A 57-year-old female patient with hepatic metastasis of breast cancer. Selected SPECT (*top*) and SPECT/CT (*bottom*) images of the liver with ^{90}Y microspheres injected into a hepatic arterial catheter showed increased activity in the right and left hepatic lobes, corresponding to metastatic lesions (Fig. 4) [13].

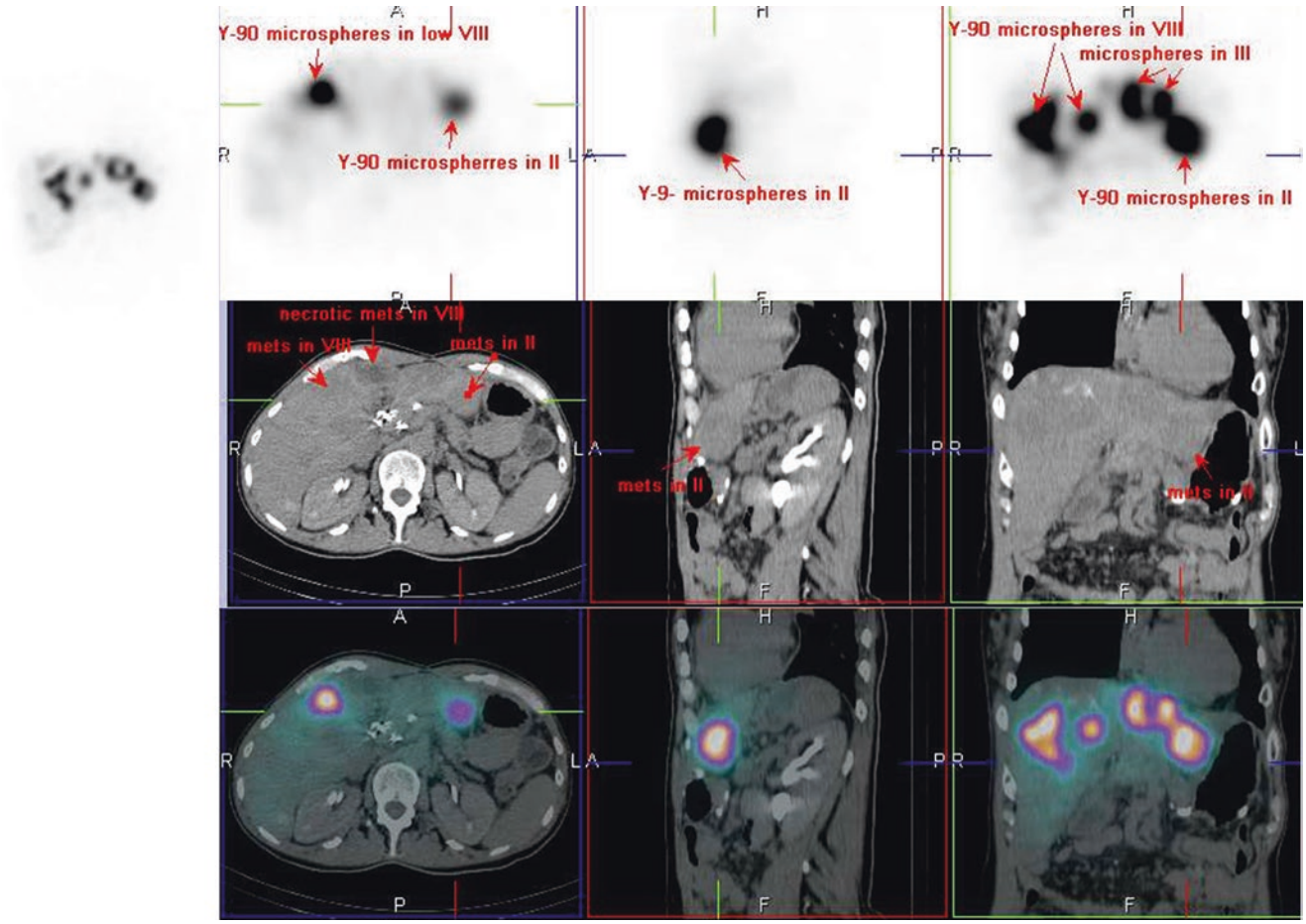

Fig. 4 ^{90}Y SPECT/CT

1.3 Neuroendocrine Tumors

1.3.1 Case 1

A 51-year-old male patient with chest tightness and dyspnea. He had prior history of a pancreatic neuroendocrine tumor, so ^{111}In-octreotide SPECT/CT was done. Images showed focal increased activity in a soft tissue mass at the pericardium, which was posteriorly confirmed to be a metastatic lesion (Fig. 5) [14].

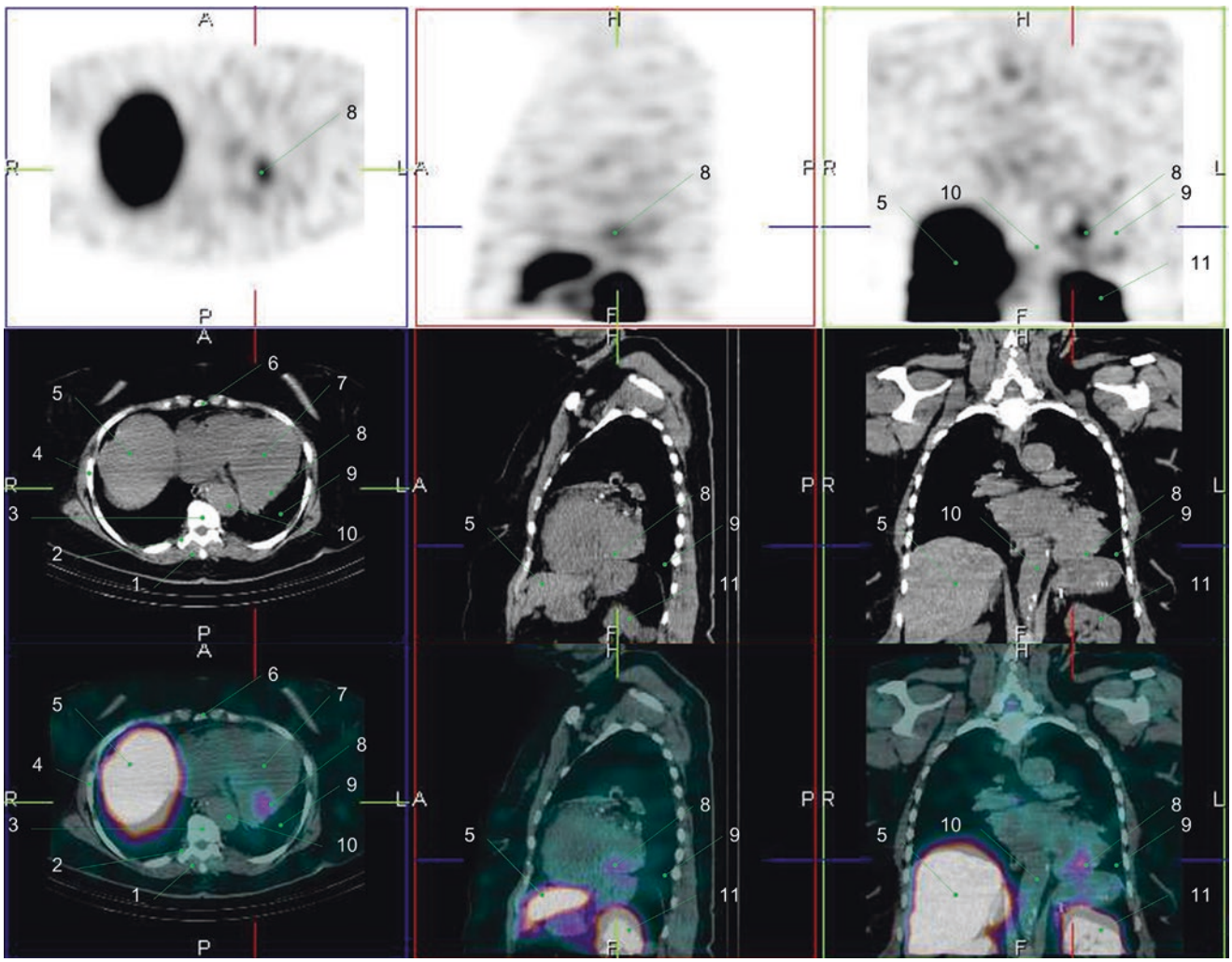

Fig. 5 1. Paraspinalis muscle
2. Transverse process
3. Vertebral body
4. Rib
5. Liver
6. Sternum
7. Left ventricle
8. Metastasis in pericardium
9. Left lower lobe of lung
10. Descending aorta
11. Left kidney

1.3.2 Case 2

A 72-year-old male patient with a history of midgut carcinoid. He attended with right shoulder and abdominal pain. ^{111}In-octreotide SPECT/CT was performed, finding focal increased activity in the right glenoid at a slerotic lesion and the right hepatic lobe at a large necrotic mass. Posterior biopsy confirmed the diagnosis of metastatic neuroendocrine tumor (Fig. 6) [15].

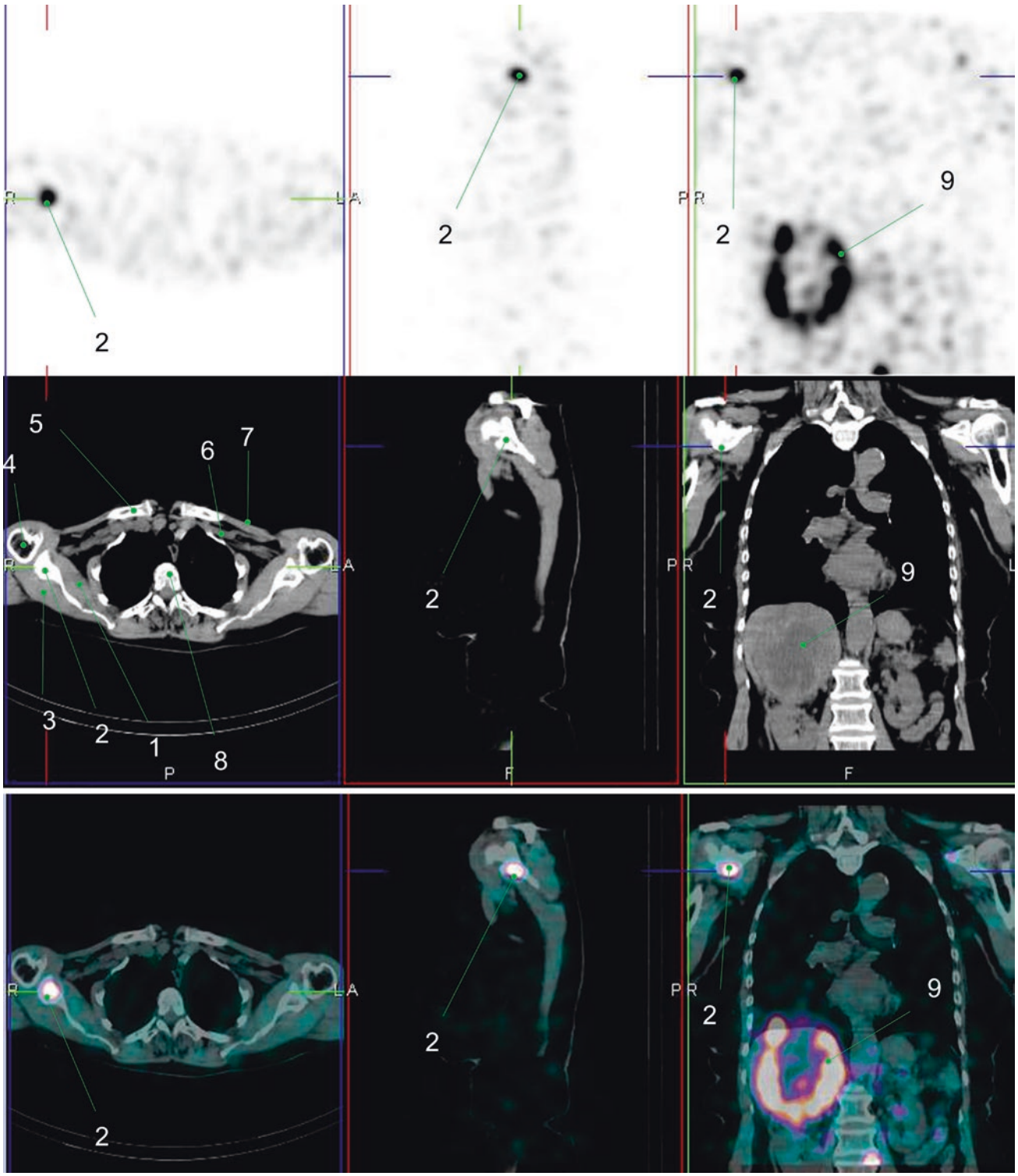

Fig. 6 1. Right subscapularis muscle
2. Metastasis in right scapula neck
3. Right supraspinatus muscle
4. Right humerus
5. Right clavicle
6. Left pectoralis minor muscle
7. Left pectoralis major muscle
8. Vertebral body
9. Liver metastasis with central necrosis

1.3.3 Case 3

A 71-year-old male patient with abdominal pain, diarrhea, and elevated chromogranin A. ^{111}In-octreotide SPECT/CT was performed, finding marked increased activity in a large pancreatic tail mass, as well as diffuse, increased activity in the portal vein. Surgical resection confirmed the diagnosis of a pancreatic neuroendocrine tumor with portal vein invasion (Fig. 7) [16].

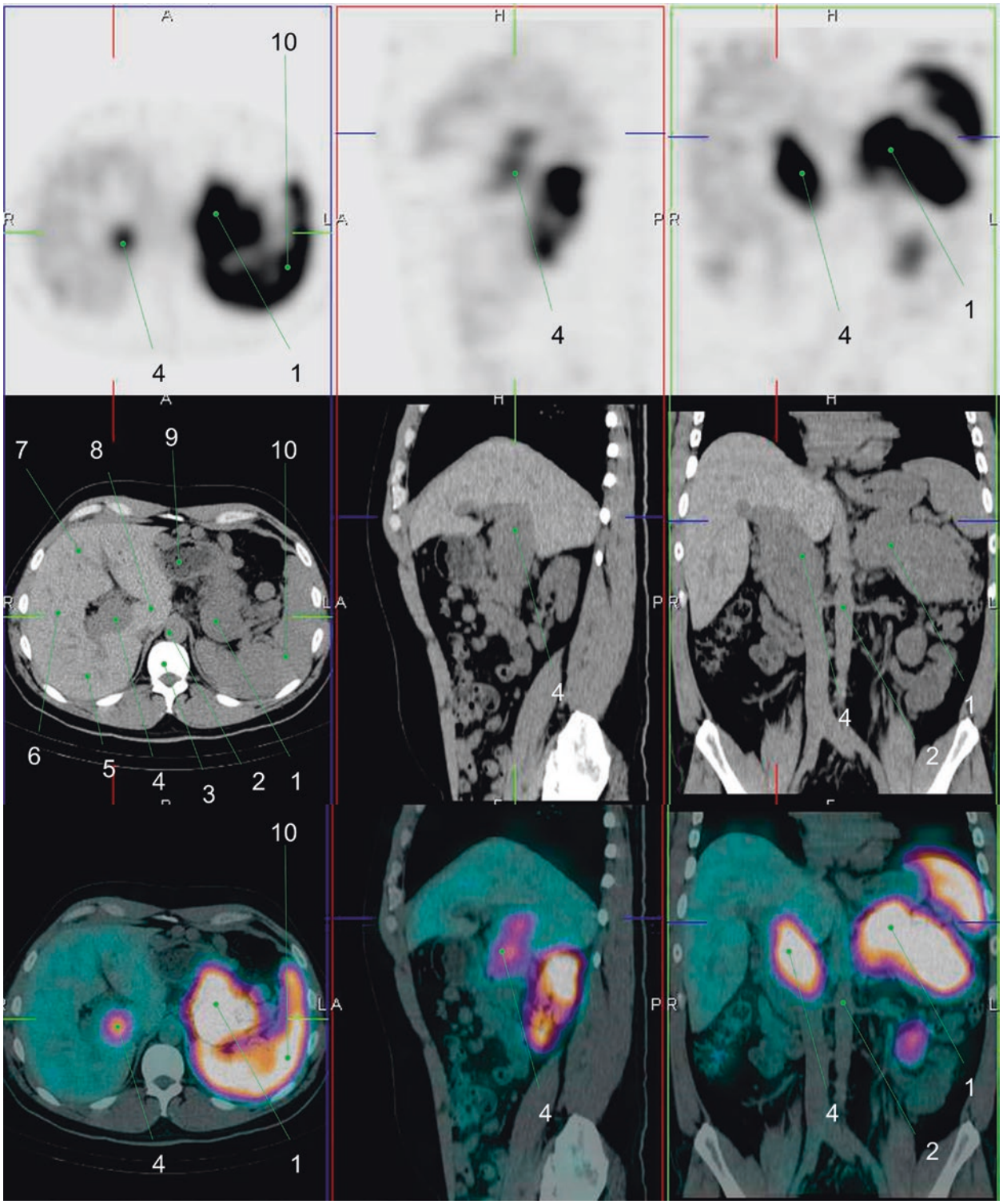

Fig. 7 1. Neuroendocrine tumor in the pancreatic tail
2. Abdominal aorta
3. Vertebral body
4. Neuroendocrine tumor in the portal vein
5. Liver, S6
6. Liver, S5
7. Liver, S4
8. Liver, S1
9. Stomach
10. Spleen

1.3.4 Case 4

A 62-year-old female patient with a history of midgut carcinoid. She presented with cough, dyspnea, and abdominal pain, so ^{111}In-octreotide SPECT/CT was done. Images showed a large mass in the right adrenal gland without abnormal increased activity. Also, diffuse, increased activity was noted in a consolidation at the right upper lung. Posterior biopsy of both lesions confirmed a right adrenal carcinoma and a metastatic neuroendocrine tumor in the right upper lung (Fig. 8) [17].

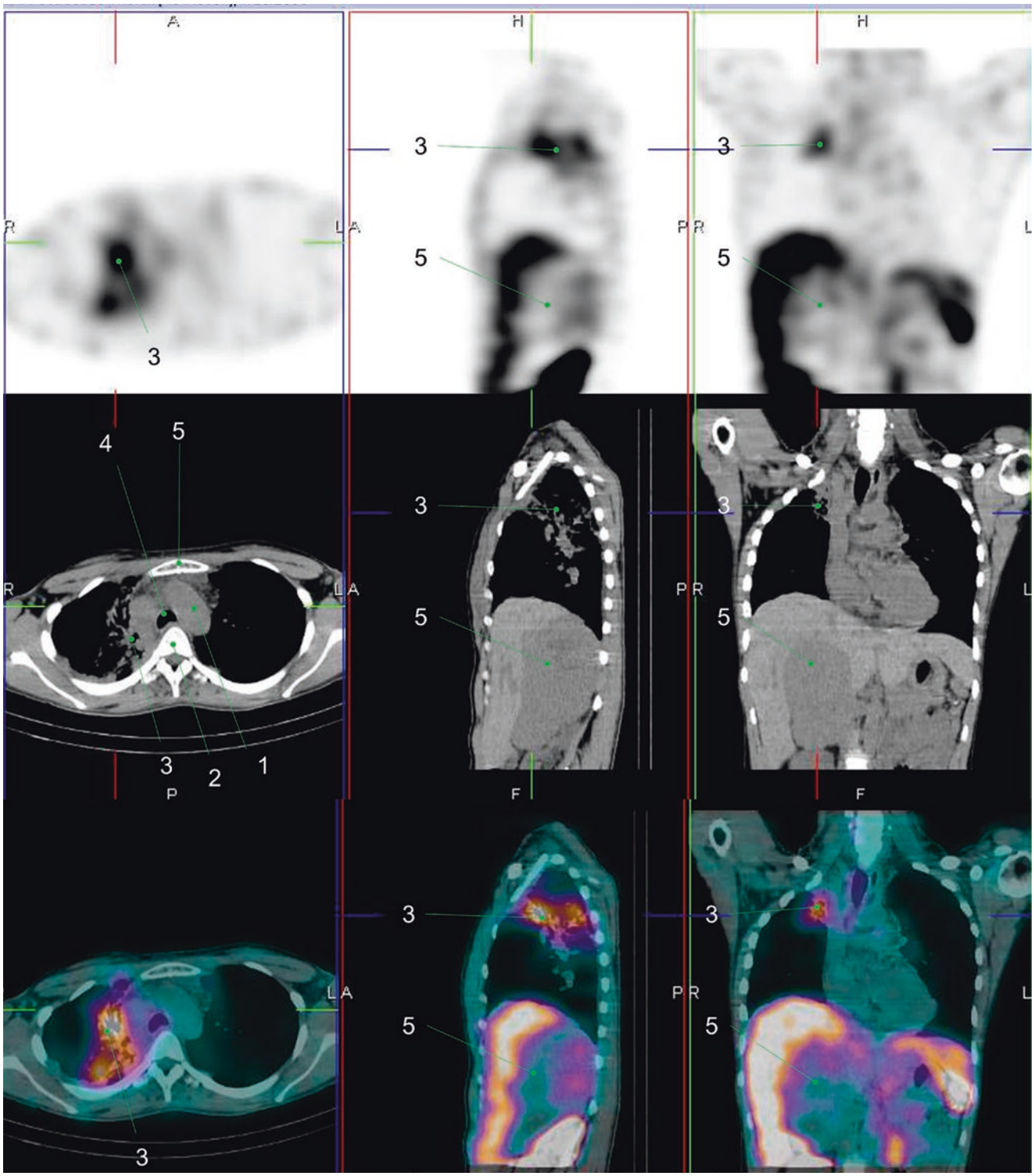

Fig. 8 1. Aortic arch
2. Vertebral body
3. Neuroendocrine tumor in RUL
4. Trachea
5. Right adrenal cancer

1.3.5 Case 5

A 54-year-old female patient with a history of rectal carcinoid. She developed abdominal pain and elevated serum levels of chromogranin A were found. ^{111}In-octreotide SPECT/CT was performed, finding multifocal increased uptake in the right hepatic lobe at several biopsy confirmed metastasis (Fig. 9) [18].

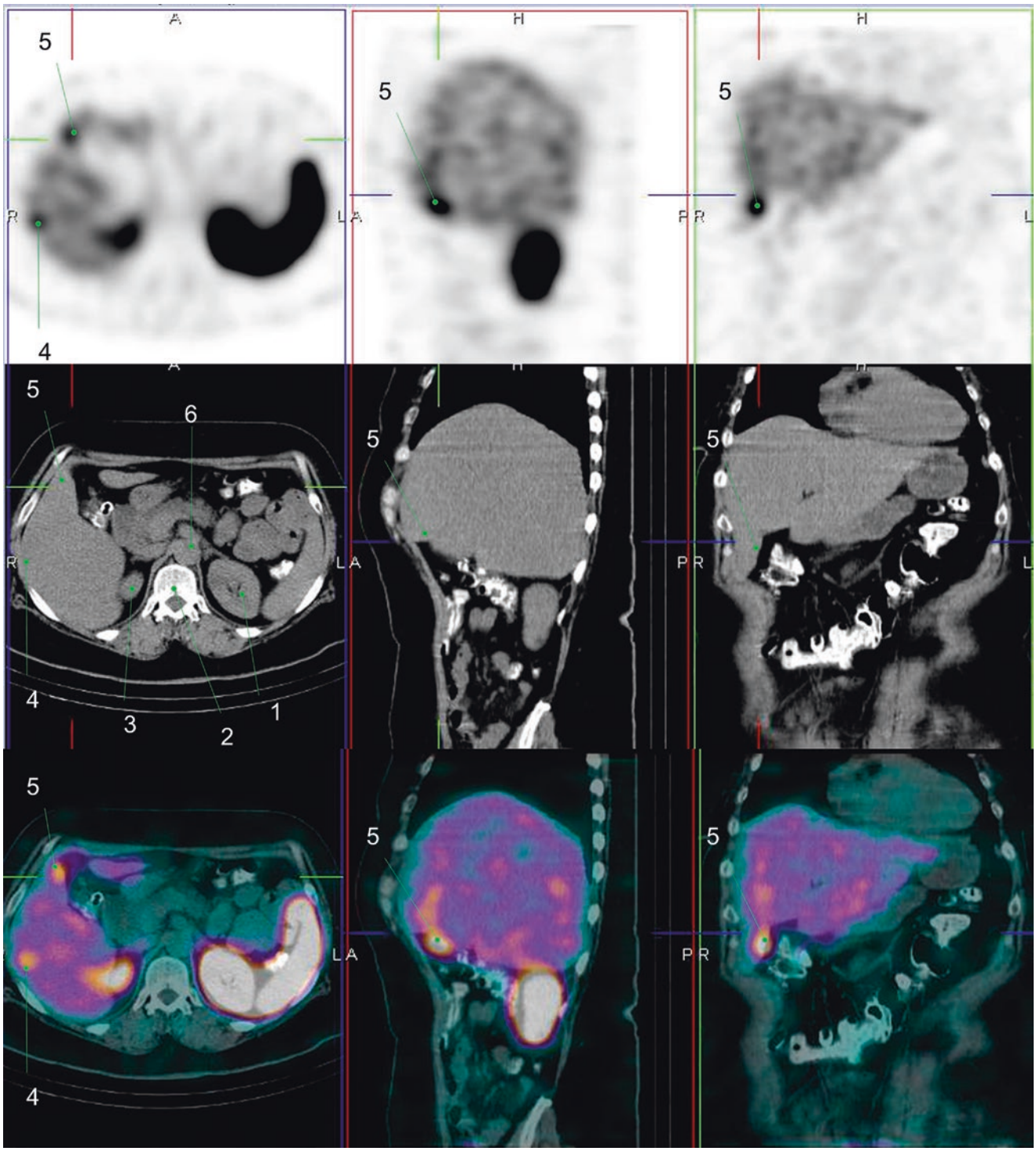

Fig. 9 1. Left kidney
2. Vertebral body
3. Right kidney
4. NE tumor in liver S6
5. NE tumor in liver S5
6. Abdominal aorta

1.3.6 Case 6

A 74-year-old female patient with abdominal pain and diarrhea. ^{111}In-octreotide SPECT/CT was done, finding focal increased activity in the pancreatic head. The surgical diagnosis was a pancreatic neuroendocrine tumor (Fig. 10) [21].

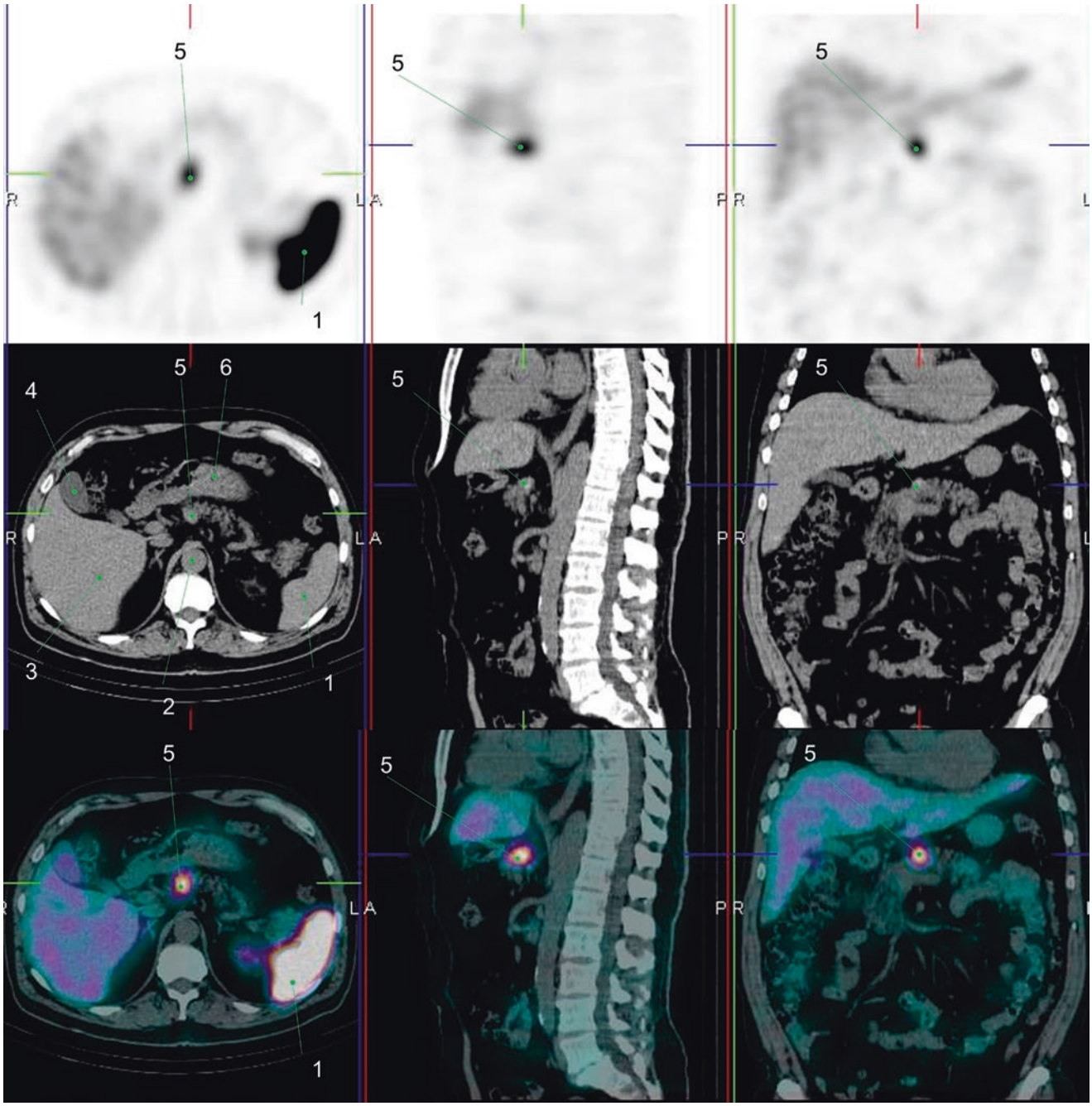

Fig. 10 1. Spleen
2. Abdominal aorta
3. Liver
4. Gallbladder
5. NE tumor in pancreatic body
6. Stomach

1.3.7 Case 7

A 67-year-old male patient with hypertension, abdominal pain, and palpitations. Elevated urinary catecholamines were found, so ^{123}I-MIBG SPECT/CT was performed. Images showed focal increased uptake in a left adrenal mass which was confirmed as a pheochromocytoma (Fig. 11) [22].

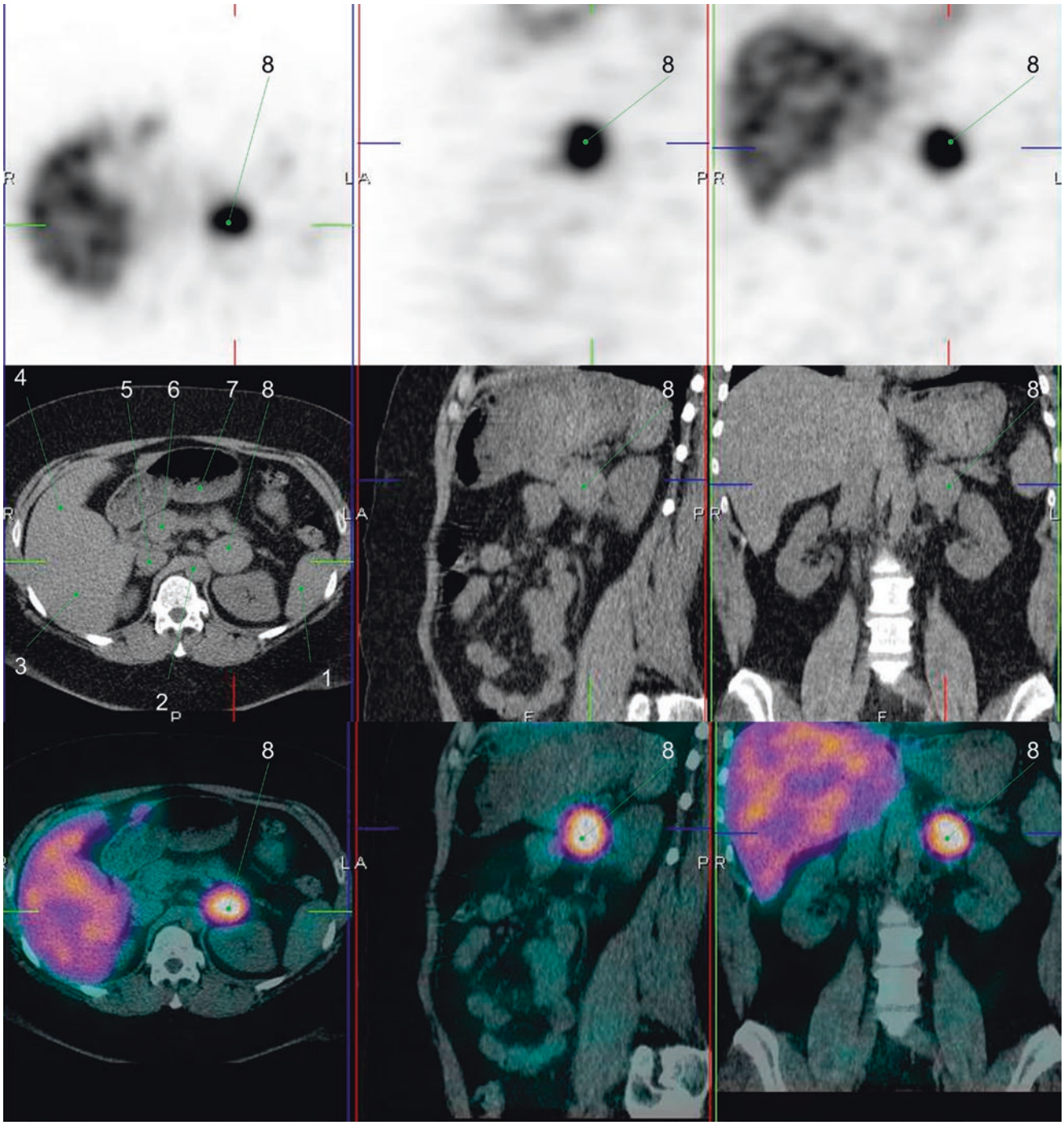

Fig. 11 1. Spleen
2. Abdominal aorta
3. Liver, S6
4. Liver, S5
5. IVC
6. Portal vein
7. Stomach
8. Left adrenal pheochromocytoma

1.3.8 Case 8

A 68-year-old female patient with a history of midgut carcinoid developed chest pain and dyspnea. Chest X-ray showed a newly developed lung nodulex nodule and she had elevated serum levels of chromogranin A, so ^{111}In-octreotide SPECT/CT was done. Images showed focal increased uptake in the right upper lung nodule, which was confirmed to be a metastatic neuroendocrine tumor (Fig. 12) [25].

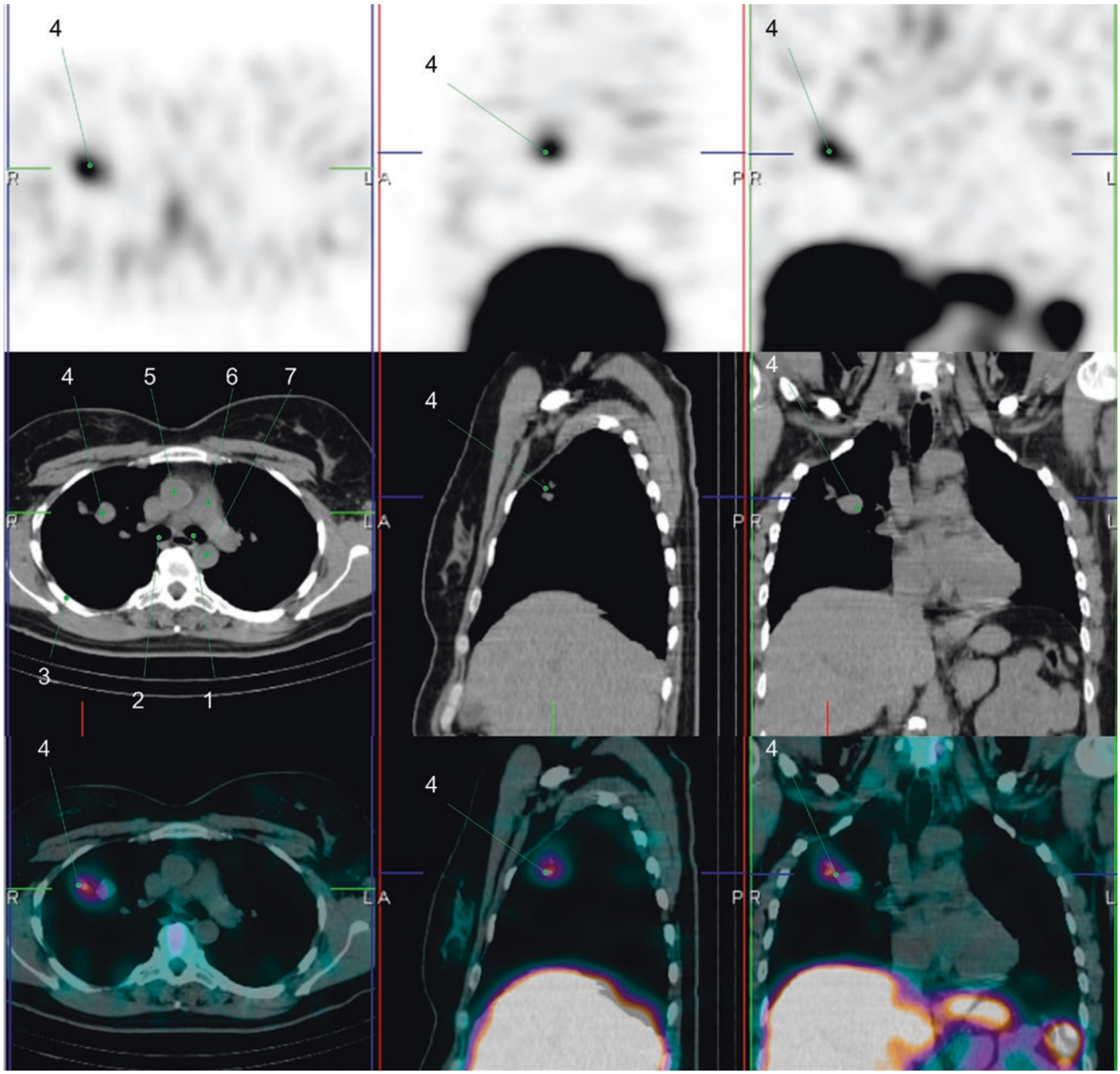

Fig. 12 1. Left main bronchus
2. Right main bronchus
3. Rib
4. Neuroendocrine tumor metastasis in right lung
5. Ascending aorta
6. Pulmonary trunk
7. Descending aorta

1.3.9 Case 9

A 64-year-old female patient with a neuroendocrine tumor in the pancreatic tail. Selected SPECT (*top*) and SPECT/CT (*bottom*) images of the upper abdomen with ^{111}In-octreotide showed a focal area of slightly increased activity in the pancreatic tail. No other lesions were observed (Fig. 13) [27].

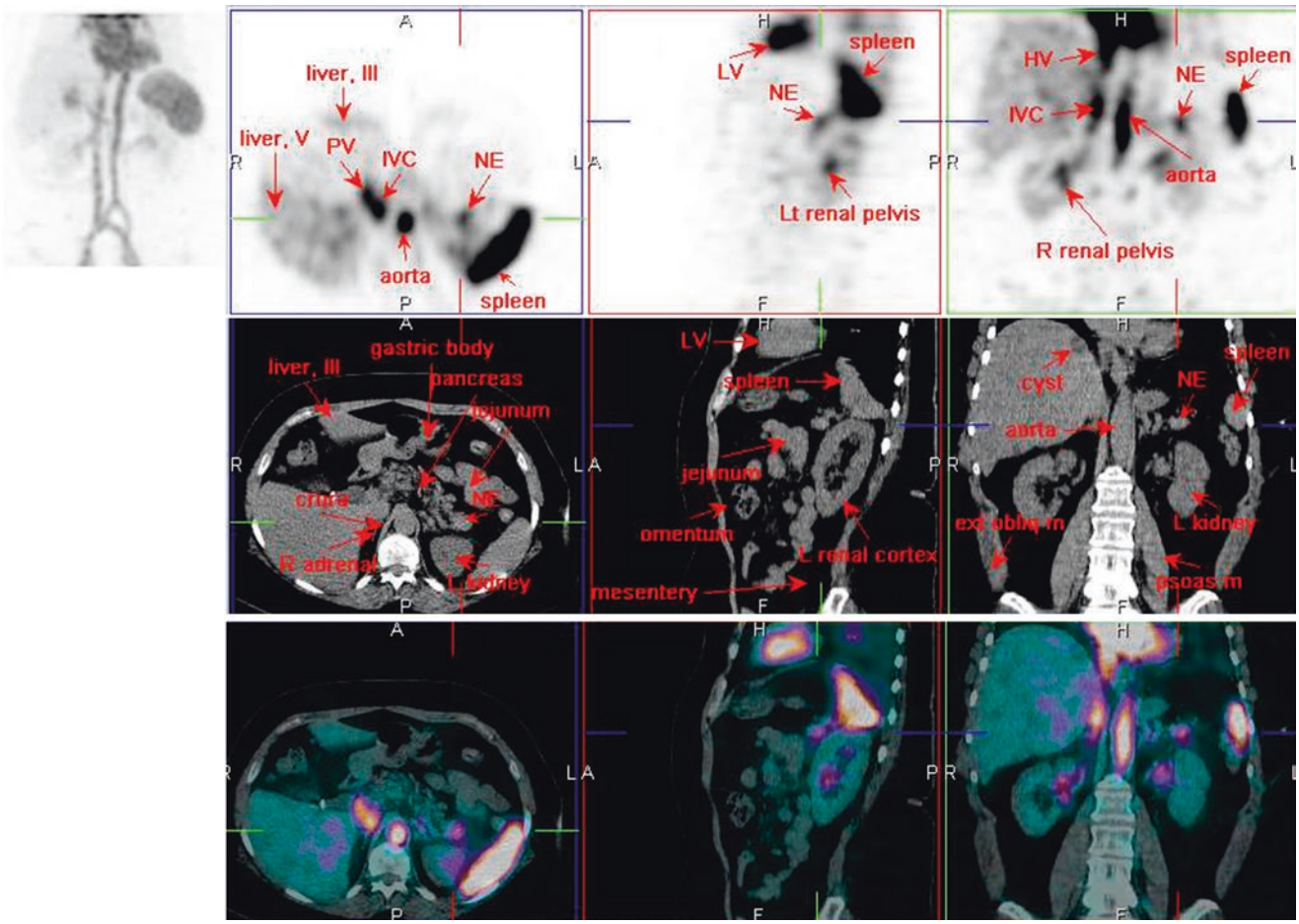

Fig. 13 ^{111}In-octreotide SPECT/CT

1.3.10 Case 10

A 41-year-old male patient with a history of carcinoid tumor, who attended for a regular check-up. ^{111}In-octreotide SPECT/CT was done, finding focal increased activity in the middle to lower abdomen corresponding to mesenteric lymph node metastases, as well as in two metastatic lesions in the right hepatic lobe (Fig. 14) [30].

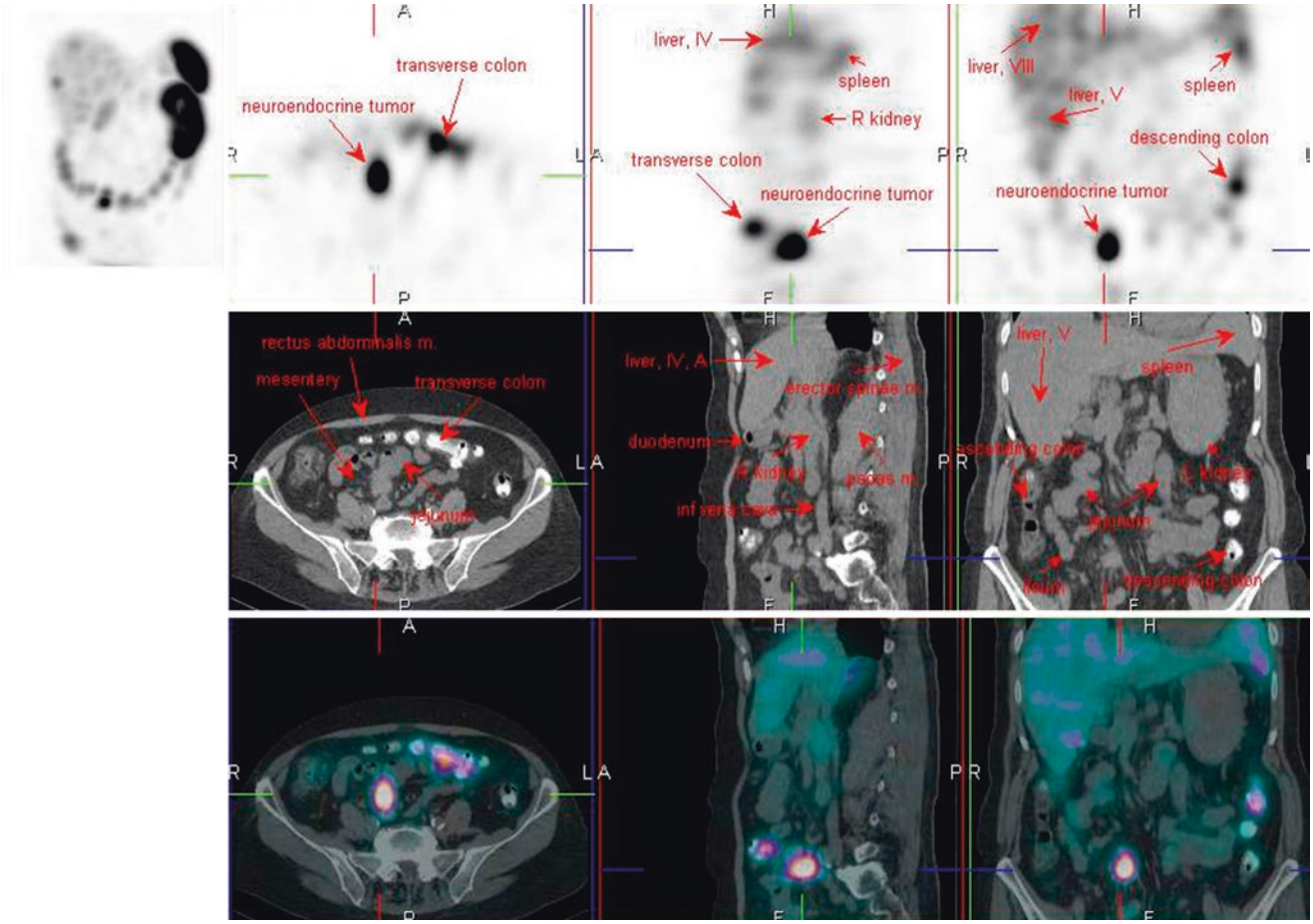

Fig. 14 ^{111}In-octreotide SPECT/CT

1.3.11 Case 11

A 39-year-old male patient with biopsy-proven lung carcinoid, who underwent ^{111}In-octreotide SPECT/CT for staging. Images showed focal increased activity in the right hilum at the primary tumor, without definite uptake in post-obstructive atelectasis (Fig. 15) [32].

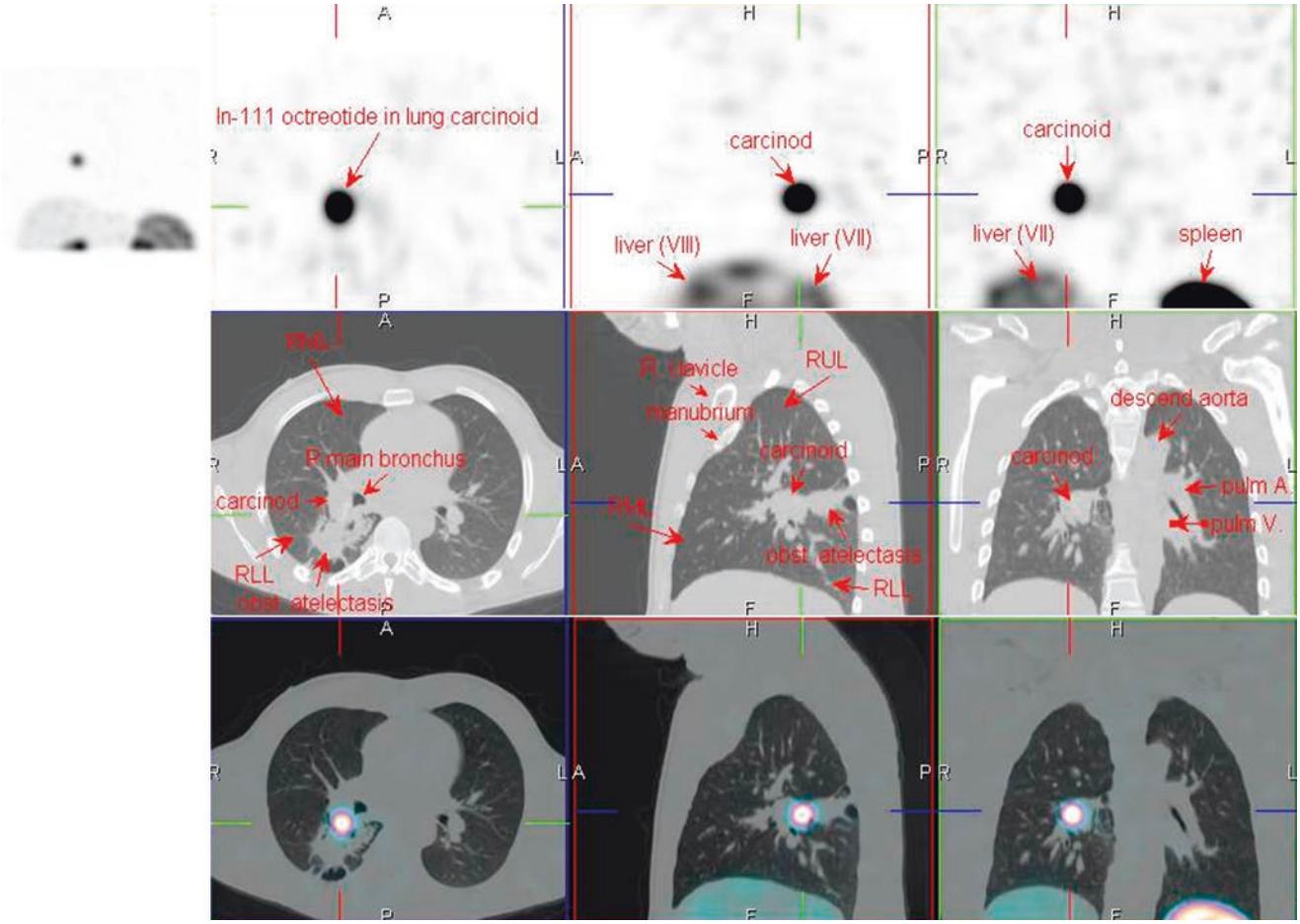

Fig. 15 ^{111}In-octreotide SPECT/CT

1.3.12 Case 12

A 51-year-old female patient with a biopsy confirmed diagnosis of transverse colon neuroendocrine tumor. ^{111}In-octreotide SPECT/CT was performed for staging, finding only focal increased uptake in the primary lesion at the proximal transverse colon (Fig. 16) [33].

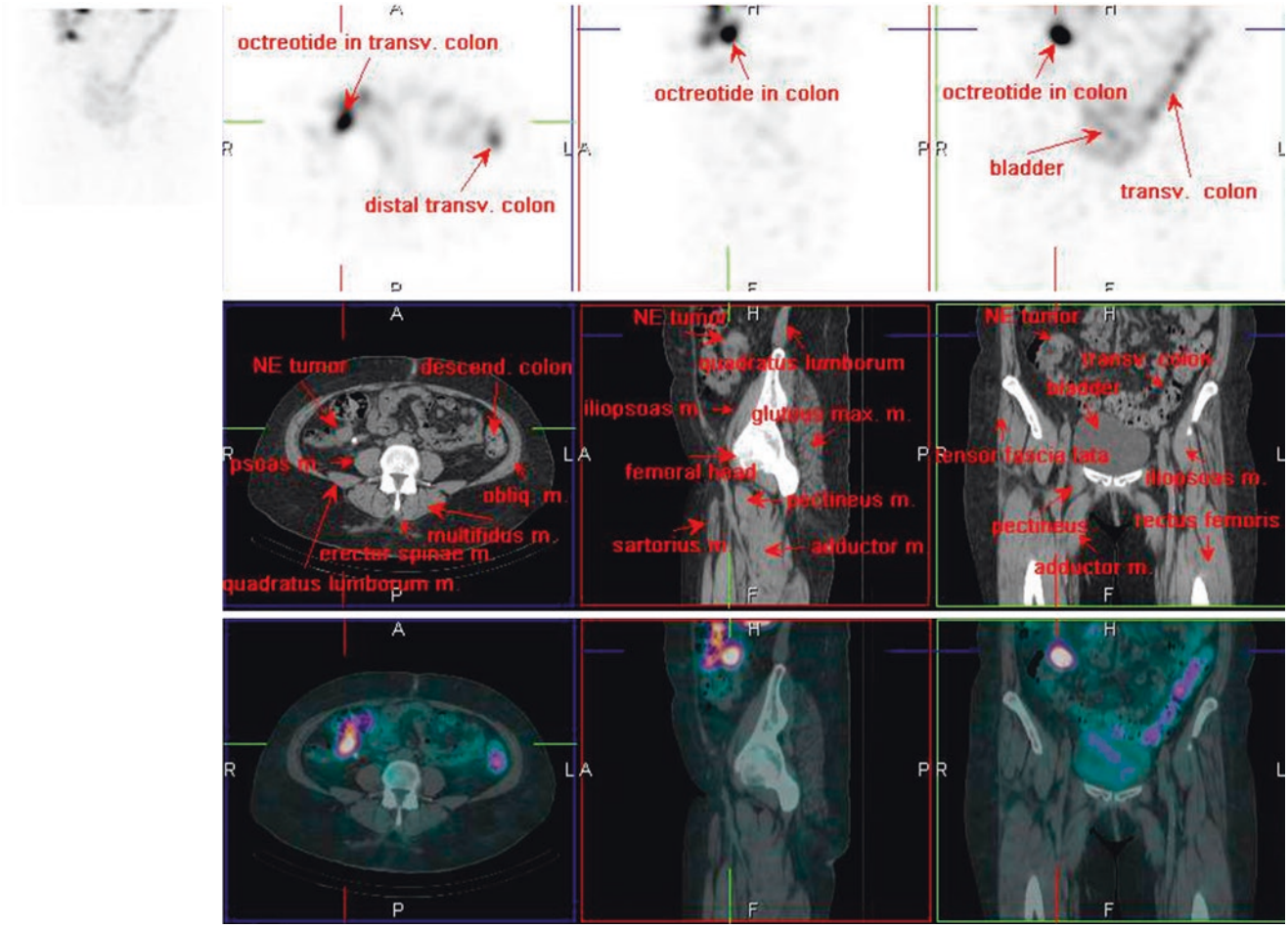

Fig. 16 ^{111}In-octreotide SPECT/CT

1.4 Neuroblastoma

1.4.1 Case 1

A 3-year-old girl with confirmed diagnosis of retroperitoneal neuroblastoma. ^{123}I-MIBG SPECT/CT was performed for further evaluation. Images showed focal increased uptake in a retroperitoneal mass adjacent to the left psoas muscle, corresponding to the primary tumor. Neuroblastoma is a neural crest cell tumor arising from the sympathetic chain, commonly in the adrenal gland, and the mean age at the diagnosis was 2 years. Metastases may be found in 75% of these patients. Meta-iodobenzylguanidine (MIBG) is similar to norepinephrine and is taken up by chromaffin granules that are in neuroblastoma and pheochromocytoma (Fig. 17) [35].

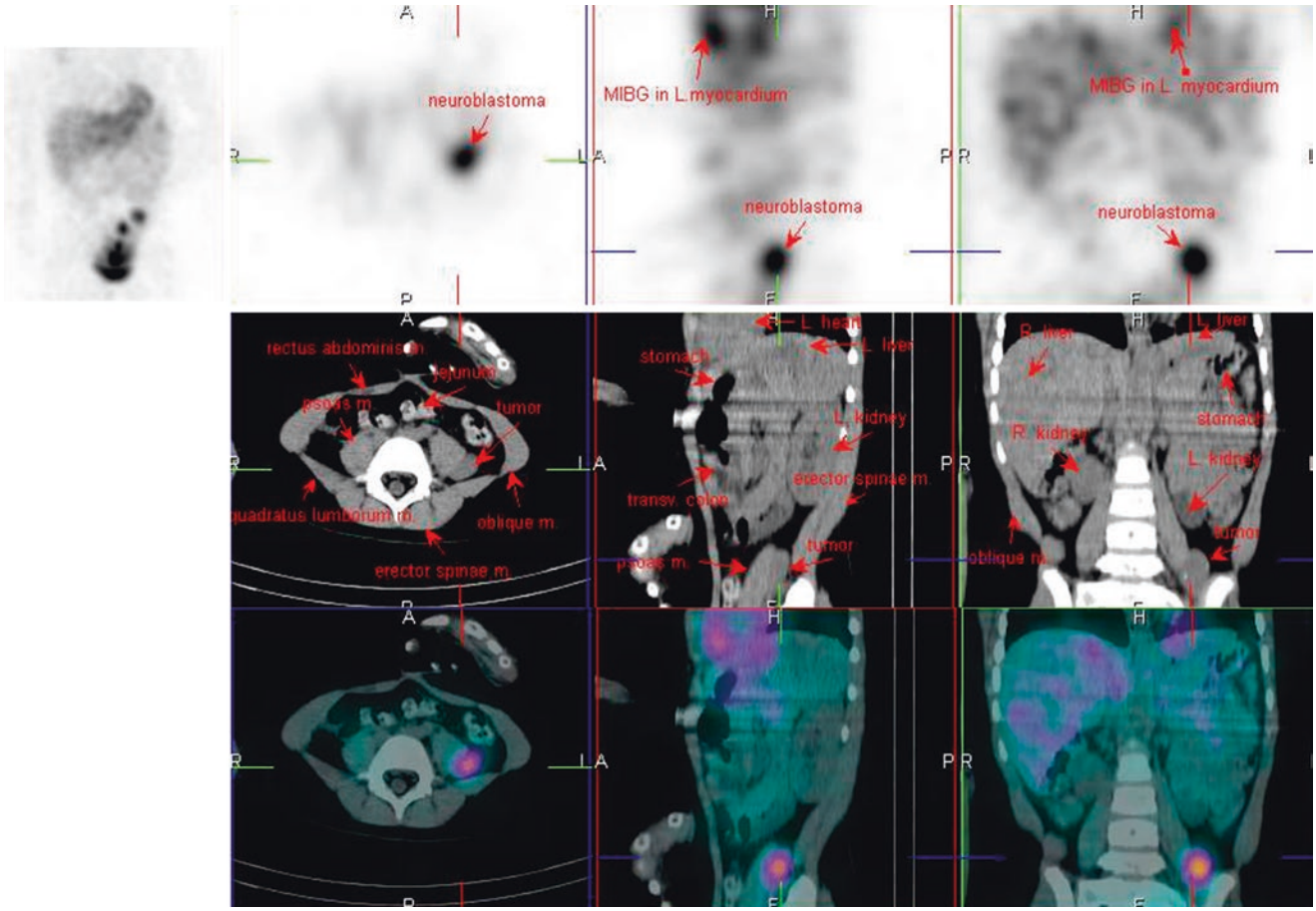

Fig. 17 ^{123}I-MIBG SPECT/CT

1.5 Paraganglioma

1.5.1 Case 1

A 59-year-old male patient, who attended with hypertension and perspiration. Elevated levels of urinary catecholamines were found, so ^{123}I-MIBG SPECT/CT was done for further evaluation. Images showed focal increased activity in a retroperitoneal mass at the aortocaval space, as well as in the left kidney superior pole. The surgical diagnosis confirmed a primary renal paraganglioma with retroperitoneal metastasis (Fig. 18).

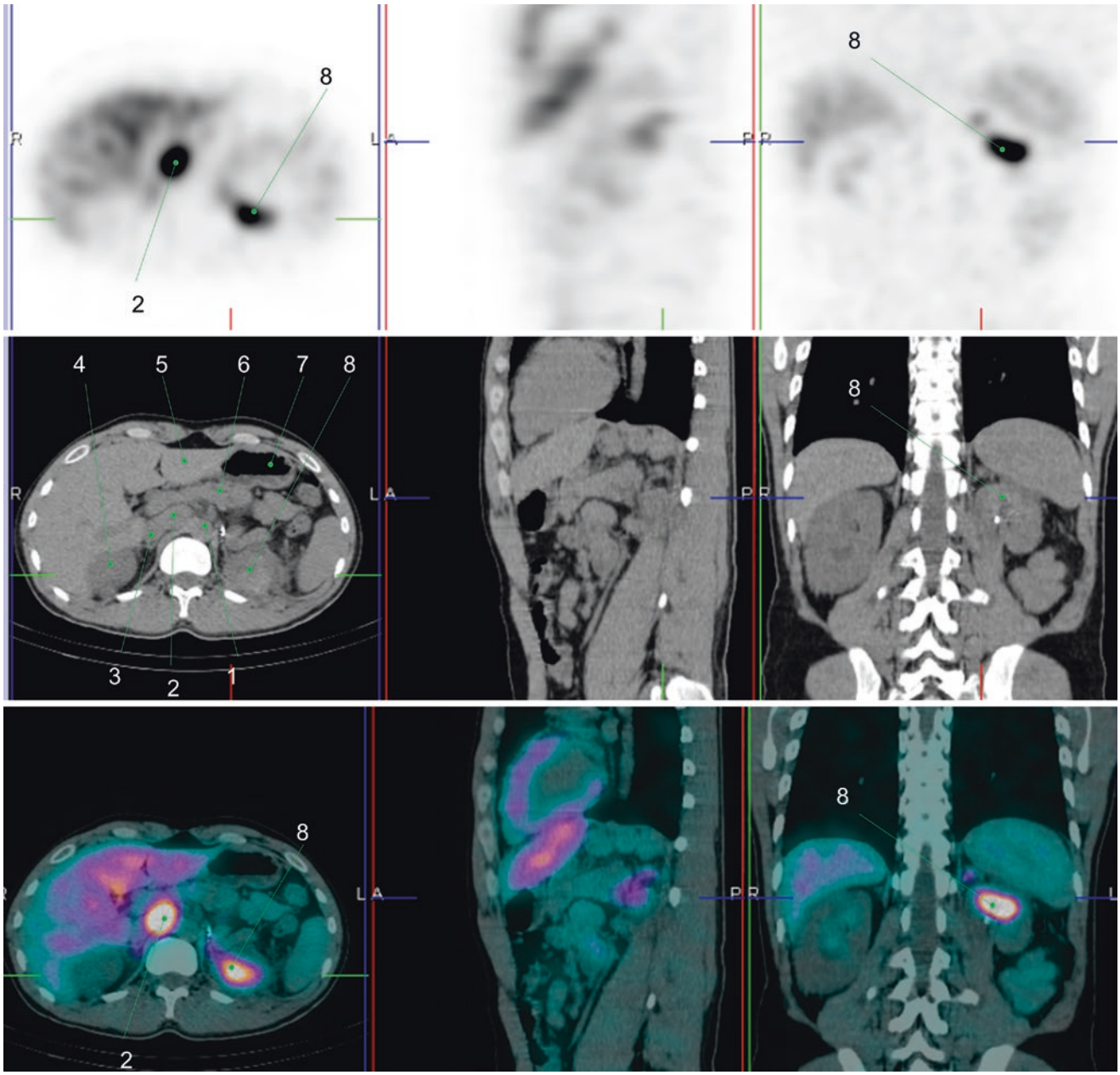

Fig. 18 1. Abdominal aorta
2. Metastatic paraganglioma in aortocaval area
3. IVC
4. Right kidney
5. Liver, left lobe
6. Pancreas
7. Stomach
8. Renal paraganglioma

1.5.2 Case 2

A 57-year-old female patient with a history of left adrenal paraganglioma, who attended for routine check-up. ^{123}I-MIBG SPECT/CT was performed, showing heterogeneous activity in the liver, with a focal nodular increased uptake in segment 5 (V). Heterogeneous activity in the liver is physiologic and related to timing of the imaging and radiotracer metabolism and excretion through the biliary system. However, focal increased uptake is an abnormal finding, and in this case, it corresponded to a metastatic lesion. Also, an active metastasis was found in the T8 vertebral body (Fig. 19) [36].

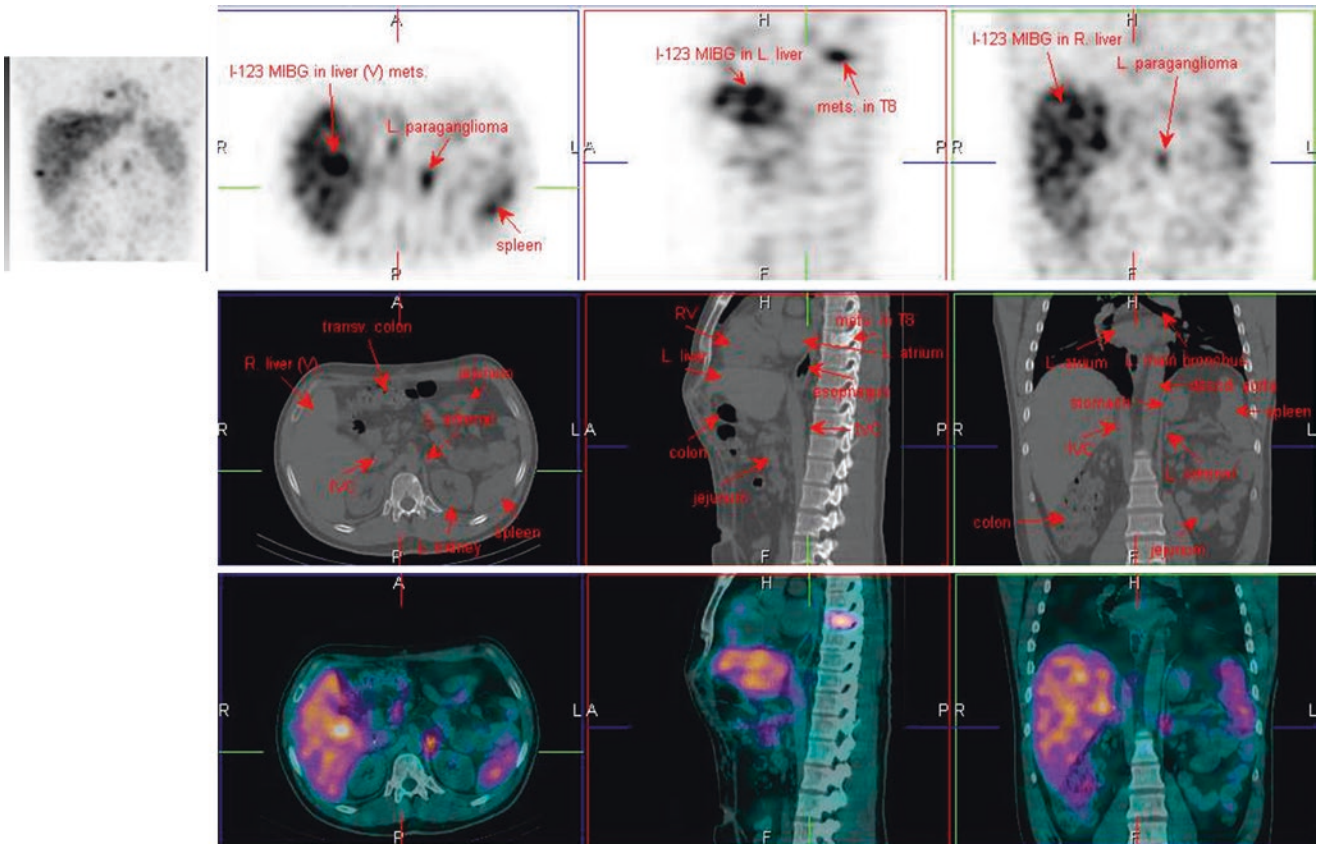

Fig. 19 ^{123}I-MIBG SPECT/CT

1.6 Thyroid Cancer

1.6.1 Case 1

A 59-year-old male patient with a history of thyroid cancer, who underwent coronary CT, finding incidentally multiple lung nodules. ^{131}I SPECT/CT showed moderately to intense increased iodine uptake in the nodules, confirming metastatic disease. Iodine therapy with 200 mCi of ^{131}I was administered (Figs. 20, 21, 22 and 23) [37].

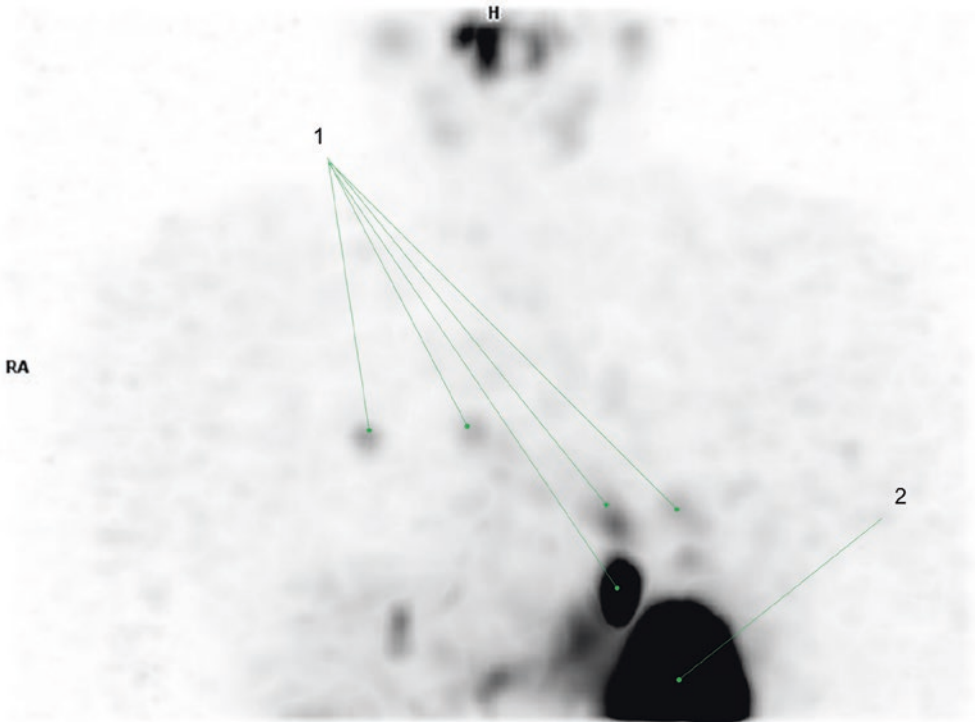

Fig. 20 1. Lung metastases
2. Physiologic colonic uptake

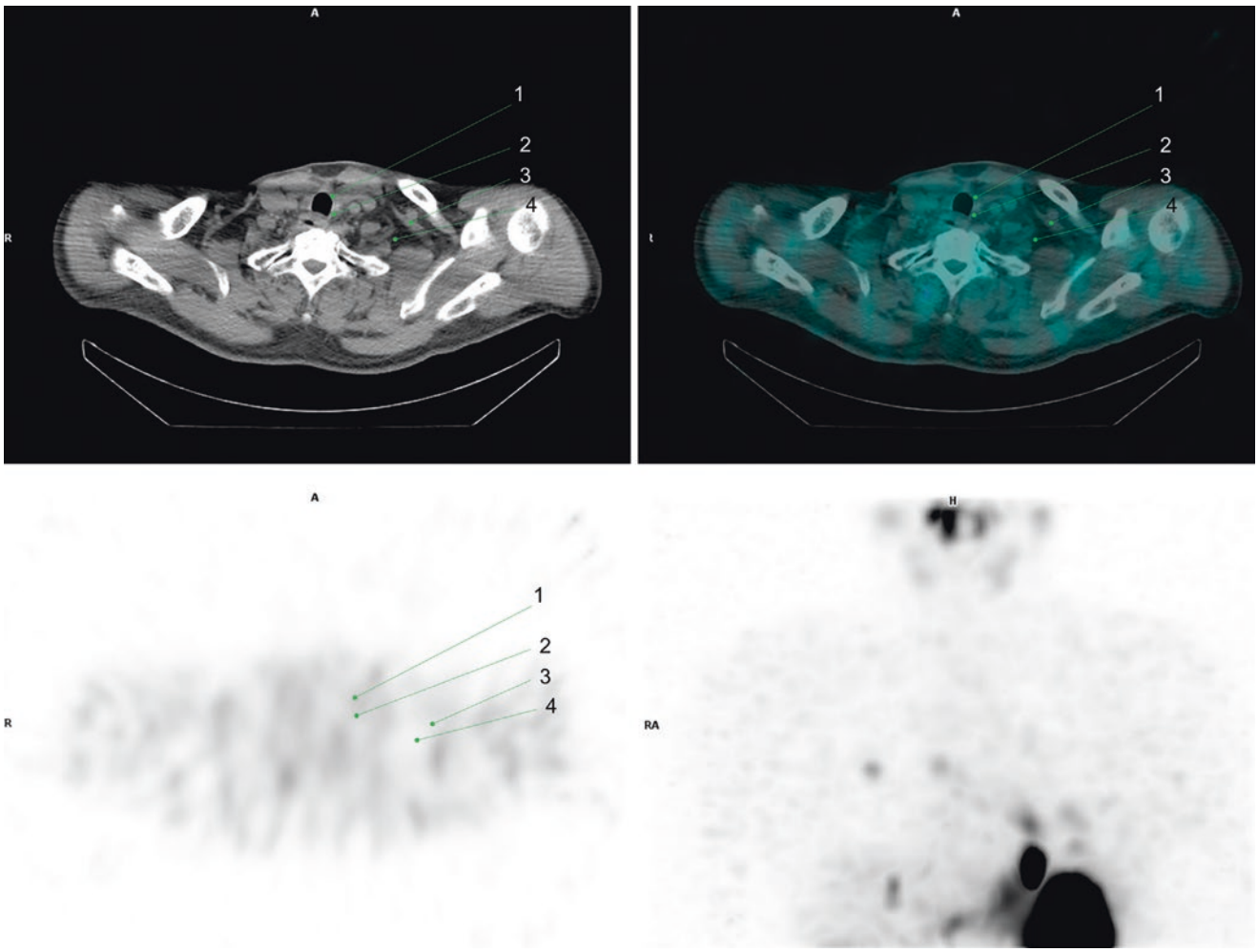

Fig. 21 1. Thyroid bed
2. Left neck, level VI
3. Left sternocleidomastoid muscle
4. Left neck, level IV

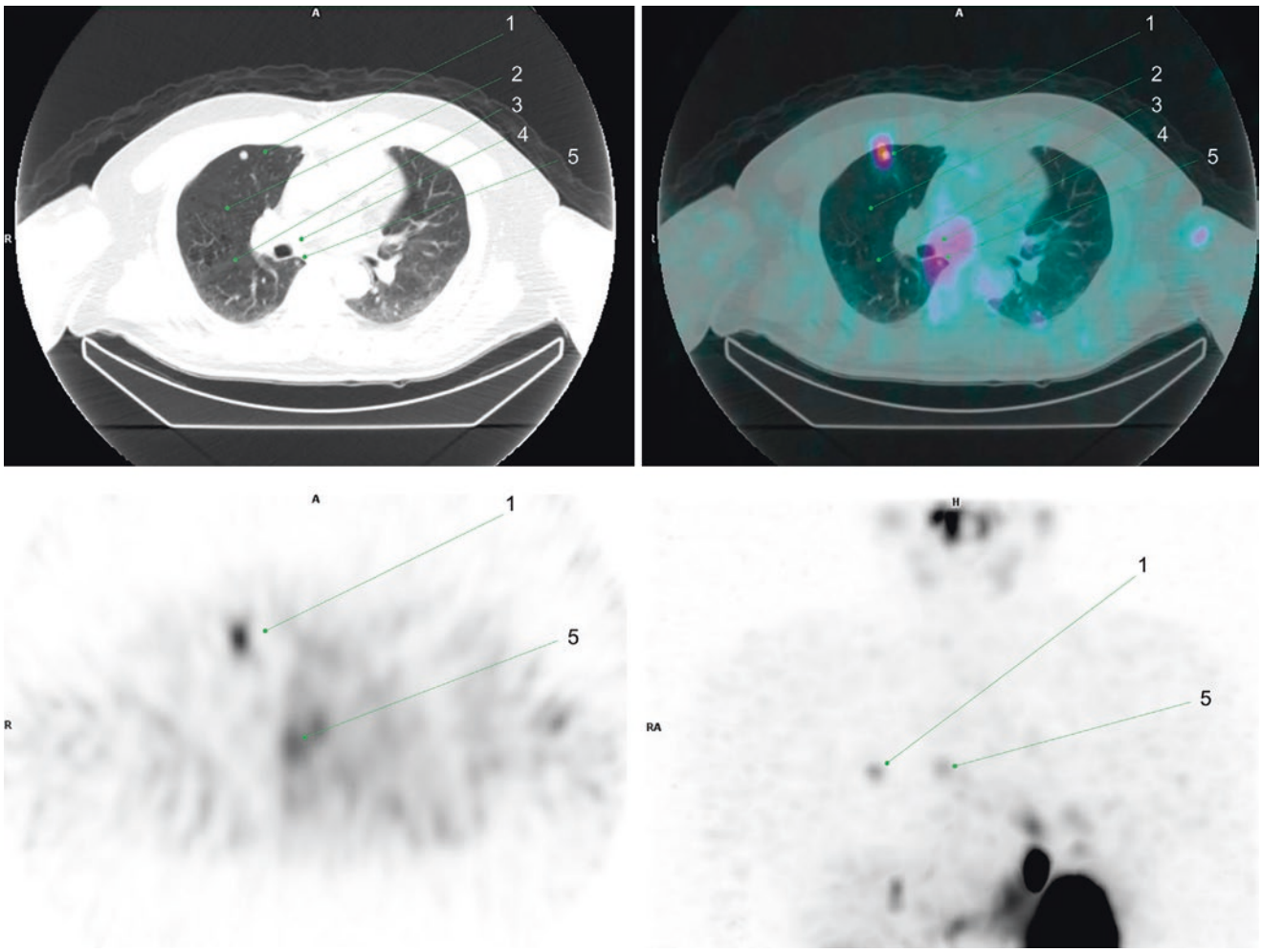

Fig. 22 1. Right middle lobe (RML) anterior segment metastatic nodule
2. Right lung minor fissure
3. Right lung major fissure
4. Right bronchus intermedius
5. Right lower lobe (RLL) superior segment metastatic nodule

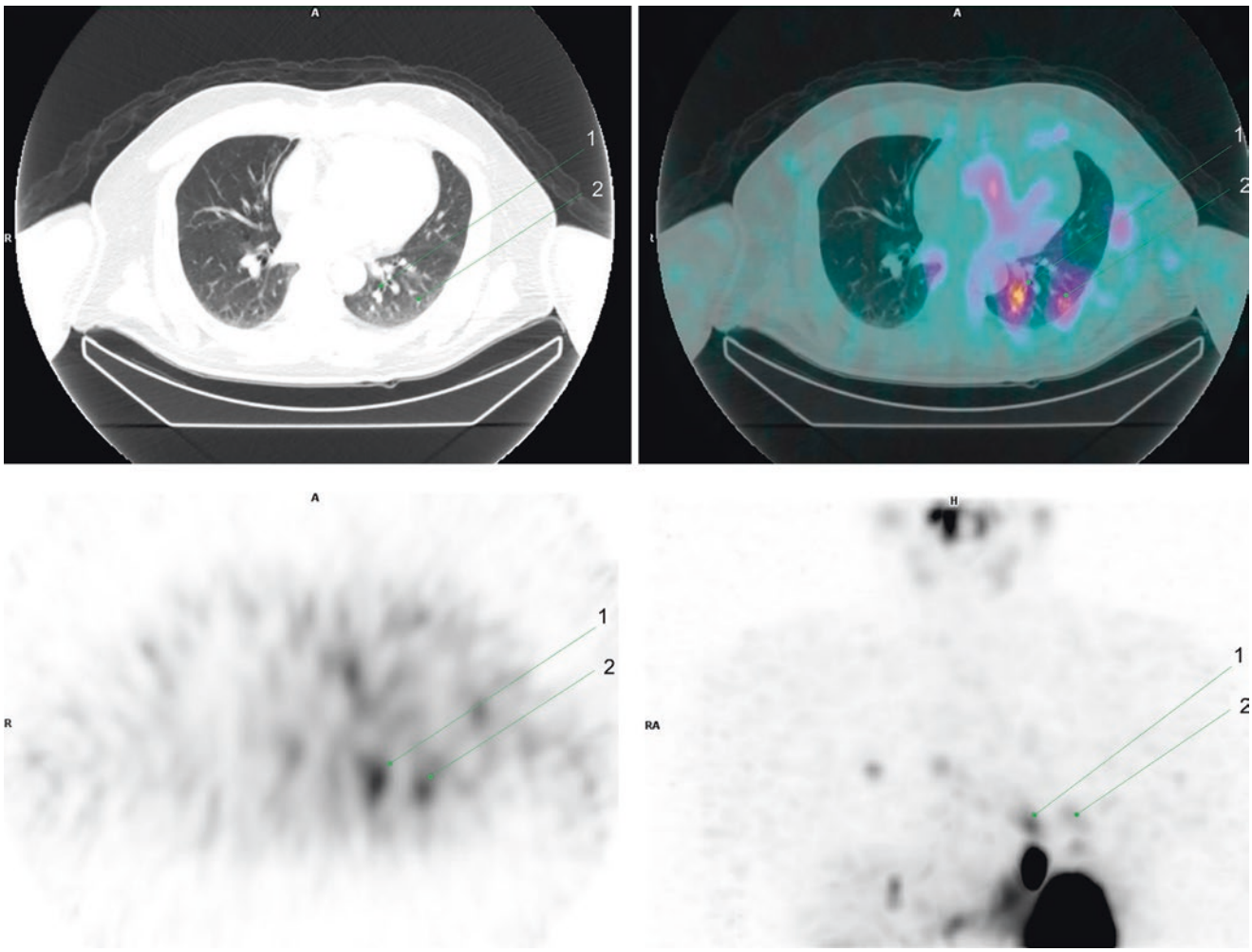

Fig. 23 1. Left lower lung lobe superior segment metastatic nodule
2. Left lower lung lobe lateral basal segment metastatic nodule

1.6.2 Case 2

A 34-year-old female patient with thyroid cancer, who underwent total thyroidectomy with central neck dissection. On ^{131}I ablation scan, bone metastases were found, which were treated with 250 mCi of ^{131}I. Post-treatment iodine scan and SPECT/CT were taken, showing intense focal iodine uptakes at T4 and T6, confirming iodine-avid bone metastases (Figs. 24, 25, 26, 27, 28, and 29) [38].

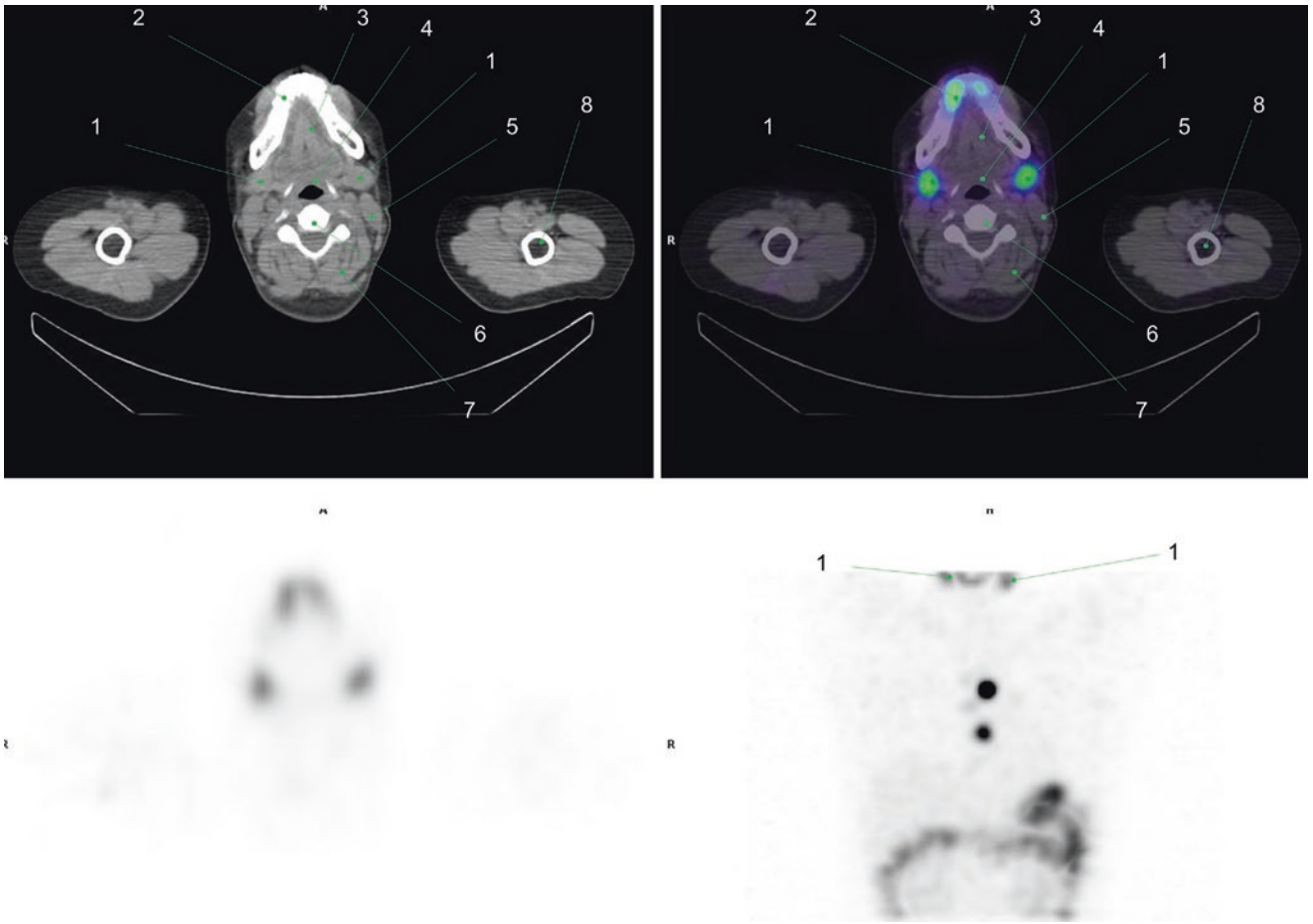

Fig. 24 1. Submandibular glands
2. Body of mandible
3. Genioglossus
4. Trachea
5. Sternocleidomastoid muscle
6. C2 spine
7. Obliquus capitis inferior muscle

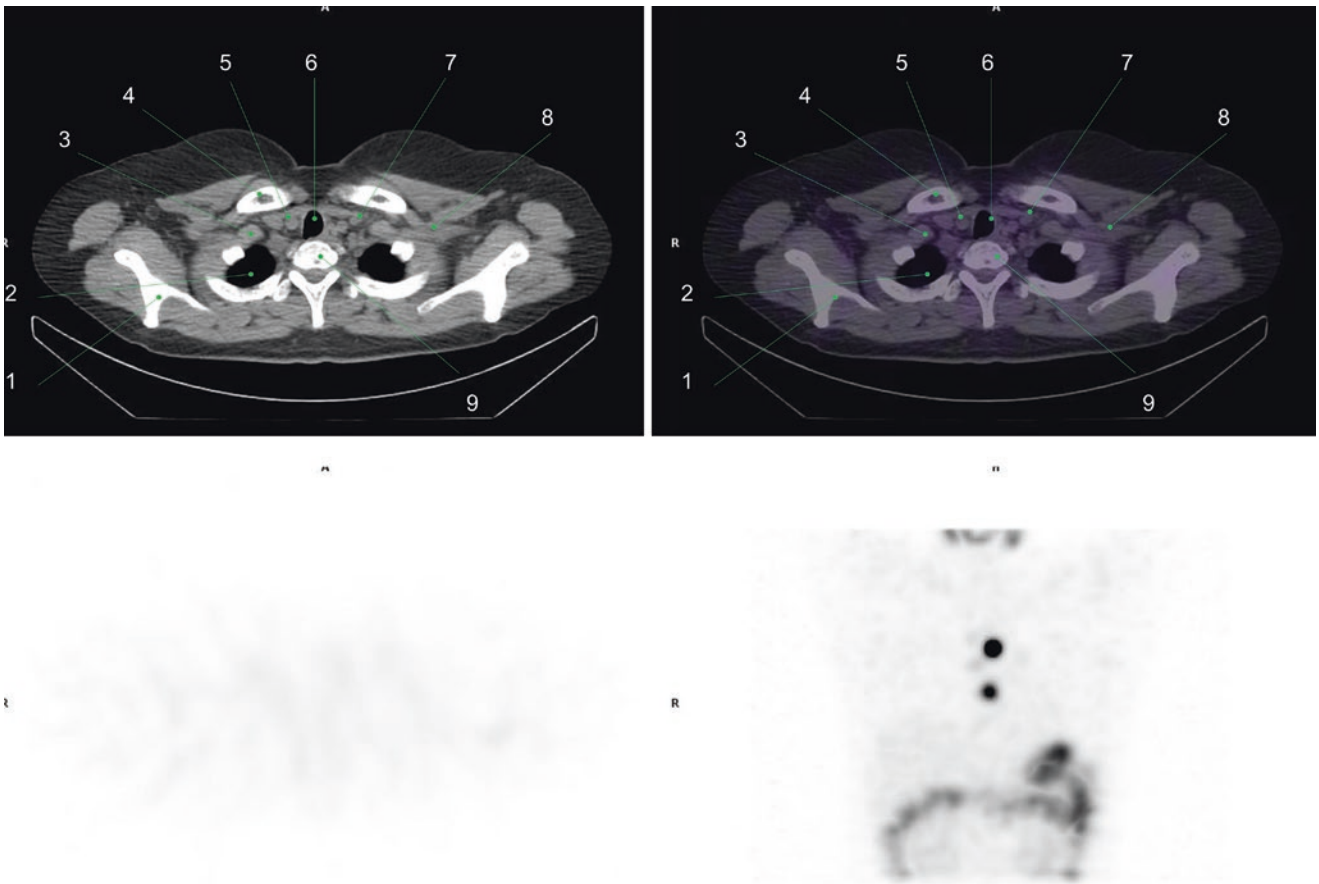

Fig. 25 1. Right scapula
2. Right lung apex
3. Right subclavian artery
4. Right clavicle
5. Right common carotid artery
6. Trachea
7. Left internal jugular vein
8. Left subclavian vein
9. T2 spine

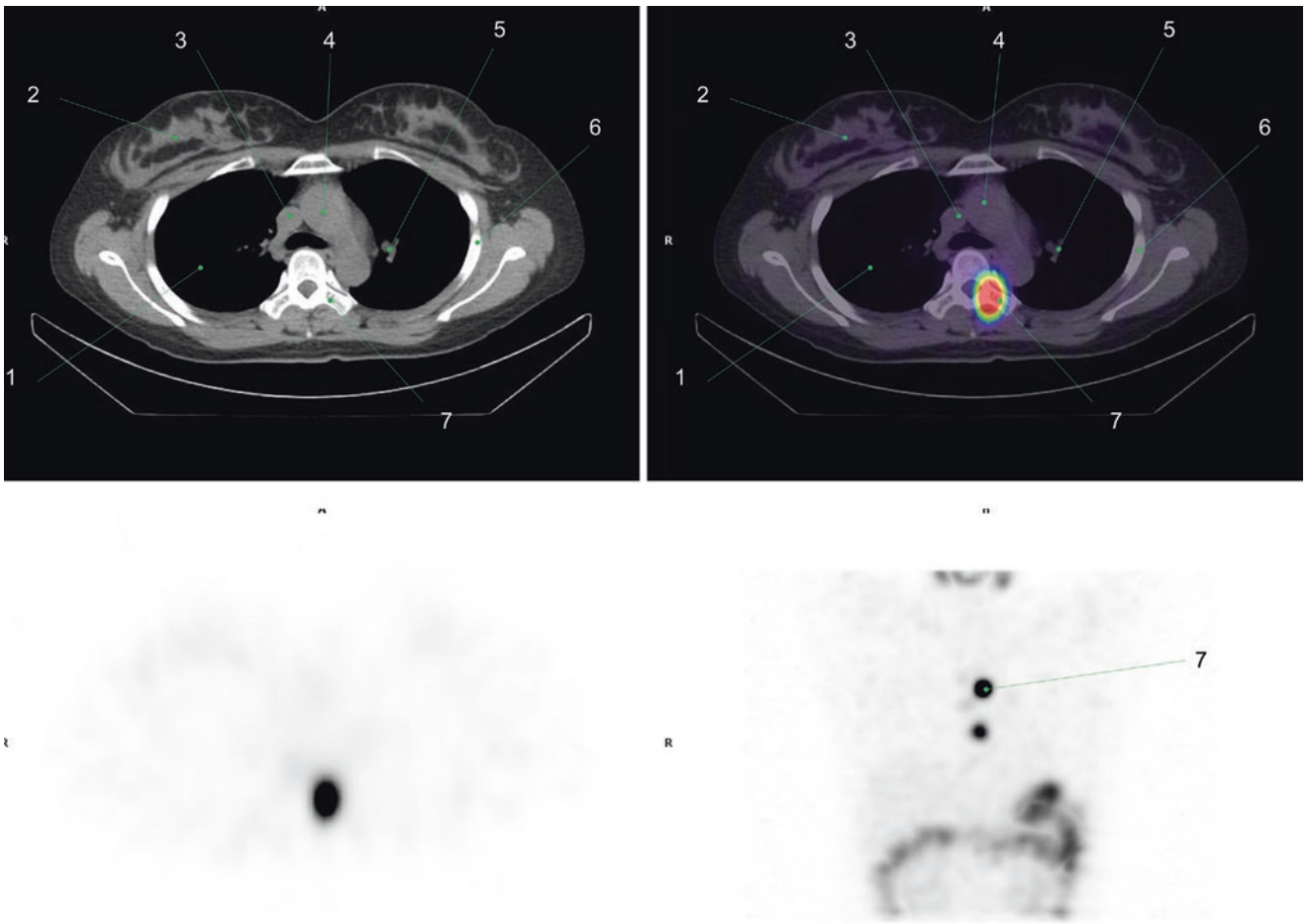

Fig. 26 1. Lung
2. Breast
3. Superior vena cava
4. Ascending aorta
5. Left pulmonary artery
6. Left fourth rib
7. Vertebral arch of T4 spine (metastasis)

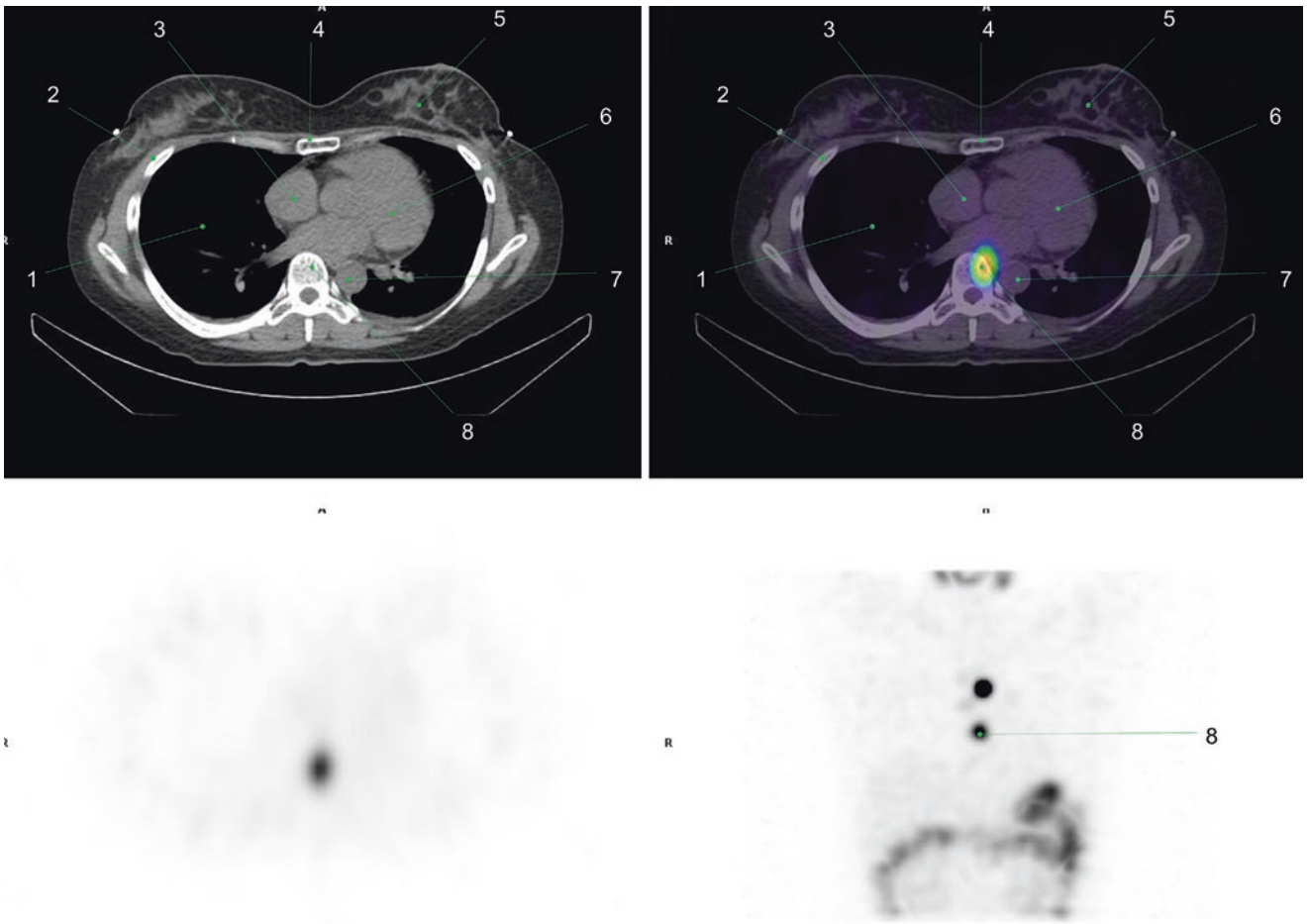

Fig. 27 1. Lung parenchyma
2. Right fourth rib
3. Right atrium
4. Sternum
5. Left breast parenchyma
6. Left ventricle
7. Descending aorta
8. Vertebral body of T6 (metastasis)

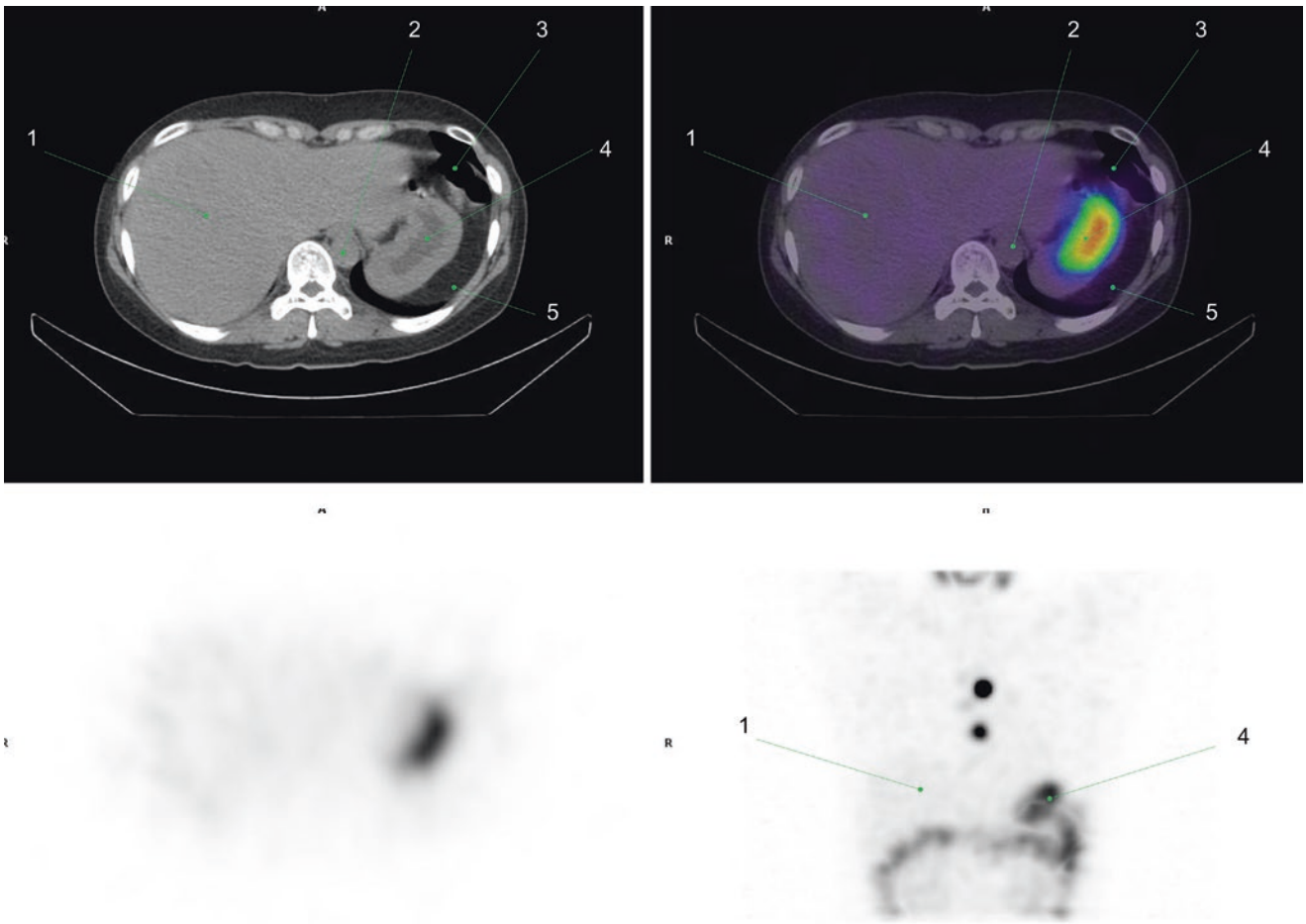

Fig. 28 1. Liver
2. Descending aorta
3. Transverse colon
4. Stomach
5. Diaphragm

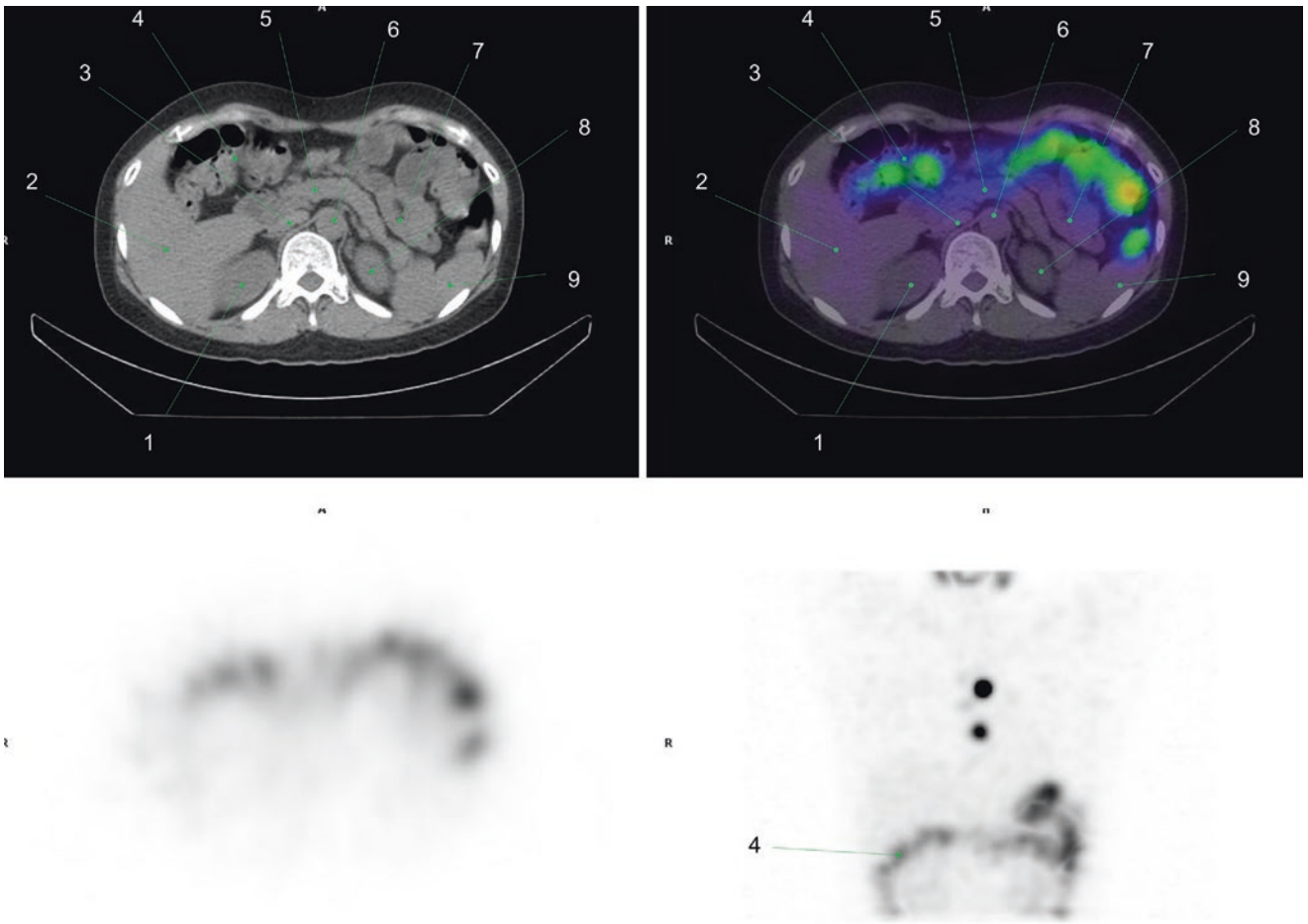

Fig. 29 1. Right kidney
2. Liver
3. Inferior vena cava
4. Transverse colon
5. Body of pancreas
6. Descending aorta
7. Jejunum
8. Left kidney
9. Spleen

1.6.3 Case 3

A 62-year-old female patient with thyroid cancer history, who was treated with thyroidectomy 6 months earlier. She attended a routine follow-up without symptoms and normal serum levels of thyroglobulin. Selected SPECT (*top*) and SPECT/CT (*bottom*) with ^{131}I demonstrated a focal area of moderately increased activity in the left thyroid bed, which was confirmed to be residual functioning thyroid tissue (Fig. 30).

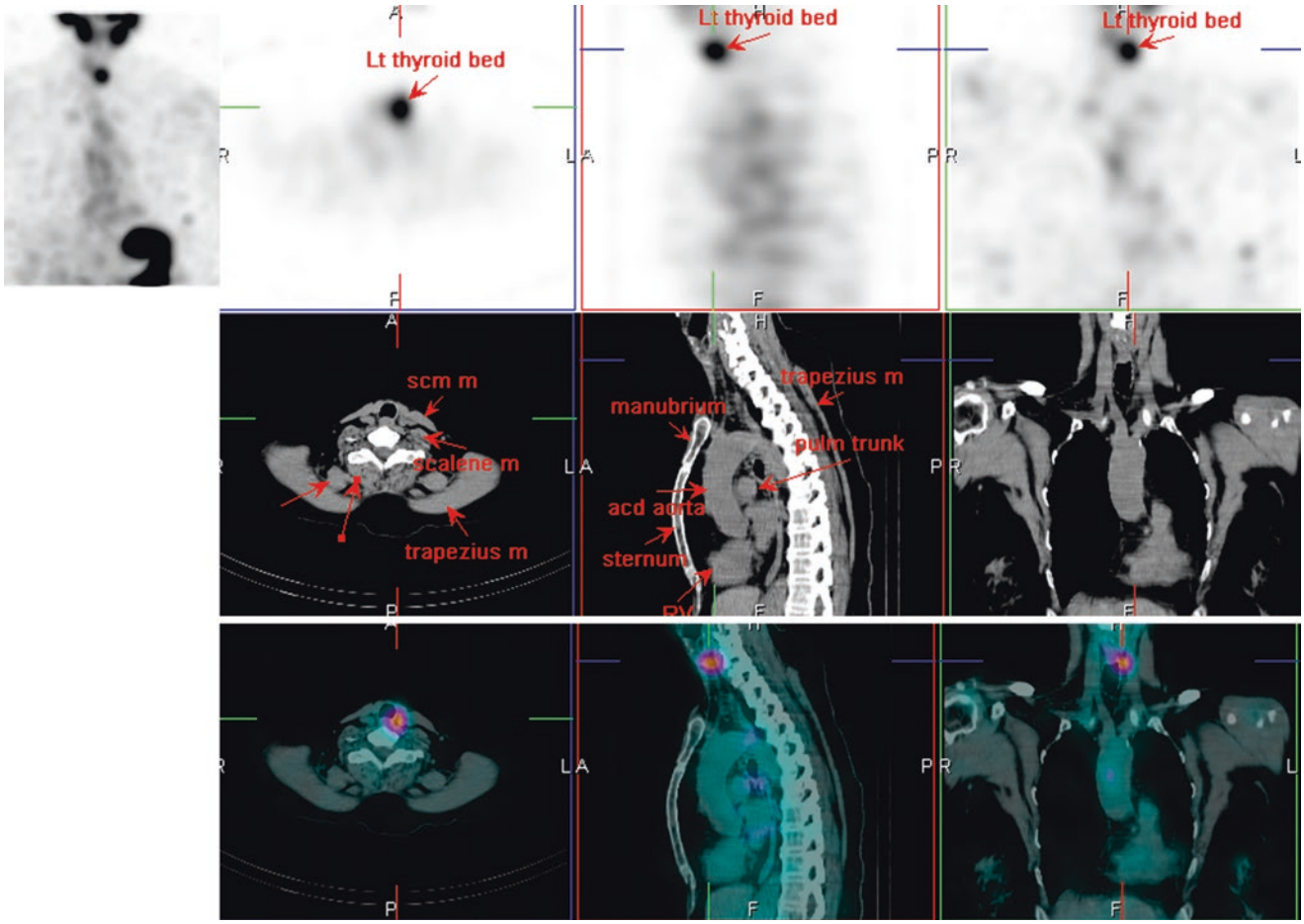

Fig. 30 ^{131}I SPECT/CT

1.7 Parathyroid Adenoma

1.7.1 Case 1

A 63-year-old male patient with hypercalcemia and weight loss. Laboratory tests showed abnormal serum calcium, phosphorus, and parathyroid hormone levels, so primary hyperparathyroidism was suspected. ^{99m}Tc-MIBI SPECT/CT was performed finding focal delayed uptake in the lower aspect of the right thyroid lobe, corresponding to a parathyroid adenoma, type E (Figs. 31, 32, 33, 34, and 35) [40, 41].

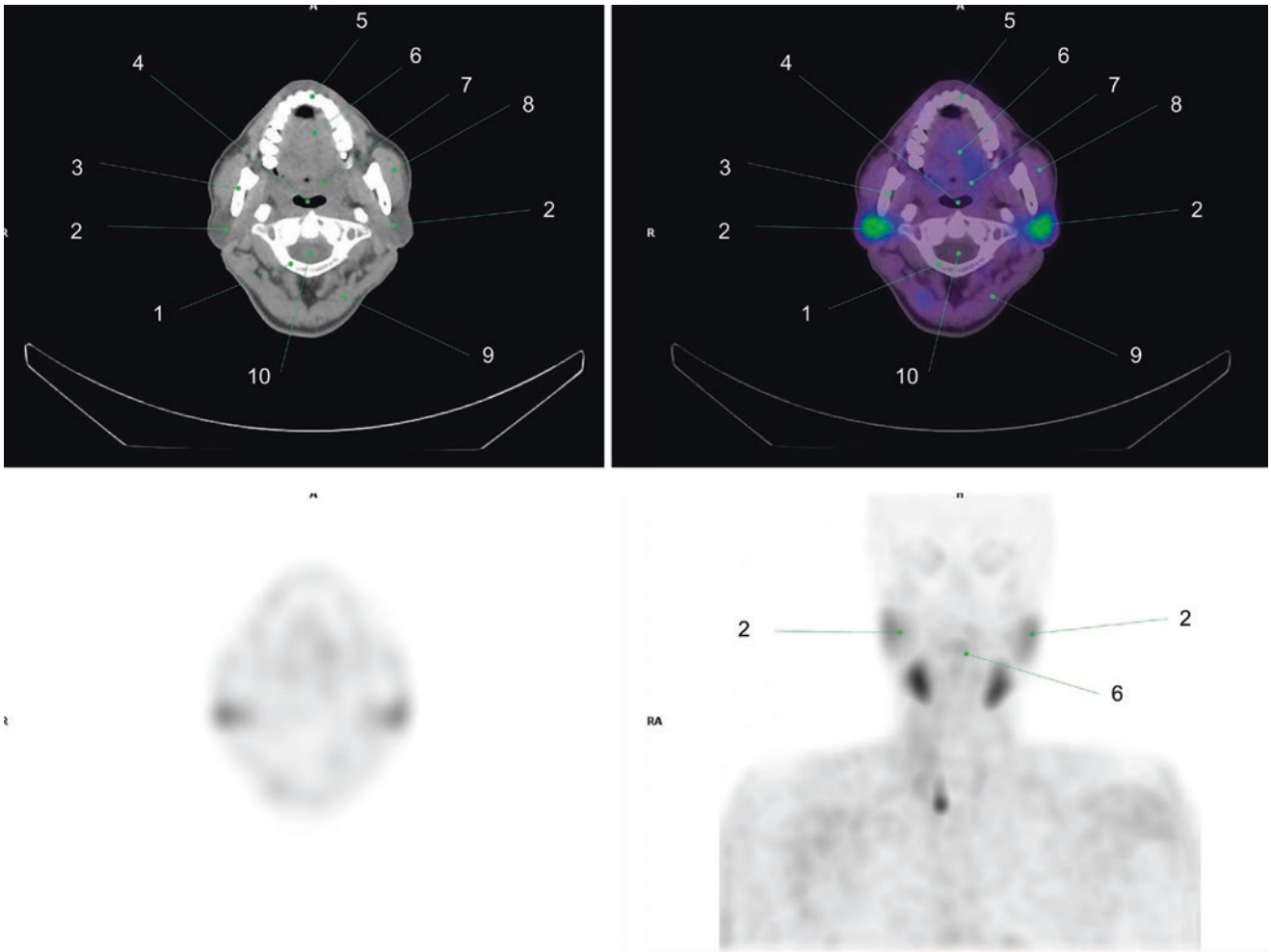

Fig. 31 1. Posterior arch of C1 spine
2. Parotid glands
3. Mandibular ramus
4. Pharyngeal space
5. Body of mandible
6. Body of tongue
7. Palatine tonsil
8. Masseter muscle (superficial part)
9. Trapezius muscle
10. Spinal cord

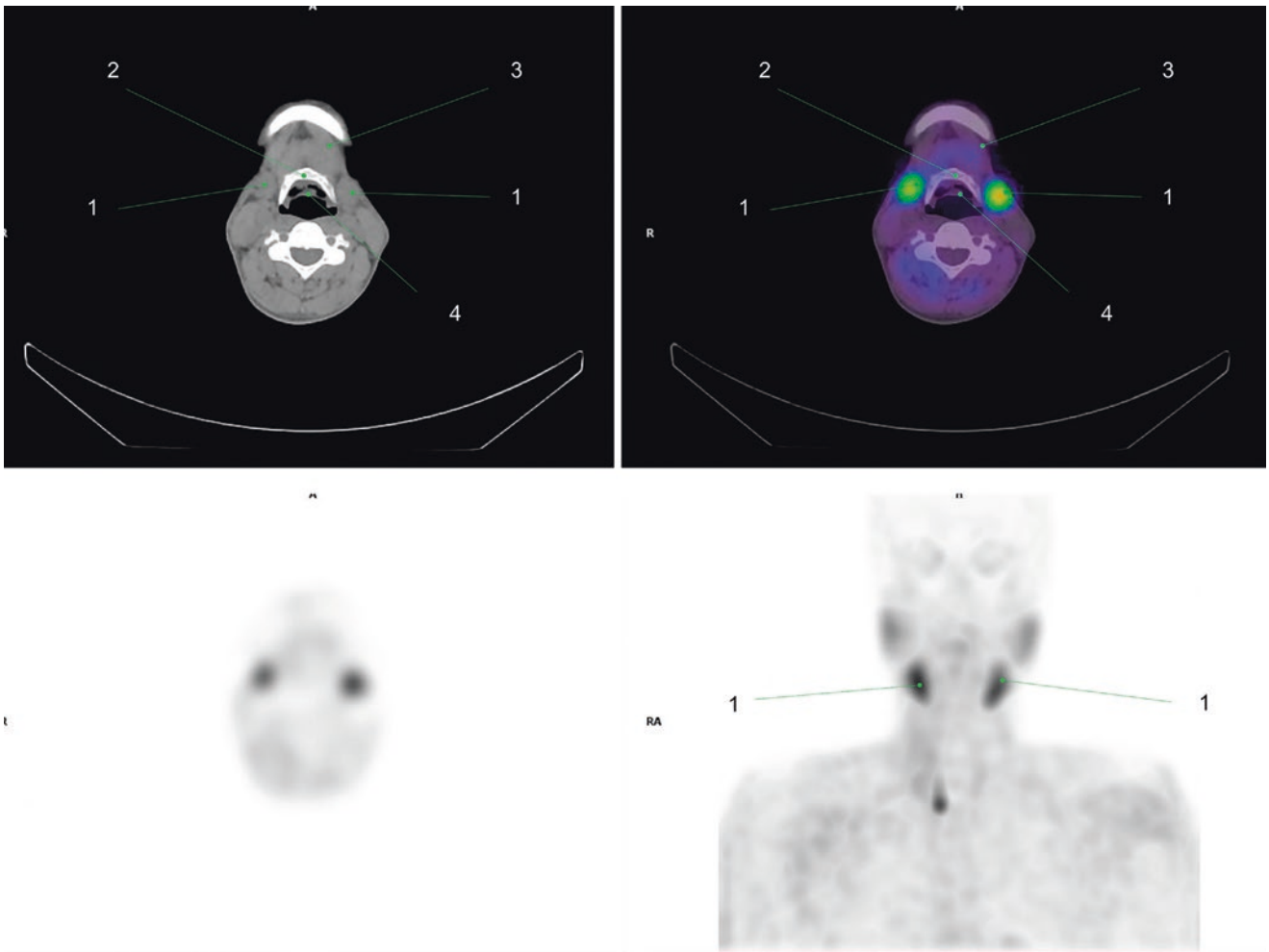

Fig. 32 1. Submandibular glands
2. Body of hyoid bone
3. Digastric muscle anterior belly
4. Epiglottis

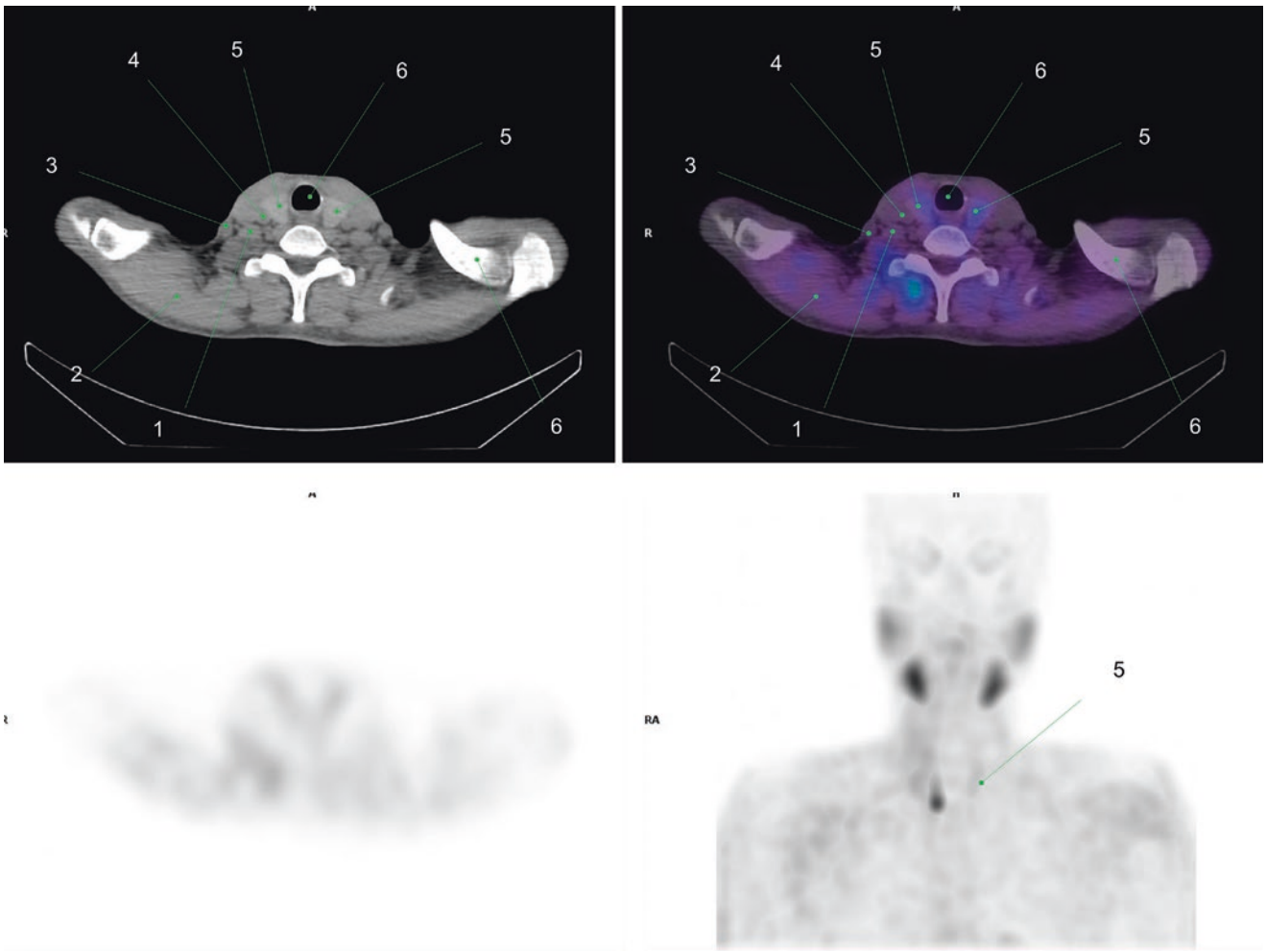

Fig. 33 1. Internal jugular vein
2. Trapezius muscle
3. External jugular vein
4. Common carotid artery
5. Thyroid gland
6. Trachea

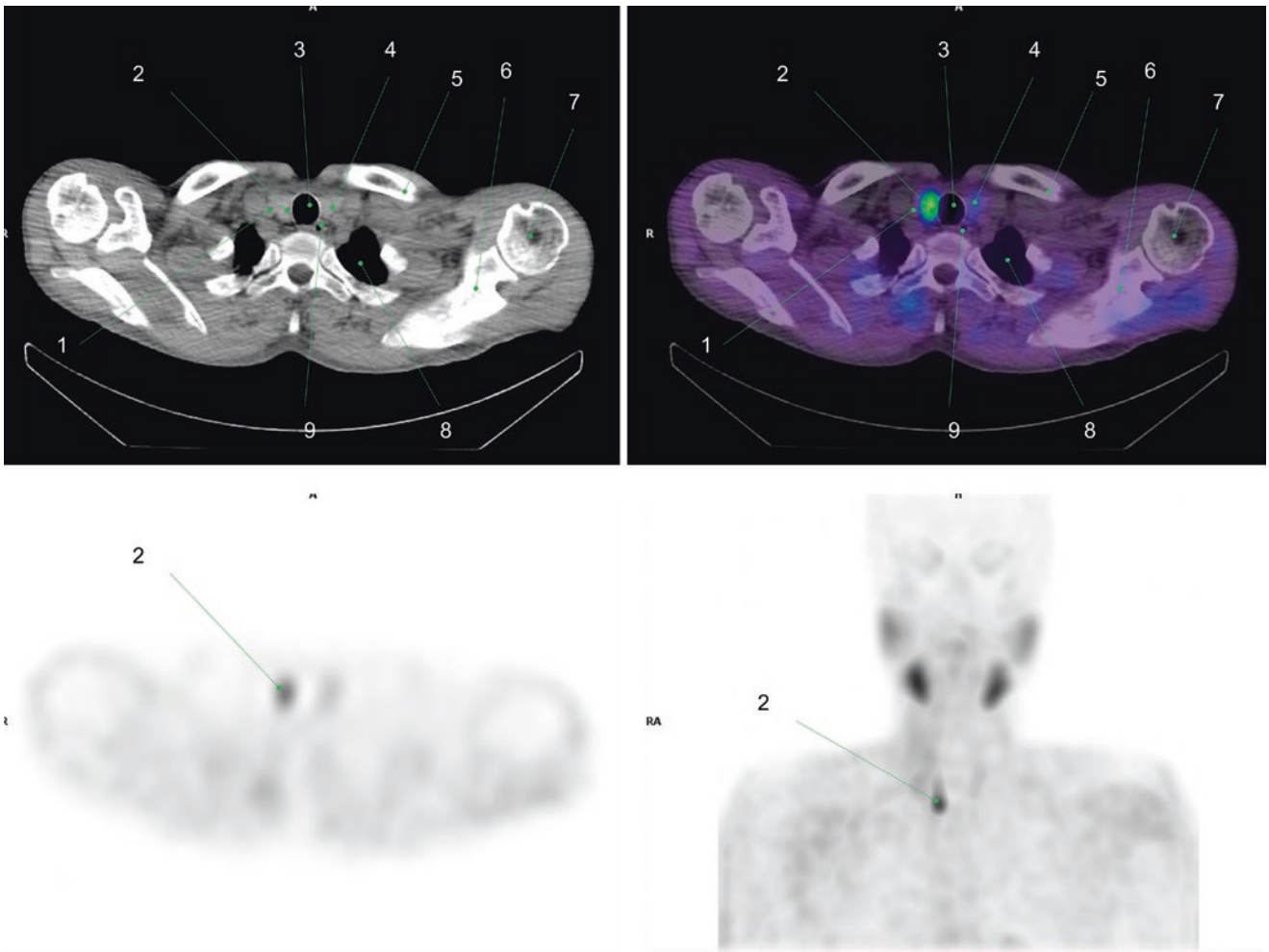

Fig. 34 1. Right common carotid artery
2. Parathyroid gland
3. Trachea
4. Thyroid Left lobe
5. Left clavicle
6. Left scapular
7. Head of left humerus
8. Left lung apex
9. Esophagus

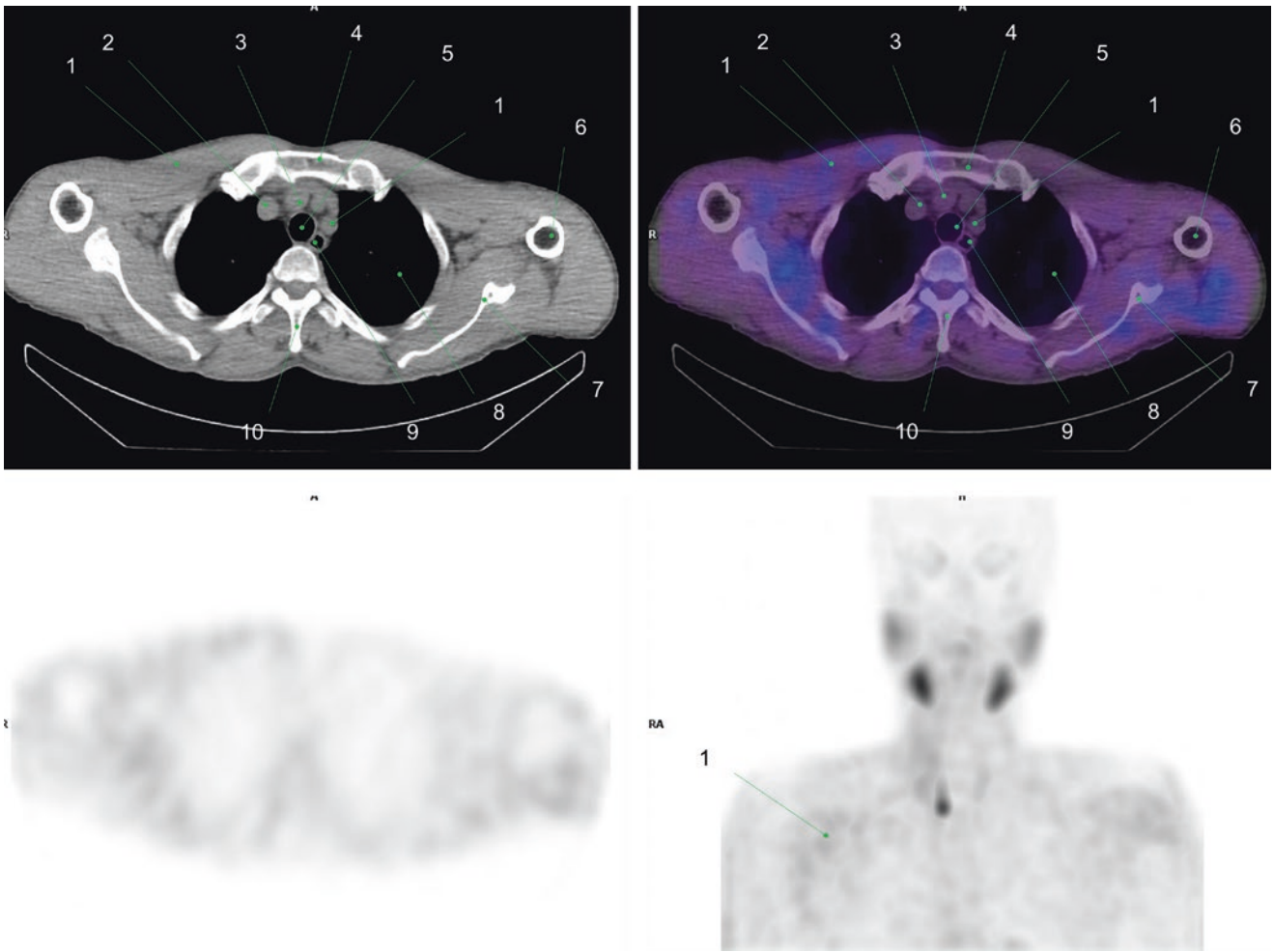

Fig. 35 1. Right pectoralis major muscle
2. Subclavian artery
3. Common carotid artery
4. Sternum
5. Trachea
6. Humeral shaft
7. Scapular
8. Left Lung
9. Esophagus
10. Spinous process of T3 spine

1.7.2 Case 2

A 63-year-old female patient with suspicion of parathyroid adenoma, who underwent ^{99m}Tc-MIBI SPECT/CT. Images showed a focal area of moderately increased activity in the right lower anterior mediastinum, which was confirmed as a parathyroid adenoma, type F (Fig. 36) [42].

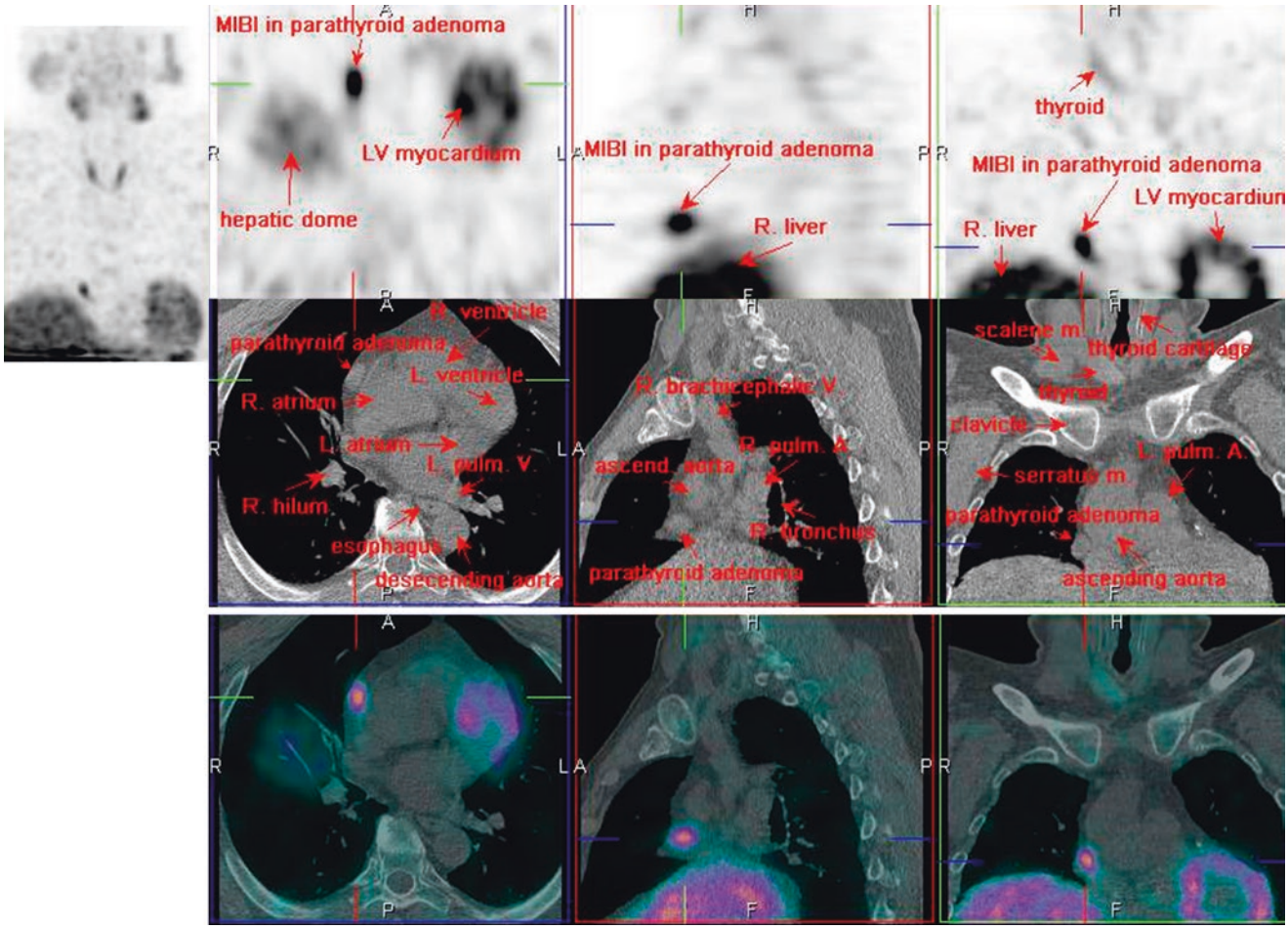

Fig. 36 ^{99m}Tc-MIBI SPECT/CT

1.7.3 Case 3

A 71-year-old female patient with primary hyperparathyroidism, who underwent ^{99m}Tc-MIBI SPECT/CT. Images showed a focal moderately increased activity in the right paraesophageal area at the level of the thoracic inlet, which corresponded to a parathyroid adenoma, type F (Fig. 37) [42].

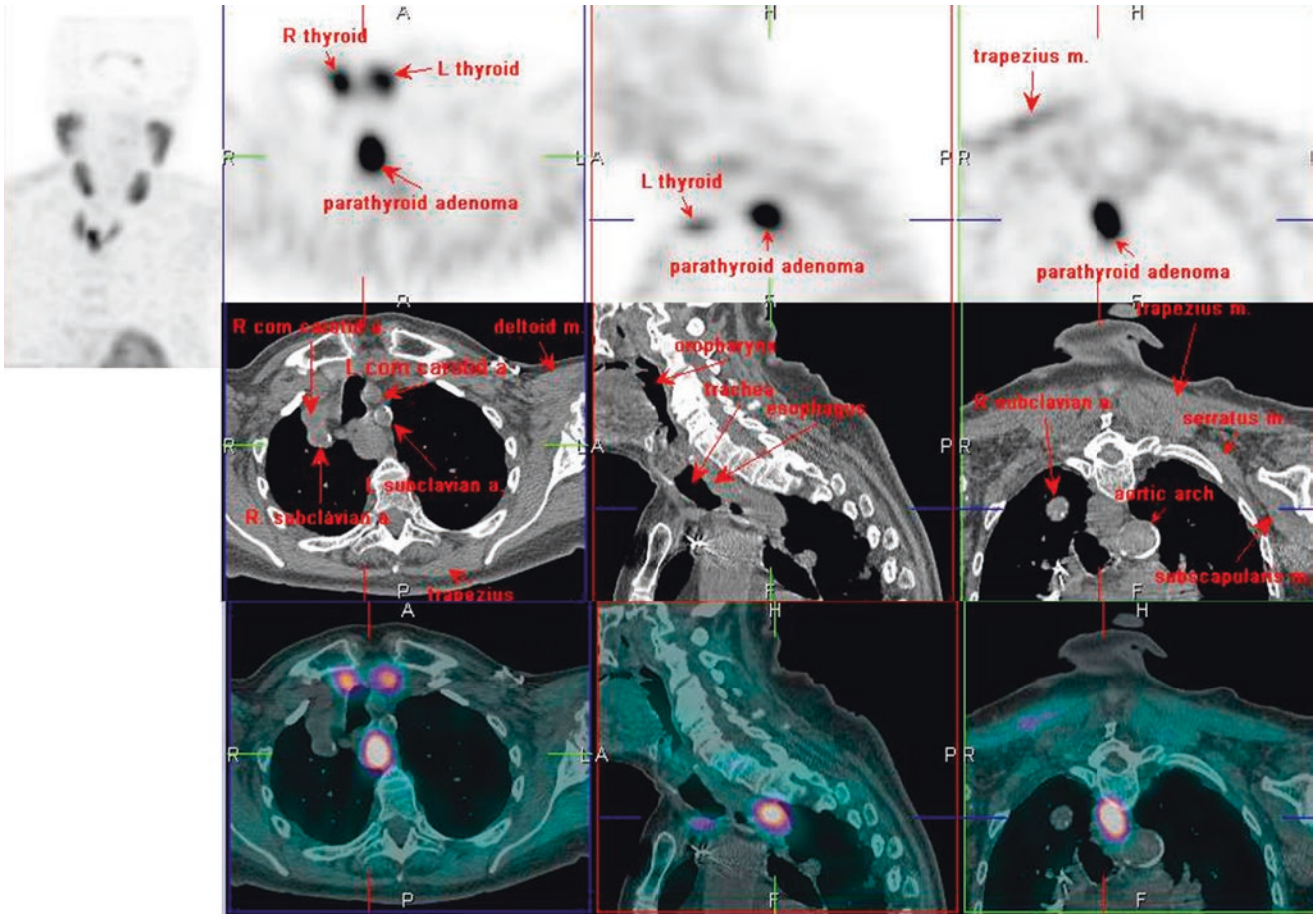

Fig. 37 ^{99m}Tc-MIBI SPECT/CT

1.7.4 Case 4

A 56-year-old male patient with confirmed diagnosis of a parathyroid adenoma (type E). Selected SPECT (*top*) and SPECT/CT (*bottom*) of the neck and chest with ^{99m}Tc-MIBI were performed. Images showed a focal moderately increased activity in the right paratracheal area at the level of the right inferior thyroid bed (Fig. 38) [42].

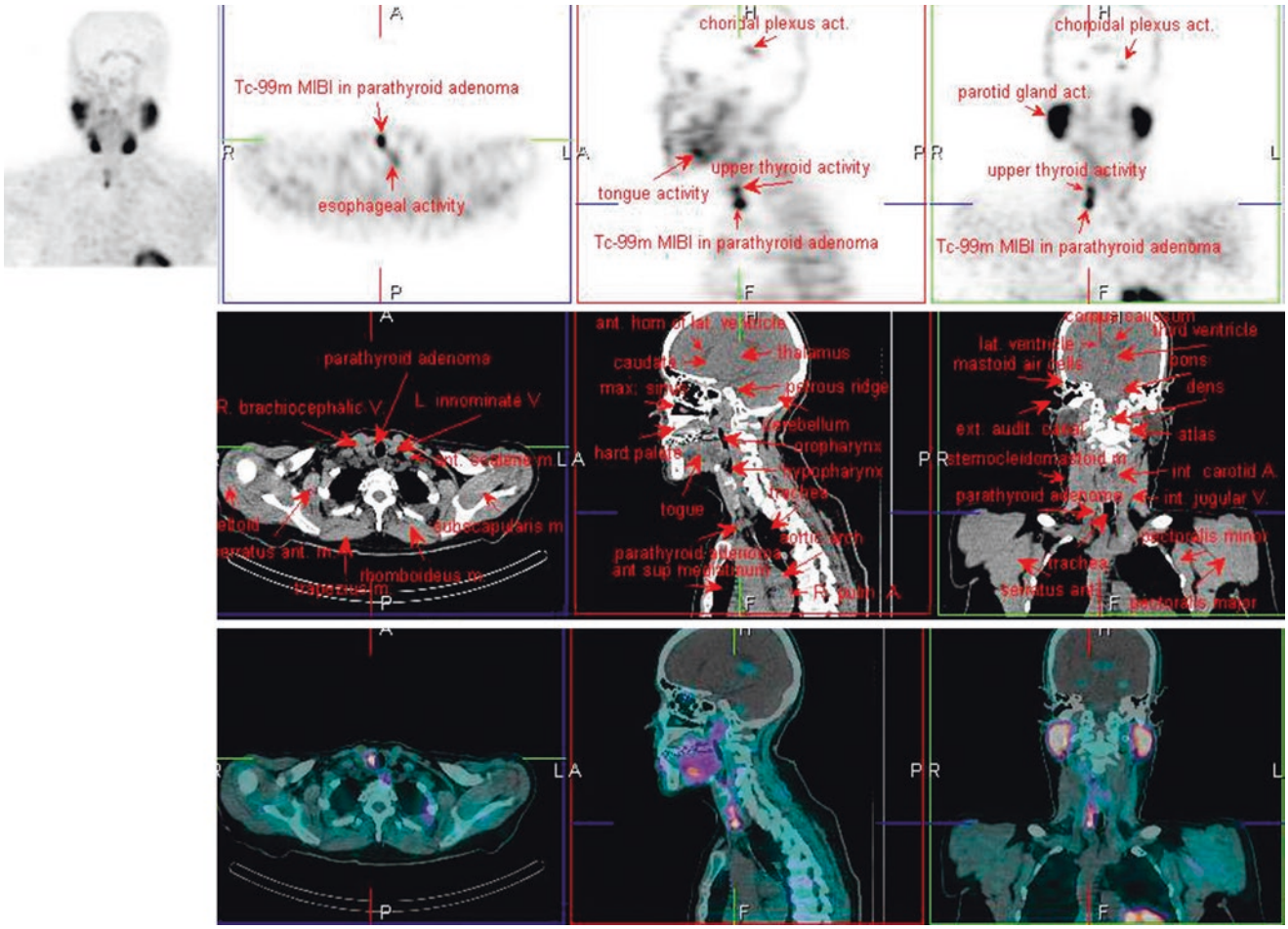

Fig. 38 ^{99m}Tc-MIBI SPECT/CT

1.7.5 Case 5

A 63-year-old female patient with suspicion of a parathyroid adenoma (type C). Selected SPECT (top) and SPECT/CT images of the neck and chest with ^{99m}Tc-MIBI showed a focal moderately increased activity in the right paraesophageal area, confirming the diagnosis (Fig. 39) [42].

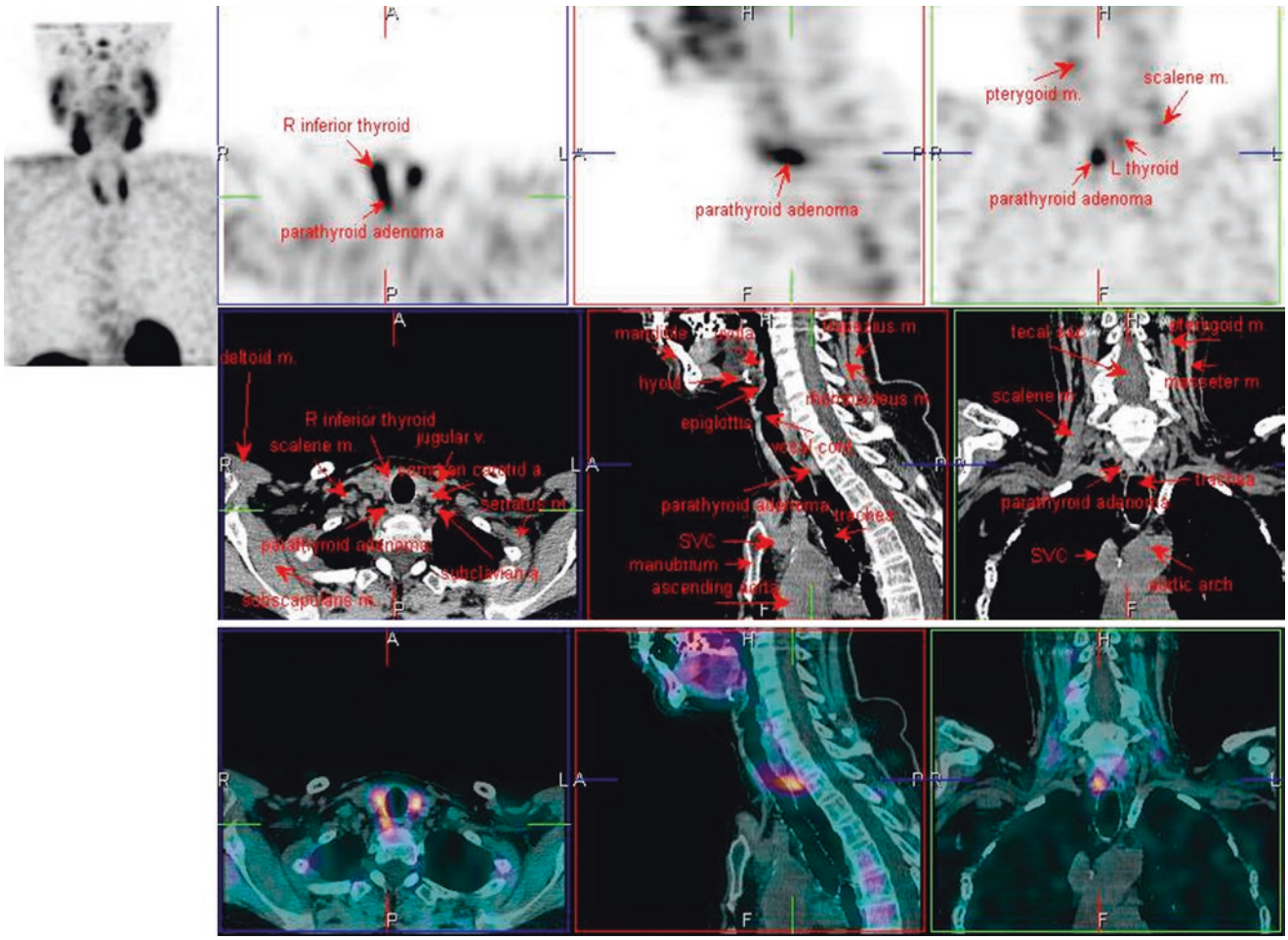

Fig. 39 ^{99m}Tc-MIBI SPECT/CT

1.8 Mesothelioma

1.8.1 Case 1

A 69-year-old male patient with chest pain and dyspnea. The diagnosis of a mesothelioma was confirmed and ^{99m}Tc-MAA SPECT/CT was performed during staging. Images showed slightly decreased activity in the right upper and middle lobes as well as moderately decreased activity in the right lower lobe. Also noted were perfusion defects along the posterolateral periphery of the right lower lobe owing to nodular pleural lesions (Fig. 40) [43].

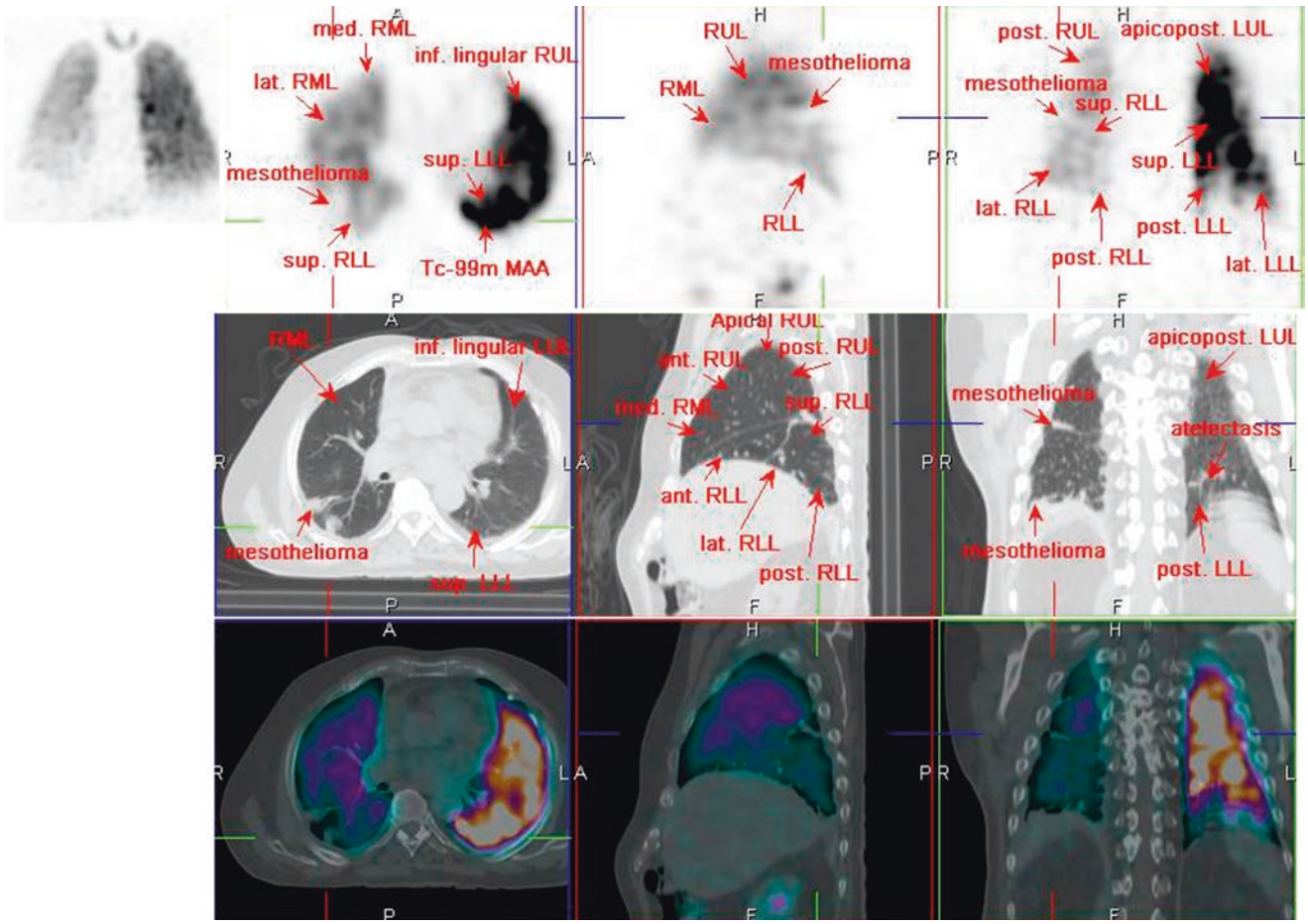

Fig. 40 ^{99m}Tc-MAA SPECT/CT

1.9 Bone Tumors

1.9.1 Case 1

A 10-year-old girl with a history of ossifying fibroma, who underwent ^{99m}Tc-methylene diphosphonate (MDP) SPECT/CT during a follow-up. Images showed moderately increased activity in the bilateral maxillary sinuses and right mandible at expansile bone lesions with fibrous matrix and peripheral sclerotic rim. Ossifying fibromas are benign bone tumors and occur often in children under 10 years in the tibia, femur, mandible, maxilla, and nasal areas (Fig. 41) [45].

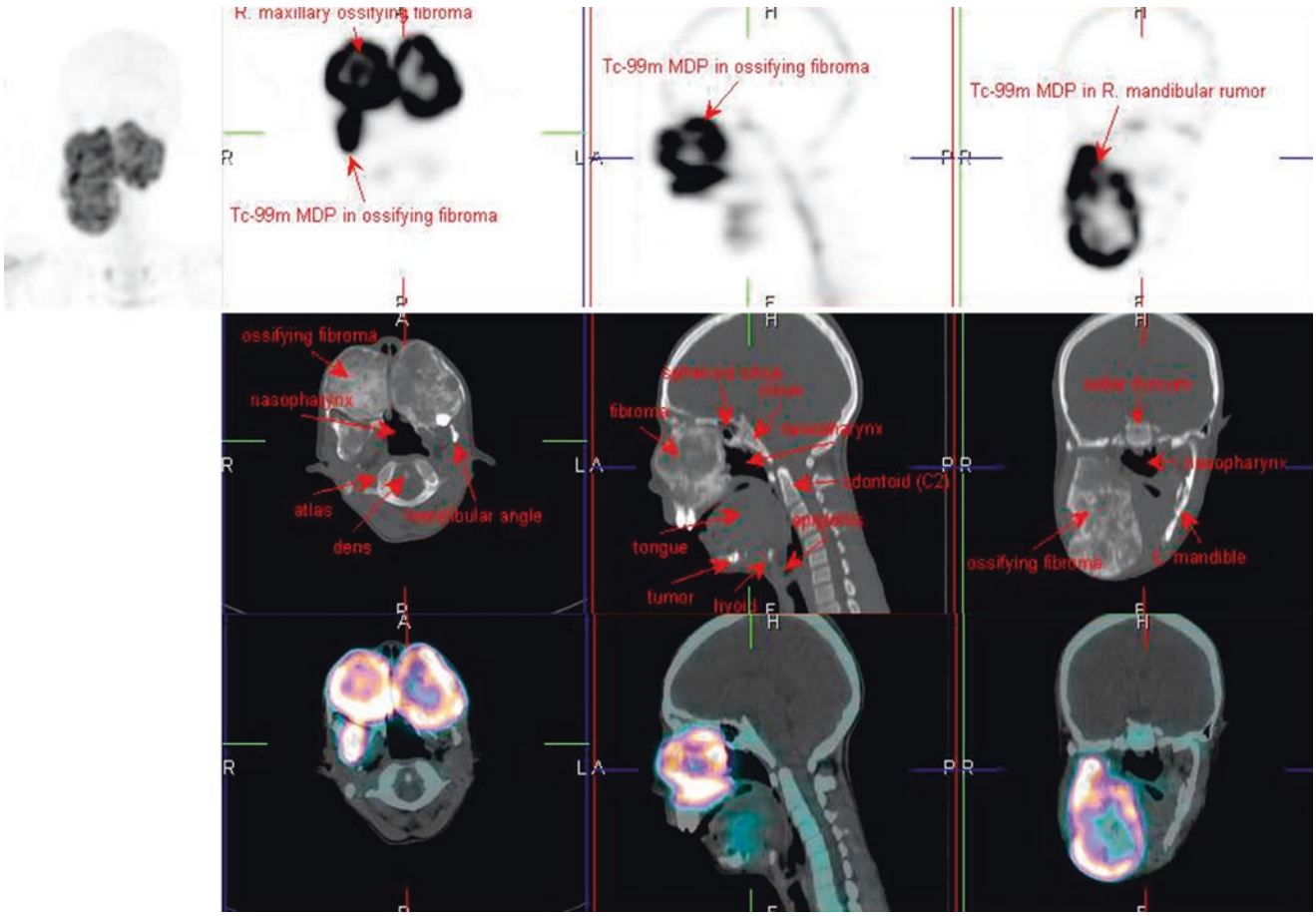

Fig. 41 ^{99m}Tc-MDP SPECT/CT

1.9.2 Case 2

A 76-year-old male patient with lower back pain. ^{99m}Tc-MDP SPECT/CT showed focal increased uptake at bilateral L5-S1 facet joints, with degenerative changes. Additionally, a focal increased uptake was noted at the superior aspect of the left iliac bone, corresponding to a non-aggressive bone lesion with a central hipodense nidus surrounded by sclerotic bone changes, which was confirmed to be an osteoid osteoma (Fig. 42).

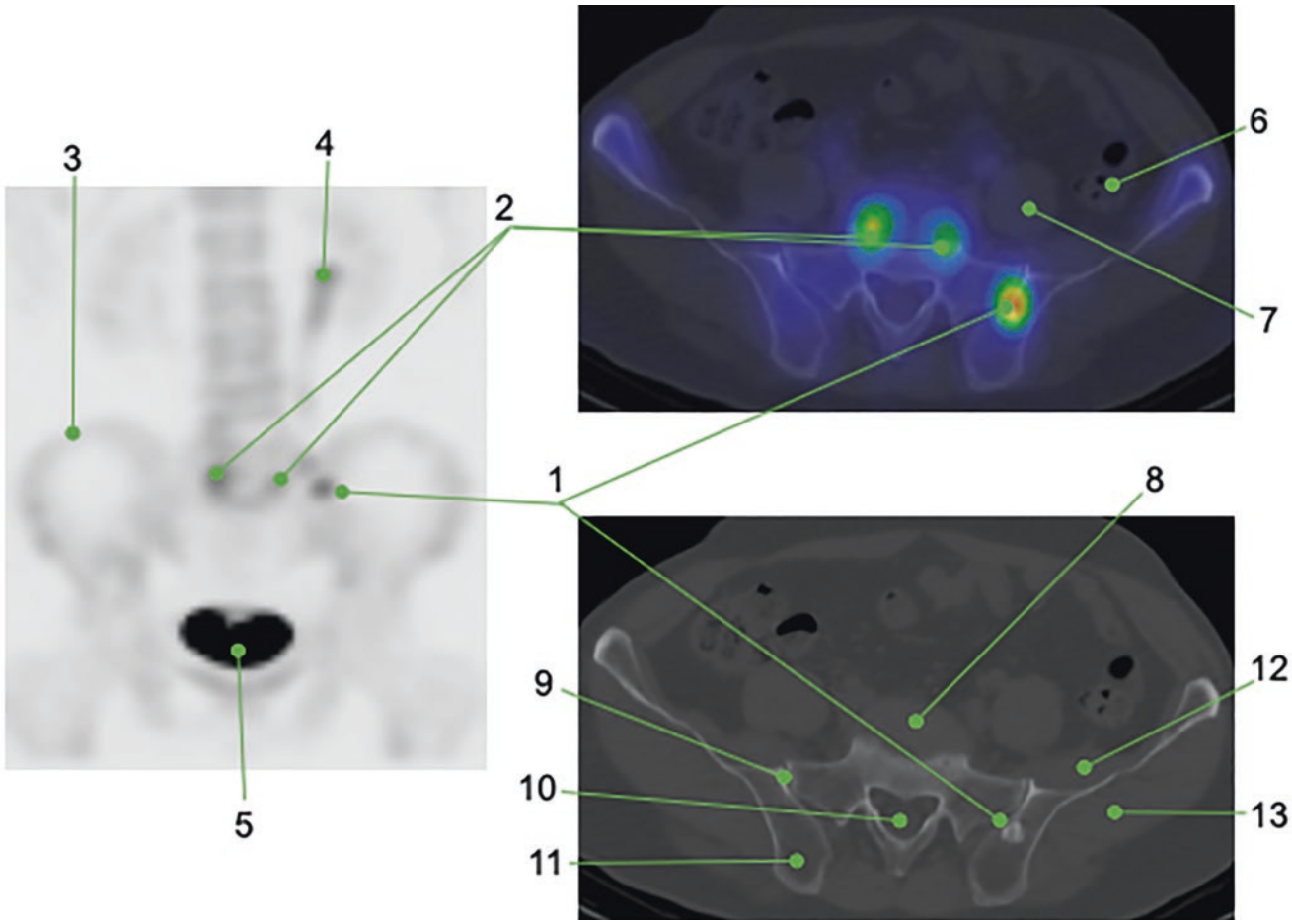

Fig. 42 1. Focal increased uptake at left iliac osteoid osteoma
2. Focal increased uptake at both L5-S1 facet joints degenerative changes
3. Right iliac crest
4. Left renal pelvis and proximal ureter
5. Bladder
6. Descending colon
7. Left psoas muscle
8. L5-S1 intervertebral disc
9. Right sacroiliac joint
10. Sacral canal
11. Right iliac tuberosity
12. Left iliacus muscle
13. Left gluteus maximus muscle

1.10 Bone Metastases

1.10.1 Case 1

A 38-year-old female patient with a history of breast cancer, who attended with right shoulder pain. ^{99m}Tc-MDP SPECT/CT was done, finding focal moderately increased activity in the right scapular body, caused by metastasis. Bone metastases are over ten times more common than primary bone tumors. Most metastases occur in the red bone marrow, most commonly in the axial skeleton. Osteoblastic metastases often occur with prostate cancer, transitional cell carcinoma, mucinous tumor, and carcinoid, whereas lytic metastases mostly occur with lung, thyroid, and renal cancers. Breast, stomach, and colon cancers can show osteolytic or osteoblastic lesions (Fig. 43) [46].

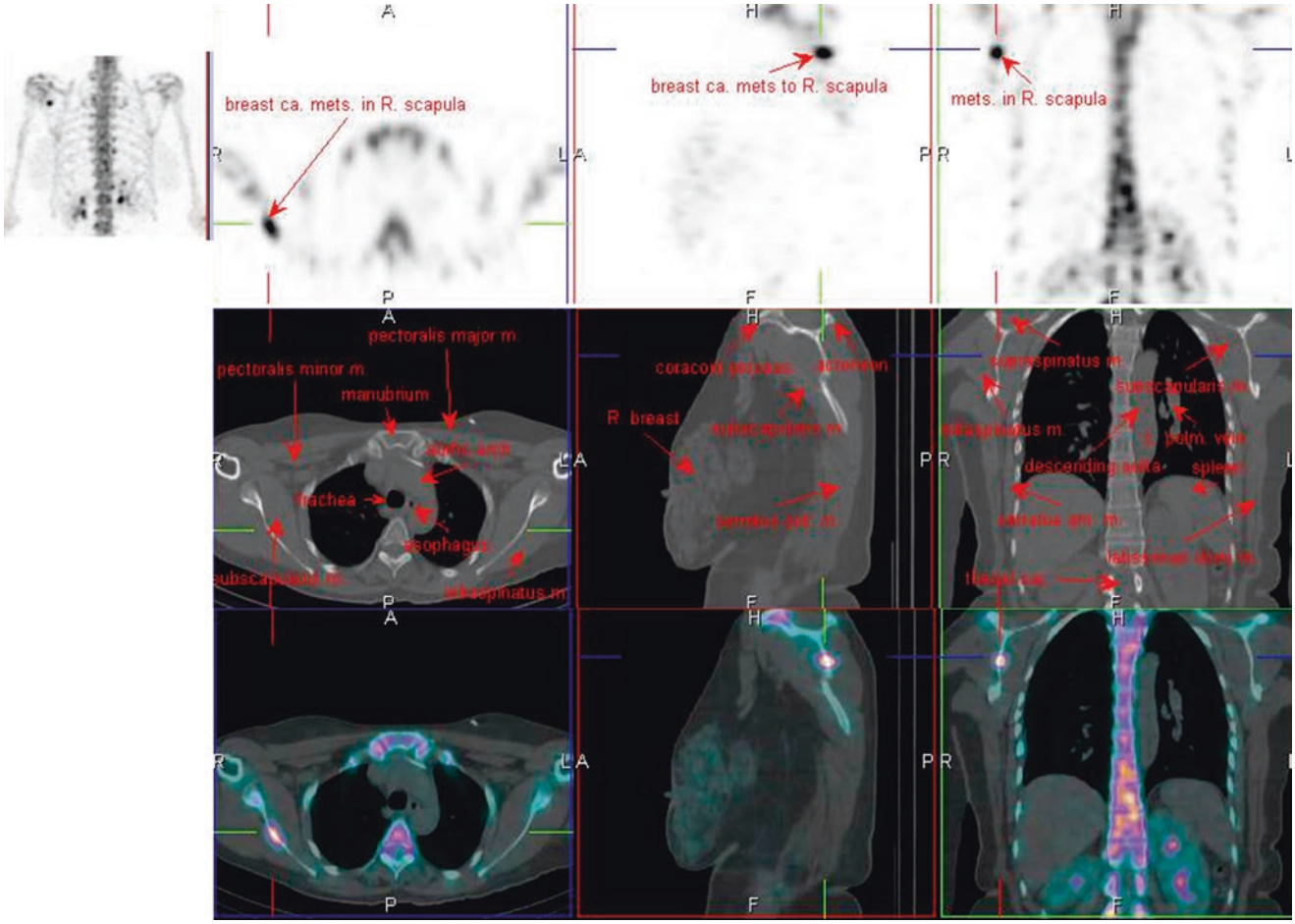

Fig. 43 ^{99m}Tc-MDP SPECT/CT

1.10.2 Case 2

A 65-year-old female patient with a history of breast cancer, who attended due to right knee pain without previous trauma. ^{99m}Tc-MDP SPECT/CT showed markedly increased activity in the lateral posterior condyle of the right distal femur at a mixed lytic and blastic bone lesion, consistent with bone metastasis (Fig. 44).

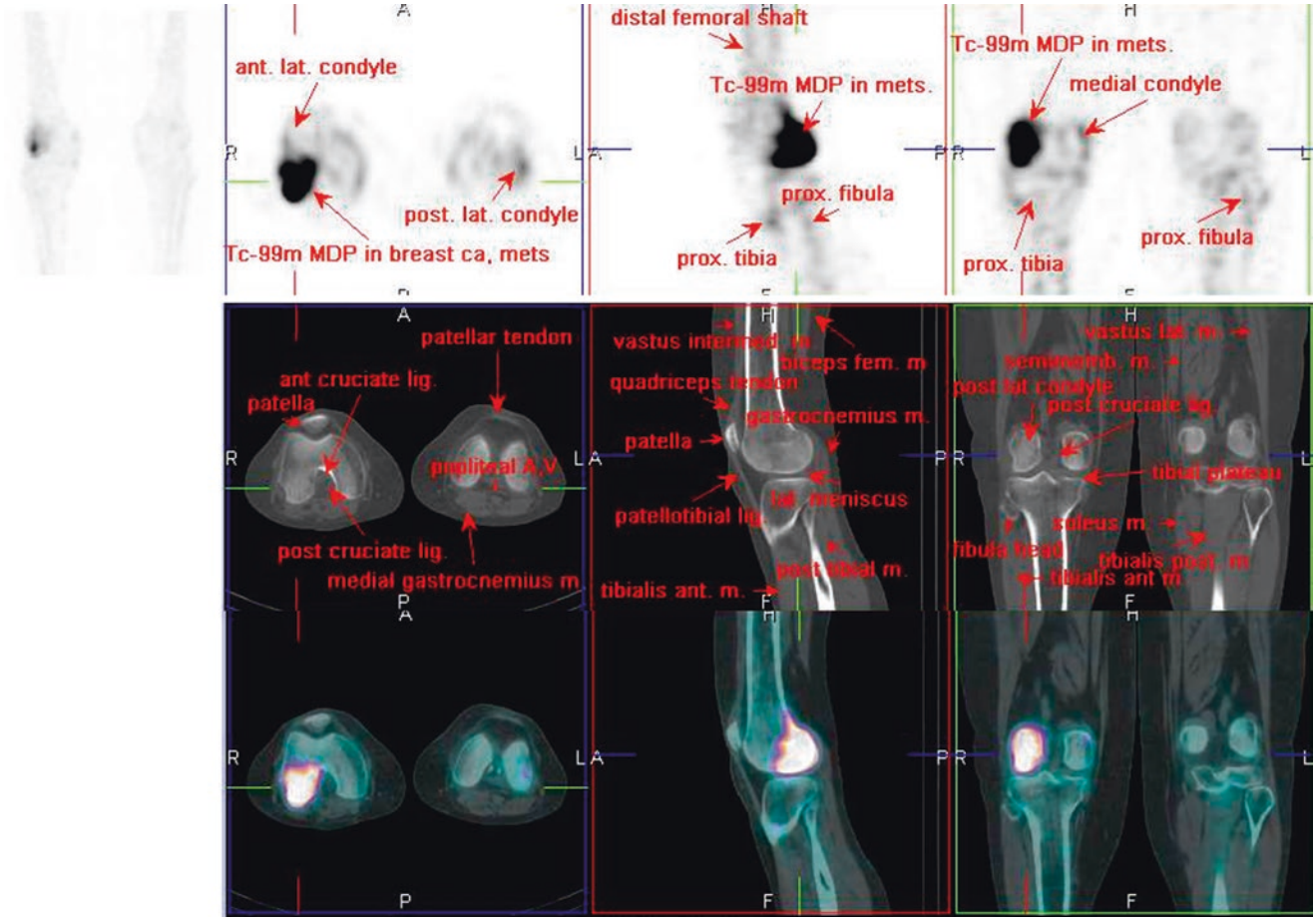

Fig. 44 ^{99m}Tc-MDP SPECT/CT

1.10.3 Case 3

A 47-year-old female patient with a history of breast cancer presented with pain in the lower back. Selected SPECT (*top*) and SPECT/CT (*bottom*) images of the pelvis with ^{99m}Tc-MDP showed markedly increased activity in the left sacral ala, abutting the sacroiliac joint (Fig. 45).

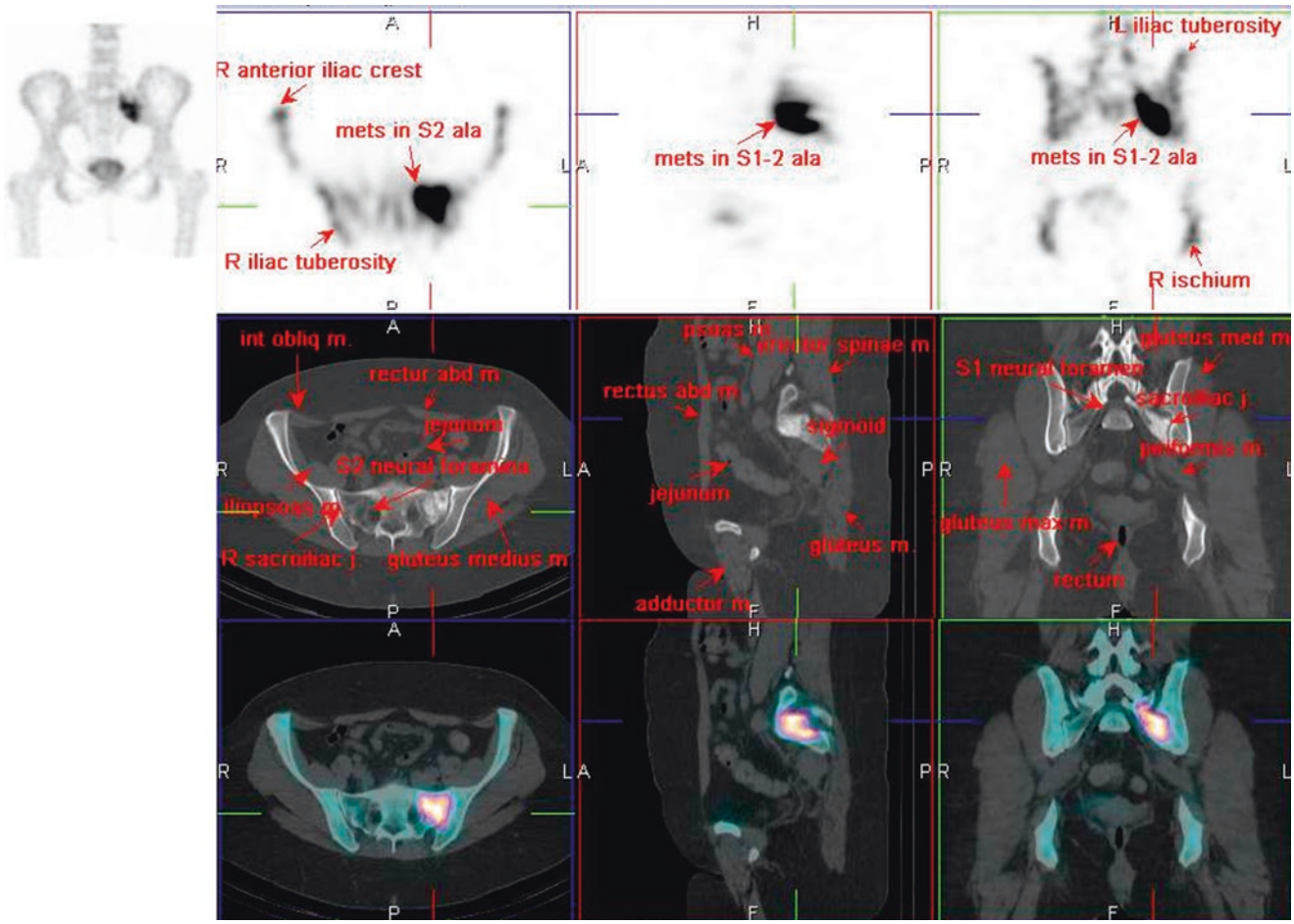

Fig. 45 ^{99m}Tc-MDP SPECT/CT

1.10.4 Case 4

A 66-year-old female patient with a history of non-Hodgkin lymphoma. She attended an early checkup due to lower back pain. ^{99m}Tc-MDP SPECT/CT was performed, finding focal areas of slightly increased activity in the bilateral iliac alae and tuberosities as well as L3-S1 vertebral bodies. Biopsy confirmed active lymphoma involvement (Fig. 46).

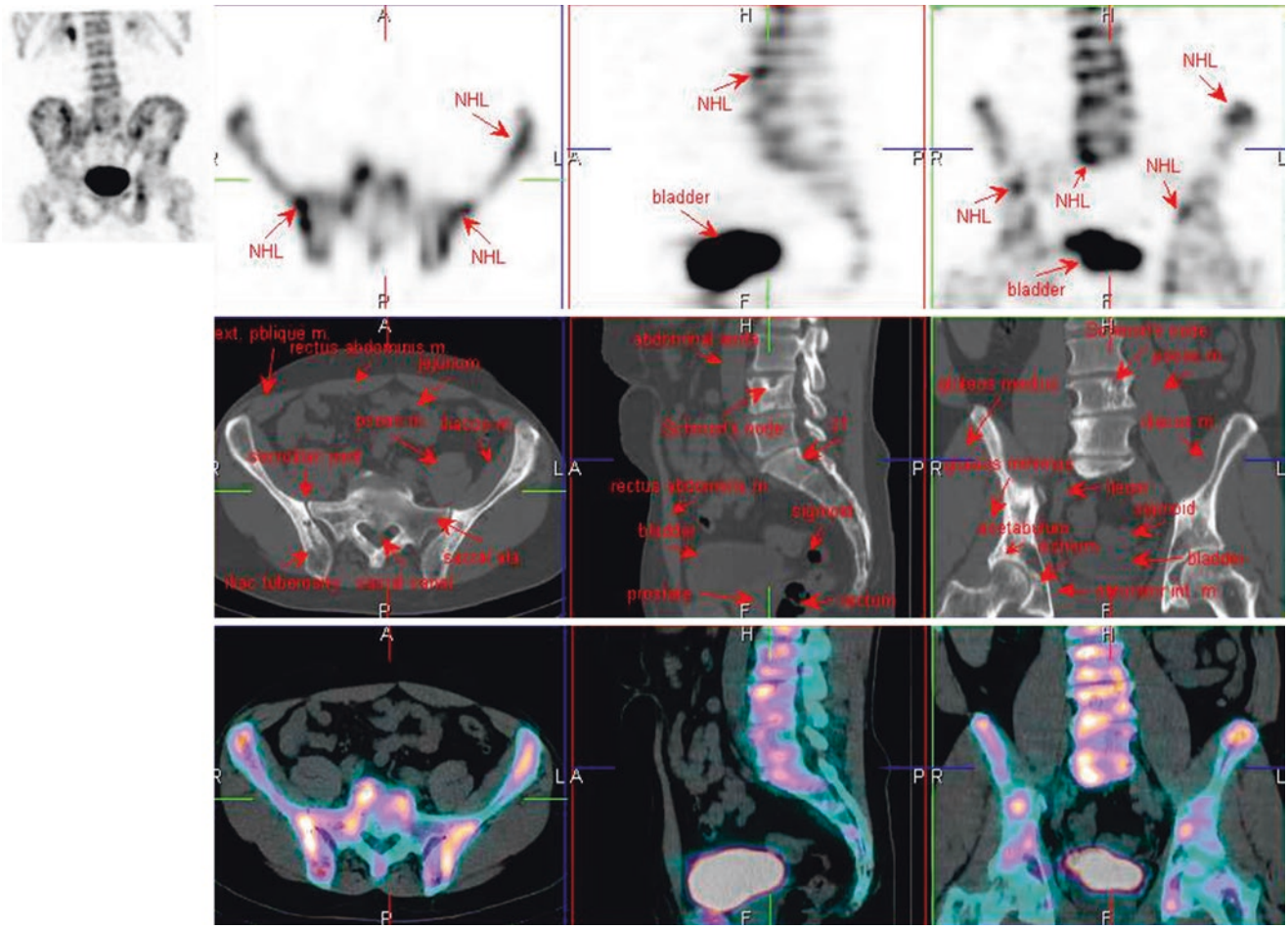

Fig. 46 ^{99m}Tc-MDP SPECT/CT

2 Non-Tumorous Conditions

2.1 Bone

2.1.1 Case 1

A 71-year-old female patient with chronic right knee pain. The clinical diagnosis was a medial meniscus tear in the right knee, and ^{99m}Tc-MDP SPECT/CT was done for further evaluation. Focal increased uptake was found in the right medial meniscus area, confirming the clinical diagnosis and associated changes in the subjacent bone (Figs. 47, 48, 49, and 50) [49].

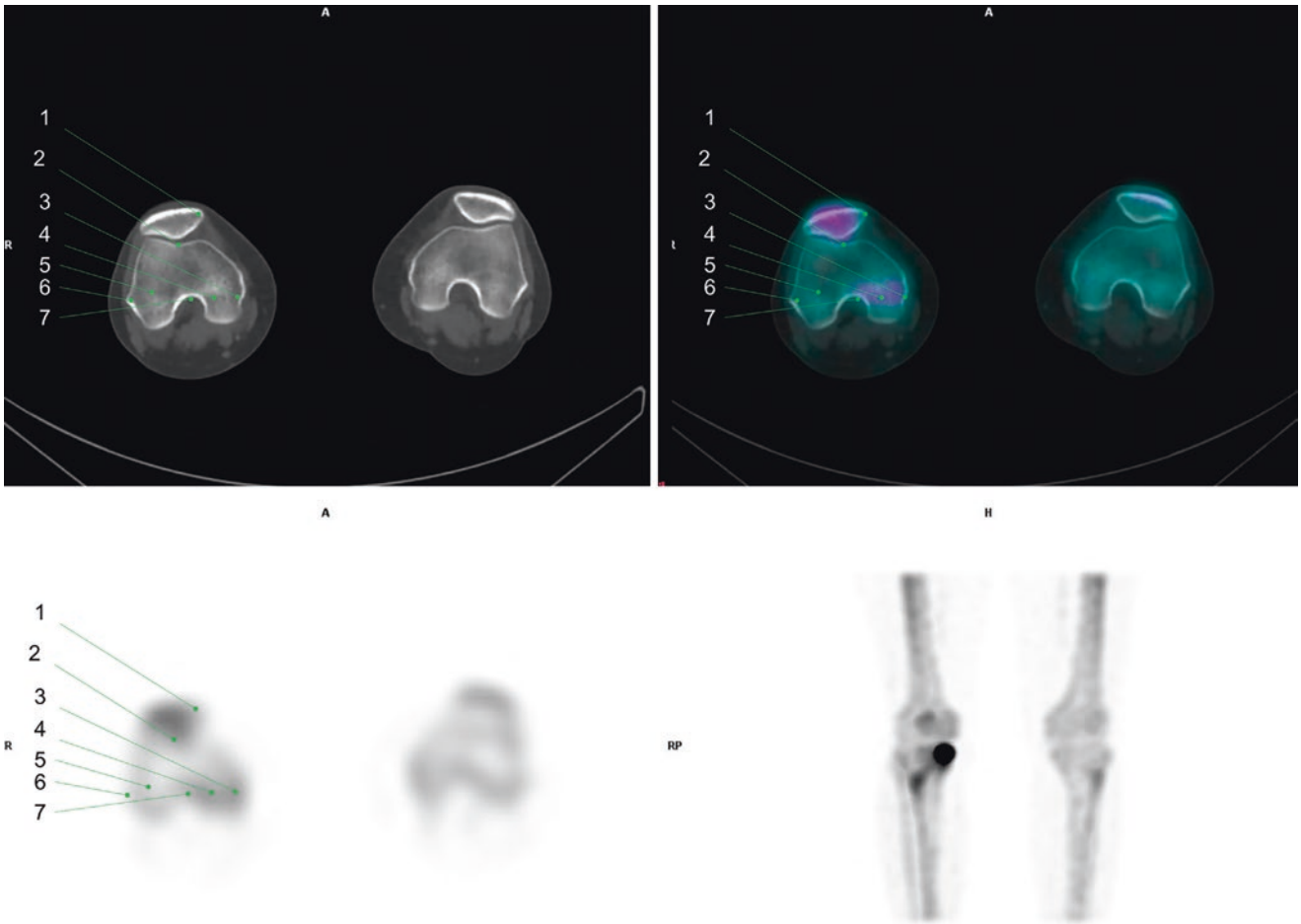

Fig. 47 1. Patella
2. Articular surface
3. Right medial epicondyle
4. Right medial condyle
5. Right lateral condyle
6. Right lateral epicondyle
7. Intercondylar fossa

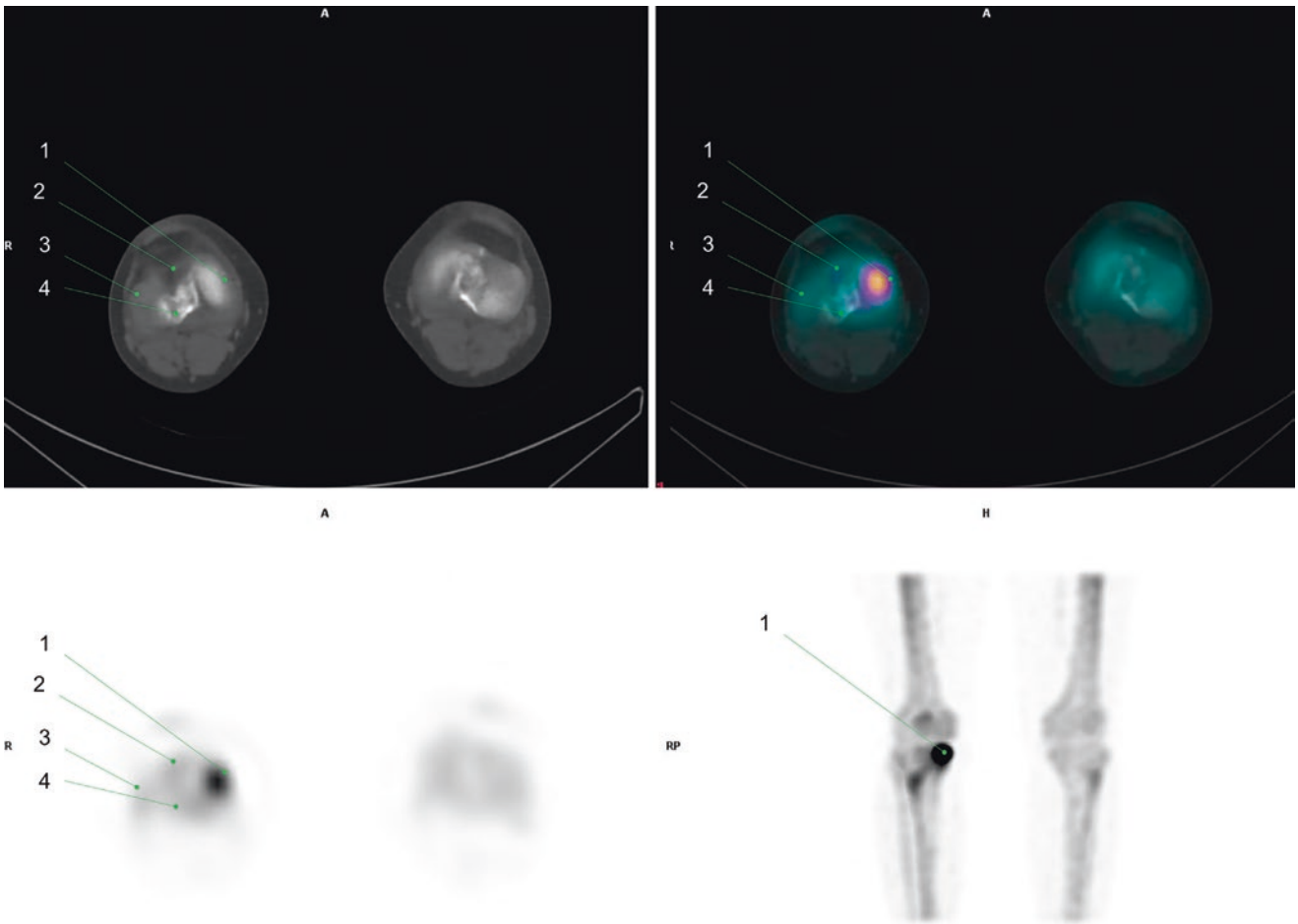

Fig. 48 1. Right medial condyle
2. Anterior intercondylar area
3. Superior articular surface
4. Posterior intercondylar

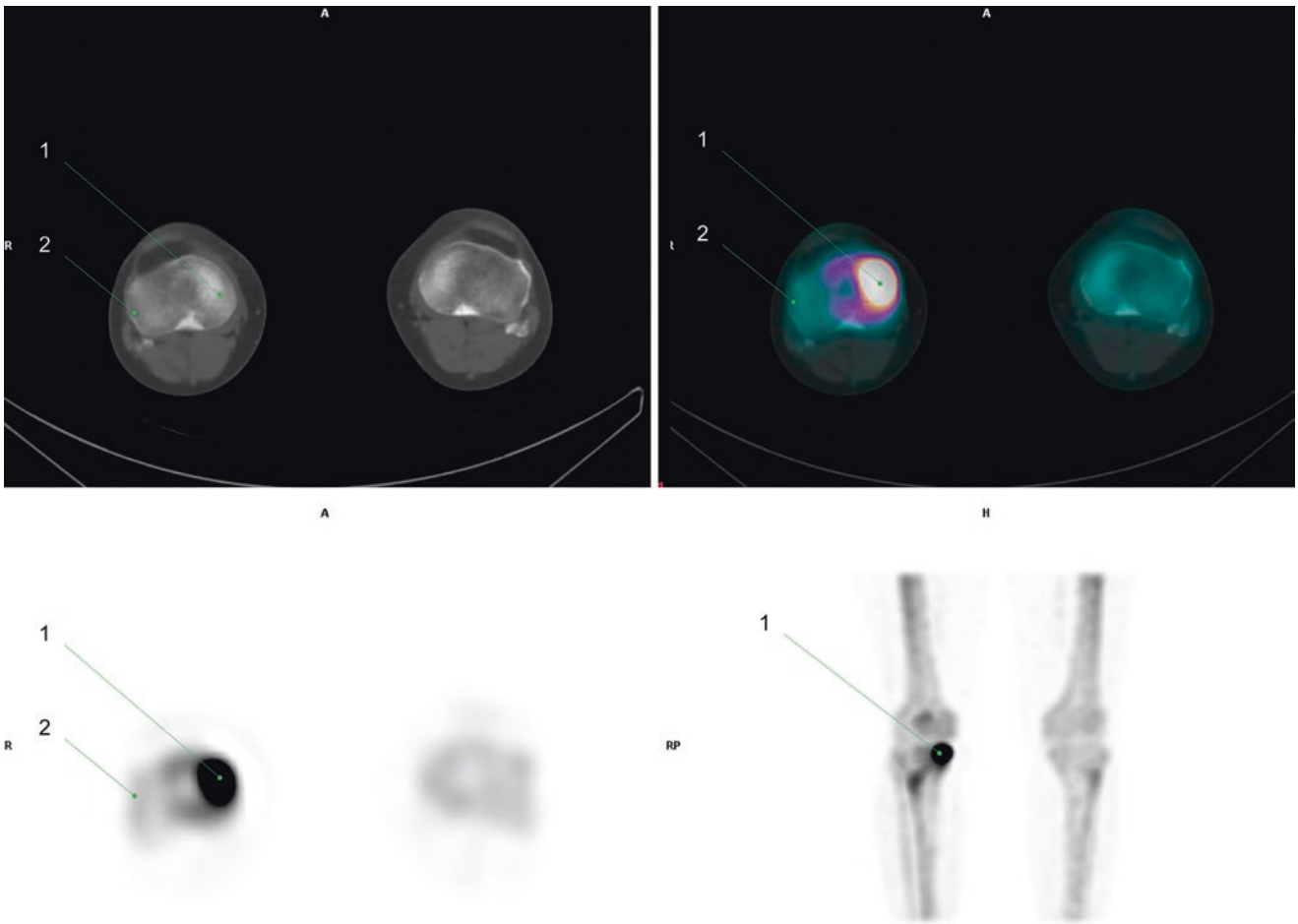

Fig. 49 1. Active lesion at right medial meniscus
2. Right tibial lateral condyle

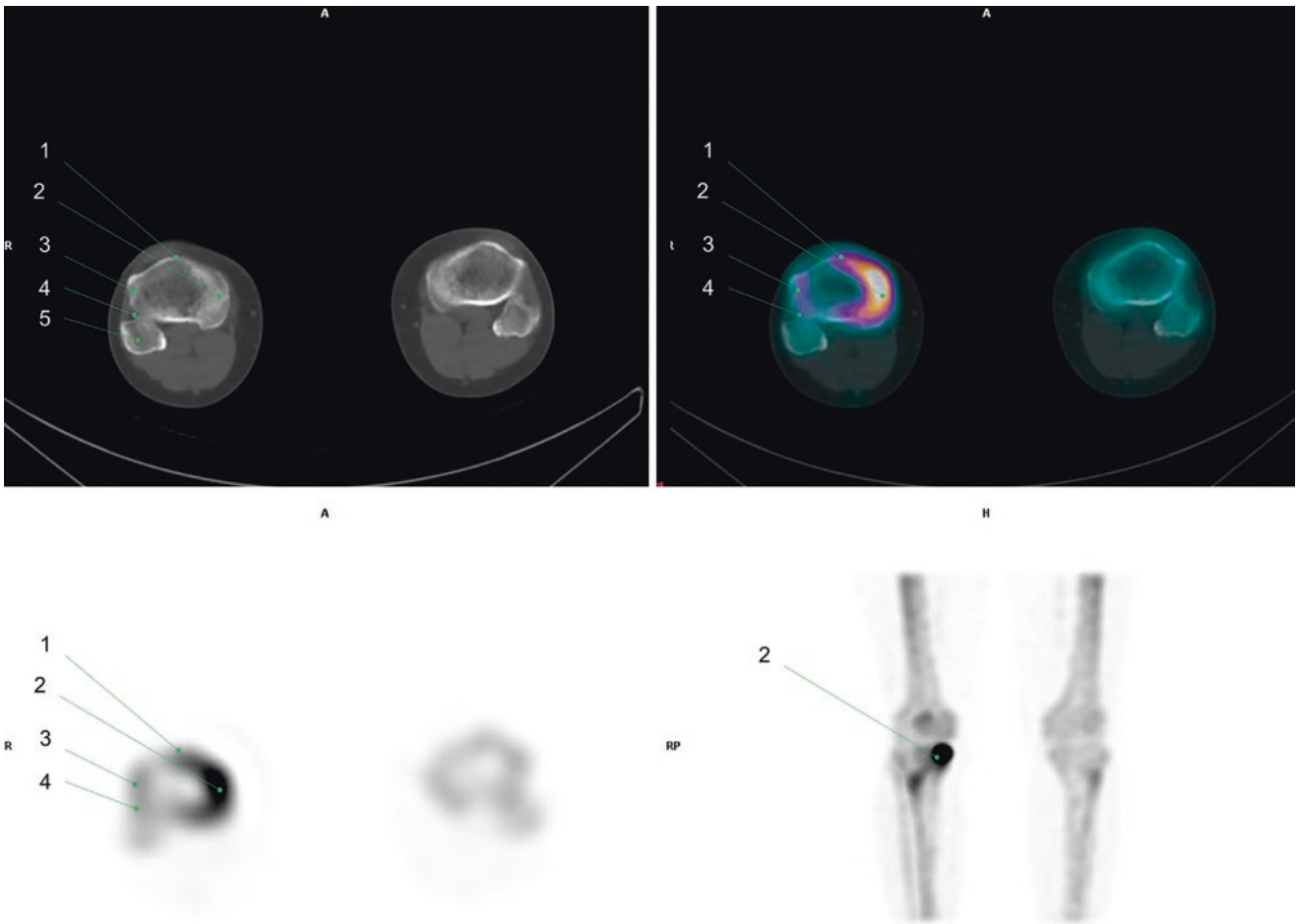

Fig. 50 1. Tibial tuberosity
2. Active lesion at right medial meniscus
3. Tibial lateral condyle
4. Fibular articular facet
5. Fibular head

2.1.2 Case 2

A 56-year-old female with a history of breast cancer complained of pain in her right lower posterior chest after a fall. ^{99m}Tc-MDP SPECT/CT showed focal increased activity in the right posterior 11th rib, corresponding to a callus formation at a fracture seen on CT. An acute fracture (up to 3–4 weeks after initial injury) will show increased radiotracer uptake surrounding the fracture site. Ninety-five percent of fractures are positive in patients under 65 years old, but skull fractures rarely show activity. In the healing phase with a variable time course, there is a gradual decrease in radiotracer activity, but 40% of fractures remain abnormal after 1 year (Fig. 51) [50].

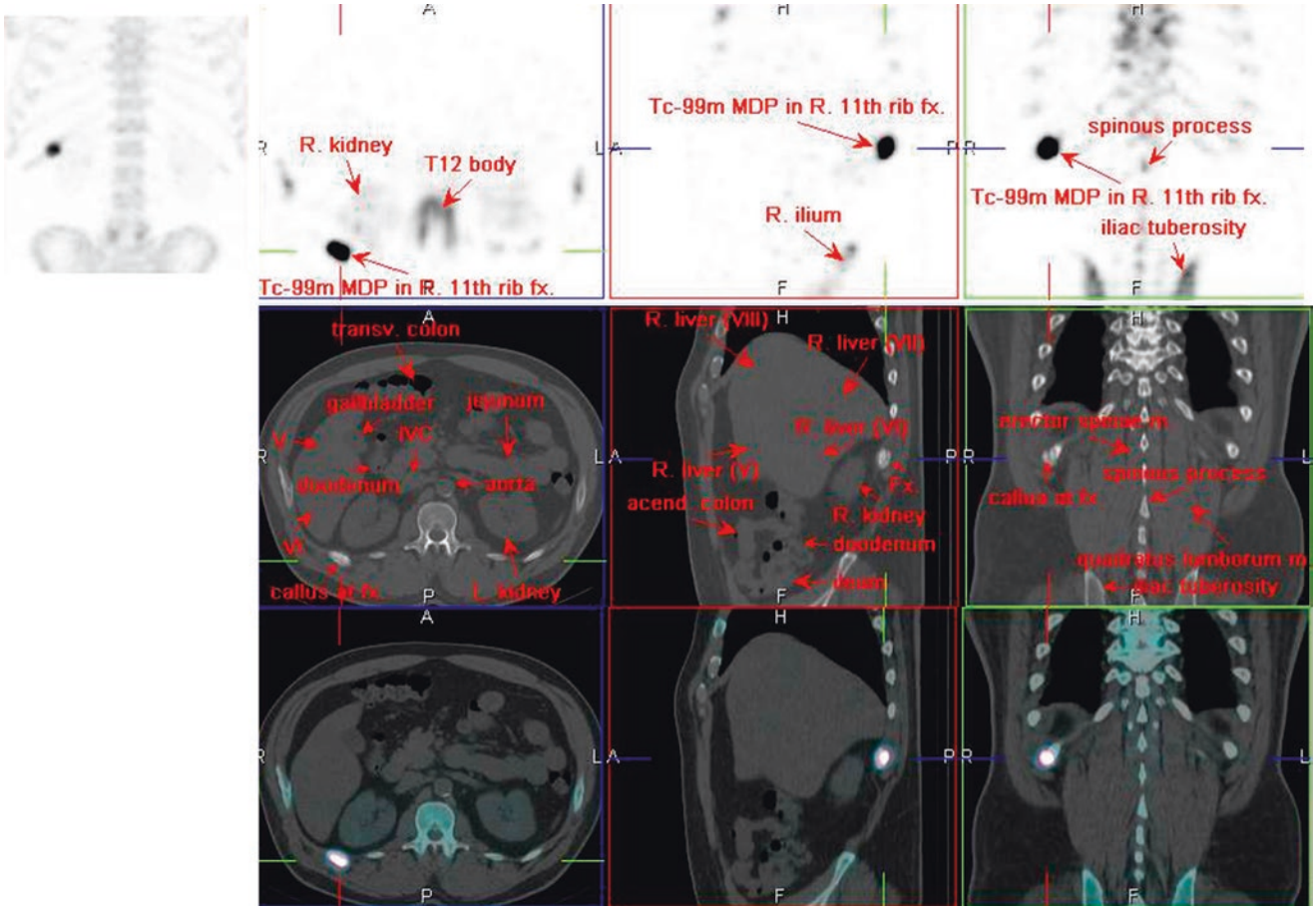

Fig. 51 ^{99m}Tc-MDP SPECT/CT

2.1.3 Case 3

A 65-year-old male patient with a history of lung cancer, who developed a backache following a car accident. ^{99m}Tc-MDP SPECT/CT showed a focal area of markedly increased activity in the spinous process of L4, corresponding to a fracture shown on CT. Slightly increased activity in the bilateral facet joints of L4 was also noted, caused by degenerative changes (Fig. 52) [51].

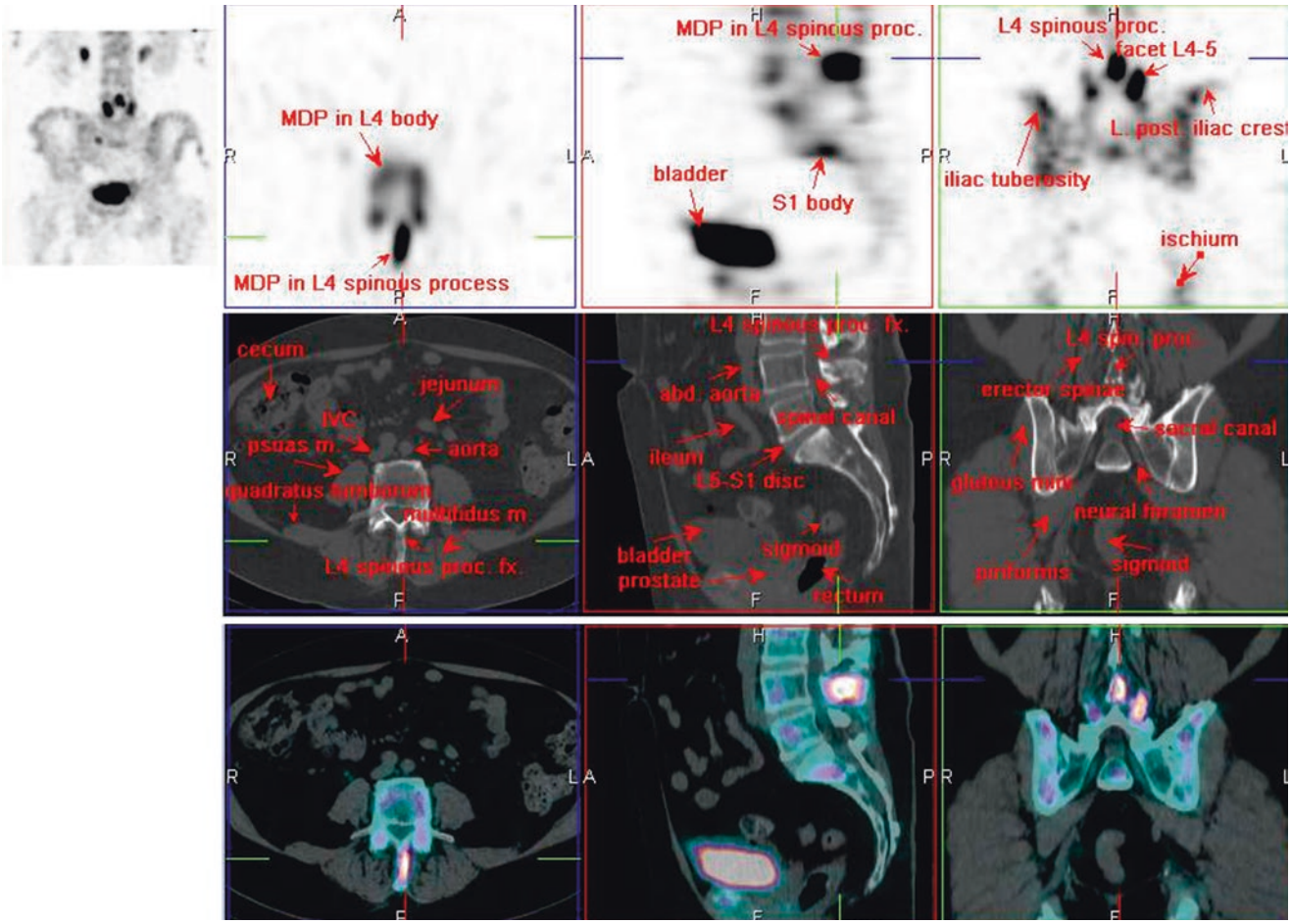

Fig. 52 ^{99m}Tc-MDP SPECT/CT

2.1.4 Case 4

A 61-year-old female patient with chronic bilateral shoulder pain and limitation was admitted for evaluation. ^{99m}Tc-MDP SPECT/CT was performed, finding diffuse increased uptake in the bilateral shoulder joint capsules and bony structures, which was consistent with adhesive capsulitis, more severe in the right shoulder (Figs. 53, 54, 55, and 56) [53].

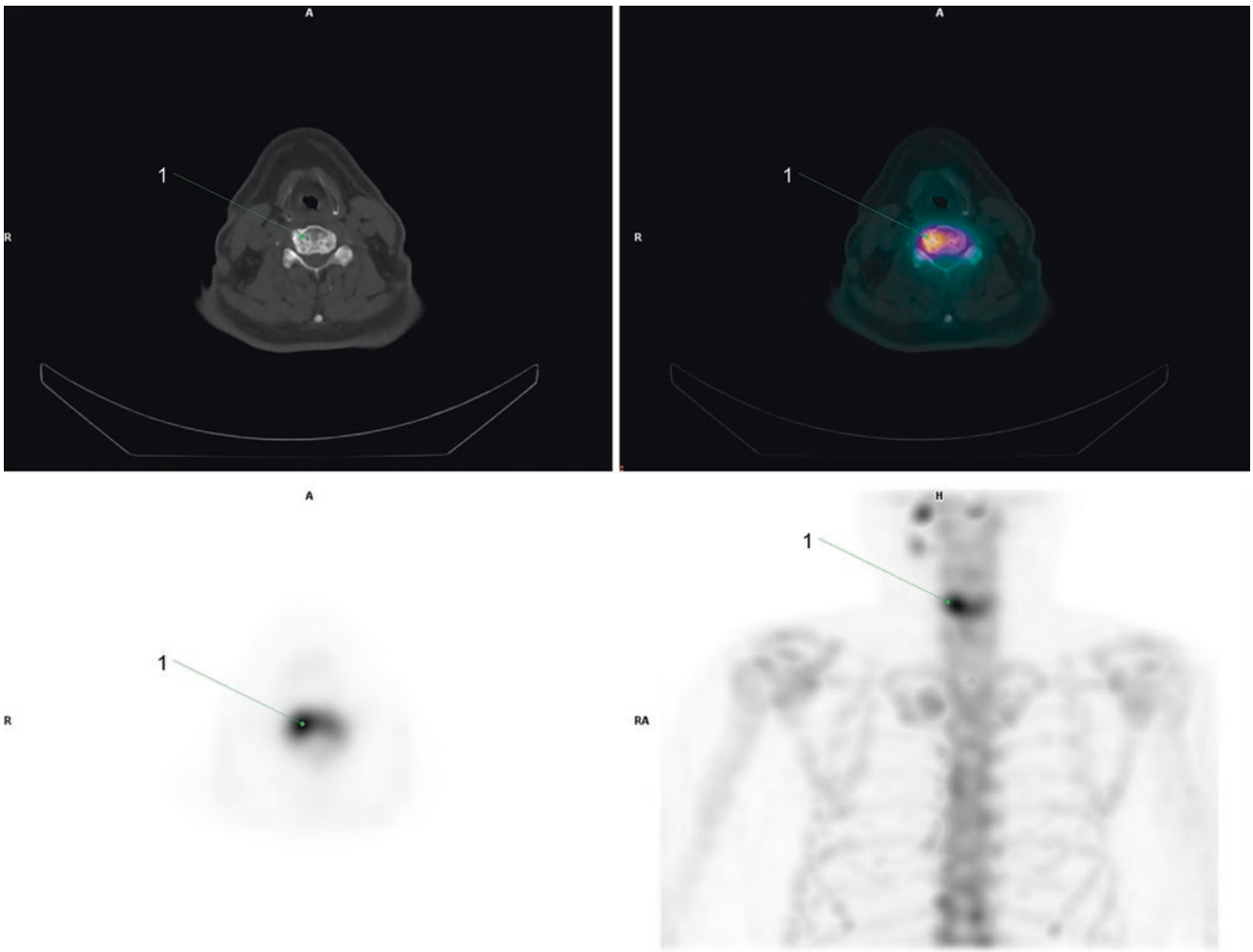

Fig. 53 1. Degenerative change in C5 spine

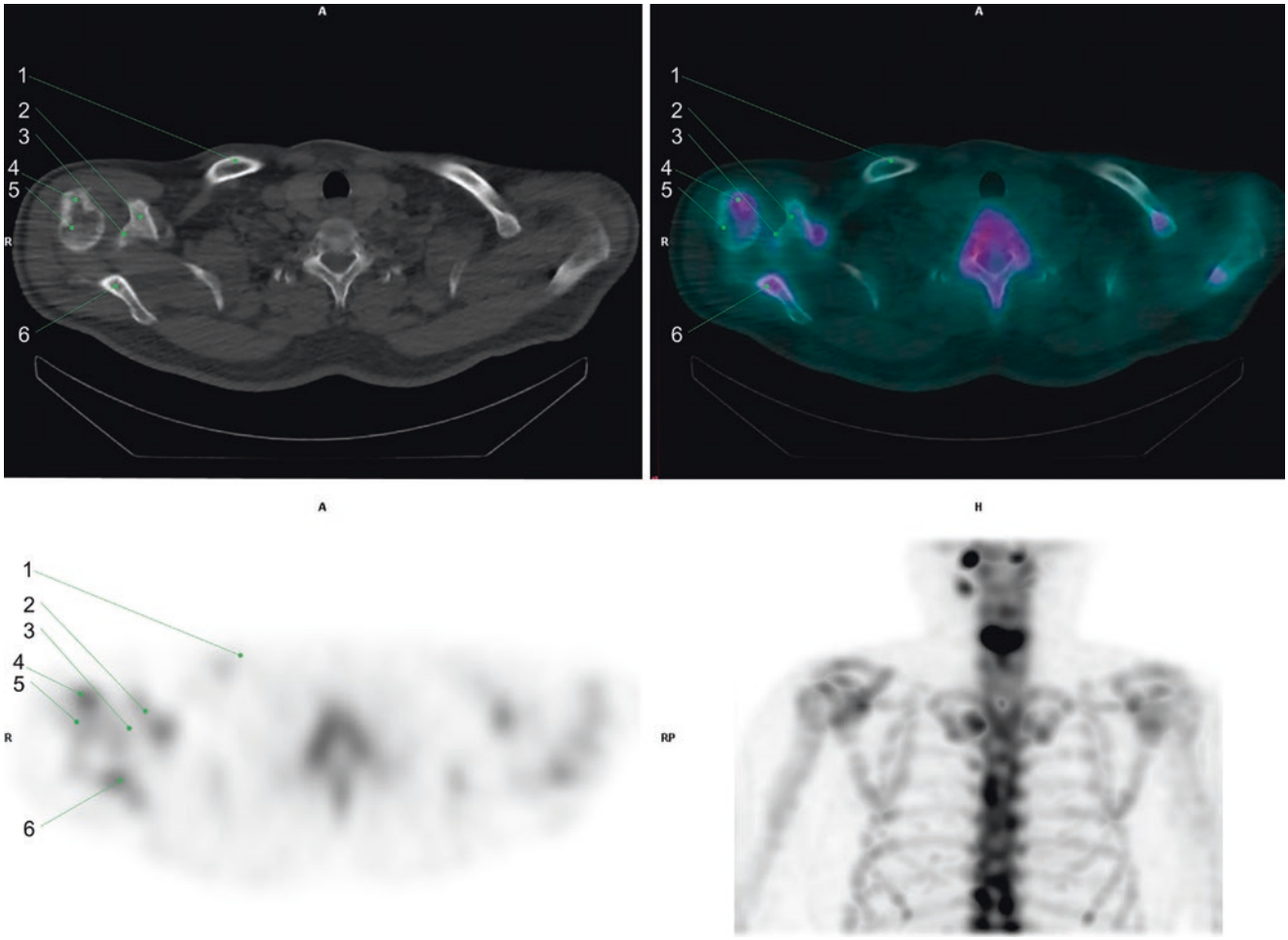

Fig. 54 1. Clavicle
2. Coracoid process
3. Supraglenoid tubercle
4. Greater tubercle of humerus
5. Humeral head
6. Scapula

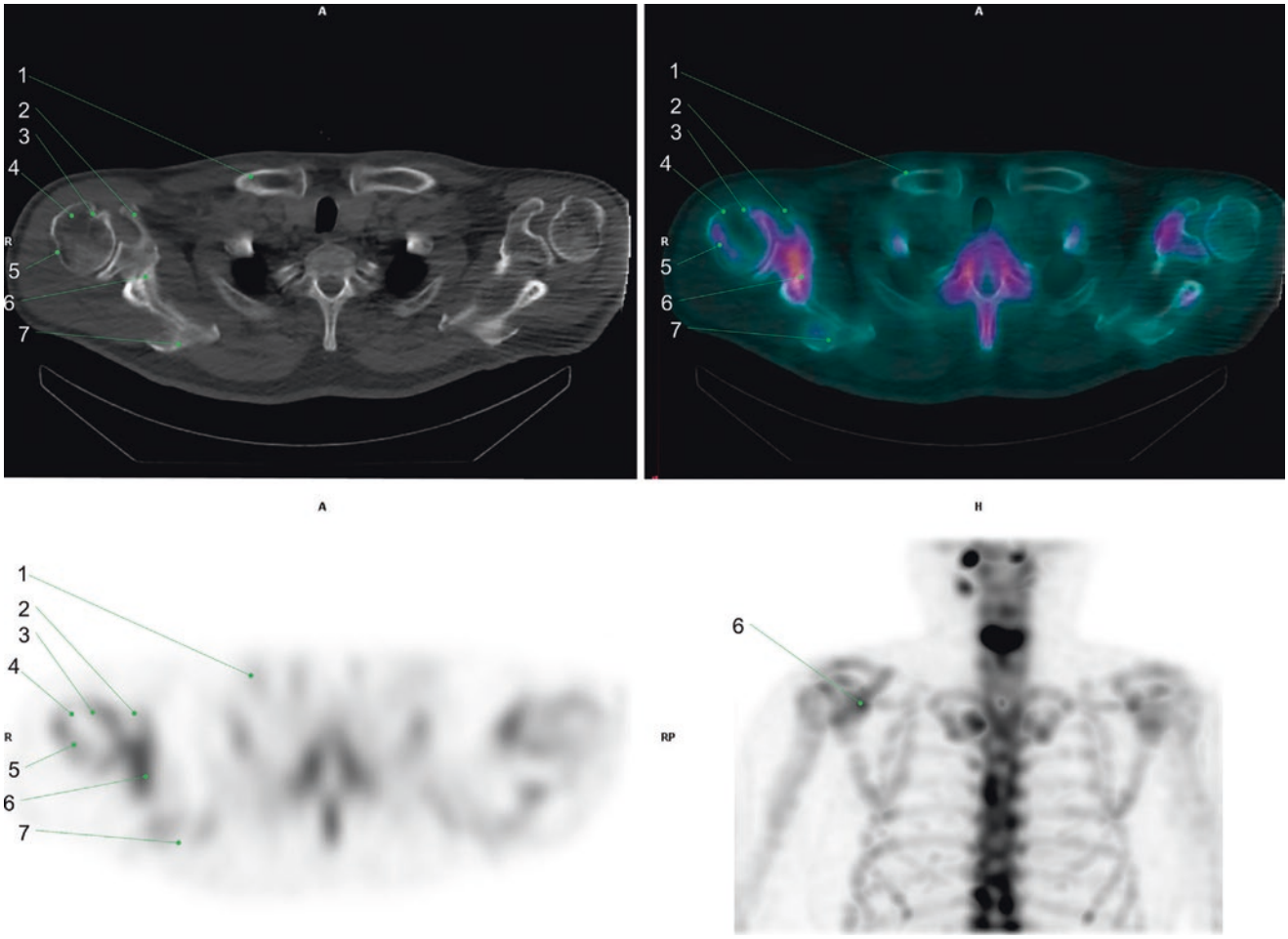

Fig. 55 1. Clavicle
2. Coracoid process
3. Lesser tubercle of humerus
4. Greater tubercle of humerus
5. Diffuse uptake in joint capsule of humeral head
6. Scapula
7. Acromion

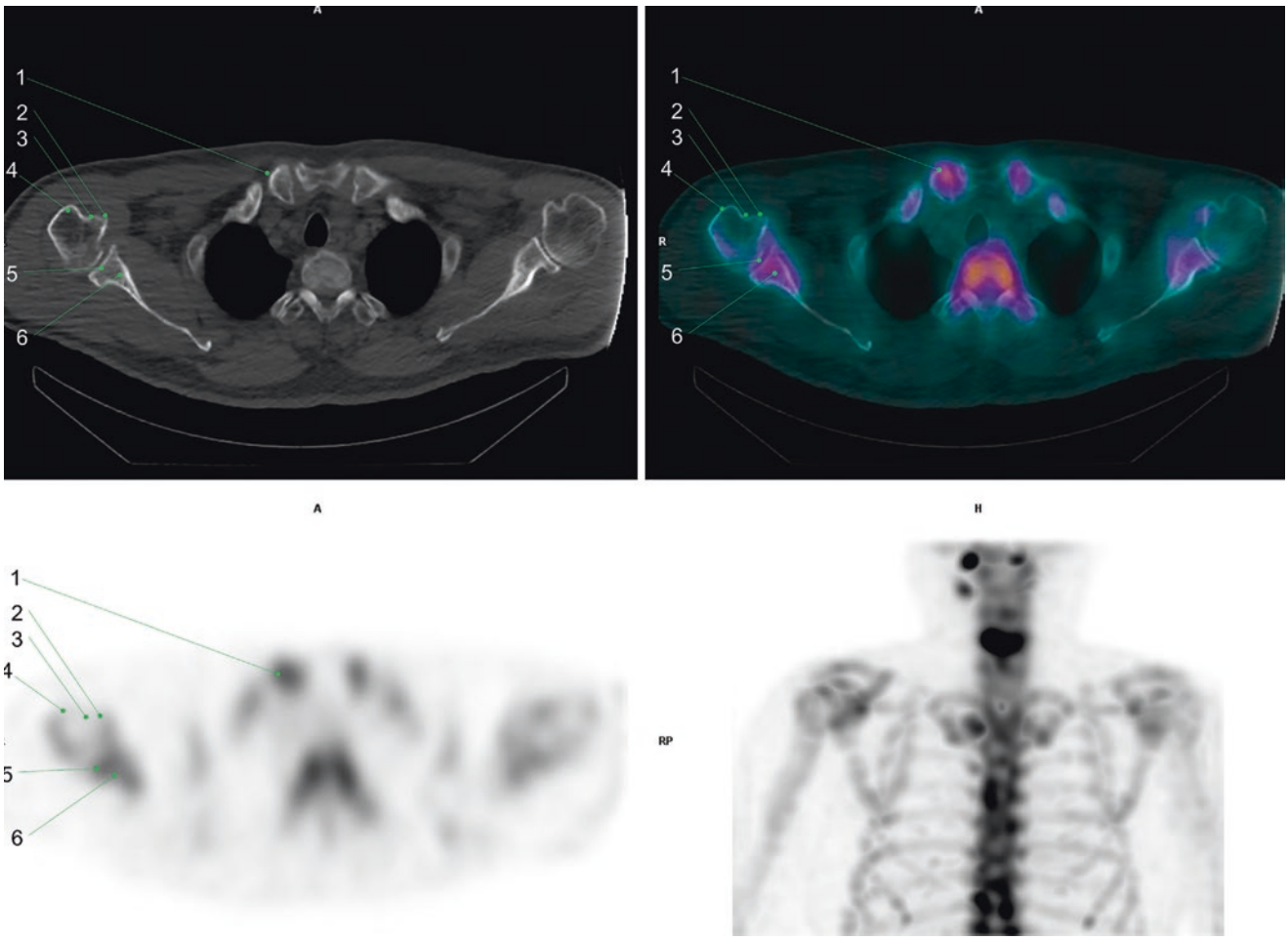

Fig. 56 1. Clavicle
2. Lesser tubercle
3. Intertubercular sulcus
4. Greater tubercle
5. Increased uptake in glenoid cavity
6. Scapula neck

2.1.5 Case 5

A 21-year-old male patient with bilateral temporomandibular joint pain. ^{99m}Tc-MDP SPECT/CT was performed, finding increased uptake in both temporomandibular joints (right > left), due to degenerative osteoarthritis (Fig. 57).

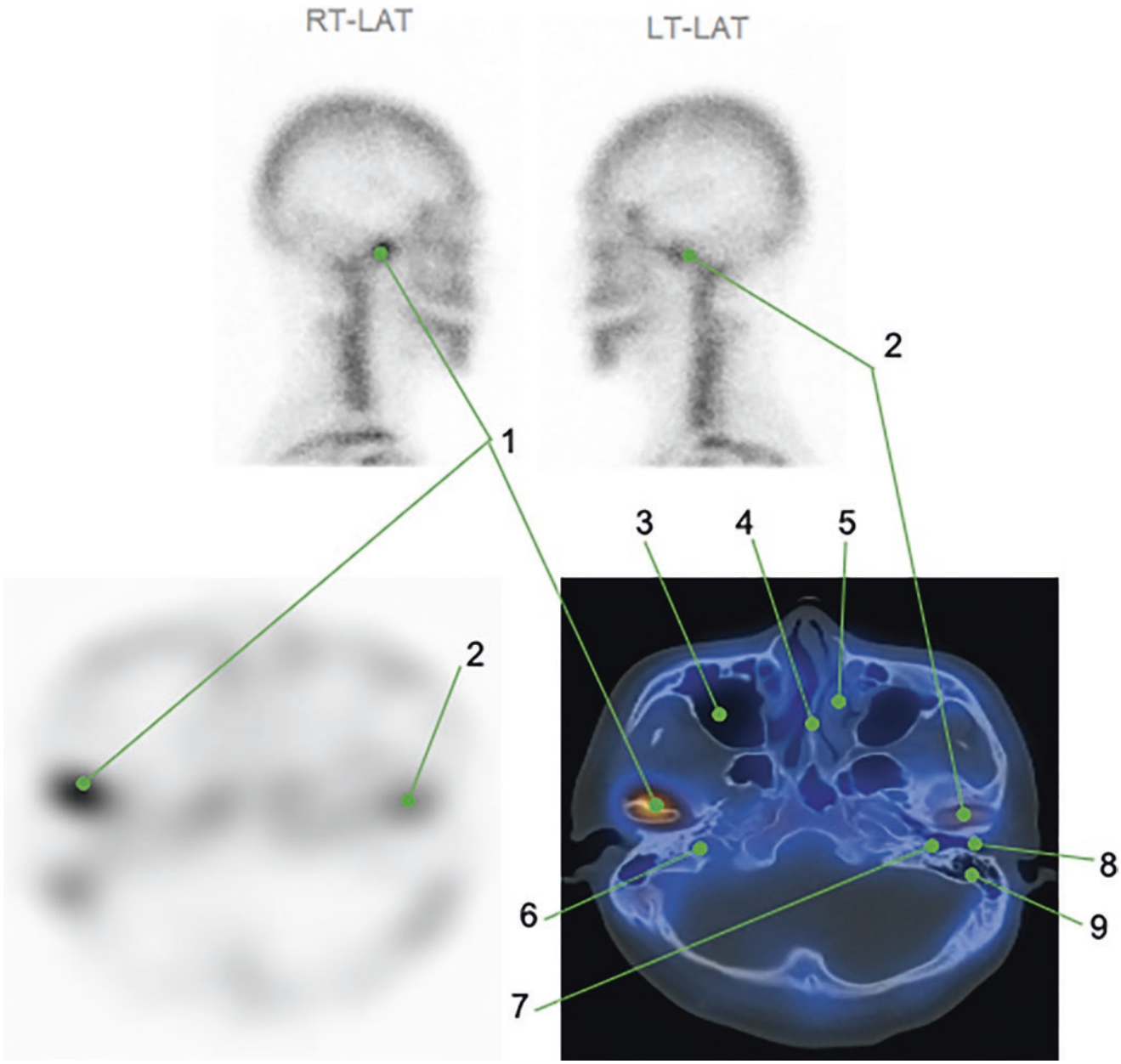

Fig. 57 1. Focal increased uptake in the right temporomandibular joint
2. Focal increased uptake in the left temporomandibular joint
3. Right maxillary sinus
4. Nasal septum
5. Left middle concha
6. Right jugular foramen
7. Left inner ear
8. Left external auditory canal
9. Left mastoid air cells

2.1.6 Case 6

A 48-year-old male patient with right knee varus deformity treated with high tibial osteotomy. In the immediate postoperative period, ^{99m}Tc-MDP SPECT/CT was performed *(top)*, finding, in addition to the normal changes of surgery, degenerative changes in the right knee with increased focal uptake in the femorotibial joint, more marked in the medial compartment, as well as in the patellofemoral joint. Three months after surgery, the patient attended with mild pain in the right knee. A new study was carried out *(bottom)* where degenerative changes showed improvement, but as a new finding, an increased uptake was observed in one of the surgical screws at the proximal tibia. Normal reactive postoperative changes were considered as the first option; however, a short-term follow-up was recommended to rule out other complications, which were later discarded (Fig. 58).

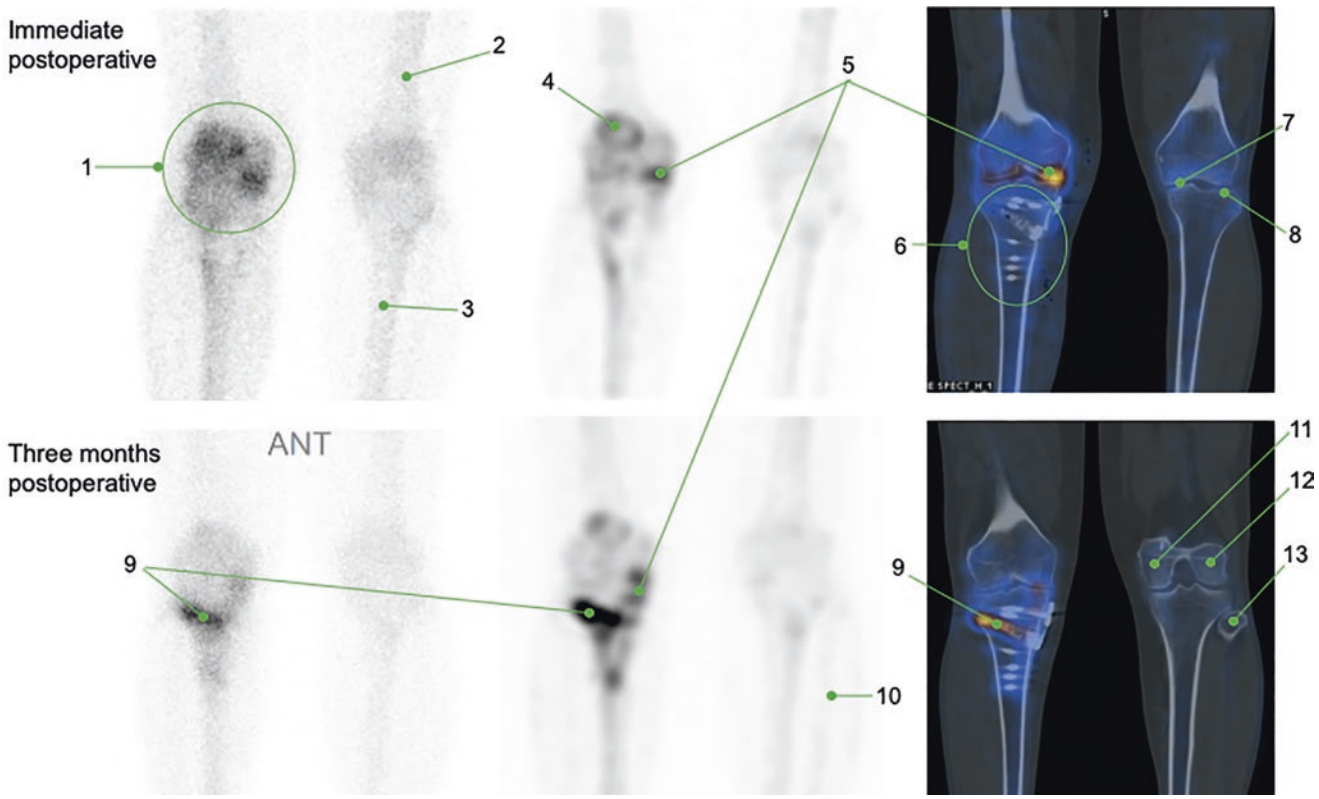

Fig. 58 1. Increased uptake in the right knee joint
2. Left femoral shaft
3. Left tibial shaft
4. Increased uptake in the right patellofemoral joint: degenerative changes
5. Increased uptake in the medial compartment of the right knee: degenerative changes
6. Surgical material (screws) in the right proximal tibia
7. Left femorotibial joint, medial compartment
8. Left femorotibial joint, lateral compartment
9. Increased uptake in the right proximal tibia at one of the surgical screws
10. Left fibula shaft
11. Left medial femoral condyle
12. Left lateral femoral condyle
13. Left fibula head

2.1.7 Case 7

A 16-year-old male patient with a history of leukemia, who developed left hip pain after completion of chemotherapy. ^{99m}Tc-MDP SPECT/CT showed a curvilinear moderately increased activity in the left femoral head at an ill-defined area of increased density on CT, caused by a healing microfracture with avascular necrosis (AVN). AVN is cellular death of bone components caused by interruption of the blood supply. It often leads to destruction of the joint articular surface. The classic sites are the head of the femur, the neck of the talus, and the waist of the scaphoid. AVN initially shows decreased radiotracer activity in the affected region, followed by a hyperemic phase with increased uptake (Fig. 59) [55].

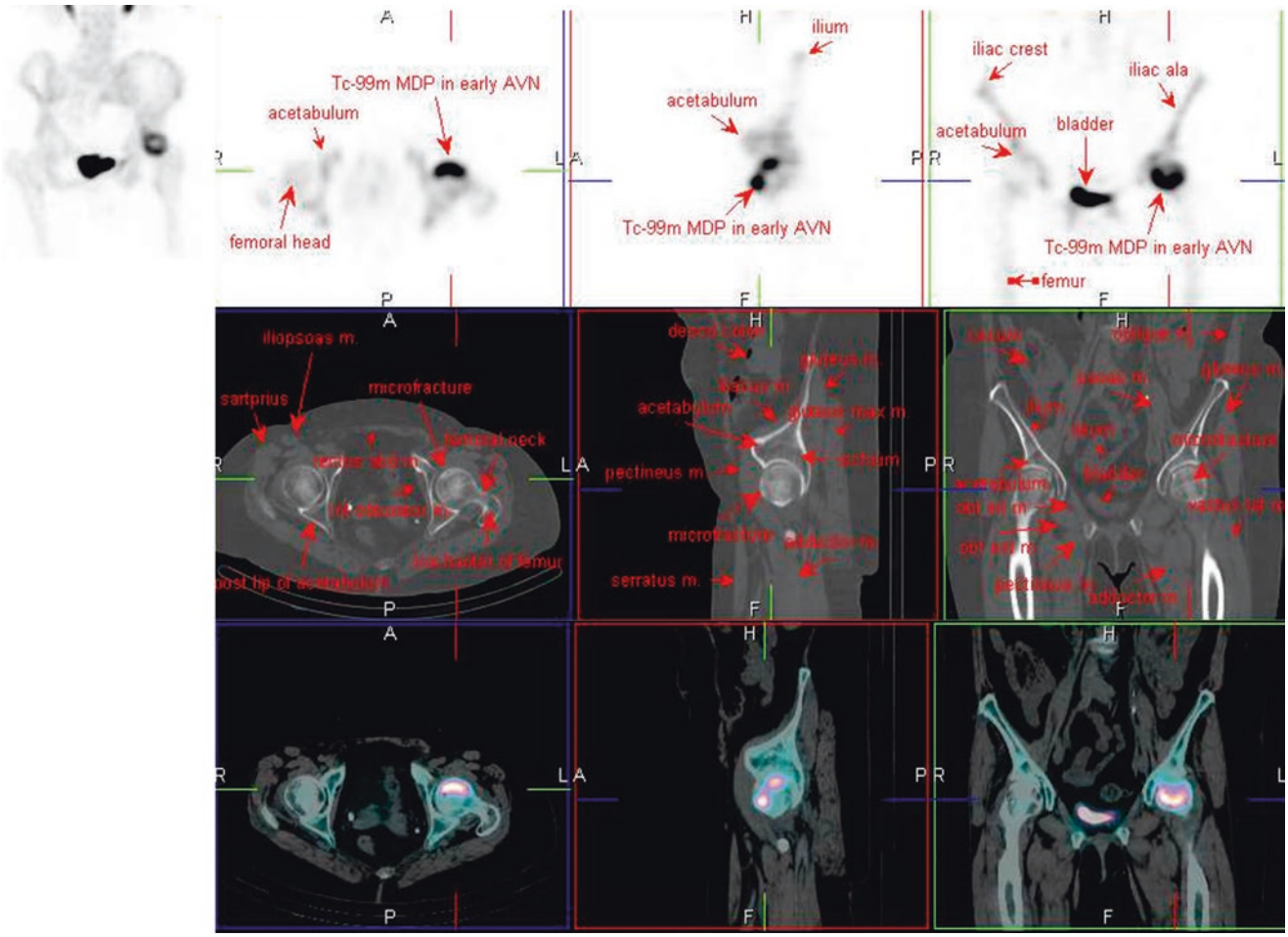

Fig. 59 ^{99m}Tc-MDP SPECT/CT

2.1.8 Case 8

A 20-year-old male patient with progressive low back pain, worsened by physical activity. ^{99m}Tc-MDP SPECT/CT was performed and showed increased uptake in the inferior aspect of bilateral sacroiliac joints, without morphologic changes. The findings were consistent with sacroiliitis (Fig. 60).

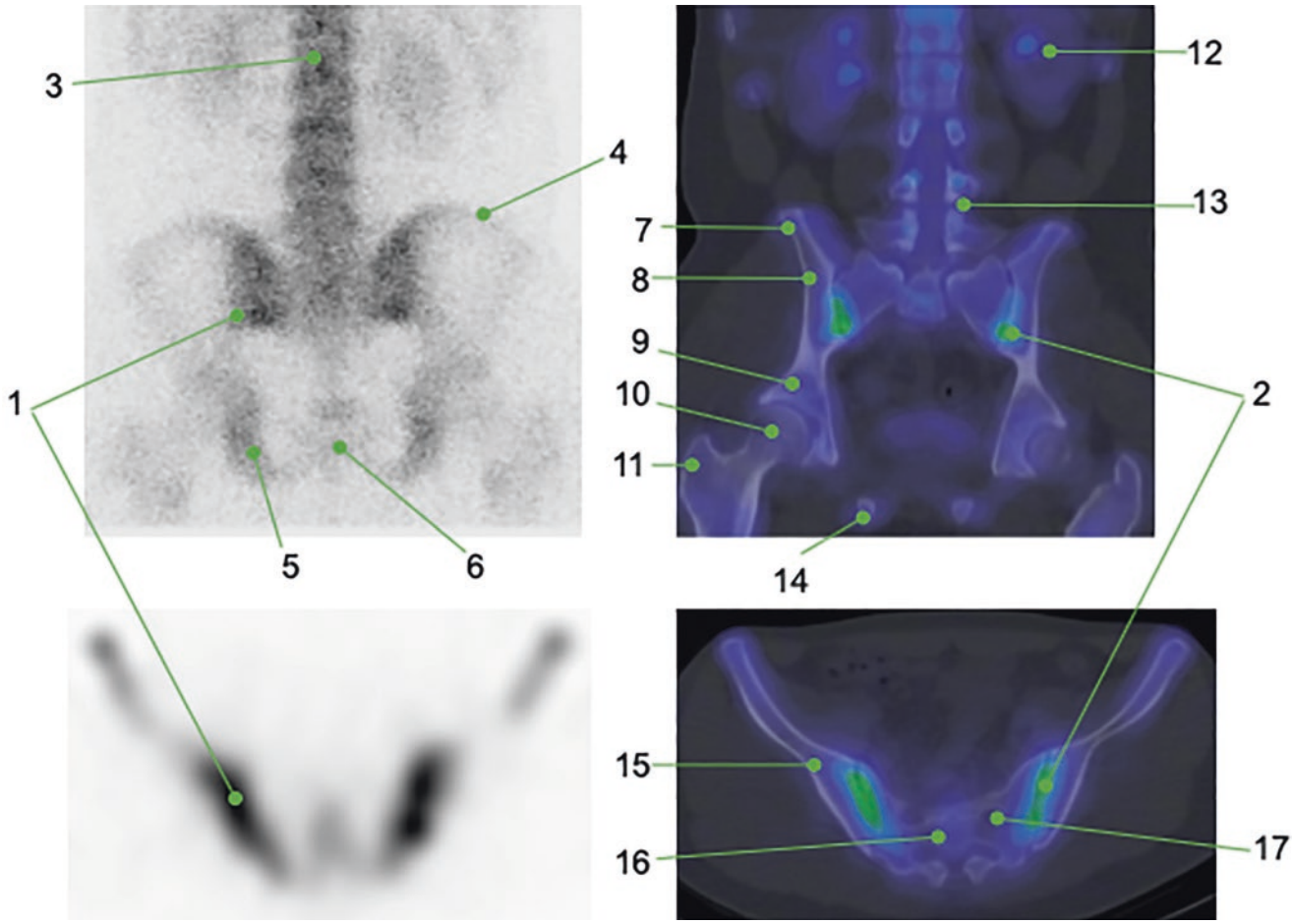

Fig. 60 1. Focal increased uptake in the right sacroiliac joint inferior aspect
2. Focal increased uptake in the left sacroiliac joint inferior aspect
3. Lumbar vertebral body, L2
4. Left iliac crest
5. Right ischium
6. Pubis
7. Right posterior superior iliac spine
8. Right ilium
9. Right acetabulum
10. Right femoral head
11. Right femur greater trochanter
12. Left kidney
13. Left L4-L5 facet joint
14. Right ischial tuberosity
15. Right iliac wing
16. Sacrum
17. Left sacral foramen

2.1.9 Case 9

A 27-year-old male patient with right foot pain. ^{99m}Tc-MDP SPECT/CT was performed finding focal increased uptake in the medial aspect of the midfoot, adjacent to the medial side of the navicular bone, at an accessory ossicle. These findings confirmed the diagnosis of accessory navicular syndrome (Fig. 61).

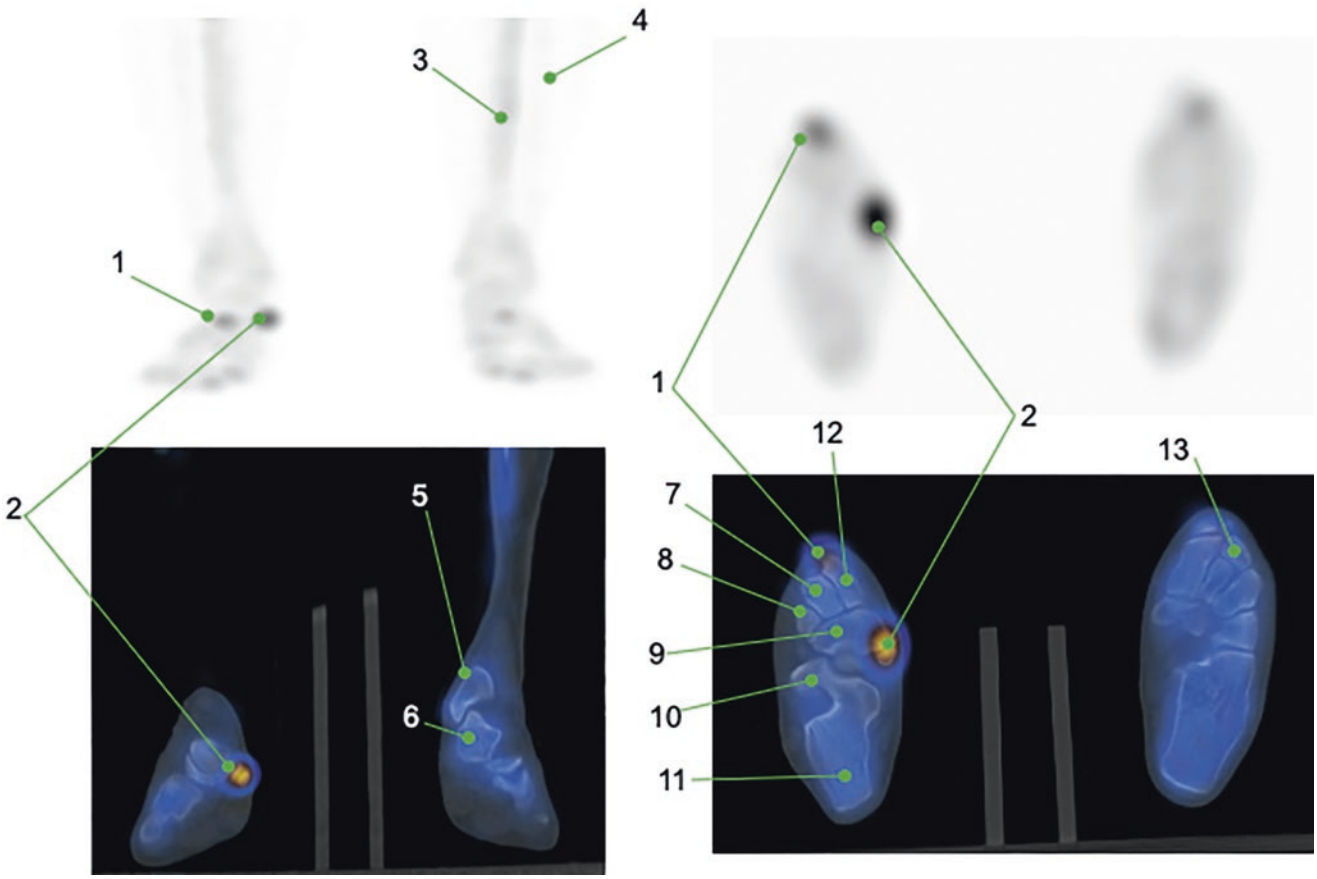

Fig. 61 1. Mild increased uptake in the right medial cuneiform-first metatarsal joint
2. Markedly increased uptake in the right midfoot at the accessory navicular bone
3. Left tibia shaft
4. Left fibula shaft
5. Left distal tibia, medial malleolus
6. Left talus bone
7. Right middle cuneiform (II)
8. Right lateral cuneiform (III)
9. Right navicular bone
10. Right sustentaculum tali
11. Right calcaneus bone
12. Right medial cuneiform (I)
13. Left proximal second metatarsal bone

2.2 Others

2.2.1 Gastrointestinal Bleeding

2.2.1.1. Case 1

A 10-year-old male patient with anaplastic large B-cell lymphoma was suffering from hematochezia caused by acute graft-versus-host disease (GVHD) after peripheral blood stem cell treatment. ^{99m}Tc-labeled red blood cell (^{99m}Tc-RBC) gastrointestinal bleeding SPECT/CT was done to find the bleeding source. A focal uptake was found in the third portion of the duodenum, corresponding to the acute bleeding site (Figs. 62, 63, 64, 65, 66, and 67) [56].

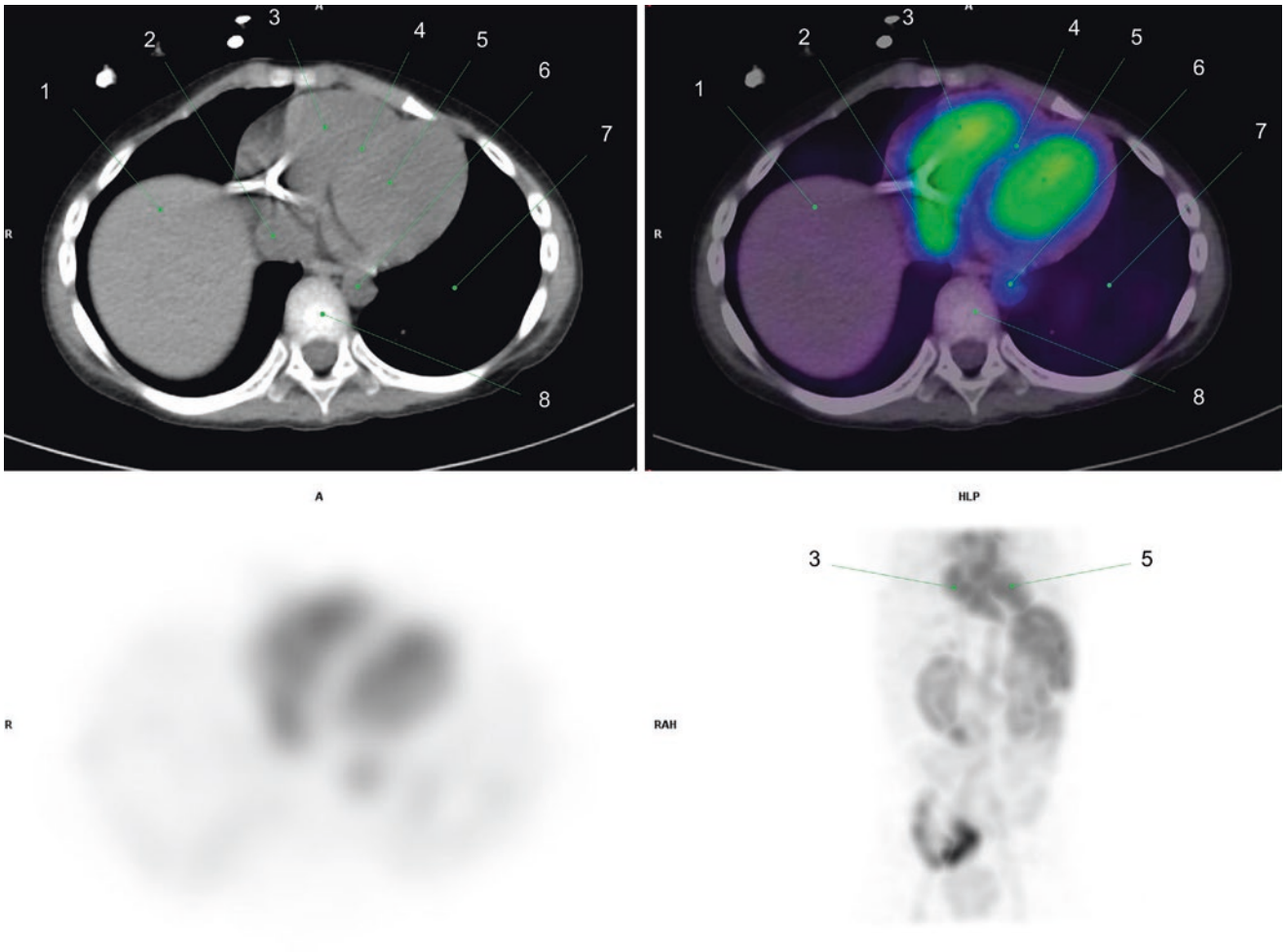

Fig. 62 1. Liver
2. Inferior vena cava
3. Right ventricle
4. Interventricular septum
5. Left ventricle
6. Aorta
7. Left lung
8. Vertebral body

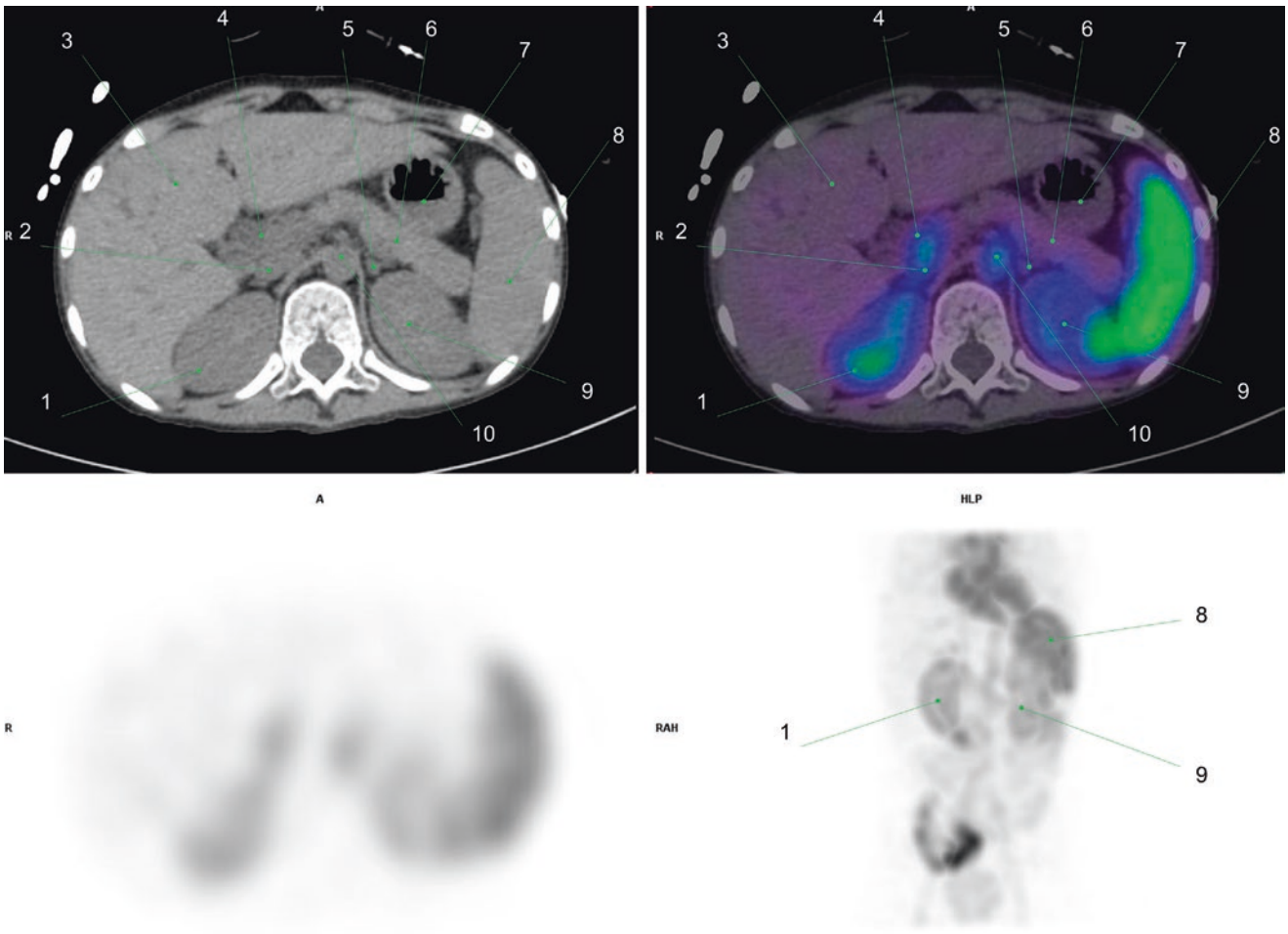

Fig. 63 1. Renal cortex
2. Inferior vena cava
3. Right lobe of liver
4. Head of pancreas
5. Left adrenal gland
6. Tail of pancreas
7. Body of stomach
8. Spleen
9. Renal pelvis
10. Abdominal aorta

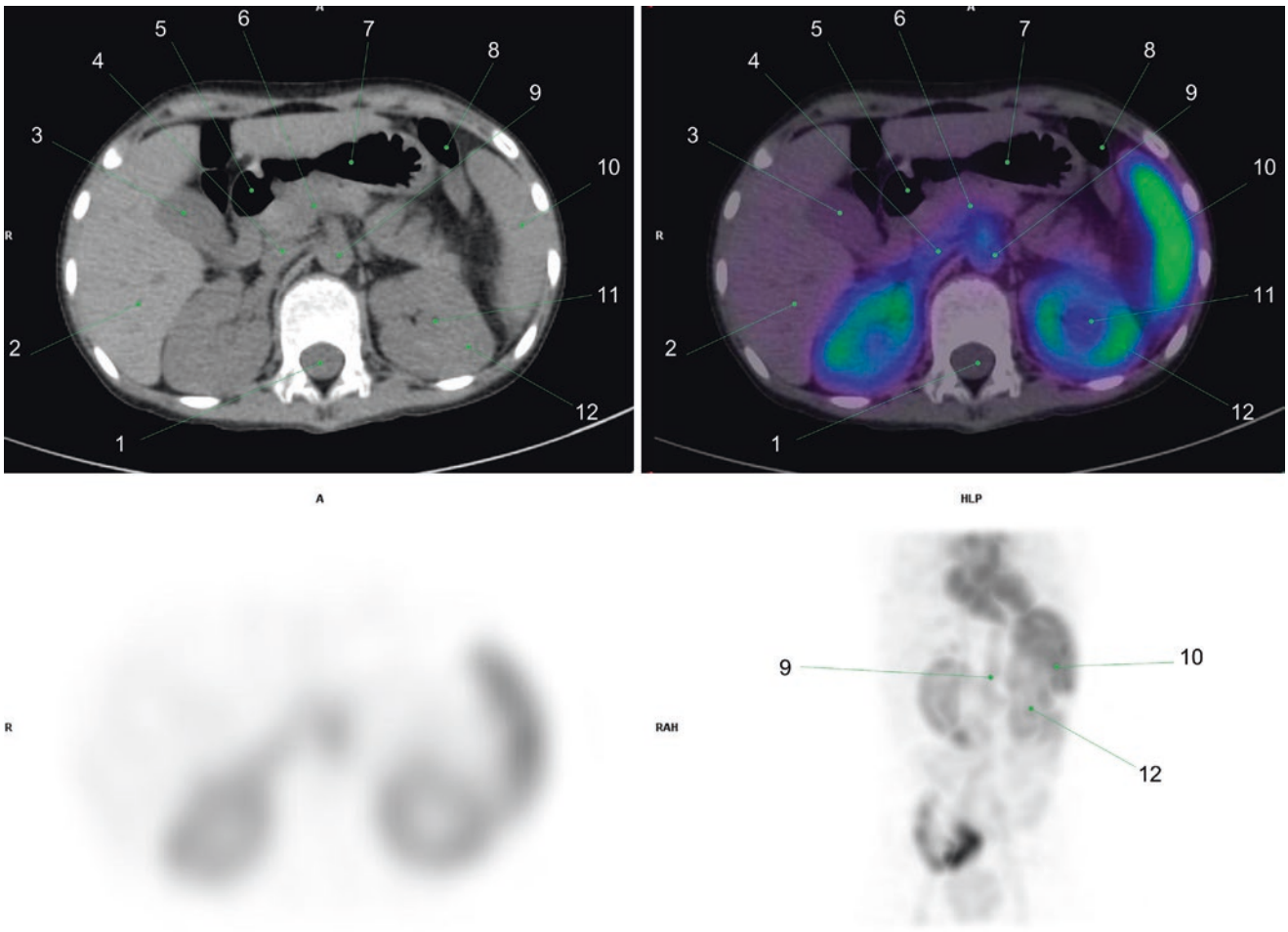

Fig. 64 1. Vertebral canal
2. Liver
3. Gallbladder
4. Inferior vena cava
5. Superior part (1st) of duodenum
6. Pancreatic head
7. Stomach lower body
8. Transverse colon
9. Abdominal aorta
10. Spleen
11. Renal pelvis
12. Renal cortex

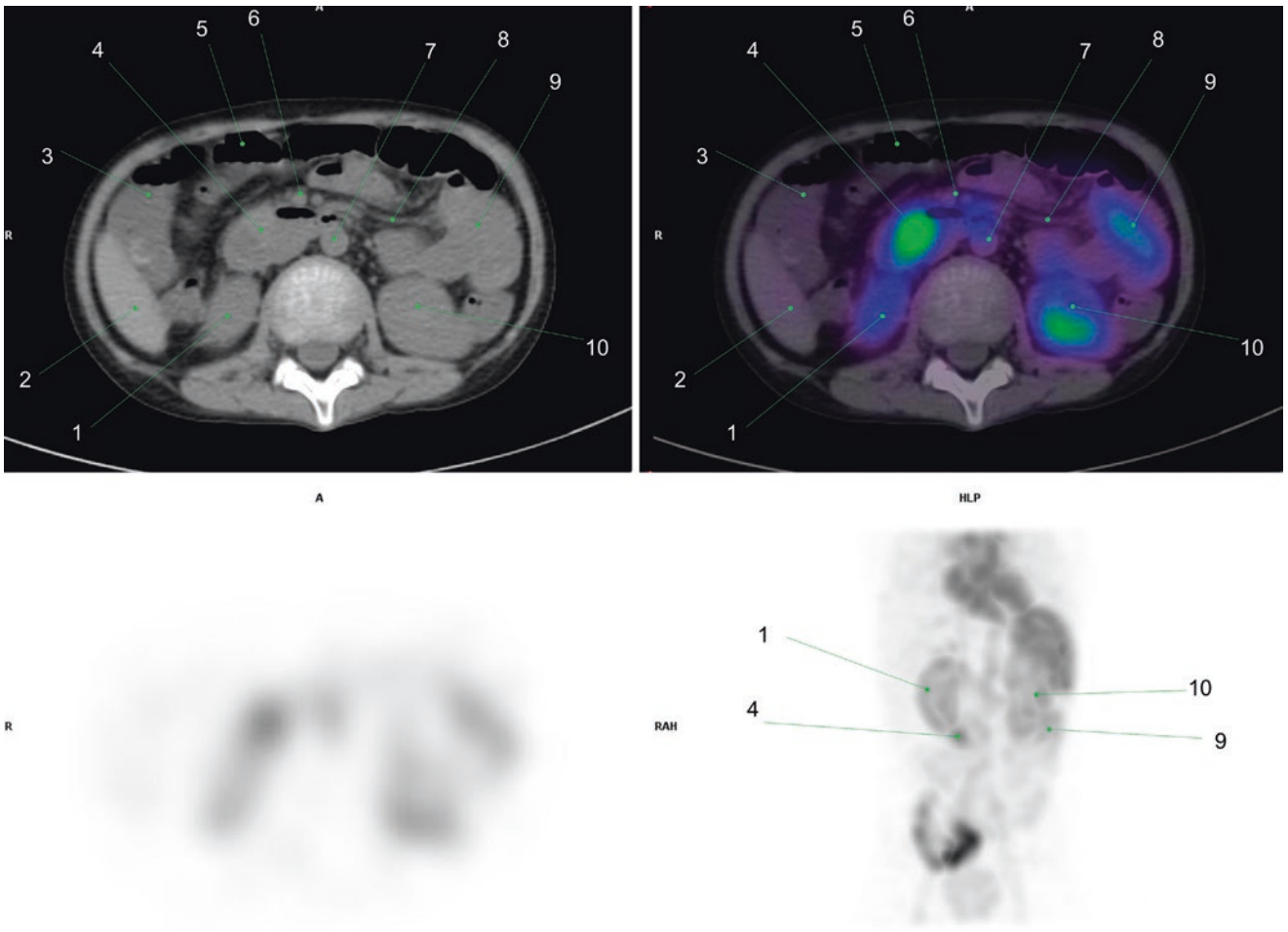

Fig. 65 1. Right kidney
2. Liver
3. Hepatic flexure of colon
4. Third portion of duodenum (Bleeding focus)
5. Transverse colon
6. Superior mesenteric vessels
7. Abdominal aorta
8. Mesenteric vessels
9. Ileum
10. Left kidney

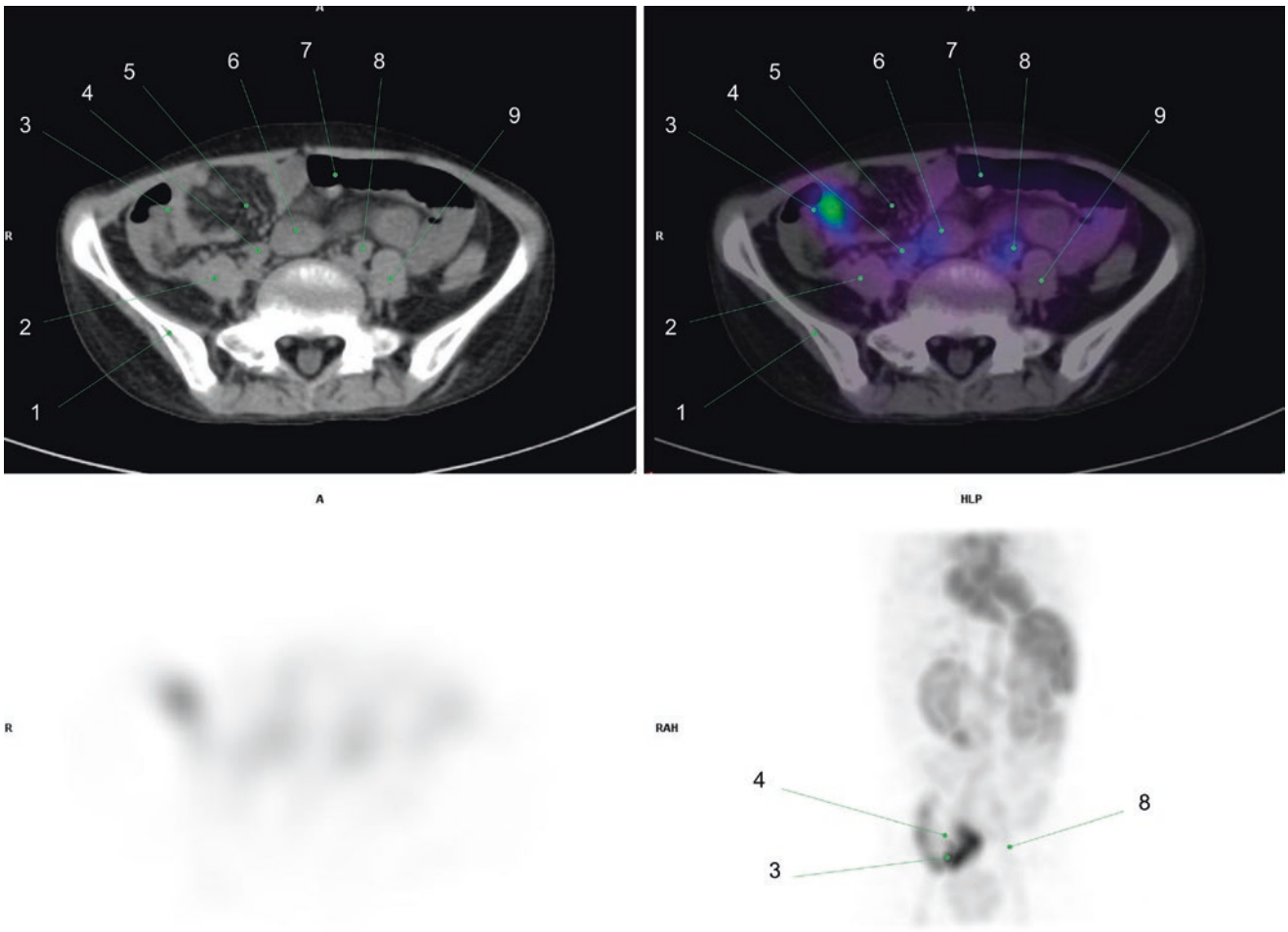

Fig. 66 1. Right ilium
2. Right psoas muscle
3. Ileocecal valve
4. Right common iliac vessels
5. Mesenteric vessels
6. Inferior vena cava
7. Transverse colon
8. Left common iliac vessels
9. Left psoas muscle

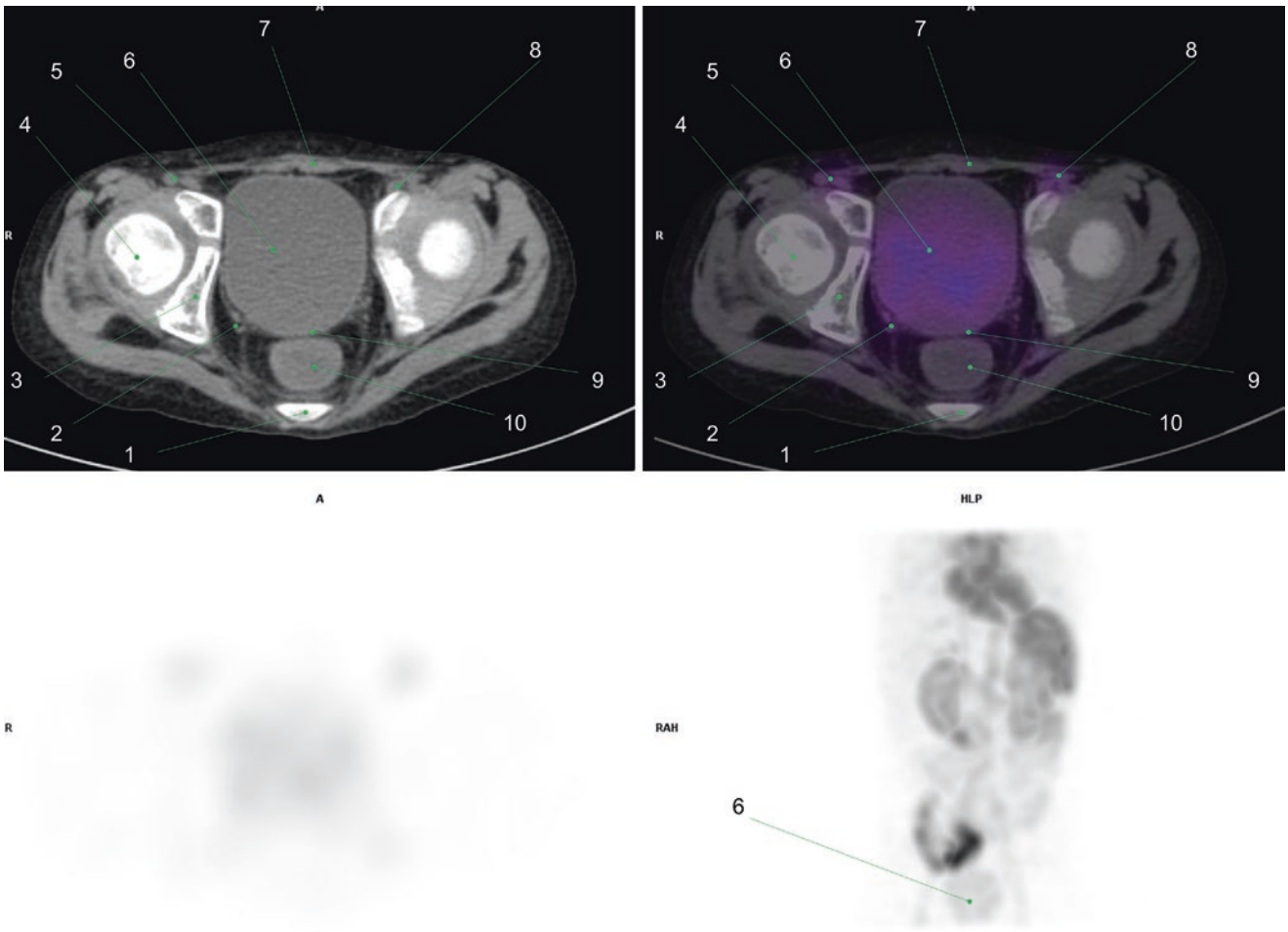

Fig. 67 1. Coccyx
2. Vesical vessels
3. Acetabulum
4. Right femoral head
5. Right external iliac vessels
6. Urinary bladder
7. Rectus abdominis
8. Left external iliac vessels
9. Rectovesical pouch
10. Rectum

2.2.1.2. Case 2

A 68-year-old male patient with a history of cystectomy for bladder cancer. He developed pain in the right lower abdomen and also noticed bloody stool. ^{99m}Tc-RBC SPECT/CT demonstrated a curvilinear moderately increased activity in the ileal conduit as well as the pouch and bag indicating active bleeding. ^{99m}Tc-RBC is useful for detecting active gastrointestinal bleeding and is prepared in vitro by mixing 1–3 mL of anticoagulated blood with stannous chloride and an oxidizing agent. The labeling procedure takes at least 20 minutes. Bleeding rates as low as 0.2 mL/min can be detected with a tagged red blood cell study compared to 1 mL/min for angiography. ^{99m}Tc-sulfur colloid requires a significant preparation time and is useful only for acute active bleeding with 2–3 minutes of vascular half-time. A positive study shows an activity that changes shape and position over time due to the peristalsis of intraluminal blood (Fig. 68) [57].

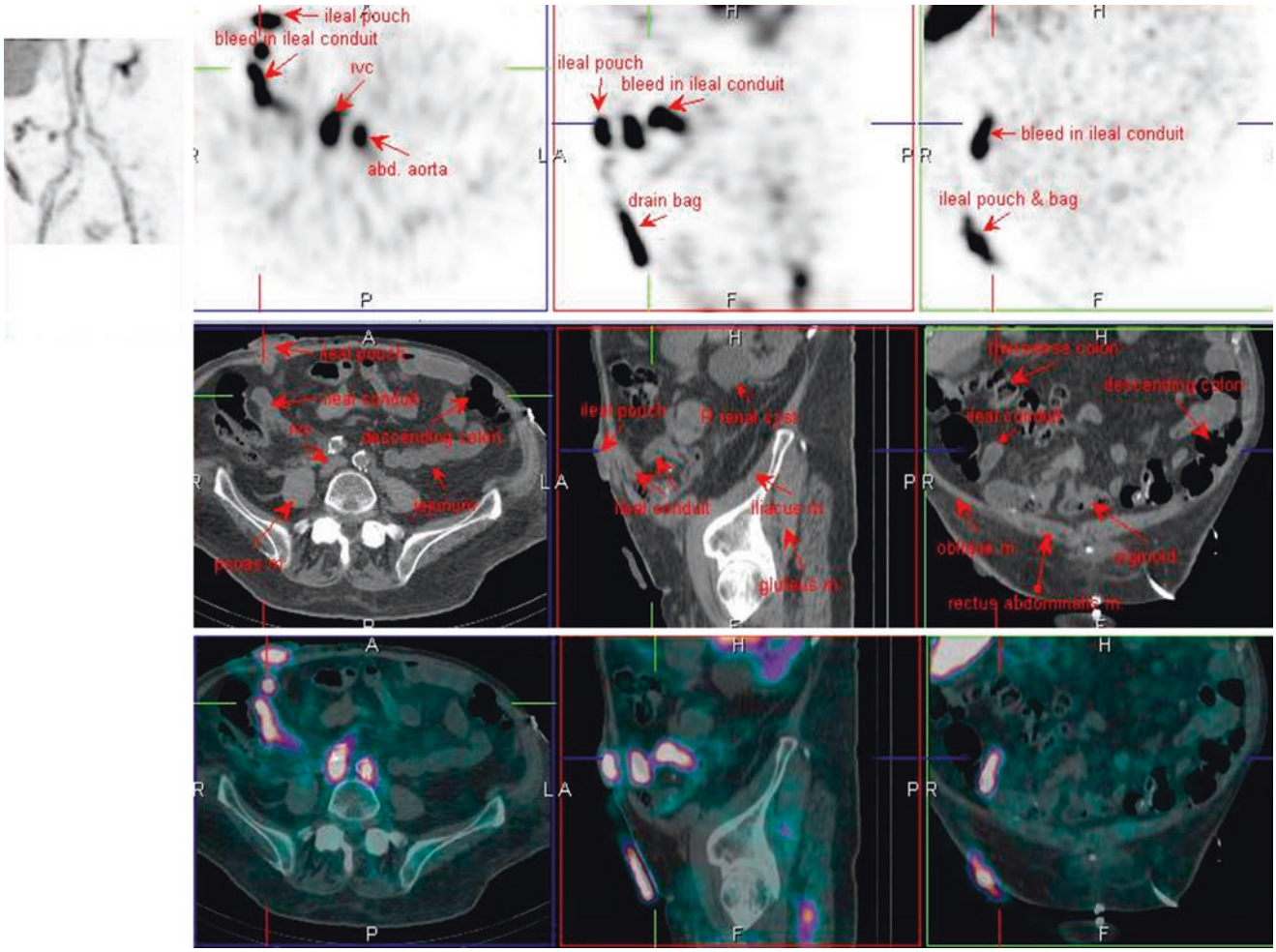

Fig. 68 ^{99m}Tc-RBC SPECT/CT

2.2.2 Abscess

2.2.2.1. Case 1

A 78-year-old female patient with a history of multiple myeloma, who attended for backache and fever. ^{111}In-WBC SPECT/CT showed a focal area of markedly increased activity in the left semispinalis muscle at the posterior lower neck adjacent to the spinous process of C6, corresponding to an ill-defined inflammatory collection. ^{111}In leukocyte, scan is helpful for detecting acute infection or inflammation. Its advantages compared to ^{99m}Tc-D, L-hexamethyl propyleneamine oxime (HMPAO) scan include the absence of interfering bowel and renal activity and the ability to perform delayed 24-hour imaging as well as simultaneous ^{99m}Tc-sulfur colloid or MDP scan. ^{67}Ga citrate scan is useful for detecting chronic infection or inflammation with lymphocytes or macrophages (Fig. 69) [58].

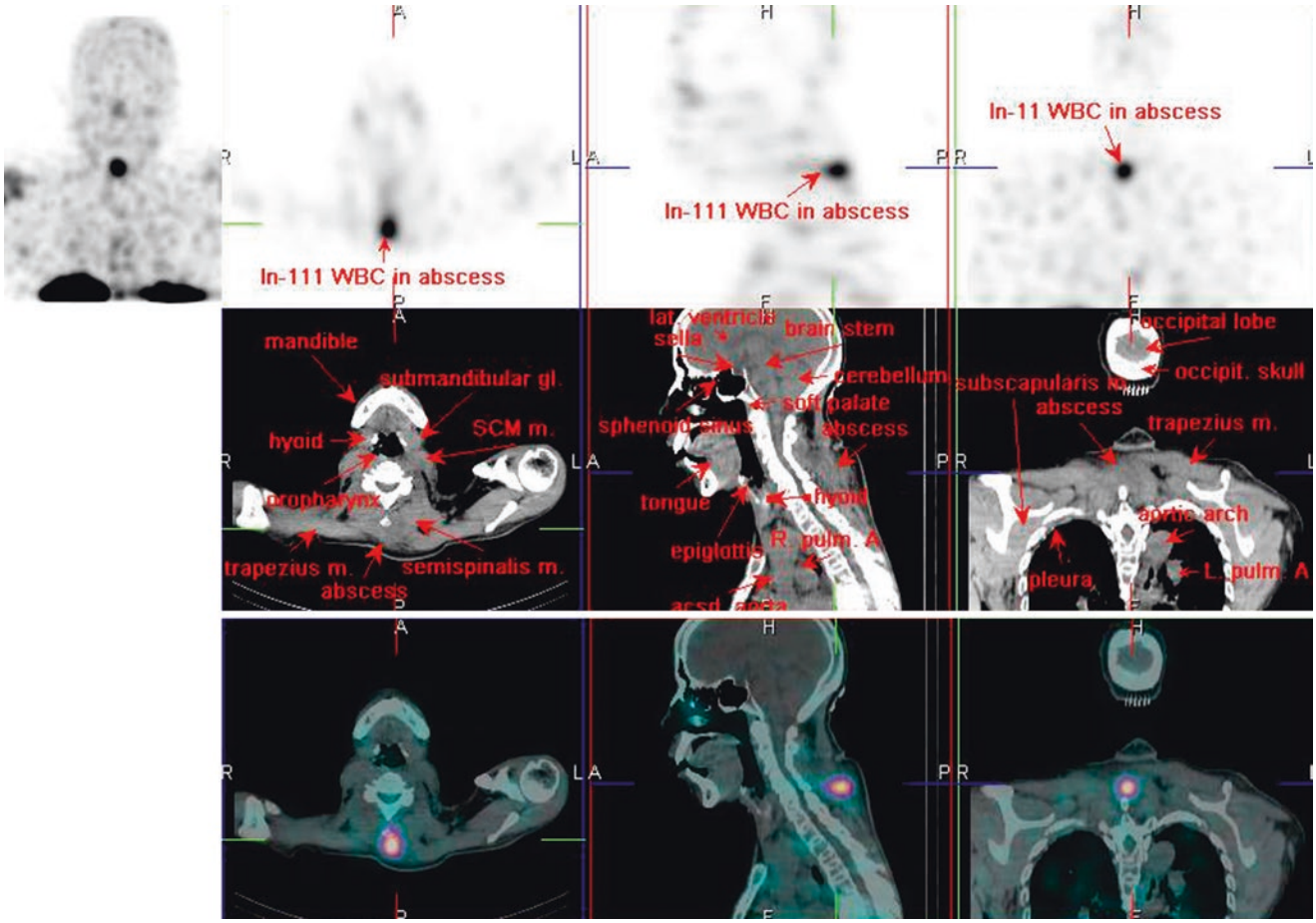

Fig. 69 ^{111}In-WBC SPECT/CT

2.2.3 Benign Thyroid Pathology

2.2.3.1. Case 1

A 57-year-old female patient with a new diagnosis of hypothyroidism.^{131}I SPECT/CT showed a focal area of moderately increased activity in the midline of the tongue base, corresponding to ectopic thyroid tissue in the thyroglossal duct. Ectopic thyroid refers to the presence of thyroid tissue in locations other than the normal anterior neck between the second and fourth tracheal cartilages. Lingual thyroid is the most common type (Fig. 70) [59].

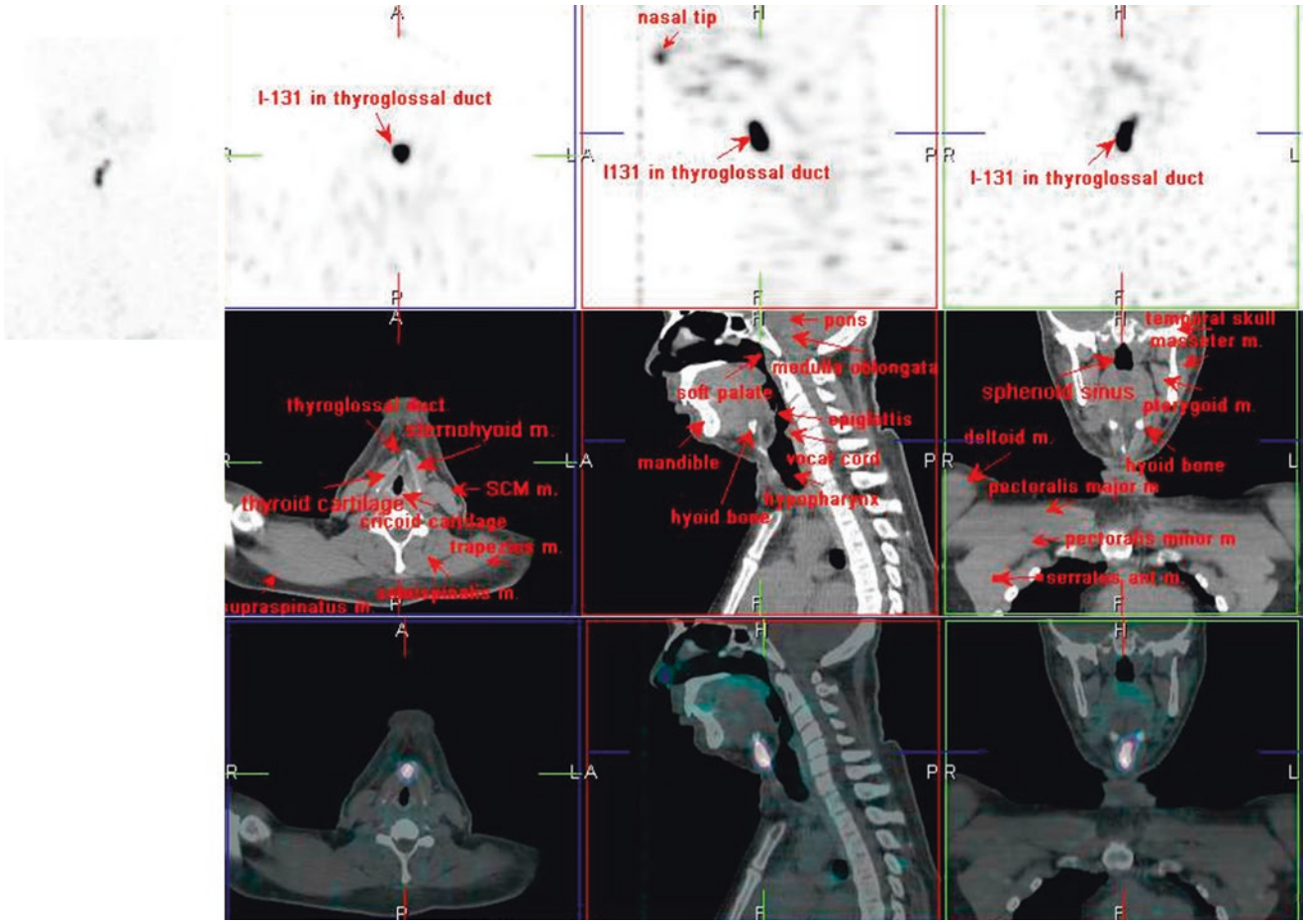

Fig. 70 ^{131}I SPECT/CT

2.2.3.2. Case 2

A 32-year-old female patient with neck pain and fever. Thyroid function studies showed low TSH with increased T3 and T4, so subacute thyroiditis was suspected. ^{99m}Tc-pertechnetate thyroid scan SPECT/CT was performed showing faintly visualized thyroid activity and decreased percentage of thyroid uptake (0.08%), so the diagnosis was confirmed (Fig. 71).

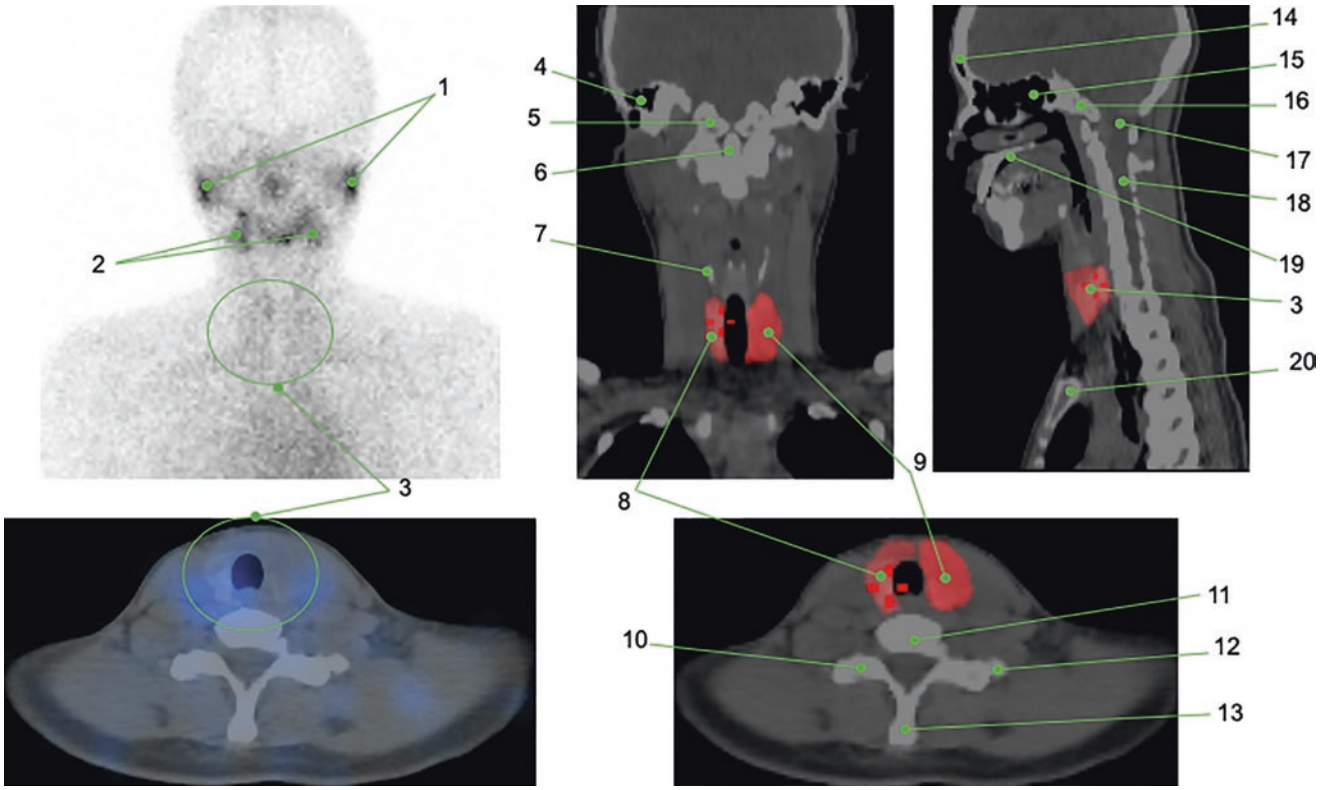

Fig. 71 1. Parotid glands
2. Submandibular glands
3. Faintly visualized thyroid gland
4. Right mastoid air cells
5. Right occipital condyle
6. Odontoid process
7. Thyroid cartilage, right superior aspect
8. Right thyroid lobe, normal size
9. Left thyroid lobe, enlarged
10. C5 right transverse process
11. C5 vertebral body
12. C5-C6 facet joint
13. C5 spinous process
14. Frontal sinus
15. Sphenoid sinus
16. Clivus
17. Foramen magnum
18. Cervical spinal canal
19. Hard palate
20. Sternum

2.2.3.3. Case 3

A 37-year-old female patient with known hyperthyroidism, Graves' disease, who attended her annual checkup. Thyroid function studies showed low TSH with increased T3 and T4, and increased TSH-R-Ab. ^{99m}Tc-pertechnetate thyroid scan SPECT/CT was performed showing diffuse enlargement of the thyroid gland with markedly increased percentage of thyroid uptake (26.32%) (Fig. 72).

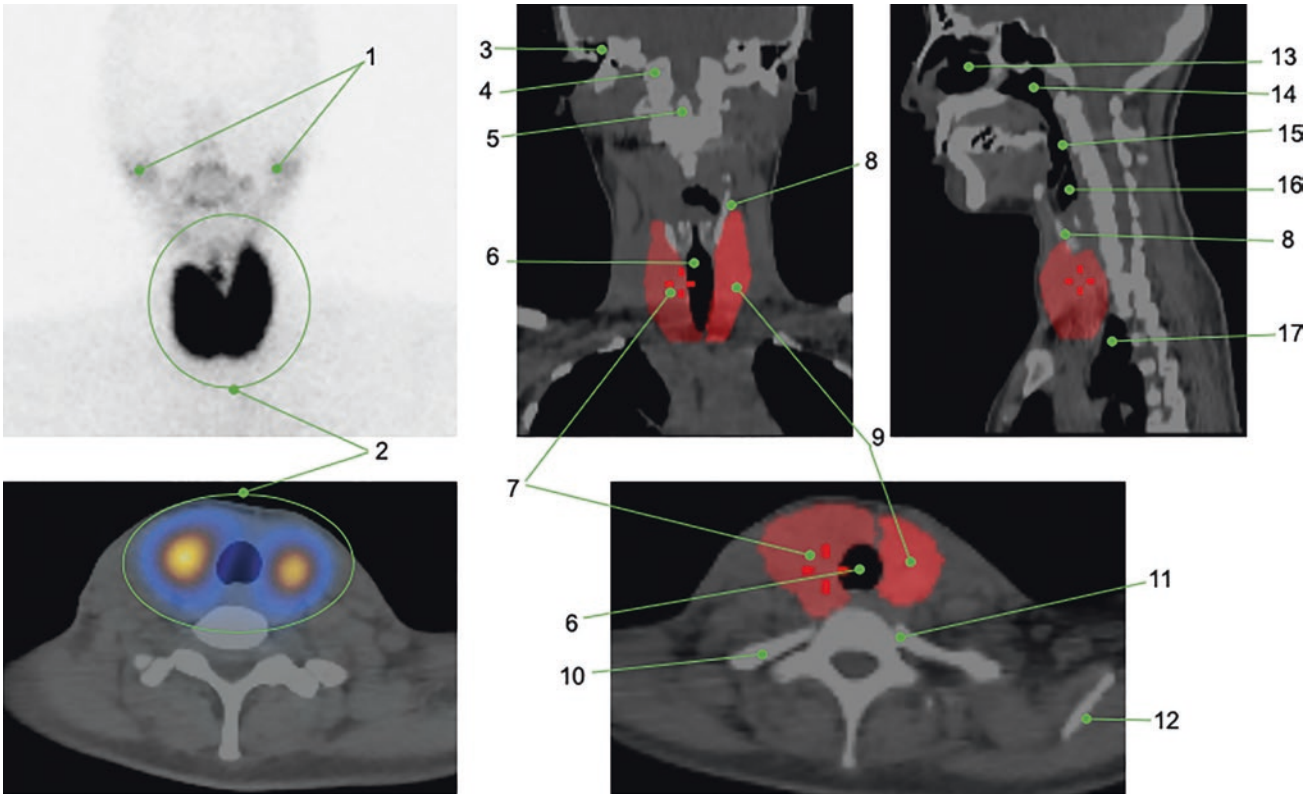

Fig. 72 1. Parotid glands
2. Diffusely enlarged thyroid gland with markedly increased uptake
3. Right mastoid air cells
4. Right occipital condyle
5. Odontoid process
6. Trachea
7. Right thyroid lobe, enlarged
8. Thyroid cartilage
9. Left thyroid lobe, enlarged
10. Right first rib
11. Left first costovertebral joint
12. Left scapula
13. Ethmoid air cells
14. Nasopharynx
15. Oropharynx
16. Larynx
17. Lung apex

2.2.4 Salivary Glands

2.2.4.1. Case 1

A 63-year-old female patient with nonspecific sicca. ^{99m}Tc-pertechnetate salivary gland scan SPECT/CT with quantitative analysis was performed and showed mild decreased uptake in bilateral parotid glands, with normal submandibular glands uptake, and normal bilateral function (Figs. 73 and 74).

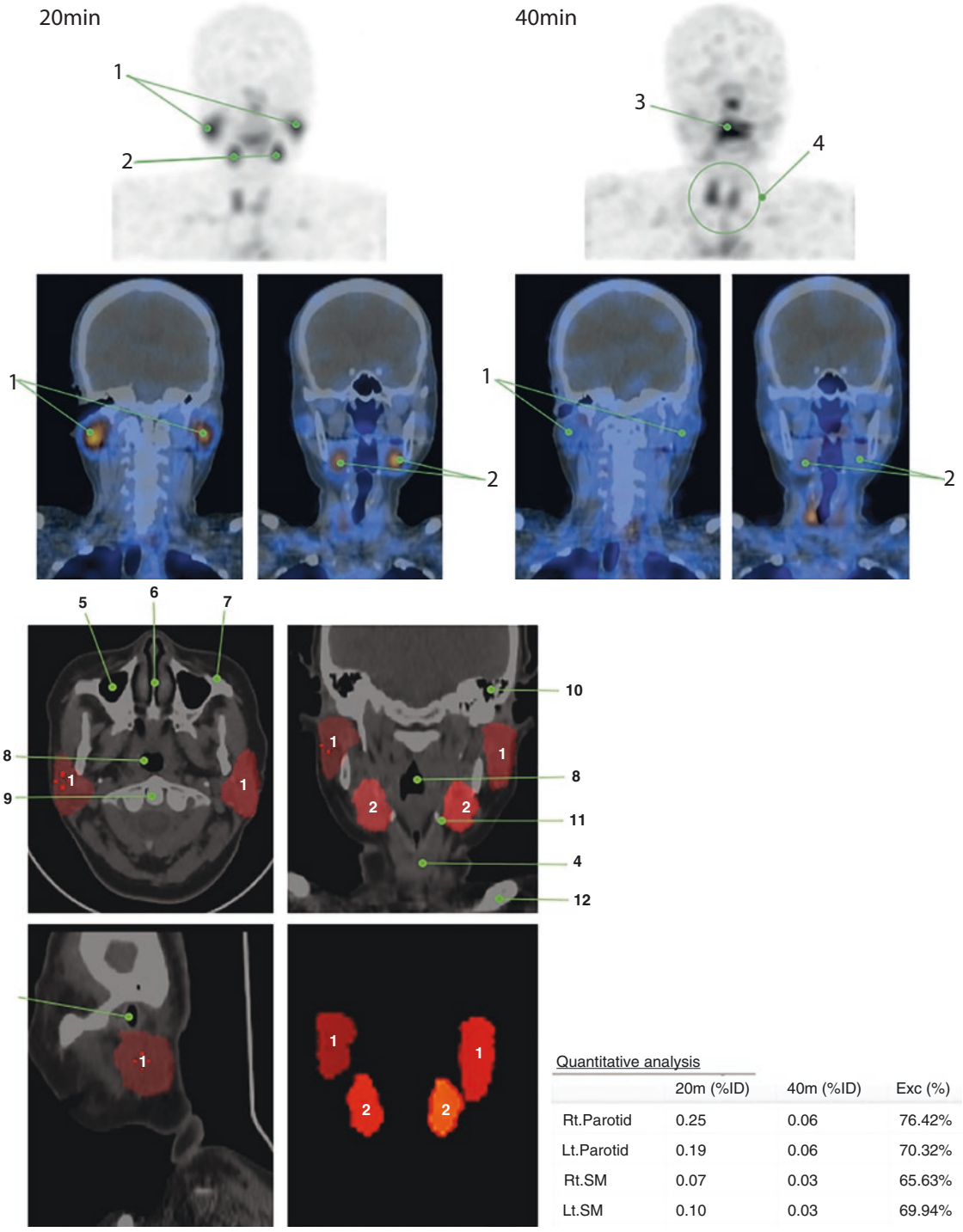

Quantitative analysis

	20m (%ID)	40m (%ID)	Exc (%)
Rt.Parotid	0.25	0.06	76.42%
Lt.Parotid	0.19	0.06	70.32%
Rt.SM	0.07	0.03	65.63%
Lt.SM	0.10	0.03	69.94%

Figs. 73 and 74 1. Parotid glands. The 20-minute scan shows bilateral mild decreased uptake, and the 40-minute scan shows complete excretion
2. Submandibular glands. The 20-minute scan shows normal bilateral uptake, and the 40-minute scan shows complete excretion
3. Radiotracer excretion in the oral cavity
4. Thyroid gland, normal uptake
5. Right maxillary sinus
6. Nasal septum
7. Left zygomatic arch
8. Trachea
9. Odontoid process
10. Left mastoid air cells
11. Left thyroid cartilage
12. Left clavicle

2.2.5 Cerebrospinal Fluid (CSF)

2.2.5.1. Case 1

A 66-year-old male patient with a history of head trauma. Moderate enlargement of ventricular size was found on CT, so after ventricular derivation, selected SPECT (*top*) and SPECT/CT (*bottom*) images of the head at 24 hours after injection of ^{111}In-DTPA into the L3-L4 spinal canal were obtained for evaluation. Images showed distribution in basal and Sylvian cisterns, without significant residual hydrocephalus or activity in the lateral ventricle, indicating non-communicating hydrocephalus (Fig. 75) [60].

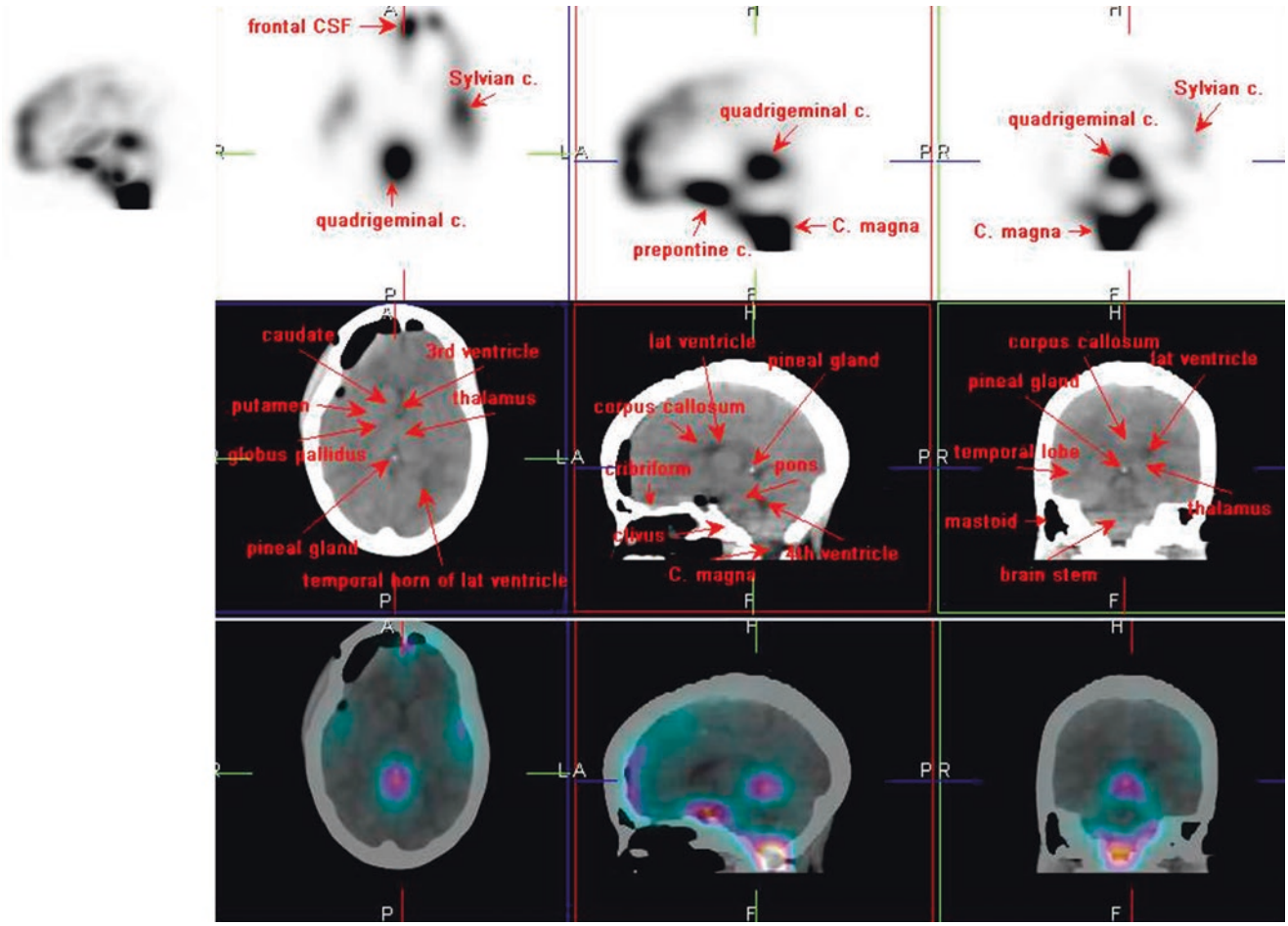

Fig. 75 ^{111}In-DTPA SPECT/CT

2.2.5.2. Case 2

A 72-year-old male patient with progressive gait disturbance, urinary incontinence, and dementia symptoms. Selected SPECT (*top*) and SPECT/CT (*bottom*) images of the head at 24 hours after injection of ^{111}In-DTPA into the L3-L4 spinal canal showed moderately increased activity in the lateral ventricles but no significant activity had migrated over to the convexity beyond the Sylvian cistern, indicating normal pressure hydrocephalus (Fig. 76).

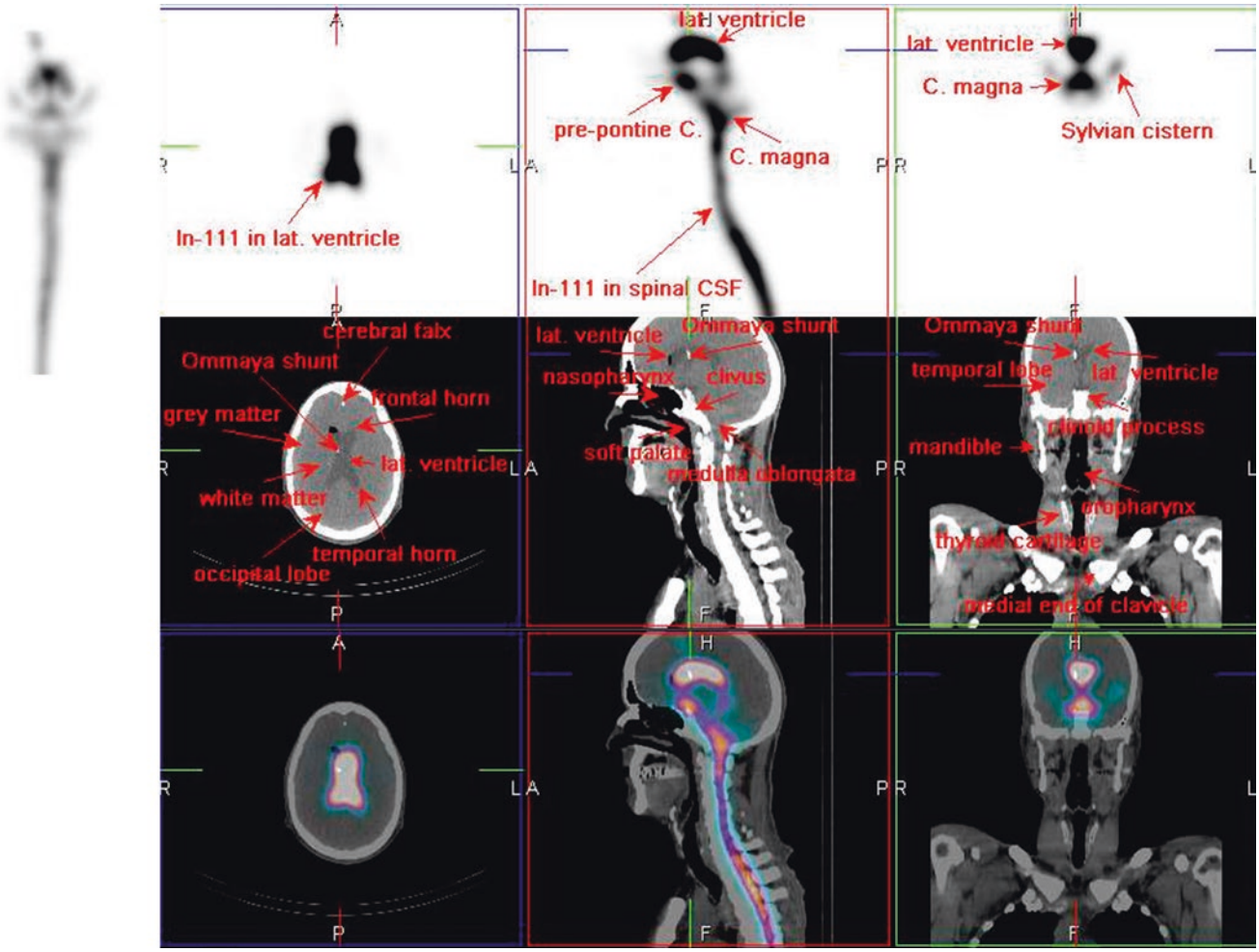

Fig. 76 ^{111}In-DTPA SPECT/CT

2.2.6 Central Venous Line Obstruction

2.2.6.1. Case 1

A 46-year-old male with a left central venous line complained of pain in the substernal area. A nuclear dynamic venous flow study using ^{99m}Tc-DTPA showed a focal area of increased activity in the distal left innominate vein, representing obstruction. Venous obstruction occurs when blood clots or vascular tissues develop and narrow the channel for flow. More than 40% of patients with a central venous line can develop a venous obstruction, and they may experience a swollen arm, neck pain, facial swelling, or shortness of breath (Fig. 77) [61].

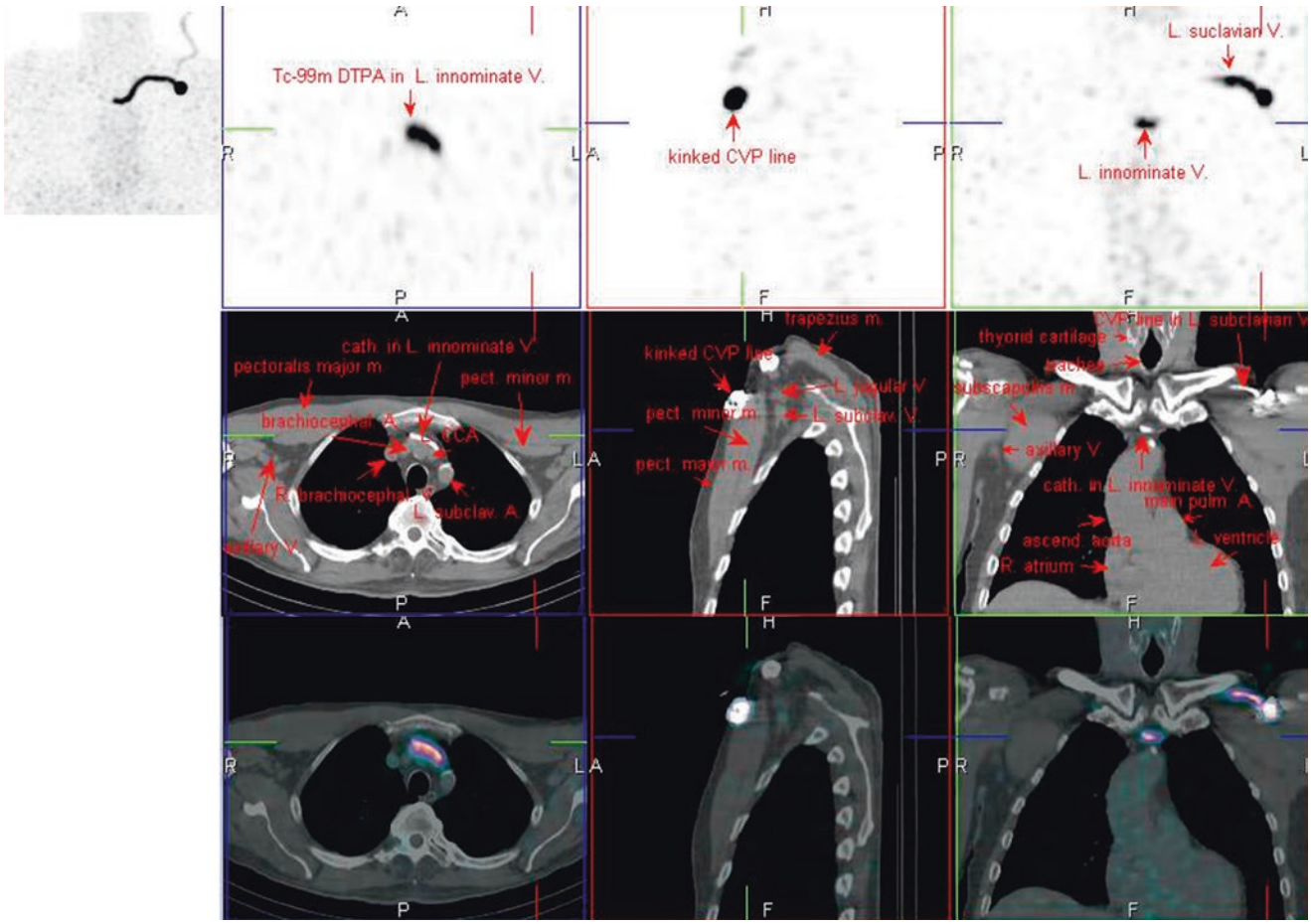

Fig. 77 ^{99m}Tc-DTPA SPECT/CT

2.2.7 Renal

2.2.7.1. Case 1

A 49-year-old male patient with right hydronephrosis due to renal pelvis stones. ^{99m}Tc-DTPA and SPECT/CT were performed for evaluation, finding decreased uptake in the right kidney with no significant effect in renal function. Calculated GFR (ml/min): left 48.58, right 42.36 (Fig. 78).

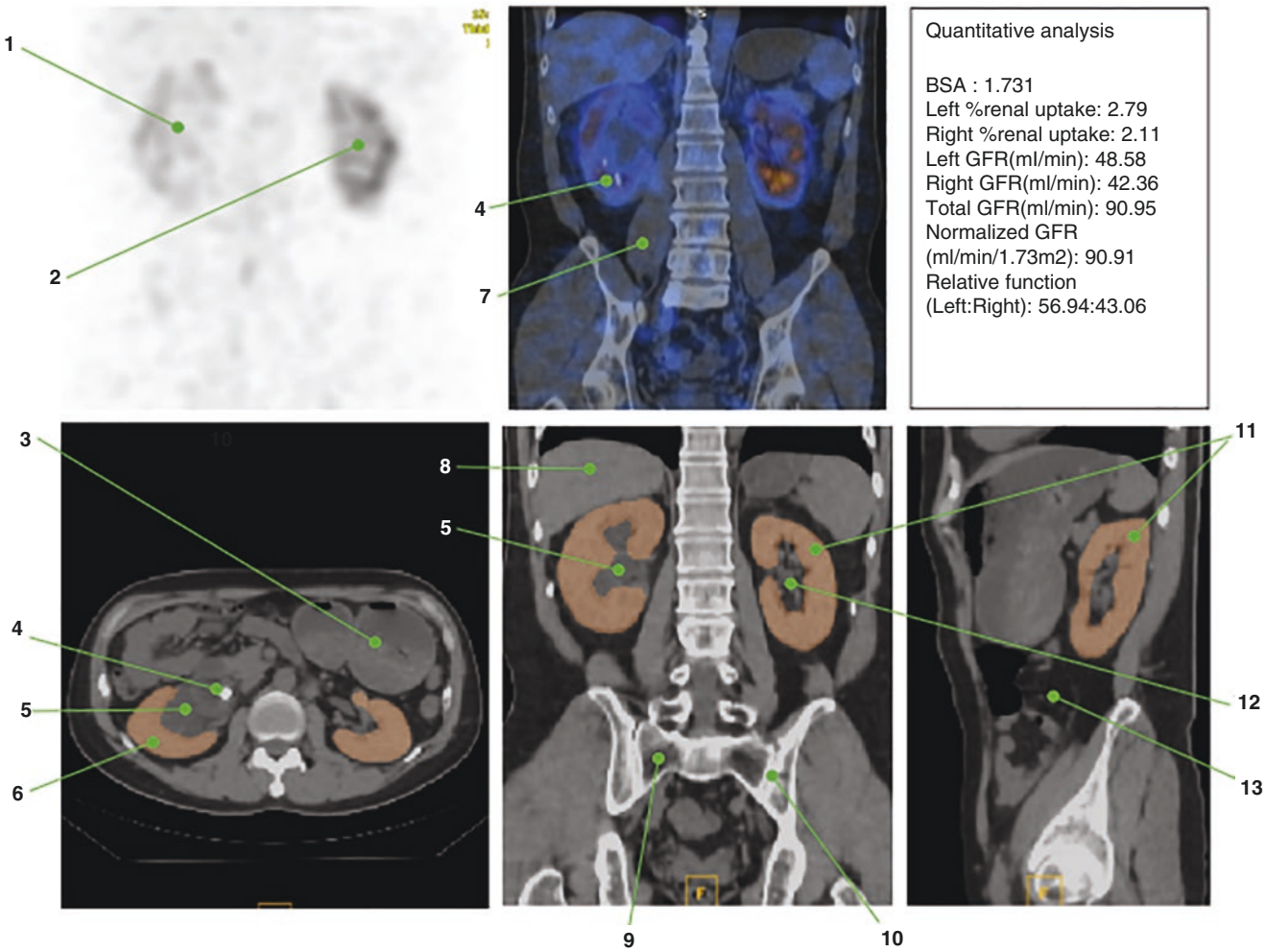

Fig. 78 1. Right kidney, decreased uptake
2. Left kidney, normal uptake
3. Stomach
4. Right renal pelvis stone
5. Right dilated renal pelvis: hydronephrosis
6. Right renal cortex, normal thickness
7. Right psoas muscle
8. Liver
9. Right sacral ala
10. Left sacroiliac joint
11. Left renal cortex
12. Left renal sinus
13. Descending colon

2.2.7.2. Case 2

A 72-year-old male patient with history of kidney transplant in 2015, who attended his annual checkup. ^{99m}Tc-DTPA and SPECT/CT were performed to find a normal functioning transplanted kidney with calculated GFR (ml/min) of 96.78. Native non-functioning kidneys showed atrophy in the right side and a large water bag kidney in the left side (Fig. 79).

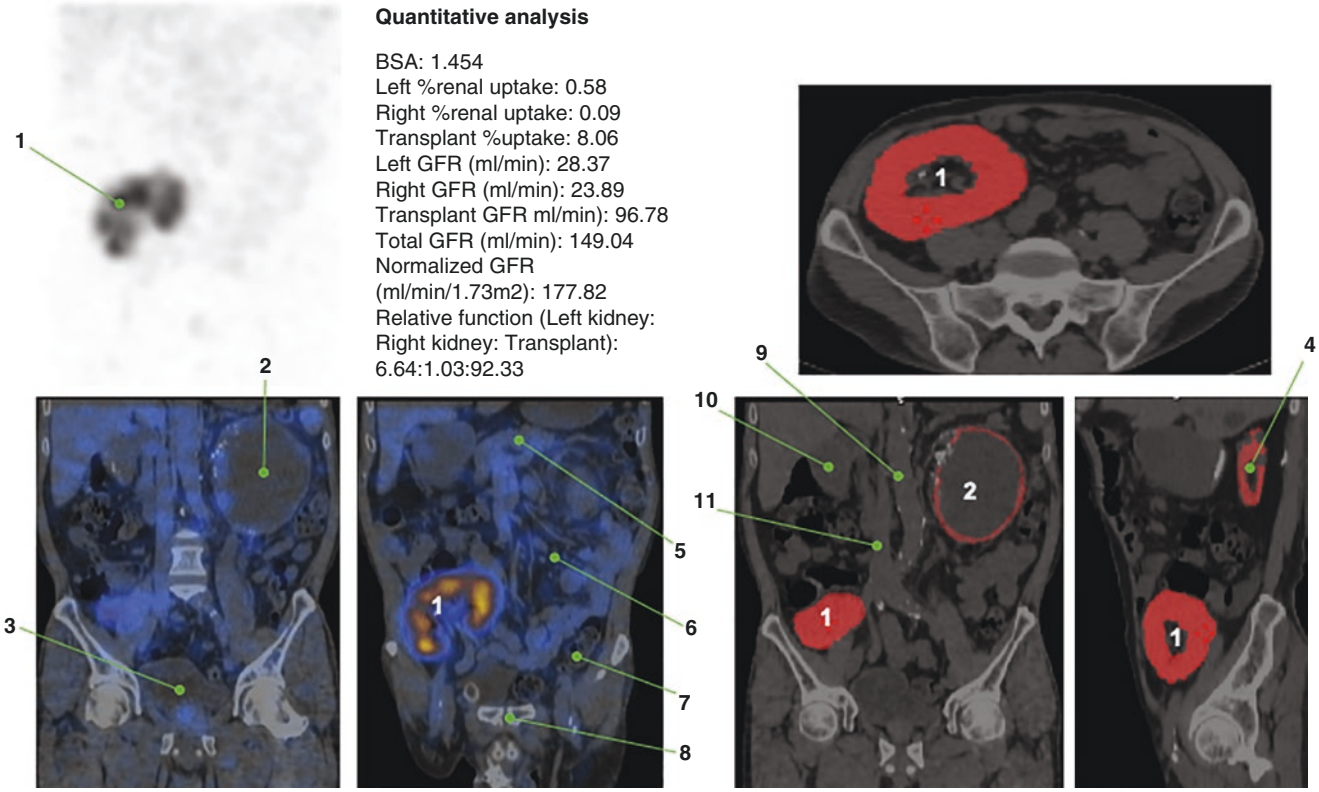

Fig. 79 1. Transplanted kidney in the right pelvis
2. Left, large, water bag kidney
3. Bladder
4. Atrophic right kidney
5. Pancreatic body
6. Small bowel mesentery
7. Distal descending colon
8. Pubic symphysis
9. Abdominal aorta
10. Gallbladder
11. Inferior vena cava

2.2.8 Lymphatic System

2.2.8.1. Case 1

A 44-year-old woman with a history of right breast cancer treated with total mastectomy and axillary lymph node dissection, who developed right arm lymphedema. ^{99m}Tc-ASC lymphoscintigraphy and SPECT/CT was performed and showed absence of main lymphatics in the right arm, as well as absence of lymph nodes and positive dermal backflow (DBF) until the elbow level. In the left arm, normal lymphatic vessels and lymph nodes were observed (Fig. 80).

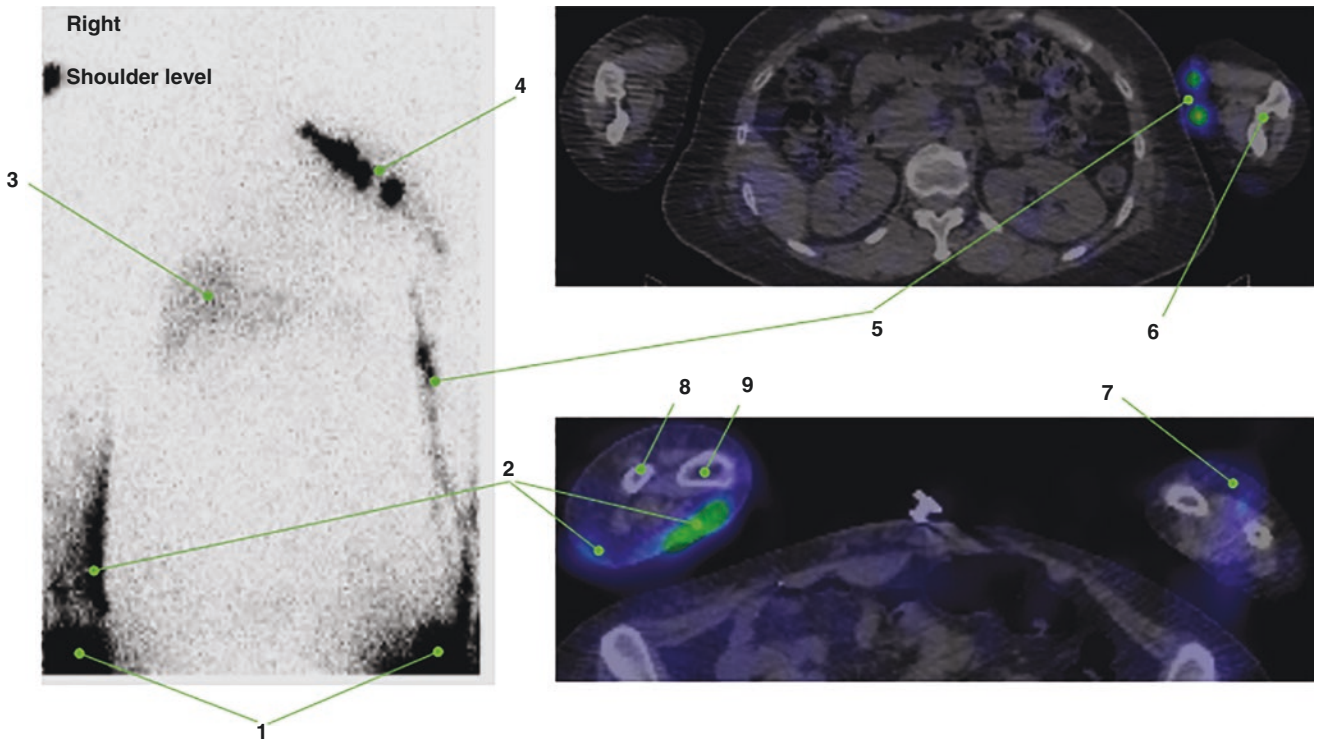

Fig. 80 1. Injection site at both hands
2. Dermal backflow in the right arm
3. Mild increased activity in the liver
4. Left axillary lymph nodes
5. Normal main lymphatics in the left arm
6. Left distal humerus
7. Left arm subcutaneous tissue, normal appearance
8. Right ulna
9. Right radius

2.2.8.2. Case 2

A 45-year-old male patient with confirmed diagnosis of left preauricular melanoma. Selected SPECT (*top*) and SPECT/CT (*bottom*) images of the neck, including the lower head, after intradermal injection of ^{99m}Tc filtered sulfur colloidal particles around the tumor, demonstrated focal areas of slightly increased activity in the left upper jugular lymphatic chain (level IIB), indicating sentinel lymph nodes. The sentinel lymph node is hypothetically the first lymph node or group of nodes to drain the cancer. It is postulated that sentinel lymph nodes are the target organs primarily reached by metastasizing cancer cells from the tumor. The spread of some forms of cancer usually follows an orderly progression (Fig. 81) [62].

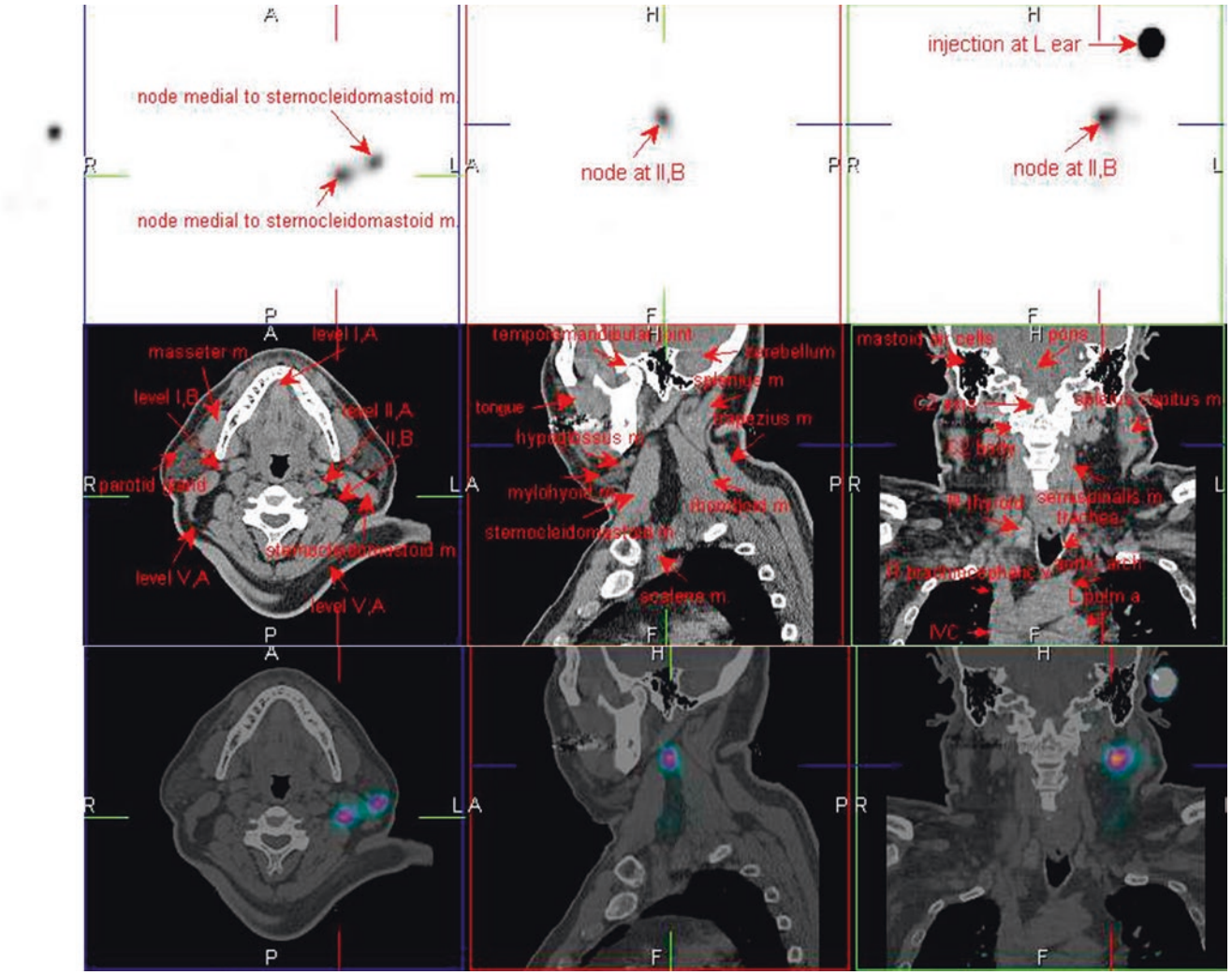

Fig. 81 ^{99m}Tc-filtered sulfur colloid SPECT/CT

2.2.8.3. Case 3

A 59-year-old female patient with uterine cervical cancer. SPECT (*top*) and SPECT/CT (*bottom*) images of the pelvis after subcutaneous injection of ^{99m}Tc-filtered sulfur colloid particles around the area were performed. Images showed moderate increased activity in the left external iliac lymph node and slightly increased activity in the left inguinal superficial lymph node, indicating sentinel lymph nodes (Fig. 82).

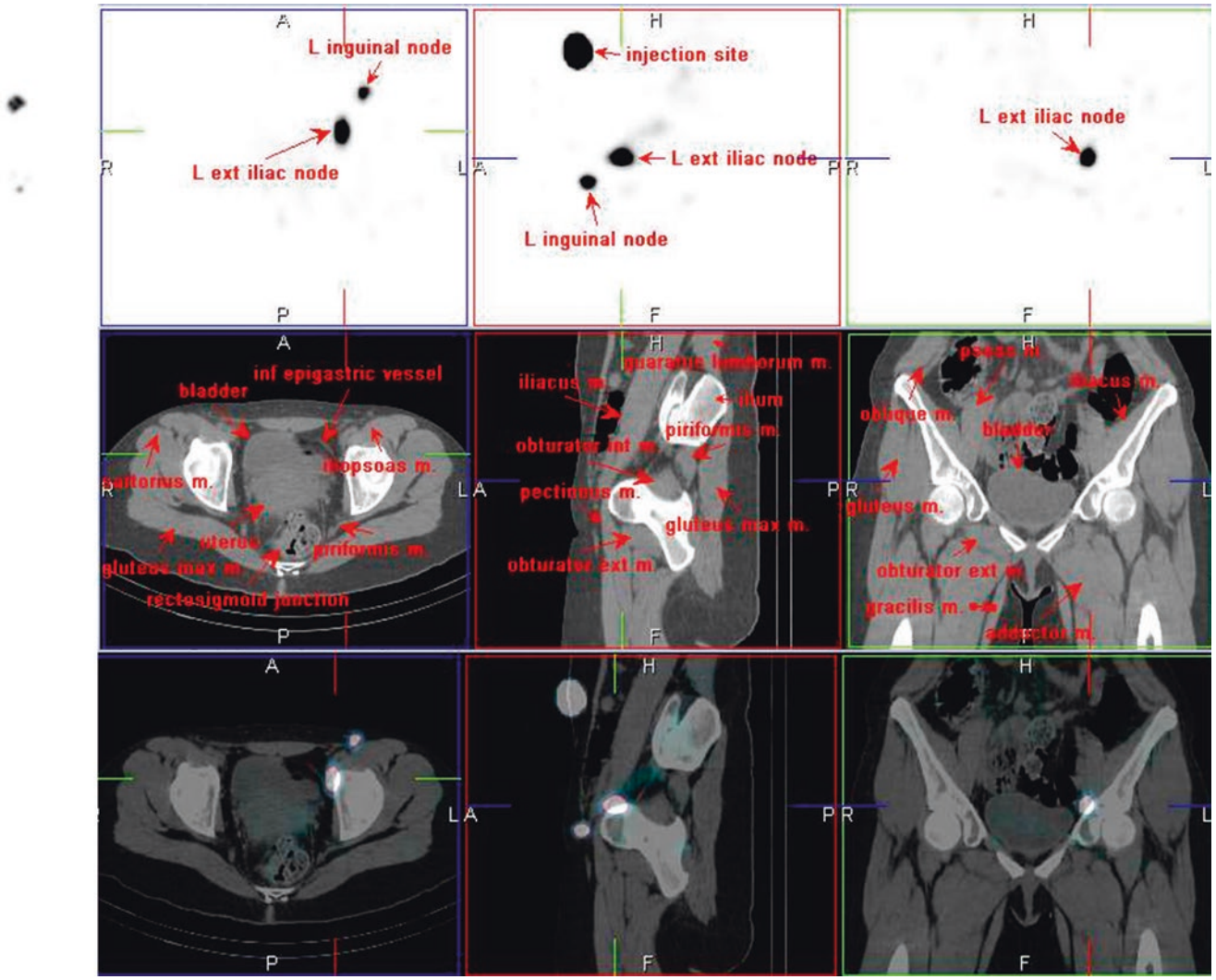

Fig. 82 ^{99m}Tc-filtered sulfur colloid SPECT/CT

2.2.8.4. Case 4

A 53-year-old female patient with recent diagnosis of melanoma in the right anterior chest wall. Selected SPECT (*top*) and SPECT/CT (*bottom*) images of the chest after intradermal injection of ^{99m}Tc-filtered sulfur colloid showed a focal area of slightly increased activity in the right superficial axillary lymph node (level I), indicating a sentinel lymph node (Fig. 83).

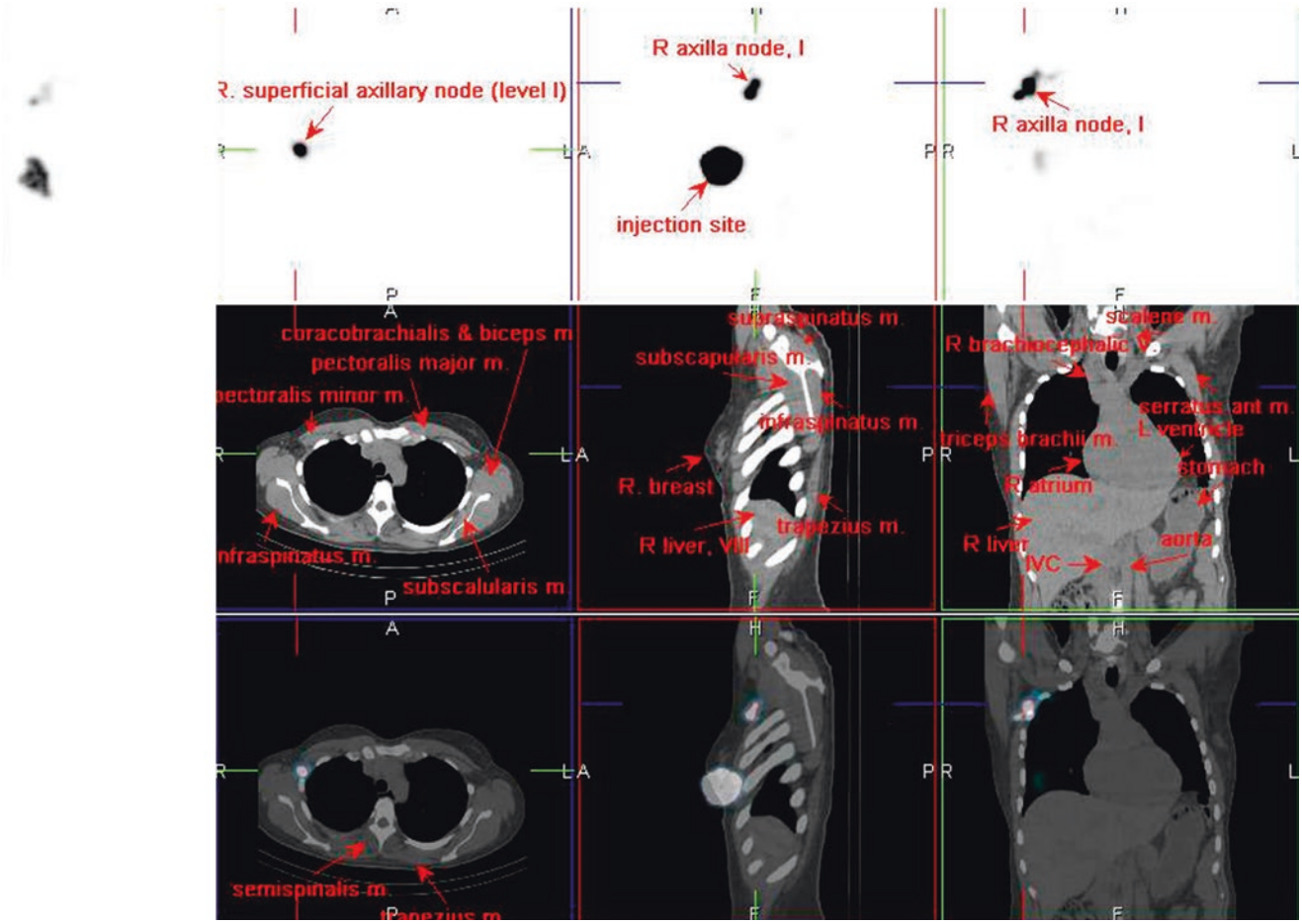

Fig. 83 ^{99m}Tc-filtered sulfur colloid SPECT/CT

2.2.8.5. Case 5

A 64-year-old male patient with a squamous cell carcinoma in the right tongue base. Selected SPECT *(top)* and SPECT/CT (*bottom*) images of the neck, including the lower head, after subcutaneous injection of ^{99m}Tc Lymphoseek showed a focal area of slightly increased activity in the right carotid space, indicating a sentinel lymph node. Lymphoseek is a radioactive diagnostic agent for lymphatic mapping and guiding sentinel lymph node biopsy (Fig. 84) [63].

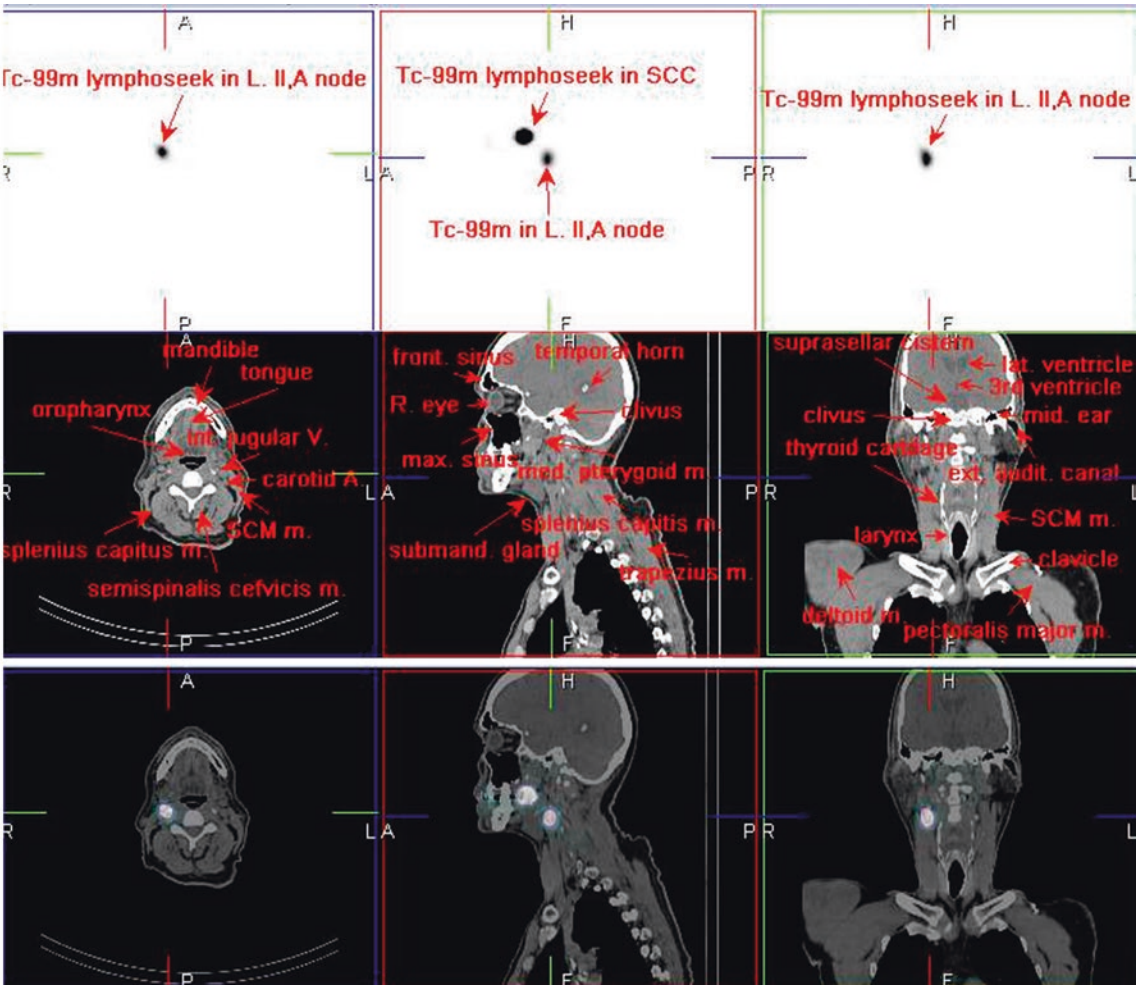

Fig. 84 ^{99m}Tc-lymphoseek SPECT/CT

2.2.9 Lung (V/Q)

2.2.9.1. Case 1

A 58-year-old male patient with non–small cell lung cancer, adenocarcinoma. ^{99m}Tc-MAA SPECT/CT was performed, finding a non-uniform distribution of the particles, indicating moderately decreased perfusion in the right upper, middle, and lower lobes. There was complete absence of particles within the tumor. ^{99m}Tc-MAA SPECT/CT is frequently performed for the presurgical evaluation of patients with lung cancer to determine the extent of surgery (Figs. 85, 86, and 87) [64, 65].

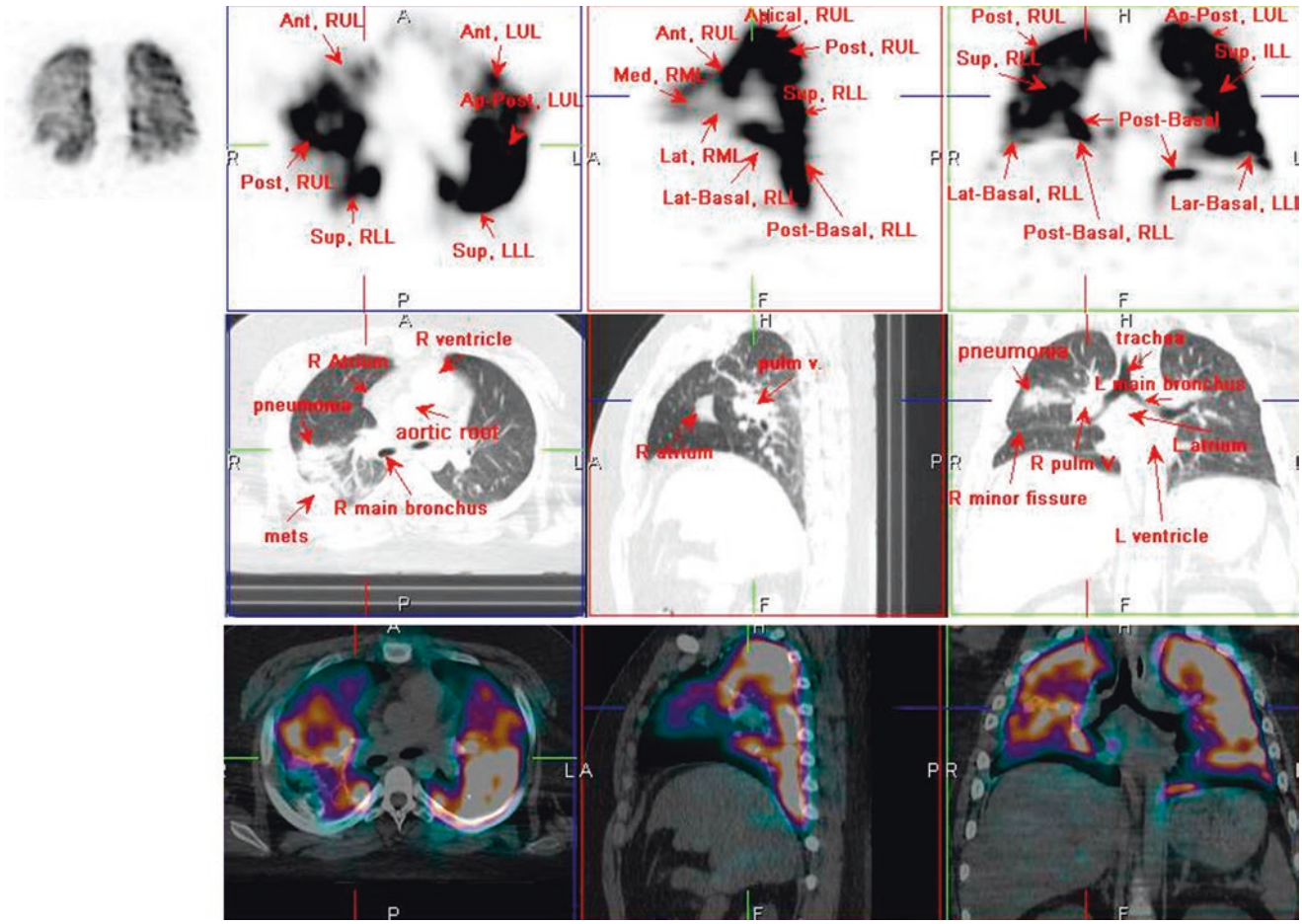

Fig. 85 ^{99m}Tc-MAA SPECT/CT

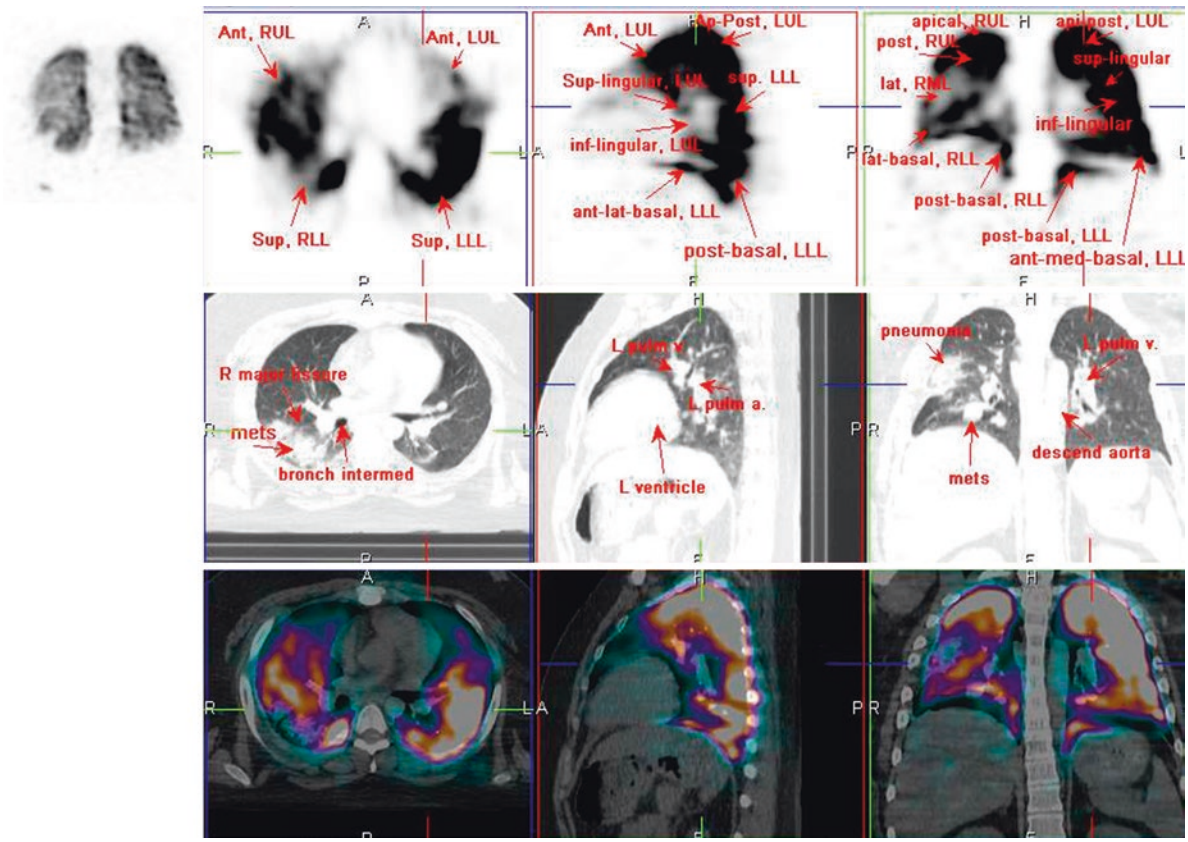

Fig. 86 ^{99m}Tc-MAA SPECT/CT

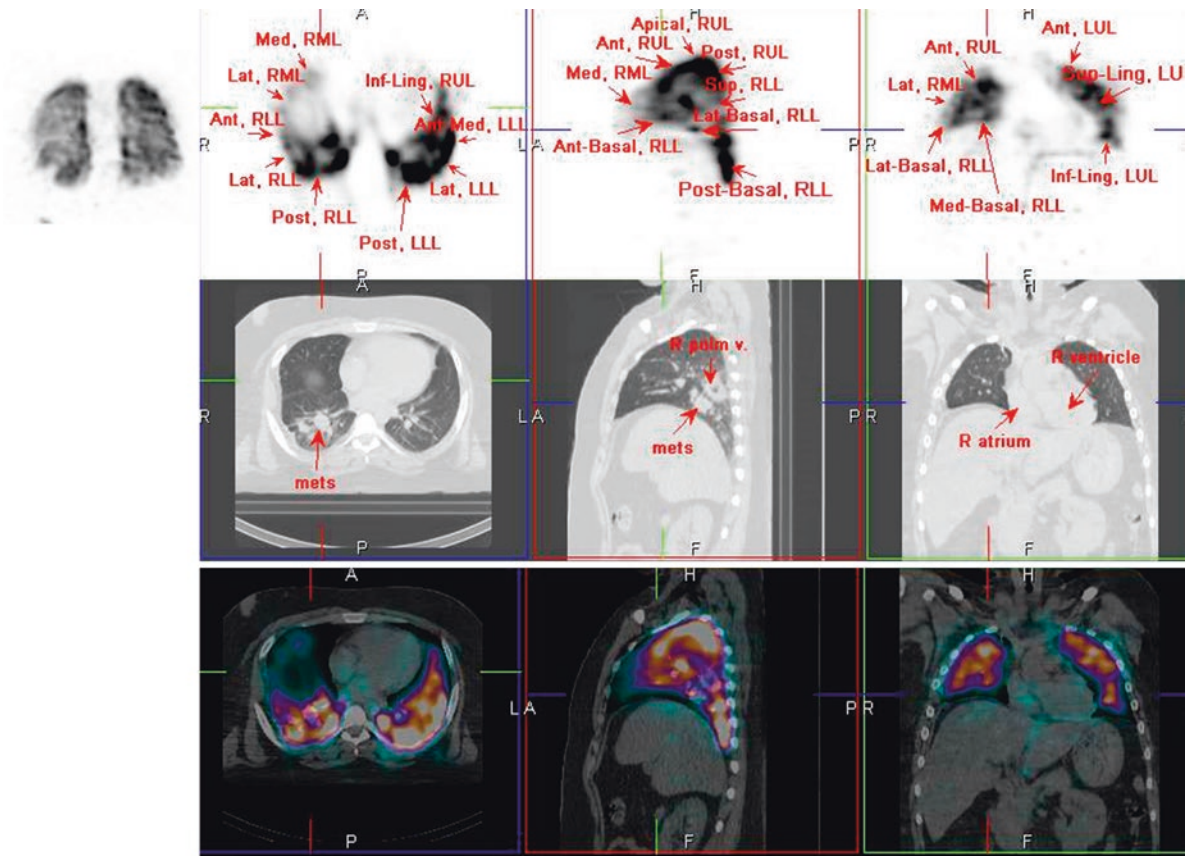

Fig. 87 ^{99m}Tc-MAA SPECT/CT

2.2.9.2. Case 2

A 26-year-old female patient with a history of recurrent respiratory papillomatosis, who developed a lung squamous cell carcinoma. Presurgical lung perfusion scan with SPECT/CT was performed to determine lung function and extent of surgery. Images showed a spiculated dense nodule in the right lower lobe, corresponding to the primary tumor, as well as complete perfusion defect in the whole lobe, probably due to obstruction (Fig. 88).

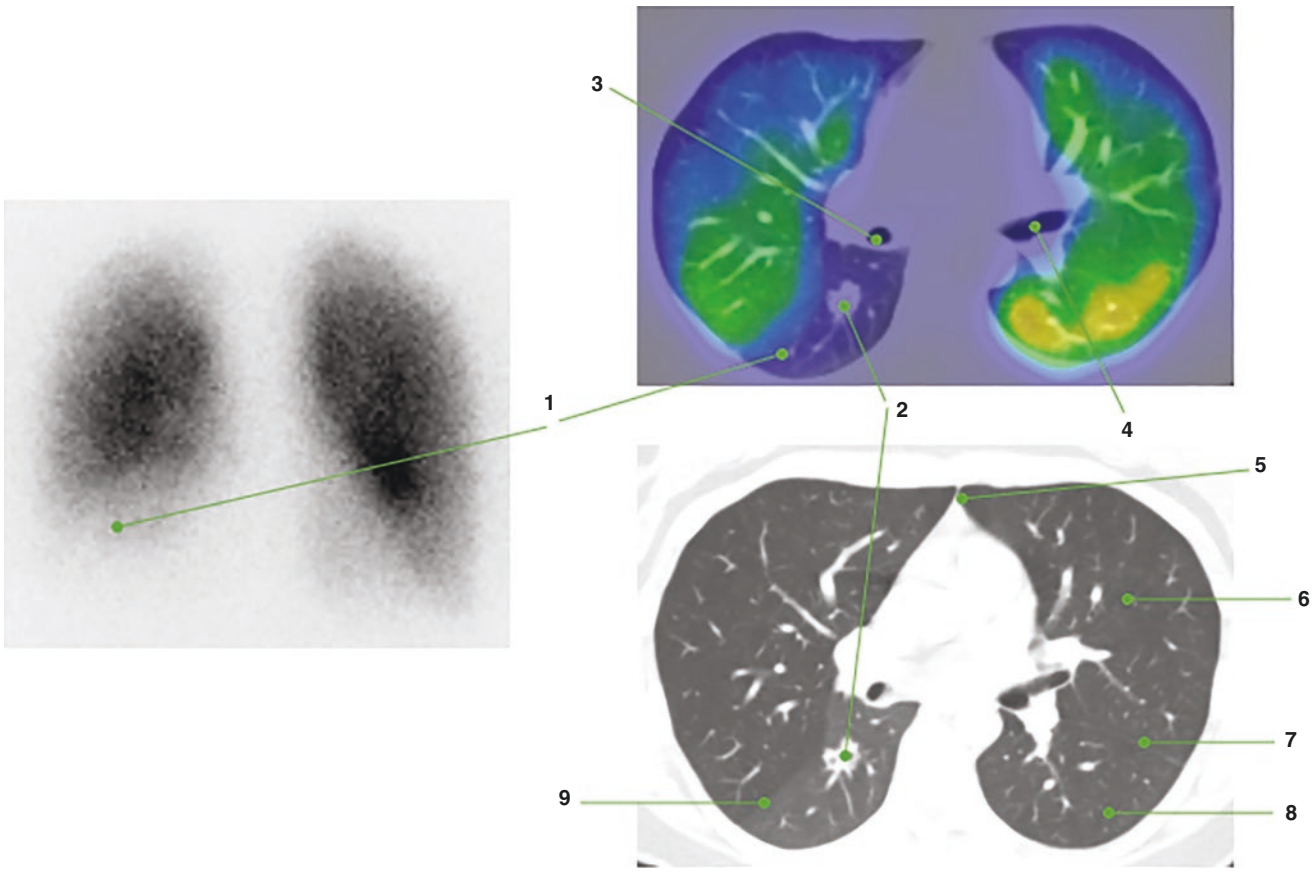

Fig. 88 1. Perfusion defect in the right lower lobe
2. Spiculated dense nodule in the right lower lobe: primary squamous cell carcinoma
3. Right main bronchus
4. Left main bronchus
5. Anterior junction line
6. Left upper lobe
7. Left major fissure
8. Left lower lobe
9. Right major fissure

2.2.10 Accessory Spleen

2.2.10.1. Case 1

A 50-year-old male patient attended a routine checkup and abdominal CT was performed finding an enhancing mass adjacent to the pancreatic tail. ^{99m}Tc-denatured RBC spleen scan was done for differential diagnosis, finding focal increased uptake in the nodular lesion at the pancreatic tail, which corresponded to an accessory spleen (Figs. 89, 90, 91, and 92) [66].

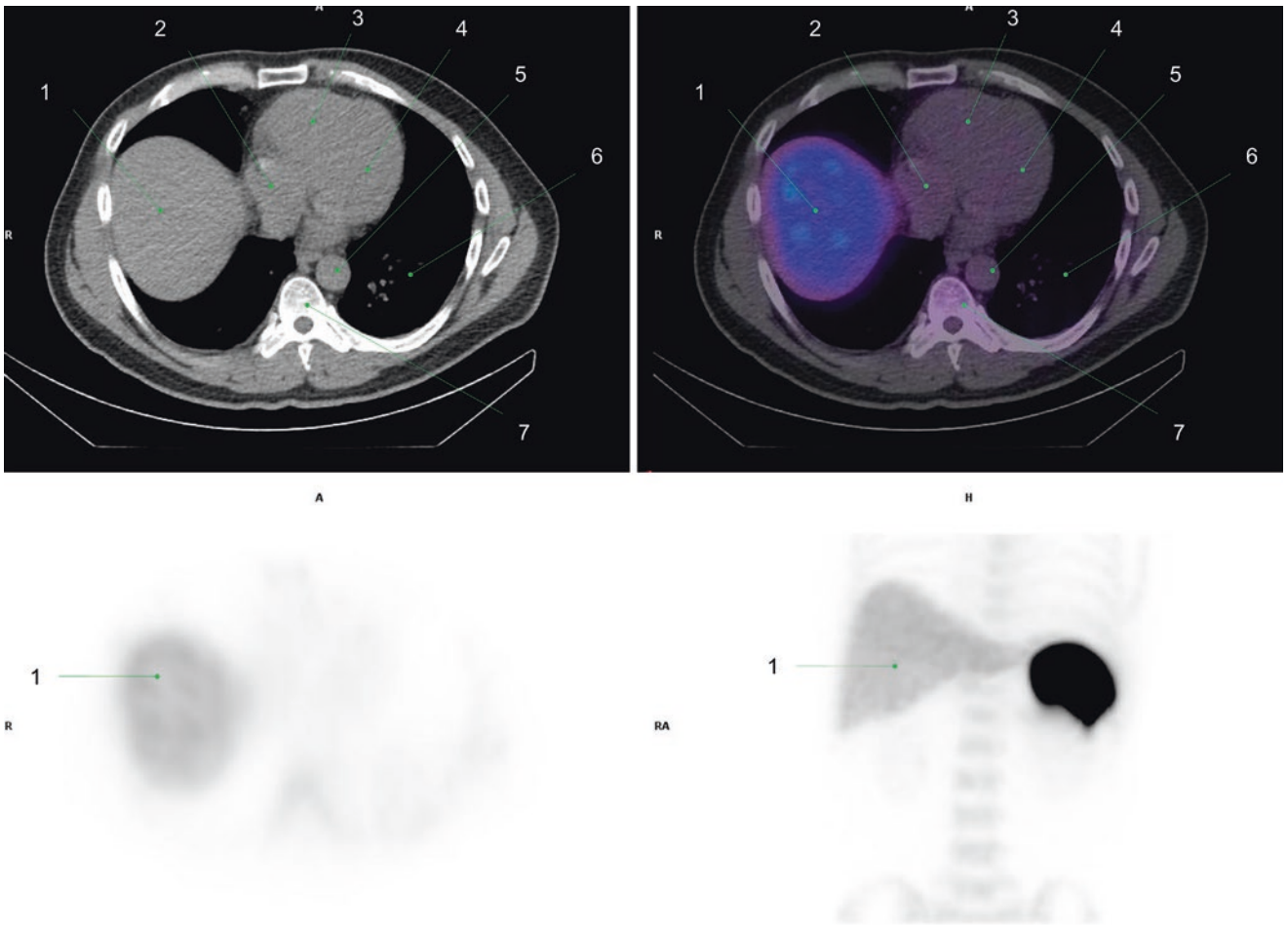

Fig. 89 1. Liver dome
2. Right atrium of the heart
3. Right ventricle
4. Left ventricle
5. Descending aorta
6. Lung parenchyma
7. Vertebral body

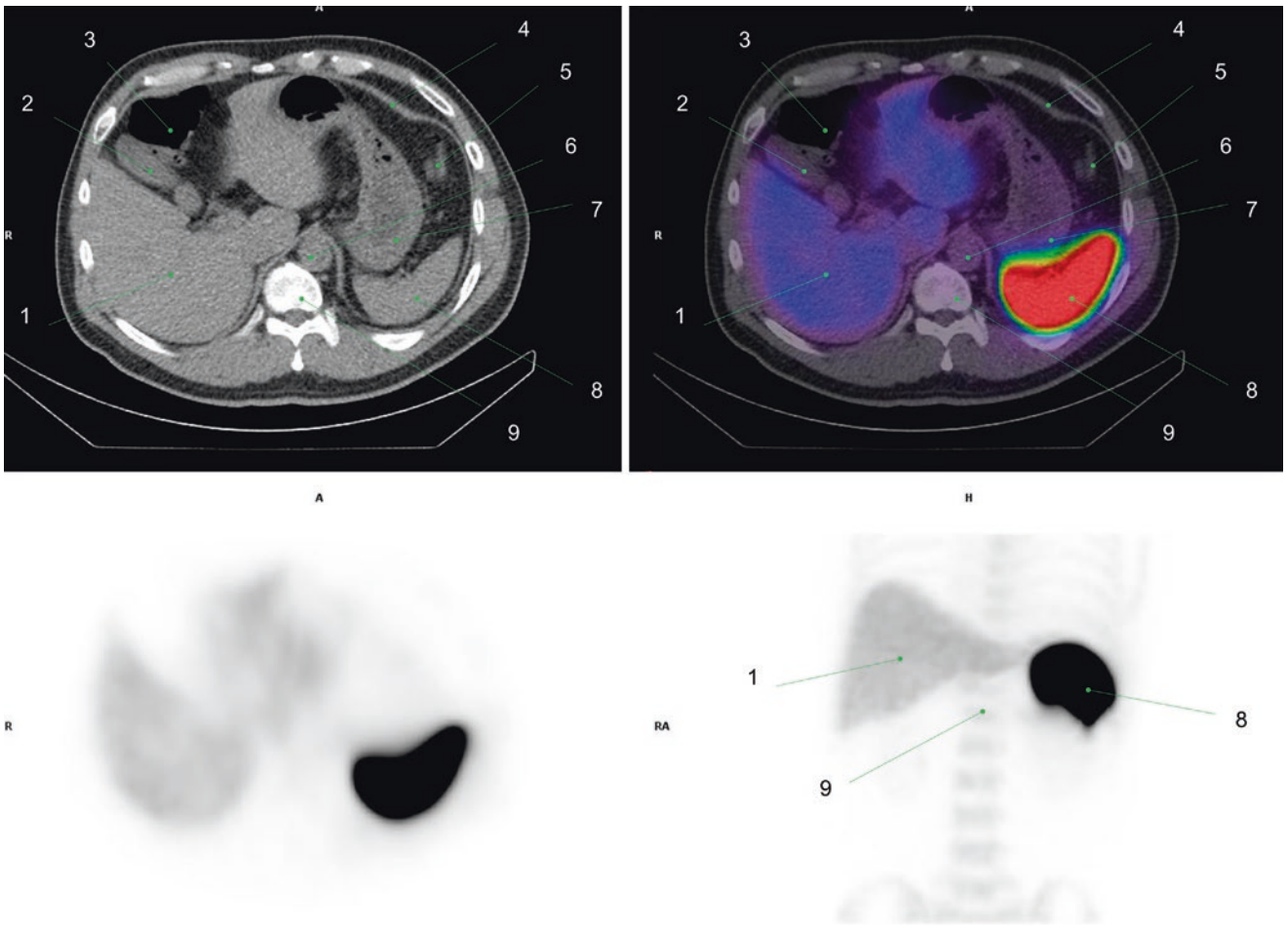

Fig. 90 1. Liver
2. Gallbladder
3. Hepatic flexure of transverse colon
4. Left diaphragm
5. Left gastroepiploic vessels
6. Spleen
7. Vertebral body

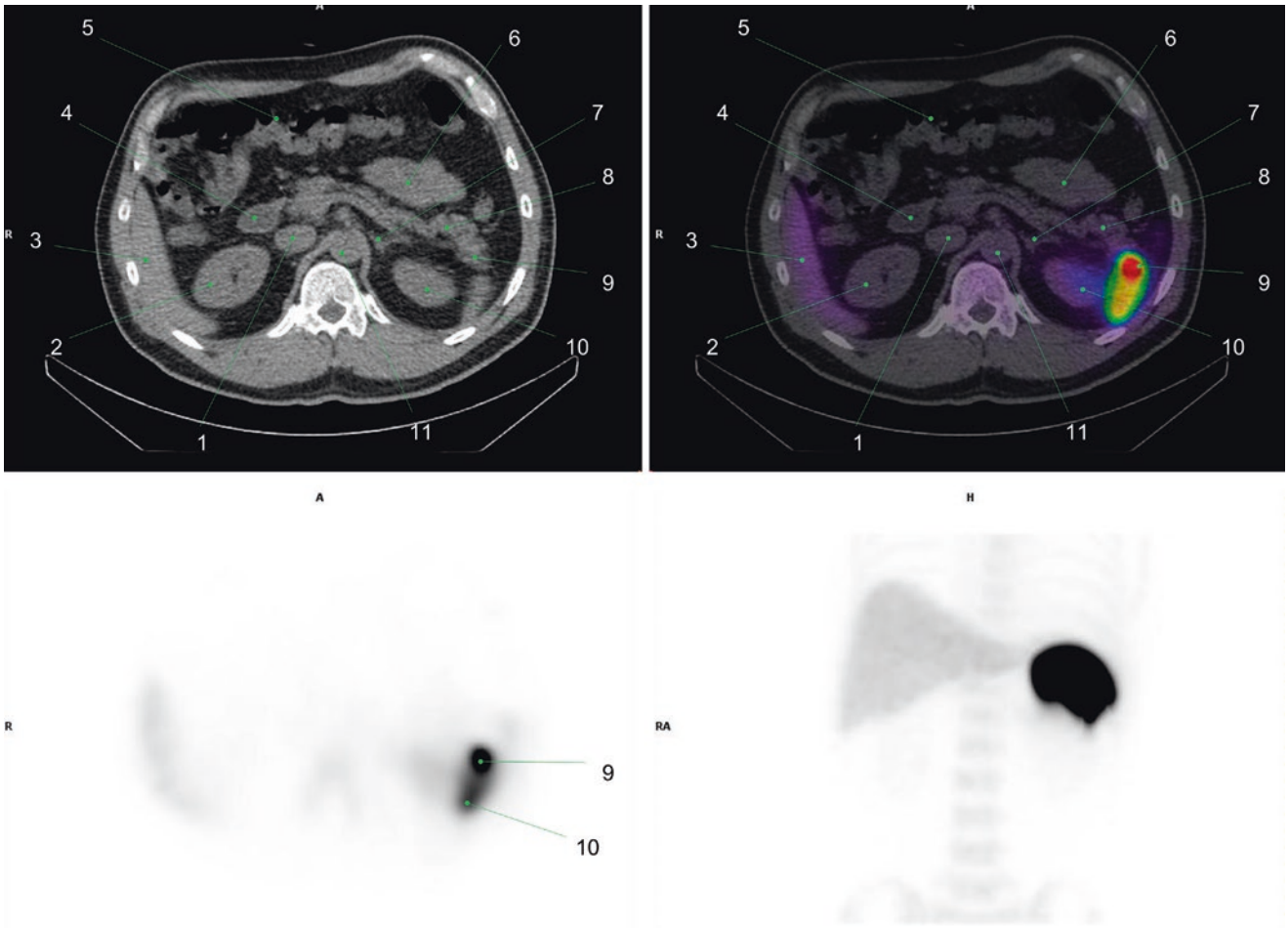

Fig. 91 1. Inferior vena cava
2. Right kidney
3. Liver tip
4. Second portion of duodenum
5. Transverse colon
6. Small bowels
7. Left adrenal gland
8. Tail of the pancreas
9. Intrapancreatic accessory spleen
10. Spleen
11. Descending aorta

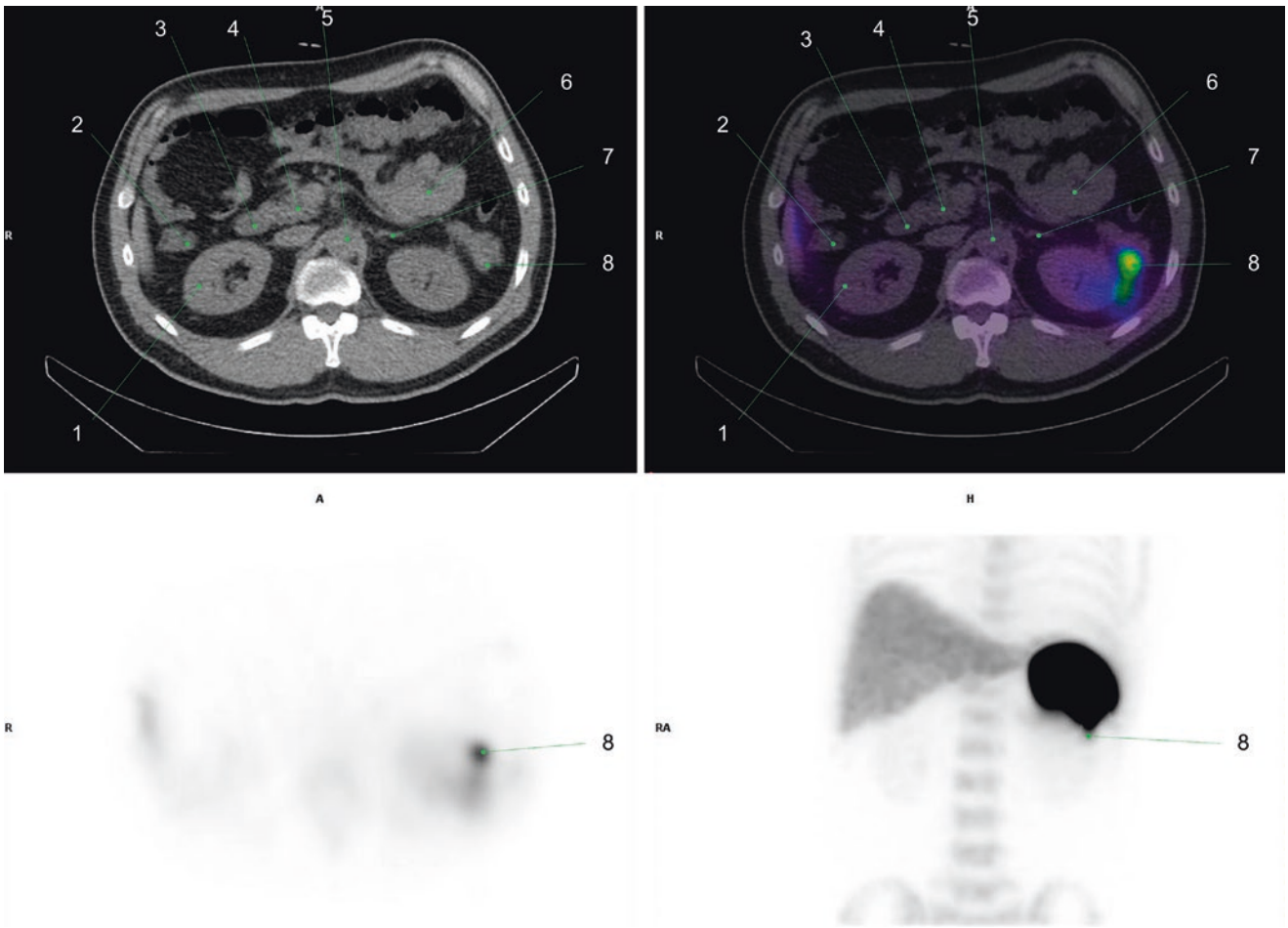

Fig. 92 1. Right kidney
2. Ascending colon
3. Duodenum
4. Uncinate process of the pancreas
5. Descending aorta
6. Small bowels
7. Left adrenal gland
8. Intrapancreatic accessory spleen

2.2.11 Adrenal Hyperplasia

2.2.11.1. Case 1

A 52-year-old male patient with right flank pain and abnormal adrenal function tests. So ^{123}I-MIBG SPECT/CT was performed for further evaluation. Images showed moderately increased activity in both adrenal glands, corresponding to adrenal hyperplasia. Also, a right renal mass was observed on CT, which was later confirmed to be a renal cell carcinoma (Fig. 93).

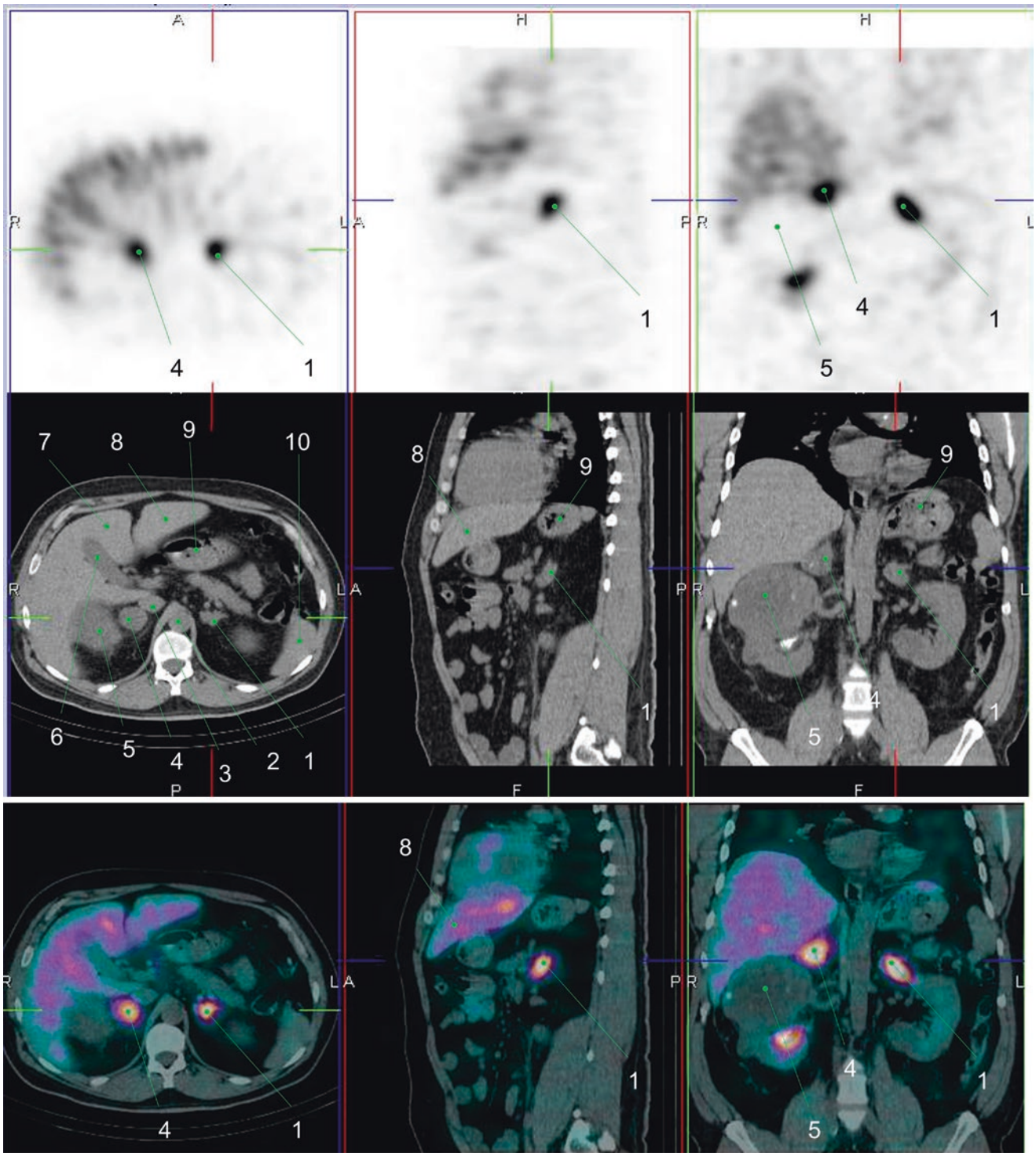

Fig. 93 1. Left adrenal gland hyperplasia
2. Abdominal aorta
3. Inferior vena cava
4. Right adrenal gland hyperplasia
5. Renal cell carcinoma in right kidney
6. Gallbladder
7. Liver, S4
8. Liver, left lobe
9. Stomach
10. Spleen

2.2.12 Heart

2.2.12.1. Case 1

An 84-year-old male patient with a history of asymptomatic coronary atherosclerosis, who attended a routine checkup and referred occasional chest pain. Laboratory studies were carried out finding increased troponin and proBNP, as well as increased free light chain of lambda and kappa (18.66 and 21.16, respectively). ^{99m}Tc-HMDP heart planar scan with SPECT/CT was performed and images showed significant heart uptake, which suggested transthyretin-related (TTR) amyloidosis, later confirmed with biopsy (Fig. 94) [67].

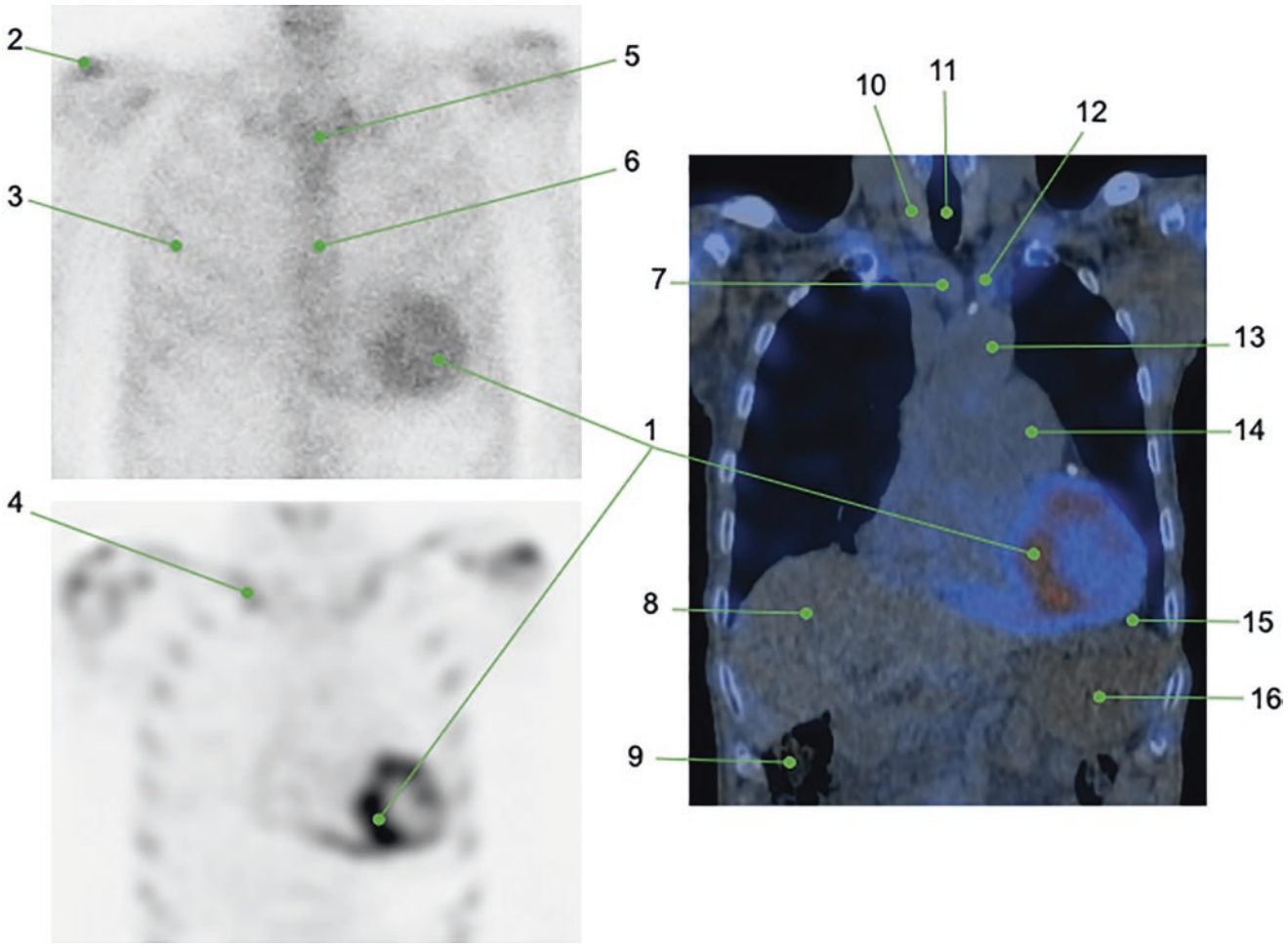

Fig. 94 1. Markedly increased uptake in the left ventricular wall: amyloidosis involvement
2. Focal increased uptake in the right acromioclavicular joint: degenerative changes
3. Right fourth rib anterior arc
4. Right sternoclavicular joint
5. Sternum manubrium
6. Sternum body
7. Right brachiocephalic artery
8. Liver
9. Hepatic angle of the colon
10. Right thyroid lobe
11. Trachea
12. Left common carotid artery
13. Aortic arch
14. Left atrium
15. Left cardio phrenic recess
16. Stomach

2.2.13 Brain

2.2.13.1. Case 1

A 35-year-old asymptomatic man with diagnosis of Moyamoya disease who attended a periodic checkup. ^{99m}Tc-HMPAO brain perfusion SPECT was performed. Basal study showed adequate perfusion in all vascular territories bilaterally. In post-acetazolamide study, perfusion is maintained and/or increased, which indicates that the vascular reserve is preserved. Anterior cerebral artery (ACA), middle cerebral artery (MCA), internal carotid artery (ICA = ACA + MCA), and posterior cerebral artery (PCA) (Fig. 95) [68].

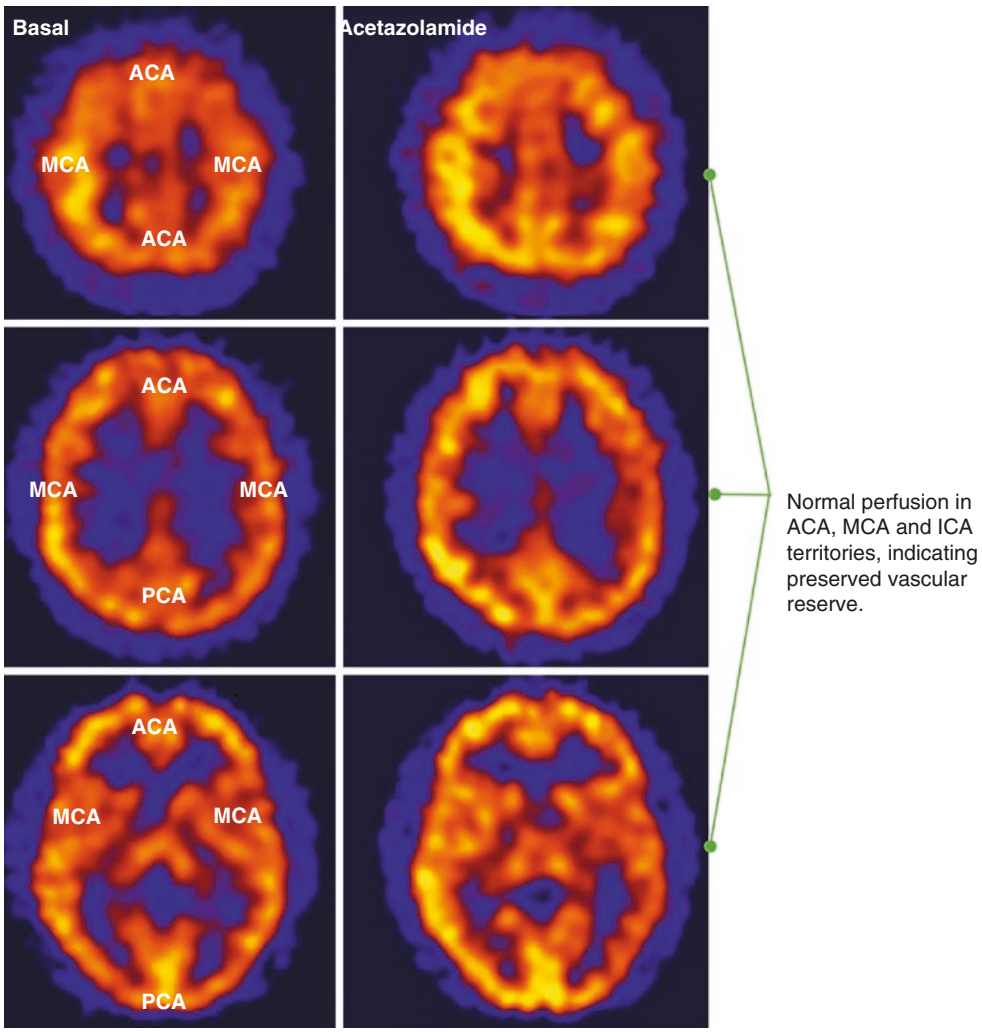

Fig. 95 ^{99m}Tc-HMPAO brain perfusion SPECT

2.2.13.2. Case 2

An 84-year-old woman with a diagnosis of severe atherosclerotic carotid stenosis of both extracranial internal carotid arteries. ^{99m}Tc-HMPAO brain perfusion SPECT was performed to determine if there was surgical indication. Basal study showed adequate perfusion in all territories. However, the post-acetazolamide study showed decreased perfusion in the left ICA (ACA + MCA) territory, indicating that the vascular reserve is compromised because the stenosis has progressed to the point of consuming compensatory capacity. These findings indicate that the patient would benefit from surgical intervention to prevent and/or reduce the risk of stroke (Fig. 96) [68].

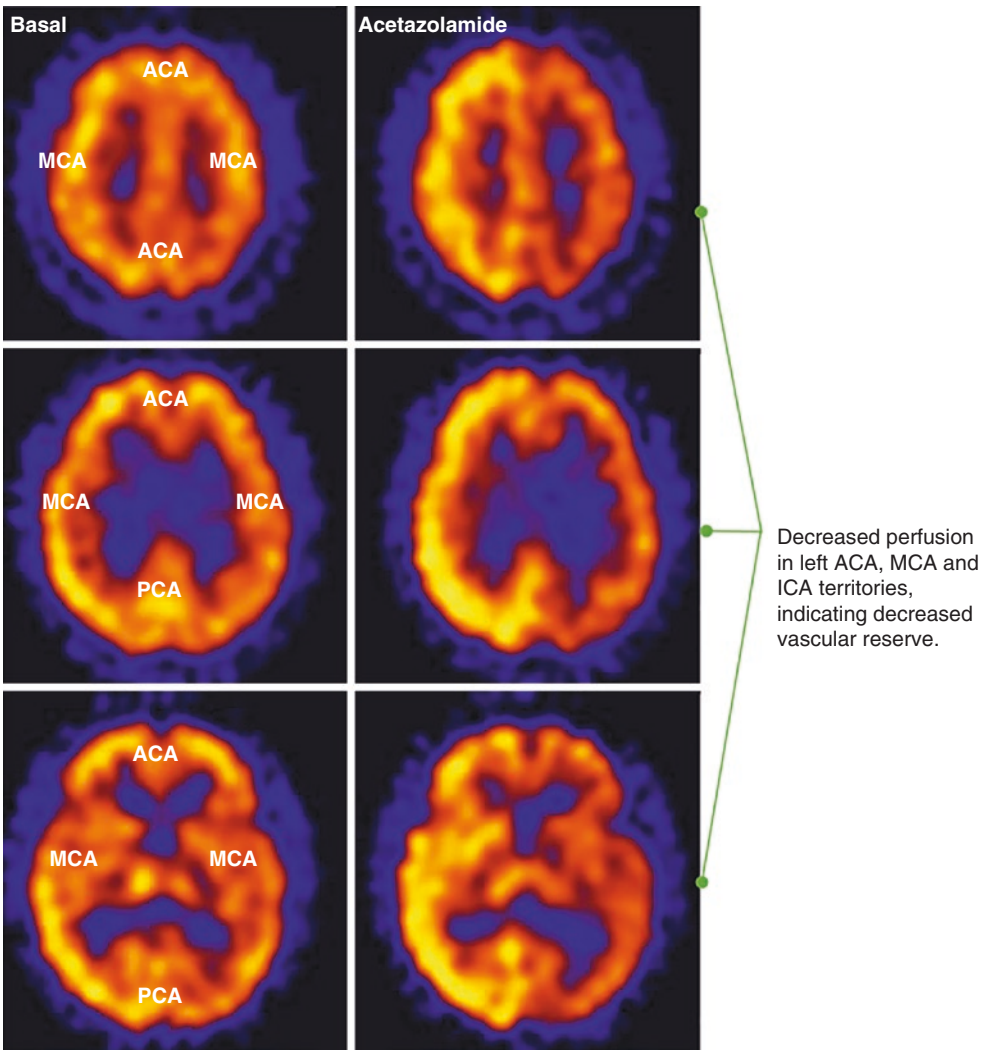

Fig. 96 ^{99m}Tc-HMPAO brain perfusion SPECT

Acknowledgments *The authors gratefully acknowledge Dr. Dong Soo Lee and Dr. Keon Wook Kang for their contributions to this chapter as it appeared in the previous edition.*

References

1. Van den Wyngaert T, Elvas F, De Schepper S, Kennedy JA, Israel O. SPECT / CT - standing on the shoulders of giants, it is time to reach for the sky! J Nucl Med. 2020:jnumed.119.236943.
2. Kinclab V, Drozdová A, Vašina J, Panovský R, Kamínek M. Cadmium – zinc – telluride SPECT scanners – new perspectives in nuclear cardiology. Cor Vasa. 2015;57(3):214–8.
3. Alenazy AB, Wells RG, Ruddy TD. New solid-state cadmium-zinc-telluride technology for cardiac single photon emission computed tomographic myocardial perfusion imaging. Expert Rev Med Devices. 2017;14(3):213–22.
4. Garcia TR, Kivenson A, Malonson S, Kudrolli H. Enhanced molecular breast image quality through improved CZT detector performance. IEEE Nuclear Science Symposium and Medical Imaging Conference (NSS / MIC) 2014, pp 1–3.
5. Mariani G, Bruselli L, Kuwert T, Kim EE, Flotats A, Israel O, et al. A review of clinical uses of SPECT / CT. Eur J Nucl Med Mol Imaging. 2010;37(10):1959–85.
6. Roarke MC, Nguyen BD, Pockaj BA. Applications of SPECT / CT in nuclear radiology. AJR. 2008;191:W135–50.
7. Ichikawa H, Miwa K, Okuda K, Shibutani T, Kato T, Nagaki A, et al. Current state of bone scintigraphy protocols and practice in Japan. Asia Oceania J Nucl Med Biol. 2020;8(2):116–22.
8. Kapoor M, Kasi A. Octreotide scan. In: StatPearls [Internet]. Treasure Island: StatPearls Publishing; 2021. 2021 Jan–. PMID: 32644756.
9. Donohoe KJ, Aloff J, Avram AM, Bennet KG, Giovanella L, Greenspan B. Appropriate use criteria for nuclear medicine in the evaluation and treatment of differentiated thyroid cancer. J Nucl Med. 2020;61(3):375–96.
10. Gandhi SJ, Babu S, Subramanyam P, Shanmuga Sundaram P. Tc-99m macro aggregated albumin scintigraphy - indications other than pulmonary embolism: a pictorial essay. Indian J Nucl Med. 2013;28(3):152–62.
11. Garin E, Rolland Y, Boucher E, Ardisson V, Laffont S, Boudjema K, et al. First experience of hepatic radioembolization using microspheres labelled with yttrium-90 (TheraSphere): practical aspects concerning its implementation. Eur J Nucl Med Mol Imaging. 2010;37(3):453–61.
12. Ahn BC. Macroaggregated albumin (MAA) injected in hepatic artery visualized in a recanalized paraumbilical vein. Clin Nucl Med. 2012;37(9):874.
13. Gulec SA, Mesoloras G, Dezarn WA, McNeillie P, Kennedy AS. Safety and efficacy of Y-90 microsphere treatment in patients with primary and metastatic liver cancer: the tumor selectivity of the treatment as a function of tumor to liver flow ratio. J Transl Med. 2007;5:15.
14. Panzuto F, Boninsegna L, Fazio N, Campana D, Pia Brizzi M, Capurso G, et al. Metastatic and locally advanced pancreatic endocrine carcinomas: analysis of factors associated with disease progression. J Clin Oncol. 2011;29(17):2372–7.
15. Berglund AS, Hulthen UL, Manheim P, Thorsson O, Wollmer P, Tornquist C. Metaiodobenzylguanidine (MIBG) scintigraphy and computed tomography (CT) in clinical practice. Primary and secondary evaluation for localization of pheochromocytomas. J Intern Med. 2001;249(3):247–51.
16. Lebtahi R, Le Cloirec J, Houzard C, Daou D, Sobhani I, Sassolas G, et al. Detection of neuroendocrine tumors: 99mTc-P829 scintigraphy compared with 111In-pentetreotide scintigraphy. J Nucl Med. 2002;43(7):889–95.
17. Zini L, Porpiglia F, Fassnacht M. Contemporary management of adrenocortical carcinoma. Eur Urol. 2011;60(5):1055–65.
18. Rufini V, Calcagni ML, Baum RP. Imaging of neuroendocrine tumors. Semin Nucl Med. 2006;36(3):228–47.
19. Bushnell DL, Baum RP. Standard imaging techniques for neuroendocrine tumors. Endocrinol Metab Clin N Am. 2011;40(1):153–62, ix.
20. Bombardieri E, Ambrosini V, Aktolun C, Baum RP, Bischof-Delaloye A, Del Vecchio S, et al. 111In-pentetreotide scintigraphy: procedure guidelines for tumour imaging. Eur J Nucl Med Mol Imaging. 2010;37(7):1441–8.
21. Pepe G, Moncayo R, Bombardieri E, Chiti A. Somatostatin receptor SPECT. Eur J Nucl Med Mol Imaging. 2012;39(Suppl 1):S41–51.
22. Ilias I, Divgi C, Pacak K. Current role of metaiodobenzylguanidine in the diagnosis of pheochromocytoma and medullary thyroid cancer. Semin Nucl Med. 2011;41(5):364–8.
23. van der Harst E, de Herder WW, Bruining HA, Bonjer HJ, de Krijger RR, Lamberts SW, et al. [(123)I]metaiodobenzylguanidine and [(111)In]octreotide uptake in benign and malignant pheochromocytomas. J Clin Endocrinol Metab. 2001;86(2):685–93.
24. Bombardieri E, Giammarile F, Aktolun C, Baum RP, Bischof Delaloye A, Maffioli L, et al. 131I/123I-metaiodobenzylguanidine (mIBG) scintigraphy: procedure guidelines for tumour imaging. Eur J Nucl Med Mol Imaging. 2010;37(12):2436–46.
25. Perri M, Erba P, Volterrani D, Lazzeri E, Boni G, Grosso M, et al. Octreo-SPECT/CT imaging for accurate detection and localization of suspected neuroendocrine tumors. Q J Nucl Med Mol Imaging. 2008;52(4):323–33.
26. Wong KK, Wynn EA, Myles J, Ackermann RJ, Frey KA, Avram AM. Comparison of single time-point [111-In] pentetreotide SPECT/CT with dual time-point imaging of neuroendocrine tumors. Clin Nucl Med. 2011;36(1):25–31.
27. Klimstra DS, Modlin IR, Coppola D, Lloyd RV, Suster S. The pathologic classification of neuroendocrine tumors: a review of nomenclature, grading, and staging systems. Pancreas. 2010;39(6):707–12.
28. Oberg K, Castellano D. Current knowledge on diagnosis and staging of neuroendocrine tumors. Cancer Metastasis Rev. 2011;30(Suppl 1):3–7.
29. Rufini V, Treglia G, Castaldi P, Perotti G, Calcagni ML, Corsello SM, et al. Comparison of 123I-MIBG SPECT-CT and 18F-DOPA PET-CT in the evaluation of patients with known or suspected recurrent paraganglioma. Nucl Med Commun. 2011;32(7):575–82.
30. Maroun J, Kocha W, Kvols L, Bjarnason G, Chen E, Germond C, et al. Guidelines for the diagnosis and management of carcinoid tumours. Part 1: the gastrointestinal tract. A statement from a Canadian National Carcinoid Expert Group. Curr Oncol. 2006;13(2):67–76.
31. Modlin IM, Oberg K, Chung DC, Jensen RT, de Herder WW, Thakker RV, et al. Gastroenteropancreatic neuroendocrine tumours. Lancet Oncol. 2008;9(1):61–72.
32. Gustafsson BI, Kidd M, Chan A, Malfertheiner MV, Modlin IM. Bronchopulmonary neuroendocrine tumors. Cancer. 2008;113(1):5–21.
33. Tan EH, Tan CH. Imaging of gastroenteropancreatic neuroendocrine tumors. World J Clin Oncol. 2011;2(1):28–43.
34. Kaemmerer D, Posorski N, von Eggeling F, Ernst G, Horsch D, Baum RP, et al. The search for the primary tumor in metastasized gastroenteropancreatic neuroendocrine neoplasm. Clin Exp Metastasis. 2014;31(7):817–27.
35. Elaini AB, Shetty SK, Chapman VM, Sahani DV, Boland GW, Sweeney AT, et al. Improved detection and characterization of adrenal disease with PET-CT. Radiographics. 2007;27(3):755–67.

36. McNicol AM. Update on tumours of the adrenal cortex, pheochromocytoma and extra-adrenal paraganglioma. Histopathology. 2011;58(2):155–68.
37. Jeong SY, Lee SW, Kim HW, Song BI, Ahn BC, Lee J. Clinical applications of SPECT/CT after first I-131 ablation in patients with differentiated thyroid cancer. Clin Endocrinol. 2014;81(3):445–51.
38. Yamamoto Y, Nishiyama Y, Monden T, Matsumura Y, Satoh K, Ohkawa M. Clinical usefulness of fusion of 131I SPECT and CT images in patients with differentiated thyroid carcinoma. J Nucl Med. 2003;44(12):1905–10.
39. Griggs WS, Divgi C. Radioiodine imaging and treatment in thyroid disorders. Neuroimaging Clin N Am. 2008;18(3):505–15.
40. Gayed IW, Kim EE, Broussard WF, Evans D, Lee J, Broemeling LD, et al. The value of 99mTc-sestamibi SPECT/CT over conventional SPECT in the evaluation of parathyroid adenomas or hyperplasia. J Nucl Med. 2005;46(2):248–52.
41. Im HJ, Lee IK, Paeng JC, Lee KE, Cheon GJ, Kang KW, et al. Functional evaluation of parathyroid adenoma using 99mTc-MIBI parathyroid SPECT/CT: correlation with functional markers and disease severity. Nucl Med Commun. 2014;35(6):649–54.
42. Mariani G, Gulec SA, Rubello D, Boni G, Puccini M, Pelizzo MR, et al. Preoperative localization and radioguided parathyroid surgery. J Nucl Med. 2003;44(9):1443–58.
43. Qureshi NR, Gleeson FV. Imaging of pleural disease. Clin Chest Med. 2006;27(2):193–213.
44. Sugarbaker DJ, Wolf AS. Surgery for malignant pleural mesothelioma. Expert Rev Respir Med. 2010;4(3):363–72.
45. Kendi AT, Kara S, Altinok D, Keskil S. Sinonasal ossifying fibroma with fluid-fluid levels on MR images. AJNR Am J Neuroradiol. 2003;24(8):1639–41.
46. Even-Sapir E, Metser U, Mishani E, Lievshitz G, Lehman H, Leibovitch I. The detection of bone metastases in patients with high-risk prostate cancer: 99mTc-MDP planar bone scintigraphy, single- and multi-field-of-view SPECT, 18F-fluoride PET, and 18F-fluoride PET/CT. J Nucl Med. 2006;47(2):287–97.
47. Maris JM, Hogarty MD, Bagatell R, Cohn SL. Neuroblastoma. Lancet. 2007;369(9579):2106–20.
48. Fish JD, Grupp SA. Stem cell transplantation for neuroblastoma. Bone Marrow Transplant. 2008;41(2):159–65.
49. Wertman M, Milgrom C, Agar G, Milgrom Y, Yalom N, Finestone AS. Comparison of knee SPECT and MRI in evaluating meniscus injuries in soldiers. Isr Med Assoc J. 2014;16(11):703–6.
50. Palestro CJ, Love C, Schneider R. The evolution of nuclear medicine and the musculoskeletal system. Radiol Clin N Am. 2009;47(3):505–32.
51. Van der Wall H, Lee A, Magee M, Frater C, Wijesinghe H, Kannangara S. Radionuclide bone scintigraphy in sports injuries. Semin Nucl Med. 2010;40(1):16–30.
52. Grant FD, Fahey FH, Packard AB, Davis RT, Alavi A, Treves ST. Skeletal PET with 18F-fluoride: applying new technology to an old tracer. J Nucl Med. 2008;49(1):68–78.
53. Huellner MW, Strobel K. Clinical applications of SPECT/CT in imaging the extremities. Eur J Nucl Med Mol Imaging. 2014;41(Suppl 1):S50–8.
54. Ryan PJ, Evans PA, Gibson T, Fogelman I. Chronic low back pain: comparison of bone SPECT with radiography and CT. Radiology. 1992;182(3):849–54.
55. DiGiovanni CW, Patel A, Calfee R, Nickisch F. Osteonecrosis in the foot. J Am Acad Orthop Surg. 2007;15(4):208–17.
56. Bentley DE, Richardson JD. The role of tagged red blood cell imaging in the localization of gastrointestinal bleeding. Arch Surg. 1991;126(7):821–4.
57. Howarth DM. The role of nuclear medicine in the detection of acute gastrointestinal bleeding. Semin Nucl Med. 2006;36(2):133–46.
58. Leder KS, Barlam TF. A case of paraspinal abscess and discitis due to Peptostreptococcus micros. Clin Infect Dis. 2000;30(3):622–3.
59. Ibrahim NA, Fadeyibi IO. Ectopic thyroid: etiology, pathology and management. Hormones (Athens). 2011;10(4):261–9.
60. Marmarou A, Young HF, Aygok GA. Estimated incidence of normal pressure hydrocephalus and shunt outcome in patients residing in assisted-living and extended-care facilities. Neurosurg Focus. 2007;22(4):E1.
61. Joffe HV, Goldhaber SZ. Upper-extremity deep vein thrombosis. Circulation. 2002;106(14):1874–80.
62. Leijte JA, Valdes Olmos RA, Nieweg OE, Horenblas S. Anatomical mapping of lymphatic drainage in penile carcinoma with SPECT-CT: implications for the extent of inguinal lymph node dissection. Eur Urol. 2008;54(4):885–90.
63. Sondak VK, King DW, Zager JS, Schneebaum S, Kim J, Leong SP, et al. Combined analysis of phase III trials evaluating [(99)mTc] tilmanocept and vital blue dye for identification of sentinel lymph nodes in clinically node-negative cutaneous melanoma. Ann Surg Oncol. 2013;20(2):680–8.
64. Hartman TE. Radiologic evaluation of the solitary pulmonary nodule. Radiol Clin N Am. 2005;43(3):459–65.
65. Kligerman SJ, Groshong S, Brown KK, Lynch DA. Nonspecific interstitial pneumonia: radiologic, clinical, and pathologic considerations. Radiographics. 2009;29(1):73–87.
66. Kim SH, Lee JM, Han JK, Lee JY, Kim KW, Cho KC, et al. Intrapancreatic accessory spleen: findings on MR imaging, CT, US and scintigraphy, and the pathologic analysis. Korean J Radiol. 2008;9(2):162–74.
67. Li W, Uppal D, Wang YC, et al. Nuclear imaging for the diagnosis of cardiac amyloidosis in 2021. Diagnostics (Basel). 2021;11(6):996.
68. Wong TH, Shagera QA, Ryoo HG, Ha S, Lee DS. Basal and acetazolamide brain perfusion SPECT in internal carotid artery stenosis. Nucl Med Mol Imaging. 2020;54(1):9–27.

Index

E. E. Kim et al. (eds.), *Atlas and Anatomy of PET/MRI, PET/CT and SPECT/CT*, https://doi.org/10.1007/978-3-030-92349-5